Optimization of the Performance of Micro Hydro-Turbines for Electricity Generation

Saeed Rajab Yassen

Ph.D

2014

Optimization of the Performance of Micro Hydro-Turbines for Electricity Generation

Saeed Rajab Yassen

A thesis submitted in partial fulfilment
of the requirements of the University of Hertfordshire
for the degree of Doctor of Philosophy

The programme of research was carried out in the School of Engineering & Technology, University of Hertfordshire, Hatfield, UK

May 2014

Abstract

Rural electrification has long been the most important topic on the development agenda of many countries. The needs for power supplies to rural areas increased significantly in the past decades. Extending electricity grids to rural areas is of a very high initial cost and is not viable economically. Micro hydroelectric power plants provide a good economical solution, which is also environmentally very friendly. The current study concentrates on selecting and optimizing a suitable cross-flow micro-turbine to be used in micro hydroelectric power plants. Cross-flow turbines are in general of simple structure, low cost, easy to fabricate and of modest efficiency. The main purpose of the present work is to optimize the performance of a selected turbine by establishing the optimal turbine's design parameters. A complete analysis of the internal flow, which is of turbulent, two-phase and three dimensional in nature, was undertaken by simulating it using various CFD simulation codes. This study reports on the flow simulation using ANSYS CFX with a two-phase flow model, water-air free surface model and shear stress transport (SST) turbulence model. Prediction velocity and pressure fields of inside the turbine are, subsequently, used to characterize the turbine performance for different geometric parameters including the number of runner blades, the angle of attack, the ratio of inner to outer diameter, the nozzle profile, the blade profile, the nozzle throat width, the nozzle to runner blades width and the runner blades width to outer runner diameter. The results revealed the highly complex nature of the flow and provided a very good insight to the flow structure and performance optimization parameters.

Acknowledgement

At first, thanks to **Almighty God** for enabling me to complete this work. I owe my deepest thanks to my principal supervisor **Dr. Nasser** for his dedication, guidance and support throughout the preparation of this work.

I would like to express my deepest appreciation to **Dr. Soorkeu A. Atrooshi** for his help and support. Cordial thanks are to my second supervisor **Dr. Byrne** for her assistance and support during my work. Also, my thanks to **Mrs. Lorraine Nicholls** and **Mrs. Avis Cowley** of the administrative office at the Science Technology and Research Center for their continuous help.

This work was supported by the Ministry of Higher Education and Scientific Research, Kurdistan Regional Government.

Finally, I wish to address my love and gratitude to my **family** for their unconditional help and support throughout my educational endeavours.

List of Contents

3 Theoretical Analysis

4 Numerical Modelling and Techniques in CFX

5 Results of Performance Improvement/Optimization and Discussion

List of Figures

List of Tables

Nomenclature

Symbol/s		Units
a	Acceleration	[m/s^2]
c	Nozzle coefficient	
c_j	Nozzle jet coefficient	
d	Diameter of the runner	[m]
g	Gravitational acceleration	[m/s^2]
$\dot{m}$	Mass flow rate	[kg/s]
n_b	Number of blades	
p	Pressure	[Pa]
r	Radius of the runner	[m]
r_b	Radius of blade curvature	[m]
s	Thickness of the jet	[m]
t	Blade spacing	[m]
u	Peripheral velocity	[m/s]
V	Absolute velocity	[m/s]
$\vec{v}$	Velocity vector of flow	[m/s]
B_w	Runner blades length	[m]
F	Force	[N]
H	Net head	[m]
M	Total amount of some properties (mass, energy, momentum)	
N	Rotational speed	[r.p.m]
P	Power	[Watt]
Q	Volume flow rate	[m^3/s]
T	Torque	[N.m]
v_r	Relative velocity	[m/s]

Greek

α	Angle of the absolute velocity	[rad]
β	Angle of the relative velocity	[rad]
γ	Specific weight of water	[N/m^3]
λ	Nozzle entry arc	[rad]
ψ	Loss coefficient	
ρ	Density	[kg/m^3]
ξ	Total amount of properties per unit mass	
η	Efficiency	
ω	Angular velocity	[rad/s]

Superscripts

'	Inner rim of the runner
$\cdot$	Time rate
$\rightarrow$	vector

Subscripts

1	Inlet of the first stage
2	Outlet of the second stage
1'	Inlet of the second stage
2'	Outlet of the first stage
1_2'	First stage
1'_2	Second stage
b	Blade
i	Input
o	Output
max	Maximum
r	Relative

Other symbols which are not listed above are defined at their occurrence in the text.

Chapter One

Introduction

Chapter One

Introduction

1.1 General Introduction

Micro hydroelectric power plants are a solution to power needs of rural and remote communities, which are not connected to the national electricity grid. In many countries, the needs for power supplies to rural areas increased significantly in the past decades. Extending electricity grids to rural areas faces very high costs. Micro hydroelectric power plants often provide an economically alternative to the grid electricity [1]. Therefore, a cross-flow turbine is proposed for micro hydroelectric power plants in this study due to its simple structure, low cost of investment and modest efficiency. A classical cross-flow turbine comprises of a cylindrical-shaped runner consisting of two parallel circular discs connected together at the perimeter with a series of curved horizontal blades. The nozzle, which has a rectangular cross-sectional area, directs the water to the full length of the runner at a specified angle of attack [2].

The site characteristics, such as the available flow rate and head, are the determinant factors in the selection of a suitable turbine. Hence, a cross-flow turbine is common and often proposed for micro hydroelectric power plants due

to its modest efficiency at part-flow conditions which may be encountered during summer season in some sites [3, 4].

A cross-flow turbine is known to be of a wide operating flow range with a good efficiency through the whole flow range. This is possible because a cross-flow turbine is designed with two inlet guide-vanes. The standard division of the inlet guide-vanes flow area is 1:2. This means that the water, during lower flow periods, can be directed through either one-third or two-thirds of the runner, thereby sustaining relatively good turbine efficiency [5, 6].

1.2 History of Hydro Power Technology

Hydropower is a renewable, clean and eco-friendly source of power generation. Hydropower is power that is derived from moving water through a turbine; the turbine turns a generator, which produces electricity. Water has been utilized as an energy source for a long time. Water energy is probably the oldest renewable energy technique utilized by human beings for mechanical energy conversion as well as electricity generation [7]. Waterwheels were utilized extensively in the ancient times, but the use of hydropower got popularized only with the invention of the water turbines at the beginning of the 19th century [8].

Originally, small scale hydro power plants were built beside waterfalls and near towns because there was not enough progress in electricity transmission means as the generated electricity cannot be sent over great distance. In the late 19th century, water energy was used to generate electricity on a large scale. The first hydroelectric power plant was installed at Niagara Falls in 1879 [9]. Some years later, many more hydroelectric power plants were installed. With the

development of technology, and the growth in energy consumption, the need of electricity generation was moved to large scale hydroelectric power plants. Such plants have been installed around the world near large rivers and dams. Large scale hydroelectric power plants require large dams such as the Hoover dam and Grand Coulee dam [10].

Over the last few decades, due to environmental concerns and sharp increase in petroleum prices, it becomes necessary to utilize the available renewable energy sources. Currently, hydropower is the biggest contributor to electricity generation from renewable energy sources [11]. Large scale hydroelectric power plants are already installed. However, it remains to harness the small scale hydro power resources. Micro hydroelectric power plants are usually installed in places where streams or small rivers can be harnessed for electric power generation. All over the world, only a little portion of the available energy in streams and small rivers is utilized for electricity generation [12].

1.3 Hydroelectric Power Plants Classification

Hydroelectric power plants are commonly classified according to their capacity, and there is no uniform standard classification criterion for hydroelectric power plants. Different countries are adopting different criteria; mainly, because of different countries have different development policies. Some countries like Portugal, Ireland, Spain, Greece and Belgium, accept 10 MW as the upper limit for an installed capacity of small hydroelectric power plants. In Italy, the limit is fixed at 3 MW (plants with larger installed power should sell their electricity at lower prices) and in Sweden 1.5 MW. In France, the limit was established at 12 MW and in the UK, 20 MW is generally accepted as the threshold for small

hydroelectric power plants [8]. The current study will concentrate mainly at micro hydro turbine, which is generally defined as an installed capacity of 100 kW or less.

Although different countries adopt different criteria, the classification of hydroelectric power plants, based on installed capacity, is shown in table 1.1.

Table 1.1 Typical hydroelectric power classification by generating capacity [13].

Type	Capacity
▪ Pico-hydropower	< 500 W
▪ Micro-hydropower	0.5 – 100 kW
▪ Mini-hydropower	100 – 1000 kW
▪ Small-hydropower	1 MW – 10 MW
▪ Full scale (large) hydropower	> 10MW

Based on the available head the classification of hydropower plants is shown in the table 1.2. These head ranges are not strict but are simply means of classification hydroelectric power plants.

Table 1.2 Typical hydroelectric power classification according to the head [14].

Type	Head range
▪ High head plants	Above 100 meters
▪ Medium head plants	30 to 100 meters
▪ Lowe head plants	Less than 30 meters

1.4 Environmental Impact

Hydropower is a renewable, clean and eco-friendly benign source of power generation. Micro hydroelectric power plants do not generate pollutants during the operation, such as carbon dioxide, sulphur dioxide, nitrous oxides or any other type of air emissions and no solid or liquid waste's production. However, they can have undesirable local environmental impacts, such as aquatic organisms' injury and mortality from passage through turbines, visual impact due to buildings, penstocks and small weirs, and have little other impacts on the atmosphere, the noise pollution [15].

As table 1.3 shows a hydroelectric power plant does not generate any oxide, especially carbon dioxide, which is main gas responsible for global warming. Hydroelectric power plants use (not consume) the water to operate the turbines, the water returns back into the stream after passing through the turbines. Micro hydroelectric power plants may not require a small reservoir if not necessary in order to power the turbines. These micro hydroelectric power plants are commonly known as run-of-river, which have a minimal local environmental impact [16].

Table 1.3 Comparative emissions from a small hydropower plant of 1000 MW, working 4500 hours/years and other sources of production of electricity [17].

	Petroleum (tons)	Coal (tons)	Natural (tons)	Hydropower
Carbon dioxide	3000	3750	2250	0
Nitrogen oxide	3.7	0.6	2.2	0
Sulphur dioxide	4.5	4.5	0.02	0

Hydropower is the most common, reliable and cost effective source of renewable energy. Even with the recent expansion of the other types of the renewable energy sources such as solar, wind and biomass, hydropower is still the largest source of renewable energy in the electricity generation in the world, as shown in the table 1.4. As a result, it is obvious that from an environmental point of view, micro hydroelectric power plants are welcome in today's world as they generate clean energy.

Table 1.4 Electricity generations from renewable energy [18].

Method of power generation	Proportion of renewable
Large hydro (>10 MW)	86 %
Small hydro (<10 MW)	8.3 %
Wind and Solar	0.6 %
Geothermal	1.6 %
Biomass	3.5 %

1.5 Components of Micro Hydroelectric Power Plants

The following information provides an overview of the two major components of a typical micro hydroelectric power plant the electro mechanical equipment and civil works. The main electro mechanical components are installed in the power house. The main civil works are illustrated by Fig.1.1, and comprise of a weir, which is used to divert a portion of water flow from the stream through an opening in the stream side called intake into an open canal. This is to channel the water from the weir to a settling basin, which is used to remove the silt from the water. A canal is used to direct the water to a forebay reservoir or tank. The major function for the forebay tank is to remove the last silt from the water

before the water enters the penstock. If the tank is at relatively large capacity, it can also be utilized as storage for water (In micro hydroelectric power plants the settling basin and forebay tank can be provided separately or combined) [19]. A closed pipe known as penstock directs the water from the forebay tank to a turbine at a lower level. Finally, the water via a tailrace flows back into the stream. The turbine extracts the water energy and converts it to mechanical energy to operate an electricity generator. Finally, and within the powerhouse, where the electricity generator is located, the generated electricity is transferred to a transformer which is then transmitted and distributed to the consumers.

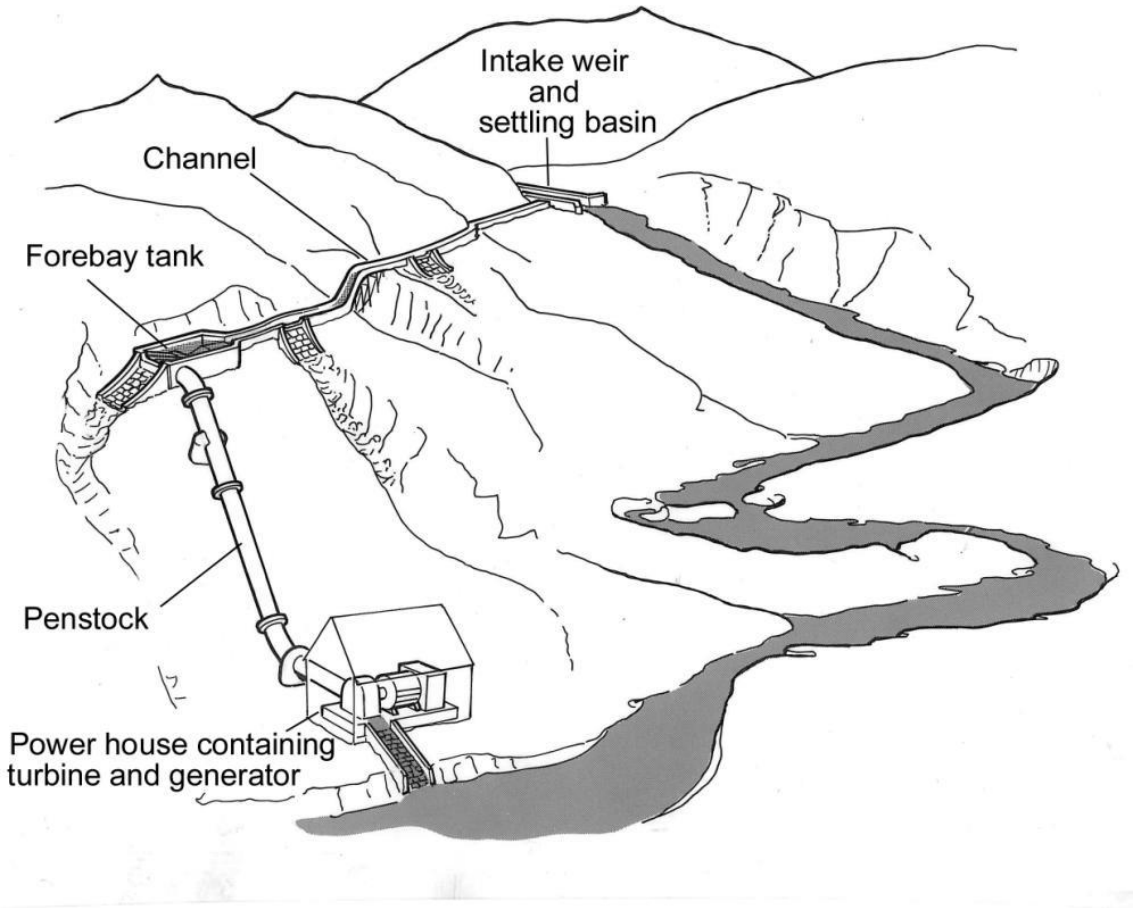

Fig. 1.1 Components of a micro-hydro scheme [20].

1.6 Advantages and Limitations of Micro Hydroelectric Power Plants

1.6.1 Advantages of Micro Hydroelectric Power Plants

Micro hydroelectric power plants have many advantages as they are reliable, effective and a clean energy source. The main advantages of micro hydropower plants may be summarized as follows:

1. A micro hydroelectric power plant has a long lifetime and it is a simple technology. It may require small hydraulic structures and a short construction period. It can be built by local staff and locally available materials.
2. It requires little or no maintenance (breakdown relatively is rare), low operating costs (compared with other technologies) and no fuel cost involved; it uses (not consume) water.
3. It is a renewable, clean and eco-friendly benign source of power generation. It does not emit pollutants as a result of electricity generation.
4. It is a reliable renewable energy source. It has the ability to run 24 hours a day continuously and the ability to be started and stopped fairly quickly. It can meet power demand due to its flexible operation and predictable power generation.
5. Micro hydroelectric power plant contributes to sustainable development in rural communities. The decentralization of micro hydroelectric power plant reduces the transmission losses and supports the national economy.

1.6.2 Limitations of Micro Hydroelectric Power Plants

Micro hydroelectric power plants have a few limitations, which may be summarized as follows:

1. A micro hydroelectric power plant is only suitable for a site which is well suited to utilize the power and water is also located close to consumers. Such a site is usually away from the central electricity distribution grid so a long transmission line is required. Long transmission line causes losses of power and also substantially increases the capital expenditure.
2. The maximum power generation by micro hydroelectric power plant is mainly dependent on the site, which in turn limits the level of expansion as the power demand increases.
3. Seasonal variation of the flow in a stream can substantially limit the maximum power generation. It is sensitive to the climate as during the summer season the power generation declined due to the drop in the level of water in a stream.
4. The environmental impact of micro hydroelectric power plants is minimal. Micro hydroelectric power plants "do not" generate pollutants during the operation, however, they can have undesirable local environmental impacts, such as aquatic organisms' injury and mortality, visual impact due to buildings, penstocks and small weirs. Also the plants may have little other impacts on the atmosphere, including noise pollution.

1.7 Types of Turbines Used in Micro Hydroelectric Power Plants

The turbine is the most important piece of equipment in a micro hydroelectric power plant. It is used to extract energy from the flowing water and convert it into mechanical work. The basic classification of the turbines is largely determined by their suitability for the available heads of water, as shown in the table 1.5. The site characteristics of a micro hydroelectric power plant location are critical factors in the selection of the suitable turbine. Therefore, a cross-flow turbine is commonly proposed for micro hydroelectric power plants due to its modest efficiency at part-flow conditions, which may be encountered during the summer season in some locations (The level of water fluctuates according to the amount of regional rainfall).

The energy of the flowing water is extracted and converted into mechanical work in the turbine, by one of two fundamental mechanisms: one mechanism is an impulse principle, which extracts the kinetic energy of water in the form of jet which strikes the blades or buckets on the periphery of the runner and converts it into mechanical work. The second mechanism is a reaction principle, which extracts the potential energy and the kinetic energy of water in the form of pressure drop across the turbine and converts it into mechanical work [21]. Francis, Kaplan and Propeller turbines are the popular turbines that operate on a reaction principle.

Table 1.5 The classification of the turbine according to the mechanisms of the work [22].

Turbine Operation Principle	High Head	Medium Head	Low Head
Impulse Turbines	Pelton Turgo Multi-Jet Pelton	Cross-Flow/Banki Multi-Jet Pelton Turgo	Cross-Flow/Banki
Reaction Turbines		Francis	Propeller Kaplan

1.8 Propeller and Kaplan Turbines

Propeller turbines are axial-flow reaction turbines, where the water is directed by the guide vanes, and flows axially through the propeller (runner blades). These are designed from complex curves to extract the potential energy and the kinetic energy of the flowing water in the form of pressure drop across their surface. The runner of a propeller turbine is completely immersed in water. Propeller turbines are generally arranged to cover a wide range of application, especially high flow discharges and low heads conditions [23]. Kaplan turbine is a unique design of propeller turbine. It is named in honour of the Austrian professor Viktor Kaplan. It is generally designed with movable runner blades and may or may not have movable guide vanes [24]. The cost and complexity of Kaplan turbine are high. In additional, the part-flow efficiency of fixed blade propeller turbines is very low [25], which makes them unusual in micro hydroelectric power plant.

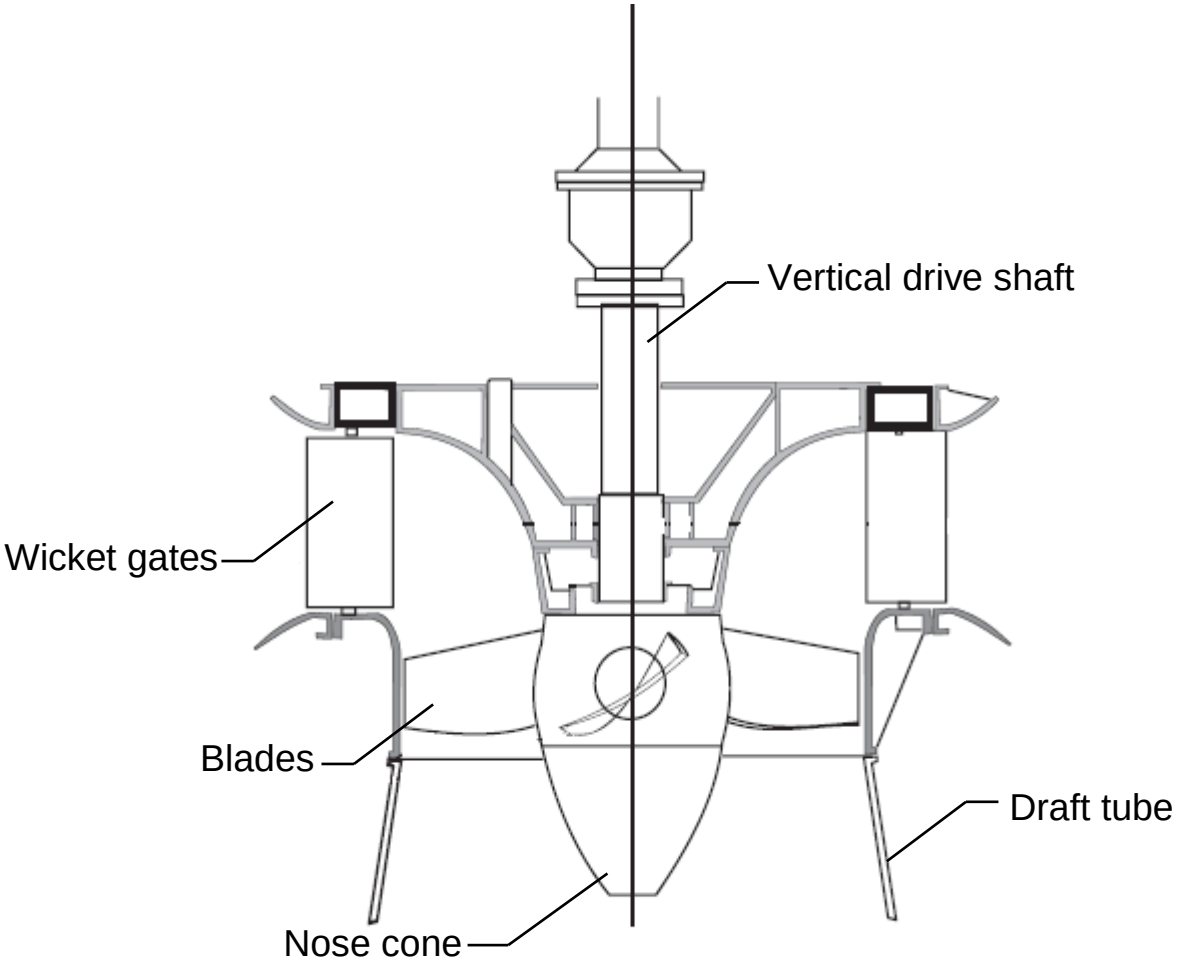

Fig. 1.2 Kaplan turbine [26].

1.9 Cross-Flow Turbine

The cross-flow turbine was first invented by an Australian engineer A. G. M. Mitchell, who got a patent for it in 1903. The turbine was based on the theory of Poncelet, a French engineer (1788-1867) who improved the classical horizontal-axis water wheel. Later, Donat Banki published a series of papers on the turbine between 1912 and 1919 in Germany. Banki specified that, the angle of attack should be as small as possible and based on this angle, he calculated the blade inner and outer angles, and the blade curvature. Thus cross-flow turbines became called as Banki-Mitchell turbines or simply, Banki turbines [27]. In 1920s, the Ossberger company in Weissenburg, Bavaria, Germany, acquired manufacturing rights and began mass-producing the turbine. As a result, cross-flow turbines became also called as Ossberger turbines [28]**.** Since then some development on a cross-flow turbine has been made in the world and have shown improved performances.

The widespread use of the cross-flow turbine in micro hydroelectric power plants is largely due to its simple structure, low cost of investment and modest efficiency. A classic cross-flow turbine comprises of a cylindrical-shaped runner consisting of two parallel circular disks connected together at the perimeter with a series of curved horizontal blades, and a nozzle, whose cross-sectional area is rectangular, directs the water flow to the full length of the runner at a specified angle of attack.

The cross-flow turbine is understood as a water turbine where the runner receives the water in a radial inward direction and discharges it in a substantially radial outward direction, the runner diameter is particularly

independent of the rate of flow, but the runner breadth can be dependent on the rate of flow.

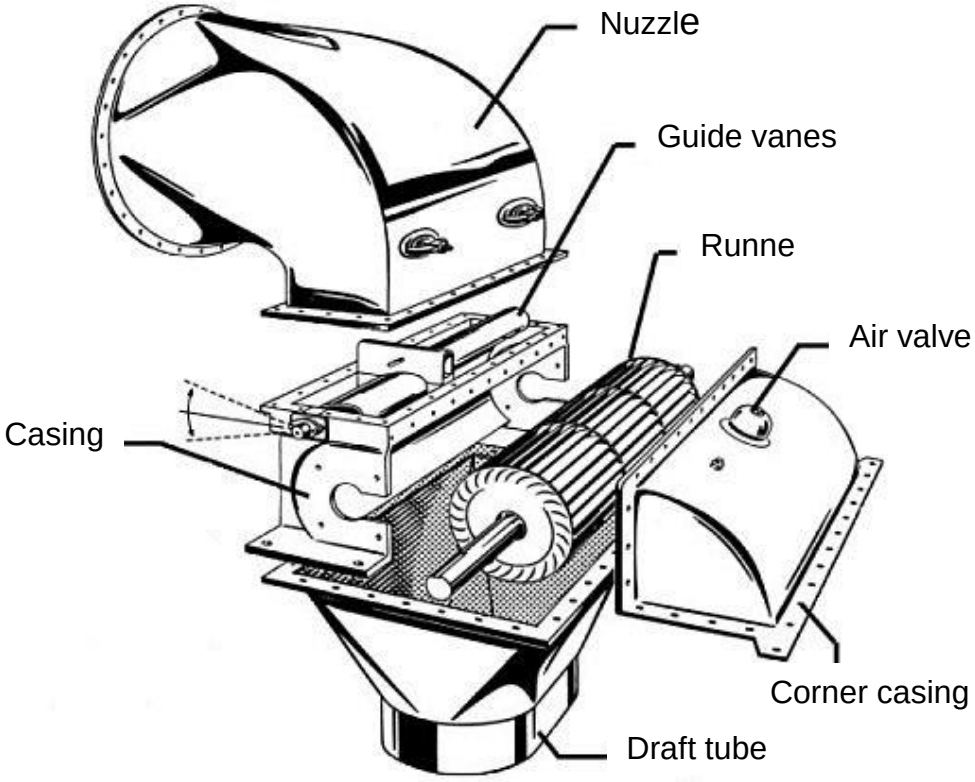

Fig. 1.3 Cross-flow turbine [29].

The advantages of partially loaded cross-flow turbine are shown diagrammatically in Fig. 1.4 along with the efficiency curve. A cross-flow turbine is known as a wide operating flow range with a good efficiency through the whole range. This is possible because a cross-flow turbine is designed with two inlet guide-vanes. The standard division of the inlet guide-vanes is 1:2. This means that the water, during lower flow periods, can be directed through either one-third or two-thirds of the runner, thereby sustaining relatively high turbine efficiency.

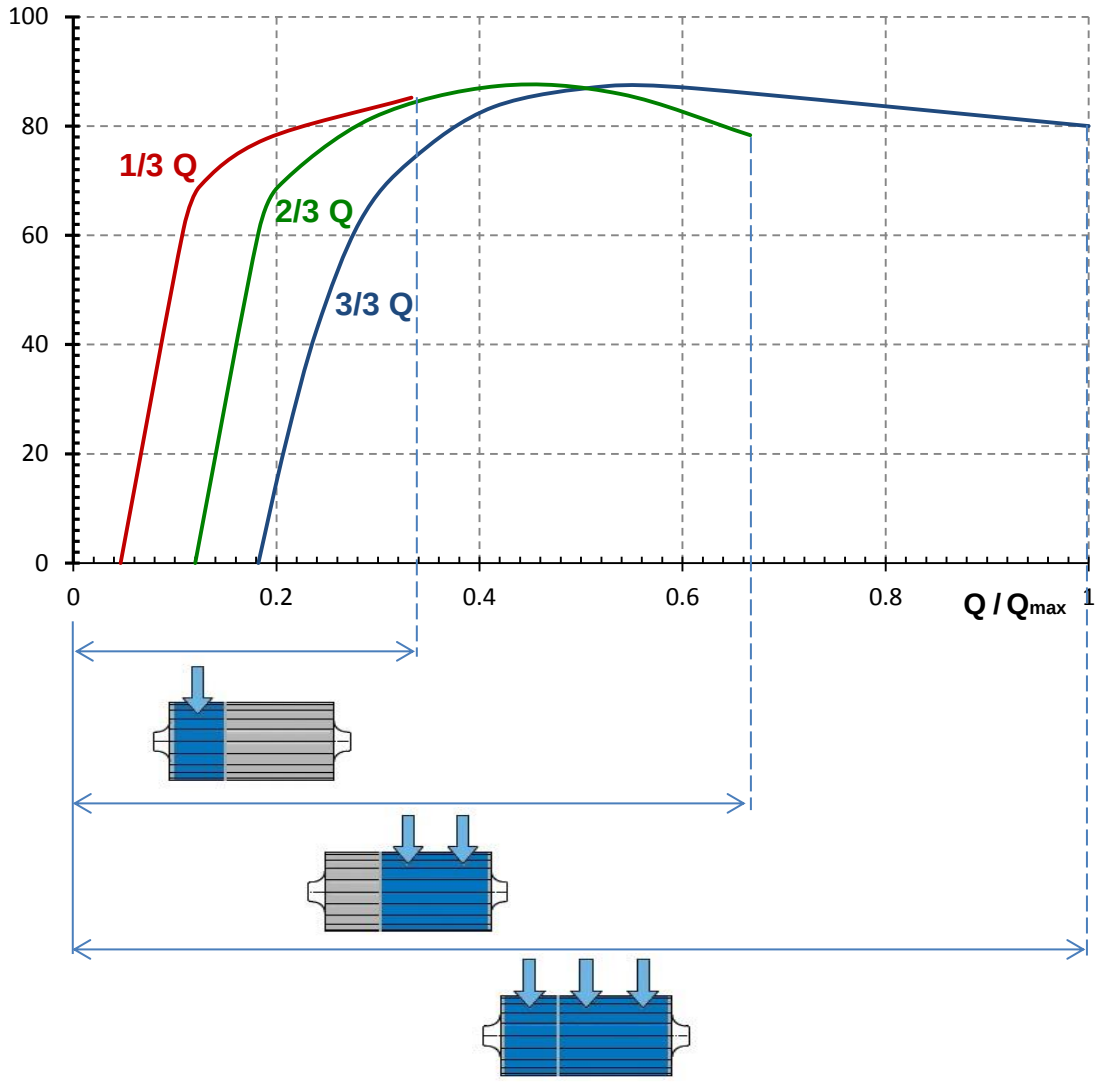

Fig. 1.4 Part-flow efficiency of a partitioned cross-flow turbine [30].

1.9.1 Principle of Operation of the Cross-Flow Turbine

The principle of operation of cross-flow turbine is illustrated in Fig. 1.5. The cross-flow operates as a rectangular jet of water is directed by the nozzle to strike the blades on the circumference of the runner. The water passes through two stages in cross-flow turbine so energy is extracted from water by the blades of the runner in two stages. The water flows over the blade first from the outside of the runner to its inside. Some of the flow is entrained between the blades and is called the uncrossed flow. The remaining water crosses the inside runner,

thus the term cross flow and strikes additional blades on the inner side of the perimeter, and discharges at the outer perimeter of the runner. The cross-flow turbine consists of the following parts:

1. Nozzle, which directs a rectangular jet of water to strike the blades on the rim of the runner at a small angle, almost converts the total flow energy into kinetic energy.
2. Runner, which is a cylindrical-shaped runner consisting of two parallel circular disks connected together at the perimeter with a series of curved horizontal blades, converts the energy of water into mechanical energy. Runners of large width have intermediate discs to support the blades.
3. Shaft, which passes through the center of the cross-flow turbine runner, transfers the torque to the generator.
4. Casing, which covers the runner and links the runner with the nozzle and draft tube, is usually fitted with an air valve when the turbine operates with a draft tube.
5. Draft tube, which is a new development on the cross-flow turbine, increases the effective head across the runner by recovering some of the remaining kinetic energy before leading the water into the river.
6. Guide vanes, which are movable vanes located just upstream of the runner inside the nozzle to control the flow of water to the runner, direct the flow into two passages, one on each side. The two passages cross-sectional areas decrease in the direction of flow to accelerate the flow. The standard division of the inlet guide-vanes is 1:2. This means that the water, during lower flow periods, can be directed through either one-third or two-thirds of

the runner, thereby sustaining relatively good turbine efficiency. A few cross-flow turbines are built without guide vane.

7. Air valve, which controls the vacuum pressure inside the turbine casing to utilize the energy of the water optimally, when a draft tube is used.

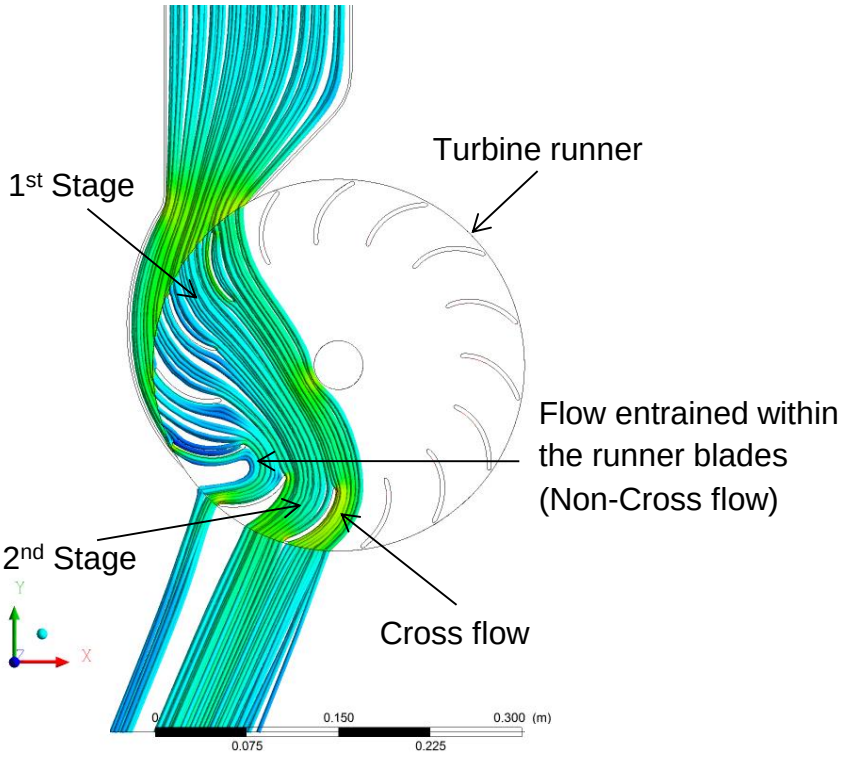

Fig. 1.5 Principle of operation of cross-flow.

1.9.2 Advantages of the Cross-Flow Turbine

The unique and inherent advantages of the cross-flow turbine may be summed up as follows:

1. The design and construction of the cross-flow turbine is easy due to its simple structure; the nozzle and runner discs can be fabricated of steel plate and the blades can be cut from a steel pipe.
2. The most valuable feature of the cross-flow turbine is the favorable shape of its efficiency curve, particularly with the use of divided guide vanes. This is particularly important for small run-of-river power plant.

3. It requires relatively limited maintenance (malfunctioning is rare), low operating costs (compared with other technologies) and no fuel cost; it uses (not consume) the water.
4. The cross-flow turbine is less cost than any other turbine used for micro hydroelectric power plants.
5. It has no effects on the environment.
6. The environmental effect of the cross-flow turbine on stream ecology is positive by increasing dissolved oxygen.
7. It is adaptable to draft tubes.
8. It is free from cavitation.
9. The cross-flow turbine installation requires simple civil works of low costs (initial low cost of investment).

1.10 Outline of the Thesis Structure

This thesis starts with an introduction to the thesis topic which followed by a comprehensive and critical review of the literature as detailed in Chapter 2.

A theoretical analysis of the geometrical parameters and other fundamental fluid mechanics principles were undertaken and detailed in Chapter 3.

Chapter 4 details the numerical techniques employed in the current study to develop the geometrical design and the necessary meshing process.

The results of the numerical simulation are presented in Chapter 5.

Chapter 6 presents the conclusions and recommendations for future studies.

1.11 Summary

In selecting an appropriate turbine design for micro hydroelectric power plants, it was taken into consideration that such turbine will be used by people who on average have moderate or little technical knowledge. Therefore, extra care was taken in the current study to avoid very complicated design structure, problematical maintenance, and difficult manufacturing process.

Chapter Two

Literature Review

Chapter Two

Literature Review

2.1 Introduction

In this chapter, the previous studies on the cross-flow turbine are presented. These are reviewed in a historical and chronological order to expose the development and the progress in this field. Theoretical and experimental studies have been undertaken to study, develop the cross-flow turbine and investigate of its feasibility for micro hydroelectric power plants. The first basic step was emerged by an Australian engineer named A. G. M. Mitchell, who got a patent for the cross-flow turbine in 1903. The turbine was based on the theory of Poncelet, a French engineer (1788-1867) who improved the classical horizontal-axis water wheel. Later, the Hungarian Prof. Donat Banki published a series of papers on the turbine between 1912 and 1919 in Germany. Thus cross-flow turbines became called as Banki-Mitchell turbines or simply, Banki turbines. In 1920s, the Ossberger company in Weissenburg, Bavaria, Germany, acquired manufacturing rights and began mass-producing the turbine. As a result, cross-flow turbines became also called as Ossberger turbines [28]. Since then some developments on a cross-flow turbine were undertaken and resulted in improved and higher turbine performances. The general features of such turbine are shown in Fig. 2.1.

The purpose of this chapter is to provide a comprehensive and critical review of the available literature in order to gain fundamental understanding of the cross-flow turbine operation and theory.

Geometrical parameters of cross-flow turbine

n_b	-	Runner's blades number
d_2/d_1	-	Runner's blades diameter ratio
α_1	-	Angle of attack
r_b	-	Blades curvature
λ	-	Nozzle entry arc
s_o	-	Nozzle throat width
N_w/B_w	-	Nozzle to runner blades width ratio
B_w/d_1	-	Runner blades width to outer diameter ratio

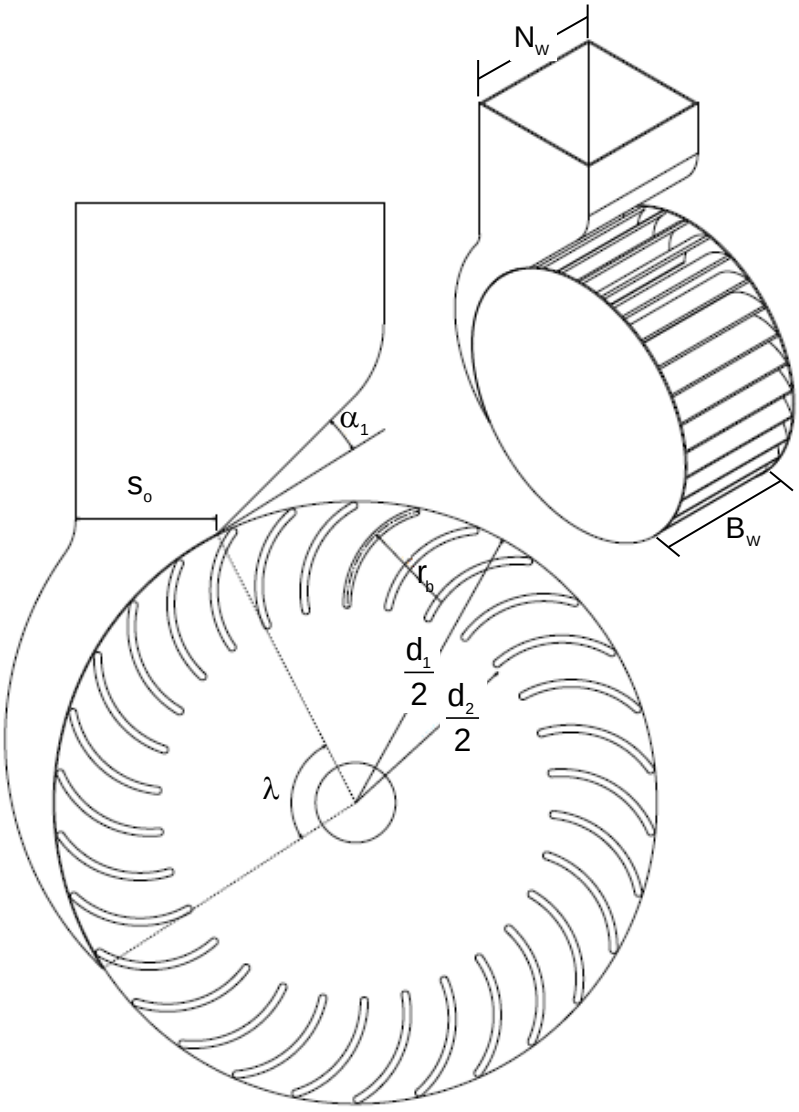

Fig. 2.1 General features of cross-flow turbine.

2.2 Literature Review

Mockmore and Merryfield [31] presented a translation of Donat Banki's paper "Neue Wasser-turbine" and conducted an experimental investigation on a laboratory turbine constructed according to the specification of Banki to study the performance of the Banki water turbine. The experimental study involved designing and manufacturing models of cross-flow turbines with variety of runner width and outer diameter. The ratio of inner to outer diameter was 0.66 and the angle of attack was 16^{o}. The blade inlet was 30^{o} while the blade outlet angle was 90^{o}. The number of blades was 20. Two Banki turbine nozzle shapes were used.

The results of the experiments indicated that the cross-flow turbine can be operated efficiently on a wide range of gate openings than most turbines. The maximum efficiency for all gate openings at constant head occurs at a practically constant speed, and finally, the effective width of the runner can be changed at various flow and electricity demands condition without changing the first stage angle of attack. The maximum efficiency recorded in this experiment was 68 %, which can be improved if efforts are concentrated on improving the performance of the turbine where estimated that 8 % of the total water never touched the runner. The detailed experimental set up and study of Mockmore and Merryfield make it one of the first and earliest comprehensive experimental studies on prototype cross-flow turbines. However, the analysis presented was rather basic and no suggestions were provided to reduce the losses of the estimated 8 % water losses that do not hit the runner.

Nakase et al [32] presented an experimental investigation to analyze the effect of nozzle shape on the cross-flow turbine performance. Three different types of nozzles were designed and manufactured to analyze their effects turbine performance. The runner outer diameter was 315 mm and the number of runner blades was 26. The angle of attack was 15^o and the nozzle entry arc was 30^o, 60^o, 90^o and 120^o. The blade inlet was 30^o while the blade outlet angle was 90^o and the ratio of inner to outer diameter was 0.68. The width of the runner and the nozzle was 315 mm and the discharge was 6.64 m^3/min at a head of 1.54 m.

This experiment resulted in an important conclusion that a cross-flow turbine cannot be treated completely as an impulse turbine. This was concluded as the flow has some pressure at the nozzle exit and the entire flow is not cross-flow where the water passes through two stages in a cross-flow turbine, is directed by the nozzle to strike the blades on the circumference of the runner. The water flows over the blade first from the outside of the runner to its inside. Some of the flow is entrained between the blades and is called the uncrossed flow. The remaining water crosses the inside runner, thus the term cross flow and strikes additional blades on the inner side of the perimeter, and discharges at the outer perimeter of the runner. A large portion of the flow is the cross flow which accelerated from the first stage to the second due to the flow contraction. They also concluded that decrease of pressure at nozzle exit is not always related to increase in maximum efficiency and finally, they concluded that the nozzle throat width ratio ($s_o/r_1\lambda$) changes slightly with the nozzle entry arc and 0.26 is the best value of nozzle throat width ratio ($s_o/r_1\lambda$), and the highest efficiency was obtained for 90^o. Nakase et al study proved that the treatment of the cross-flow turbine as an impulse turbine is incorrect. Although, their study was

predominantly experimental, no detailed theoretical analysis was presented to support this important conclusion.

Makansi, J. [33] investigated the effect of flow variation and low-head, high-flow situations on the performance of the cross-flow turbine. Makansi concluded that the cross-flow turbine has a flat efficiency over a wide range of operations. The cross-flow turbine improves flow utilization depending on the degrees of flow variation and continuously increases the power production at the site. The improved flow utilization is generally more important to a run-of-river site than to one with a dam. Makansi stated that, in low-head applications, the cost of the cross-flow turbine may be reduced from the use of plastics, since bending forces at low head applications are relatively small. Makansi also stated that, in high-flow, low-head situations, the cross-flow turbines require larger unit dimensions than other turbines, and because capacities are limited by the size of the runners, so multi-unit installations may be required to obtain performance equivalent to that of other turbines.

Chappell, J. R. [34] demonstrated the potential for reducing the cost of micro hydroelectric power plants. In low head applications, the cross-flow turbine can be manufactured of plastics, since fluid forces at such heads are relatively small. The use of standard plastic pipes or sheets in the manufacture of the cross-flow turbines can be considered cost-effective. Chappell estimated the capital cost savings of about 50 % for micro-hydro power plants. Chappell did not provide any data regarding the durability of the plastic turbines as compared to that of the normal ones. Also, no analysis was provided on the stresses associated with the operation of the normal or plastic turbines.

The magnitude of these forces and stresses were determined by ***Van Dixhorn et al [35].*** They conducted an experimental investigation to determine the magnitude of the fluid forces on the runner blades of the cross-flow turbine. The tangential and radial forces as well as the pitching moment were measured on a test runner blade. In addition, the pattern of blade loading was tested during a revolution over a non-dimensional speed range of 0.35 to 1.10 and a head of 1 to 2.6 m. In these experiments, the runner outer diameter was 0.277 m, the number of runner blades was 22, the angle of attack was 15^{o}, the nozzle entry arc was 90^{o}, the ratio of inner to outer diameter was 0.66, and the width of the runner was 0.197 m.

The sides of the runner in the model were made of Plexiglas to enable the researchers to visualize the flow and the attack angle effects at various speeds. They were able to observe the attack angle in the first stage and the validity of full passage assumption. Full passage assumption appeared reasonable only near the optimum speed, and separation off the suction and pressure sides of blades was seen at both low and high speeds.

The results of Van Dixhorn et al experiments revealed that the maximum efficiency was between 65 and 70 % at a non-dimensional speed of 0.47, and it was found that the maximum blade forces occur when the blade is about 10 degrees before the nozzle exit, where there is a spike in force. The centrifugal force and the pitching moment were found by spinning the runner in the air, and were found to agree well with the measured forces during the operation of the cross-flow turbine in the empty regions. However, there are healthy scepticisms regarding the validity of this analysis in the absence of the water forces. With varying the head, the blade loading pattern remains nearly constant but the

magnitudes changes at a given speed. At runaway speed, the fluid forces were not substantially higher than those at optimum speed. The tangential forces were found to be in good agreement with the results of a full passage control volume analysis, while the radial forces were slightly lower than predicted. Finally, Van Dixhorn et al provided charts for determining the blade forces on the runner of the cross-flow turbine.

Hothersall, R. J. [36] discussed the advantages of cross-flow turbines in general and the cross-flow turbines with partitioned runners in particular. He concluded that cross-flow turbines have good part-load efficiencies and this is a desirable feature when a run-of-river micro hydroelectric power plant is subjected to considerable flow variations. Cross-flow turbines fitted with partitioned runners can handle this type of flow fluctuations effectively. Hothersall also concluded that the cost of the cross-flow turbine is lower than other turbines. Finally, a selection chart for water turbines less than 100 kW and some guidelines in the selection of a suitable turbine for a micro hydro application were presented. The chart and the guidelines can be used to avoid mismatching of the turbine with the site conditions.

Khosrowpanah et al [28] discussed the historical development of the cross-flow turbine both theoretically and experimentally and concluded that there are serious constraints with regard to the use of other turbines for small hydroelectric power plants. These constraints are particularly applicable to the developing countries in which the cross-flow turbine would be highly appropriate to small-scale hydroelectric power plants. It was clear from this study that the cross-flow turbine has attracted the attention in such countries because of its unique design as it can be fabricated and built in a simple factory capable of

welding and cutting sheet metal in remote areas. Khosrowpanah et al listed the unique and inherent advantages of the cross-flow turbine such as:

1. The design and construction of the cross-flow turbine is simple, the nozzle and runner discs can be fabricated of steel plate and the blades can be cut from steel pipe of an appropriate diameter.
2. The most important aspect of the turbine is the favorable shape of its efficiency curve, particularly with the use of divided guide vanes. This is particularly important for small run-of-river power plant.
3. It requires relatively limited maintenance (malfunctioning is rare), low operating costs (compared with other technologies) and no fuel cost; it uses (not consume) the water.
4. The capital cost of a cross-flow turbine is less than any other turbine used for micro hydroelectric plants.
5. Positive effect on stream ecology by increasing dissolved oxygen (No measurements or qualification of such effect is reported in support of this conclusion).
6. Adaptability to draft tubes.
7. Freedom from cavitation.
8. Low civil works costs.

Although Khosrowpanah et al work contributed to our understanding of the cross-flow turbines, it lacked extensive theoretical analysis. This analysis is necessary to support the conclusion raised about blade’s angles and general shape.

Durgin and Fay [37] undertook an experimental investigation to investigate the internal hydrodynamics of the cross-flow turbine. The experimental study involved designing and constructing a special model of the cross-flow turbine with a Plexiglas casing and an open ended runner supported on a cantilever shaft. The open end runner allowed objects to be placed inside the rotating runner to alter the internal flow patterns so a cross flow could be collected by inserting a pipe with a slot inside the runner. The nozzle entry arc was varied from 35^o to 80^o.

This experimental investigation revealed that a significant amount of flow is entrained between the runner blades and did not cross to the blades second stage. It was also revealed that the amount of uncross-flow varied directly with the runner speed from zero to the maximum, as expected. It was also shown that the amount of uncross-flow increased from zero to the maximum with changing the nozzle entry arc from 35^o to 80^o. The maximum efficiency of such turbines was in the range of 61 % and the second stage contributes was approximately 17 % of the generated power. As a result of the observation of the uncross-flow in this study, they modified the equations of the theory of cross-flow turbines to account for the portion of uncross-flow in the runner introducing a different loss factor (ψ), entrance nozzle loss coefficient (c), and the ratio of uncross-flow to total flow. It is interesting to note that Durgin and Fay Plexiglas model with the cantilever runner modified the real flow in the turbine. Indeed, their work ignored the fact that the elimination of the solid walls on the free side of the cantilever modified the flow as compared to that of pivoting side. This made the flow unsymmetrical and ignored the effect of the boundary layer interference and the pressure forces on the flow of the cantilever side. This

renders any study involving physical interference with the flow invalid, and make CFD analysis ideal for such studies.

Fukutomi et al [38] presented a numerical method to analyze the effects of nozzle shape on the exit flow and the cross-flow turbine performance, the flow from a nozzle with arbitrary asymmetric curved surfaces is calculated numerically as a two dimensional flow by Schwarz-Christoffel method. The nozzle exit radius was 124 mm and the width of the nozzle was 100 mm. The parameters which prescribe the nozzle shape were as follows, the nozzle tip angle was 15^o and the nozzle entry arc was 30^o, 60^o, 90^o and 120^o.

The study revealed that the exit pressure had a larger value with an increase of the nozzle entry arc. Therefore, the nonuniformity of pressure distribution along the peripheral position at the nozzle exit increase with an increase of the nozzle entry arc. The study also revealed that the nozzle throat width was a significant parameter because an increase of flow angle results in a shock loss at the blade inlet. It is interesting to note that Fukutomi et al results show that the flow at the nozzle exit of a cross-flow turbine has a considerable value of pressure and the exit pressure increases with an increase of the nozzle throat width.

In a general and highly descriptive but valid study, ***Thapar and* Albertson *[39]*** revealed that cross-flow turbines are free from cavitation but are subject to wear when the water contains excessive silt and sand particles are present in. *Thapar and Albertson [39]* also stated in general cross-flow turbines require less maintenance than other types of turbines as the runner is self-cleaning. And also the cross-flow turbine is a less complex structure and cost than any other turbine.

Smith, G. J. [40] discussed the technical design and the use of the cross-flow turbine in hydroelectric development projects in developing countries and, more specifically, development of hydroelectric power plants in a remote area. It was stressed that the cross-flow turbine is the appropriate turbine for the low head hydroelectric power plants because of its advantages. The most important of these advantages are its low cost, its low civil work cost, and its simplicity of design and construction so that the turbine can be manufactured locally, and finally, the using of the cross-flow turbines with the flexibility to operate efficiently over a wide range of flows in low head hydroelectric power plants would provide an economic benefit to the country by promoting the growth of local industry. No data were provided to support the view that the efficiency of such turbine remains high over a wide range of flow. Also, there was no explanation provided as to why the efficiency remains high over a wide range of flow. Smith seems to have re-stated some conclusions from previous research.

Panasyuk et al [41] conducted an extensive investigation on the utilization of local energy resources as an alternative to centralized electrical supply for mountainous regions of the Central Asian part of Russia. Various options were considered such as water power, wind power, solar power and internal combustion engines. They compared the energy, operational and economic parameters of autonomous energy sources, and concluded that for territorially scattered and difficulty accessible economic objects with power consumption up to 30 – 50 kW, the use of micro hydroelectric power plants is the most prospective. During investigations, they created and tested experimental models of a micro hydroelectric power plant with a capacity of 1, 2, 10 and 30 kW. The problems associated with creating automated systems for controlling

the processes of water intake, water distribution, and irrigation on the basis of using a micro hydroelectric power plant was examined. The typical design of a hydro power block of a micro hydroelectric power plant was also studied. Their study indicated that cross-flow turbines along with propeller turbines as the most appropriate for use under those conditions. However, their study lacked in depth analysis of the characteristics of such turbines under the prevailing local conditions.

Kpordze, C. S. K. [42] prepared a new methodology for the selection of hydraulic turbines. A new methodology was introduced to guide hydropower planners, designers and developers logically and consistently through all phases of turbine selection during planning and feasibility studies for hydropower developments. Kpordze analyzed 174 turbines (the sample period considered was between 1965 and 1984) he proposes the following empirical equations and also a homograph for selection of cross-flow turbine runner speed and size when head, discharge, and power output are known.

$$D = 0.329\left(P/H\right)^{0.275} \quad \ldots (2.1)$$

$$D = 1.730\left(Q/N\right)^{0.191} \quad \ldots (2.2)$$

$$D = 0.814\left(H^{0.5}/Q\right)^{-0.222} \quad \ldots (2.3)$$

$$N = 38.45\left(H^{0.5}/D\right)^{1.032} \quad \ldots (2.4)$$

$$N = 74.927\left(H^{3/2}/Q\right)^{0.331} \quad \ldots (2.5)$$

$$P/H = 341.218\left(Q/N\right)^{0.641} \quad \ldots (2.6)$$

Where, D is turbine diameter in metres, P is turbine rated power output in kW, H is turbine rated head in m, Q is turbine rated flow in m^3/s and N is turbine rotational speed in rpm. The study was rather comprehensive over a very long period and resulted in good empirical equations that based on solid experimental work/data. It produced good and excellent guide lines and data bank for micro-turbine design.

Khosrowpanah et al [43] conducted an experimental investigation on cross-flow turbine performance by varying the runner diameter, the number of the runner blades and the nozzle entry arc under both flow and head variations. A model was designed, constructed and tested at Colorado States University. Four runners were tested. The outer diameter was 15.24 cm for one of them and 30.48 cm for the rest. The blade inlet was 30^o while the blade outlet angle was 90^o. The width of the runner blades was 15.24 cm and the number of runner blades ranged from 10 to 20 blades. Three vertically admitting nozzles were tested. The nozzles had the same width as the blades but varying entry arcs of 58^o, 78^o and 90^o. The model was without draft tube and open at the top.

The results of this experiment showed that the unit discharge increases by increasing the ratio of the outer diameter to the runner width, increasing the nozzle entry arc from 58^o to 90^o or reducing the number of runner blades. With an increase in the nozzle entry arc from 58^o to 90^o the maximum efficiency increased. The maximum efficiency for the runner tested occurs at the same unit rotational speed for a constant nozzle throat width ratio, regardless of the diameter of runner, the nozzle entry arc, number of runner blades or the flow/head variations. The efficiency decreases about 20 % by reducing the ratio of outer diameter to runner width from 2.0 to 1.0 and the maximum efficiency

occurs at about 0.53 – 0.54 of the peripheral velocity of the runner to absolute velocity of the flow at the first stage. The number of runner blades strongly affects the efficiency and the optimum number was approximately 15 for the 30.48 cm runner diameter with the outer diameter to the runner width ratio 2.0. The total pressure decreases, for each nozzle entry arc, with a decrease in the number of blades for a constant flow rate. The optimum value of the ratio of radial distance from outer to inter edge of the blade to blade spacing was 1.03 for the nozzle entry arc of 90^o and the ratio of inner to outer diameter 0.68. Khosrowpanah et al experiments were concluded on a realistic geometry prototype turbine. However, no attempt was made to relate the impact of the changes in the turbine parameter on the turbine flow fields and the dynamic forces in the rotor/blades. This is despite of the strong link between those fields/forces on the performance characteristics of the turbine.

Tongco, A. F. [44] conducted an experimental investigation to investigate the effect of the number of runner blades to the field performance of the cross-flow turbine. The experimental study involved designing and constructing of the cross-flow turbine. The turbine was constructed so that runners of the same size, but with a different number of blades, can be interchanged. Four runners with identical 10, 15, 20 and 30 blades were tested with the outside diameter of runner was 15.24 cm. The blade inlet was 150^o. The length of the runner was 20.32 cm. The entry angle of the nozzle was 90^o.

The results of the experiments revealed that the 20-blade runner was the most efficient where the maximum efficiency was 50 %. A further increase of the number of blades did not increase turbine efficiency to a significant degree. The results also revealed that the effect of flow rate is highly insignificant on the

cross-flow turbine efficiency, and finally, the turbine's low cost, the simplicity of its design and the ease by which available materials can be substituted for its construction make this water turbine ideal to provide electrical power to many rural communities.

Ott and Chappel [45] conducted an experimental investigation to build and test an inexpensive new cross-flow turbine and to provide information to the U.S. Department of Energy on efficiency, operation, maintenance and cost of the project. The experimental study involved designing, manufacturing and installing a new cross-flow turbine with a flow control slide gate at a remote run-of-river site in Northern California. The detailed dimensions for the cross-flow turbine were as follows; the inner and outer diameters of the runner were 62 and 92 cm, respectively and the runner width was 112 cm. The number of the blades was 20 and the entry arc of the nozzle was 90^{o}. The blade inlet was 30^{o} while the blade outlet angle was 90^{o}. The angle of attack was 16^{o}.

The results of the experiments showed that the cross-flow turbine with an adjustable gate can operate efficiently (maximum efficiency was between 70 and 80 per cent) on a wide range of flow and head conditions experienced in typical run-of-river projects where the available flow varies rapidly. Ott and Chappel studies were merely a repeat of previous studies and did not include any new study features or conclusions.

Aziz and Desai [46] conducted an experimental investigation to investigate the effect of certain parameters on the efficiency of the cross-flow turbine. The experimental study was conducted at Clemson Hydraulic Laboratory in Clemson University and involved designing and manufacturing models of cross-

flow turbines with variety of number of runner blades, inner to outer diameter ratios and angles of attack. Three nozzles shape and twenty seven runners were investigated.

The results of the experiments revealed that the cross-flow turbine efficiency increased with the increase in the number of runner blades from 15 to 25 which is contrast to Khosrowpanah et al [43] study which indicated that the maximum efficiency is when the runner is of 15 blades. Also the study revealed that the maximum efficiency of the turbine increased by increasing in the value of the inner to outer diameter ratio as well as the most efficient value of the inner to outer diameter ratio was 0.68 of the runners investigated due to the contribution of the second stage, and finally, these experiments indicated that an increase in the angle of water entry into the runner from 24^o to 32^o results in an increase in the predicted maximum efficiency in only 2 out of 18 tests. Therefore, the angle of water entry into the runner should be around 24^o.

Fukutomi et al [47] developed a method of numerical analysis for flow inside the runner of the cross-flow turbine. The internal flow inside the runner of the cross-flow turbine was analyzed as a two dimensional unsteady flow. They found that the flow is exceedingly nonuniform along the periphery in the runner of the cross-flow turbine, especially at the runner outlet. The nonuniformity is responsible for a decrease of the cross-flow turbine efficiency and finally, they found that the nonuniform flow increases with the diameter ratio.

Fiuzat* and Akerkar *[48] conducted an experimental investigation to improve the efficiency by identifying the contribution of the two stages of power generation to the shaft power in a cross-flow turbine. The experimental study

was conducted at Clemson Hydraulic Laboratory in Clemson University and involved designing and constructing a special model of the cross-flow turbine so a flow diverter could be mounted in the runner. The model (except the shaft) was built of acrylic material for ease of observing the flow path. Two nozzles were constructed. The nozzle entry arc was 90^o and 120^o, and the width of the nozzle and the runner was 15.24 cm. The runner outer diameter was 30.48 cm.

The results of the experiments showed that the cross-flow turbine second stage has an important effect on the efficiency, where the second stage of the cross-flow turbine contributes of at least 45 % of the total shaft power for the 90^o nozzle entry arc and at least 41 % for the 120^o nozzle. The results also showed that the overall efficiency of the cross-flow turbine, for a 90^o nozzle entry arc, is higher because the cross flow is more, which result in higher efficiencies for both stages of the turbine.

Olgun **and Ulku** ***[49]*** conducted an experimental investigation to test the performance of the cross-flow turbine by varying the number of the runner blades, the inner to outer diameter ratio and the gate openings of the nozzle under head variations. The experimental investigation involved designing and constructing an experimental rig of the cross-flow turbine. Two different nozzles and thirteen different runners were tested. The outer diameter for all runners was 170 mm and the width of the runner was 114 mm. The nozzles and the runner blades nearly had the same width. The blade inlet was 30^o while the first-stage blade outlet angle was 90^o and the diameter ratios were 0.75, 0.67, 0.58 and 0.54. The numbers of runner blades were 20, 24, 28 and 32 blades and the angle of attack was 16^o. The head ranged from 8 to 30 m.

The results of this experiment showed that the difference in efficiency for all of the runner configurations within the range of head from 8 to 30 m was about 4% and the maximum efficiency recorded in this experiment was about 73 %, which obtained by using a runner with 28 blades and an inner to outer diameter ratio of 0.67. Again those results contrast those of Khosrowpanah et al [23].

Desai* and Aziz *[50] conducted an experimental investigation to investigate the effect of certain parameters on the efficiency of the cross-flow turbine. They tested the effect of flow rate, diameter ratio, flow-stream spreading, number of blades, runner aspect ratio and blade exit angle. The experimental study was conducted at Clemson Hydraulic Laboratory in Clemson University and involved designing and manufacturing models of cross-flow turbines with a total of 39 runners and 11 nozzles were tested in 75 different combinations.

The results of the experiments revealed that the maximum efficiency of the turbine increased with the decrease in the first-stage inlet angle of attack in the range of 22^o – 32^o, and also the efficiency increased by increasing the number of runner blades from 15 to 30. The results also revealed that the maximum efficiency of the turbine reduced slightly by increasing in the diameter ratio in the range of 0.6 – 0.75. The ratio 1.5 of the runner width to the nozzle width is better than one of either 1, 2 or 3, and the ratio 0.33 of the runner width to the outer diameter is better than 0.5. The efficiency increased by decreasing the first-stage blade exit angle, an angle of 55^o is better than 90^o, and finally, the effect of flow rate is highly insignificant on the cross-flow turbine maximum efficiency.

Desai* and Aziz *[51] conducted an experimental investigation to investigate the effect of some geometric parameters on the efficiency of the cross-flow turbine.

The experimental study was conducted at Clemson Hydraulic Laboratory in Clemson University and involved designing and manufacturing models of cross-flow turbines with three different numbers of runner blades, three different inner to outer diameter ratios and three different of the first-stage inlet angles of attack. The runners, blades and nozzles were built of acrylic material for ease of observing the flow path.

The results of the experiments indicated that the geometric parameters have a significant effect on the overall performance of the cross-flow turbine and also indicated that the efficiency of the cross-flow turbine increased by increasing the number of runner blades from 15 to 25. The increase in the first-stage inlet angle of attack in the range of 24^o – 32^o did not improve the performance of the turbine and finally, 0.68 inner to outer diameter ratio produce a higher turbine efficiency within the range of 0.6 – 0.75. The efficient geometric parameters in the experiment were as follows; the first-stage inlet angle of attack was 24^o, the inner to outer diameter ratio was 0.68 and the number of the blades was 25.

Costa Pereira **and Borges** ***[52]*** conducted an experimental investigation to analyze the flow inside the nozzle of a cross-flow turbine. They measured the pressure distribution on the nozzle inside walls for two different configurations of the nozzles one installed with an inside guide vane while the other without it, both when the nozzle mounted alone and in the presence of a runner. In addition, the efficiency for the cross-flow turbine was measured in the tests carried out with a runner installed. The tests in the case of a runner installed covered a wide range of working conditions. The internal width of nozzles and the width of the runners were 210 and 215 respectively and the number of runner blades ranged from 10 to 25 blades.

This experiment gave an important conclusion that the head has no significant effect on the efficiency, and also the guide vane inside the nozzle improves the efficiency of cross-flow turbine. They also claimed that there are some changes in the pressure distribution in the case of a runner installed which varied significantly with the flow rate, and the influence of the number of blades was not clear on the pressure distribution, because most of the changes were small and dependent markedly on the position of the point considered. They also revealed that the influence of the runner on the pressure distribution is less on the lower wall of the nozzle than the upper wall.

Fukutomi et al [53] conducted an experimental and theoretical study to determine the magnitude of the fluid forces on the runner blades of the cross-flow turbine. In the experiment, the tangential and radial forces are measured on a test blade using strain gauges. In their theoretical study, the tangential and radial forces are calculated numerically using the two dimensional unsteady momentum equations. The dimensions of the test impulse cross-flow turbine were as follows; the entry arc of the nozzle was 90^o and the width of the throat of the nozzle was 64 mm. The inner and outer diameters of the runner were 214 and 315 mm, respectively and the runner width was 100 mm. The number of the blades was 26 with a circular profile whose thickness was 5.7 mm. The blade inlet was 30^o while the blade outlet angle was 90^o. The angle of attack was 15^o.

The results of the study revealed that the tangential and radial forces take maximum values near the nozzle tip where the blade escapes from the jet which is issuing from the nozzle. The fluid forces on the runner blades increase by decreasing the rotational speed of the runner, and finally, the results showed

that the values of radial forces are about 60 % of corresponding values of tangential forces.

Joshi et al [54] presented an experimental investigation to analyze the effect of the number of the blades, the nozzle entry arc, and the head of water on the performance characteristics of a cross-flow turbine. The first-stage inlet angle of attack was 16^o and the nozzle entry arc was 12^o, 26^o, 32^o and 36^o. The width of the nozzle was held constant at 25 mm less than that of the runner. The width of the runner was 325 mm, the runner outer diameter was 300 mm and the runner inner diameter was 198 mm. The number of runner blades ranged from 8 to 30 blades. The head ranged from 2 to 9 m.

This experimental investigation was shown that the cross-flow turbine is not a pure impulse turbine where a significant static pressure was measured at the nozzle exit and the static pressure at the nozzle exit increases with an increase in the head. The performance of the cross-flow turbine improves with an increase in nozzle entry arc, supply head and number of runner blades. The optimum number was approximately 20 for this experimental investigation.

Reddy et al [55] conducted an experimental investigation to study the effect of using different sizes of draft tubes on the performance of a 5-kW cross-flow turbine. The experimental study was carried out in the fluid mechanics laboratory of IIT Delhi. A cross-flow turbine model with variety of draft tubes (203, 259, and 300 mm) and without draft tubes were investigated in head range 3 to 9 m. The outer diameter of the cross-flow turbine was 300 mm and the inner diameter was 198 mm. The width of the runner was 325 mm and the

number of runner blades was 24. The angle of attack was 16^{o} and the nozzle entry arc was 36^{o}.

The results of the experiments indicated that the cross-flow turbine is not a pure impulse turbine because of the existence of static pressure at the nozzle exit and also indicated that the installation of the right draft tube size improves the performance of the cross-flow turbine at all heads, the improvement being only slight at higher heads (2-3 %) and considerable at lower heads (5-6 %), and finally, these experiments indicated that the maximum efficiency of the turbine decreases gradually with increasing head due to increased turbulence and losses due to the runner being partly flooded at higher heads.

Kenyery* and Alcala *[56] carried out an experimental study to analyze the effect of installing a guide vane in the interior of the runner, to guide the water flow after crossing the first stage effectively, on the cross-flow turbine performance. The experimental study involved designing and manufacturing of a model of cross-flow turbine with two types of guide vanes inside the runner. The dimensions of the model were as follows; the number of runner blades was 24 and the runner outer diameter was 294 mm while the runner inner diameter was 200 mm. The blade inlet was 30^{o} while the blade outlet angle was 90^{o} and the angle of attack was 20^{o}.

The results of the experiment indicated that the cross-flow turbine performance can be improved through the use of the proper internal guide vanes. The efficiency, which obtained by using internal guide vanes, was between 1.50 % and 6.0 % higher than the efficiency without using the internal guide vanes of the cross-flow turbine.

Olgun, H. [57] conducted an experimental investigation to analyze the effect of some geometric parameters of nozzle and runner on the cross-flow turbine efficiency by changing the diameter ratio of runner and gate opening of two different nozzles under different heads. Four different types of cross-flow turbine runners were designed and manufactured to analyze the effect of the diameter ratio on the cross-flow turbine efficiency. The runner outer diameter was 170 mm and the number of runner blades was 28. The angle of attack was 16^o. The blade inlet was 30^o while the blade outlet angle was 90^o and the diameter ratios were 0.75, 0.67, 0.58 and 0.54. The width of the runner and the nozzle was 114 mm and the head ranged from 8 to 30 m.

This experiment gave important conclusions that cross-flow turbines can be worked efficiently on a wider range of operating gate openings than most turbines, maximum efficiency almost can be obtained at a constant speed for all operating gate openings at a constant head, the increase of the head at constant gate openings changes the speeds for maximum efficiency, the cross-flow turbine with a diameter ratio of 0.67 is more efficient than the cross-flow turbines with diameter ratios of 0.54, 0.58 and 0.75 and finally, he concluded that the cross-flow turbine is a distinct selection in the micro turbine field.

Olgun, H. [58] conducted an experimental investigation to determine the effect of an interior guide tube on the cross-flow turbine efficiency at different positions of interior guide tubes and gate openings of a nozzle. Three different types of interior guide tubes were used to direct the flow inside the cross-flow turbine runner towards the second stage of the runner. The dimensions of the nozzle and runner were as follows; the nozzle throat width ratio ($T_r = 2s_o / \lambda d_1$) was

0.249 and the width of the runner and the nozzle was 114 mm. The runner outer diameter was 170 mm and the number of runner blades was 24. The ratio of inner to outer diameter (d_2/d_1) was 0.54 and the discharge (Q) range was 0.014 – 0.055 m^3/s while the head (H) was 4–30 m. The angle of attack was 16^o.

Olgun indicated that the interior guide tube did not improve the cross-flow turbine efficiency. The maximum efficiency which obtained by using an interior guide tube was about 5 % less than the maximum efficiency without interior guide tube due to a choking effect.

Kaniecki, M. [59] presented a numerical method to analyze the internal flow in a classical impulse cross-flow turbine and a reaction cross-flow turbine. A two dimensional flow simulation of the turbine was performed to analyze the velocity and pressure in these turbines by adopting a computer program FLUENT 5.0™. The AutoCAD™ design program was applied to build the geometry of the flow system of both the turbines. The dimensions of both the model cross-flow turbines were as follows; the runner outer diameter was 300 mm, the inner diameter was 200 and the number of runner blades was 30. The blade thickness was 3.6 mm and the blade inlet was 150^o while the blade outlet angle was 90^o. The width of the impulse turbine runner was 150 mm while the width of the reaction turbine runner was 300 mm.

The results showed that the CFD analysis is an useful tool to aid the design of cross-flow turbine, and the results of the reaction turbine showed that the proper design of the draft tube reduces some undesirable phenomena like back flows and separations.

Choi et al [60] presented a numerical method to analyze the effects of various turbine structures on the internal flow and performance of cross-flow turbine by adopting a commercial code ANSYS-CFX. The dimensions of the cross-flow turbine model were as follows; the runner outer diameter was 250 mm and the width of the runner and the nozzle was 150 mm. On the top of chamber casing an air suction pipe was installed. Three different cross sectional area types of vertical nozzle shape without guide vane were used to simplify the internal passage of the cross-flow turbine model to confirm the effects of nozzle shape on the internal flow and performance of the cross-flow turbine. Five different types of blade angle were used by changing the inlet and outlet angles of the runner blade model. Moreover, three different numbers of runner blades 15, 26 and 30 and three inlet blade angles 25^o, 30^o and 35^o were used.

They concluded that the using of the air suction pipe in runner passage reduces collision loss between the runner passage flow and shaft and eliminates loss by recirculation flow which results in improving the cross-flow turbine efficiency and finally, they concluded that nozzle shape has the largest effect on the internal flow and turbine performance. Relatively narrow nozzle passage gives high turbine efficiency.

Choi et al [61] suggested a newly developed air suction method for the cross-flow turbine. They presented a numerical method to analyze the effects of air layer located in the cross-flow turbine chamber on the internal flow and the performance of the cross-flow turbine by adopting a commercial code ANSYS-CFX. The internal flow inside the runner of the cross-flow turbine was analyzed as a two dimensional unsteady-state two-phase flow. The dimensions of the cross-flow turbine model were as follows; the number of runner blades was 30.

The width of the runner and the nozzle was 500 mm and the blade inlet was 30^o while the blade outlet angle was 87^o. Two air suction valves were used, one installed at the top of chamber casing and the other on the casing side wall.

They concluded that the using of the air suction pipe on the casing side wall of the runner has significant effects on the internal flow and the performance of cross-flow turbine and thus, the efficiency increased by the increase of the supplied air flow rate through the air suction pipes on the casing side wall. The efficiency increased is resulted from the effect of suppressing the hydraulic loss by recirculation flow and reducing the collision loss between the runner passage flow and shaft.

Haurissa and Soenoko [62] conducted an experimental investigation to investigate the effect of an interior nozzle on the second stage performance for a cross-flow turbine by installing nozzle inside the runner to guide the water after crossing the first stage into the second stage effectively. The experimental study involved designing and manufacturing of a nozzle inside the cross-flow turbine runner. The dimensions of the model were as follows; the number of runner blades was 20 and the runner outer diameter was 200 mm while the runner inner diameter was 130 mm. The first stage nozzle angle was 32^o and the second stage nozzle angle was 20^o.

They indicated that the installation of the nozzle inside the runner has significant effects on the performance and the efficiency of the cross-flow turbine. The maximum efficiency, which obtained by using a nozzle inside the runner with 32^o for the first stage inlet angle and 20^o for the second stage inlet blade angle, was about 11 % higher than the maximum efficiency without using the interior

nozzle of the cross-flow turbine. The efficiency increased because of increasing the contribution of the second stage.

De Andrade et al [63] presented a numerical method to analyze the internal flow in a cross-flow turbine. A three dimension-CFD steady state flow simulation of the turbine was performed to analyze the velocity and pressure in the cross-flow turbine by adopting a commercial code ANSYS-CFX. The dimensions of the cross-flow turbine model were as follows; the runner outer diameter was 295 mm, the inner diameter was 200 mm and the number of runner blades was 24. The width of the runner blades was 150 mm and the blade inlet was 150^{o} while the blade outlet angle was 90^{o}. The angle of attack was 16^{o}.

The CFD simulation results showed that 68.5 % of the energy transfer happens in the first stage and 31.5 % of the energy transferred happens in the second stage, and also the results were able to recognize the shocks with the runner shaft and recirculation flow zone in the cross-flow turbine which result in decrease the efficiency of the turbine significantly.

Son et al [64] presented a numerical method to examine the effect of various structures on the internal flow and the performance of the cross-flow turbine. They examined the inlet nozzle shape, diffuse angle and length of the draft tube. A two-dimensional CFD steady state flow simulation of the turbine was performed to examine the velocity and pressure in the cross-flow turbine by using ANSYS-CFX code. The dimensions of the cross-flow turbine model were as follows; the runner outer diameter was 280 mm, the number of runner blades was 23. The width of the runner blades and the nozzle was 135 mm and the blade inlet was 35^{o} while the blade outlet angle was 100^{o}. The CFD simulation results revealed that the circular nozzle upper wall provides better effect on the

cross-flow flow turbine performance than the straight nozzle upper wall. And the diffuse angle and length of the draft tube do not affect considerable on the performance of the cross-flow turbine because the recovery head of the diffuse angle and length of the draft tube is very small in comparison with net head at the turbine inlet. However, the internal flow characteristics of the cross-flow turbine are strongly influenced by the diffuse angle and length of the draft tube.

Kokubu et al [65] presented a numerical method to analyze the flow inside a new type of cross-flow turbine which has an anti-recirculation block (ARB) in the interior of the runner and investigate the effect of this anti-recirculation block (ARB) on the flow characteristics and the performance of the cross-flow turbine performance. A CFD steady state flow simulation of the turbine was performed to examine the velocity and pressure in the cross-flow turbine by using ANSYS-CFX code. Four different kinds of cross-flow turbine runners were adopted for CFD simulation analysis. The runner outer diameter was 250 mm and the number of runner blades was 30. The blade inlet was 30^{o} while the blade outlet angle was 87^{o} and the width of the nozzle and the runner was 17 mm for the models 1 and 2 and 100 mm for the models 3 and 4. An anti-recirculation block (ARB) was installed for the models 2 and 4.

The CFD simulation results revealed that the using of the anti-recirculation block in runner passage reduces collision loss between the runner passage flow and shaft and eliminates loss by recirculation flow which results in improving the cross-flow turbine efficiency. The results also revealed that the widening of the width of the nozzle and the runner and increasing the flow rate reduces the friction loss and improve the performance of the cross-flow turbine. Finally, the most efficient model was the model 4 where the efficiency was 62.9 %.

2.3 Main Observations from Previous Work

It is evident from the literature available that the impact of various geometrical parameters on the cross-flow turbine performance is not well understood. The previous studies on the cross-flow turbine development may be summed up as in table 2.1, where attention has been focused on investigating the effects of the first three of the following geometrical parameters:

i. the angle of attack,
ii. the diameter ratio,
iii. the number of blades,
iv. the blade profile,
v. the nozzle profile,
vi. the nozzle entry arc,
vii. the nozzle throat width,
viii. the nozzle to runner blades width, and
ix. the runner blades width to outer diameter.

However, little attention was directed towards the complex flow structure associated within such turbines. Such flow characteristics (which is three dimensional in nature with complex hydrodynamic forces) can greatly affect the performance and the working life of such turbines. In addition this review has shown some conflicting results of the previous investigation reported by various researchers. The current study is undertaken with the purpose of optimizing the performance of the cross-flow turbine for micro hydroelectric power plants to resolve any previous conflicting views or conclusions. It aims at analyzing the impact of such parameters change on the flow characteristics and the

hydrodynamics forces within the turbine. It was interesting to note from the literature that despite the importance of the flow field and structure within the turbine, which can influence the turbine performance immensely, this was not investigated in the literature thoroughly and comprehensively.

Table 2.1 Summary of previous investigations on the cross-flow turbine (*Reference can be made to Fig. 2.1 for the geometric parameters of this table*).

Investigator(s)	Type of Study	Year	Geometric parameters values						
			Number of Blades (n_b)	Diameter ratio (d_2/d_1)	Angle of attack (α_1)	Nozzle entry arc (λ)	Nozzle throat width (S_o)	Nozzle to runner blades width (N_w/B_w)	Runner blades width to outer diameter (B_w/d_1)
Mockmore and Merryfield [31]	Experimental	1949	20	0.66	16^o	-	-	-	0.92
Nakase et al. [32]	Experimental	1982	26	0.68	15^o	90^o	$0.2d_1$	1	1
Makansi, J. [33]	Review	1983	-	-	-	-	-	-	-
Chappell, J. R. [34]	Review	1983	-	-	-	-	-	-	-
Van Dixhorn et al. [35]	Experimental	1984	22	0.66	15^o	90^o	-	-	0.71
Hothersal, R. J. [36]	Review	1984	-	-	-	-	-	-	-
Khosrowpanah et al. [28]	Comprehensive Rview	1984	-	-	-	-	-	-	-
Durgin and Fay [37]	Experimental	1984	-	-	-	-	-	-	-

Fukutomi et al. [38]	Numerical	1985	-	-	-	-	-	-	-
Thaper and Albertson [39]	Review	1985	-	-	-	-	-	-	-
Smith, G. J. [40]	Review	1985	-	-	-	-	-	-	-
Panasyuk et al. [41]	Review	1987	-	-	-	-	-	-	-
Kpordze, C. S. K. [42]	Comprehensive Rview	1987							
Khosrowpanah et al. [43]	Experimental	1988	15	0.68	16^o	90^o	$0.32d_1$	1	0.5
Tongco, A. F. [44]	Experimental	1988	20	0.67	-	90^o	$0.2d_1$	-	1.34
Ott and Chappel [45]	Experimental	1989	20	0.67	16^o	90^o	-	-	1.22
Aziz and Desai [46]	Experimental	1991	25	0.68	24^o	90^o	$0.32d_1$	1	0.5
Fukutomi et al. [47]	Numerical	1991	-	-	-	-	-	-	-
Fiuzat and Akerkar [48]	Experimental	1991	-	-	-	90^o	-	1	0.5
Olgun and Ulku [49]	Experimental	1992	28	0.67	16^o	-	-	1	0.67

Aziz and Desai [50]	Experimental	1994	30	0.6	22^o	90^o	-	0.67	0.34
Desai and Aziz [51]	Experimental	1994	25	0.68	24^o	90^o	$0.32d_1$	1	0.5
Costa Pereira and Borges [52]	Experimental	1995	-	0.67	15^o	80^o	-	1	0.86
Fukutomi et al. [53]	Experimental and Analytical	1995	26	0.68	15^o	90^o	$0.2d_1$	-	0.32
Joshi et al. [54]	Experimental	1995	20	0.66	16^o	36^o	-	0.92	1
Reddy et al. [55]	Experimental	1996	24	0.66	16^o	36^o	-	-	1
Kenyery and Alcala [56]	Experimental	1997	24	0.68	20^o	-	-	-	0.44
Olgun, H. [57]	Experimental	1998	28	0.67	16^o	-	-	1	0.67
Olgun, H. [58]	Experimental	2000	24	0.54	16^o	-	-	1	0.67
Kaniecki, M. [59]	Numerical/ Modelling	2002	30	0.67	16^o	-	-	-	1
Choi et al. [60]	Numerical/ Modelling	2008	26	-	-	-	-	1	0.6
Choi et al. [61]	Numerical/ Modelling	2010	30	-	-	-	-	1	-

Haurissa and Soenoko [62]	Experimental	2010	20	0.65	32^o	-	-	1	-
De Andrade et al. [63]	Numerical/ Modelling	2011	24	0.68	16^o	70^o	$0.16d_1$	1	0.5
Son et al. [64]	Numerical/ Modelling	2012	23	-	-	-	-	1	0.48
Kokubu et al. [65]	Numerical/ Modelling	2012	30	0.67	17^o	109^o	-	1	0.4

Where there are no details shown in the above table, the author did not specify any technical details, dimensions or geometries.

Chapter Three

Theoretical Analysis

Chapter Three

Theoretical Analysis

3.1 Introduction

The cross-flow turbine is normally classified as an impulse turbine but this is not strictly correct because there is a slight static pressure at nozzle exit [32]. The cross-flow turbine comprises of a cylindrical-shaped runner consisting of two parallel circular disks connected together at the perimeter with a series of curved horizontal blades, and a nozzle, whose cross-sectional area is rectangular, directs the water flow to the full length of the runner at a specified angle of attack to strike the blades on the circumference of the runner. The water passes through two stages in cross-flow turbine so energy is extracted from water by the blades of the runner in two stages.

3.2 Theory of the Cross-Flow Turbine

The turbine is the most important piece of equipment in a micro hydroelectric power plant in which energy transfers take place from the water to the runner as a result of a change of momentum occurring when the water flows through the blades of the runner.

The energy of the flowing water is extracted and converted into mechanical work in the hydraulic turbine using one of two fundamental mechanisms: one

mechanism is an impulse principle, which extracts the kinetic energy of water in the form of jet which strikes the blades on the periphery of the runner and converts it into mechanical work. The extraction of energy (the change of momentum) happens because of changing in direction of the water where no change in pressure in the blade passages and no change in the magnitude of the relative velocity vector. The second mechanism is a reaction principle, which extracts the potential energy and the kinetic energy of water in the form of pressure drop across the turbine and converts it into mechanical work.

The water in cross-flow turbine runner passes through two stages so energy is extracted from the water by the blades of the runner in two stages. The first stage may have reaction effect because water piles up during operation and the reaction effect becomes zero at a low flow. The second stage that the blade passages are not full of water operates at a constant pressure since the pressures are balanced through these blade passages.

The fundamental design relationship for all turbo machinery is derived using the momentum law, which can be obtained by using control volume. Control volume approach refers to a region in a space, and is useful in the analysis of situation where flow occurs into and out of the space. The boundary of a control volume (c.v) is its control surface (c.s).

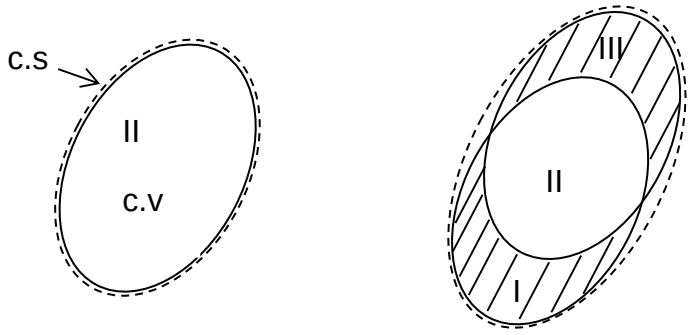

(a) Time (t) (b) Time (t+δt)

Fig. 3.1 Control volume: (a) system at time t; (b) at time t + δt system I begins to enter system II and system III leaves.

Let M be the total amount of properties such as mass, energy, momentum. ξ be the amount of this property per unit mass through the fluid M/m.

At time $t+\delta t$ the system comprises volume II and III while in time t occupies II.

The increase in M

$$M_{t+\delta t} - M_t = \left(\int_{II} \xi\rho dV + \int_{III} \xi\rho dV\right)_{t+\delta t} - \left(\int_{II} \xi\rho dV\right)_t \quad \dots (3.1)$$

Where dV is the element volume of control volume, and ρ is the density

Rearrangement after adding and subtracting $\left(\int_{I} \xi\rho dV\right)_{t+\delta t}$ and dividing by δt

$$\frac{M_{t+\delta t} - M_t}{\delta t} = \frac{\left(\int_{II} \xi\rho dV + \int_{I} \xi\rho dV\right)_{t+\delta t}}{\delta t} - \frac{\left(\int_{II} \xi\rho dV\right)_t}{\delta t} + \frac{\left(\int_{III} \xi\rho dV\right)_{t+\delta t}}{\delta t} - \frac{\left(\int_{I} \xi\rho dV\right)_{t+\delta t}}{\delta t} \quad \dots (3.2)$$

The average time rate of increasing of M within the system at time δt in the limits as $\delta t \to 0$ becomes

$$\frac{dM}{dt} \quad \dots (3.3)$$

The amount of M in the control volume at time t and $t+\delta t$. The limit is

$$\frac{\partial}{\partial t}\int_{c.v} \xi\rho dV \quad \dots (3.4)$$

The rate of flow of M out the control volume in the limit may be written as

$$\lim_{\delta t\to 0}\frac{\left(\int_{III} \xi\rho dV\right)_{t+\delta t}}{\delta t} = \int_{out} \xi\rho\vec{v}\cdot dA \quad \dots (3.5)$$

where $\vec{v}$ is the velocity vector of flow

The rate of the flow of M into the control volume

$$\lim_{\delta t\to 0}\frac{\left(\int_{I} \xi\rho dV\right)_{t+\delta t}}{\delta t} = -\int_{in} \xi\rho\vec{v}\cdot dA \quad \dots (3.6)$$

Equations (3.5) and (3.6) can be written as

$$\int_{c.s} \xi\rho\vec{v}\cdot dA \quad \dots (3.7)$$

In general, equation (3.2) becomes

$$\frac{dM}{dt} = \frac{\partial}{\partial t}\int_{c.v} \xi\rho dV + \int_{c.s} \xi\rho\vec{v}\cdot dA \quad \dots (3.8)$$

It is necessary to restrict the flow to steady flow which means the state of the fluid at any given point is constant.

For steady state

$$\frac{dM}{dt} = \int_{c.s} \xi \rho \vec{v} \cdot dA \quad \dots (3.9)$$

Conservation of momentum based on the control volume theorem let $M = m\vec{v}$ then $\xi = \frac{M}{m} = \frac{m\vec{v}}{m} = \vec{v}$

$$\frac{d(m\vec{v})}{dt} = \int_{c.s} \rho \vec{v}\,\vec{v} \cdot dA \quad \dots (3.10)$$

Newton's second law states that the sum of external forces acting on a moving system is equal to the time rate of change of momentum of the system.

$$\sum \vec{F} = \frac{d}{dt}(m\vec{v}) \quad \dots (3.11)$$

Now, we are going to write the system formulation of Newton's law in control volume formulation.

$$\sum \vec{F} = \sum_{out} \dot{m}\vec{v} - \sum_{in} \dot{m}\vec{v} \quad \dots (3.12)$$

$$F = \frac{\gamma}{g} Q v_{out} - \frac{\gamma}{g} Q v_{in} \quad \dots (3.13)$$

$$F = \frac{\gamma}{g} Q\left(v_2 \cos\alpha_2 - \left(-v_1 \cos\alpha_1\right)\right) \quad \dots (3.14)$$

$$F = \frac{\gamma}{g} Q\left(v_2 \cos\alpha_2 + v_1 \cos\alpha_1\right) \quad \dots (3.15)$$

General view of
the turbine runner

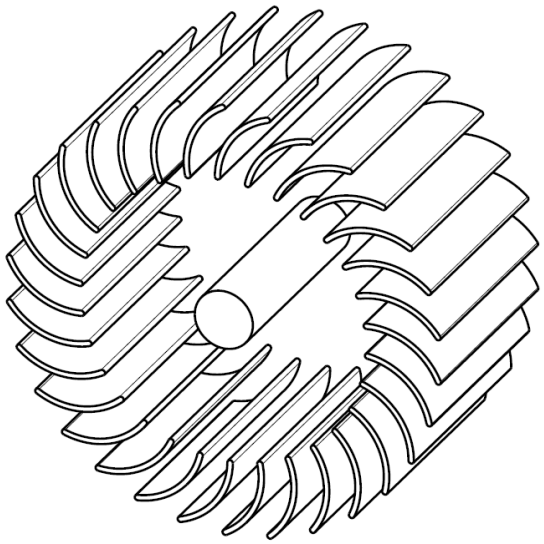

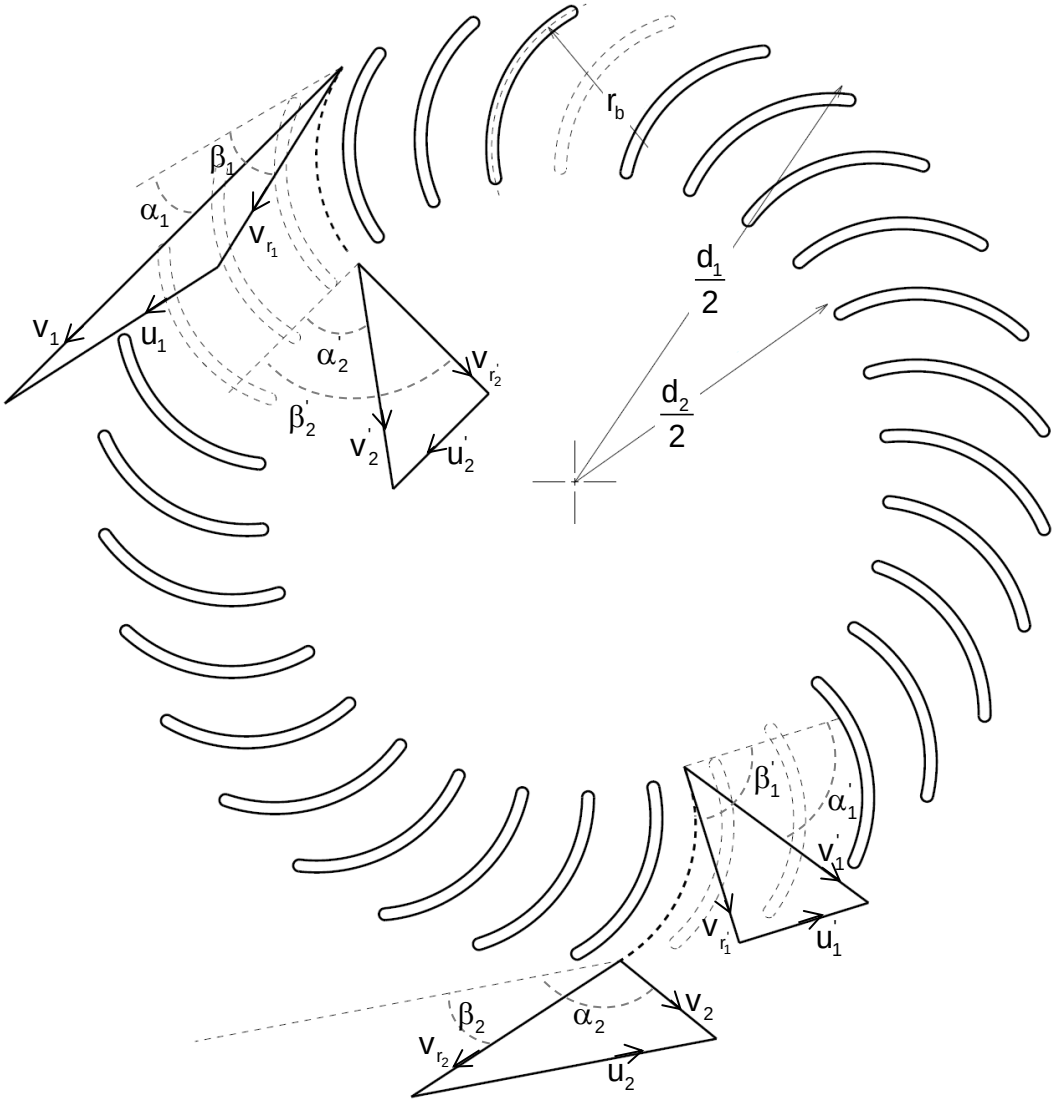

Fig. 3.2 Water path through the runner blades and the velocity diagrams.

The rate at which useful work is done by the runner can be calculated by the product of the force and the velocity.

$$P_o = \frac{\gamma}{g} Q\left(v_2 \cos\alpha_2 + v_1 \cos\alpha_1\right) u_1 \qquad \ldots (3.16)$$

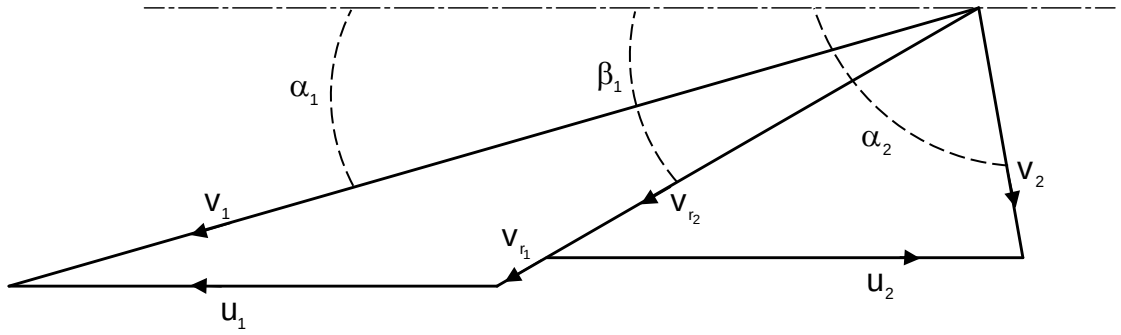

Fig. 3.3 Velocity diagrams.

The equation (3.16) can be simplified by using the velocity triangles, Fig. 3.3.

$$u_2 = v_{r_2} \cos\beta_2 + v_2 \cos\alpha_2 \qquad \ldots (3.17)$$

Since $u_1 = u_2$

$$v_2 \cos\alpha_2 = v_{r_2} \cos\beta_2 - u_1 \qquad \ldots (3.18)$$

Neglecting the increase in velocity of water due to the difference in the elevation between points 1 and 2 (Fig. 3.2) which is small in most cases,

$$v_{r_2} = \psi v_{r_1} \qquad \ldots (3.19)$$

Where ψ is an empirical coefficient less than unity (about 0.98) [31]. From the velocity diagram Fig. 3.3,

$$v_1 \cos\alpha_1 = u_1 + v_{r_1} \cos\beta_1 \qquad \ldots (3.20)$$

$$v_{r_1}\cos\beta_1 = v_1\cos\alpha_1 - u_1 \quad \ldots (3.21)$$

$$v_{r_1} = \frac{\left(v_1\cos\alpha_1 - u_1\right)}{\cos\beta_1} \quad \ldots (3.22)$$

Substituting equations (3.18), (3.19), and (3.22) in the power equation (3.16).

$$P_o = \frac{\gamma}{g}Q\left(v_{r_2}\cos\beta_2 - u_1 + v_1\cos\alpha_1\right)u_1 \quad \ldots (3.23)$$

$$P_o = \frac{\gamma}{g}Q\left(\psi v_{r_1}\cos\beta_2 - u_1 + v_1\cos\alpha_1\right)u_1 \quad \ldots (3.24)$$

$$P_o = \frac{\gamma}{g}Q\left(\psi\left(\frac{v_1\cos\alpha_1 - u_1}{\cos\beta_1}\right)\cos\beta_2 - u_1 + v_1\cos\alpha_1\right)u_1 \quad \ldots (3.25)$$

$$P_o = \frac{\gamma}{g}Q\left(v_1\cos\alpha_1 - u_1\right)\left(1 + \psi\frac{\cos\beta_2}{\cos\beta_1}\right)u_1 \quad \ldots (3.26)$$

The power available from a river or falling water is a combination of volume flow rate of water and net elevation head. It is possible to produce a power with any combination of volume flow rate of water and head, low flow and high head, high flow and low head or any combination of both values. The input power is given by the formula

$$P_i = \gamma QH \quad \ldots (3.27)$$

Consider the forces acting on the element as shown in Fig. 3.4, and apply Newton's law. The head at the inlet can be derived as

$$\sum \text{Forces} = \text{mass} * \text{acceleration} \quad \ldots (3.28)$$

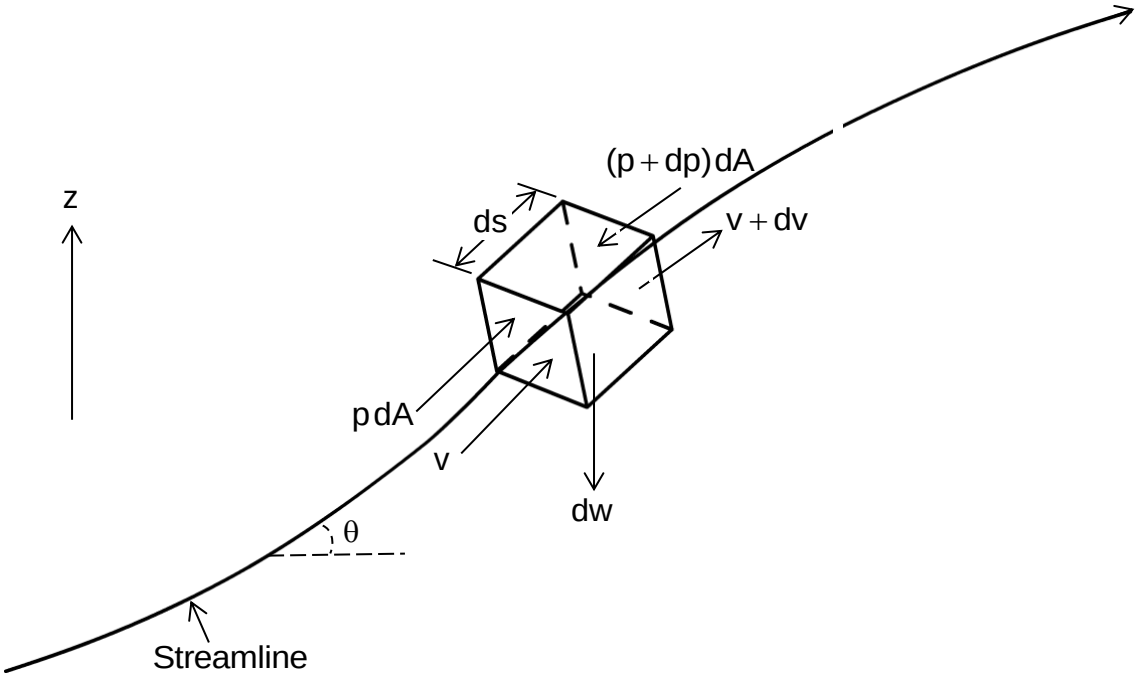

Fig. 3.4 Forces action on fluid on streamline

$$pdA - (p + dp)dA - dw\sin\theta = \frac{dw}{g} * a \qquad \ldots (3.29)$$

where a is the acceleration

$$w = \rho g dA ds \qquad \ldots (3.30)$$

$$a = \frac{dv}{dt} = v\frac{dv}{ds} \qquad \ldots (3.31)$$

Thus

$$-dpdA - \rho g dA ds\frac{dz}{ds} = \rho dA ds * v\frac{dv}{ds} \qquad \ldots (3.32)$$

$$dpdA + \rho g dA dz + \rho dA * vdv = 0 \qquad \ldots (3.33)$$

$$\frac{dp}{\rho} + gdz + vdv = 0 \qquad \ldots (3.34)$$

Dividing by g gravitational acceleration

$$\frac{dp}{\gamma} + dz + \frac{vdv}{g} = 0 \quad \ldots (3.35)$$

$$\frac{dp}{\gamma} + dz + d\left(\frac{v^2}{2g}\right) = 0 \quad \ldots (3.36)$$

For incompressible fluid, specific weight is constant

$$d\left(\frac{p}{\gamma}\right) + dz + d\left(\frac{v^2}{2g}\right) = 0 \quad \ldots (3.37)$$

Integration between any two points (1) and (0)

$$\left(\frac{p}{\gamma} + \frac{v^2}{2g} + z\right)_1 = \left(\frac{p}{\gamma} + \frac{v^2}{2g} + z\right)_0 \quad \ldots (3.38)$$

Thus the total hydraulic head at the exit of the nozzle is H and c be taken as nozzle coefficient, which covers the loss of kinetic energy through the nozzle, then equation (3.38) can be written as follows,

$$H = \frac{v_1^2}{c^2 2g} \quad \ldots (3.39)$$

Since the head at the nozzle exit is $\frac{v_1^2}{c^2 2g}$ where c is a nozzle coefficient that accounts for the losses in the nozzle, the inlet power becomes,

$$P_i = \gamma Q H = \frac{\gamma Q v_1^2}{c^2 2g} \quad \ldots (3.40)$$

The efficiency of turbine can be calculated from the ratio of the output and input power,

$$\eta = \frac{\frac{\gamma}{g} Q\left(v_1 \cos\alpha_1 - u_1\right)\left(1+\psi\frac{\cos\beta_2}{\cos\beta_1}\right)u_1}{\frac{\gamma Q v_1^2}{c^2 2g}} \quad \ldots (3.41)$$

$$\eta = 2c^2 \frac{u_1}{v_1}\left(1+\psi\frac{\cos\beta_2}{\cos\beta_1}\right)\left(\cos\alpha_1 - \frac{u_1}{v_1}\right) \quad \ldots (3.42)$$

$\beta_1 = \beta_2$ (β_1 & β_2 are corresponding angles of the same blade)

$$\eta = 2c^2 \frac{u_1}{v_1}(1+\psi)\left(\cos\alpha_1 - \frac{u_1}{v_1}\right) \quad \ldots (3.43)$$

Differentiating

$$\frac{d\eta}{d\left(\frac{u_1}{v_1}\right)} = 0 \quad \ldots (3.44)$$

The velocity coefficient at maximum theoretical power output becomes

$$\frac{u_1}{v_1} = \frac{1}{2}\cos\alpha_1 \quad \ldots (3.45)$$

And for maximum the cross-flow turbine efficiency

$$\eta_{max} = 2c^2(1+\psi)\frac{1}{2}\cos\alpha_1\left(\cos\alpha_1 - \frac{1}{2}\cos\alpha_1\right) \quad \ldots (3.46)$$

$$\eta_{max} = 2c^2(1+\psi)\frac{1}{2}\cos\alpha_1\left(\frac{1}{2}\cos\alpha_1\right) \quad \ldots (3.47)$$

$$\eta_{max} = 2c^2(1+\psi)\frac{1}{4}\cos^2\alpha_1 \quad \ldots (3.48)$$

The maximum theoretical cross-flow turbine efficiency is

$$\eta_{max} = \frac{1}{2}c^2(1+\psi)\cos^2\alpha_1 \quad \ldots (3.49)$$

Therefore maximum theoretical power output becomes

$$P_{o_{max}} = \frac{\gamma}{g} Q v_1^2 \left(\frac{u_1}{v_1}\right)^2 (1+\psi) \quad \ldots (3.50)$$

The theoretical power developed for each stage could be started with the conservation of momentum based on the control volume theorem let $M = m\vec{v}.\vec{r}$

then $\xi = \frac{M}{m} = \frac{m\vec{v}.\vec{r}}{m} = \vec{v}.\vec{r}$

$$\frac{d(m\vec{v}.\vec{r})}{dt} = \int_{c.s} \rho(\vec{v}.\vec{r})\vec{v} \cdot dA \quad \ldots (3.51)$$

Angular moment is an extension of the consideration made for linear momentum.

$$\sum \vec{r} \times \vec{F} = \sum_{out} (\vec{r} \times \vec{v})\dot{m} - \sum_{in} (\vec{r} \times \vec{v})\dot{m} \quad \ldots (3.52)$$

This equation is three dimensions equation. In turbo machinery, it is convenient to use coordinates of rotating body.

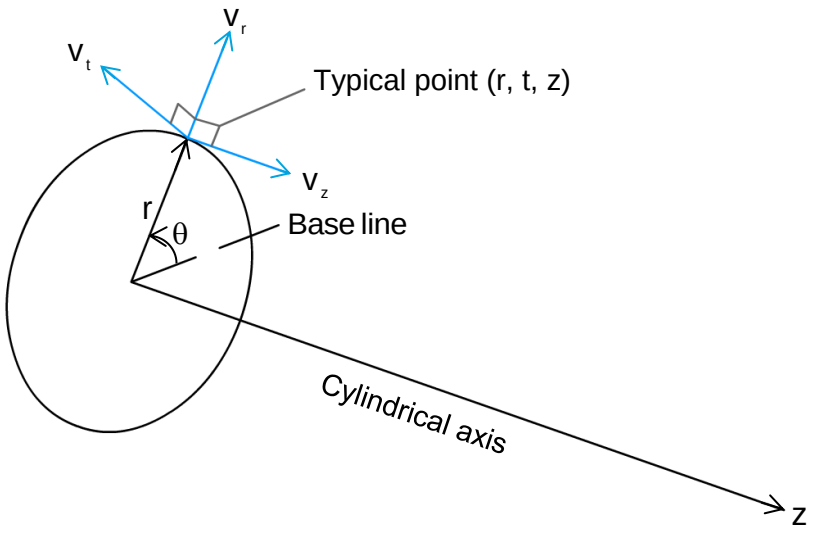

Fig. 3.5 Definition sketch for the cylindrical coordinate system.

It is clear that the tangential form is the important where, it is the torque producer

$$\sum r.F_t = \sum_{out}(v_t.r)\dot{m} - \sum_{in}(v_t.r)\dot{m} \quad \dots (3.53)$$

But

$$T = r.F_t \quad \dots (3.54)$$

the power developed becomes,

$$P_o = T.\frac{u}{r} \quad \dots (3.55)$$

The water passes through two stages in cross-flow turbine so energy is extracted from water by the blades of the runner in two stages. Therefore, the Euler energy equation for the cross-flow turbine can be written from the sum of the energy developed from each stage as follows,

$$P_o = \frac{\gamma}{g}Q\left(\underbrace{\left(u_1 v_{t_1} - u_2' v_{t_2'}\right)}_{\text{First Stage}} + \underbrace{\left(u_1' v_{t_1'} - u_2 v_{t_2}\right)}_{\text{Second Stage}}\right) \quad \dots (3.56)$$

The theoretical power developed for each stage

$$P_o = P_{1\_2'} + P_{1'\_2} \quad \dots (3.57)$$

$$P_{1\_2'} = \frac{\gamma}{g}Q\left(u_1 v_{t_1} - u_2' v_{t_2'}\right) \quad \dots (3.58)$$

$$P_{1'\_2} = \frac{\gamma}{g}Q\left(u_1' v_{t_1'} - u_2 v_{t_2}\right) \quad \dots (3.59)$$

Since $(u_1 = u_2)$ and $(u_1' = u_2')$ with using the velocity diagrams (Fig. 3.2) and assuming the empirical coefficient ψ is equal one.

$$v_{t_1} = u_1 + v_{r_1}\cos\beta_1 \quad \dots (3.60)$$

$$v_{t_2} = u_1 - v_{r_2}\cos\beta_1 \quad \dots (3.61)$$

Assume $v_{t_1} = u_1$ [66]

$$v_{t_2'} = u_2' \quad \ldots (3.62)$$

$$v_{t_1'} = u_1' \quad \ldots (3.63)$$

Further with

$$u_2' = \left(\frac{d_2}{d_1}\right) u_1 \quad \ldots (3.64)$$

$$P_{1\_2'} = \frac{\gamma}{g} Q u_1^2 \left((1+\cos\beta_1) - \left(\frac{d_2}{d_1}\right)^2 \right) \quad \ldots (3.65)$$

$$P_{1'\_2} = \frac{\gamma}{g} Q u_1^2 \left(\left(\frac{d_2}{d_1}\right)^2 - (1+\cos\beta_1) \right) \quad \ldots (3.66)$$

The power ratio of the two stages, therefore, is

$$\frac{P_{1\_2'}}{P_{1'\_2}} = \frac{(1+\cos\beta_1) - \left(\frac{d_2}{d_1}\right)^2}{\left(\frac{d_2}{d_1}\right)^2 - (1-\cos\beta_1)} \quad \ldots (3.67)$$

Assuming $d_2/d_1 = 2/3$ and $\beta_1 = 30^o$

$$\frac{P_{1\_2'}}{P_{1'\_2}} = 4.58 \quad \ldots (3.68)$$

Which means that the theoretical power developed in the first stage is 4.58 times that of the second stage. In terms of proportion of the total power

$$P_{1\_2'} + \frac{P_{1'\_2}}{4.58} = P_o \quad \ldots (3.69)$$

$$P_{1\_2'} = 0.82 P_o \quad \ldots (3.70)$$

$$P_{1'\_2} = 0.18 P_o \quad \ldots (3.71)$$

3.3 Design Calculations of the Cross-Flow Turbine

3.3.1 Blade Angles

The inlet and outlet blade angles have a significant effect on the cross-flow turbine performance [67]. In the design, they have to be chosen so that the water transfers useful work efficiently to the runner in the first and second stages. The blade angle β is the angle between the relative velocity of water v_r and the peripheral velocity of the runner u. The nozzle of the cross-flow turbine, whose cross-sectional area is rectangular, discharges the jet to the full width of the runner and enters the runner at a small angle of attack to the tangent of the periphery of the runner. The first stage entrance blade angle is related to the first stage angle of attack α_1, according to the inlet velocity triangle as shown in Fig. 3.6.

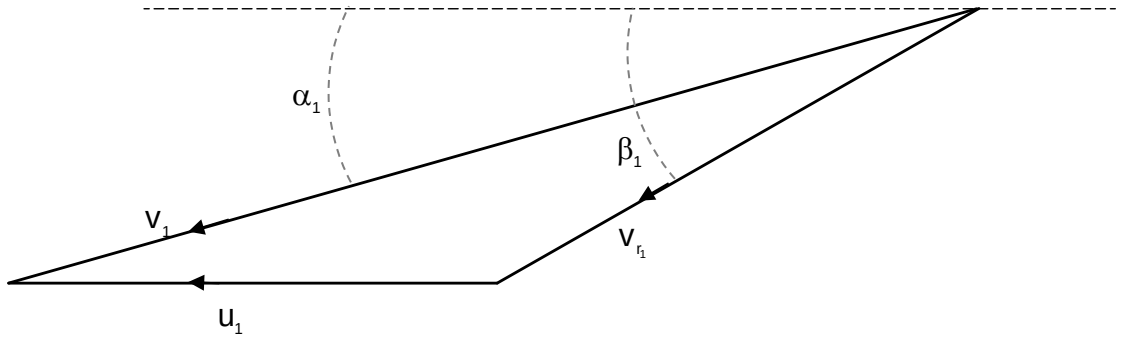

Fig. 3.6 Inlet velocity diagram.

$$v_1 \cos\alpha_1 = u_1 + v_{r_1} \cos\beta_1 \qquad \ldots (3.72)$$

Rearranging equation (3.45) we find that

$$u_1 = \frac{v_1}{2} \cos\alpha_1 \qquad \ldots (3.73)$$

Substituting equation (3.73) into equation (3.72) we find that

$$v_{r_1} \cos\beta_1 = \frac{v_1}{2}\cos\alpha_1 \quad \ldots (3.74)$$

Therefore, using equation (3.74) and the velocity diagram (Fig. 3.6)

$$\tan\beta_1 = \frac{v_1 \sin\alpha_1}{\frac{v_1}{2}\cos\alpha_1} \quad \ldots (3.75)$$

$$\tan\beta_1 = 2\tan\alpha_1 \quad \ldots (3.76)$$

Assuming no shock loss at entrance of the second stage and the deviation angle is nearly zero for the flow leaving the blades in the first stages; therefore, the inter stage angle of the blades is taken equal to 90^o (the first stage exit blade angle β_1' and the second stage inlet blade angle β_2' are equal to 90^o). On account of the small difference in elevation between the exit and entrance to the inner periphery, we assume that the water absolute velocity at exit to the blade of first stage, v_2', and the water absolute velocity at entrance to the blade of the second stage, v_1', are equal ($v_2' = v_1'$). Assuming that the inner exit and entrance water absolute velocities are equal and because the inner periphery velocities of the runner at the exit and entrance to the inner periphery are equal ($u_2' = u_1'$) and because ($\beta_2' = \beta_1'$) the inner velocities are congruent as shown in Fig. 3.2, accordingly ($\alpha_1' = \alpha_2'$). And also ($\beta_1 = \beta_2$) since they are corresponding angles of the same blade [68].

3.3.2 The Diameter Ratio

The thickness of the jet at the blade entrance s_1 and the thickness of the jet at the blade exit s_2 are related to the ratio of the inner to outer diameters (d_2/d_1) or radius ratio (r_2/r_1) as shown in Fig. 3.7. However, the thickness of the jet can be expressed in terms of the blade spacing. Therefore, if the thickness of the jet is measured at a right angle to the relative velocity,

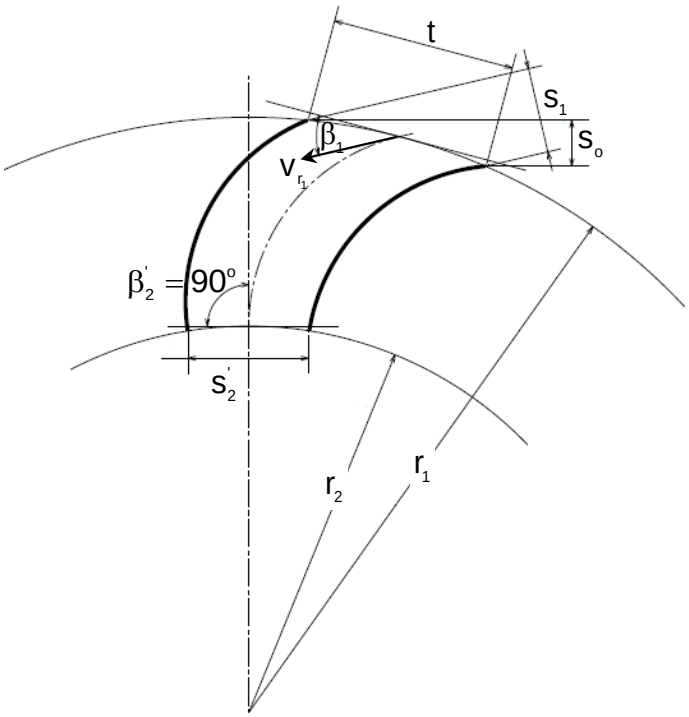

Fig. 3.7 Blade spacing.

$$s_1 = t_1 \sin\beta_1 \qquad \ldots (3.77)$$

and

$$s_2' = t_2' \sin\beta_2' \qquad \ldots (3.78)$$

Where t_1 is the entrance blade spacing and t_2' is the inner exit blade spacing.

However, $t_2' = \left(\frac{r_2}{r_1}\right) t_1$ and $\beta_2' = 90^o$ so equation (3.78) becomes

$$s_2^{'} = \left(\frac{r_2}{r_1}\right) t_1 \quad \ldots (3.79)$$

From conservation law of mass, the volume flow rate at the entrance and exit of the blade must be equal. However, as long as the diameter ratio is small, blades' passages will not be filled by the jet. As the diameter ratio increases the thickness of the jet at the blade exit s_2 decreases so the diameter ratio will be limited by

$$s_2^{'} = s_1 \left(\frac{v_{r_1}}{v_{r_2}^{'}}\right) \quad \ldots (3.80)$$

Increasing the ratio of the inner to outer diameters (d_2/d_1) over a limit range is not advisable because the amount of the water, which strikes the blades on the circumference of the runner, could not flow through so small blades' passages cross-section and reverse flow could result. On the other hand, decreasing the ratio of the inner to outer diameters under a limit range would not be efficient as separated jets would flow out of the wide blades' passages at the inner periphery.

In order to determine the ratio of the inner to outer diameters (d_2/d_1) it is necessary to know the change in the relative velocity, which is affected by the centrifugal force,

$$\left(v_{r_1}\right)^2 - \left(v_{r_2}^{'}\right)^2 = \left(u_1\right)^2 - \left(u_2^{'}\right)^2 \quad \ldots (3.81)$$

Rearrangement equation (3.81)

$$\left(v_{r_2}^{'}\right)^2 = \left(u_2^{'}\right)^2 - \left(u_1\right)^2 + \left(v_{r_1}\right)^2 \quad \ldots (3.82)$$

Substituting equations (3.77) and (3.79) in equation (3.80) and rearrangement so

$$v_{r_2}' = v_{r_1}\left(\frac{r_1}{r_2}\right)\sin\beta_1 \quad \ldots (3.83)$$

$$u_2' = u_1\left(\frac{r_2}{r_1}\right) \quad \ldots (3.84)$$

Substituting equations (3.83) and (3.84) in equation (3.82)

$$\left(v_{r_1}\left(\frac{r_1}{r_2}\right)\sin\beta_1\right)^2 = \left(u_1\left(\frac{r_2}{r_1}\right)\right)^2 - (u_1)^2 + (v_{r_1})^2 \quad \ldots (3.85)$$

$$\left(\left(\frac{v_{r_1}}{u_1}\right)\left(\frac{r_1}{r_2}\right)\sin\beta_1\right)^2 = \left(\frac{r_2}{r_1}\right)^2 - 1 + \left(\frac{v_{r_1}}{u_1}\right)^2 \quad \ldots (3.86)$$

$$\left(\frac{r_2}{r_1}\right)^2 - 1 + \left(\frac{v_{r_1}}{u_1}\right)^2 - \left(\frac{v_{r_1}}{u_1}\right)^2\left(\frac{r_1}{r_2}\right)^2 \sin^2\beta_1 = 0 \quad \ldots (3.87)$$

$$\left(\frac{r_2}{r_1}\right)^4 - \left(\frac{r_2}{r_1}\right)^2 + \left(\frac{v_{r_1}}{u_1}\right)^2\left(\frac{r_2}{r_1}\right)^2 - \left(\frac{v_{r_1}}{u_1}\right)^2 \sin^2\beta_1 = 0 \quad \ldots (3.88)$$

$$\left(\frac{r_2}{r_1}\right)^4 - \left(1 - \left(\frac{v_{r_1}}{u_1}\right)^2\right)\left(\frac{r_2}{r_1}\right)^2 - \left(\frac{v_{r_1}}{u_1}\right)^2 \sin^2\beta_1 = 0 \quad \ldots (3.89)$$

$$\left(\frac{r_2}{r_1}\right)^2 = \frac{\left(1 - \left(\frac{v_{r_1}}{u_1}\right)^2\right) + \sqrt{\left(1 - \left(\frac{v_{r_1}}{u_1}\right)^2\right)^2 + 4\left(\frac{v_{r_1}}{u_1}\right)^2 \sin^2\beta_1}}{2} \quad \ldots (3.90)$$

The diameter ratio $\left(\frac{d_2}{d_1}\right)$ can be calculated from rearrangement equation (3.90)

$$\frac{d_2}{d_1}=\left(\frac{\left(1-\left(\frac{v_{r_1}}{u_1}\right)^2\right)+\sqrt{\left(1-\left(\frac{v_{r_1}}{u_1}\right)^2\right)^2+4\left(\frac{v_{r_1}}{u_1}\right)^2\sin^2\beta_1}}{2}\right)^{\frac{1}{2}} \quad \ldots (3.91)$$

$$\frac{d_2}{d_1}=\left(\frac{\left(1-\left(\frac{1}{\cos\beta_1}\right)^2\right)+\sqrt{\left(1-\left(\frac{1}{\cos\beta_1}\right)^2\right)^2+4\left(\frac{1}{\cos\beta_1}\right)^2\sin^2\beta_1}}{2}\right)^{\frac{1}{2}} \quad \ldots (3.92)$$

The angle of absolute velocity at the first stage blade exit $\alpha_2^{'}$ can be determined from equation (3.82).

Substituting equations (3.84) in equation (3.82)

$$\left(v_{r_2^{'}}\right)^2=\left(\frac{r_2}{r_1}u_1\right)^2-\left(u_1\right)^2+\left(v_{r_1}\right)^2 \quad \ldots (3.93)$$

$$\left(v_{r_2^{'}}\right)^2=u_1^2\left(\left(\frac{r_2}{r_1}\right)^2-1+\left(\frac{v_{r_1}}{u_1}\right)^2\right) \quad \ldots (3.94)$$

$$\left(v_{r_2^{'}}\right)^2=u_1^2\left(\left(\frac{r_2}{r_1}\right)^2-1+\left(\frac{1}{\cos\beta_1}\right)^2\right) \quad \ldots (3.95)$$

$$v_{r_2^{'}}=u_1\left(\left(\frac{r_2}{r_1}\right)^2-1+\left(\frac{1}{\cos\beta_1}\right)^2\right)^{\frac{1}{2}} \quad \ldots (3.96)$$

$$\tan\alpha_2^{'}\frac{v_{r_2^{'}}}{u_2^{'}} \quad \ldots (3.97)$$

Substituting equations (3.84) and equation (3.96) in equation (3.97)

$$\tan\alpha_2' = \frac{u_1\left(\left(\frac{r_2}{r_1}\right)^2 - 1 + \left(\frac{1}{\cos\beta_1}\right)^2\right)^{\frac{1}{2}}}{u_1\left(\frac{r_2}{r_1}\right)} \quad \ldots (3.98)$$

$$\alpha_2' = \tan^{-1}\frac{\left(\left(\frac{r_2}{r_1}\right)^2 - 1 + \left(\frac{1}{\cos\beta_1}\right)^2\right)^{\frac{1}{2}}}{\left(\frac{r_2}{r_1}\right)} \quad \ldots (3.99)$$

3.3.3 Blade Radius of Curvature

The blade radius of curvature can be determined from a circle whose center lies at the intersection of two lines, one perpendicular on the relative velocity of the entrance blade at first stage and the other perpendicular on the tangent to the inner periphery as shown in Fig. 3.8,

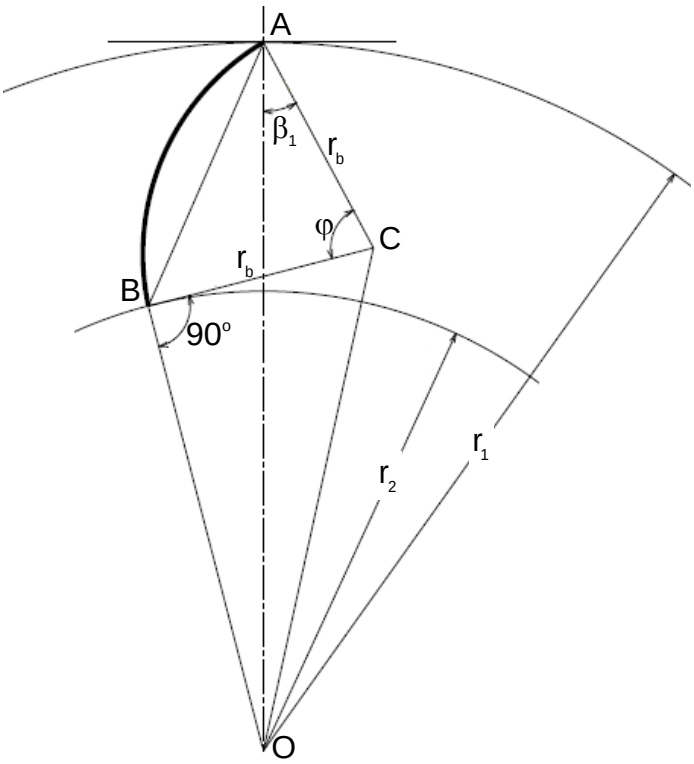

Fig. 3.8 Blade radius of curvature

From the Fig. 3.8 and using the cosine rule we can obtain

$$r_2^2 + r_b^2 = r_1^2 + r_b^2 - 2r_1 r_b \cos\beta_1 \quad \ldots (3.100)$$

When r_1 is the outer radius of the runner blade, r_2 is the inner radius of the runner blade and r_b is the radius of the blade curvature.

$$r_2^2 + r_b^2 - r_1^2 - r_b^2 = -2r_1 r_b \cos\beta_1 \quad \ldots (3.101)$$

$$r_2^2 - r_1^2 = -2r_1 r_b \cos\beta_1 \quad \ldots (3.102)$$

$$r_1^2 - r_2^2 = 2r_1 r_b \cos\beta_1 \quad \ldots (3.103)$$

$$r_b = \frac{r_1^2 - r_2^2}{2r_1 r_b \cos\beta_1} \quad \ldots (3.104)$$

3.3.4 The Dimension of the Runner

The runner diameter can be determined from the following equation,

$$u_1 = \frac{\pi d_1 N}{60} \quad \ldots (3.105)$$

Substituting equations (3.73) in equation (3.105),

$$\frac{v_1}{2}\cos\alpha_1 = \frac{\pi d_1 N}{60} \quad \ldots (3.106)$$

$$\frac{c(2gH)}{2}\cos\alpha_1 = \frac{\pi d_1 N}{60} \quad \ldots (3.107)$$

$$d_1 = \frac{30c(2gH)^{\frac{1}{2}}\cos\alpha_1}{\pi N} \quad \ldots (3.108)$$

$$d_1 = \frac{42.3c\sqrt{H}\cos\alpha_1}{N} \quad \ldots (3.109)$$

The width of the cross-flow turbine runner can be determined by knowing the diameter of the runner and the head of the water as well as the volume flow rate, which is equal to the velocity of water through the nozzle times the nozzle area. Therefore,

$$Q = s_o B_w c(2gH)^{\frac{1}{2}} \quad \ldots (3.110)$$

Where Q is the volume flow rate, s_o the thickness of the jet in the nozzle,

$$Q = c_j d_1 B_w c(2gH)^{\frac{1}{2}} \quad \ldots (3.111)$$

$$d_1 = \frac{Q}{c_j B_w c(2gH)^{\frac{1}{2}}} \quad \ldots (3.112)$$

Substituting equations (3.108) in equation (3.112),

$$\frac{Q}{c_j B_w c(2gH)^{\frac{1}{2}}} = \frac{30c(2gH)^{\frac{1}{2}}\cos\alpha_1}{\pi N} \quad \ldots (3.113)$$

$$B_w = \frac{\pi N Q}{30 c_j c^2 (2gH)\cos\alpha_1} \quad \ldots (3.114)$$

c_j is an experimental coefficient which relates the thickness of the jet in the nozzle to the runner diameter. c_j value lies between 0.075 and 0.10 according to [31]. Therefore, substituting c_j into equation (3.114) and assuming $c = 0.98$ so the equation becomes

$$Q = 0.074\frac{NQ}{H\cos\alpha_1} \quad \text{to} \quad 0.055\frac{NQ}{H\cos\alpha_1} \quad \ldots (3.115)$$

3.3.5 The Number of the Runner Blades

The number of blades is one of the important considerations of the runner design. A large number of runner blades will increase losses and the cost of the turbine. On the other hand, a small number of runner blades will increase losses by flow separation on the back side of the blades.

$$n_b = \frac{2\pi r_1}{t_1} \quad \ldots (3.116)$$

Where n_b is the number of blades and t_1 is the entrance blade spacing

$$t_1 = \frac{s_1}{\sin\beta_1} \quad \ldots (3.117)$$

Substituting equations (3.117) in equation (3.116) and $s_1 = k\,d_1$

$$n_b = \frac{\pi}{k}\sin\beta_1 \quad \ldots (3.118)$$

3.4 Outline of the Theoretical Analysis

The geometry of turbine was investigated in this chapter and the parameters/equations controlling the performance of the cross-flow turbine were identified. The parameters/equations are used in the modelling and performance improvement of the turbine reported in Chapters 3 and 4.

Chapter Four

Numerical Modelling and Techniques in CFX

Chapter Four

Numerical Modelling and Techniques in CFX

4.1 Introduction

In this chapter, the background theories of computational fluid dynamics (CFD) and the numerical tools used in flow simulation are introduced. Accordingly, understanding CFD complexity is very important in any flow simulation investigation. The flow field numerical simulation of cross-flow turbine was undertaken using various available computational fluid dynamics (CFD) simulation codes based on the Reynolds Averaged Navier Stokes equations (RANS) and Shear Stress Transport (SST) turbulence models. Most CFD codes, are powerful tools, utilize a finite volume to solve the governing equations of fluid motion numerically on a user defined computational grid and have been designed for use in a Computer Aided Engineering (CAE) environment.

“Computational Fluid Dynamics (CFD) can be described as the use of computers to produce information about the ways in which fluids flow in given situations. CFD embraces a variety of technologies including mathematics, computer science, engineering and physics, and these disciplines have to be brought together to provide the means of modelling fluid flows. Such modelling

is used in many fields of science and engineering but, if it is to be useful, the results that the model yields must be a realistic simulation of a fluid in motion. At present, this depends entirely on the problem being simulated, the software being used and the skill of the user" [69].

The concept of computational fluid dynamics (CFD) is to predict the flow of the fluid and any related phenomena (separation, re-attachment, pulsation … etc.) scientifically to a given situation. To do that the CFD code utilizes the computer in the numerical calculation of the equations that govern the fluid flow. In order to achieve acceptable results, it is necessary for the CFD user to have an understanding of the main characteristics of fluid flow to be modelled as well as the equations that govern such flow. The differential equations that govern the flow must be transformed to a large number of algebraic equations. The solution can be achieved from intensive iteration of these equations by utilizing powerful computer hardware and software; hence, some of the hydrodynamics simulations can be obtained using these computer tools.

Computational fluid dynamics (CFD) is a very powerful technique and covers a wide range of engineering applications. Its application and development have undergone considerable growth. In the discipline of flow hydrodynamics research this technique has become increasingly significant, and prominent for investigating the hydrodynamics of hydraulic turbomachines. This is mainly due to the tremendous technological advancements in the computer power. However, before start modelling any turbomachine, it is extremely important to select appropriate code that can accurately and quickly simulate the problem [70].

A complete analysis of the internal flow, which is turbulent, two-phase and three dimensional in nature, was undertaken by simulating it using various CFD simulation codes. The procedures involved in the modelling fluid flows, comprise the following steps. First, the geometry of a cross-flow turbine was designed by the CATIA V5 computer aided design (CAD) program. This was then imported into CFD simulation code meshing tool for grid generation. The generated mesh was then imported into the pre-processor, for setting the suitable boundary conditions. Once the changes in pre-processor were saved, a new definition file (*.def) was created for later import into CFD code solver. That file was the starting point in each simulation, and the subsequent simulation results were processed in post-processor.

4.2 CFD Simulation Codes

Various computational fluid dynamics (CFD) simulation codes, which are available nowadays, have been designed for use in a computer aided engineering (CAE) environment. However, in turbomachine modelling, it is especially important at the start of the process more accurate CFD code is chosen which can accurately and quickly simulate the problem. In order to do this, it is necessary for the CFD user to have an understanding of the fundamental characteristics of fluid flow for a given situation, as well as the numerical tools used for flow simulation [71].

University of Hertfordshire has access to several CFD simulation codes, such as PHOENICS (it is the first commercial CFD software [72]), STAR-CCM+, ANSYS CFX and so on. Students, researchers and staff have taken advantage of available CFD simulation codes to prepare themselves and specialize in

simulating and coping with high levels of complexity in a wide range of engineering application through the use of these CFD simulation codes.

PHOENICS, STAR-CCM+ and ANSYS CFX were selected in the current investigation to choose a suitable CFD simulation code. After consulting a number of experts, and attending several training courses held by companies such as CHAM (PHOENICS), CD-adapco (STAR-CCM+) and ANSYS. A number of code's interesting features were investigated including the geometry modelling and geometry import capabilities; grid generation or meshing capabilities; the solver capabilities; post-processing capabilities; available information and user support.

Available information and user support enable users to overcome some of the difficulties and understanding the CFD simulation code properly in a short period of time. When users and especially new CFD simulation code users try to simulate a difficult case, it is helpful if there is easy access to CFD simulation code's information and very active research and development team with good quality user support. However, the main critical factors to choose a CFD simulation code are its capabilities and high-performance to simulate a particular case. ANSYS CFX was chosen (as explained in section 4.7, hereafter) to simulate the entire internal flow for cross-flow turbine, which is turbulent, two-phase and three dimensional in nature. ANSYS CFX advanced solver technology is the key for accomplishing accurate and reliable solutions quickly and robustly [73]. ANSYS CFX also possesses ANSYS TurboGrid which is a powerful tool that lets users create high quality hexahedral meshes for turbomachinery [74]. Turbine designers and manufacturers use widely CFX in their simulations [75-77], which proves the reliability and accuracy of ANSYS

CFX.Typically, CFD simulation codes consist of three main structures, which are pre-processor, solver and post-processor. These three main structures influenced accurate and quick simulation of CFD simulation codes.

4.3 Pre-Processor

The pre-processing of the CFD simulation code is the first step in performing a CFD simulation analysis through which the user identifies the computational domain. It is used to input the problem and subsequently transform the input into a suitable form to be used by the solver. The accuracy of CFD simulation results strongly depends on the capability of the pre-processor tools to prepare and also be able to efficiently modify a high quality CFD model, overcoming all the difficulties that arise by the large model size and their complexity [78]. However, the accuracy and the model simulation time are influenced by the skill of the simulation user. The pre-processing includes

- Defining the geometry of the region for computational domain [79],
- Design and create the grid or Meshing,
- Defining the physical models, and
- Defining the boundary conditions.

4.4 Solver

The numerical solver of CFD simulation code is the second step in performing a CFD simulation analysis. The CFD solver is used to set the numerical factors, compute and monitor the solution as shown Fig. 4.1. In CFD simulation codes, the solver is often operated as a “black box” [80]. However, understanding the numerical tools and the pre-processing including geometry, mesh, physical

models and boundary conditions are required in order to produce the desired results from solving the discretised governing equations by utilizing powerful computer hardware and software. The results obtained in solver step are fed into the post-processor for examination.

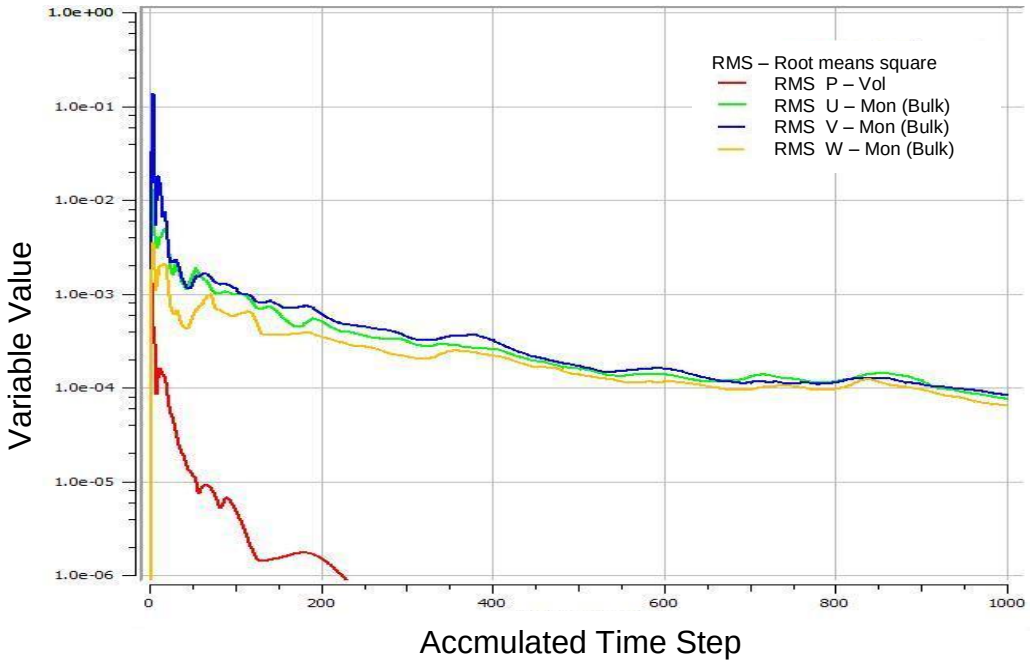

Fig. 4.1 Plot of residual proceeding with accumulated time step for simulation in CFX.

4.5 Post-Processor

The post-processing of the CFD simulation code, is the last step in performing a CFD simulation analysis, and performs flow field visualization and quantitative data analysis on CFD results. CFD simulation codes provide full-field data in their results files. Plotting (graphical result) is the quickest and the most efficient technique to display enormous quantities of the data. CFD simulation codes have the capability to represent and plot the flow variables on a point, a line and a plane or over a three dimensional region of interest. Most CFD post-processor includes many tools for analyzing CFD results [81].

- Isosurfaces
- Vector plots
- Contour plots
- Streamlines and pathlines
- XY plotting
- Animation creation

The flowchart of the three processes detailed in sections 4.3 to 4.5 is depicted in Fig. 4.2.

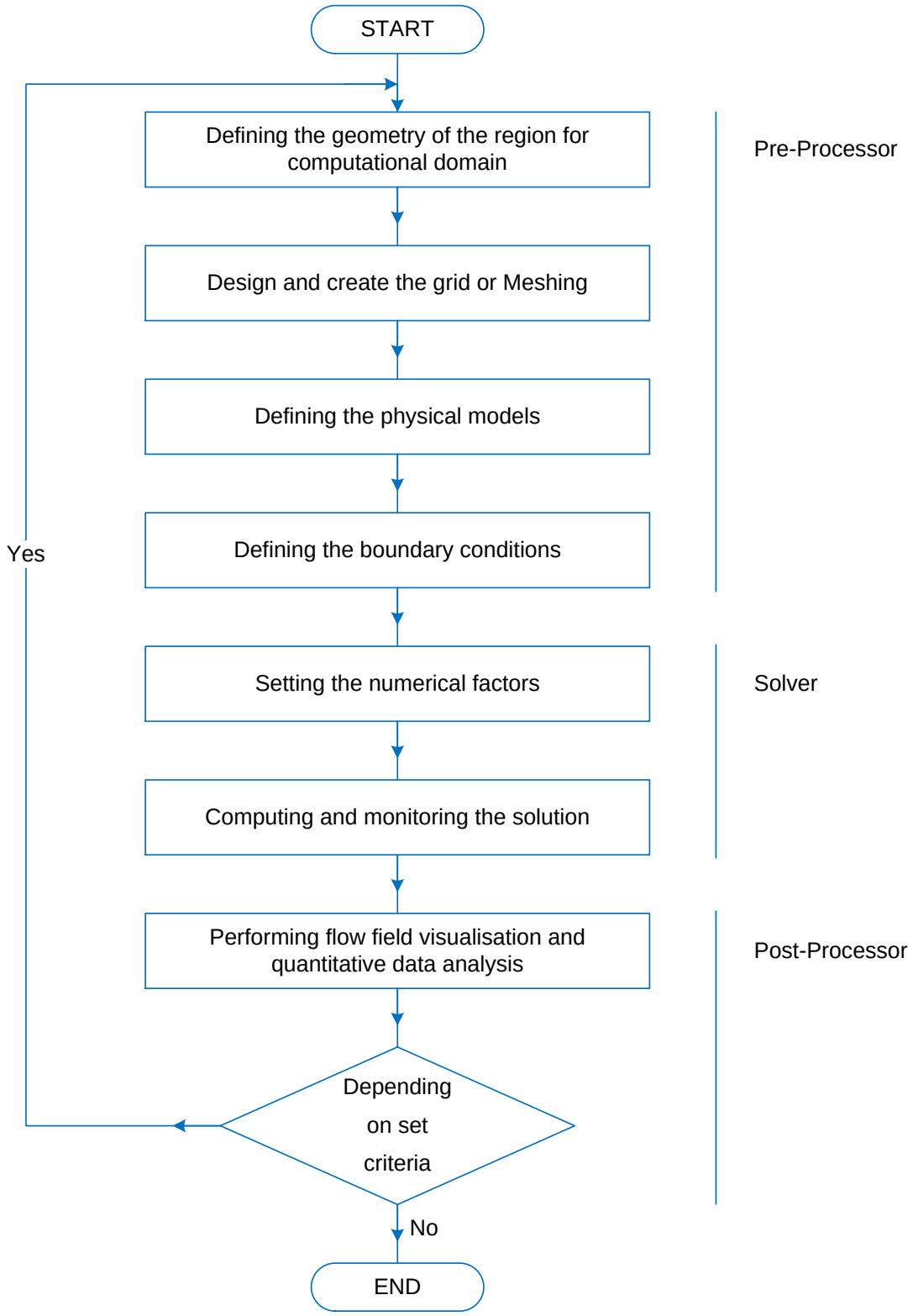

Fig. 4.2 A Flowchart of the CFD analysis processes.

* As detailed in Chapter 4 (*The number and quality of the selected cells*).

4.6 Geometry Modelling and Grid Generation

4.6.1 Geometry Modelling

The design created for the cross-flow turbine was based on the specifications provided by Mockmore and Merryfield [31], Aziz and Desai [46] and Kaniecki [59]. However, some modifications were made in order to obtain optimum performance. The drafting and design capabilities of computer aided design software (CAD), CATIA V5, were utilized to create the geometry model of the turbine. CATIA V5, by Dassault Systemes, at its core is a full functioned geometry modelling tool that is widely used in the industry [82]. The turbine case was created in the simplest way so as to get a better mesh distribution as the quality of the mesh depends on the complexity of the geometry. This resulted in good mesh quality as shown in Fig. 4.3.

The most important aspect of CATIA V5 is that it integrates efficiently with CFD simulation codes. This aspect allows file formats like IGES, STEP and STL for the complex geometry created in CATIA V5 to be smoothly imported into CFD simulation codes such as PHONIES, STAR CCM+, and ANSYS. Particularly, ANSYS CFX has the capability to import CAD data file directly without need to transfer it to another format, for example, in International Graphical Exchange Standard (IGES) format. This direct translation makes ensure an optimum geometry quality input. In addition, all information, such as part, property names and numbers, as well as assembly hierarchy, are also transferred exactly as built in the CAD system [77].

The quality of the imported geometry is one of the principal factors governing the time taken to extract the proper computational domain. The time and

accuracy of the simulation in any CFD simulation code depend on the quality of the mesh, which in turn depends on the computational domain. Modern CFD simulation codes, including ANSYS CFX have the capability to import existing computer aided design (CAD) geometry or create the three-dimensional geometry from scratch. ANSYS DesignModeller™ software provides powerful tools to create three-dimensional geometry (however, the software is not as advanced as CATIA V5) as well as to import and manipulate existing CAD geometry. ANSYS BladeModeller™ software is specialized for three-dimensional design of rotating machinery components [83]. It is also able to import and manipulate existing blade CAD geometry.

As the flow, in the cross-flow turbine, is of a complex and a three-dimensional nature, ANSYS BladeModeller™ software was utilized to design and optimize the runner. ANSYS BladeModeller™ software was selected because it, has the capability to modify individual parameters smoothly, is exclusively developed to design runner blades and configuration of the turbine runner. Finally, ANSYS DesignModeller™ software was utilized to extract the computational domain as shown in Fig. 4.4.

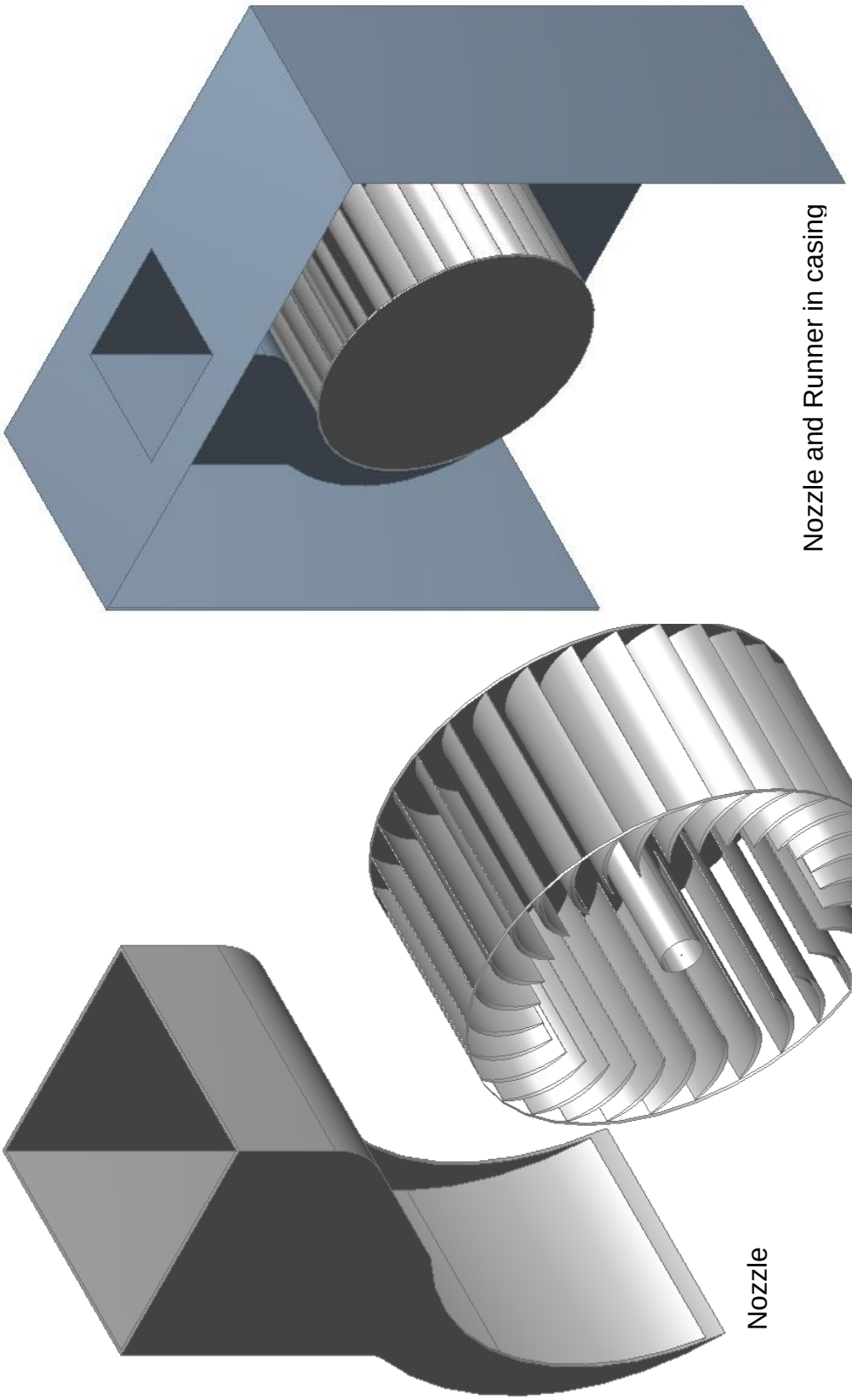

Fig. 4.3 3D Views of the cross-flow turbine tested.

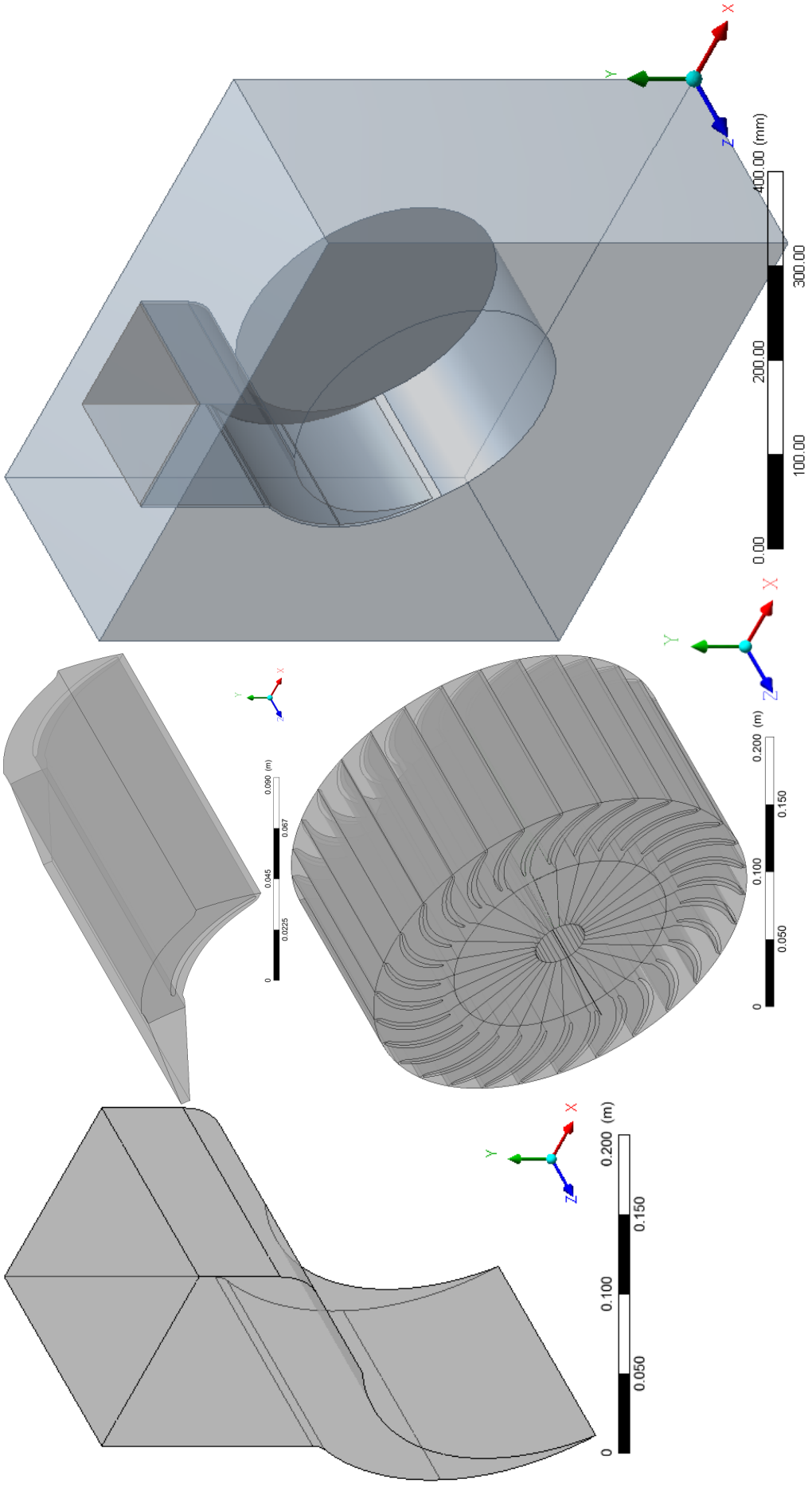

Fig. 4.4 3D Views of the computational domains of the cross-flow turbine tested.

4.6.2 Mesh Generation

Mesh generation is a discretization of a computational domain into numerous small control volumes. The governing equations are integrated over each control volume, such that the relevant quantity (mass, momentum, energy, etc.) is conserved in a discrete sense for each control volume [84]. All together, these small control volumes comprise the mesh [85]. Before constructing the mesh a computational domain for the simulation of the cross-flow turbine must be available. The computational domain includes the whole cross-flow turbine was made with a full scale model, from the inlet to the outlet, which composed of the casing, the nozzle and the runner as shown in Fig. 4.4. ANSYS CFX-Mesh and TurboGrid mesh software are employed to generate an adapted mesh for the turbine components using structured & unstructured grid.

ANSYS CFX-Mesh provides a mesh generator with high quality meshes for use in CFD simulations [86]. ANSYS CFX-Mesh imports computational domain definitions from DesignModeller^{TM} or any similar tools supported by ANSYS e.g. CATIA V5. It has powerful tools with a number of features enable the user to manipulate and control the mesh resolution in the each portion of the computational domain, including bodies, faces and edges. These features are utilized to get better distribution of the mesh density, finer mesh in regions where the variations of the flow variables are larger and coarser anywhere else. Controlling the mesh resolution can be accomplished by controlling the size of the elements, inflation layers and virtual topology of the entire computational domain or different sections may be individually controlled. Generally, Variable gradients on smaller element's size are more accurately calculated. Therefore, finer mesh was required where the variations of the flow variables were large.

Inflation layers are significantly important, in order to get better mesh merge between different regions, and capture the boundary layer effects. Finally, ANSYS CFX-Mesh creates finer meshes at the edge of each face. Virtual topology was used to merge the faces where a finer mesh is unnecessary.

ANSYS TurboGrid software offers designers and analysts of turbomachinery with mesh creation tailored for specific the blade geometries [74]. The runner blades' computational domain was meshed in ANSYS TurboGrid using the ATM optimization mesh method which imports computational domain definitions from ANSYS BladeModeller™ software. ANSYS TurboGrid was selected for meshing because it is a highly hexahedral mesh generator, specifically developed for turbomachinery applications. As mentioned earlier, the time and accuracy of the simulation in any CFD simulation code depend on the mesh quality, which in turn depends on the number of the elements and the mesh aspect ratio. The fine mesh was employed in the numerical simulation to ensure an appropriate development of flow in the whole runner channels and to resolve/capture the entire internal flow especially flow separation when operating at different conditions. A fine and high quality hexahedral structured mesh was obtained for the runner blades' computational domain by using the ATM optimization mesh method as shown in Fig. 4.5.

Meshes for other components of the cross-flow turbine (casing and nozzle) were performed with ANSYS CFX-Mesh, utilizing tetrahedral cells with adding inflation layers at desired surfaces as shown in Fig. 4.6. The cross-flow turbine model was created using the computer aided design software, CATIA V5. The unstructured tetrahedral mesh generation is one of the most useful features available in ANSYS CFX-Mesh, which allows smoothly meshing of complex

geometries (it has great flexibility in fitting complicated domains [87]). In order to capture the velocity and pressure gradients near a wall. A very fine structured mesh was generated using the mesh inflation option available in CFX Mesh. By adopting various mesh control parameters it was possible to get the required mesh quality.

As mentioned earlier, the time and accuracy of the simulation in any CFD simulation code depend on the mesh quality, which in turn depends on the number of the elements and the mesh aspect ratio. Therefore, it is essential before CFD simulation results are obtained, to optimize the number of the elements in the computational domain. The solution mesh dependency was tested by starting with a coarse mesh. The number of the elements was increased until the CFD simulation results were no longer significantly affected by any further. A minimum residual target of 10^{-4} was set as a convergence criterion. According to the mesh independency test, shown in Figs. 4.7 and 4.8, the total number of the elements in the entire cross-flow turbine computational domain was 1,713,426. The number of the elements in the runner computational domain was 986,370 and for the rest of the turbine were 727,056.

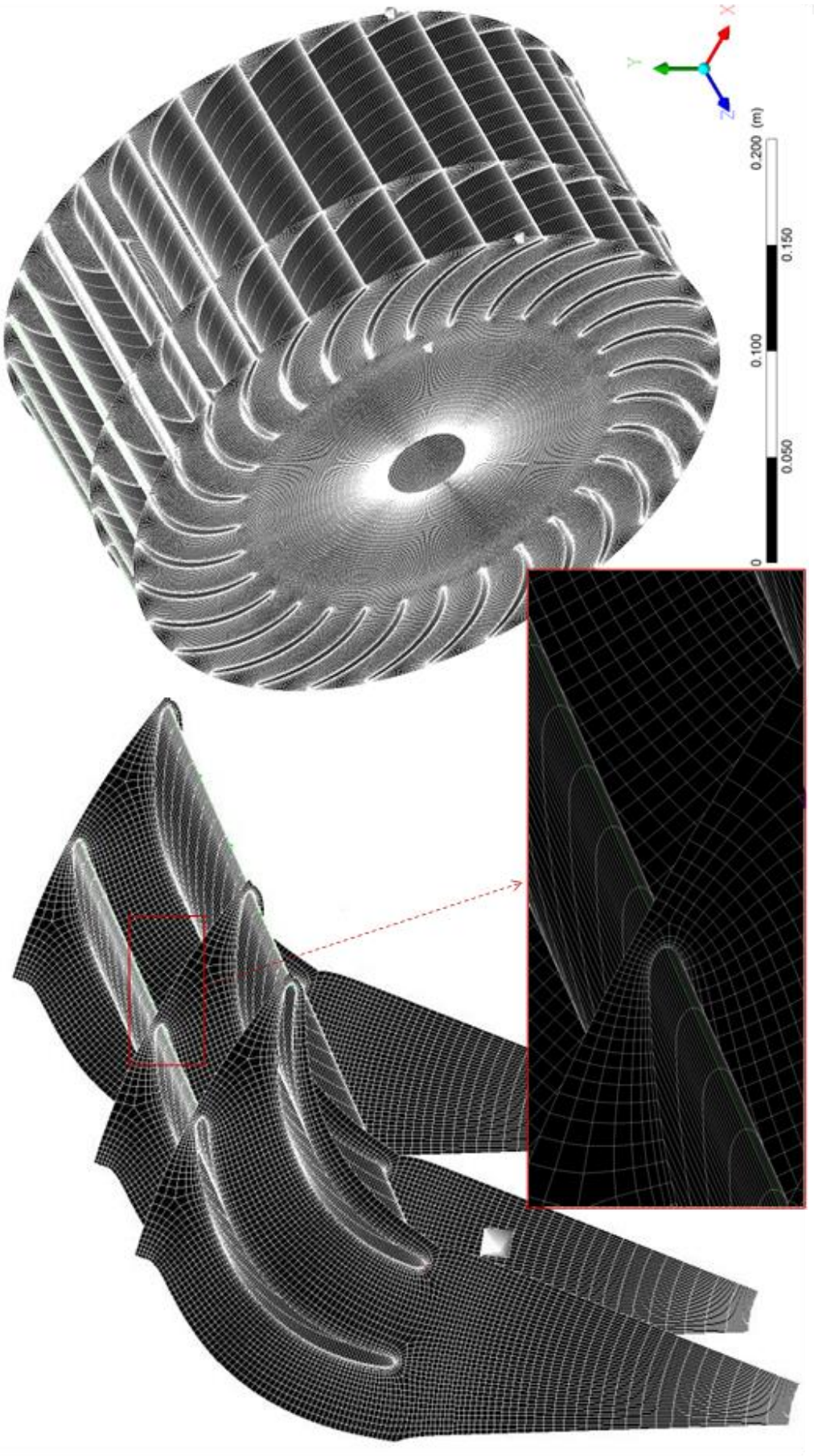

Fig. 4.5 Hexahedral mesh of the runner.

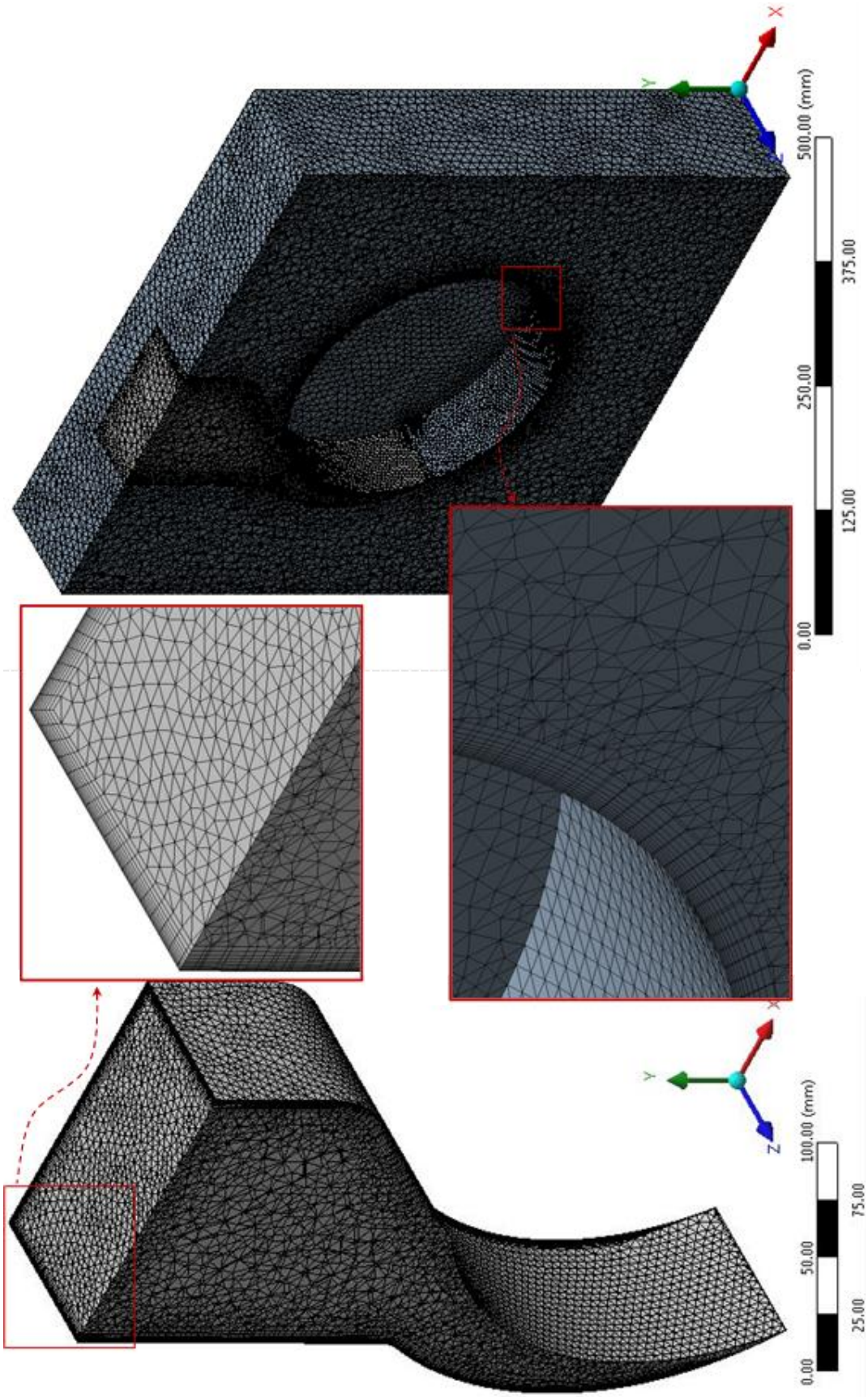

Fig. 4.6 Tetrahedral mesh with inflation layers of the half cross-flow turbine tested without the runner.

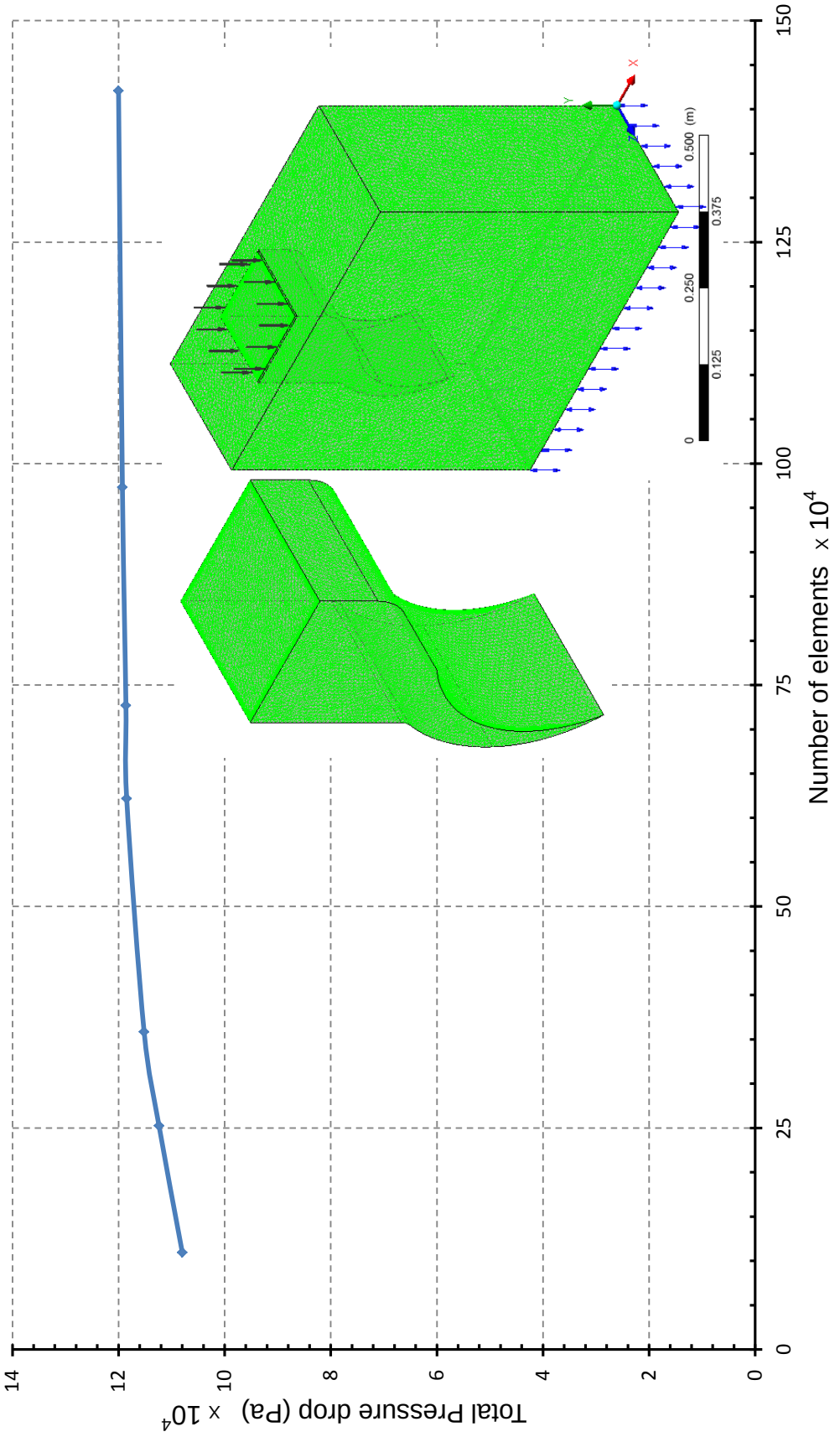

Fig. 4.7 Results of mesh dependency analysis of the turbine without runner.

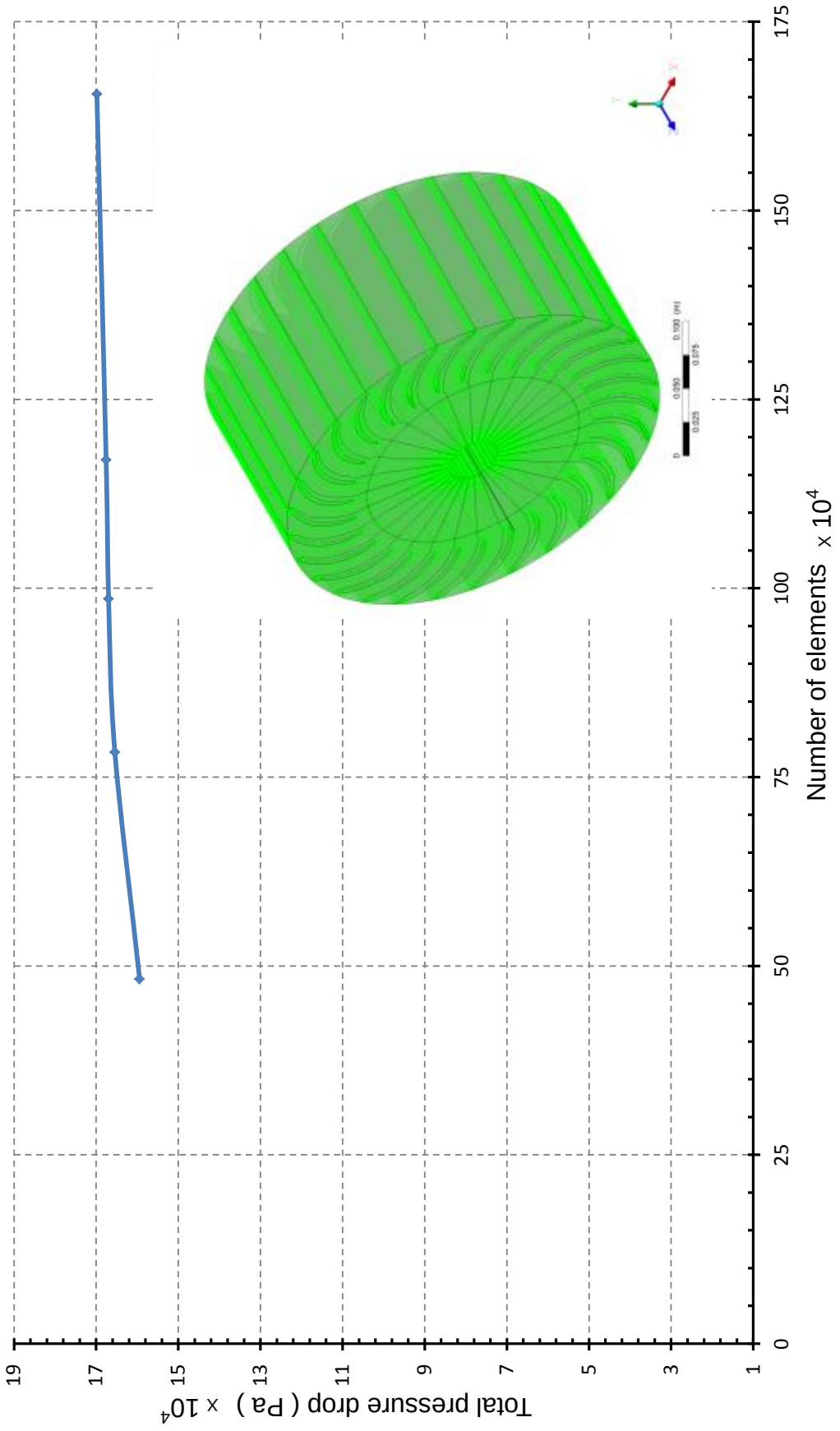

Fig. 4.8 Results of mesh dependency analysis of the runner.

4.6.2.1 Mesh Quality

Mesh quality plays an important role in the accuracy of the CFD simulation results. A high quality mesh is required to resolve satisfactorily the fundamental flow physics implied within the computational domain. This can be accomplished by generating a mesh contains the highest number possible of the elements which have properties similar to the optimal element. The optimal element is an element with the best nodes' distribution [88]. The numbers of the elements and the mesh aspect ratio as well as rapid changes in the mesh density are parameters that can affect mesh quality. Therefore, it is essential to check the quality of the mesh in order to avoid any numerical problems further on and to achieve accurate results. A guideline for ANSYS CFX mesh quality is in mesh "quality metrics", one represents the perfect quality and zero represents the worst quality. It is recommended to keep mesh quality higher than 0.1 [89]. The mesh quality of cross-flow turbine apart from the runner is shown in Fig. 4.9. The horizontal axis represents the mesh quality and the vertical axis represents the quantity of elements.

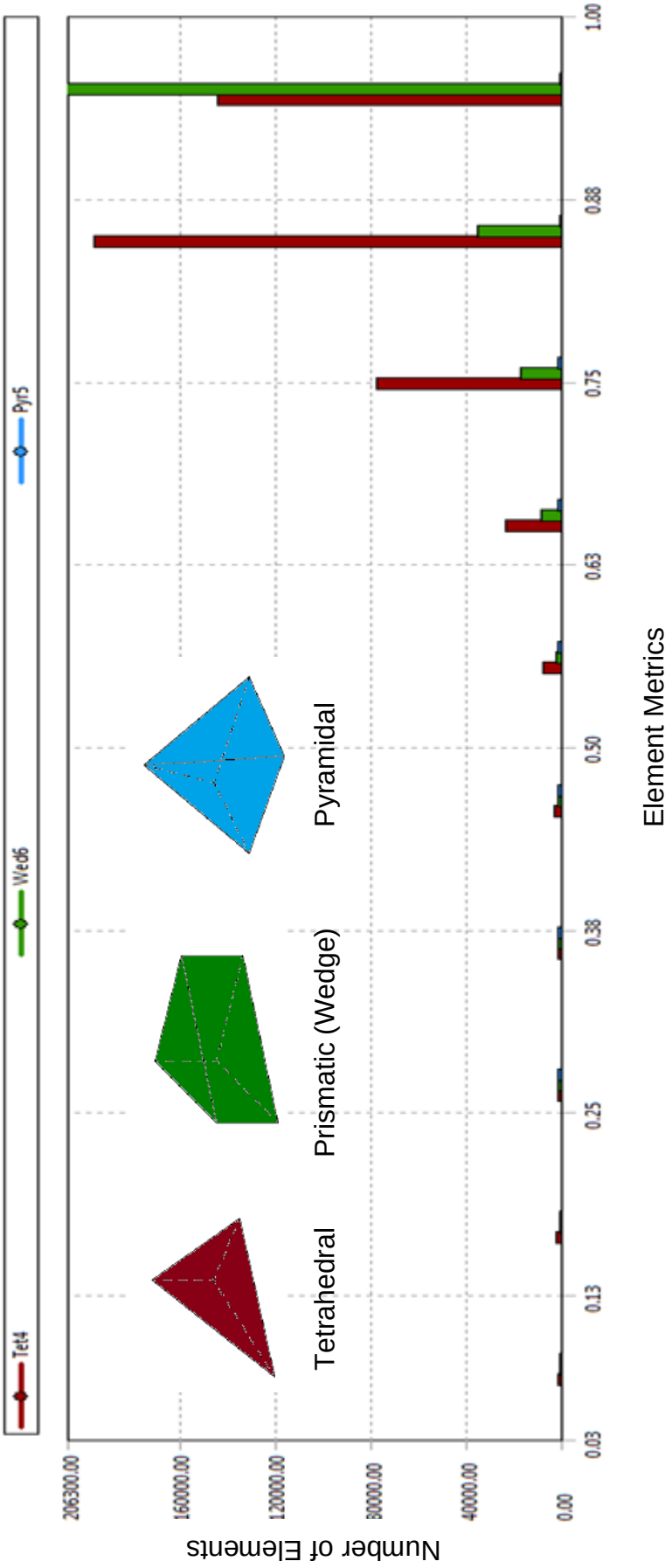

Fig. 4.9 Mesh quality of the cross-flow turbine tested without runner (as detailed in section 4.6.2.1).

A guideline for ANSYS TurboGrid mesh quality is in mesh limits. The mesh quality with mesh limits of the cross-flow turbine runner blade is shown in Fig. 4.10.

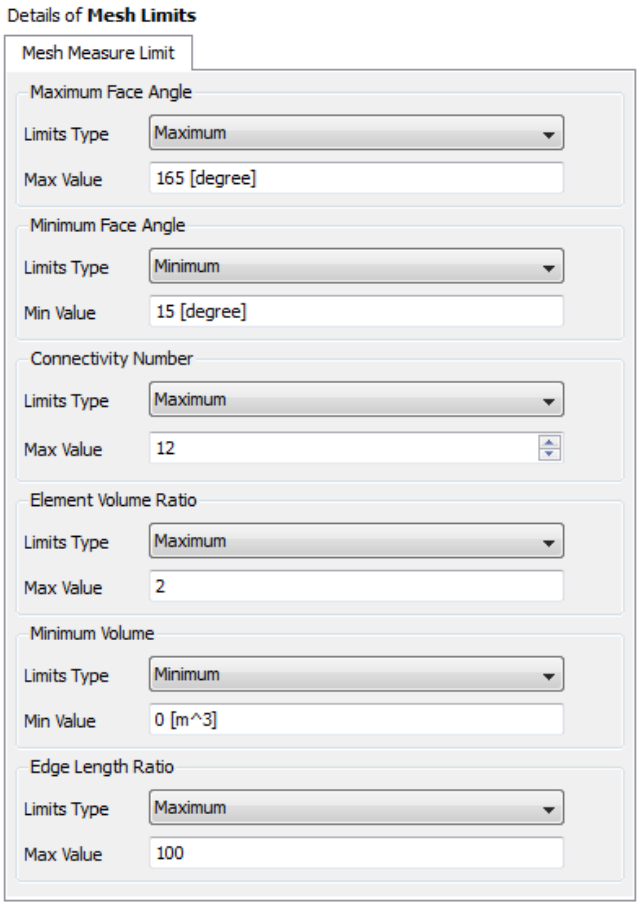

Fig. 4.10 (a) Mesh quality of the runner blade of the cross-flow turbine tested.

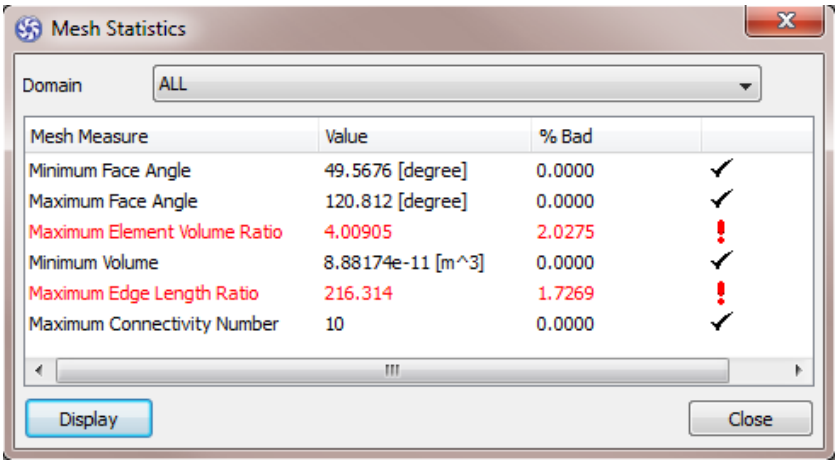

Fig. 2.10 (b) Mesh quality of the runner blade of the cross-flow turbine tested.

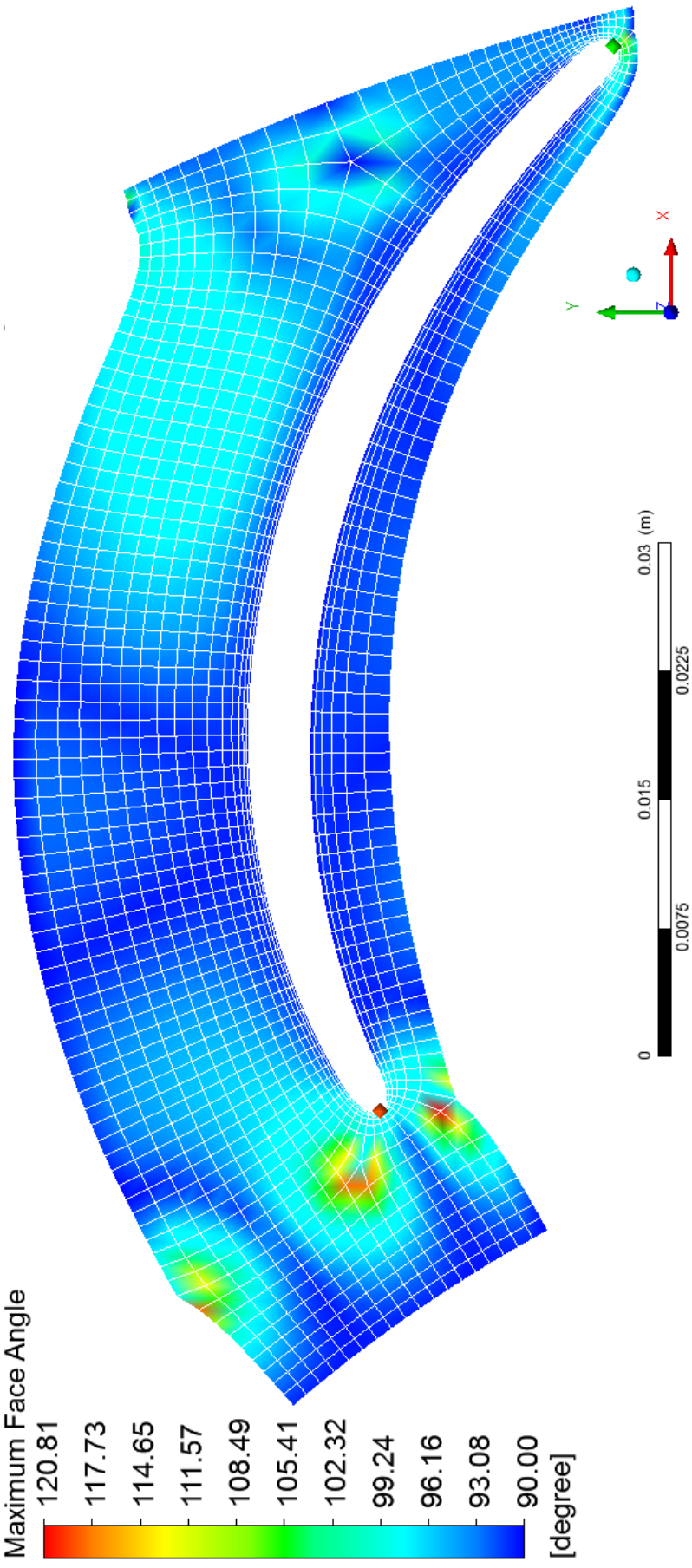

Fig. 4.10 (c) Mesh quality of the runner blade of the cross-flow turbine tested.

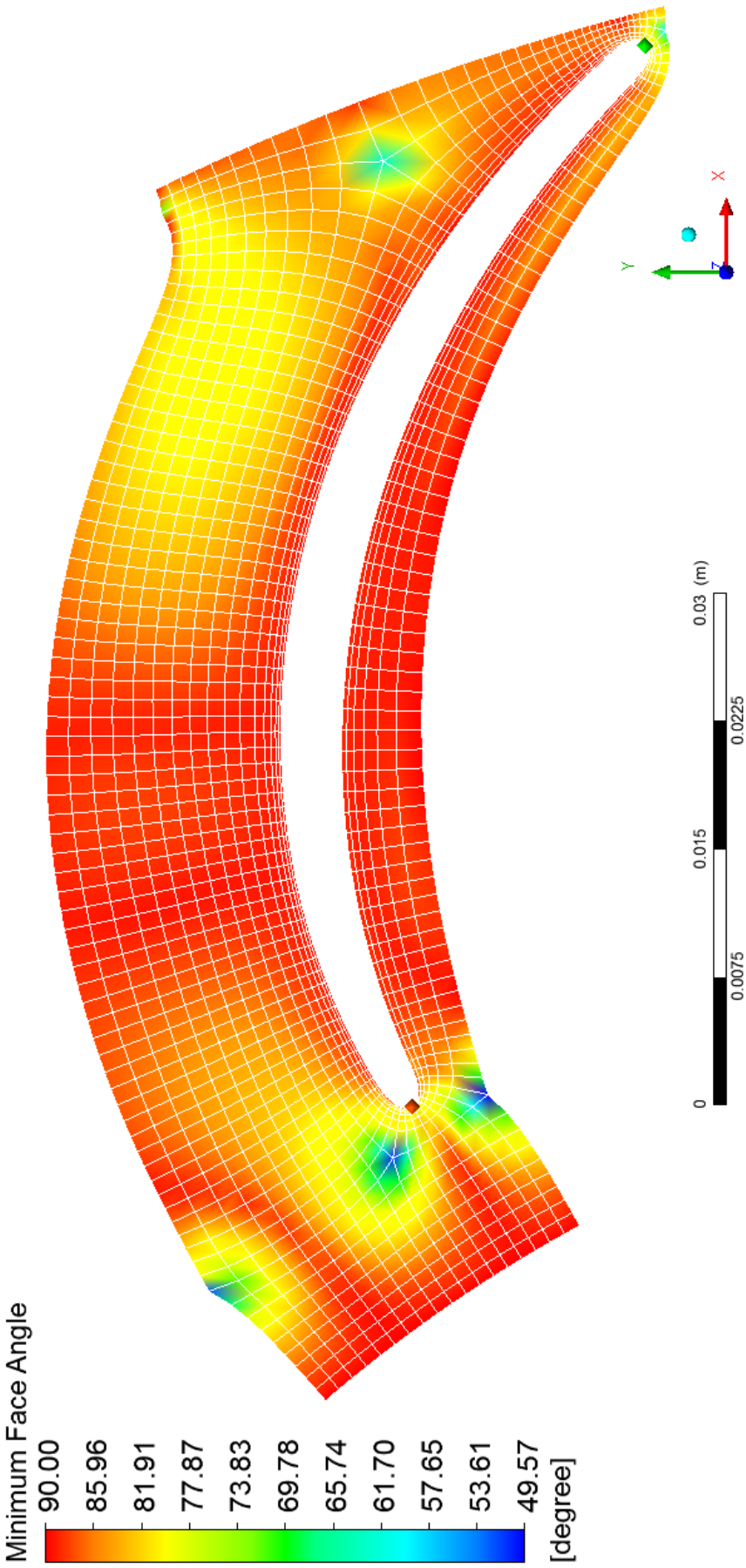

Fig. 4.10 (d) Mesh quality of the runner blade of the cross-flow turbine tested.

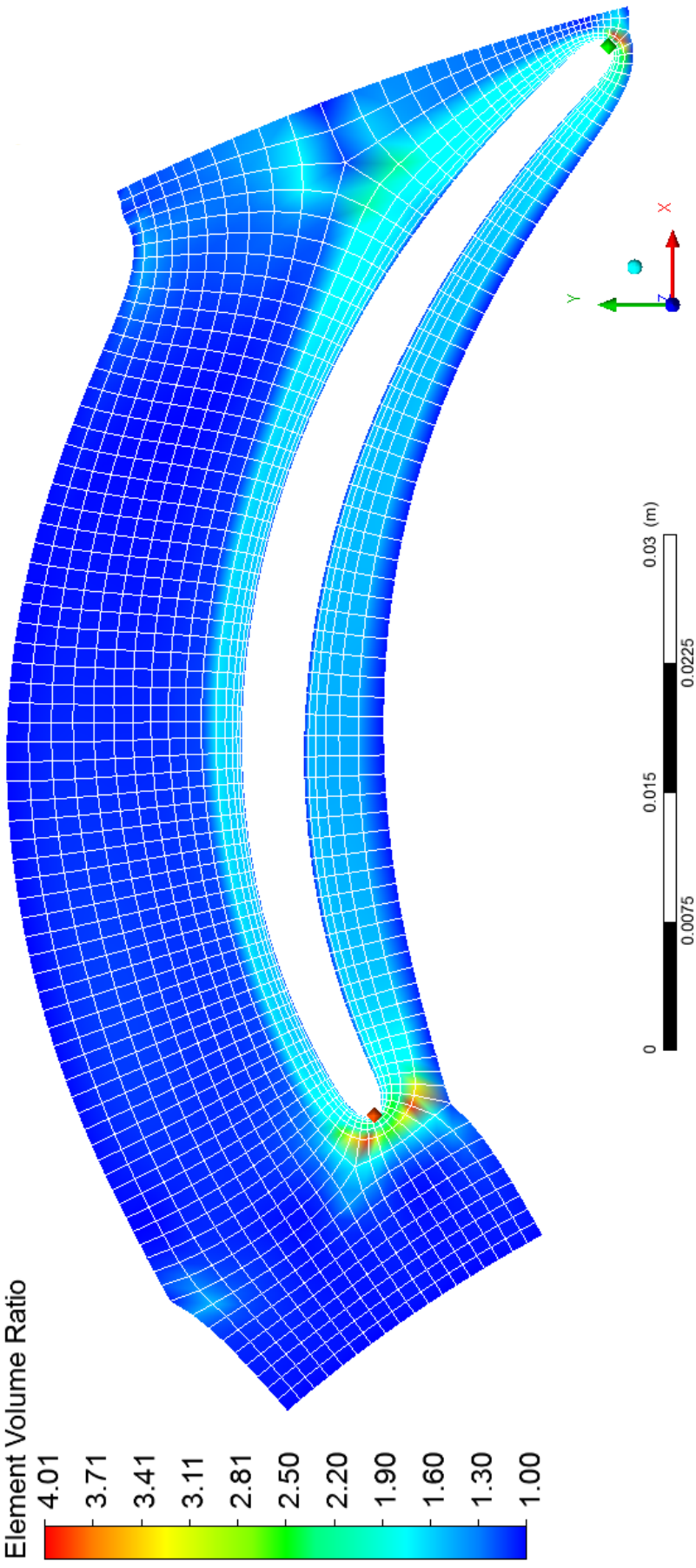

Fig. 4.10 (e) Mesh quality of the runner blade of the cross-flow turbine tested.

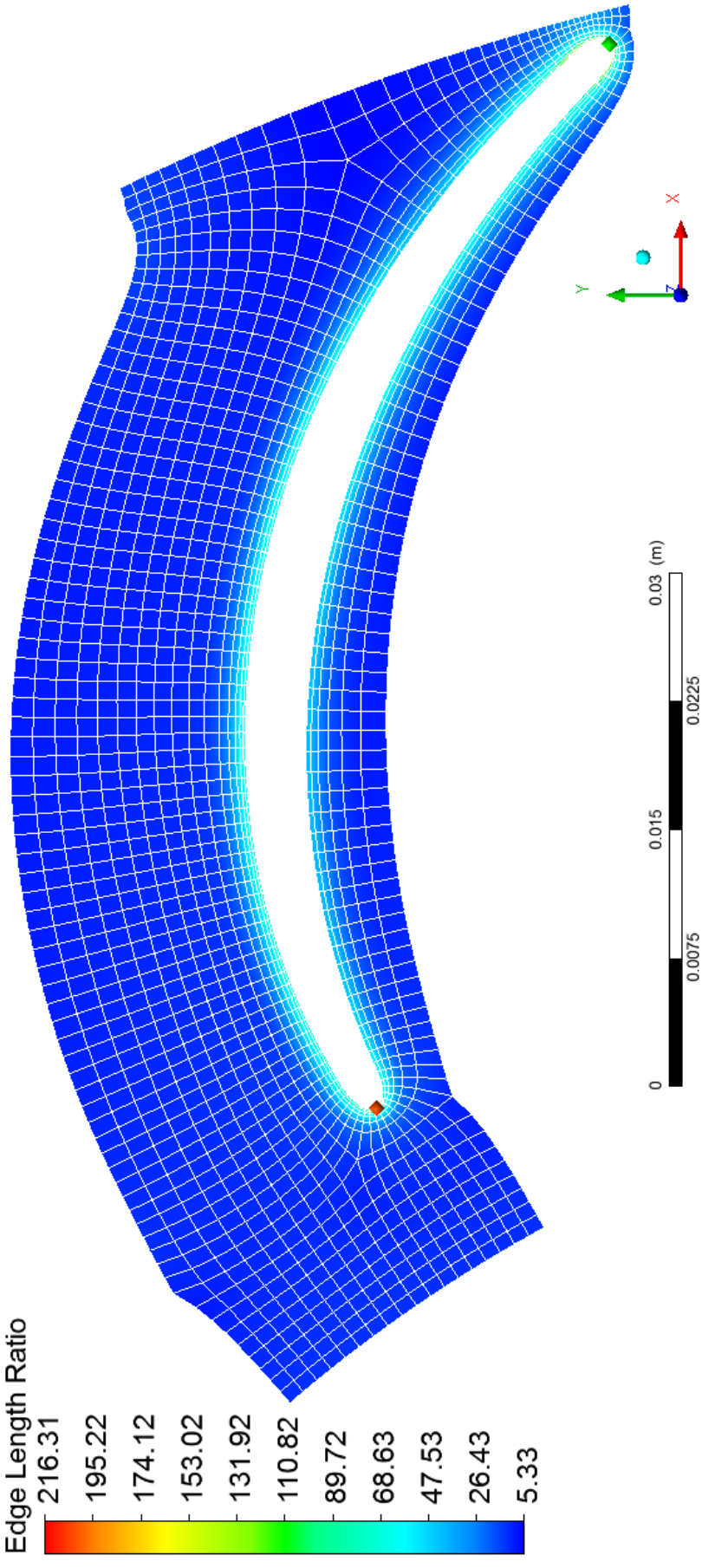

Fig. 4.10 (f) Mesh quality of the runner blade of the cross-flow turbine tested.

4.7 Outline of the Modelling Techniques

ANSYS CFX, advanced and high-performance modelling capabilities, was chosen among several CFD simulation codes (such as PHOENICS, STAR-CCM+ and ANSYS CFX) to perform an accurate and quick simulation of cross-flow water turbines. The main capabilities of ANSYS CFX simulation code are:

- ANSYS CFX has the capability to import CAD data file directly without the need to transfer it to another format, for example, in International Graphical Exchange Standard (IGES) format. This direct translation ensures an optimum geometry quality input.

- It has a very powerful tool “TurboGrid” to design and create high quality grid/mesh for turbomachinery “cross-flow turbine”.

- It has an advanced and high-performance solver technology which provides an accurate and quick solution.

In this chapter, the mesh generation and mesh quality were investigated. Structured & unstructured high quality meshes were generated for the computational domain of the cross-flow turbine. A fine and high quality hexahedral structured mesh was obtained for the runner blades’ computational domain and for other components’ computational domain a high quality tetrahedral unstructured mesh was obtained. The governing equations for fluid flow to predict the ways in which fluid flows in the cross-flow turbine were investigated. Direct Numerical Simulation (DNS), Large Eddy Simulation (LES) and Reynolds Averaged Navier-Stokes Simulation (RANS) approaches to make

turbulence computationally tractable were discussed. The flow field numerical simulation of cross-flow turbine was undertaken based on the Reynolds Averaged Navier Stokes equations (RANS).

Finally, the ANSYS software was found to be a good fluid dynamics simulation code with complete high-performance tools for comprehensive turbomachinery optimization.

Chapter Five

Results of Performance Improvement/Optimization and Discussion

Chapter Five

Results of Performance Improvement/Optimization and Discussion

5.1 Introduction

In this chapter, the details of establishing the optimal values for some geometric parameters of the main cross-flow turbine elements (runner and nozzle) are presented and discussed. A cross-flow turbine comprises of a nozzle and a cylindrical-shaped runner. The nozzle, which has a rectangular cross-sectional area, converts the flow energy into kinetic energy by directing the water to the full length of the runner at a specified angle of attack. The cylindrical-shaped runner consists of two parallel circular disks connected together at the perimeter with a series of curved horizontal blades. The runner converts the energy of water into mechanical energy. Both the nozzle and the runner were investigated, numerically, for the optimization of their geometrical parameters. These include the number of runner's blades n_b, the runner's blades diameter ratio d_2/d_1, the angle of attack α_1, the nozzle entry arc λ, the blade profile, the nozzle profile, the throat width s_o, the ratio of the nozzle width to the blades width N_w/B_w and the ratio of the blades width to the runner outer diameter B_w/d_1. They are plotted as velocity streamlines and pressure contours.

Complete details of the nature of the complex flow structure were revealed, which is presented and fully discussed in sections 5.2.1 to 5.2.9 of this chapter.

5.2 Performance Improvement and Optimization

The main parameter which characterizes the performance of a cross-flow turbine is its efficiency, which is the percentage of the energy obtained from the blades of the runner to the available energy of water prior to its entry to the turbine. This fundamental process of energy conversion is described by the efficiency equation (5.1), defined as the ratio of the power delivered by the cross-flow turbine to the power of the water passing through the blades of the runner. The general expression for this efficiency η is given in equation (5.1)

$$\eta = \frac{P_{out}}{P_{in}} \quad \ldots (5.1)$$

Where P_{out} is the power generated by the turbine. The power is calculated by simply multiplying the torque T by the rotational speed ω of the runner. P_{in} is the power supplied to the turbine, and it is equal to $\rho \times g \times Q \times H$, where ρ is the density of water, g is the acceleration of gravity, Q is the water flow rate to the turbine and H is the total head.

The theory of cross-flow turbine, discussed fully in Chapter 3, indicates that the geometric parameters can strongly influence the performance characteristic of this type of turbine. The geometric parameters are the properties of the main cross-flow turbine two components (the runner and the nozzle). These include the number of blades n_b, the diameter ratio d_2/d_1, the runner outer diameter d_1, the diameter of the shaft d_s, the thickness of the blades t_b, the first stage inlet

angle β_1, the first stage exit angle β_2', the curvature of the blades r_b, the angle of attack α_1, the shape of the nozzle rear wall, the nozzle entry arc λ, the throat width s_o etc.,

It was evident from the literature available on the cross-flow turbine development, reported in Chapter 2, that attention has been paid to investigate the effects of few of these geometric parameters such as the angle of attack, the diameter ratio and the number of blades on the cross-flow turbine performance. However, little or no attention was paid to the complex flow structure associated with the change of such parameters in these turbines. Such flow characteristics (which is three dimensional and of two phases with complex hydrodynamic forces) can greatly affect the performance and the working life of such turbines. The current study was undertaken with the purpose of optimizing the performance of the cross-flow turbine for micro hydroelectric power plants by varying all of the geometric parameters of the turbine. It is aimed at analyzing the impact of such parameter changes on the flow characteristics and the hydrodynamic forces within the turbine. These ultimately determine the power output, torque and the efficiency of turbine. It was interesting to note from the literature review, which is reported in Chapter 2, that despite the importance of the flow field and structure within the turbine this was not investigated thoroughly and comprehensively.

5.2.1 Optimization of the Runner's Blades Number (n_b)

The number of runner's blades is one of the most important geometric parameters of cross-flow turbine as the energy is extracted from water by the blades. The principle was fully described in Chapter 3. Therefore, it is essential to improve and optimize the turbine operation by selecting the optimum number of runner's blades. It must be noted that selecting too many runner's blades for certain turbine tends to increase the friction losses, weight of the runner and the cost of the turbine. However, too few blades tend to increase the flow separation loss on the back side of the blades [90]. An experimental investigation on cross-flow turbine performance by varying the number of the runner's blades was conducted by Khosrowpanah et al [43]. The results of this experiment showed that the number of the runner's blades strongly affects the efficiency. An optimum blades number of 15 was identified in a series of experiments with runners of 10 to 20 blades. In 1996, Costa Pereira and Borges [52] conducted an experimental investigation of cross-flow turbine with the number of the runner's blades ranged from 10 to 25 blades. Unusually, and surprisingly they concluded that the influence of the number of blades on the performance was unclear. Both Olgun and Ulku [49] and Desai and Aziz [50], also, undertook experiments to study the effect of the number of the runner's blades on the efficiency of the cross-flow turbine. Olgun and Ulku [49] concluded that a runner with 28 blades was more efficient than the runner with 20, 24 and 32 blades. However, Desai and Aziz [50] revealed that the efficiency of the cross-flow turbine increased by increasing the number of runner's blades from 15 to 30. As it is clearly evident from the above review summary, the observations regarding the effect of the number of the runner's

blades on the performance of the cross-flow turbine are very "unclear" and rather "contradictory". According to few previous studies, an increase in the number of runner's blades has a favorable impact on performance of the cross-flow turbine, whereas in other studies it is not. Therefore, it was rather important to resolve this contradiction and determine the optimum number of runner's blades necessary for the best performance of the cross-flow turbine. In order to achieve this goal in the current study, certain blades geometrical details were selected. These are listed in table 5.1.

Table 5.1 Details of the runner's blades number tested.

Geometrical parameter	Specification
Number of blades	$n_b = ?$ $15, 20, 25, 30, 35 \& 40$
External diameter	$d_1 = 300\,mm$
Diameters ratio	$d_2/d_1 = 0.67$
Angle of attack	$\alpha_1 = 16^o$
Inlet blade angle	$\beta_1 = 150.166^o$
Internal blade angle	$\beta_1^{'} = \beta_2^{'} = 90^o$
Outlet blade angle	$\beta_2 = 29.834^o$
Blade thickness	$t_b = 3.6\,mm$
Blade radius of curvature	$r_b = 47.65\,mm$
Nozzle entry arc	$\lambda = 90^o$
Throat width	$s_o = 60\,mm$
Width of the nozzle	$N_W = 150\,mm$
Shaft (axle) diameter	$d_s = 40\,mm$ *Note: Symbols as detailed in Fig. 3.2.*

The simulation results employing the parameters of table 5.1 are shown in Figs. 5.1 to 5.7 and Figs. B.1 to B.2. The details of the internal flow of the turbine's runners with various numbers of blades, which is turbulent and two phases are shown in Figs. 5.1 (a) to (f). These figures show the water superficial velocity streamlines in both the nozzle and the runner. They clearly show that in all cases water passes only through part of the runner. The impact of the number of blades on the flow exit angle is quite evident. Increasing the number of runner's blades increases the exit angle of the water leaving the runner. As a result of a considerable obstruction to the flow at an increase runner's blades number the entry velocity of the water to the runner increased as shown in Fig. 5.1 (f). An increase in the number of runner's blades also reduces the area available for the water leaving the runner. This also causes the increase in the flow velocity (activity) at the second stage of the runner. As it is anticipated, in all cases some separation of the main flow was detected particularly in the convergent part of the nozzle and close to the runner entry. However, this is not entirely clear from Figs. 5.1 (a) to (f) and warrant further clarification.

The streamlines of the flow at the mid span of the turbine runner of various blade numbers are shown in Figs. 5.2 (a) to (f). These confirm the conclusion from the previous set of results that increasing the number of runner's blades causes an increase in the velocity of the flowing water at the entry and exit to the runner. It is rather interesting to note the effect of the volute shape, particularly near the end of the nozzle, on the flow between the blades. It seems that flow creates an air bubble (pocket) region. The size of such bubble or pocket relates inversely to the number of blades in the runner. Inspecting Figs. B.2 (a) to (f) closely also reveals the flow tendency to separate along the line

close to where the nozzle meets the volute. This will be discussed further, hereafter, and suggests that such sharp line (edge) should be eliminated in future design in order to reduce losses and improve power output and efficiency.

Water superficial velocity vectors at the mid span of the turbine of various runner's blades are shown in Figs. 5.3 (a) to (f). Here, it is interesting to note that as the number of blades increases, water splatter from the inner side and outer side of the blades (runner center and rim) also increases. This splatter, which is in the form of very small water droplets of fine diameter, concentrates close to the runner rim. The water eventually loses momentum and descends to lower part of the turbine casing where they mix the rest of the water leaving the turbine. The water drops are of much lower velocity than mainstream water; hence, they appear as very small dots as clearly shown in Fig. 5.3 (f). A comparison of the water superficial velocity of Figs. 5.3 (a) to (f) shows clearly that such velocity vectors are rather uniform for a runner with 30 blades with minimum flow separation at the runner center and rim (Fig. 5.3 (d)). Accordingly, it is expected that such blades number results in high efficiency and power output as the flow separation regions are almost eradicated in this case. Such regions are clearly shown in Fig. 5.3 (a). They most certainly cause lower power output and lower efficiency as well as undesirable vibration and noise, which are associated with the operation of turbines with runners of a low number of the runner's blades. As the number of the runner's blades increased above 30 (as in Figs. 5.3 (e) and (f)) two distinctive phenomena can be seen. The first is the tendency of the water to impinge on the axle of the runner. The second is the regions of increasing activities at the runner entry of the upper

blades row and the runner outlet. Both of these phenomena are associated with unnecessary loss of water energy and reduce the power output/efficiency of the turbine.

Figures B.1 (a) to (f) show the total pressure distribution in both the nozzle and runner. As almost a uniform high total pressure can be seen in the nozzle in all cases. Regions in the runner where the pressure is almost atmospheric indicate regions of no flow. Such regions are empty of water and these are indicated by atmospheric pressure. It is very clear that such region encapsulates two or more blades in runners of high blades number. This represents loss of interaction between the blades and the water which causes a reduction in power output/efficiency. In runners of low blades number (Figs. B.1 (a) and (b)), blades separation is such that it allows the water to leave the runner at high total pressure. This represents a loss of water potential energy or power output.

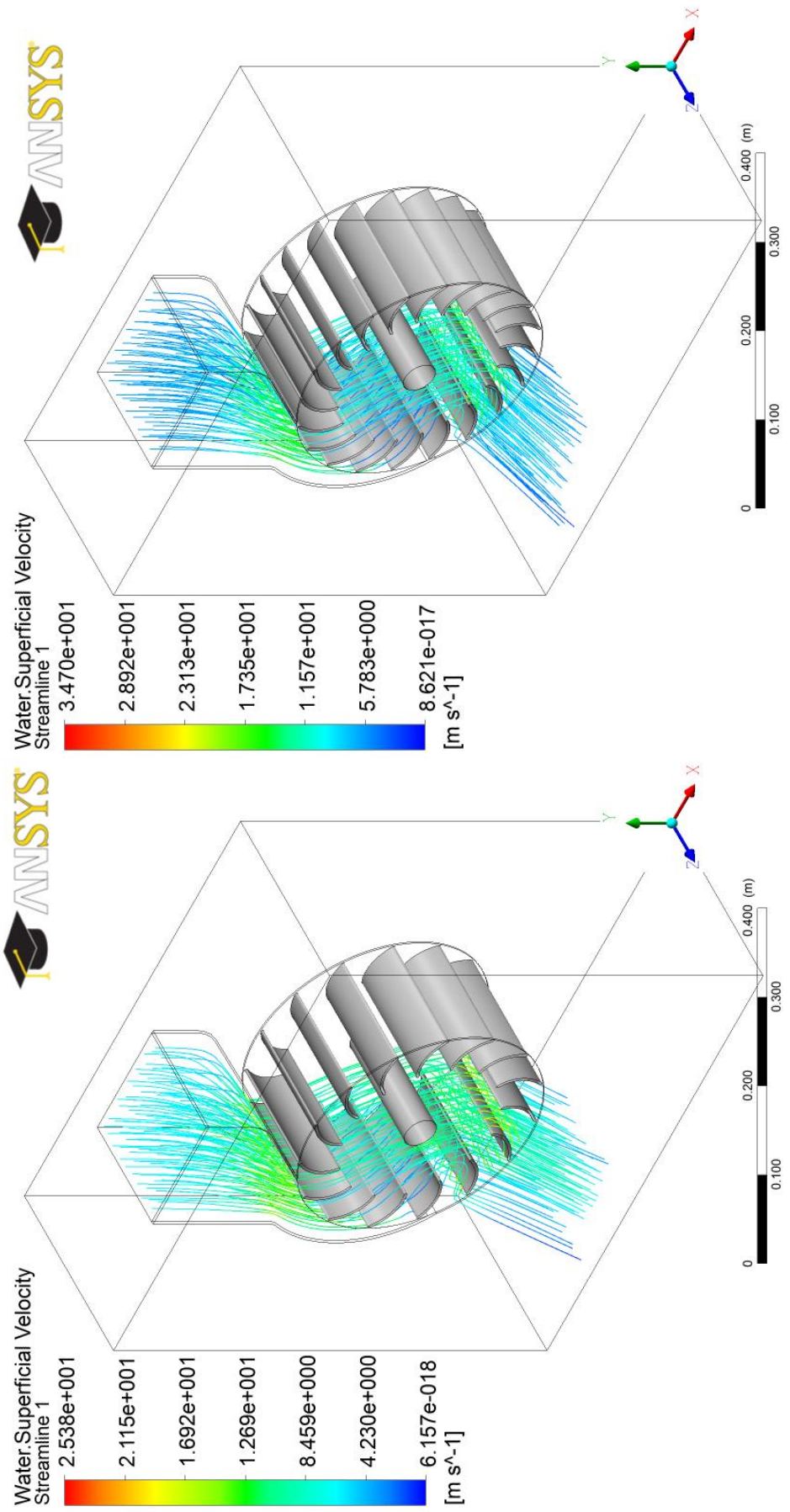

(b) 20-blade

(a) 15-blade

Fig. 5.1 (a) and (b) Water superficial velocity streamlines in cross-flow turbine for various number of runner's blades.

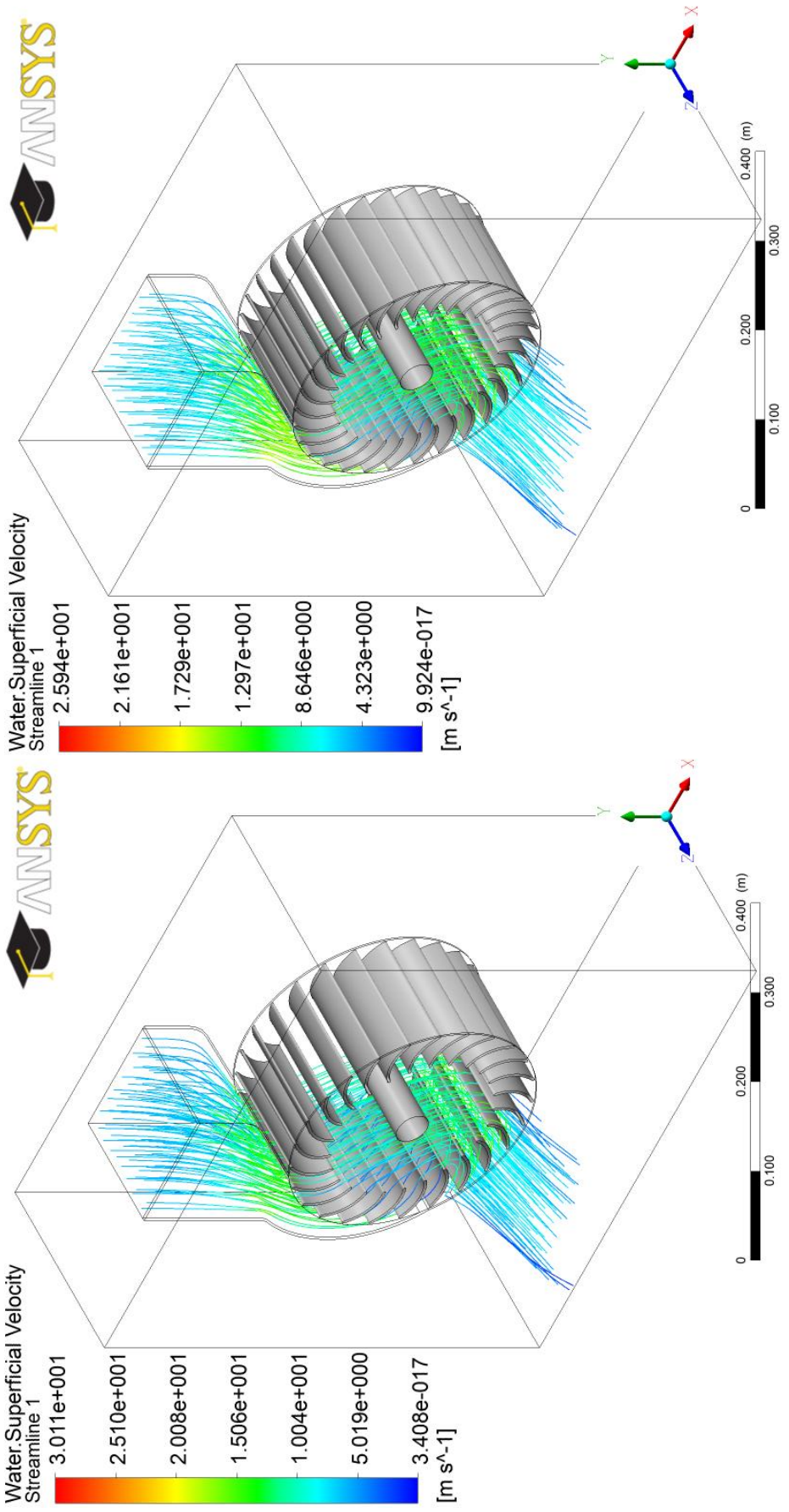

(d) 30-blade

(c) 25-blade

Fig. 5.1 (c) and (d) Water superficial velocity streamlines in cross-flow turbine for various number of runner's blades.

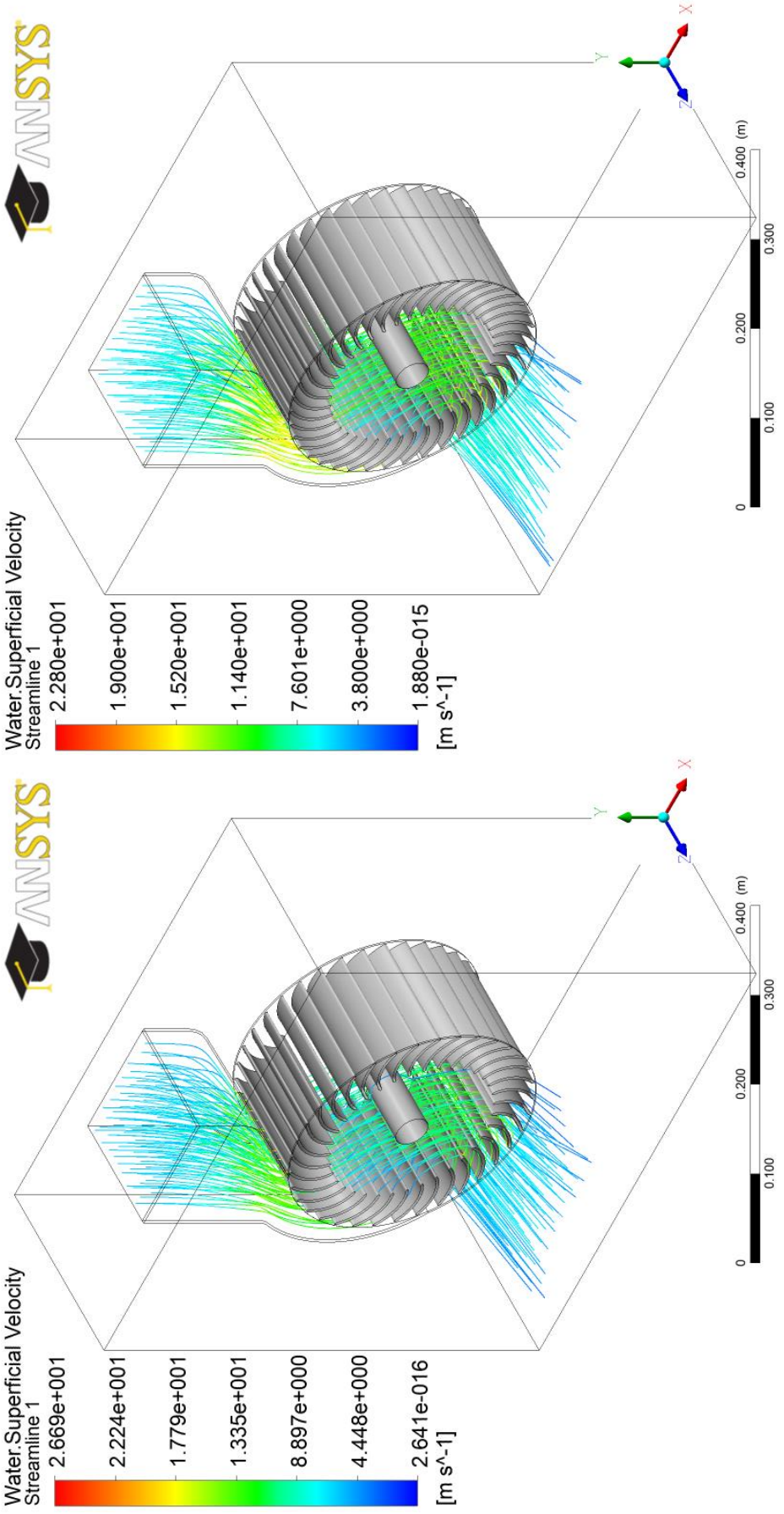

(f) 40-blade

(e) 35-blade

Fig. 5.1 (e) and (f) Water superficial velocity streamlines in cross-flow turbine for various number of runner's blades.

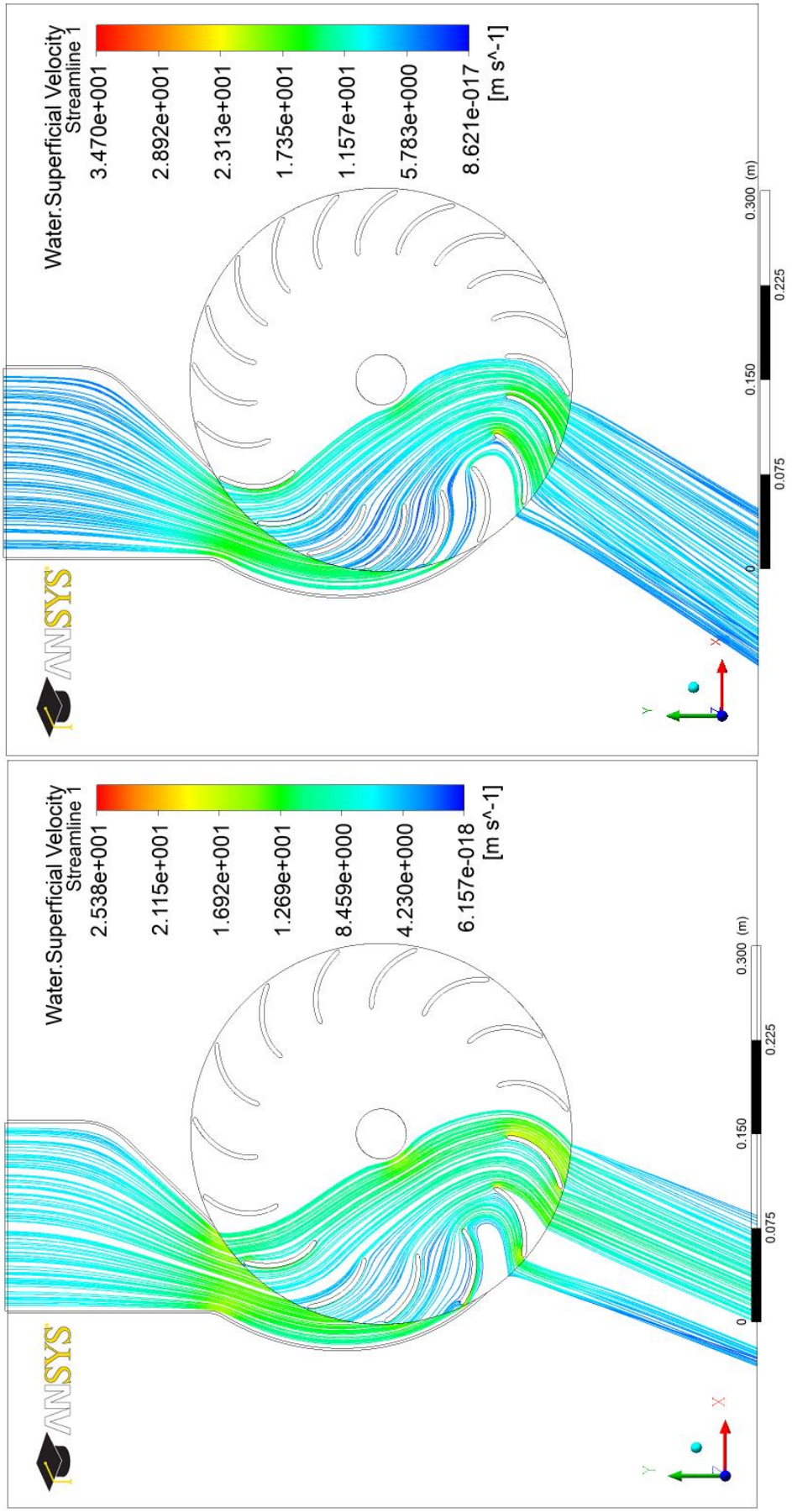

(a) 15-blade (b) 20-blade

Fig. 5.2 (a) and (b) Water superficial velocity streamlines at the mid span of cross-flow turbine for various number of runner's blades.

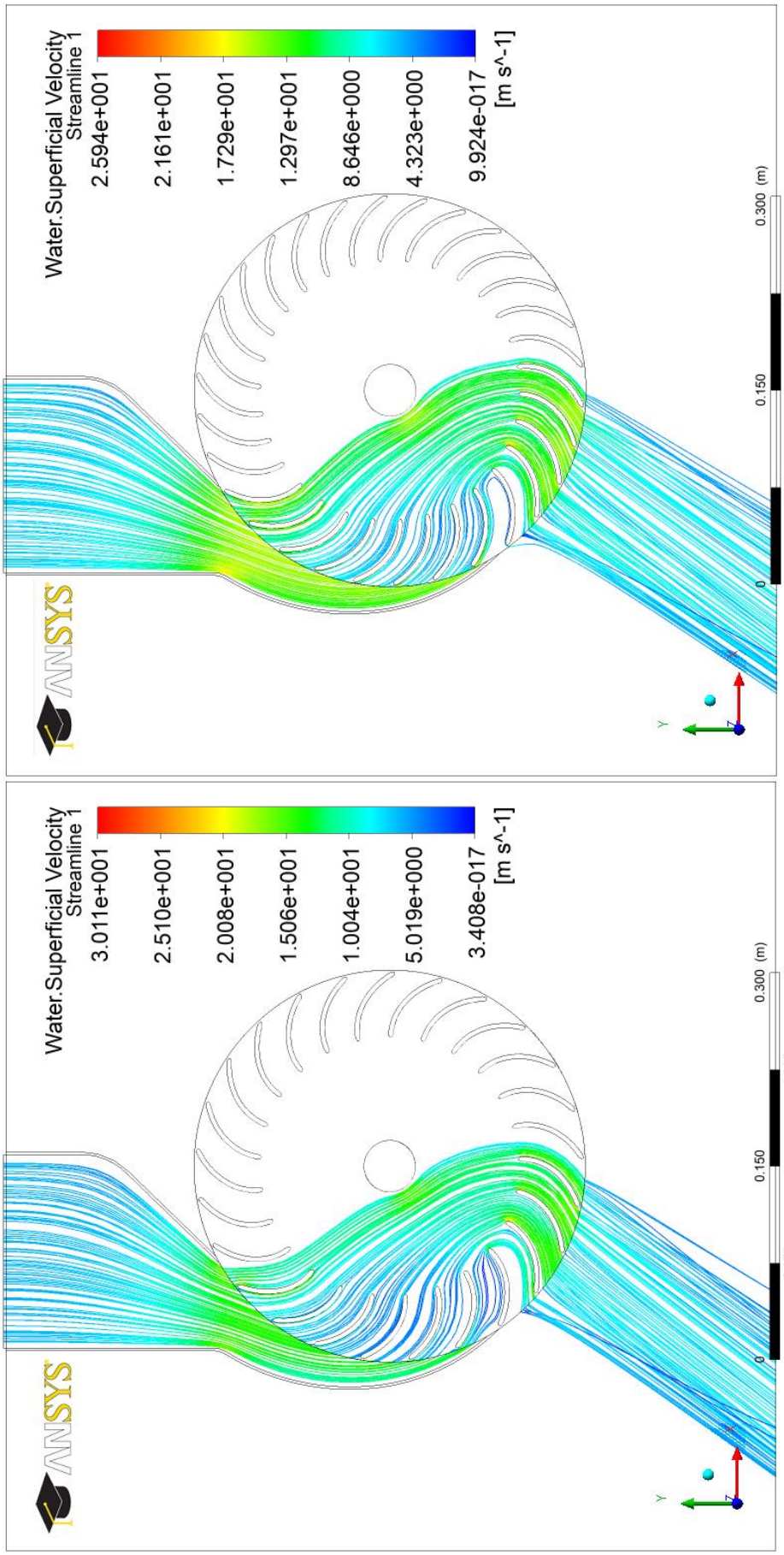

(c) 25-blade (d) 30-blade

Fig. 5.2 (c) and (d) Water superficial velocity streamlines at the mid span of cross-flow turbine for various number of runner's blades.

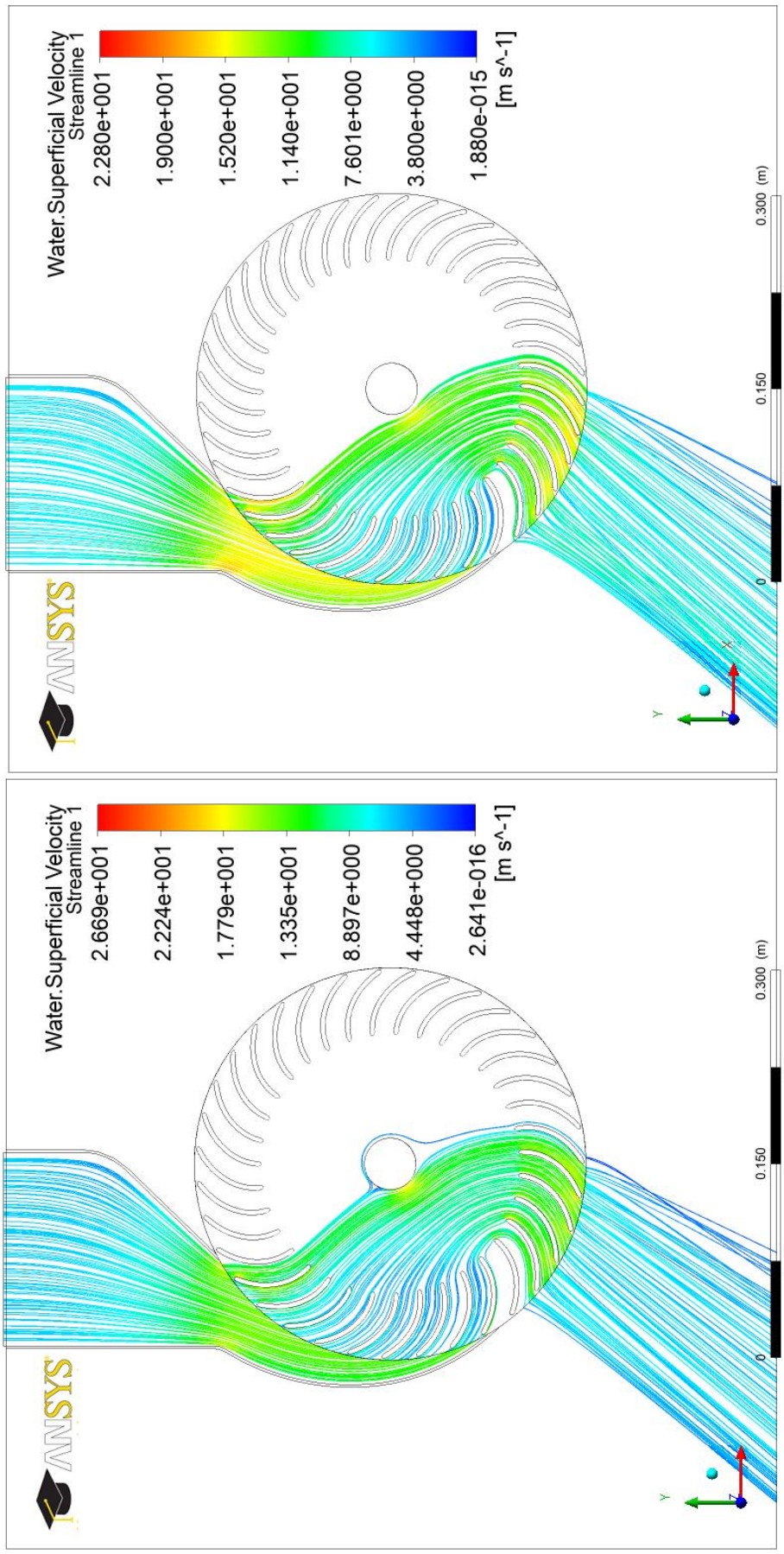

(e) 35-blade (f) 40-blade

Fig. 5.2 (e) and (f) Water superficial velocity streamlines at the mid span of cross-flow turbine for various number of runner's blades.

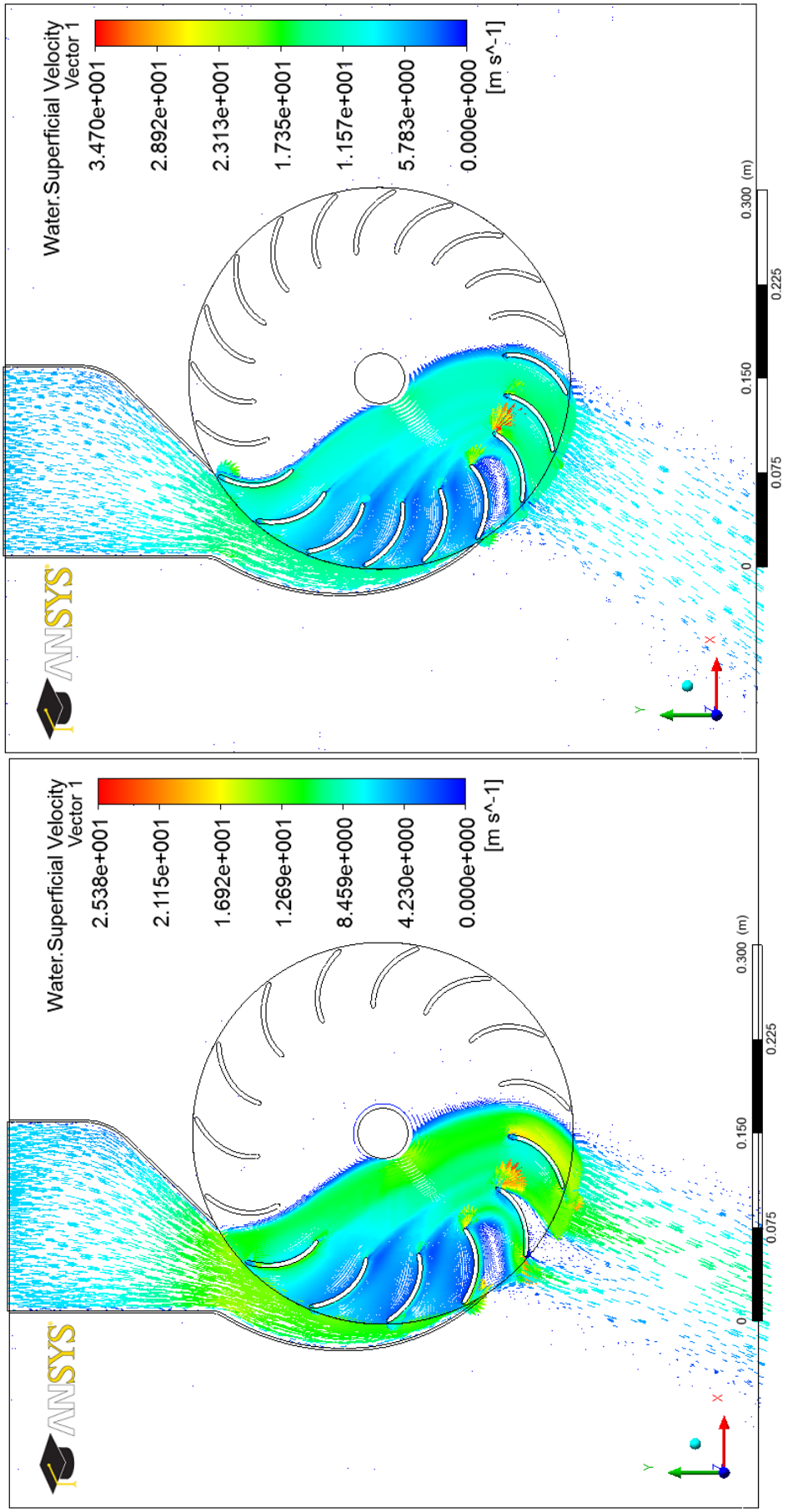

(a) 15-blade (b) 20-blade

Fig. 5.3 (a) and (b) Water superficial velocity vectors at the mid span of cross-flow turbine for various number of runner's blades.

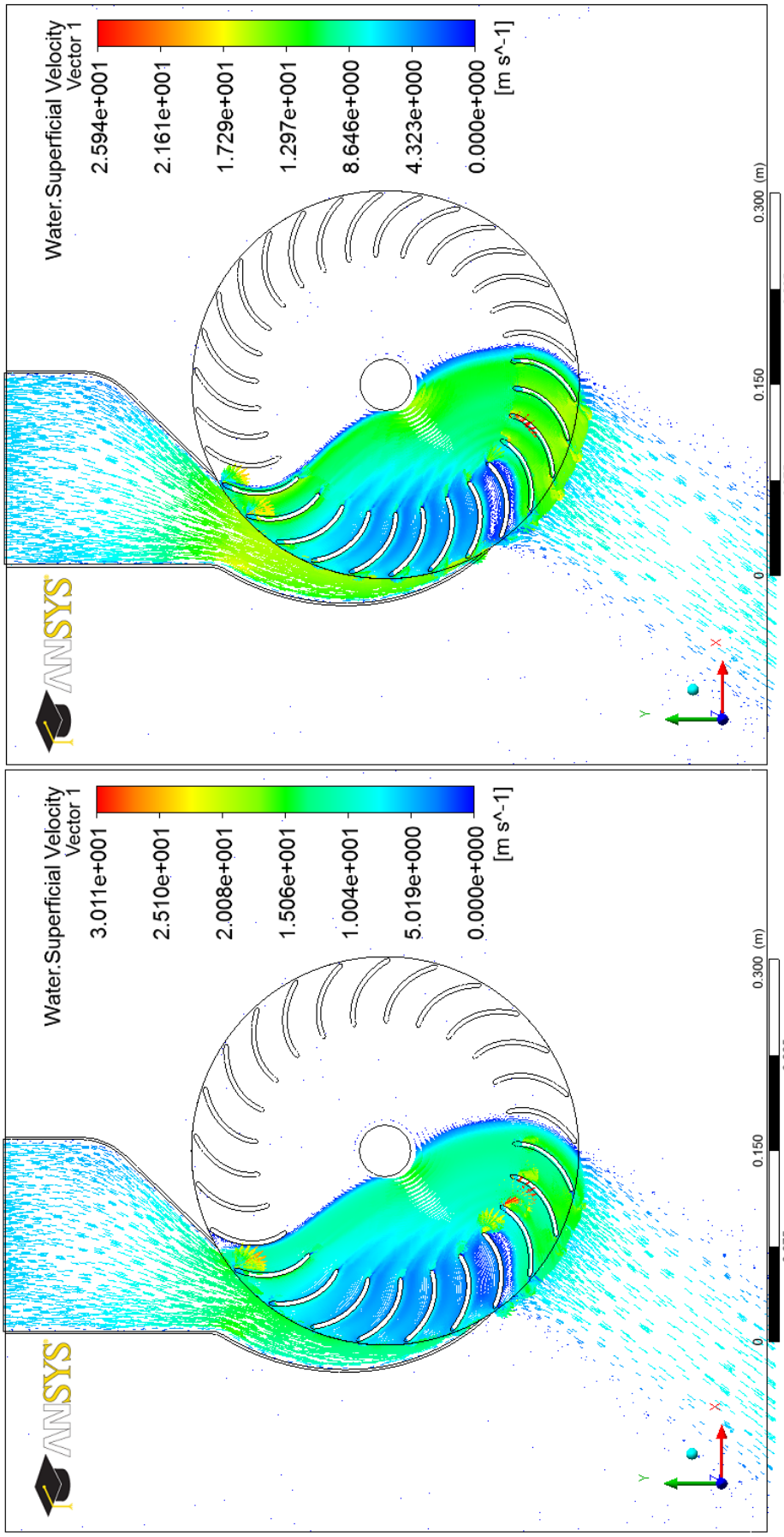

(c) 25-blade (d) 30-blade

Fig. 5.3 (c) and (d) Water superficial velocity vectors at the mid span of cross-flow turbine for various number of runner's blades.

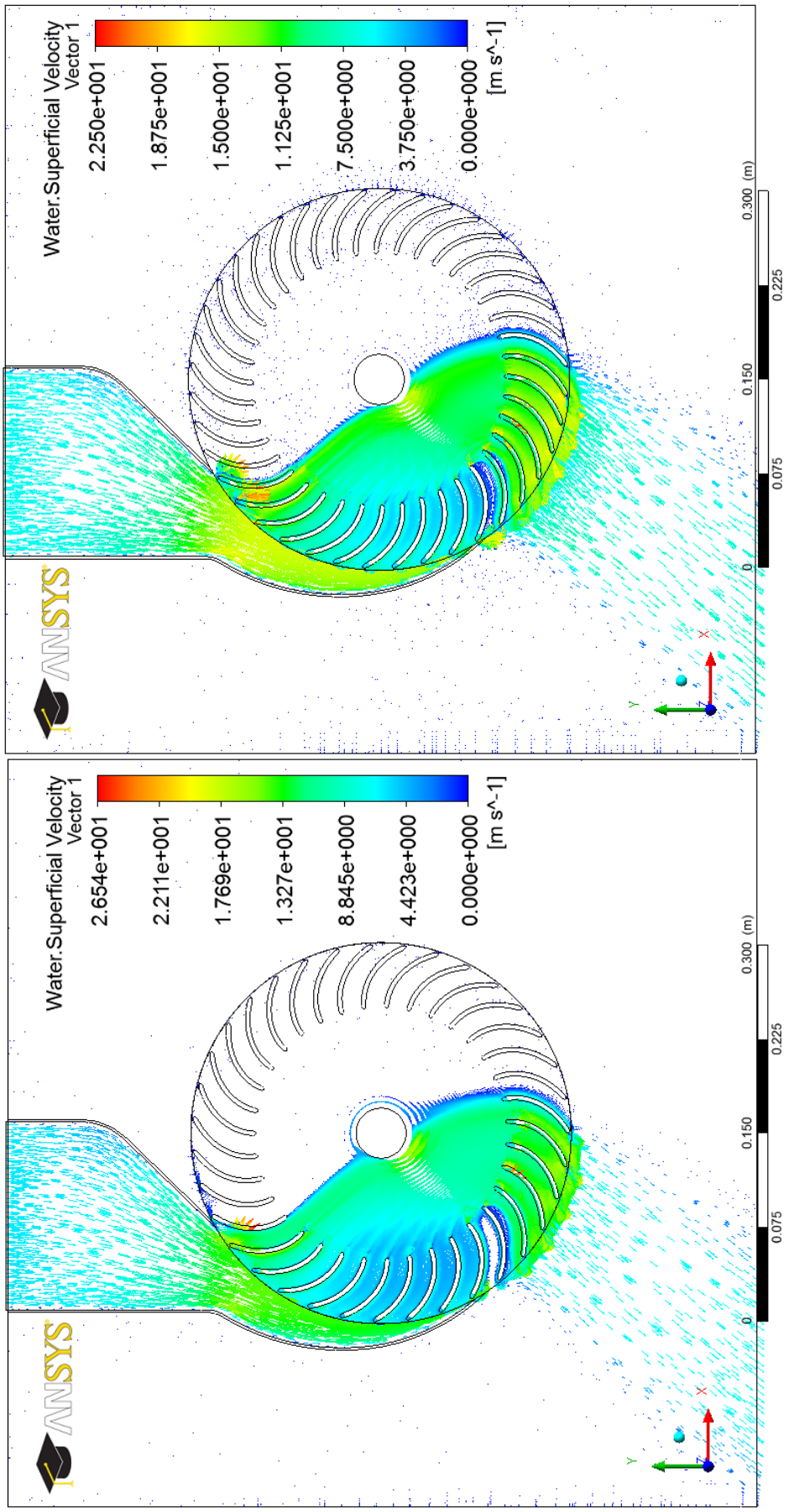

(e) 35-blade (f) 40-blade

Fig. 5.3 (e) and (f) Water superficial velocity vectors at the mid span of cross-flow turbine for various number of runner's blades.

The effect of the number of runner's blades on the efficiency of the cross-flow turbine is shown in Fig. 5.4. It is clear that an increase in the number of runner's blades from 15 to 30 has a favorable effect on the efficiency of the cross-flow turbine. This can be explained, firstly, by the fact that the energy extracted from water by the blades increases with increasing the number of the runner's blades [32], secondly non-cross flow increases with decreasing the number of runner's blades as shown in Figs. 5.2 and 5.3, and thirdly, the size of the separation/ recirculation flow on the back of the runner's blades increases with decreasing the number of the runner's blades as shown in Fig. 5.3. A further increase in the number of the runner's blades from 30 to 40 has an undesirable impact of reducing the efficiency. This can be explained, firstly, by the fact that the collision loss increases with increasing the number of the runner's blades as shown in Figs. B.1 and B.2, secondly the increase in the weight of the runner, and thirdly, the runner's blades causes a reduction in the flow area which in turn increases the flow velocity and causes a reverse flow at the runner's blades exit. According to this, the most effective number of runner's blades noticed was 30 where the efficiency was 73.387 %. Therefore, the optimum number of runner's blades can be considered to be 30, which is in agreement with Desai and Aziz [50] conclusion. Their results also showed that the efficiency of the cross-flow turbine increased by increasing the number of the runner's blades from 15 to 30.

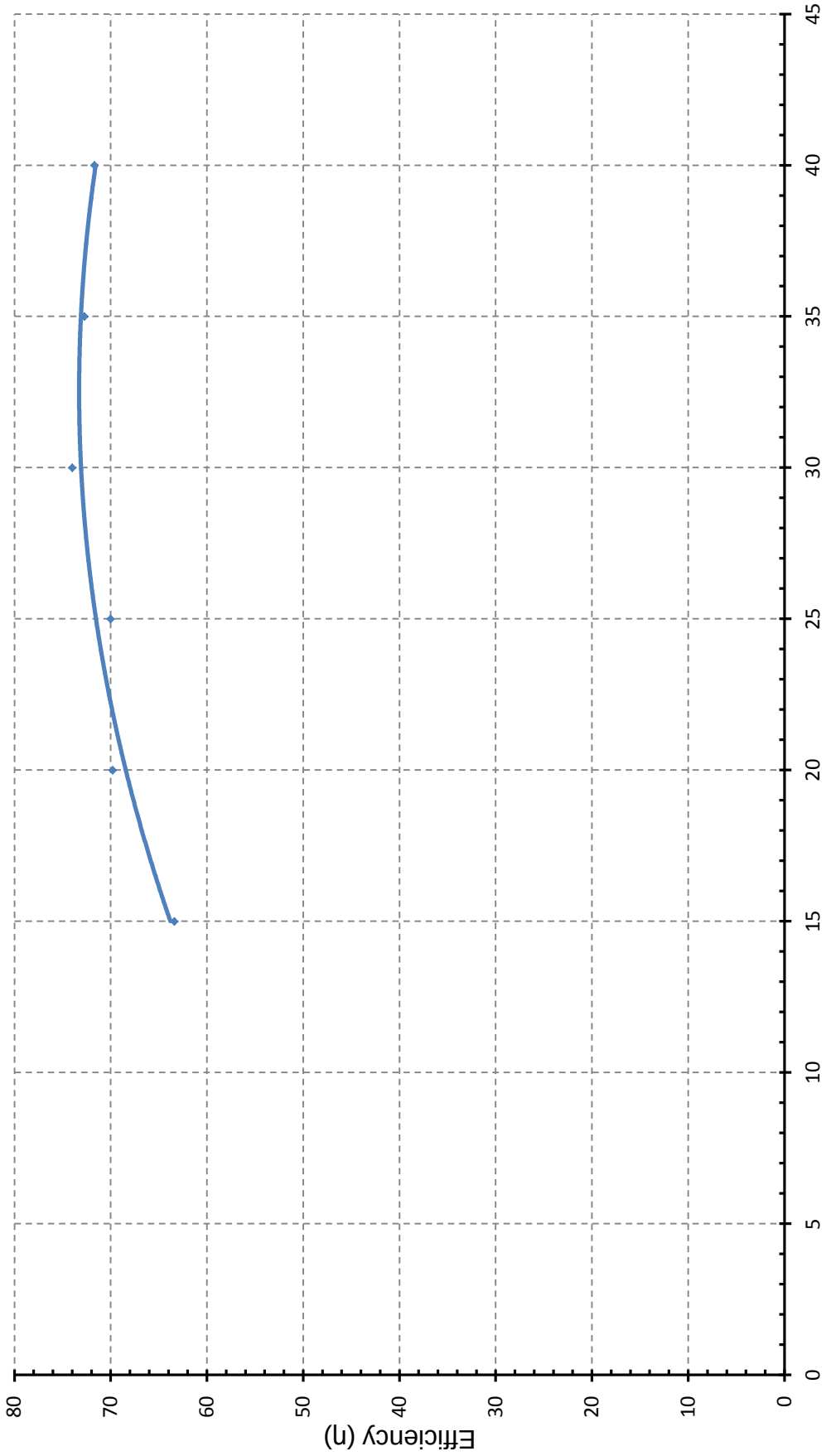

Fig. 5.4 Cross-flow turbine performance characteristics curve for runner with various blades.

An enlarged view of the blades in a runner of 15 blades is shown in Fig. 5.5. It is clear that a vortex is stationed in part of the space in between two blades. Such vortex causes non-cross flow or flow reversal at the back of the blades as can be seen in both Figs. 5.5 and 5.6. However, the flow reversal and the recirculation zones tend to minimize when the blades number increase to 40. This effect is counter-balanced by the development of impingement regions at the blades tip in runners of high blades number as shown in Fig. 5.7. This tends to reduce the efficiency of turbines with runner of high blades number. It can be seen from Fig. 5.4 that at high blades number, the turbine efficiency is lower than the maximum.

It is important to take into consideration the combined effects of the regions of non-cross flow (flow reversal), flow recirculation zones and the flow impingement in the enlarged views of Figs. 5.5 to 5.7 on the turbine overall performance.

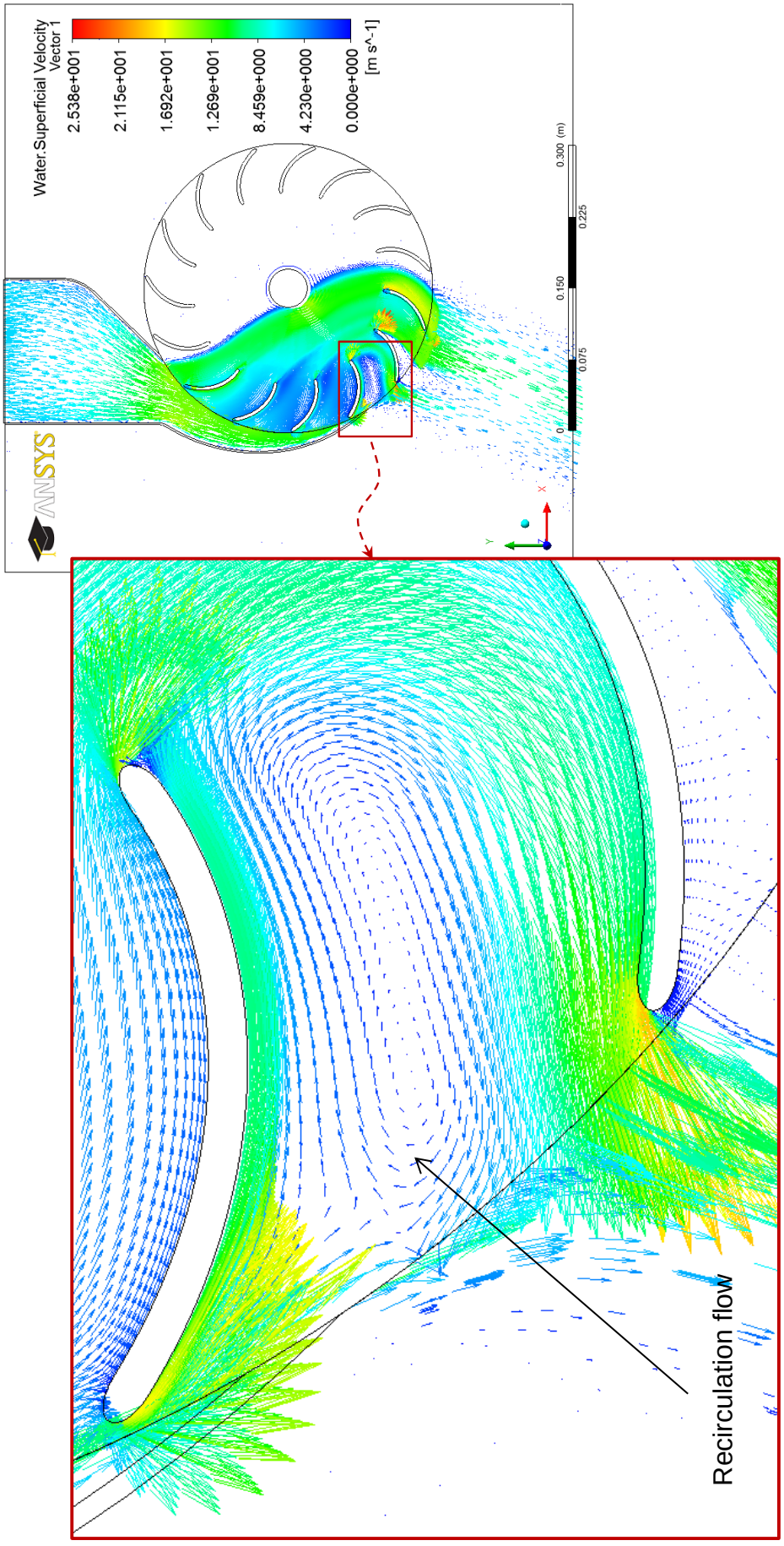

Fig. 5.5 Enlargement of the water superficial velocity vectors at the mid span of cross-flow turbine of 15 blades runner.

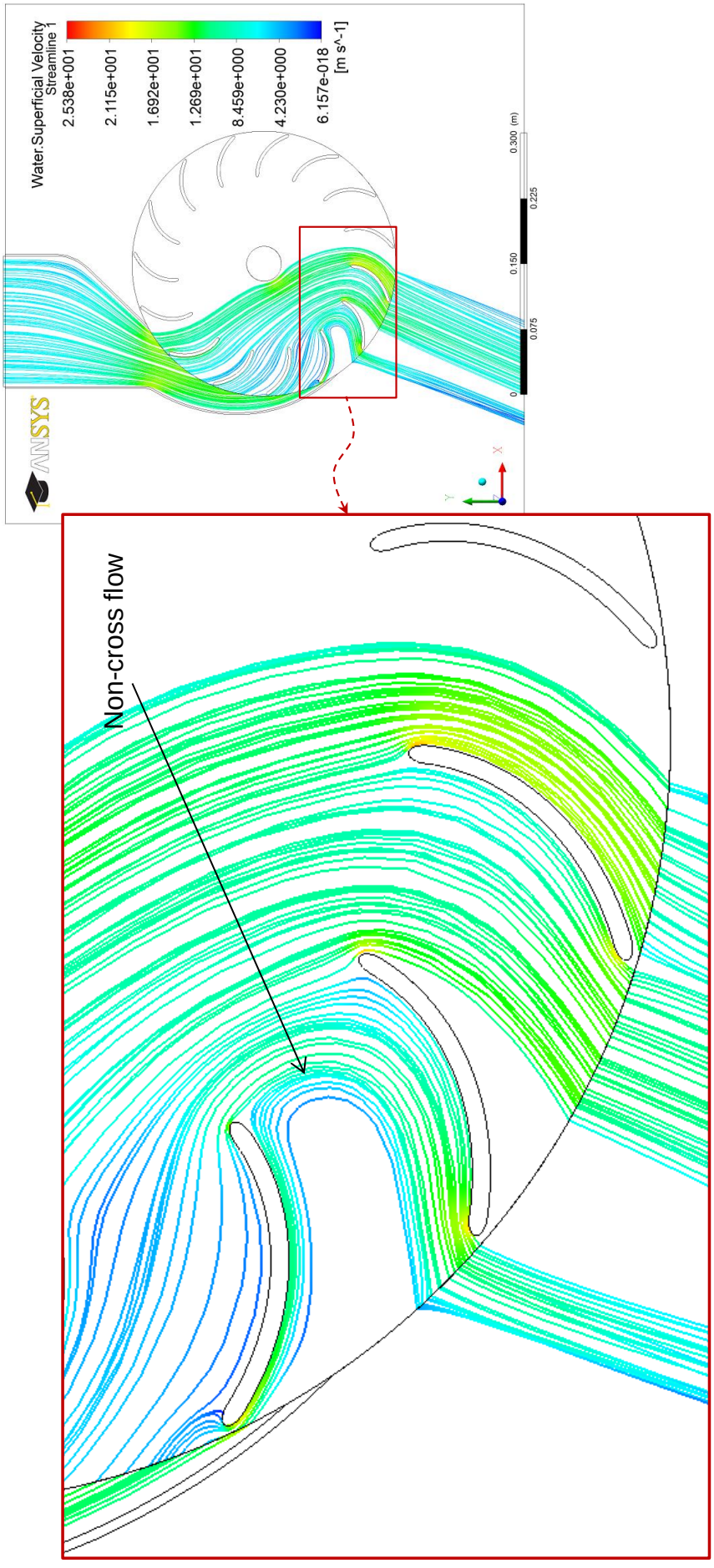

Fig. 5.6 Enlargement of the water superficial velocity streamlines at the mid span of cross-flow turbine of 15 blades runner.

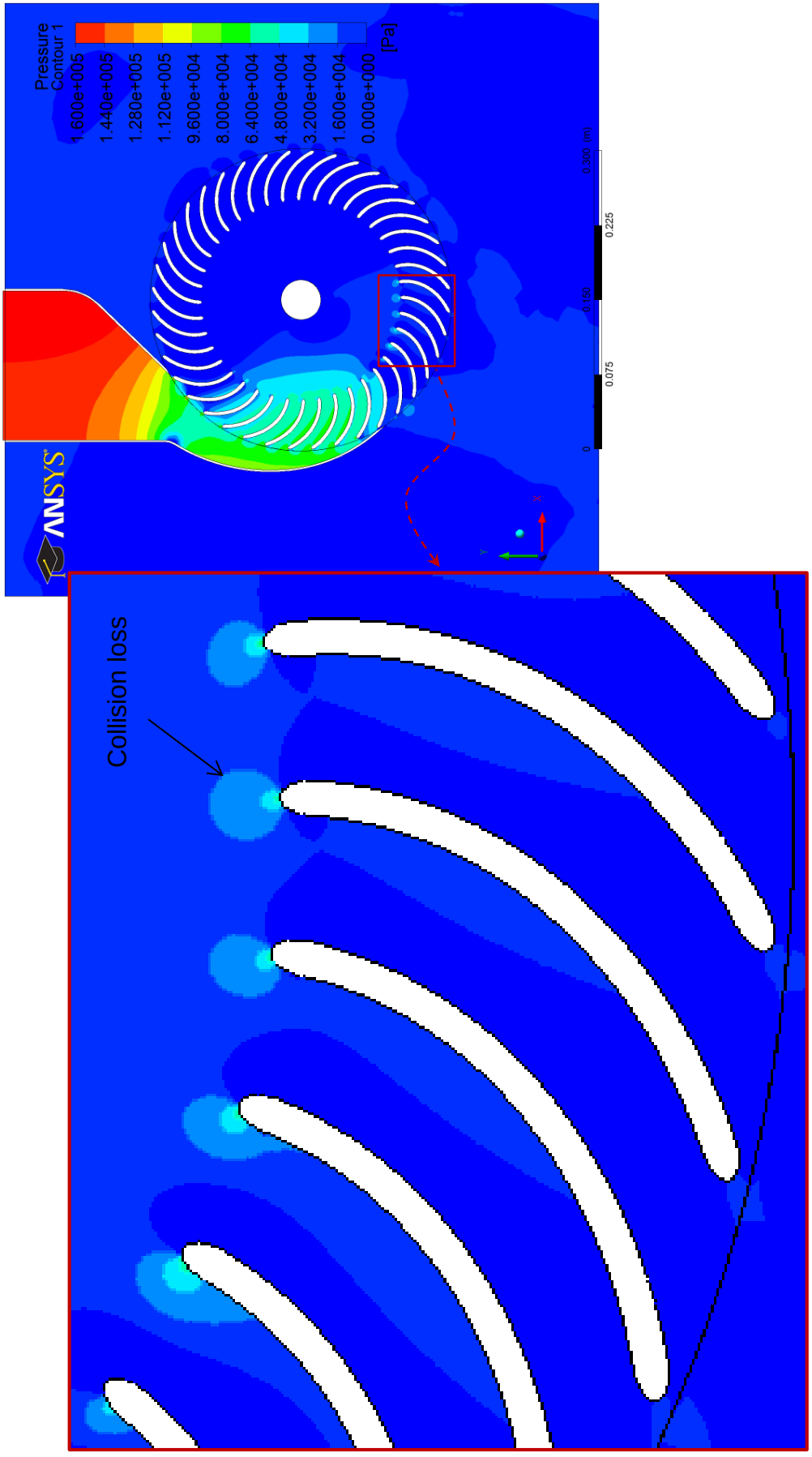

Fig. 5.7 Enlargement of the pressure contours at the mid span of cross-flow turbine of 40 blades runner.

5.2.2 Optimization of the Runner's Blades Diameter Ratio (d_2/d_1)

The diameter ratio has a considerable impact on the flow characteristics and the hydrodynamic forces within the cross-flow turbine as it controls the length of the blades and this in turn controls the width of the passages between the blades. A narrow passage between the blades may cause a reverse flow. A wide passage between the blades, on the other hand, may cause a separation. Mockmore and Merryfield [31], who presented a translation of Donat Banki's paper "Neue Wasser-turbine", conducted an experimental investigation on a laboratory turbine. It was constructed with a diameter ratio of 0.66, according to the specifications of Banki. The impact of the diameter ratio on the efficiency of the cross-flow turbine was also experimentally investigated by Desai and Aziz [50]. They concluded that 0.68 inner to outer diameter ratio produce a higher turbine efficiency within the range of ratios of 0.6 – 0.75. Olgun [57] experimental investigation led to the conclusion that, the cross-flow turbine with a diameter ratio of 0.67 is more efficient than the cross-flow turbines with diameter ratios of 0.54, 0.58 and 0.75. In order to provide a comprehensive understanding of the effect of the diameter ratio on performance of the cross-flow turbine ratios of 0.56, 0.60, 0.65, 0.66, 0.67, 0.68 and 0.70 were selected for investigation in the present work. The geometrical parameters' details of the tested cross-flow turbines are listed in table 5.2. It must be stressed that optimized parameter from the previous section is employed in the table and this is also done with the current parameter and the others to follow.

Table 5.2 Details of the diameter ratios tested.

Geometrical parameter	Specification
Number of blades	$n_b = 30$
External diameter	$d_1 = 300\,mm$
Diameters ratio	$d_2/d_1 = ?$ $0.56, 0.6, 0.65, 0.66, 0.67, 0.68 \& 0.7$
Angle of attack	$\alpha_1 = 16^o$
Inlet blade angle	$\beta_1 = 150.166^o$
Internal blade angle	$\beta_1^{'} = \beta_2^{'} = 90^o$
Outlet blade angle	$\beta_2 = 29.834^o$
Blade thickness	$t_b = 3.6\,mm$
Blade radius of curvature	$r_b = ?$ 59.34, 55.33, 49.93, 48.8, 47.65, 46.48 & 44 mm
Nozzle entry arc	$\lambda = 90^o$
Throat width	$s_o = 60\,mm$
Width of the nozzle	$N_w = 150\,mm$
Shaft (axle) diameter	$d_s = 40\,mm$

Note: Symbols as detailed in Fig. 3.2.

Figures 5.8 (a) to (f) show the result of the simulation of the water volume fraction in both the nozzle and runner for various blades internal to external diameter ratio d_2/d_1. The two-phase flow, which is well-defined by the interface between the air and water. Here, the water was represented by the water volume fraction contours by red color and the air by blue color.

The runner's blades diameter ratio d_2/d_1 has a significant impact on the impingement of the flow leaving the upper row of blades on the runner shaft

(axle). The impingement clearly increases by decreasing the diameter ratio. For a diameter ratio of 0.6, Fig. 5.8 (a) clearly shows a vacuum region created in between the blades facing the tip end of the nozzle. It is highly probable that such region is created by a combination of two factors. The first is an increase in the frictional forces on the water as it has to move over longer surfaces. The second is a reduction in the gravitational forces acting on the water as it is not in a free fall state (the position of this region is almost horizontal). The exit angle of the water with a low diameter ratio (depicted in Fig. 5.8 (a)) also shows evidence of impingement of the outer core of the water leaving the runner on the turbine casing. This causes a very low volume fraction of the water to move in the upward direction and parallel to the casing surface. Naturally, such impingement is associated with some degree of noise and possibly vibration. The total pressure distribution in the nozzle and runner depicted in Figs. B.3 (a) to (f) confirms some of the details of the flow revealed by Figs. 5.8 (a) to (f). It is not surprising that the pressure distribution of Figs. B.3 (c) and (d) are almost identical as the diameter ratio corresponds to 0.66 and 0.67, respectively. Both show almost a cross-flow stream which is of high total pressure extending from the inlet to the outlet of the runner this is followed by regions of relatively less total pressure crossing the runner from the inlet to the exit of the runner. A region of a total pressure which is almost identical to the atmospheric pressure which corresponds to intense recirculation in the blades facing the tip of the nozzle is also indicated in the same figures. This region is of a very interesting structure which is investigated further in the superficial velocity vectors of Figs. 5.9 (a) to (f).

The complex nature of the flow in the runner and the nozzle is revealed in Figs. 5.9 (a) to (f), which shows the water superficial velocity vectors in the runner and nozzle. It is important to note that although the general details of the water superficial velocity vectors are similar to those of Figs. 5.3 (a) to (f); the flow details are evidently different. Changing the diameter ratio can change the flow structure in the blades. Regions of intense flow activities are shown in various parts of the runner. It seems that the flow activities in the blades to differ with the diameter ratio. As an example, Fig. 5.9 (a) shows an interesting vortex structure in the blades facing the tip of the nozzle. When this is enlarged (Fig. 5.12) a clear tri-contra rotating vortices can be clearly seen in between these blades. Naturally, energy lost in these vortices is taken from the water energy available at the entrance to the nozzle. This in turn explains the low efficiency associated with the runner's blades of the diameter ratio of 0.6. The flow associated with Fig. 5.9 (d) display fewer vortices in the blades which in turn associated with less losses and higher turbine efficiency. Figure 5.9 (f) displays entirely different phenomena of small proportion of the water or droplets moving towards the outer rim in the direction of the incoming blades. This encounters the movement of the runner and exerts opposing forces. In order to overcome these forces, energy is absorbed from that available at the nozzle outlet which tends to reduce the power generated and the turbine efficiency.

The water superficial velocity and pressure contours were plotted on the mid span plane to illustrate more clearly, the effect of a diameter ratio on the fluid flow through the passages of the runner blades as shown in Figs. 5.9 and B.4. These figures clearly show the effect of the diameter ratio on the internal flow characteristics and the hydrodynamic forces within the cross-flow turbine where

the runner blade profile is controlled by the diameter ratio. Here, it is interesting to note that as the diameter ratio reduces, the collision on the runner shaft increases and the separation on the flow in the convergent part of the nozzle and close to the runner entry decreases due to increase the blade radius curvature which narrowing the passages between the runner blades. It is rather interesting to note that increases the diameter ratio has a strong effect on the length of the blades by decreasing the blade radius curvature which may decrease the energy extracted from the water due to decrease the length of the blades. Accordingly, it is expected that a runner blade profile with diameter ratio 0.65 may result in high power output as the collision on the runner shaft is reduced significantly and the length and blade curvature increase which certainly cause higher efficiency.

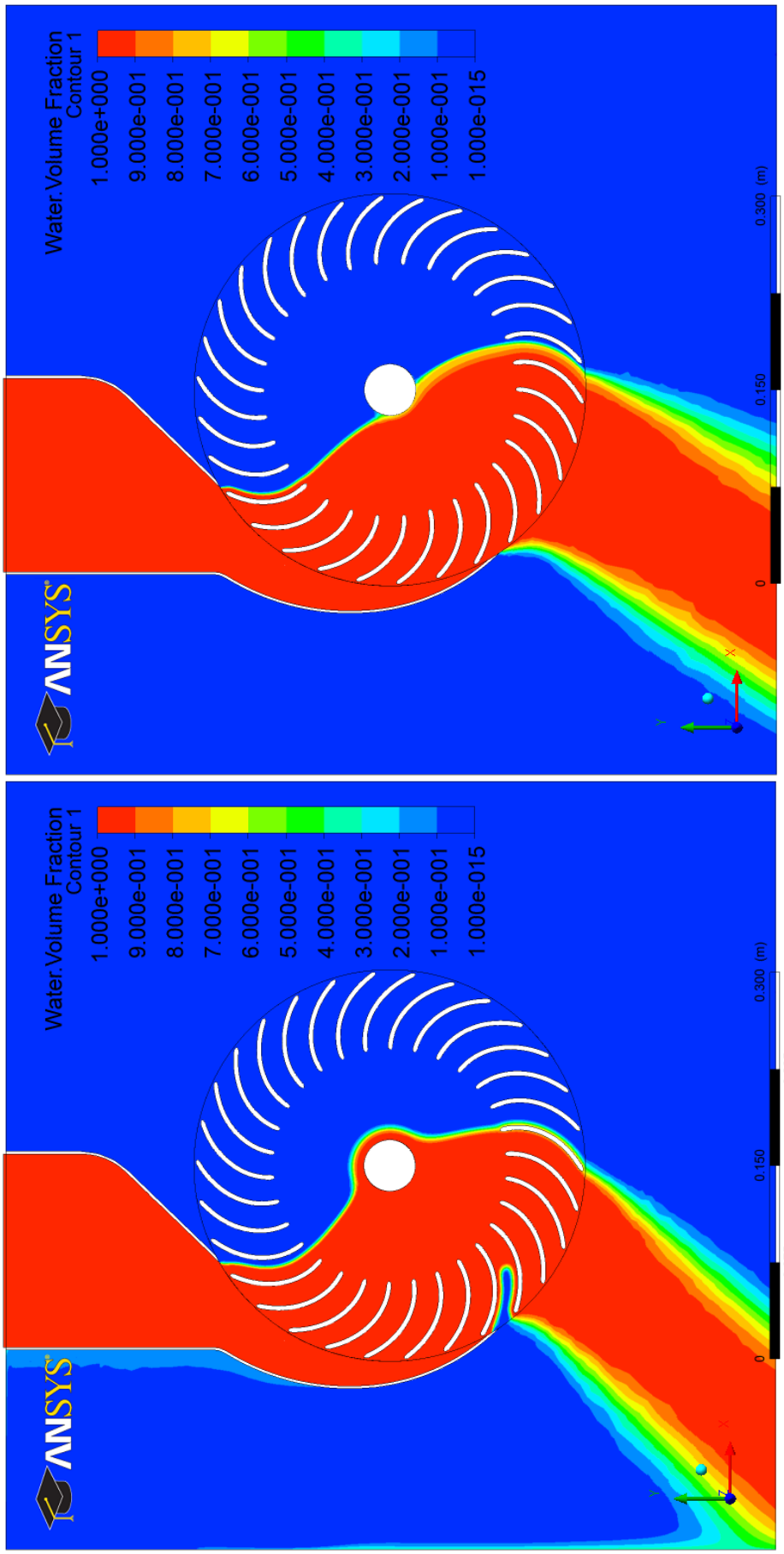

(a) $d_2/d_1 = 0.60$ (b) $d_2/d_1 = 0.65$

Fig. 5.8 (a) and (b) Water volume fraction contours at the mid span of cross-flow turbine of various diameter ratios.

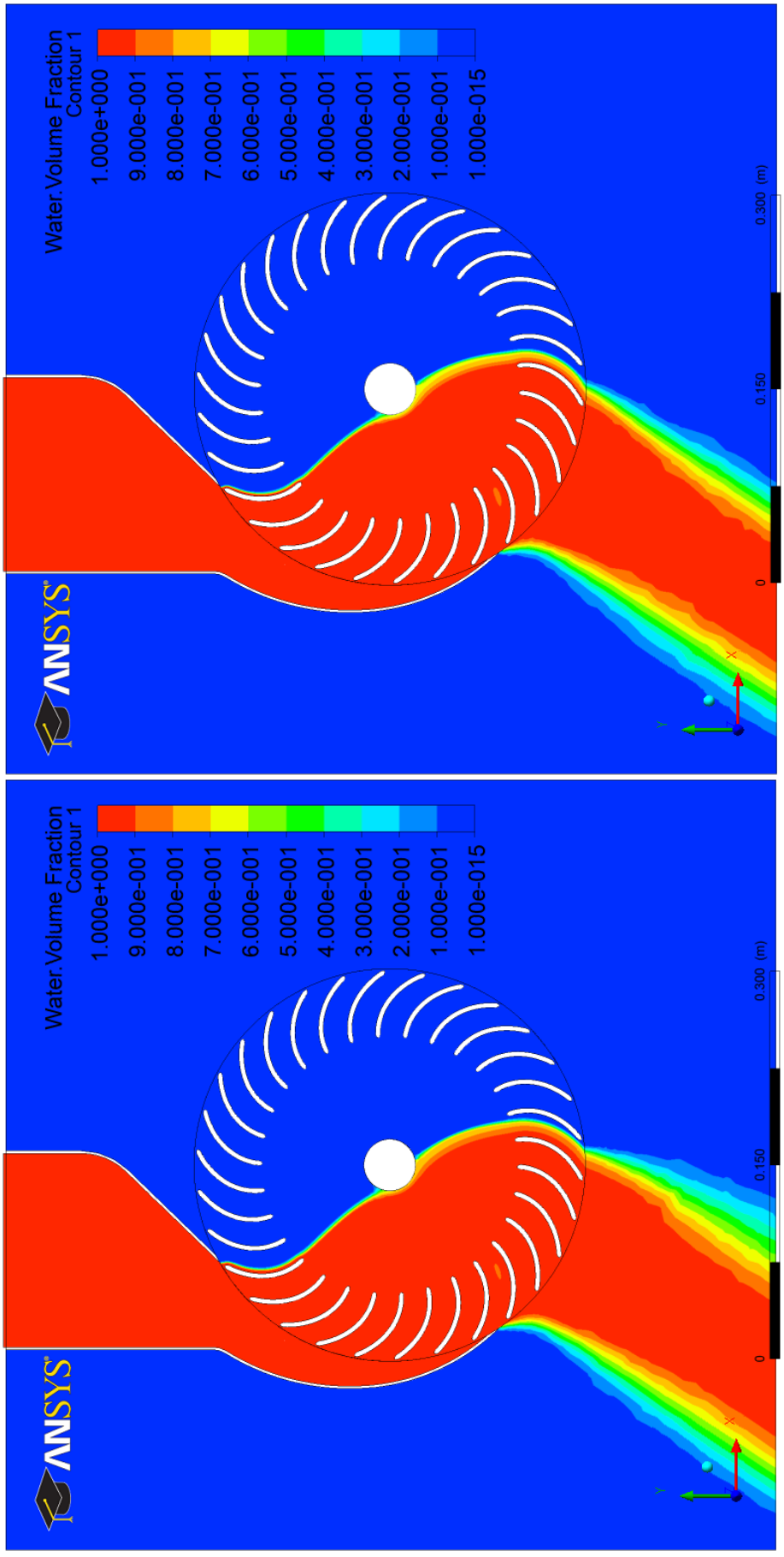

(c) $d_2/d_1 = 0.66$ (d) $d_2/d_1 = 0.67$

Fig. 5.8 (c) and (d) Water volume fraction contours at the mid span of cross-flow turbine of various diameter ratios.

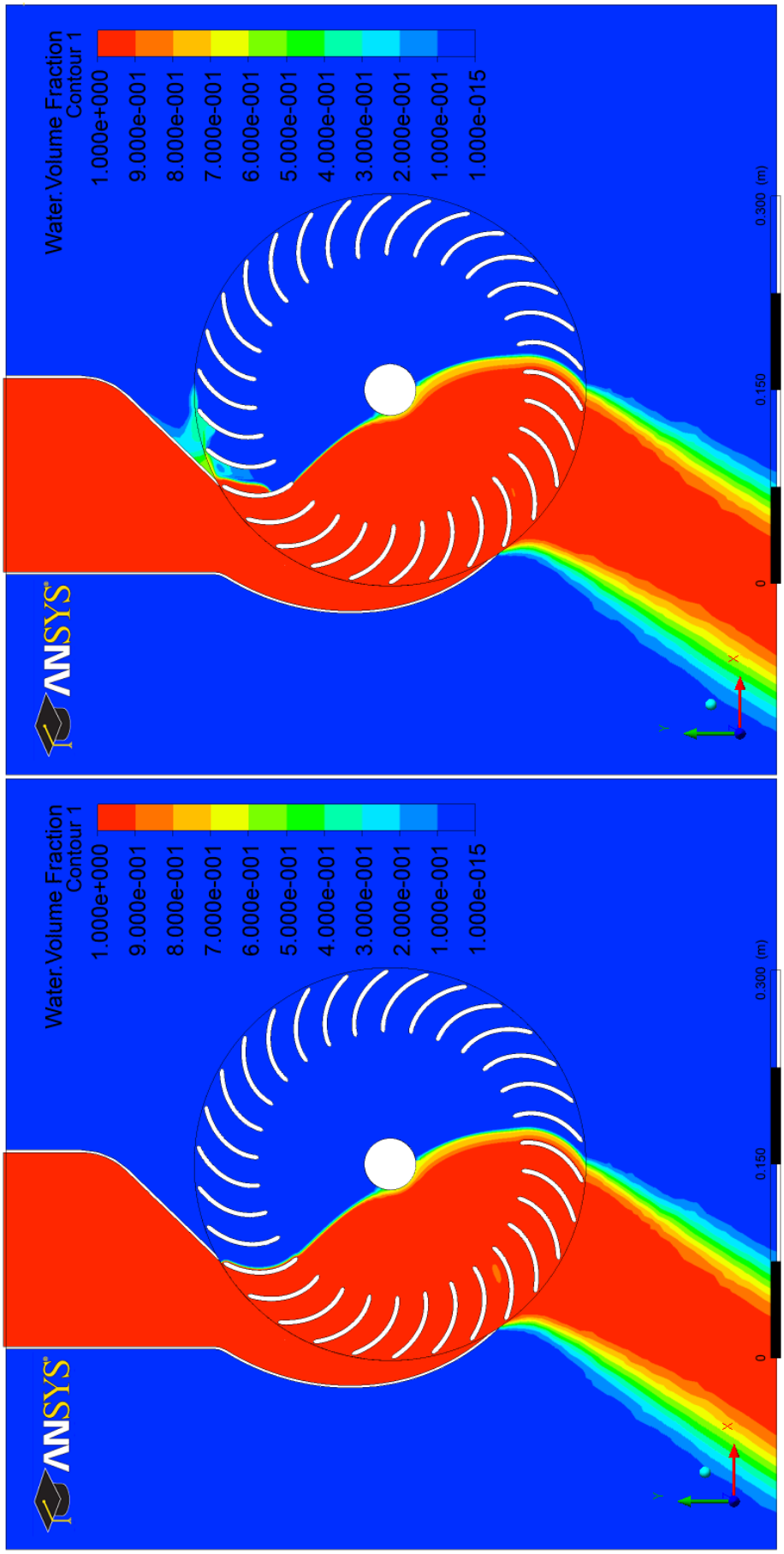

(e) $d_2/d_1 = 0.68$ (f) $d_2/d_1 = 0.70$

Fig. 5.8 (e) and (f) Water volume fraction contours at the mid span of cross-flow turbine of various diameter ratios.

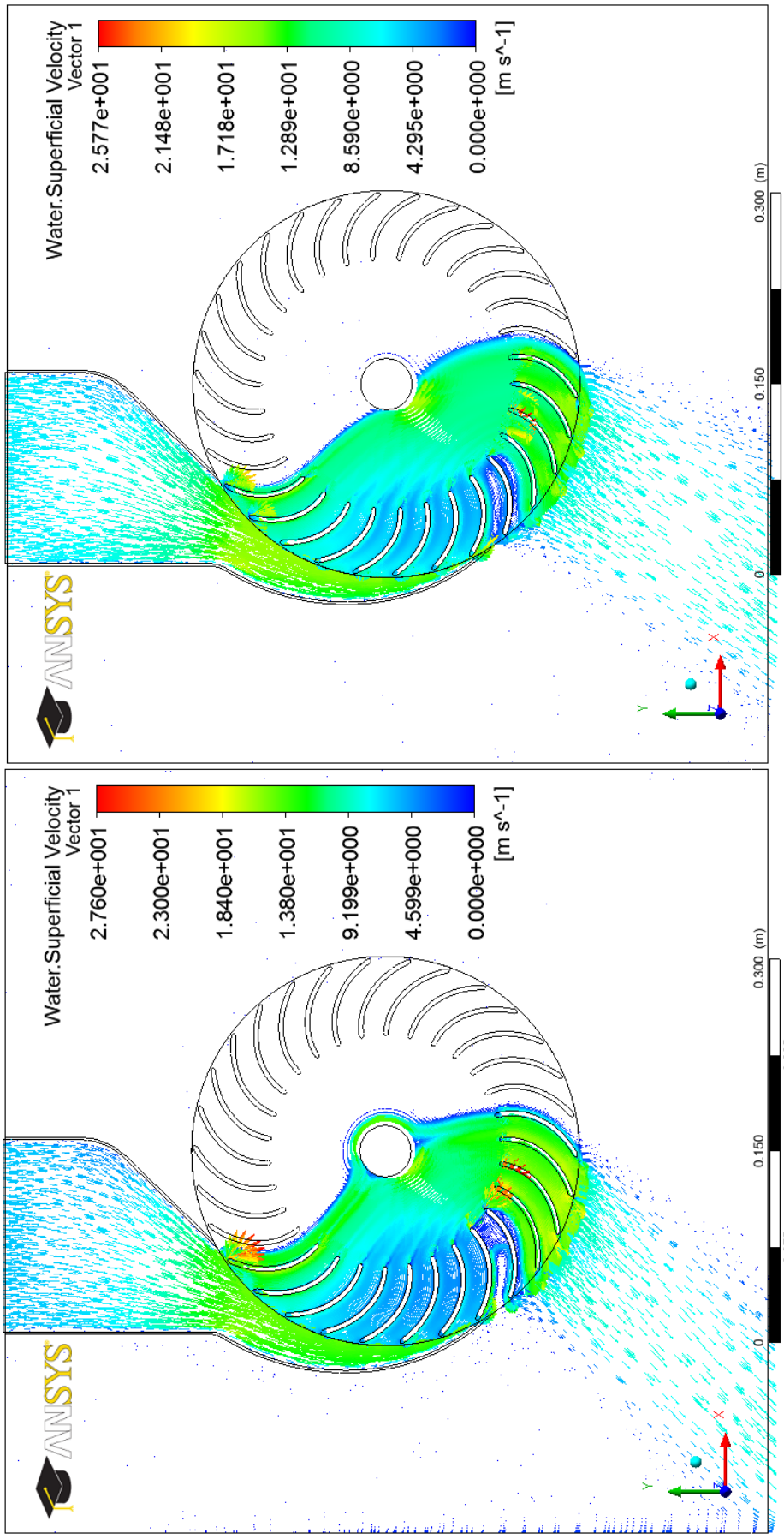

(a) $d_2/d_1 = 0.60$ (b) $d_2/d_1 = 0.65$

Fig. 5.9 (a) and (b) Water superficial velocity vectors at the mid span of cross-flow turbine of various diameter ratios.

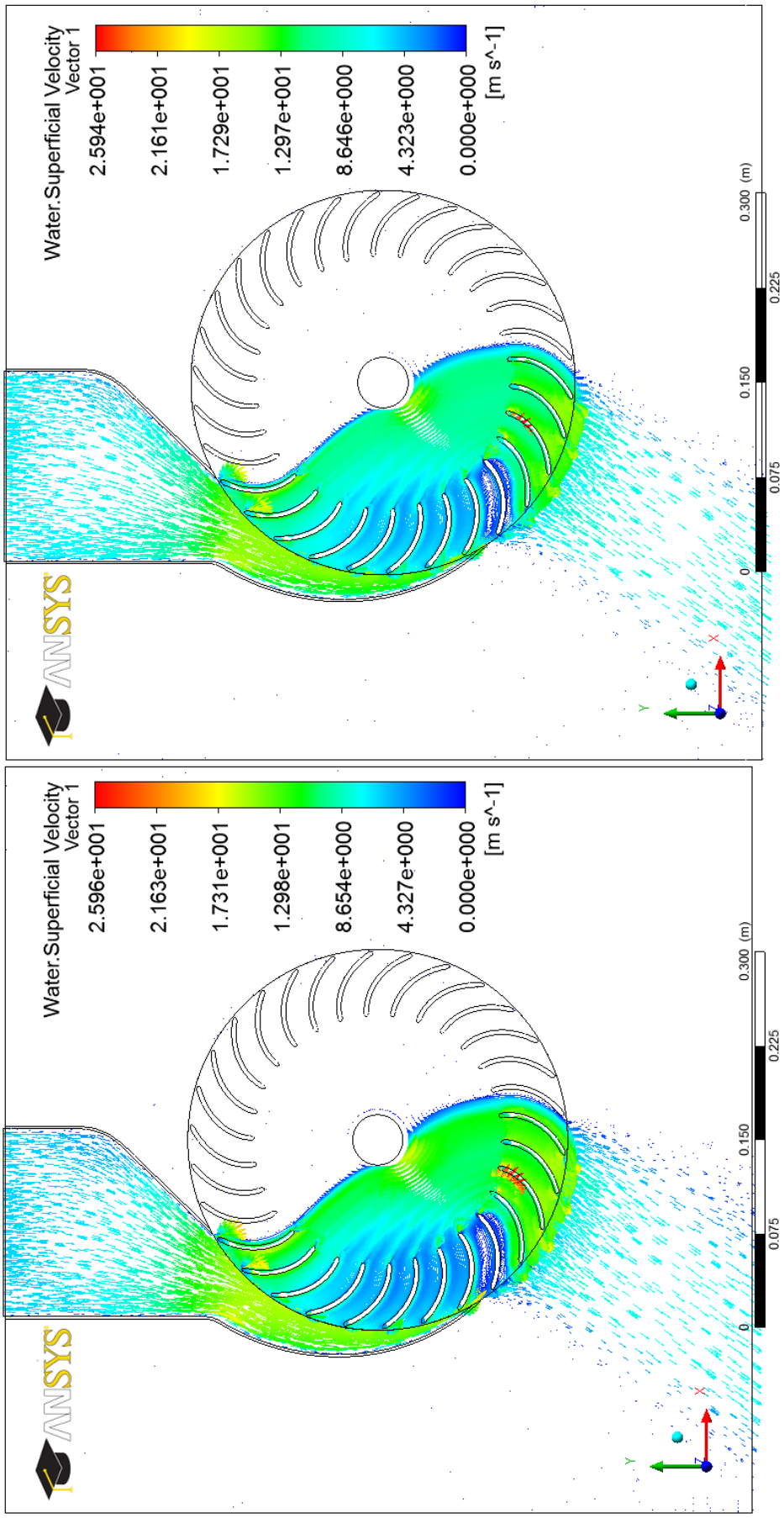

(c) $d_2/d_1 = 0.66$ (d) $d_2/d_1 = 0.67$

Fig. 5.9 (c) and (d) Water superficial velocity vectors at the mid span of cross-flow turbine of various diameter ratios.

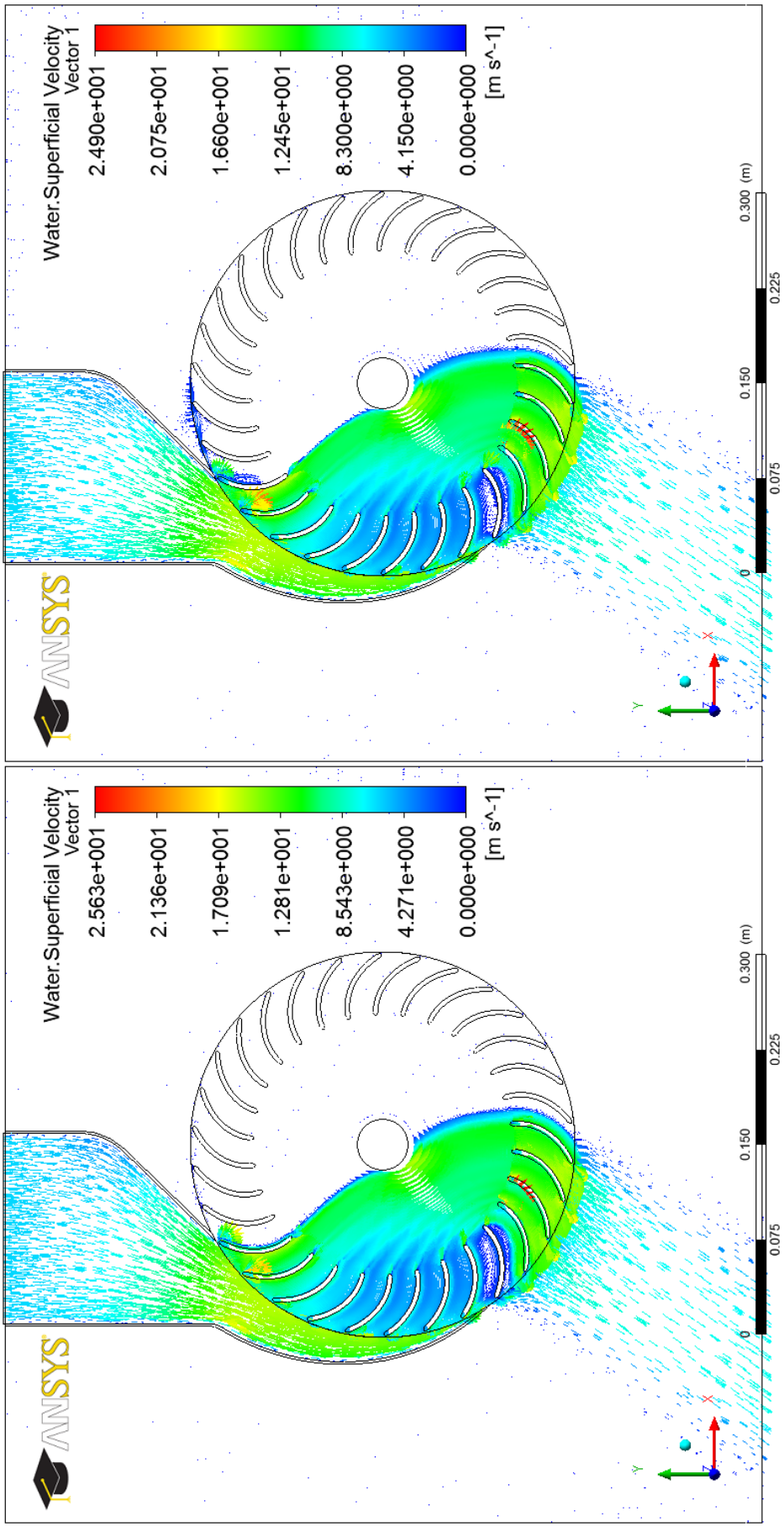

(e) $d_2/d_1 = 0.68$ (f) $d_2/d_1 = 0.70$

Fig. 5.9 (e) and (f) Water superficial velocity vectors at the mid span of cross-flow turbine of various diameter ratios.

The effect of the diameter ratio (inner-to-outer diameter d_2/d_1) on the efficiency of the cross-flow turbine is shown in Fig. 5.10. The results revealed that there was a minimal drop in the efficiency when the diameter ratio changed from 0.65 to 0.68. Most of the previous studies employed a diameter ratio within this range. A further decrease in the diameter ratio under 0.65 tends to cause further reduction in the efficiency. This can be explained by the fact that the energy drop loss increases with decreasing the value of the diameter ratio as shown in Figs. 5.8, 5.9, B.3 and B.4, and also decreasing the diameter ratio under this range is inefficient because the amount of water striking the blades could not flow through narrow passages and reverse flow would result. At small diameter ratio (d_2/d_1 = 0.56), the turbine efficiency was so low (66.021 %). Moreover, a diameter ratio which would be over this range would be inefficient since separated flow would flow out of the wide passages at the inner periphery [31]. At large diameter ratio (d_2/d_1 = 0.70), the turbine efficiency was 72.831 %. According to this the most effective diameter ratio value was 0.65 where the efficiency was 73.88 %. Therefore, the optimum value of the diameter ratio can be considered to be 0.65.

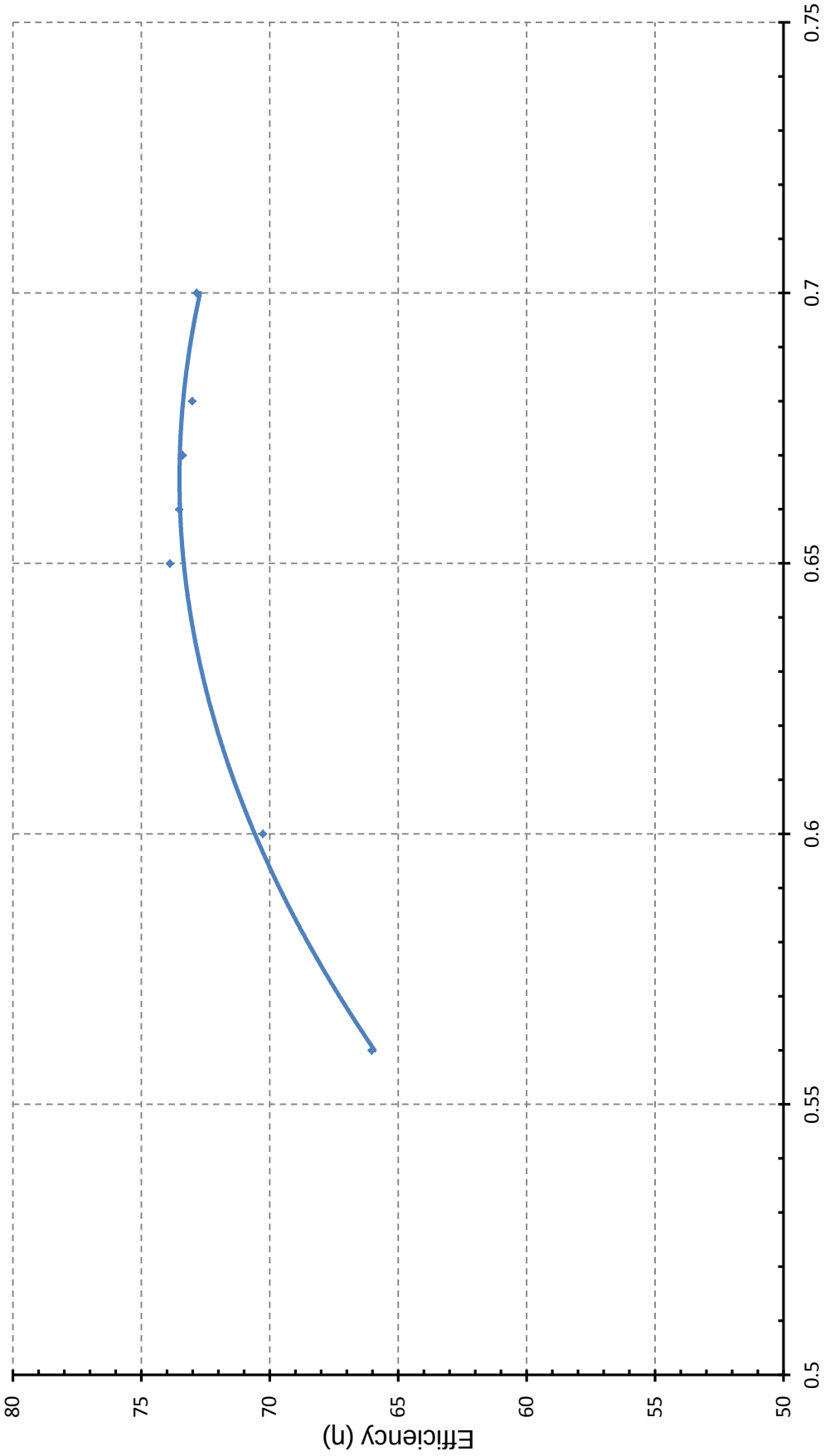

Fig. 5.10 Cross-flow turbine performance characteristic curve for runner with various blades diameter ratio.

An enlarged view of total pressure and flow structure for a diameter ratio of 0.60 is shown in Figs. 5.11, 5.12 and 5.13. These pressure contours reveal some very interesting details on the flow structure. Figure 5.11 reveals clearly the impingement of the water onto the runner shaft (axle). This explains the drop in efficiency as some of the water energy is lost during this collision. Further decrease in the efficiency of turbine resulted from the generation of "Tri-Contra-Rotating Vortices" in the passage between certain blades as shown in Fig. 5.12. Those vortices absorb a significant amount of the available energy which cause a drop in the generated power of the turbine. The power drop increased further by the flow reversal caused by the vortex which is generated close to the outlet of the passage of Fig. 5.12. Here, the flow direction encourages the entrainment of the water leaving the passage above and cause the reversed flow. This flow structure (impingement and vortices) disappear at higher diameter ratio. It can be seen from Fig. 5.10 that at 0.60 inner to outer diameter ratio, the turbine efficiency is low (70.258 %).

The tri-contra-rotating vortices structure seems to convert to a single vortex due to frictional and pressure changes when the distance between the blades increases as shown in Fig. 5.5.

Water of high velocity (as indicated by the velocity vectors' colors) coming from the end of the nozzle moves close to the back surface as shown in Fig. 5.16. There it experiences friction with the blade surface and loses some of its momentum, as a result, and as it approaches the end of the blade surface, some of it entrained with water coming from the upper blades. The rest of the water experiences a change in the directional velocity and turns towards the surface of the next blade. This situation creates a vortex sandwiched between

the two blades and as shown in Fig. 5.16. At the end of the blade, some of the water leaves under the action of gravity. The rest of the water seems to unite with combined portions coming from the upper blades and the lower one. As a result, it moves in the direction of the resultant velocity. This phenomenon can also be confirmed in Figs. 5.17, 5.19 and 5.21.

Fig. 5.14 shows the water superficial velocity as it impinges on the tip of the first couple of blades as it leaves the nozzle. Here, Fig. 5.14 shows clearly that a portion of the water impinging on the tips. As a result, water droplets, generated as a result of the collision with blade tips, travel in direction of reduced regional density. In such regions, because of the existence of the air, there is little resistance to the droplets' movements, and hence they travel with velocity, which exceeds that of the water in the nozzle. At a diameter ratio of 0.66 and 0.68 which are shown in Figs. 5.15 and 5.18 identical phenomena occur. However, it is evidently less intense, which explain why the efficiency is so low in case of a low diameter ratio of Fig. 5.10.

Fig. 5.20 shows the water superficial velocity vectors at the diameter ratio of 0.7. At this ratio and as indicated by Fig. 5.10, the turbine efficiency is rather low. This can be explained by the flow of water droplets opposing the movement of the runner. These droplets originated from the impingement of the nozzle water with the first blade. As these droplets move towards the center of the runner and close to the back surface of the same blade, they tend to lose momentum. Eventually, they are pushed in the upward direction by the centrifugal forces of the rotating runner. As they reverse direction, they create a vortex at "part" of the back surface of the first blade. The water stream containing the droplets leaving the vortex collides with the tip of the nozzle and

eventually bifurcates into two parts. One entrained by the main flow at the tip of the nozzle. The other moves in direction opposing the movement of the runner. As this continues, it collides with the tips and back of the incoming blades producing vortices as shown in Fig. 5.20. This complicated flow regime tends to reduce the efficiency of the turbine and, hence, the low efficiency value at $d_2/d_1 = 0.7$ observed in Fig. 5.10.

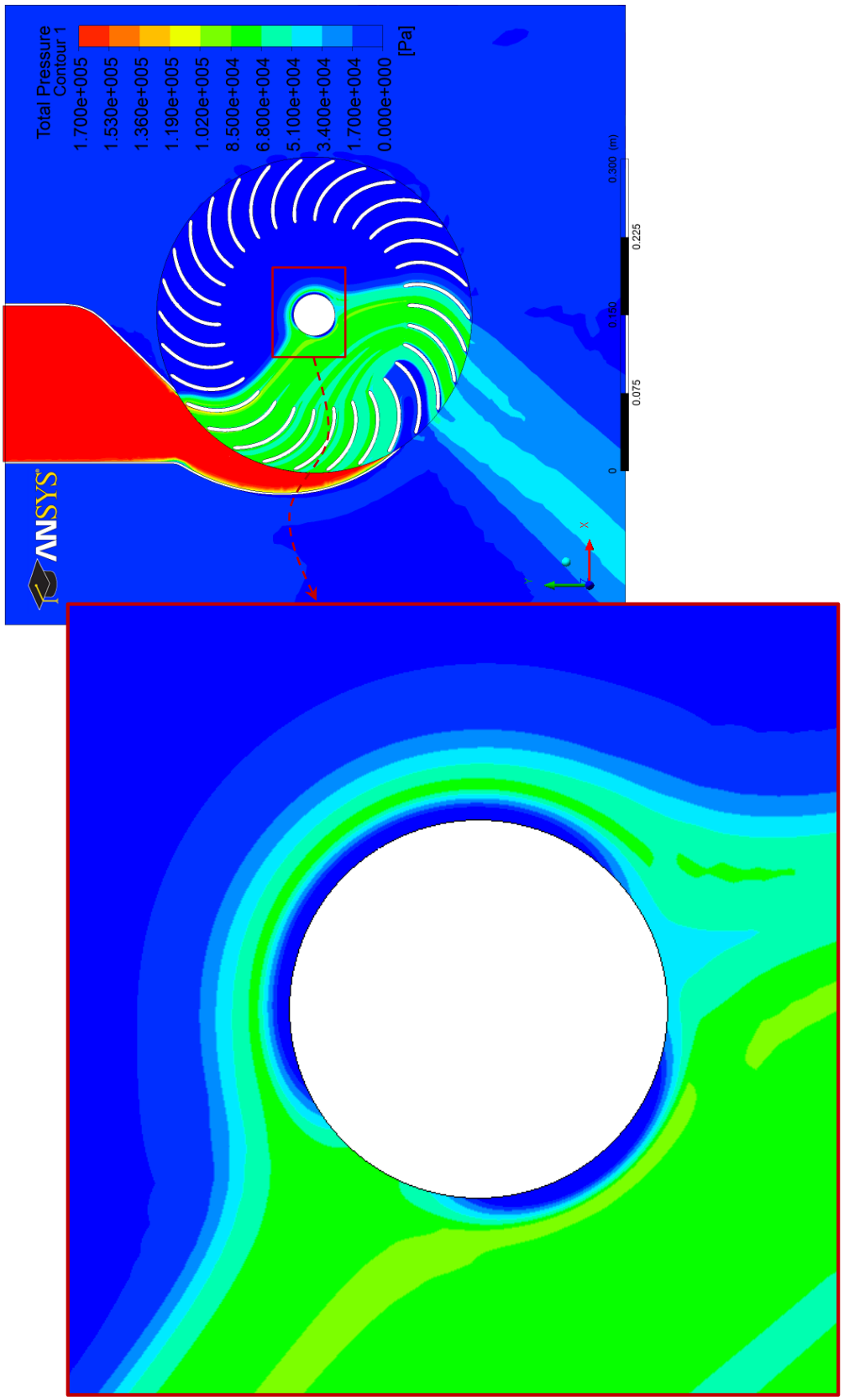

Fig. 5.11 Enlargement of the total pressure contours on the runner shaft at the mid span of cross-flow turbine for the diameter ratio 0.60.

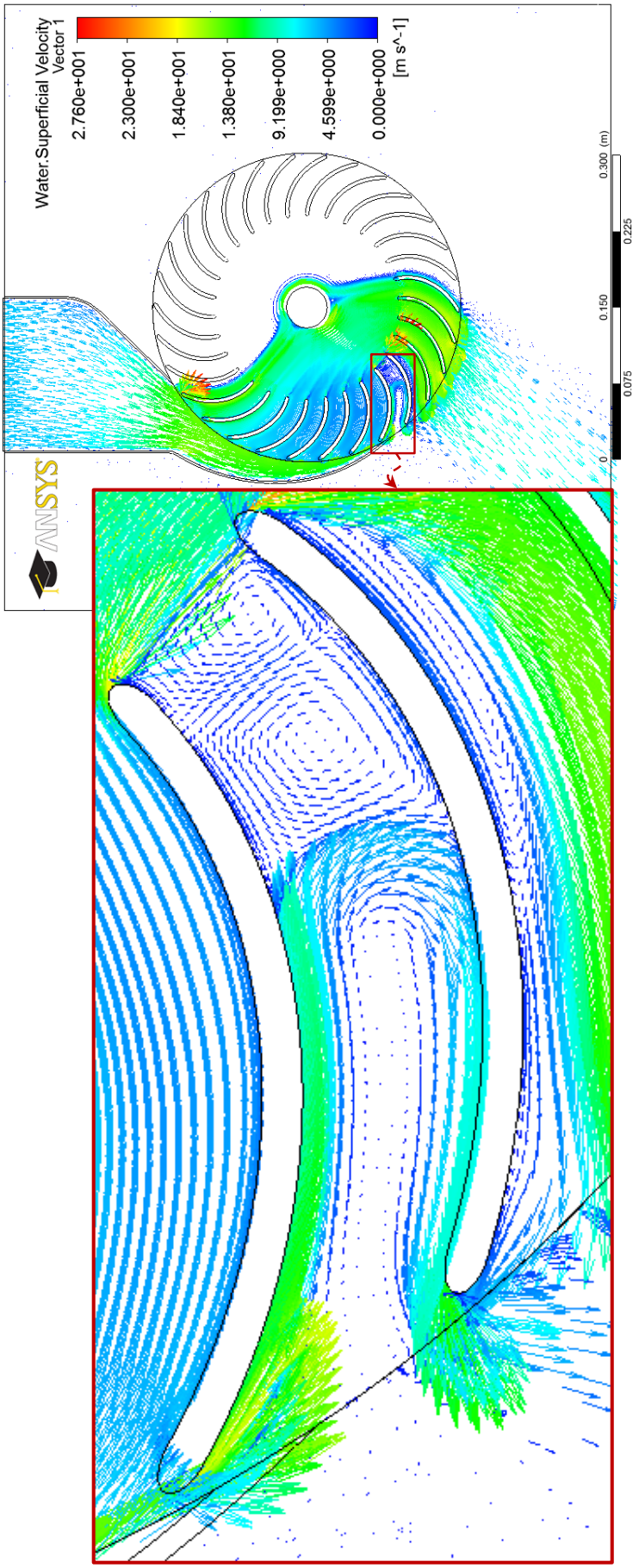

Fig. 5.12 Enlargement of the water superficial velocity vectors on the blades' passages facing the end of the nozzle at the mid span of cross-flow turbine for the diameter ratio 0.60.

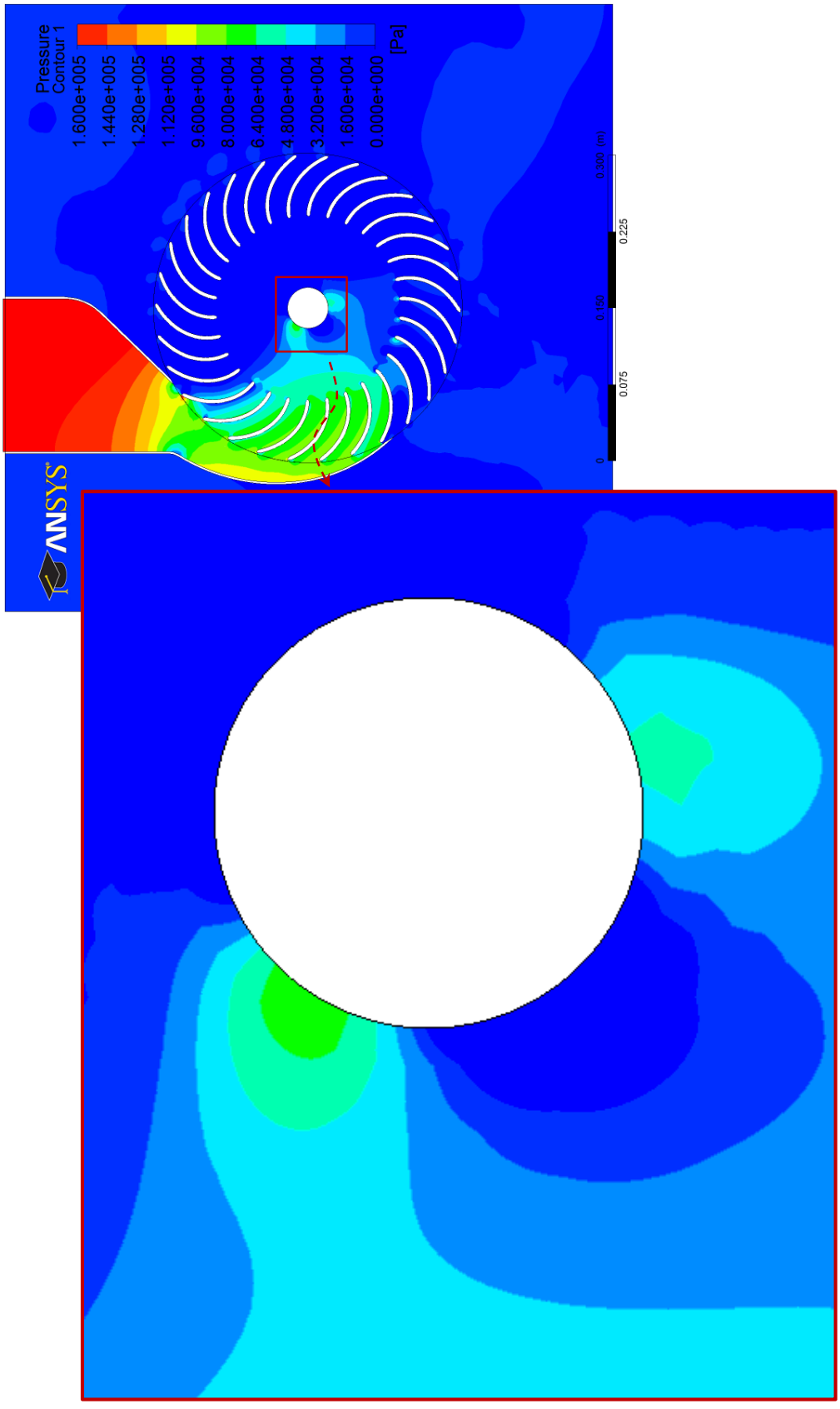

Fig. 5.13 Enlargement of the pressure contours on the runner shaft at the mid span of cross-flow turbine for the diameter ratio 0.60.

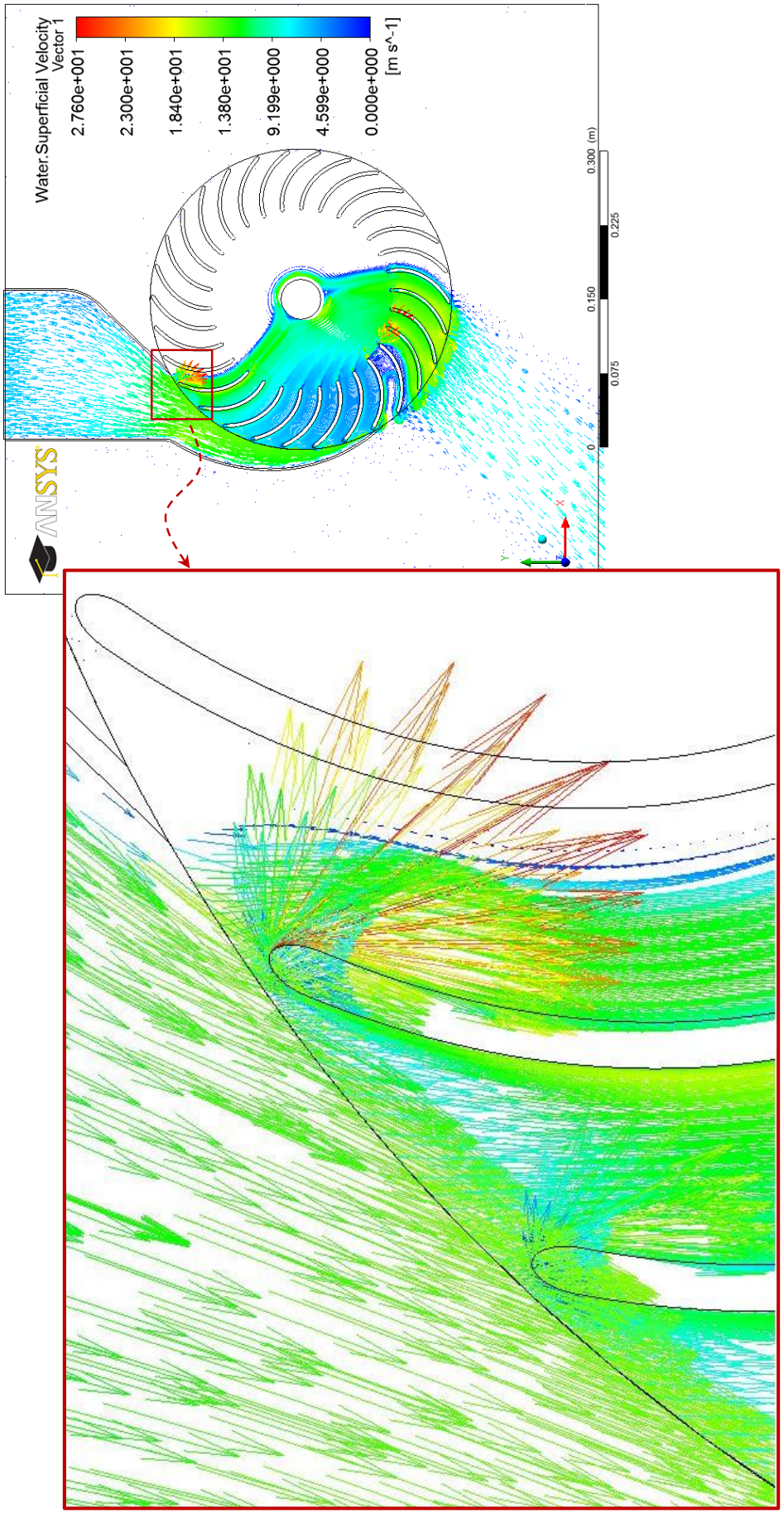

Fig. 5.14 Enlargement of the water superficial velocity vectors on the tip of the first couple of blades at the mid span of cross-flow turbine for the diameter ratio 0.60.

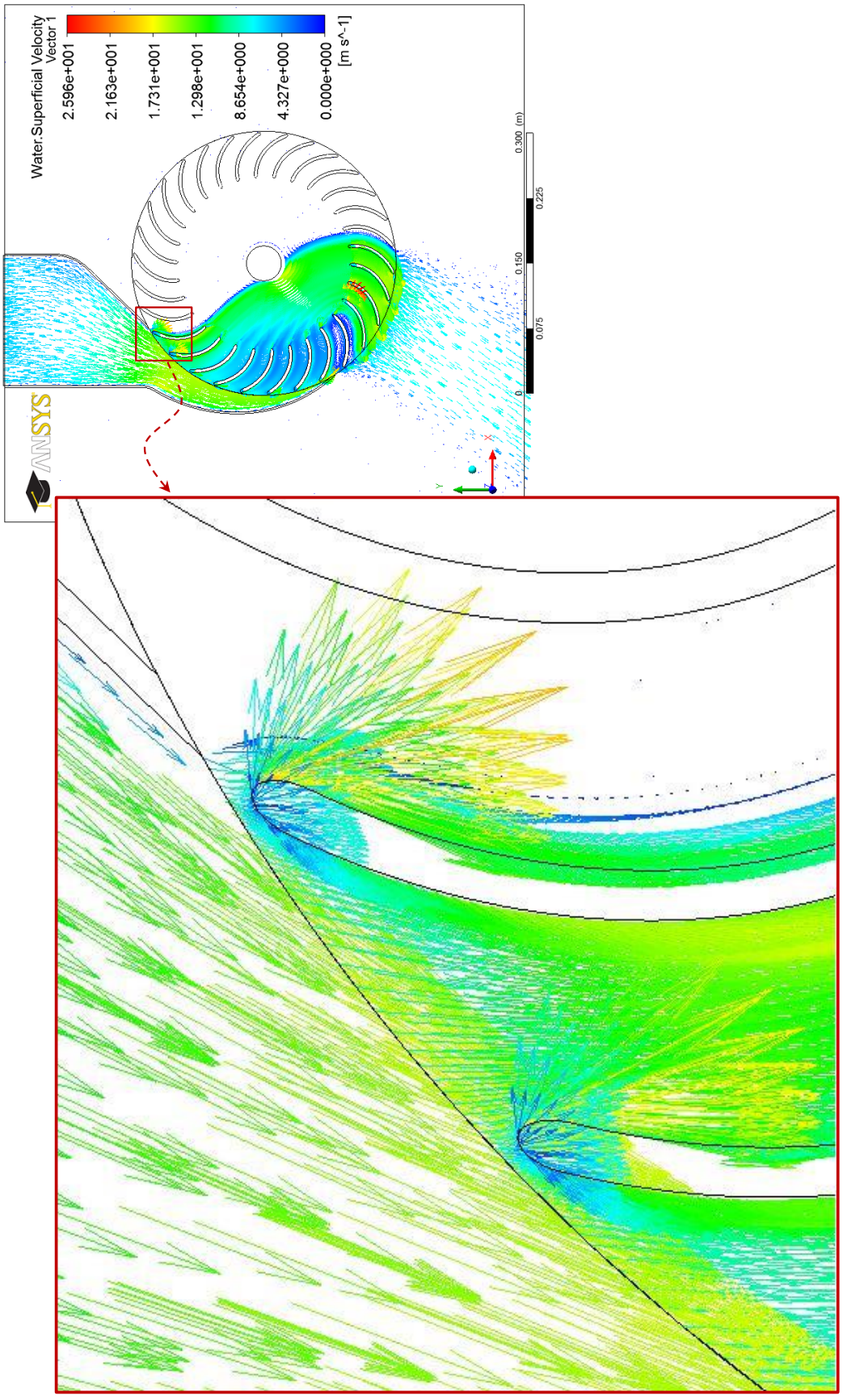

Fig. 5.15 Enlargement of the water superficial velocity vectors on the tip of the first couple of blades at the mid span of cross-flow turbine for the diameter ratio 0.66.

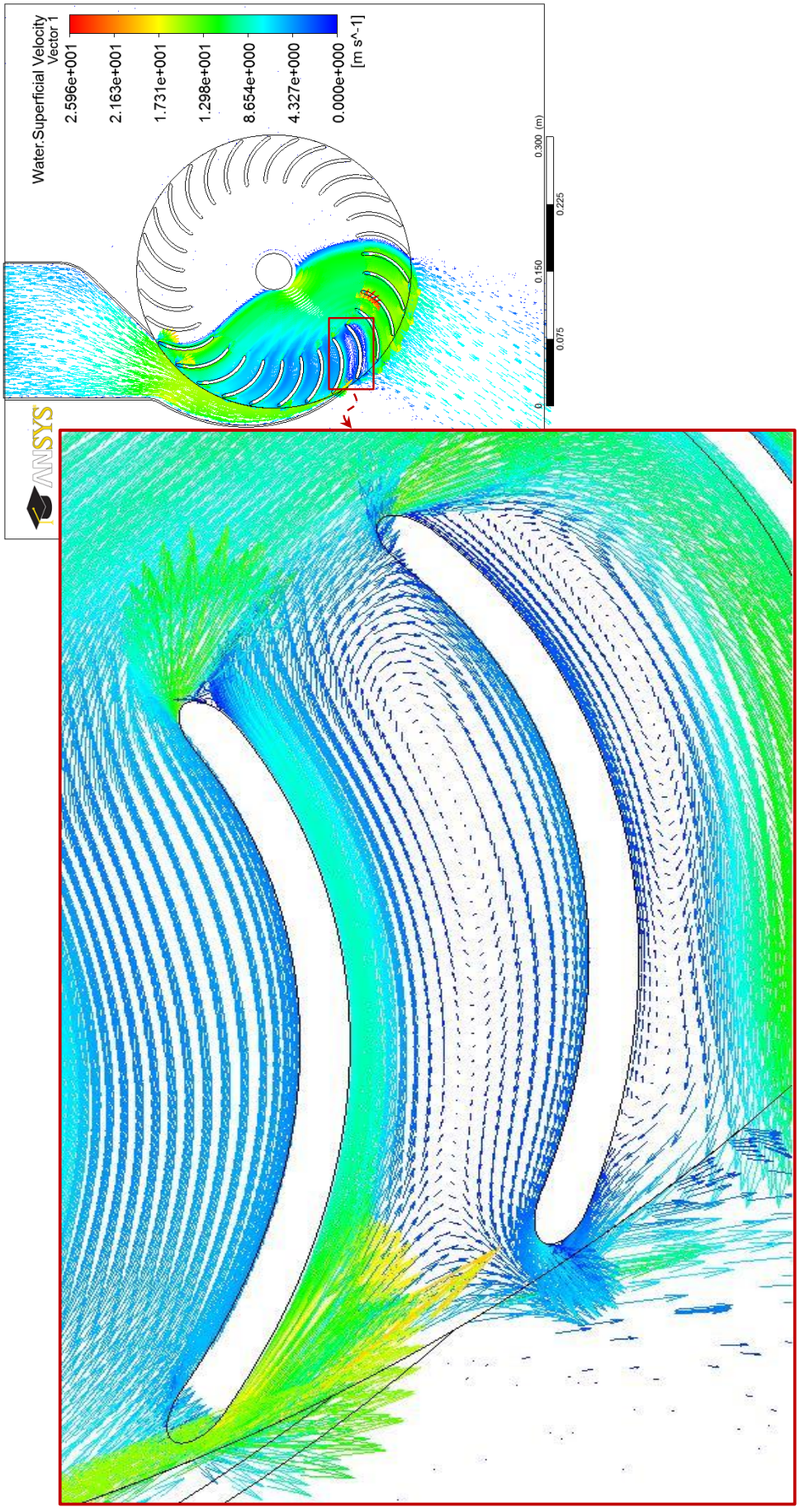

Fig. 5.16 Enlargement of the water superficial velocity vectors on the blades' passages facing the end of the nozzle at the mid span of cross-flow turbine for the diameter ratio 0.66.

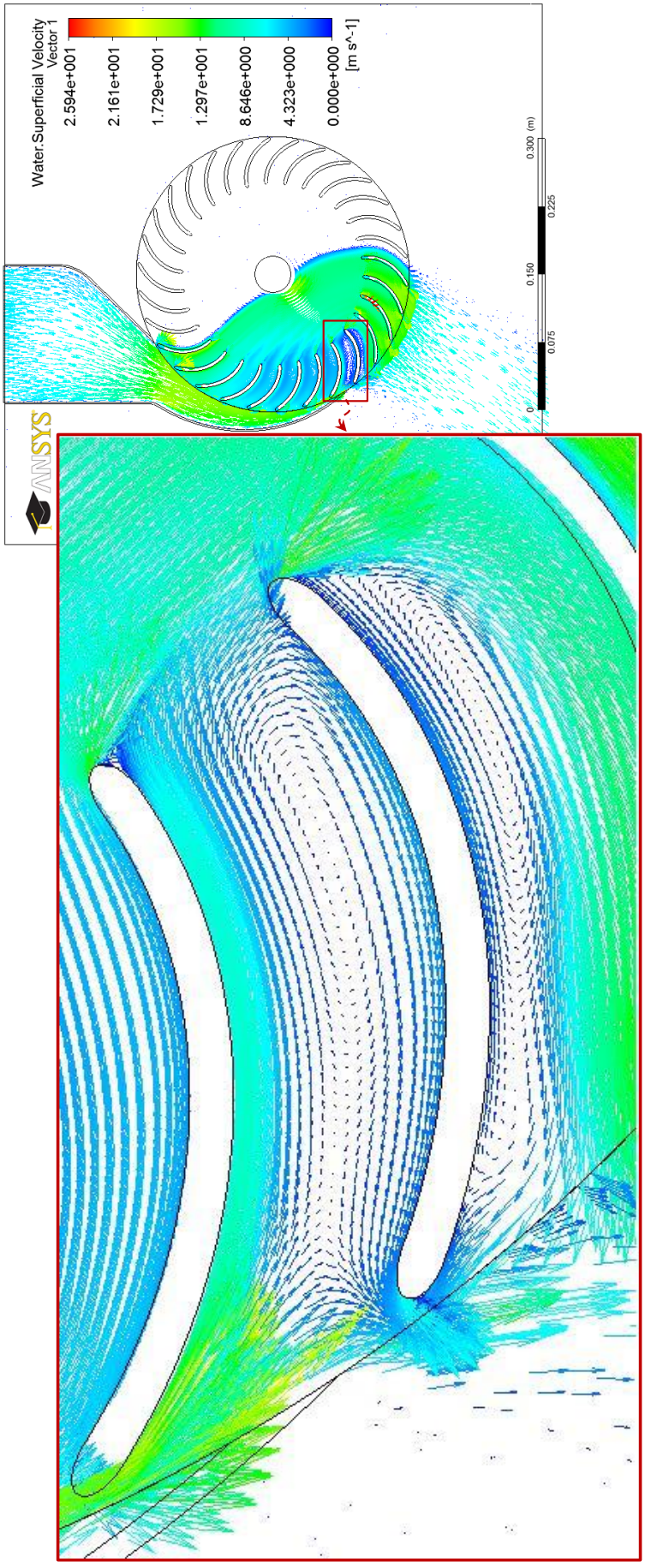

Fig. 5.17 Enlargement of the water superficial velocity vectors on the blades' passages facing the end of the nozzle at the mid span of cross-flow turbine for the diameter ratio 0.67.

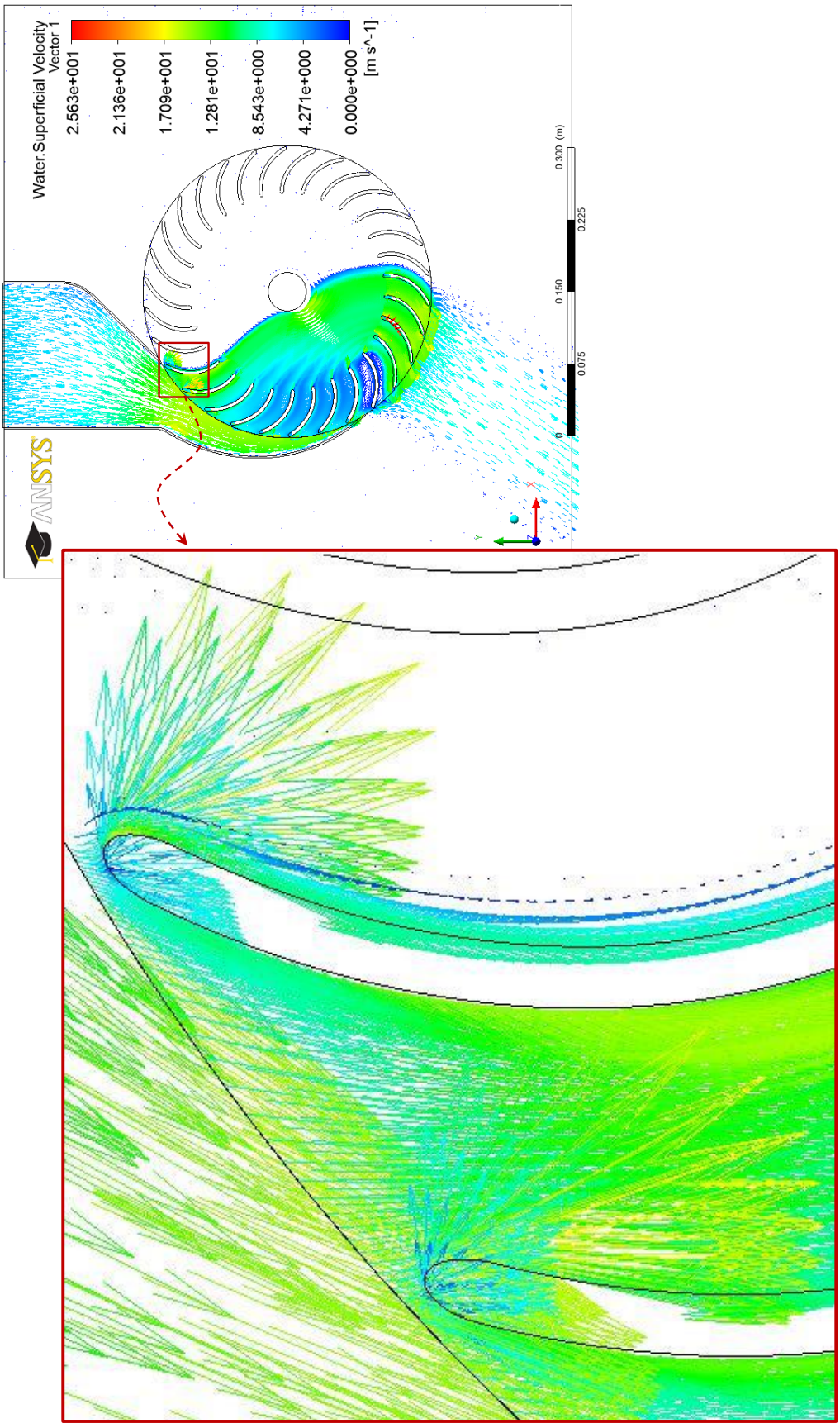

Fig. 5.18 Enlargement of the water superficial velocity vectors on the tip of the first couple of blades at the mid span of cross-flow turbine for the diameter ratio 0.68.

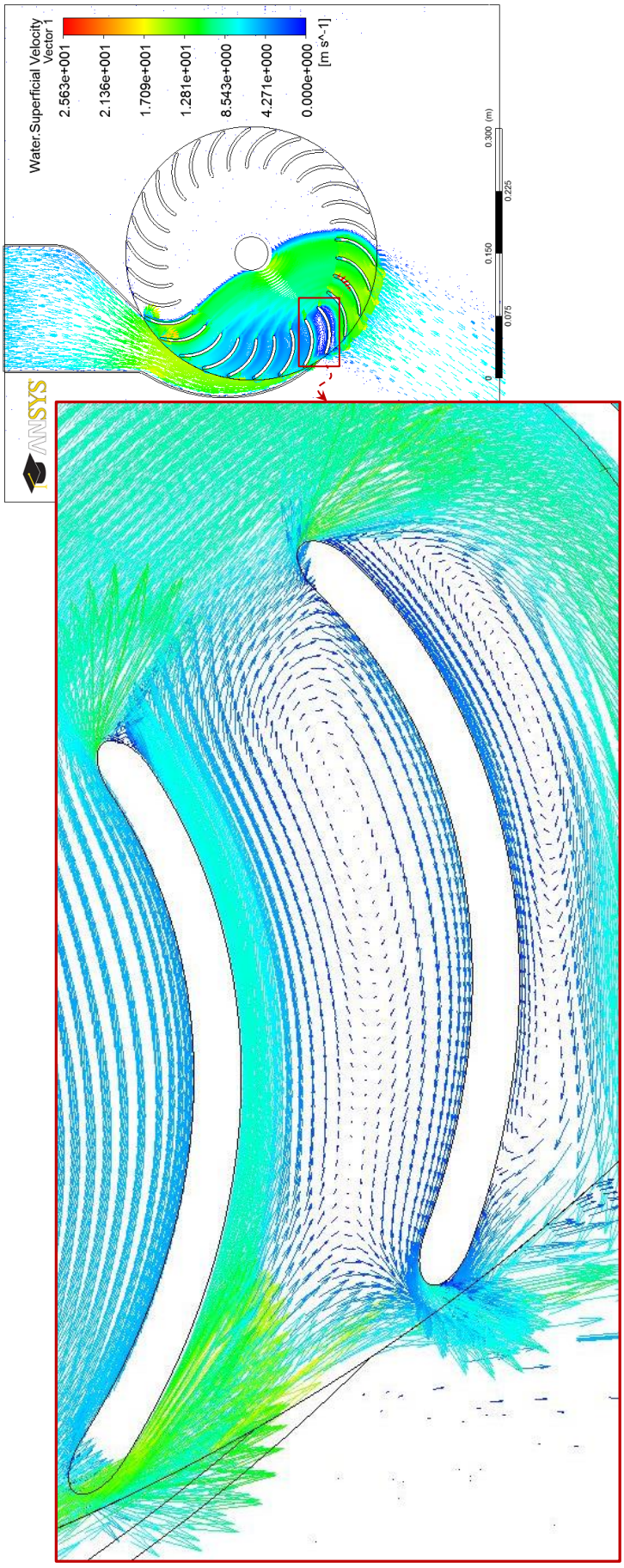

Fig. 5.19 Enlargement of the water superficial velocity vectors on the blades' passages facing the end of the nozzle at the mid span of cross-flow turbine for the diameter ratio 0.68.

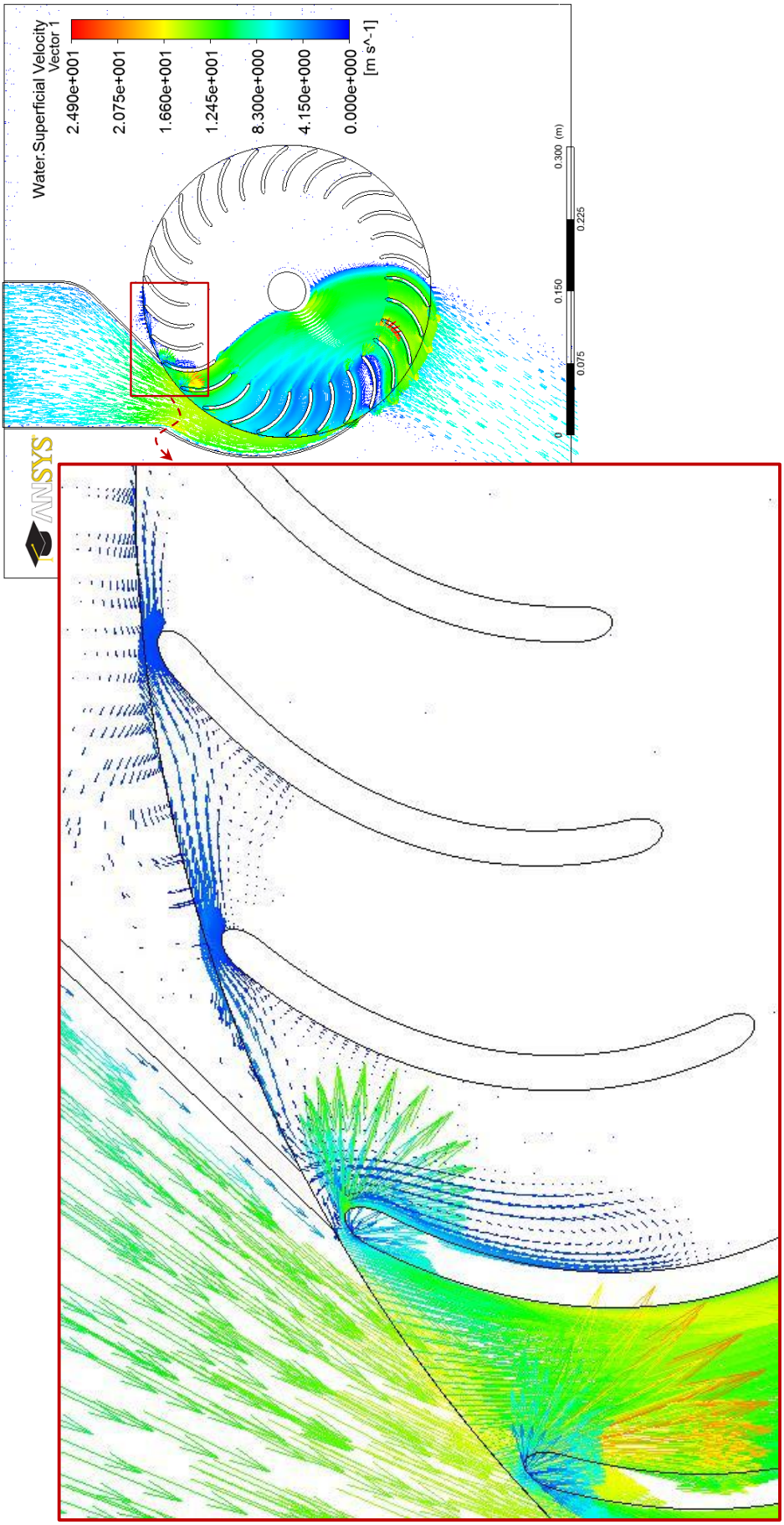

Fig. 5.20 Enlargement of the water superficial velocity vectors on the tip of the first couple of blades at the mid span of cross-flow turbine for the diameter ratio 0.70.

Fig. 5.21 Enlargement of the water superficial velocity vectors on the blades' passages facing the end of the nozzle at the mid span of cross-flow turbine for the diameter ratio 0.70.

5.2.3 Optimization of the Angle of Attack (α_1)

According to Banki's paper "Neue Wasser-turbine" translated by Mockmore and Merryfield [31], the maximum efficiency equation (3.49) shows that in order to achieve the maximum efficiency, the angle of attack α_1 should be kept as small as possible.

$$\eta_{max} = \frac{1}{2} c^2 (1+\psi) \cos^2 \alpha_1 \qquad \text{… (From Chap. 3, Eq. 3.49)}$$

The angle of attack α_1 shown in Fig. 3.2, for a laboratory turbine constructed by Mockmore and Merryfield [31], was 16^o according to the specifications of Banki. Most of the studies afterwards were conducted using this angle value. The angle of attack has a significant effect on the internal flow characteristics and the hydrodynamic forces within the cross-flow turbine. The flow angle at the runner inlet (nozzle exit) and the water passages between the runner blades are controlled by such angle. An experimental investigation to study the effect of the angle of attack on the cross-flow turbine efficiency was conducted by Aziz and Desai [46]. The results of these experiments indicated that an increase in the angle of water entry into the runner from 24^o to 32^o produces in an increase in the predicted maximum efficiency in only 2 out of 18 tests. Therefore, the angle of water entry into the runner should be around 24^o. In 2008, Choi et al [60] presented a numerical method to analyze the effects of the angle of attack on the internal flow and performance of cross-flow turbine by adopting a commercial code ANSYS-CFX. They concluded that an inlet blade angle of 25^o produces a higher turbine efficiency within the angles range of 25^o – 35^o tested. In order to determine the optimum angle of attack, the runner and nozzle of

cross-flow turbine were simulated in the present work by ANSYS CFX code with angles of attack of 15^o, 16^o, 20^o, 24^o and 32^o. This wide angles range covers almost the entire range of the angle of attack in the previous studies. The geometrical parameters' details of the tested cross-flow turbines are listed in table 5.3. Here, the optimize parameters of the runner's blades number and the runner's blades diameter ratio employed in the table/simulation.

Table 5.3 Details of the angle of attacks tested.

Geometrical parameter	Specification
Number of blades	$n_b = 30$
External diameter	$d_1 = 300\,mm$
Diameters ratio	$d_2/d_1 = 0.65$
Angle of attack	$\alpha_1 = ?$ $15, 16, 20, 24 \& 32^o$
Inlet blade angle	$\beta_1 = 151.814^o$
Internal blade angle	$\beta_1^{'} = \beta_2^{'} = 90^o$
Outlet blade angle	$\beta_2 = 28.186^o$
Blade thickness	$t_b = 3.6\,mm$
Blade radius of curvature	$r_b = 49.139\,mm$
Nozzle entry arc	$\lambda = 90^o$
Throat width	$s_o = 60\,mm$
Width of the nozzle	$N_W = 150\,mm$
Shaft (axle) diameter	$d_s = 40\,mm$ *Note: Symbols as detailed in Fig. 3.2.*

In order to view the effect of the angle of attack α_1 on the internal flow of the cross-flow turbine, the water superficial velocity streamlines were plotted for

entire cross-flow turbine as shown in Figs. 5.22 (a) to (d). These figures clearly show that the cross-flow turbine operates as a rectangular jet of water which is directed by the nozzle to strike the blades on the circumference of the runner at a small angle of attack converting the flow energy into kinetic energy. The runner receives the water from the nozzle in a radial inward direction and discharges it in a substantially radial outward direction. The runner with a series of curved horizontal blades converts the energy of the incoming water into mechanical energy.

A comparison of the water volume fraction contours of the flow at the mid span of the turbine runner of various angle of attacks is shown in Figs. 5.23 (a) to (d). Clearly, the nozzle and blades shape are influenced by changing the angle of attack, as the inlet blade angle increases by increasing the angle of attack. The impact of inlet blade angle on the flow exit angle is quite evident.

It is interesting to note the flow regime in each of the water volume fraction results. At the low angle of attack, the shape of the blades changes, in particular, its length. This will increase the conversion of the water energy into a mechanical energy as the blades' passages are longer and more curved. This in turn causes the water to move away from the runner axle which minimizes the impingement losses. It also causes the water to exit the blades/runner at a sharp angle. The above explains the high efficiency of the turbine at a low angle of attack.

In Fig. 5.23 (e), the angle of attack increased to a maximum of 32^{o}, the flow regime changes completely. In this case, both the shape and length of the runner's blades change. The blades are evidently shorter and less curved. This

affects the energy transfer as the incoming water interaction with blades is reduced considerably. In this case, the water leaving the upper row of runner's blades still possesses a significant amount of energy to cause it to impinge on the runner axle. This in turn increases losses and ultimately reduces the efficiency of the turbine as indicated by Fig. 5.31. An enlarged view of the region close to the nozzle outlet is shown in Figs. 5.26 to 5.27. The water volume fraction shows a region of intense activities close to the entry of upper tip of the blades. There some of the incoming water escapes from the clearance between the nozzle and the blade upper tips. This is caused by the low pressure in the regions closed to the runner inlet. A reverse flow generates a stream which impinges on the incoming blades. This stream seems to be growing bigger in case of higher angle of attack as shown in Fig. 5.27. Consequently, this will reduce the water energy conversion as it opposes the runner movement. Ultimately, this will reduce the efficiency of the turbine as evident in Fig. 5.31.

The above phenomena, which associated with the high angle attack, can also be seen in Figs. 5.24 (d) and (e). The escape of a portion of the water from the high pressure region at the tip of the nozzle in the direction of low pressure can be clearly seen also in the enlarged sections of the above figures shown in Figs. 5.28 to 5.29. This cannot be avoided as there must be a clearance between the runner and the nozzle which allow the former to rotate freely. The escape of the water contributes to the parasitic losses as it opposes the movement of the runner.

Figure 5.30, shows the structure of the flow in the blades at the lower part of the runner at a higher nozzle angle of attack of 32^{o}. The structure of the flow is

highly complex, which is associated with changing vortex structure in each blade passage. As indicated in this figure the lowest blade passage shows that the water acquires high velocity, which prevent it from forming large separation regions as in the passages above it. It is little wonder that the efficiency of the turbine at this specific large nozzle angle of attack (32^{o}) is very low as indicated by Fig. 5.31.

To visualize the fluid flow more clearly, vectors of water superficial velocity, contours of total pressure and streamlines of water superficial velocity were plotted on the mid span planes as shown in Figs. 5.24 to 5.25 and Figs. B.5 (a) to (d). These figures clearly show the interaction between the water leaving the nozzle and entering the runner such interaction decreases by increasing the angle of attack. This interaction also decreases as the blade radius increases and as described above. Inspecting Figs. B.5 (a) to (d) closely reveals the tendency of the water to separate along the nozzle rear wall with increasing the angle of attack.

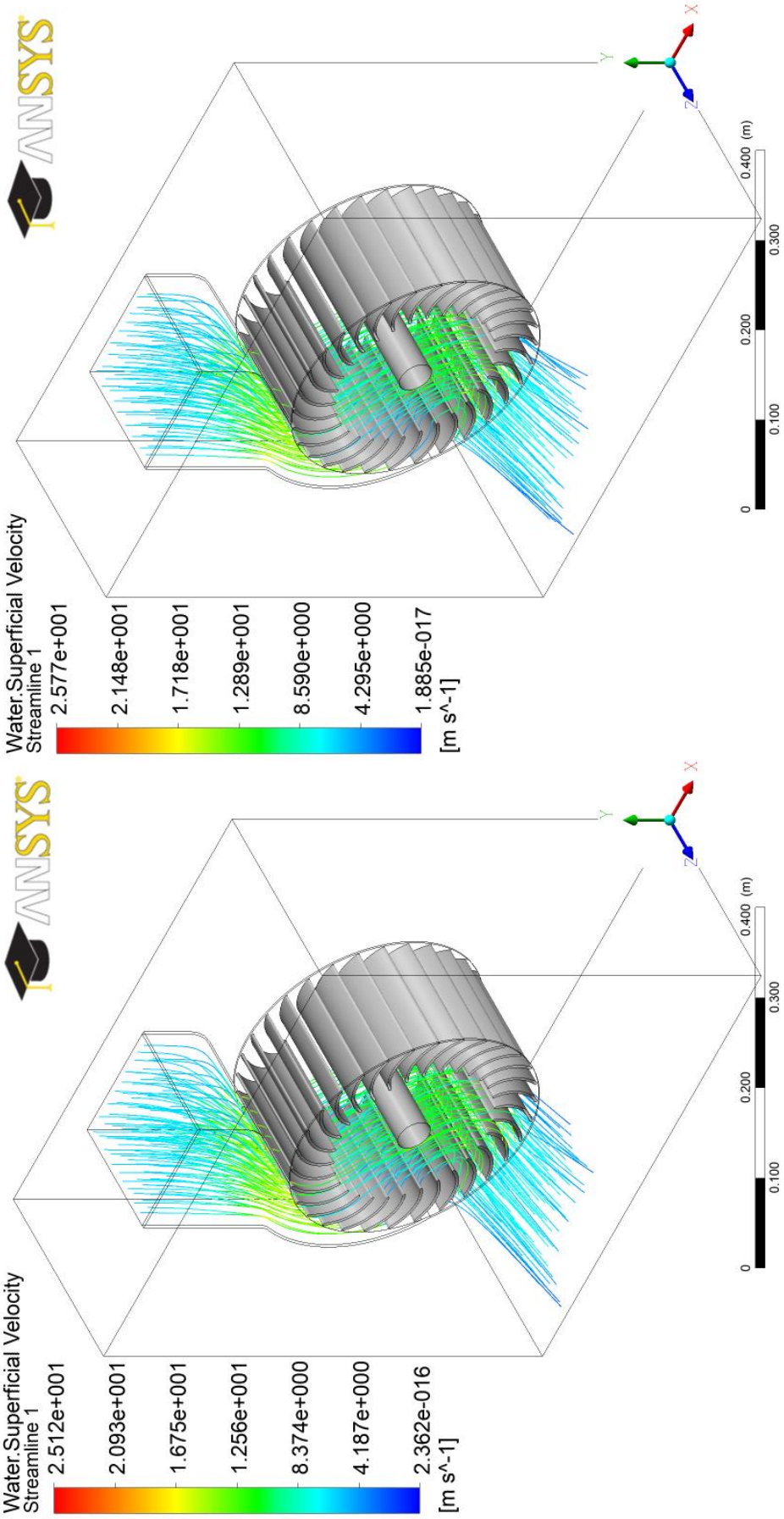

(a) Angle of attack 15^{o} (b) Angle of attack 16^{o}

Fig. 5.22 (a) and (b) Water superficial velocity streamlines in cross-flow turbine of various angles of attack.

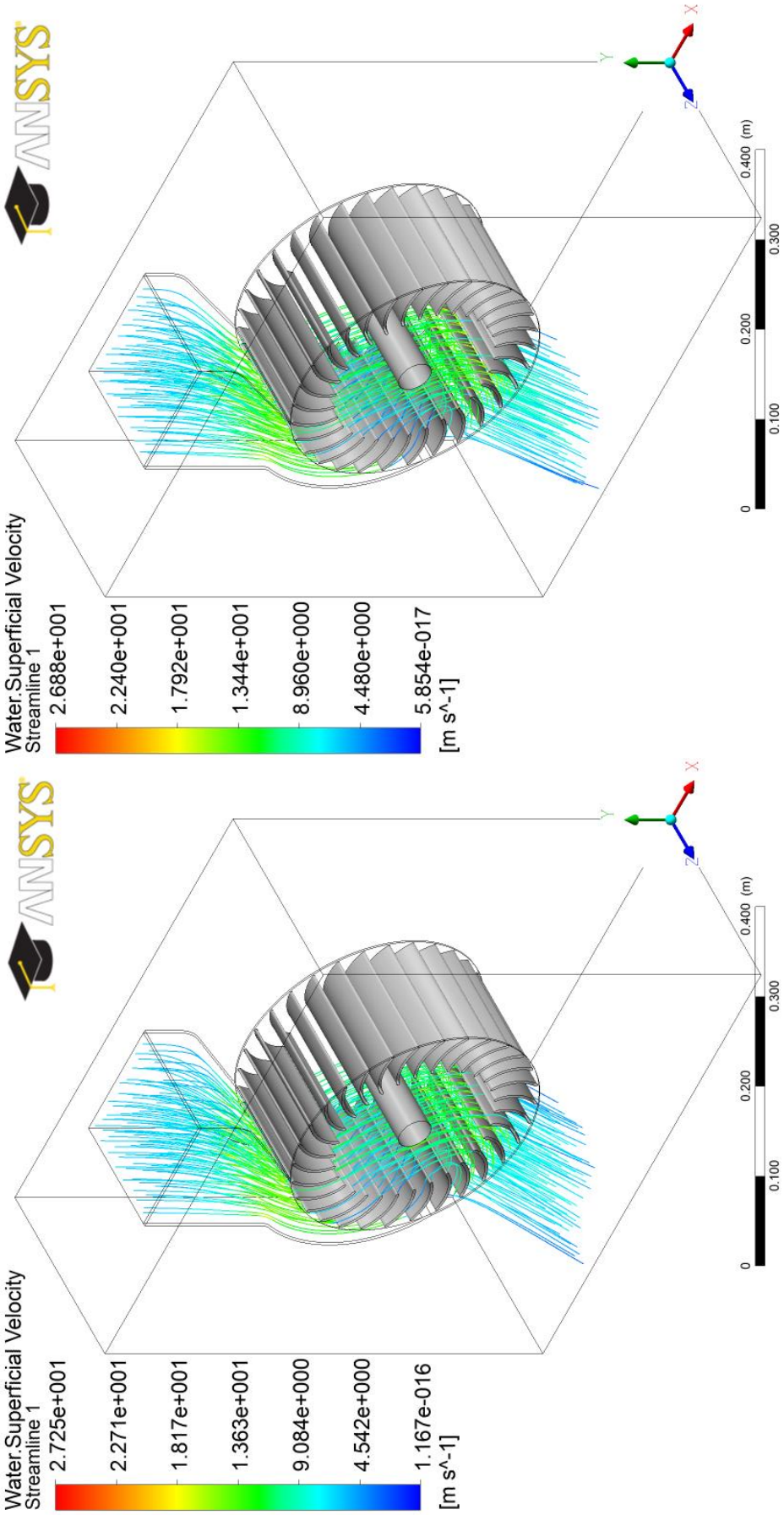

(c) Angle of attack 20°

(d) Angle of attack 24°

Fig. 5.22 (c) and (d) Water superficial velocity streamlines in cross-flow turbine of various angles of attack.

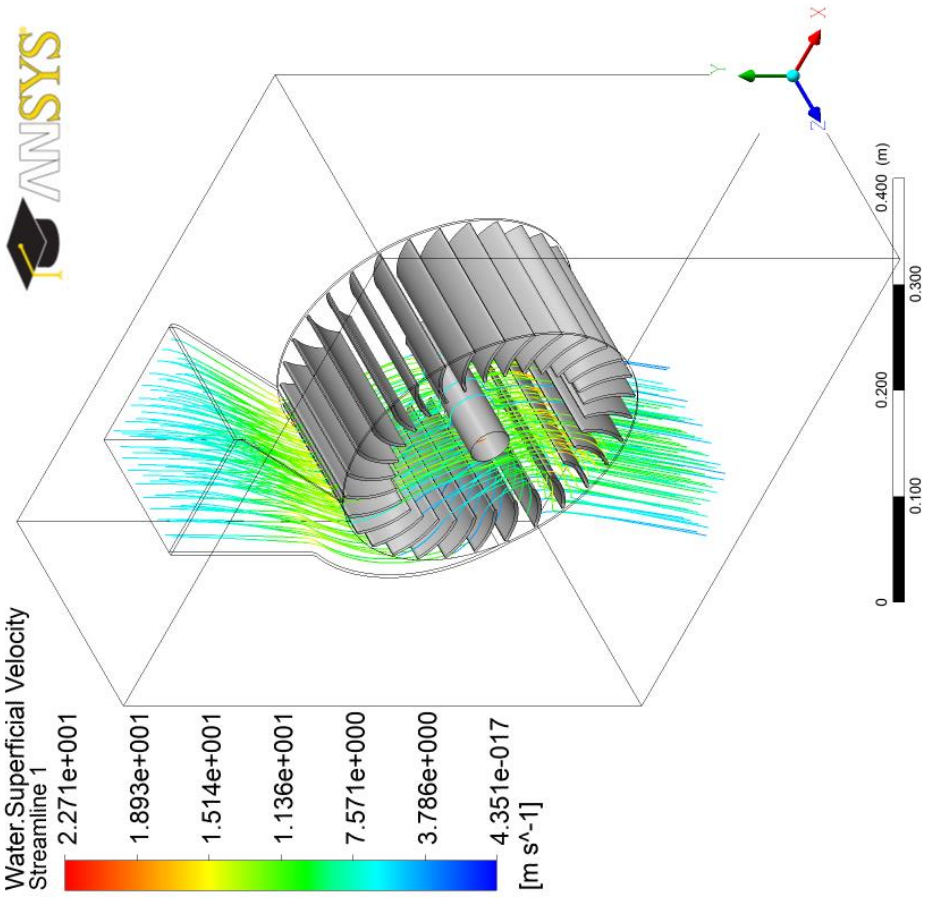

Fig. 5.22 (e) Water superficial velocity streamlines in cross-flow turbine for nozzle angle of attack 32^{o}.

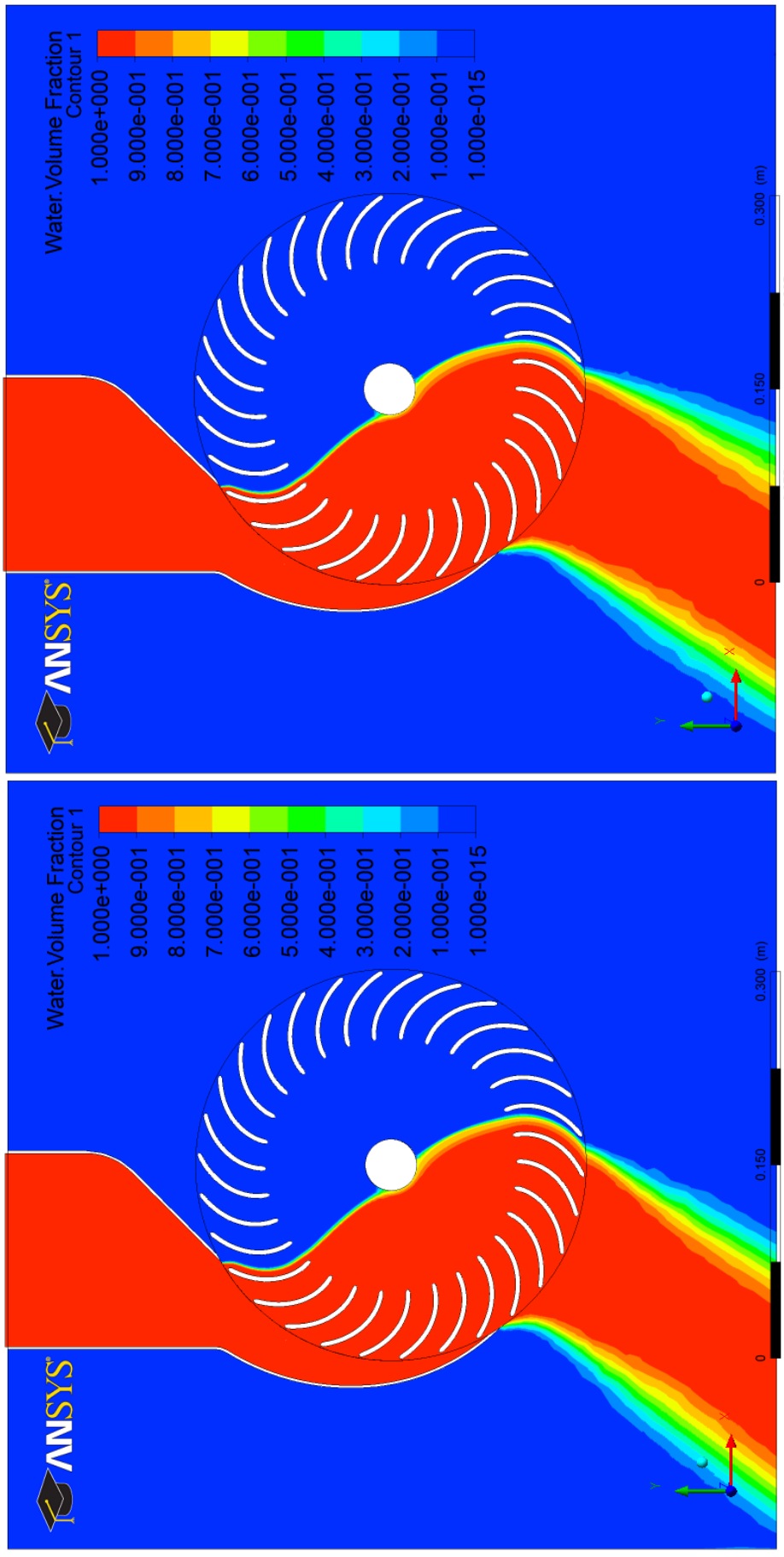

(a) Angle of attack 15^{o} (b) Angle of attack 16^{o}

Fig. 5.23 (a) and (b) Water volume fraction contours at the mid span of cross-flow turbine of various angles of attack.

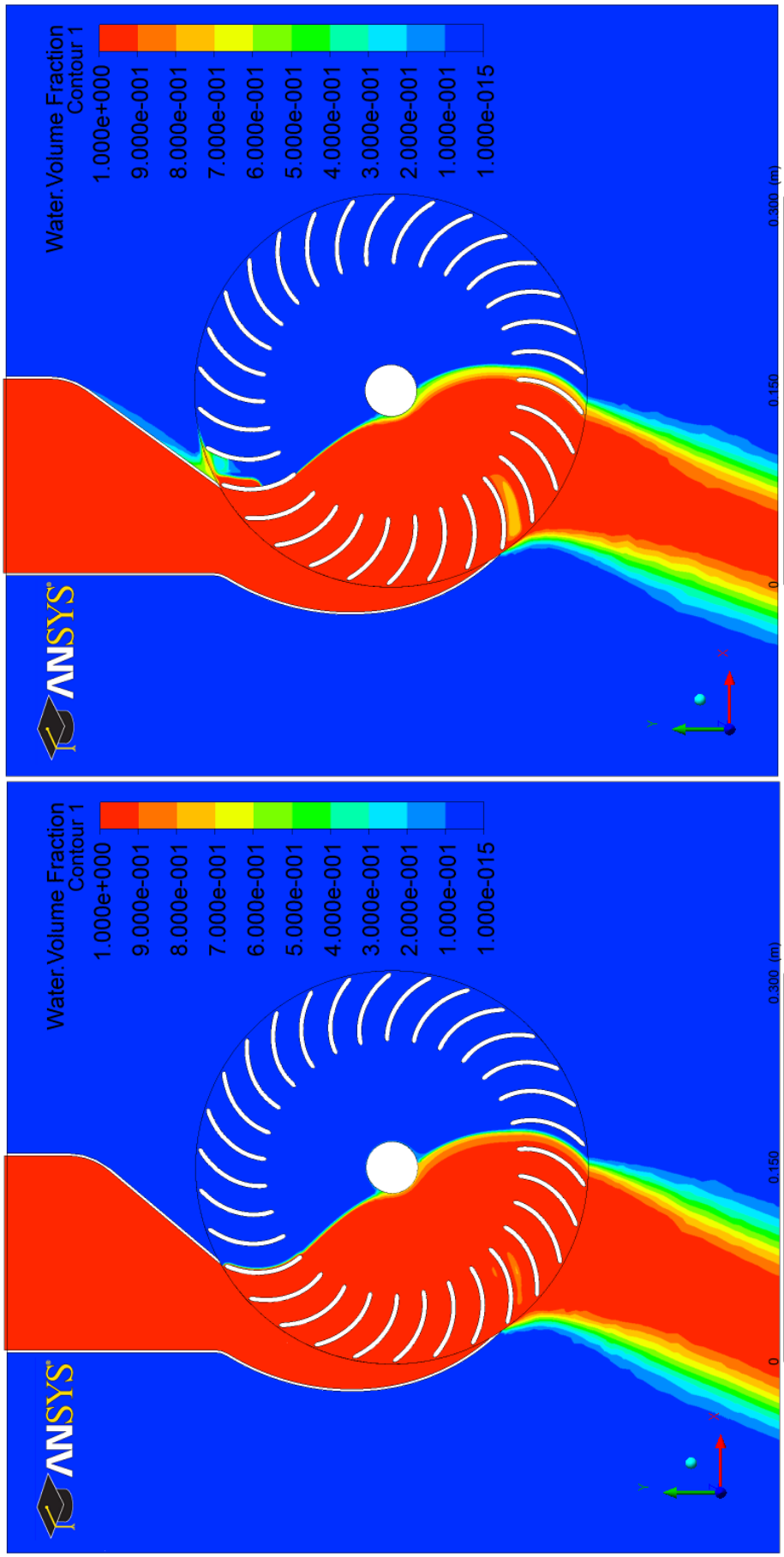

(c) Angle of attack 20° (d) Angle of attack 24°

Fig. 5.23 (c) and (d) Water volume fraction contours at the mid span of cross-flow turbine of various angles of attack.

Fig. 5.23 (e) Water volume fraction contours at the mid span of cross-flow turbine for nozzle angle of attack 32^{o}.

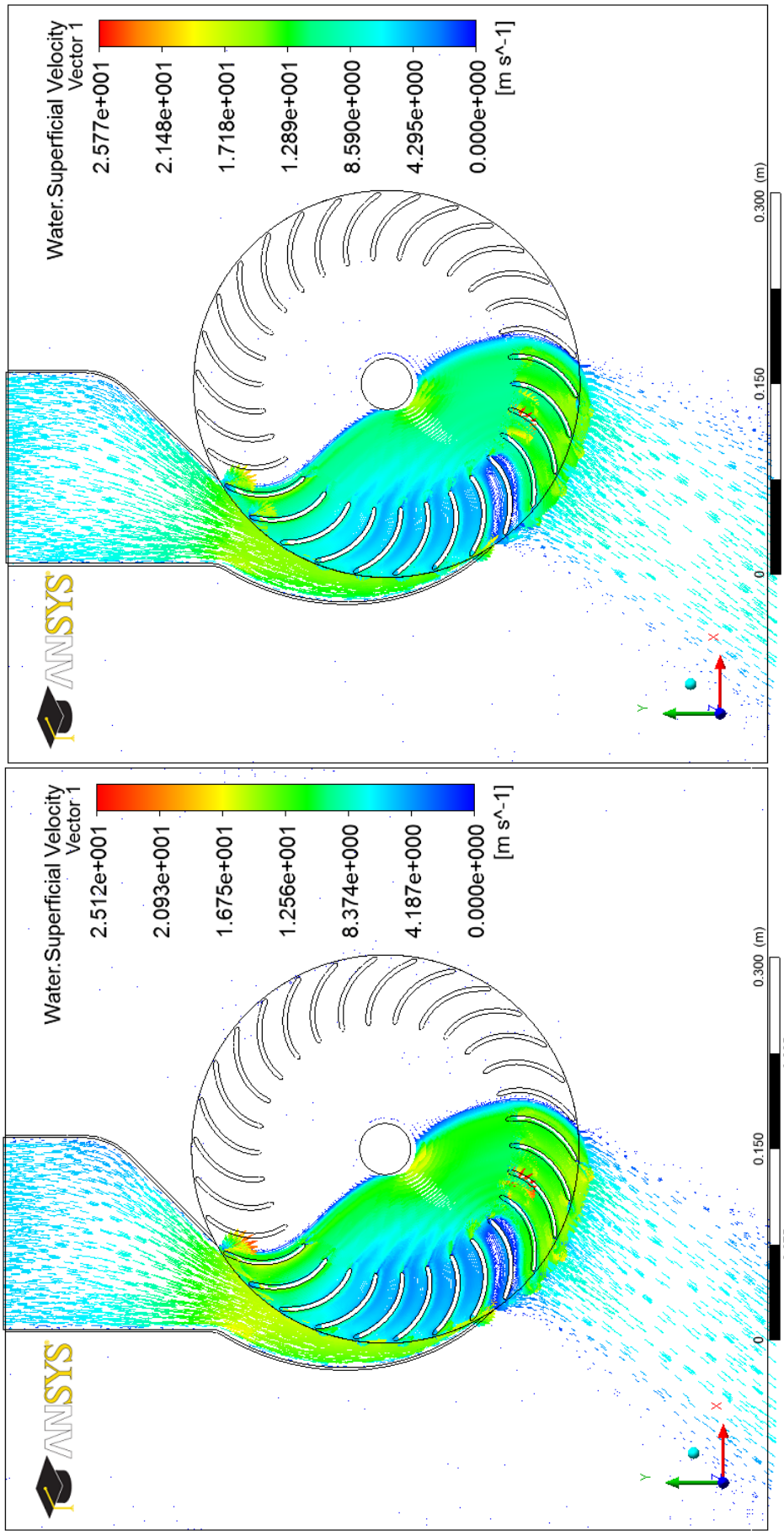

(a) Angle of attack 15^{o} (b) Angle of attack 16^{o}

Fig. 5.24 (a) and (b) Water superficial velocity vectors at the mid span of cross-flow turbine of various angles of attack.

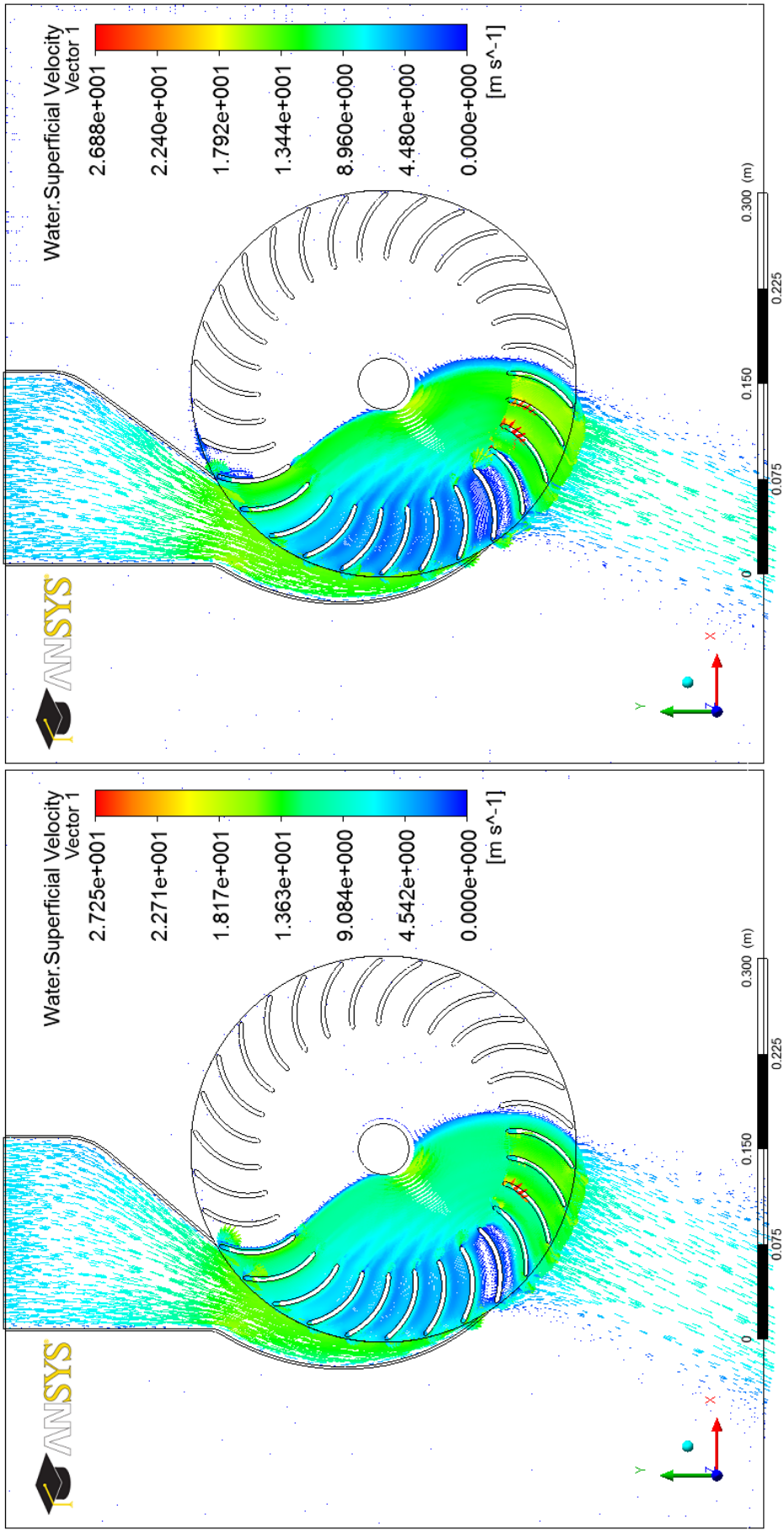

(c) Angle of attack 20° (d) Angle of attack 24°

Fig. 5.24 (c) and (d) Water superficial velocity vectors at the mid span of cross-flow turbine of various angle of attack.

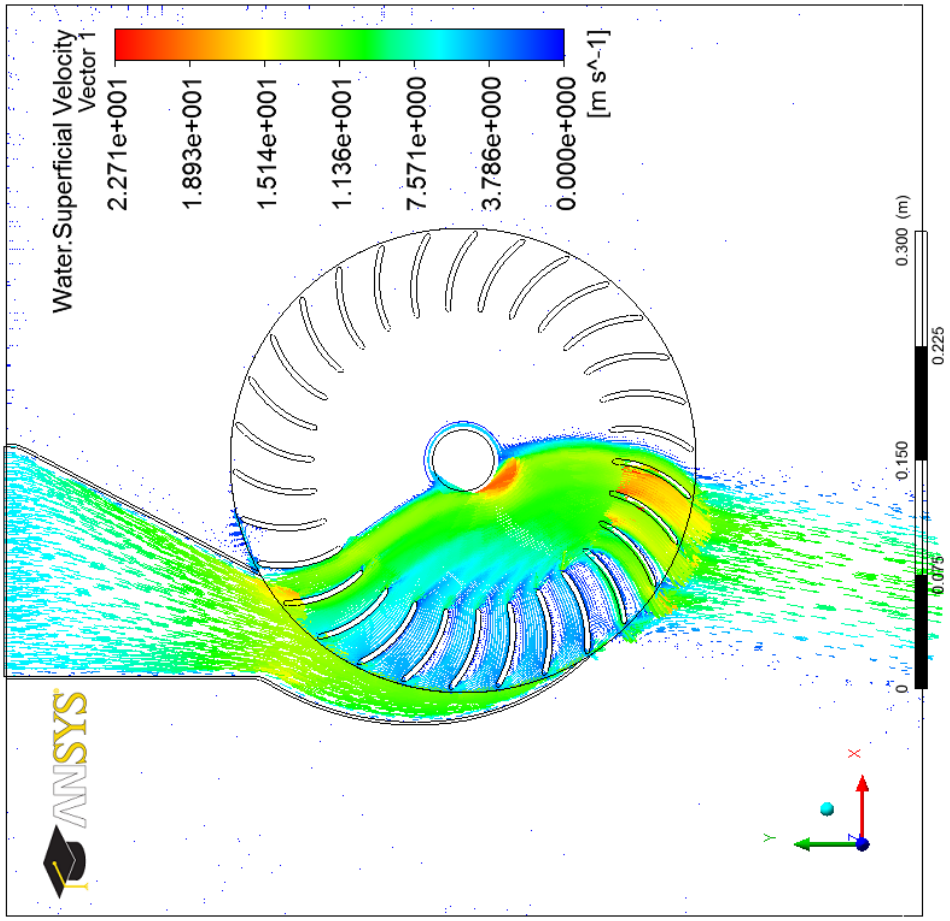

Fig. 5.24 (e) Water superficial velocity vectors at the mid span of cross-flow turbine for nozzle angle of attack 32°.

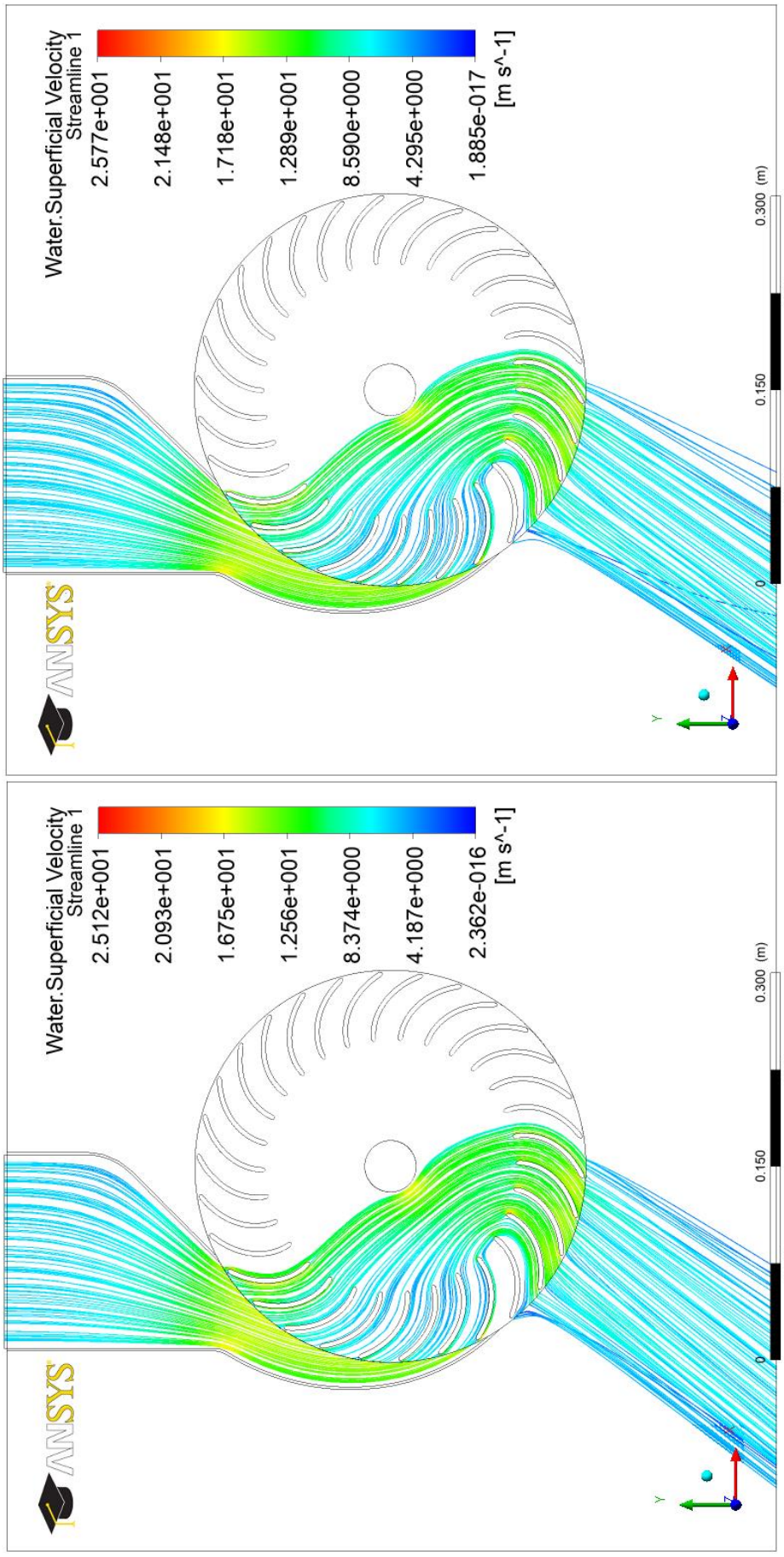

(a) Angle of attack 15^{o} (b) Angle of attack 16^{o}

Fig. 5.25 (a) and (b) Water superficial velocity streamlines at the mid span of cross-flow turbine Of various angles of attack.

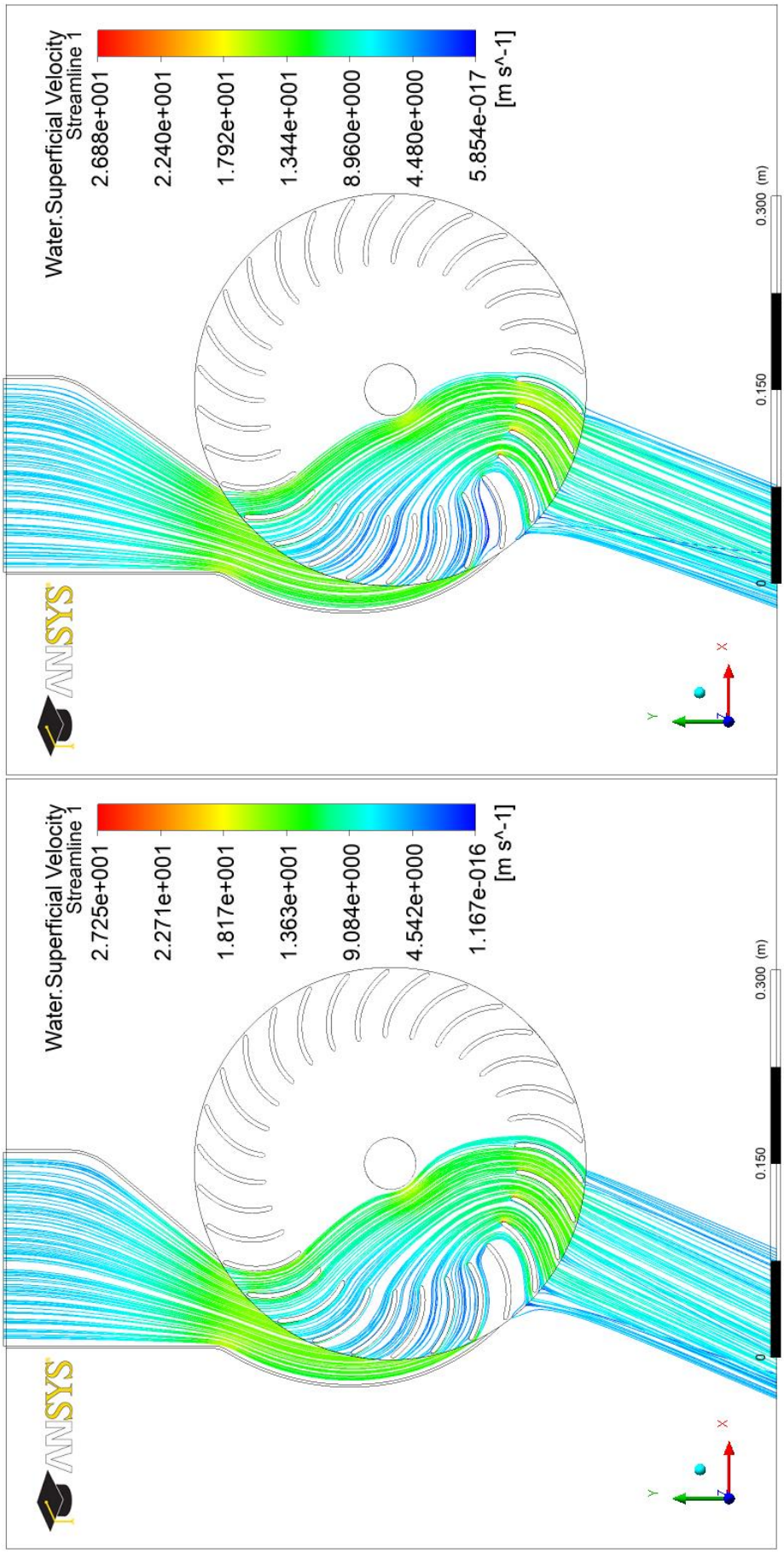

(c) Angle of attack 20^{o} (d) Angle of attack 24^{o}

Fig. 5.25 (c) and (d) Water superficial velocity streamlines at the mid span of cross-flow turbine Of various angles of attack.

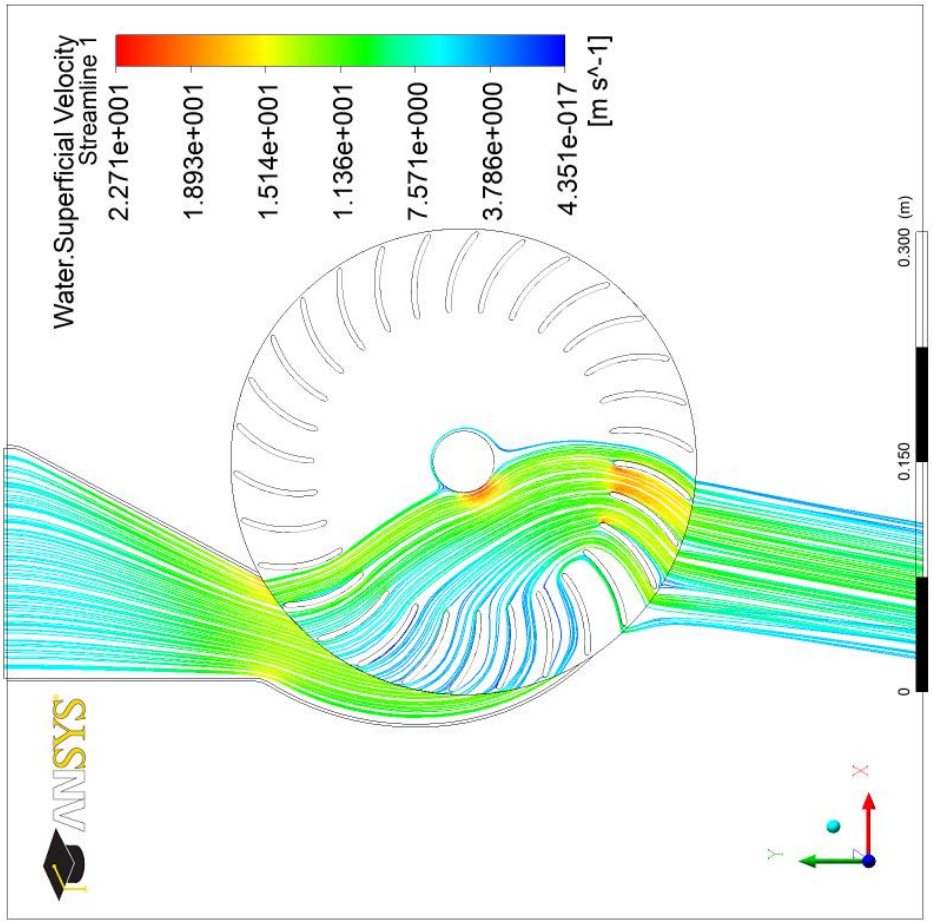

Fig. 5.25 (e) Water superficial velocity streamlines at the mid span of cross-flow turbine for nozzle angle of attack 32^{o}.

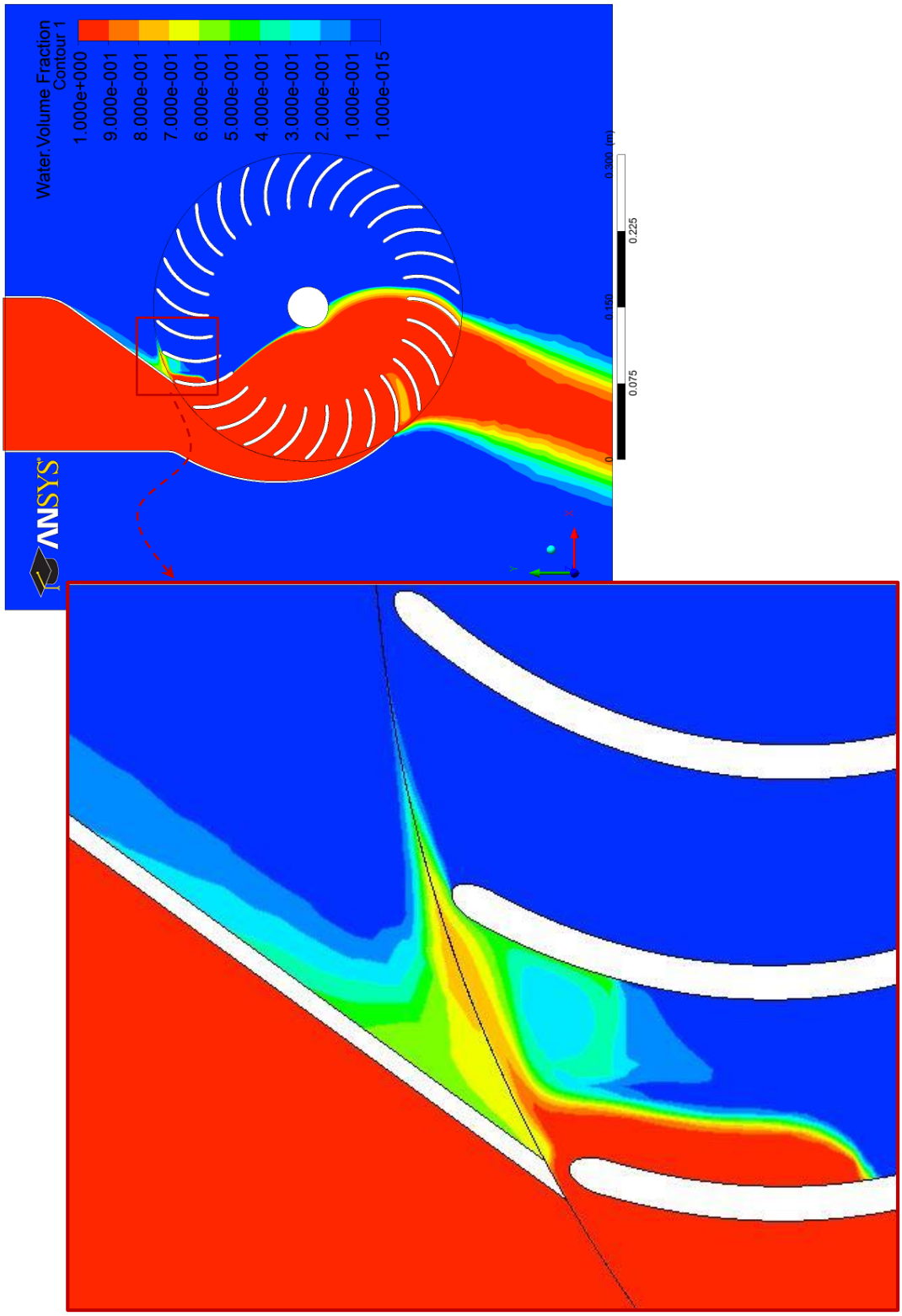

Fig. 5.26 Enlargement of the water volume fraction contours on the tip of the first couple of blades at the mid span of cross-flow turbine for nozzle angle of attack 24^{o}.

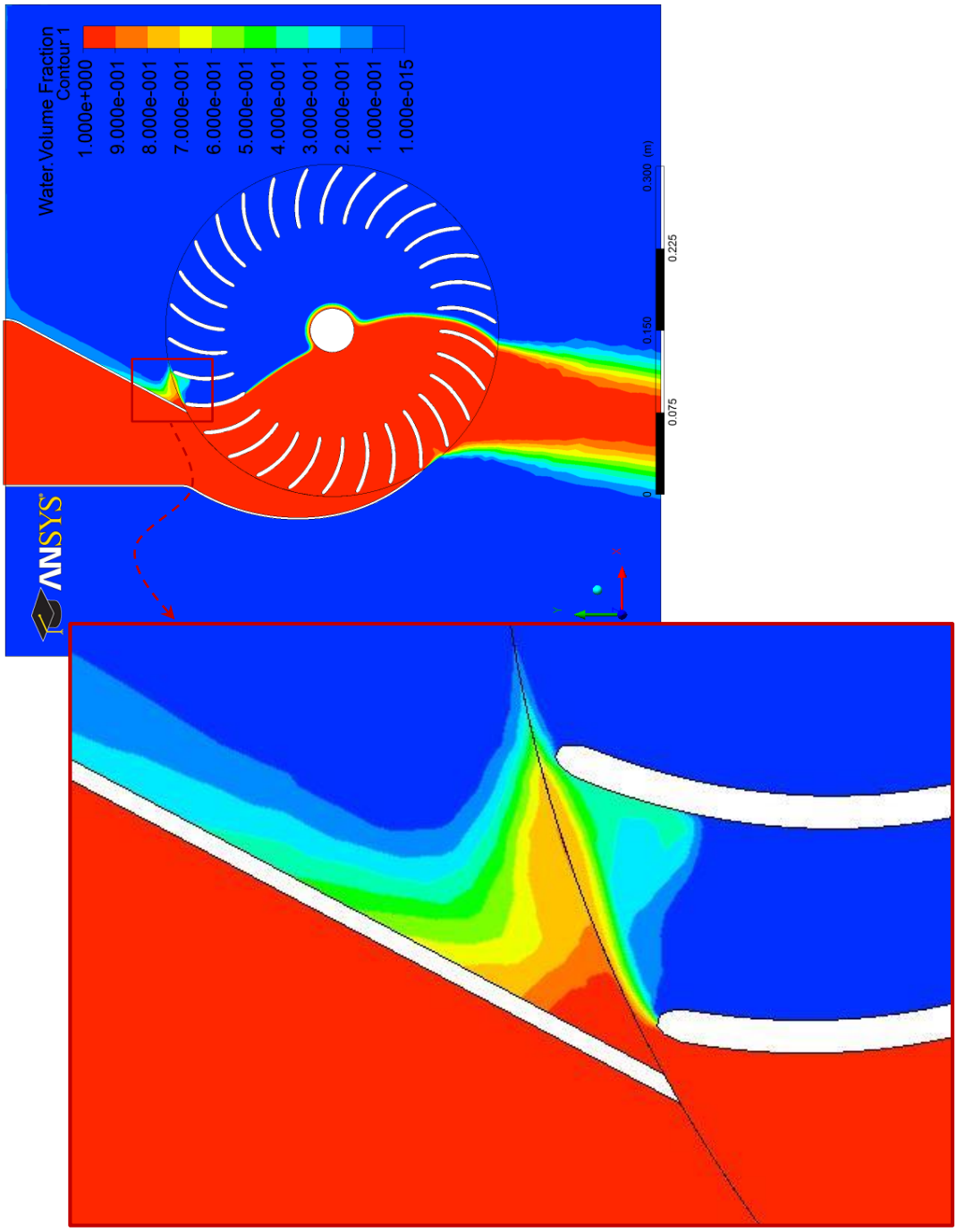

Fig. 5.27 Enlargement of the water volume fraction contours on the tip of the first couple of blades at the mid span of cross-flow turbine for nozzle angle of attack 32^{o}.

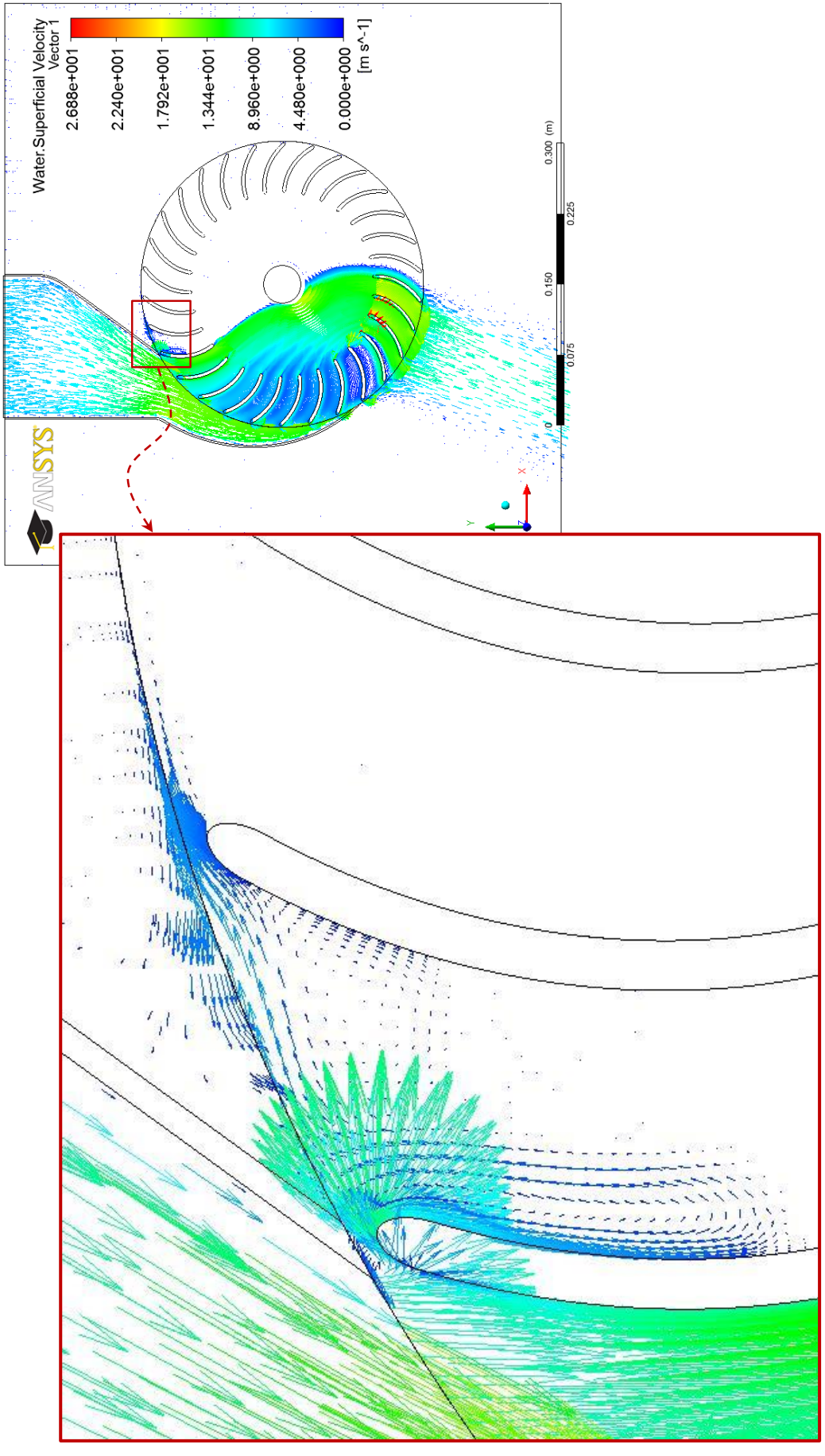

Fig. 5.28 Enlargement of the water superficial velocity vectors on the tip of the first couple of blades at the mid span of cross-flow turbine for nozzle angle of attack 24^{o}.

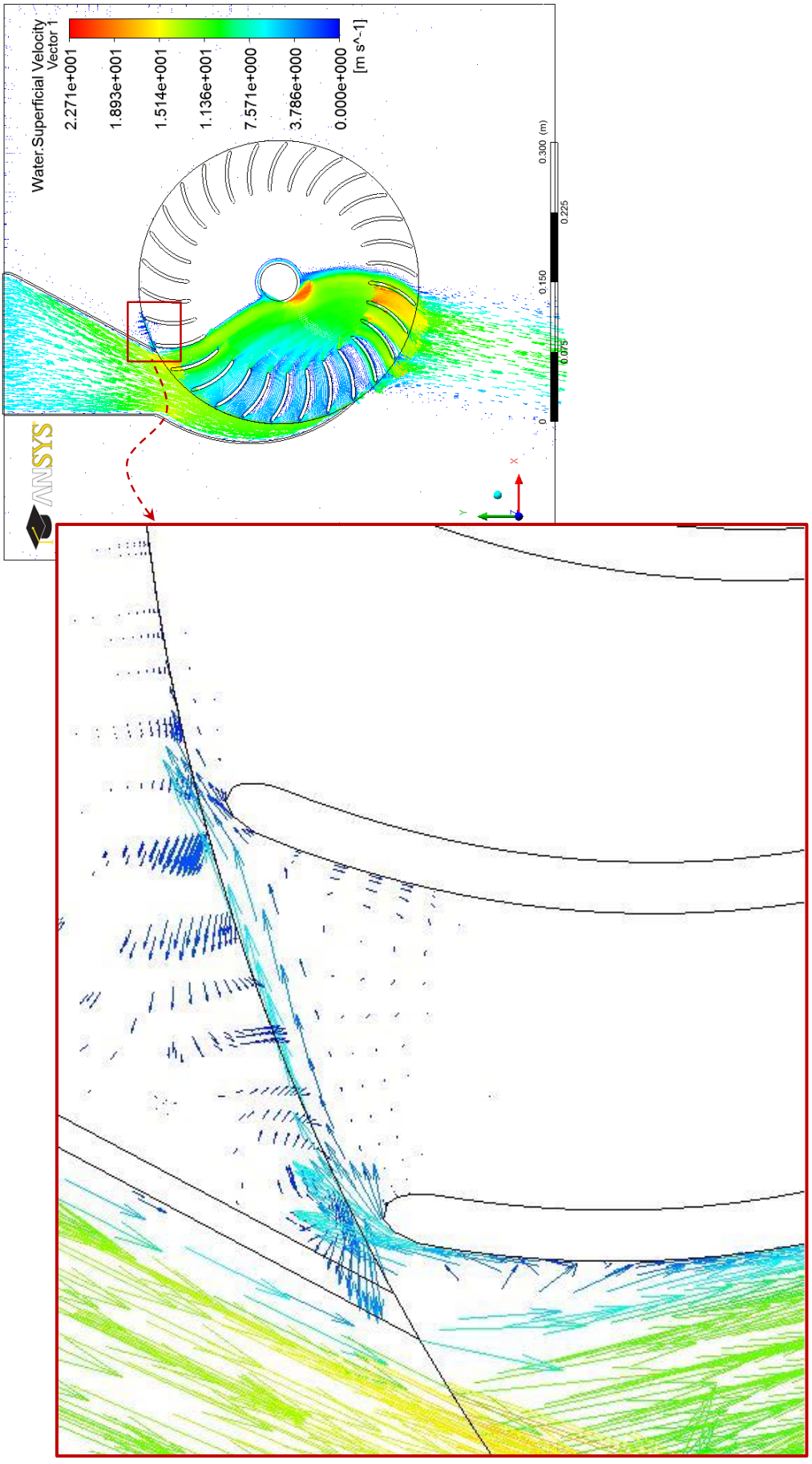

Fig. 5.29 Enlargement of the water superficial velocity vectors on the tip of the first couple of blades at the mid span of cross-flow turbine for nozzle angle of attack 32^{o}.

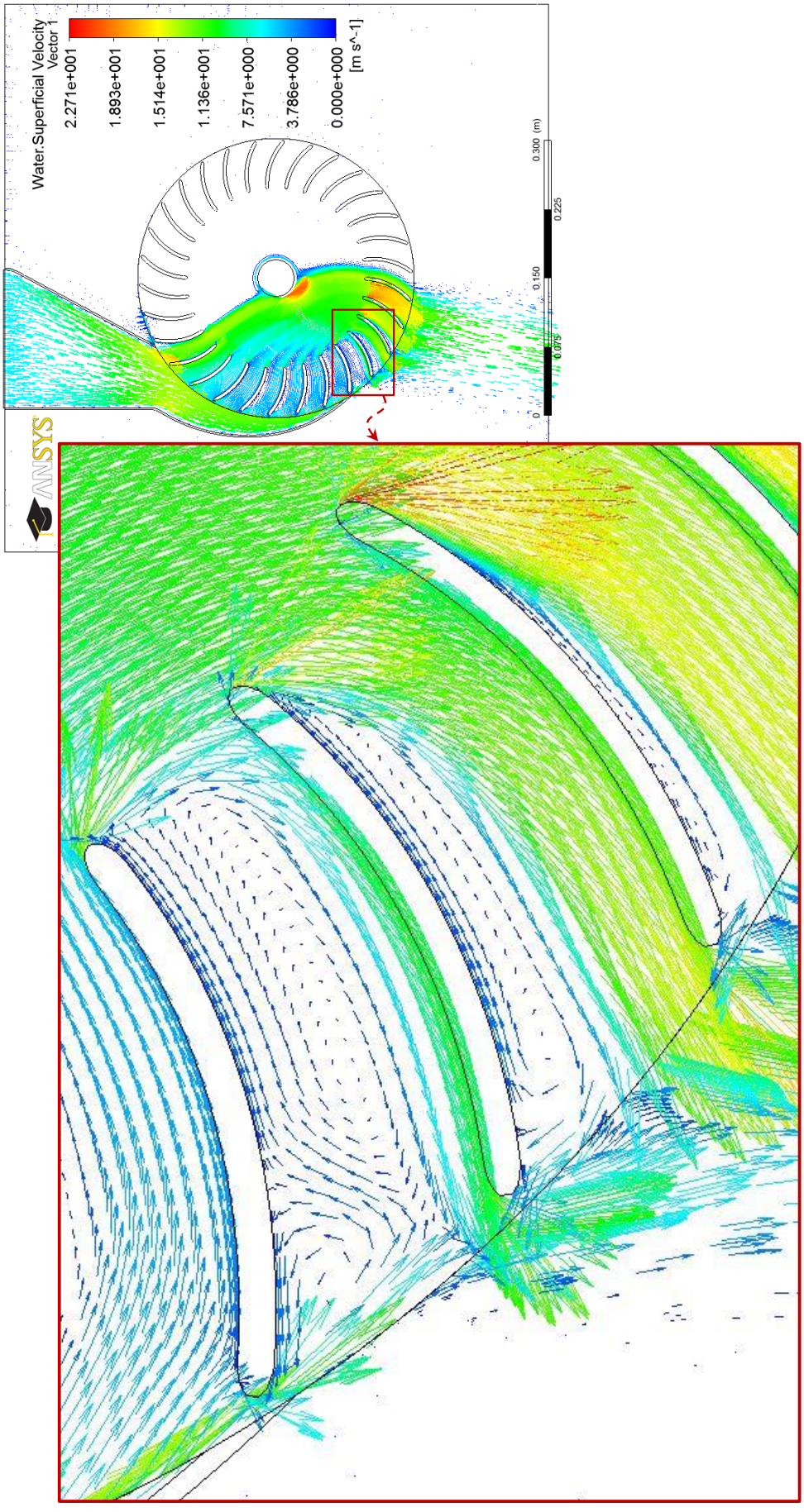

Fig. 5.30 Enlargement of the water superficial velocity vectors on the blades' passages facing the end of the nozzle at the mid span of cross-flow turbine for nozzle angle of attack 32^{o}.

The effect of the angle of attack α_1 on the efficiency of the cross-flow turbine was calculated and depicted in Fig. 5.31. It is clear that decreasing the angle of attack α_1 from 32^o to 15^o has a favorable effect on the efficiency of the cross-flow turbine. This indicates agreement with the Banki's theory as was explained in details earlier in this section. In summary, increasing the angle of attack means increasing the inlet blade angle β_1 which in turn increases the blade curvature r_b. This leads to reduce the blade curve as a result of that the extracted energy from water by the blades decreases significantly. According to this, the most effective angle of attack noticed was 15^o where the calculated efficiency was 75.339 %. Therefore, the optimum angle of attack can be considered to be 15^o, which provides higher interaction between the water flow in the passages and the blades than the rest of the angles of attack 16^o, 20^o, 24^o and 32^o. It can also be seen from Fig. 5.31 that at the high angle of attack 32^o, the turbine efficiency was considerably low (51.213 %).

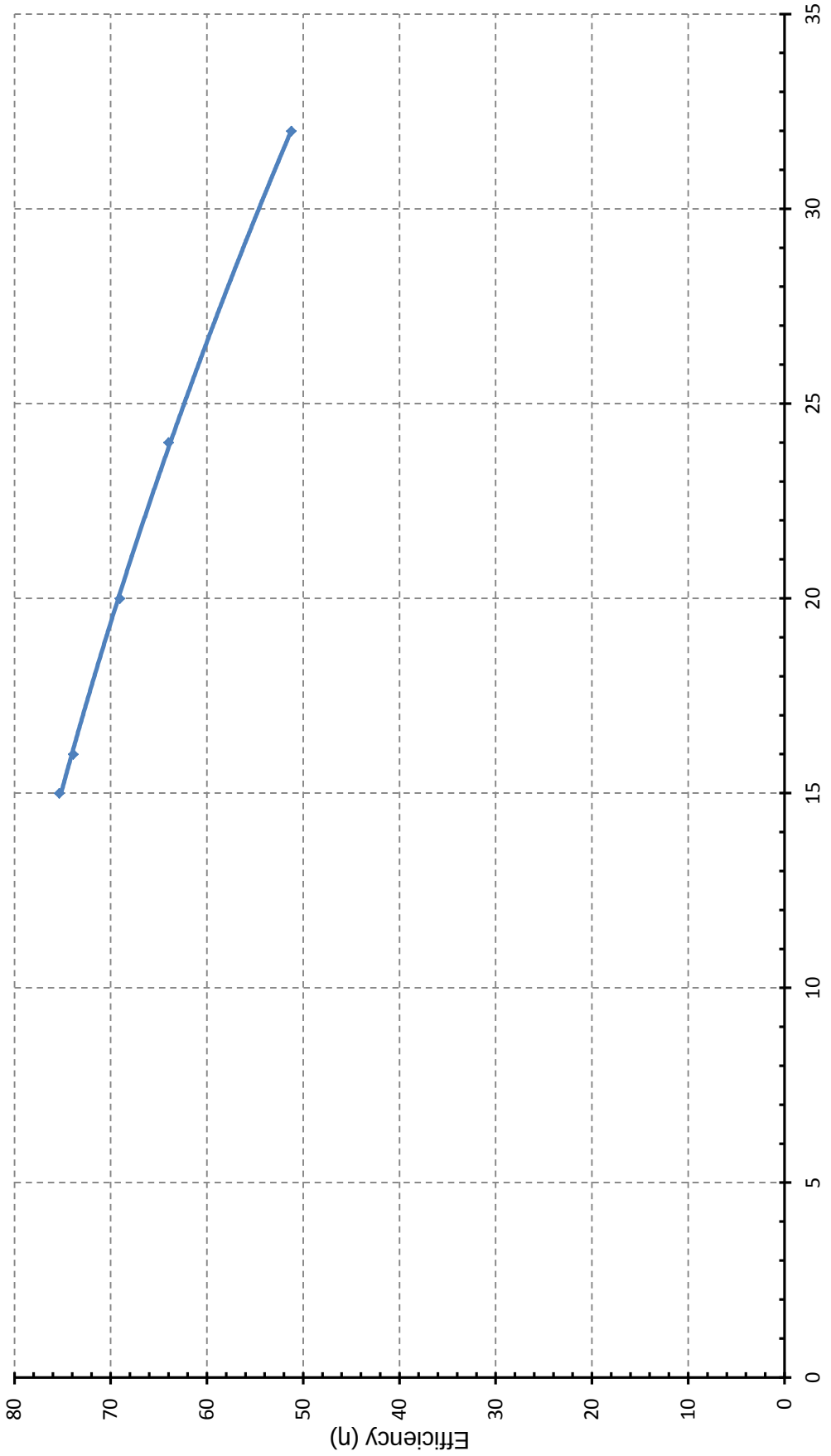

Fig. 5.31 Cross-flow turbine performance characteristics curve for blade with various angles of attack.

5.2.4 Optimization of the Nozzle Entry Arc (λ)

Nozzle entry arc λ is the part of the cross-flow turbine runner circumference that facilitates the water flow steadily and smoothly into the runner. Various nozzle entry arc angles λ are depicted in Figs. 5.32 – 5.35. The connection area between the main cross-flow turbine elements (the runner and the nozzle) is formed by multiplying the nozzle entry arc λ by nozzle width N_w. The nozzle entry arc has a significant effect on the flow characteristics and the hydrodynamic forces within the cross-flow turbine as it controls the angle of attack and the number of the effective blades which can be struck by the water from the nozzle. A large nozzle entry arc may cause an uncertain angle of attack of the flow at the runner inlet. A small nozzle entry arc, on the other hand, reduces the number of the effective blades (blades which simultaneously in contact with incoming water) and this in turn reduces the energy extract from water by the blades. Therefore, it is essential to improve and optimize the performance of a cross-flow turbine by selecting the optimum nozzle entry arc. An experimental investigation to analyze the effect of nozzle shape on the cross-flow turbine performance by varying the nozzle entry arc was conducted by Nakase et al [32]. The results of this experiment revealed that a nozzle with entry arc 90^o was more efficient than that of 30^o, 60^o and 120^o. Durgin and Fay [37] undertook an experimental investigation to investigate the internal hydrodynamics of the cross-flow turbine with the nozzle entry arc ranged from 35^o to 80^o. They concluded that the efficiency of the cross-flow turbine increased by increasing the nozzle entry arc from 35^o to 63^o and the efficiency decreased for a further increase in the nozzle entry arc. Fiuzat and Akerkar [48] experimental investigation led to the conclusion that, the overall efficiency of the

cross-flow turbine, for a 90^o nozzle entry arc, is higher than 120^o because the quantity of the cross flow is more. This results in higher efficiencies for both the upper and lower stages of the turbine. The impact of the nozzle entry arc on the efficiency of the cross-flow turbine was also experimentally investigated by Joshi et al [54]. The results of this experiment led to the conclusion that the efficiency of the cross-flow turbine increased by increasing the nozzle entry arc from 12^o to 36^o.

It is evident from the literature available that the impact of nozzle entry arc on the performance of the cross-flow turbine is not yet very well established or understood. Therefore, it is important to find the optimum nozzle entry arc in order to optimize the performance of the cross-flow turbine. In the current study, the geometrical parameters and nozzle entry arcs' details of the tested cross-flow turbines are shown in table 5.4 and Figs. 5.32, 5.33, 5.34 and 5.35. Figures 5.32 to 5.35 provide details of the nozzle entry arc angles which employed in the current investigation. They cover a higher angles range than those employed by the previous workers reported above.

Table 5.4 Details of the nozzle entry arc tested.

Geometrical parameter	Specification
Number of blades	$n_b = 30$
External diameter	$d_1 = 300\,mm$
Diameters ratio	$d_2/d_1 = 0.65$
Angle of attack	$\alpha_1 = 15^o$
Inlet blade angle	$\beta_1 = 151.814^o$
Internal blade angle	$\beta_1^{'} = \beta_2^{'} = 90^o$
Outlet blade angle	$\beta_2 = 28.186^o$
Blade thickness	$t_b = 3.6\,mm$
Blade radius of curvature	$r_b = 49.139\,mm$
Nozzle entry arc	$\lambda = ?$ $60^o, 90^o(a), 90^o(b) \,\&\, 120^o$
Throat width	$s_o = 60\,mm$
Width of the nozzle	$N_W = 150\,mm$
Shaft (axle) diameter	$d_s = 40\,mm$ *Note: Symbols as detailed in Fig. 3.2.*

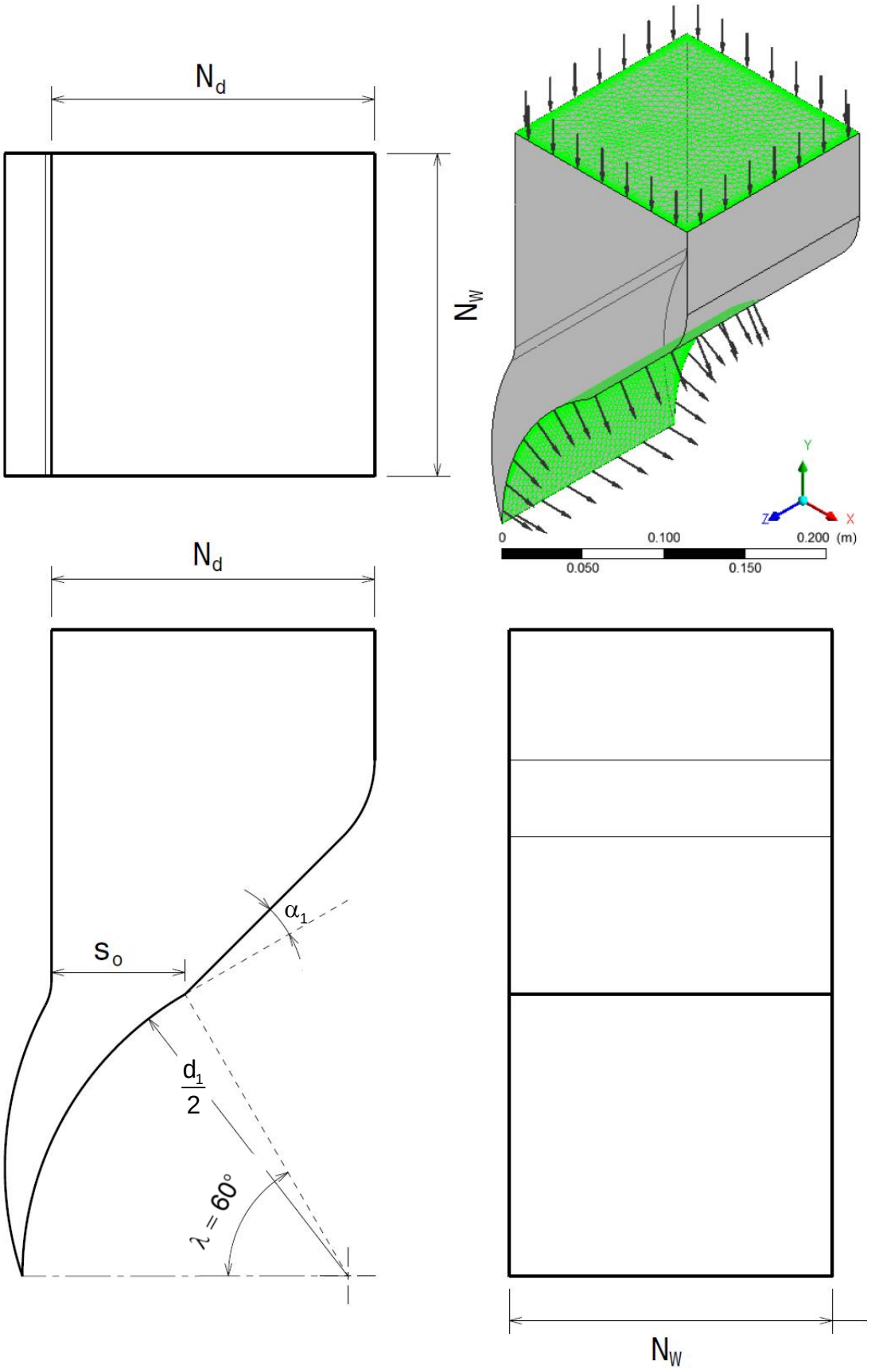

Fig. 5.32 Schematic view of the test nozzle with entry arc angle ($\lambda = 60^{o}$).

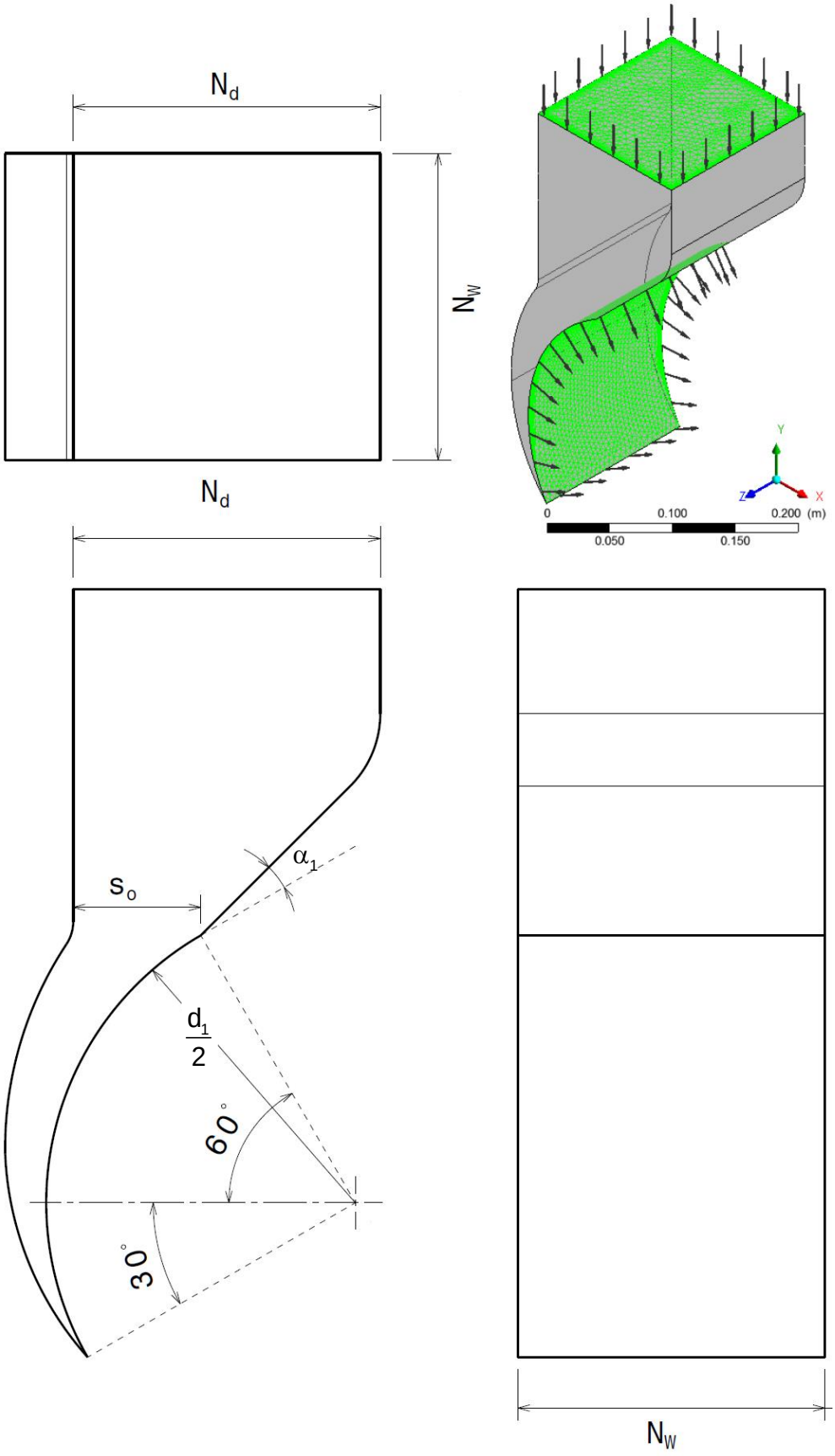

Fig. 5.33 Schematic view of the test nozzle with entry arc angle of $\lambda = 90^{o}$ (a).

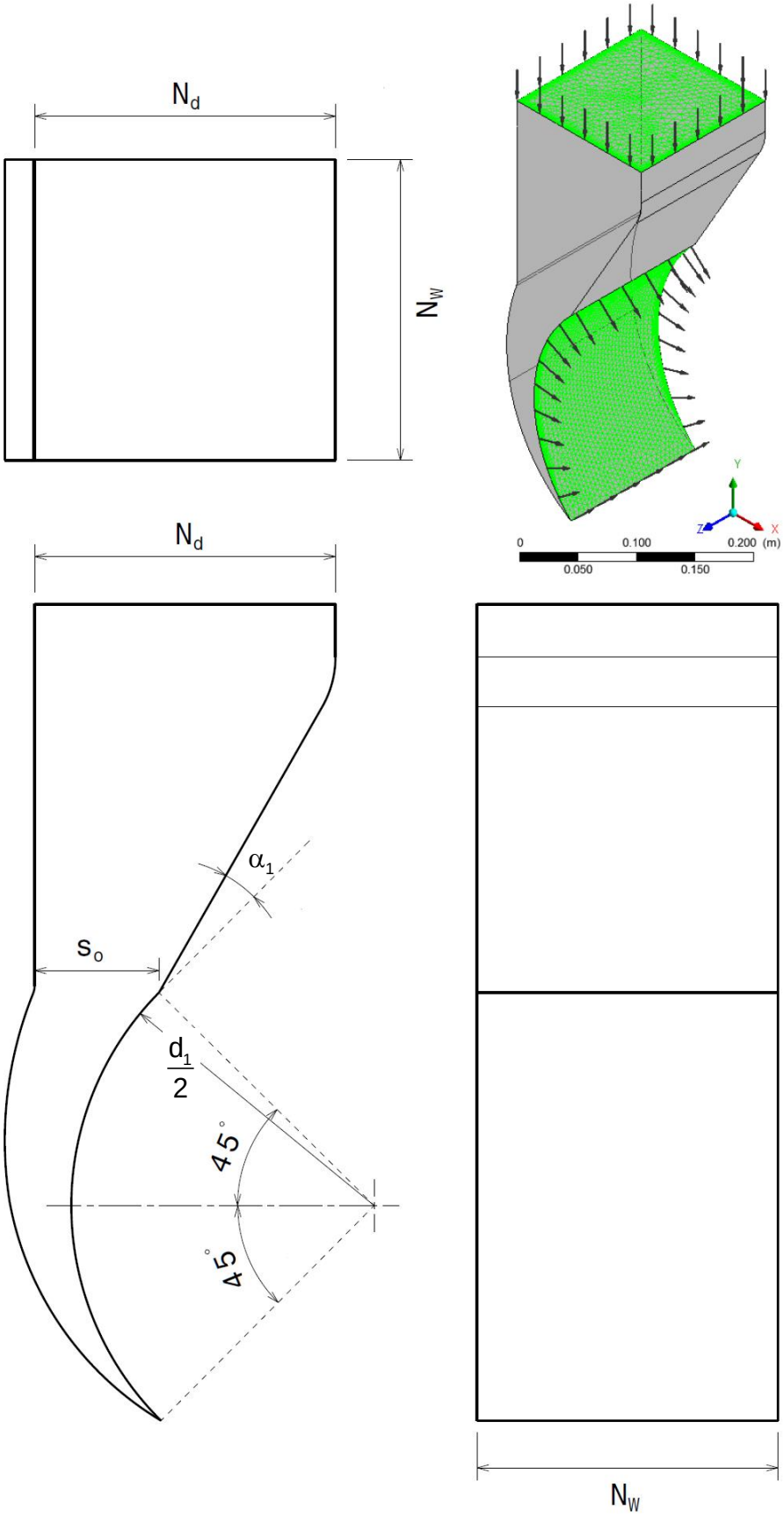

Fig. 5.34 Schematic view of the test nozzle with entry arc angle of $\lambda = 90^{o}$ (b).

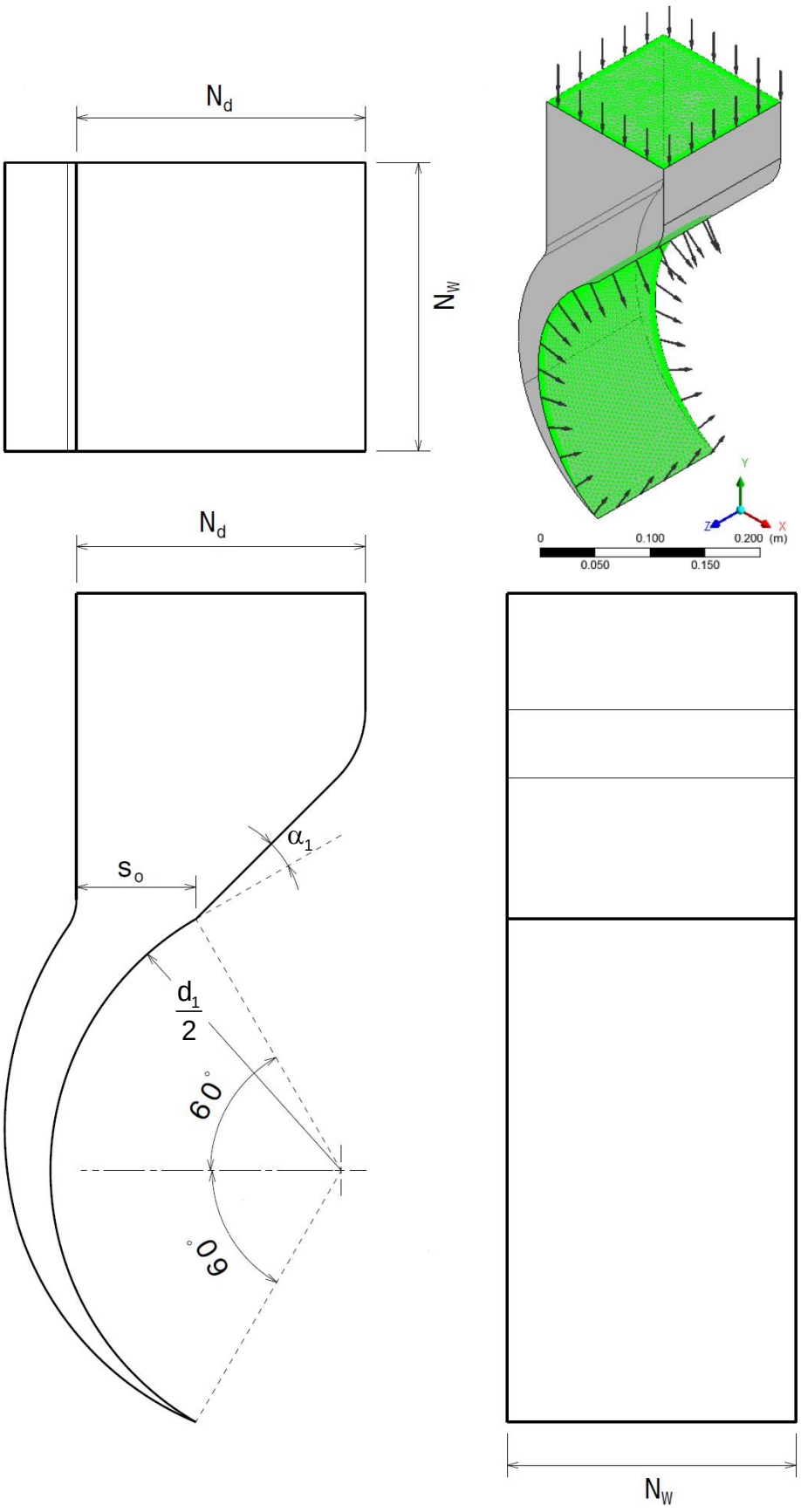

Fig. 5.35 Schematic view of the test nozzle with entry arc angle ($\lambda = 120^{o}$).

The structure of the internal flow in the cross-flow turbine was obtained as a result of computations by ANSYS CFX simulation code. Details of the internal flow of the turbine, with various values of the nozzle entry arc angle and orientation, are shown in Figs. 5.36 to 5.37 and Figs. B.6 to B.7. These provide a comprehensive understanding of the structure of the turbulent, two-phase and three dimensional flow and the related phenomena (separation, re-attachment, impingement and vortex structure). These figures clearly show that the fluid flow in the cross-flow turbine is strongly influenced by the nozzle entry arc angle and orientation. Also, the splatter of the water droplets from bulk of the flow is clearly shown in Fig. 5.36 (a). Such droplets which have high velocity and momentum, at a low nozzle entry arc angle tend to separate from the main flow when leaving the runner. This is confirmed by the velocity vectors' results of Fig. 5.37 (a). The water superficial velocity streamlines, were plotted for entire cross-flow turbine as shown in Fig. 5.36 (a) to (d). These streamlines show the number of the effective blades which is stricken by the water from the nozzle and the complexity of the turbulent two-phase three dimensional flow in the runner. In order to view the effect of nozzle entry arc and visualize the fluid flow more clearly, contours of total pressure, vectors of water superficial velocity and contours of pressure were plotted on the mid span planes as shown in Fig. 5.37 and Figs. B.6 to B.7. Figures B.6 and B.7 show the impingement of the flow leaving the upper raw of blades on the runner shaft (axle) which increase by increasing the nozzle entry arc. This represents parasitical losses, which reduce the power output from the turbine, reduces the efficiency, and increases the noise and vibration associated with the turbine operation. Figures B.6 (d) and B.7 (d) also demonstrate clearly the water impingement phenomena at large

nozzle entry arc (120^o). The water superficial velocity vectors in Figs. 5.37 (a) to (d) show the passages between the effective blades. A large nozzle entry arc may cause an uncertain angle of attack and flow separation, on the other hand; small nozzle entry arc reduces the number of the effective blades. Figure 5.37 (a) shows the number of the blades that in which water is moving through the runner (approximately 6 blades). This figure is changed significantly (to approximately 11 blades) in Fig. 5.37 (d). Those are not associated with re-circling vortices as shown in Fig. 5.37 (a). This explains the higher efficiency of the arrangement of Fig. 5.37 (a) in a similar manner the number of blades interacting with the water in Fig. 5.37 (c) is equivalent to that of the nozzle entry arc arrangement of Fig. 5.37 (b). However, it is clearly shown that there is "dead area" in which the water is re-circulating, which tends to increase the losses. This in turn explains why the efficiency of turbine with the nozzle entry arc of 90^o (a) is higher than the efficiency of turbine with the nozzle entry arc of 90^o (b). It is also clear from Fig. 5.37 (d) that larger nozzle entry arc angle should allow higher quantity of water to interact with a larger number of blades. However, this arrangement is associated with vortices, which companied with higher quantity of water impinging on the shaft (axle) of the runner. This explains the lower turbine efficiency resulted from the arrangement of nozzle entry arc (120^o). In addition, the exit angle of the water leaving the runner in Fig. 5.37 (a) is much sharper than the rest of the arrangements (Figs. 5.37 (b) to (d)) and this tends to cause splatter of some of the water droplets as a result of the impingement of the water on the turbine boundary (cover). This is clearly visible in Fig. 5.37 (a) and was not observed in the result of the other nozzle entry arc arrangements (90^o (a), 90^o (b) and 120^o).

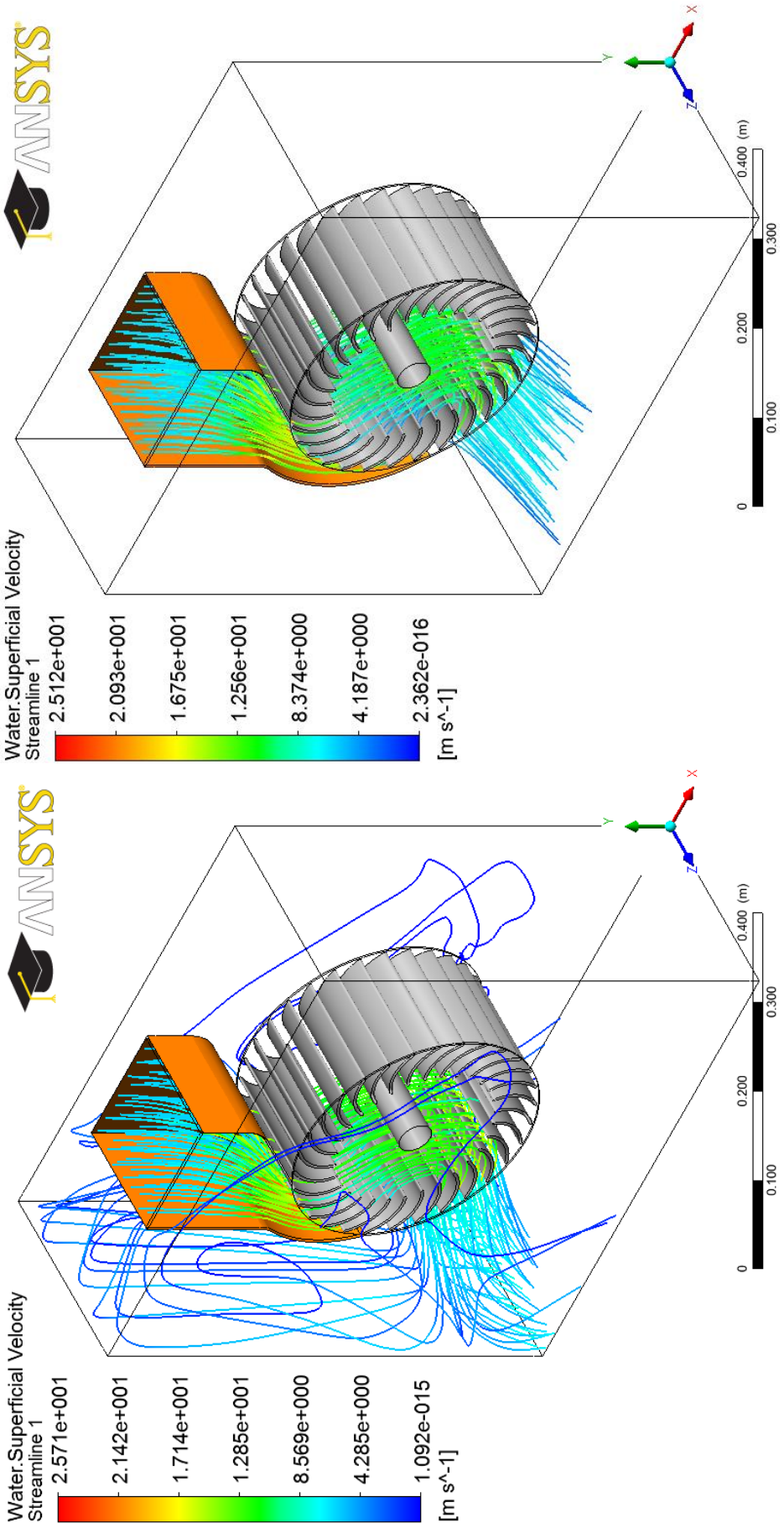

(a) Nozzle entry arc (60^{o}) (b) Nozzle entry arc 90^{o} (a)

Fig. 5.36 (a) and (b) Water superficial velocity streamlines in cross-flow turbine of various nozzle entry arcs.

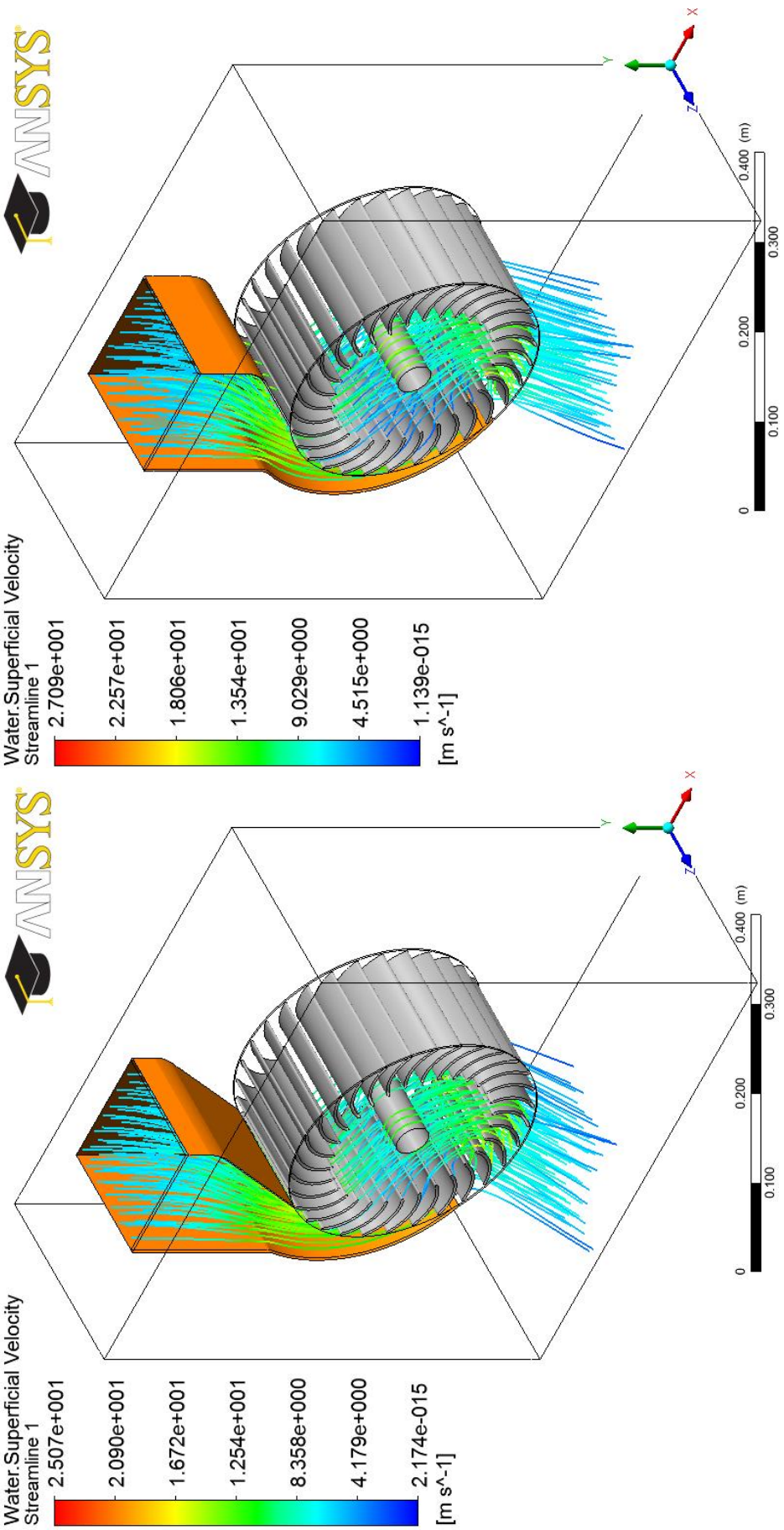

(d) Nozzle entry arc (120^o)

(c) Nozzle entry arc 90^o (b)

Fig. 5.36 (c) and (d) Water superficial velocity streamlines in cross-flow turbine of various nozzle entry arcs.

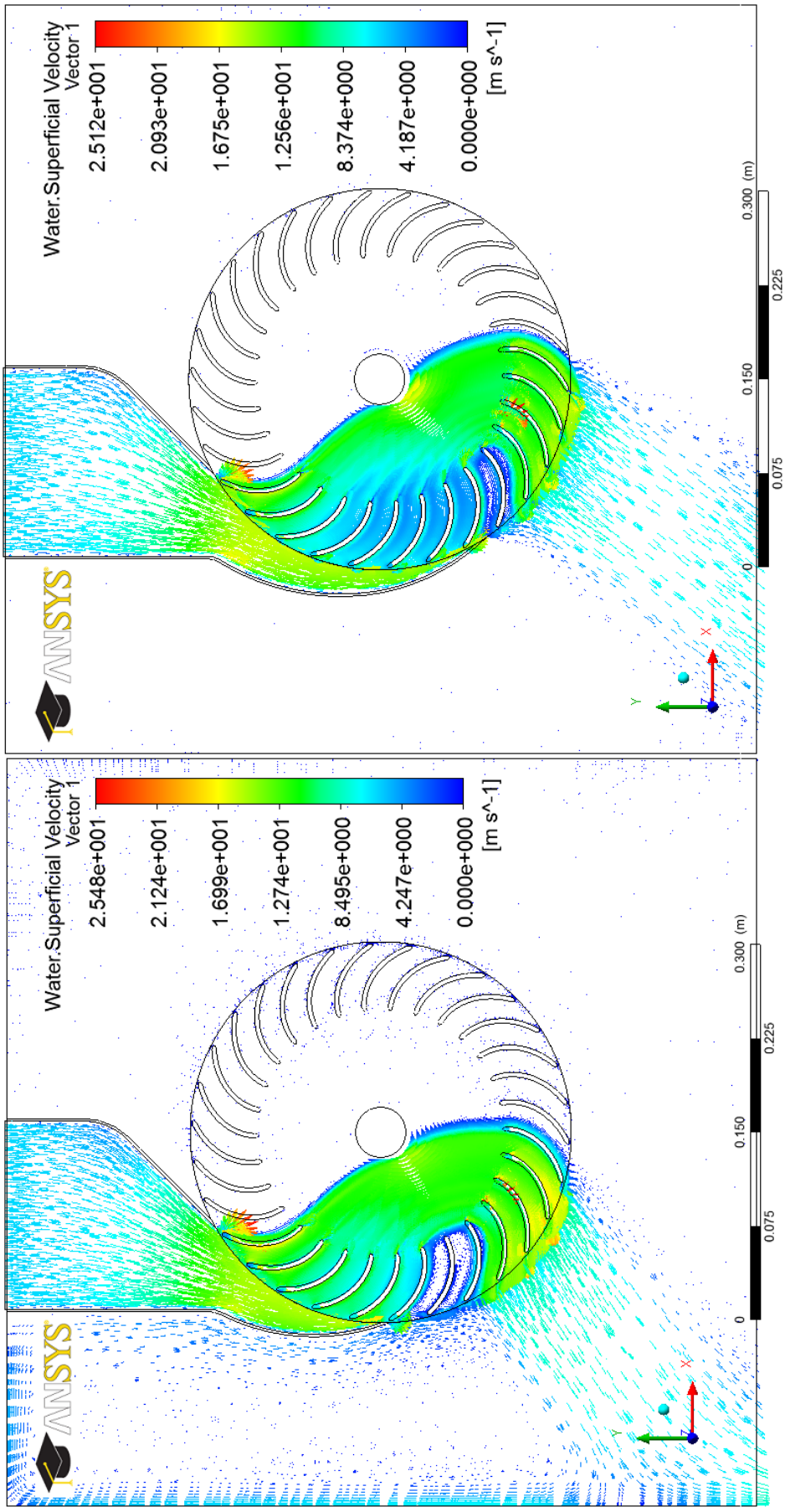

(a) Nozzle entry arc (60^o) (b) Nozzle entry arc 90^o (a)

Fig. 5.37 (a) and (b) Water superficial velocity vectors at the mid span of cross-flow turbine of various nozzle entry arcs.

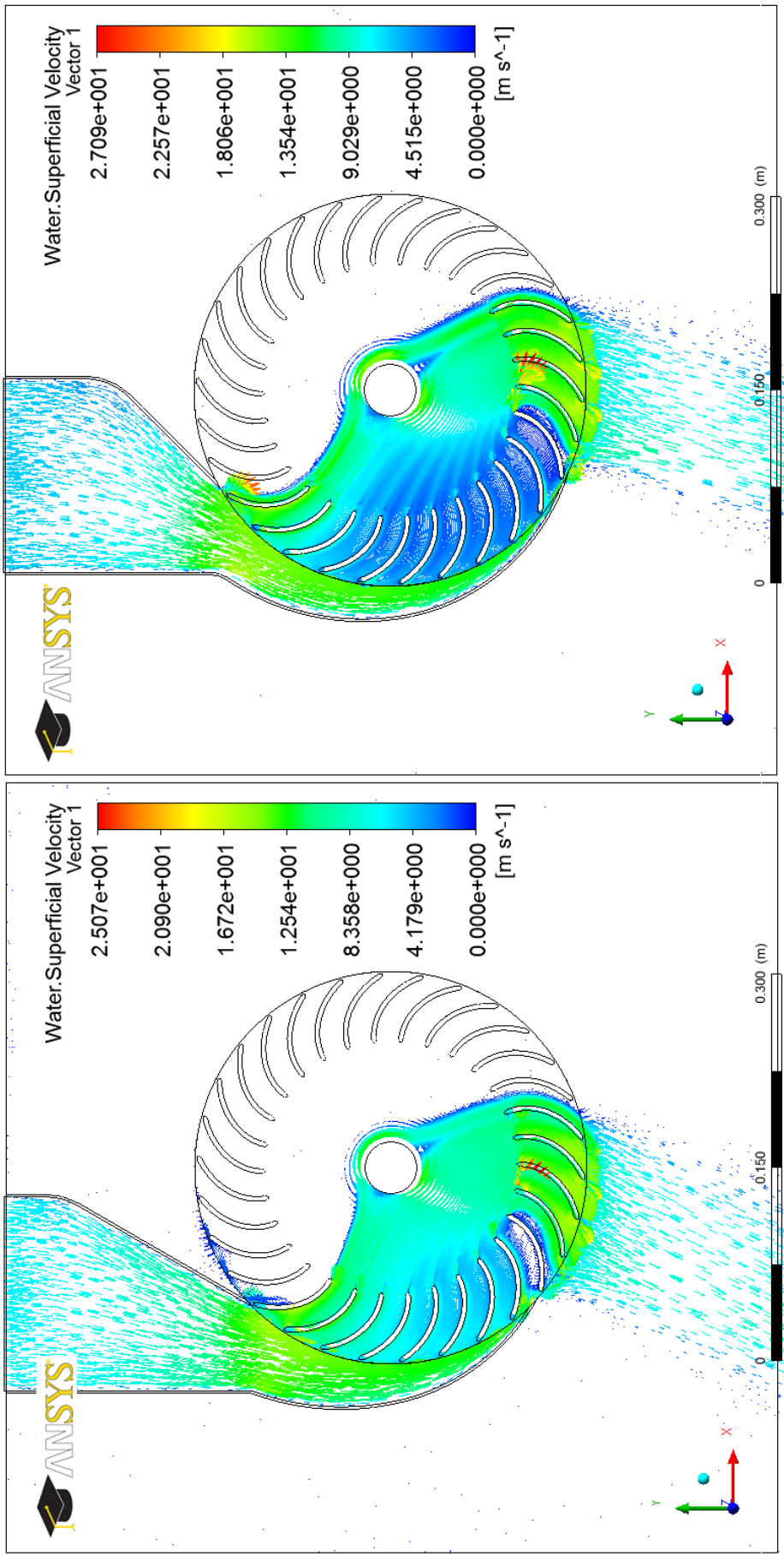

(c) Nozzle entry arc 90° (b) (d) Nozzle entry arc (120°)

Fig. 5.37 (c) and (d) Water superficial velocity vectors at the mid span of cross-flow turbine of various nozzle entry arcs.

Figure 5.38 clearly shows the summary of the effect of the nozzle entry arc λ on the efficiency of the cross-flow turbine. It is clear that an increase in the nozzle entry arc λ from 60^o to 90^o has a favorable effect on the efficiency of the cross-flow turbine. This can be explained by the fact that the increase in the nozzle entry arc increases the number of the effective blades. The energy extracted from water by the blades increase with increasing the number of the runner blades [32]. At small nozzle entry arc ($\lambda = 60^o$), the turbine efficiency was low (73.524 %). A further increase in the nozzle entry arc from 90^o to 120^o has an undesirable impact of reducing the efficiency. This can be explained firstly by the fact that the impingement of the flow leaving the upper raw of blades on the runner shaft (axle) increases by increasing the nozzle entry arc as shown in Figs. 5.40 and 5.41, secondly the increase in the flow separation as shown in Fig. 5.39, and thirdly the increase in the nozzle entry arc causes an uncertain angle of attack to the water flow at the runner inlet. At large nozzle entry arc ($\lambda = 120^o$), the turbine efficiency was so low (68.148 %). Therefore, the 90^o nozzle entry arc produces higher turbine efficiency within the range of 60^o – 120^o. Aiming to increase the performance of the cross-flow turbine through improving the performance of the nozzle entry arc, the 90^o nozzle entry arc was rearranged to match the nozzle entry arc of 90^o (b) by Fukutomi et al [53]. The efficiency of the cross-flow turbine with the nozzle entry arc of 90^o (b) was 72.257 %. The nozzle with entry arc of 90^o (a) was more efficient than the nozzle with entry arc of 90^o (b). The impingement of the flow leaving the upper raw of blades on the runner shaft (axle) increases by lowering the low end of the nozzle entry arc. According to this, the most effective nozzle entry arc noticed was of 90^o (a) where the efficiency was 75.339 %. Therefore, the

optimum nozzle entry arc can be considered to be of 90^o (a), which is in agreement with Nakase et al [32] conclusion. Their results showed that the highest efficiency was obtained with a nozzle entry arc 90^o.

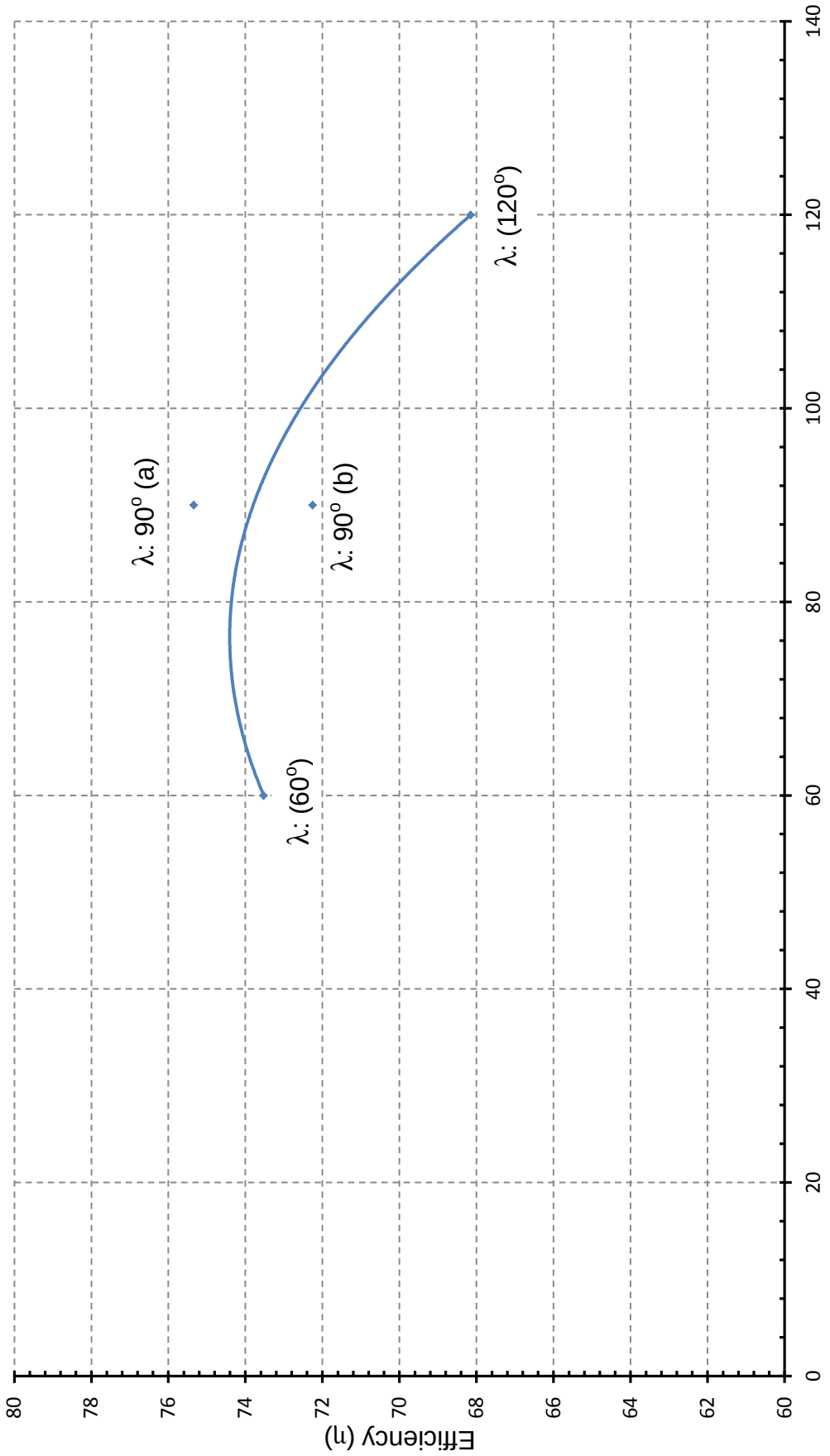

Fig. 5.38 Cross-flow turbine performance characteristics curve for nozzle of various entry arcs.

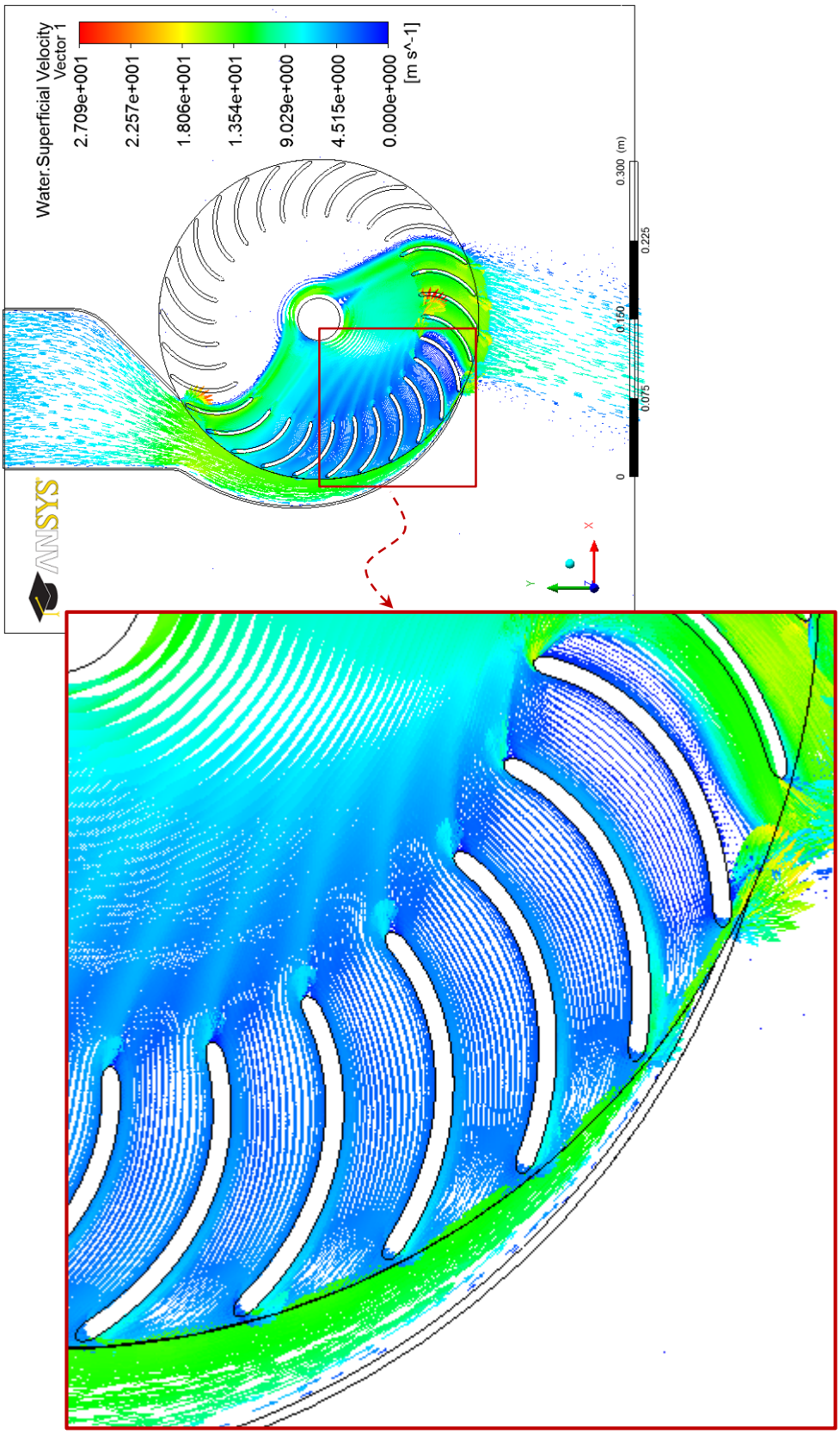

Fig. 5.39 Enlargement of the water superficial velocity vectors at the mid span of cross-flow turbine for nozzle entry arc 120^{o}.

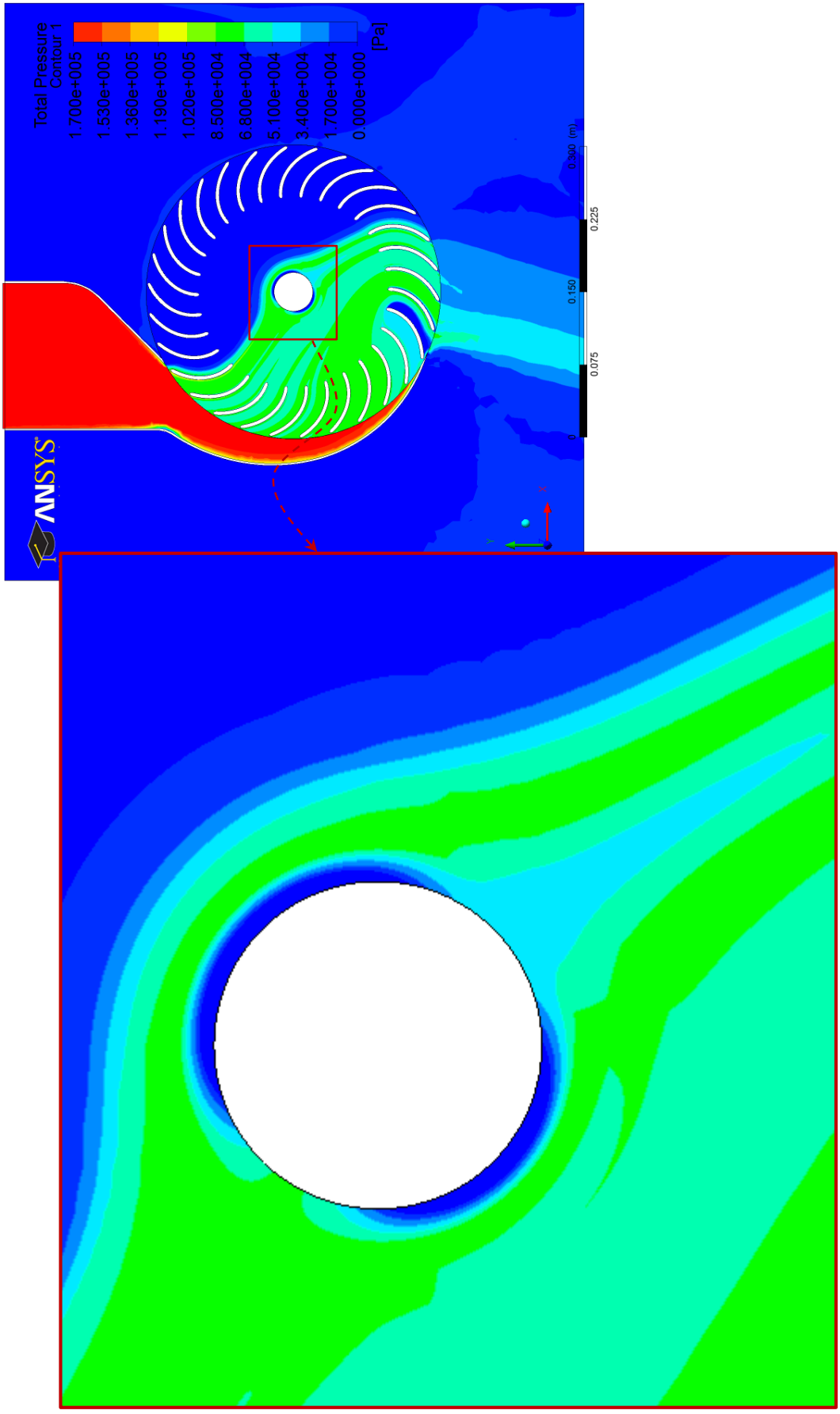

Fig. 5.40 Enlargement of the total pressure contours at the mid span of cross-flow turbine for nozzle entry arc 120°.

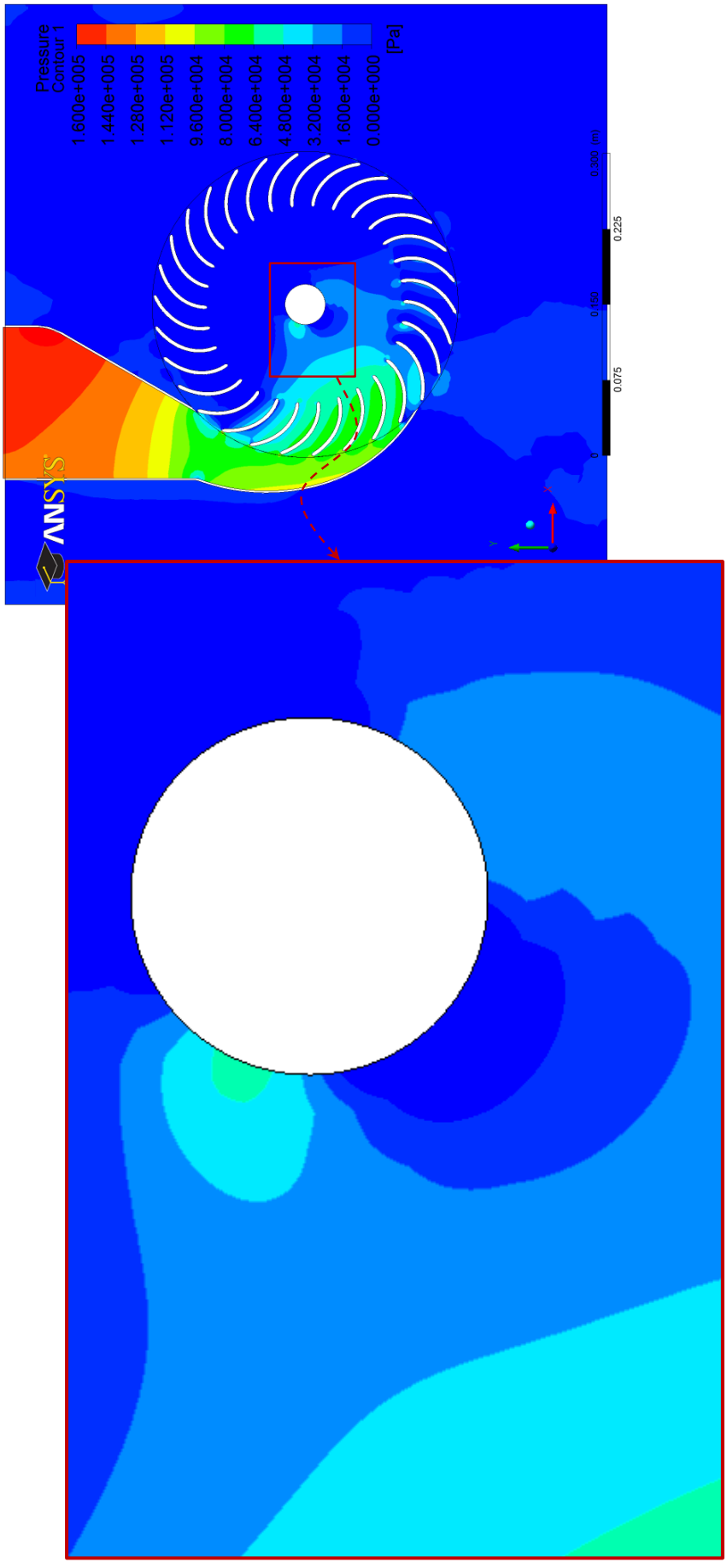

Fig. 5.41 Enlargement of the pressure contours at the mid span of cross-flow turbine for nozzle entry arc 90^{o}(b).

5.2.5 Optimization of the Runner Blade Profile

As indicated previously, optimization of cross-flow turbine involves establishing the best geometrical parameters within the imposed hydrodynamic restrictions. These restrictions necessitate that the blades are of a cylindrical annulus with radial entrance/outlet as well as with double interaction between water and the runner blades. Hence, the blade is the most important part of cross-flow turbine as it is the part that extracts the energy from water. Therefore, this study investigates improvements in blade profile and how the changes in the blade profile would affect the performance of cross-flow turbine. Based upon Banki's blade profile, four runner blade profiles were investigated including that of Banki [31]. The blades were designed and investigated by ANSYS CFX simulation code. The geometrical parameters and runner blades profiles' details of the tested cross-flow turbines are shown in table 5.5 and Figs. 5.42, 5.43, 5.44 and 5.45. Figure 5.42 shows Banki's blade profile which is of uniform thickness as indicated. The first of the new three blades designed for use in the current investigation (blade profile (1)) has maximum thickness in the center and a minimum thickness at both ends as indicated in Fig. 5.43. The blades of variable thickness with maximum thickness skewed to the right and to the left, respectively, are shown in Figs. 5.44 and 5.45. The refined mesh used in each case is also shown in each respective figure. In addition, a three dimensional meshing system around the blade also show in the same figures.

Table 5.5 Details of the blades profiles tested.

Geometrical parameter	Specification
Number of blades	$n_b = 30$
External diameter	$d_1 = 300\,mm$
Diameters ratio	$d_2/d_1 = 0.65$
Angle of attack	$\alpha_1 = 15^o$
Inlet blade angle	$\beta_1 = 151.814^o$
Internal blade angle	$\beta_1^{'} = \beta_2^{'} = 90^o$
Outlet blade angle	$\beta_2 = 28.186^o$
Blade thickness	$t_b = 3.6\,mm$
Blade radius of curvature	$r_b = 49.139\,mm$
Nozzle entry arc	$\lambda = 90^o$
Throat width	$s_o = 60\,mm$
Width of the nozzle	$N_W = 150\,mm$
Shaft (axle) diameter	$d_s = 40\,mm$
Blade profile	1, 2, 3 and 4 *Note: Symbols as detailed in Fig. 3.2.*

Blade profile

1 Banki's symmetrical and uniform blade thickness.

2 None – uniform maximum blade thickness in center.

3 None – uniform blade thickness (skewed to right – trailing edge).

4 None – uniform blade thickness (skewed to left – leading edge).

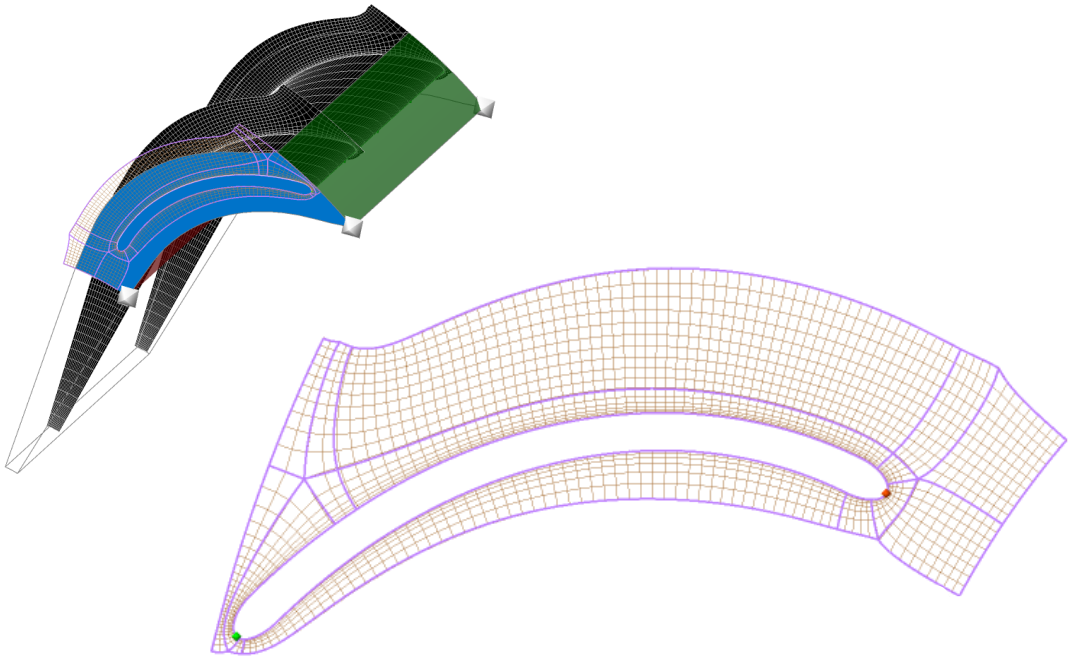

Blade domain mesh

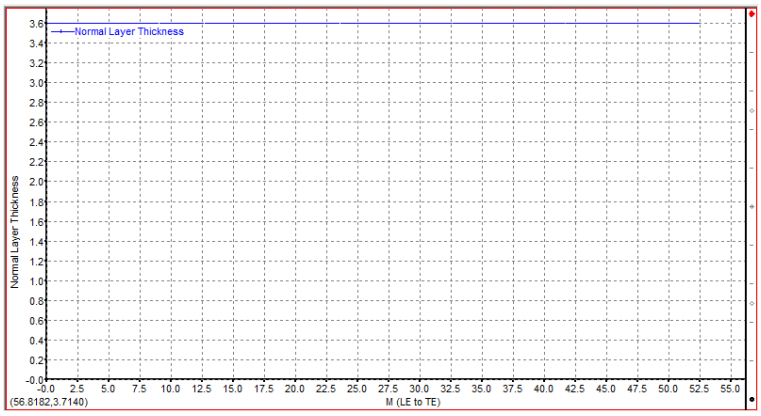

Blade thickness

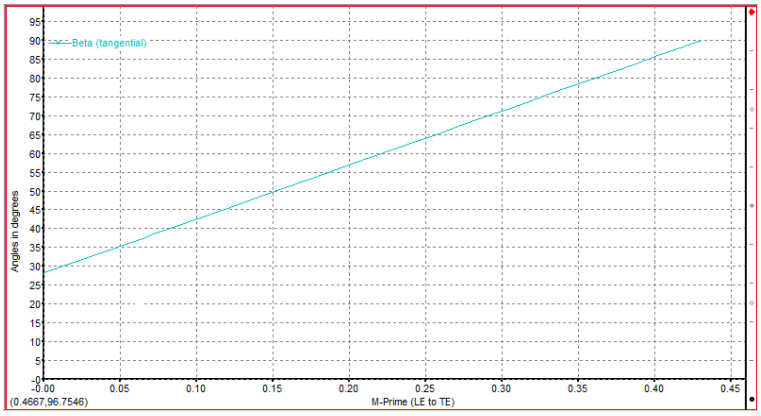

Blade angle (β)

Fig. 5.42 The runner normal-blade profile (Banki's).

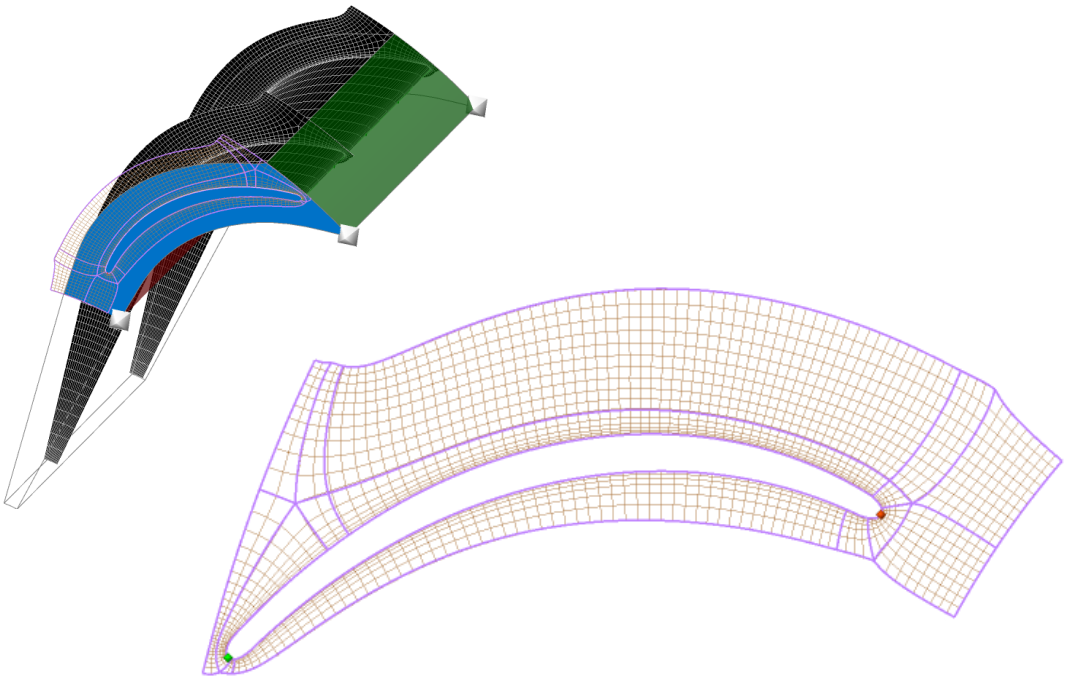

Blade domain mesh

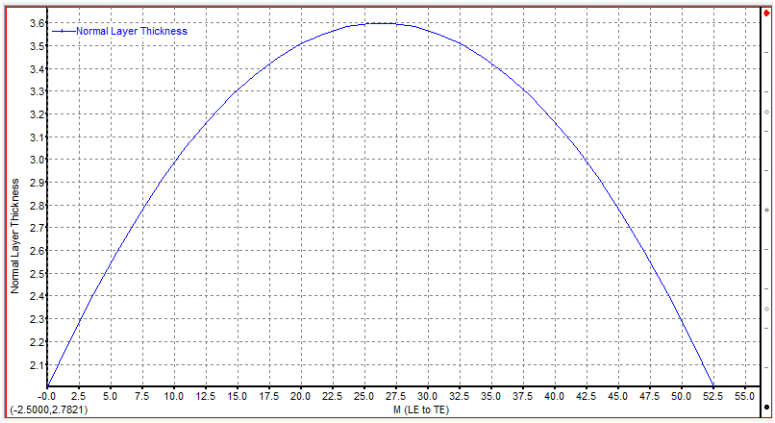

Blade thickness

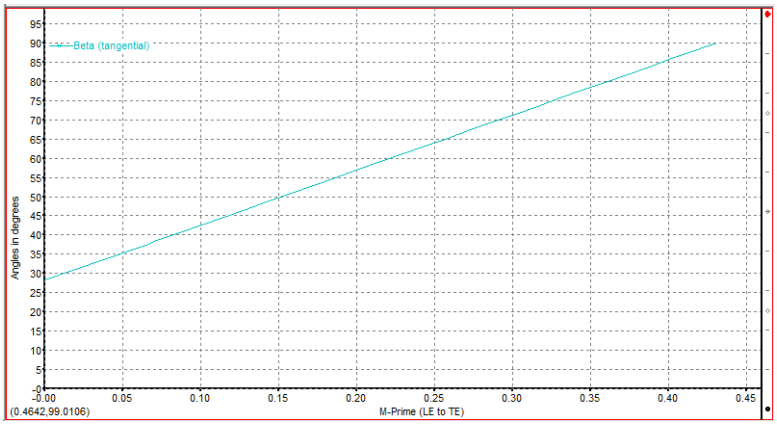

Blade angle (β)

Fig. 5.43 The runner blade profile (1).

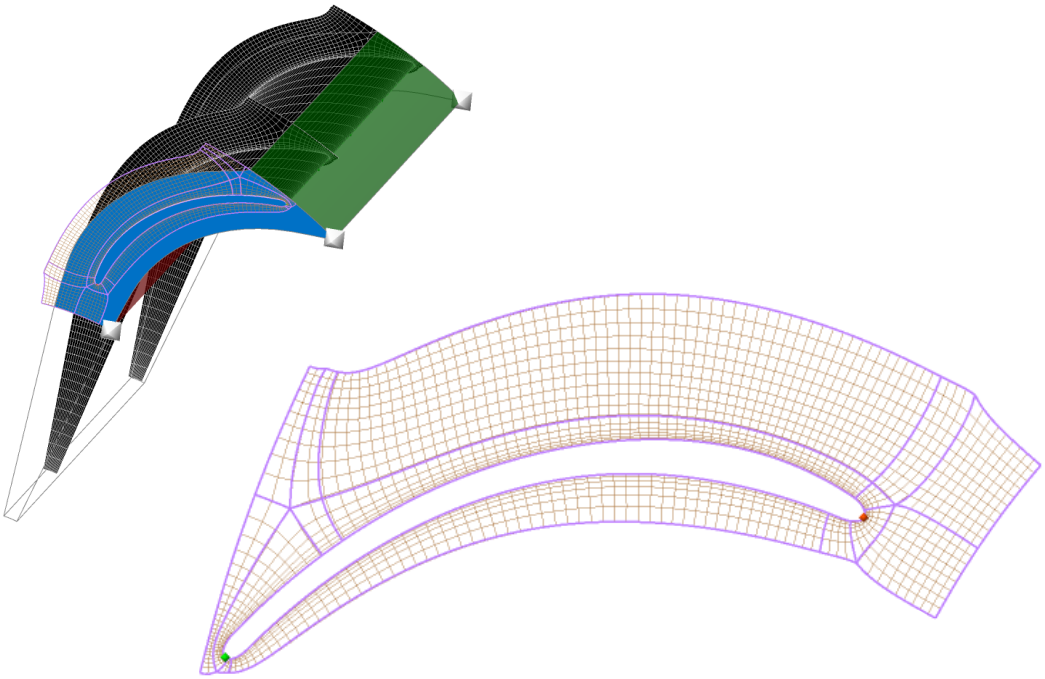

Blade domain mesh

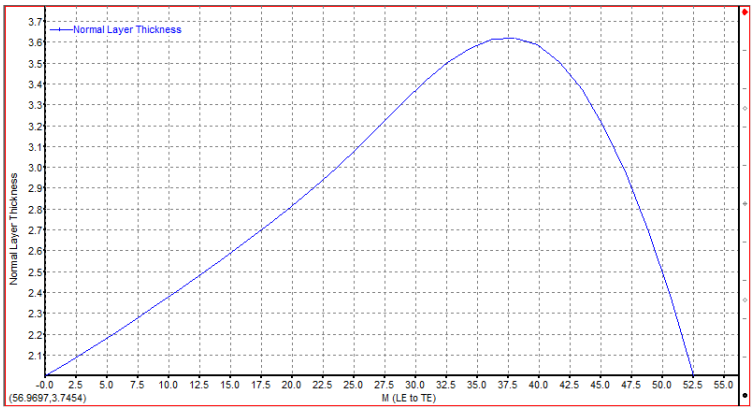

Blade thickness

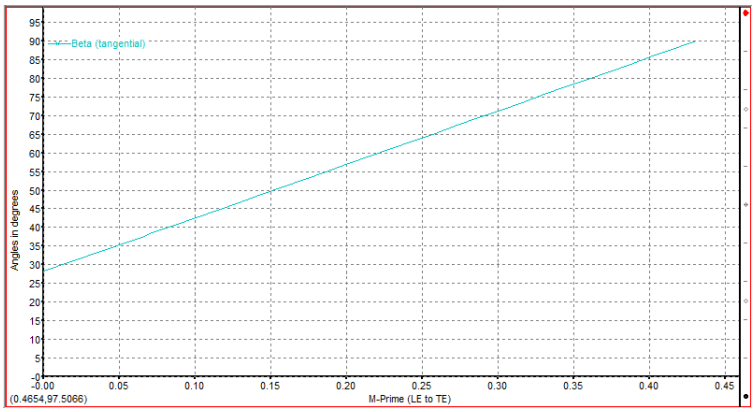

Blade angle (β)

Fig. 5.44 The runner blade profile (2).

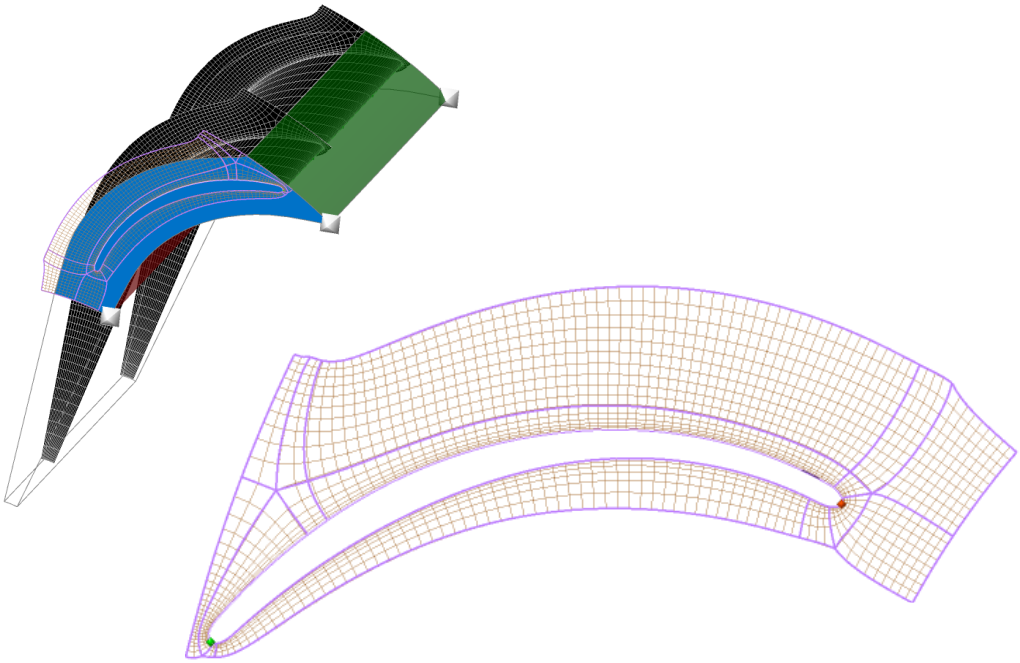

Blade domain mesh

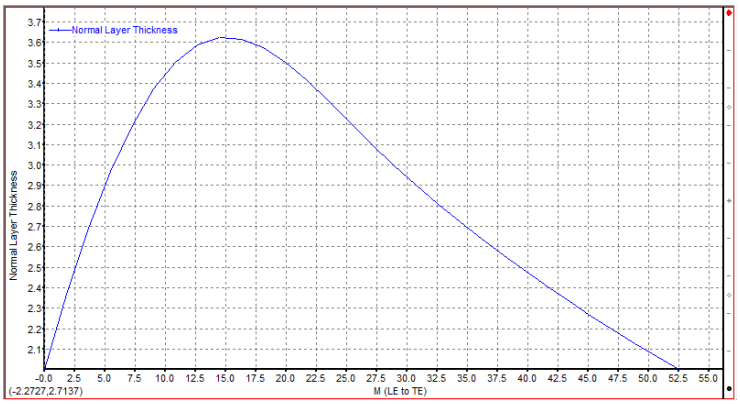

Blade thickness

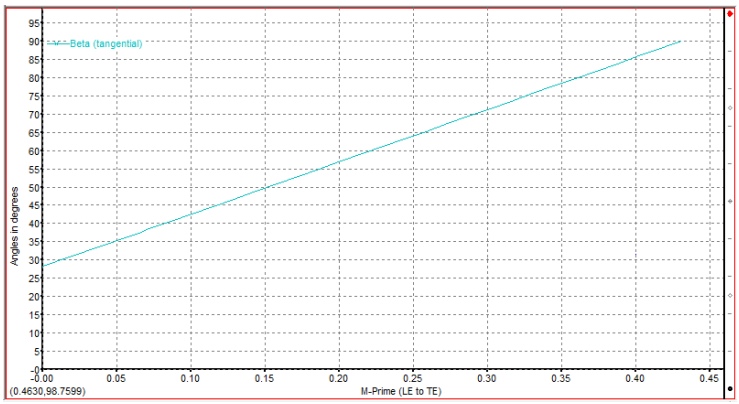

Blade angle (β)

Fig. 5.45 The runner blade profile (3).

As it was, previously, undertaken in this study general views of the flow in the nozzle and the runner are shown in Figs. 5.46 (a) to (d). These figures confirm the general internal flow in its three dimensional state. They all show that water flows only through part of the runner facing the nozzle. The water volume fraction contours of the flow at the mid span of the turbine of various blade profiles are shown in Figs. 5.47 (a) to (d). These figures reveal the interface of the air and water two-phase flow. Figures 5.48 (a) to (d) show more details of the fluid flow, in term vectors of water superficial velocity. These figures show clearly that the runner with Banki's blade profile shows less water impingement on the axle of the runner. It is expected, therefore, that turbine of runners fitted with Banki's blade profile should be of high efficiency. This clearly contradicts the results reported in Fig. 5.49. The reasons for this contradiction will become apparent in Figs. 5.48 (a) to (d) and the enlarged sections of Figs. 5.48 (a) and 5.48 (b) which are reported in Figs. 5.50 and 5.51. These show very interesting details of the internal flow in the runner in all cases. Some features of flow impingement on the blades' upper edges and vortices generated in between some blades and these undoubtedly affect the performance of the turbine. Therefore, it was decided to study these features in more details by scaling-up the regions of intense activities in the runner's blades. These are depicted in Figs. 5.50 and 5.51, respectively, and will be discussed hereafter.

Contours of total pressure were plotted on the mid span plane as shown in Figs. B.8 (a) to (d). The pressure distribution in the runner clearly has a significant impact on the turbine performance. It is clear that there are regions of low pressure (almost atmospheric) inside the runner's blades and these regions are almost empty of water. However, they contain enough water droplets to cause

vortices inside them and this reduces the developed energy. Although Fig. B.8 (b) shows the larger regions than Fig. B.8 (a) of low pressure, but in this case, the fine ends of the blades allow the bulk of the water to enter the runner through the first half of the nozzle entry arc smoothly. This in turn causes a greater water energy conversion into mechanical energy and result in higher efficiency.

Inspecting Figs. 5.48 (a) to (d) closely reveals that the impingement of the flow on the tip of the new blade profiles is less than the impingement of the flow on the tip of Banki's blade profile. Accordingly, it is expected that the new blade profiles may result in improve the performance of the cross-flow turbine. Inspecting Figs. 5.50 and 5.51 confirms the above explanation. These figures show clearly that a runner fitted with Banki's blade profile has indeed more water energy wasted through the impingement process at the leading edge of the lower row of the blades. Furthermore, they show high velocity (energy) water leaving the trailing edge of the lower row of the runner's blades.

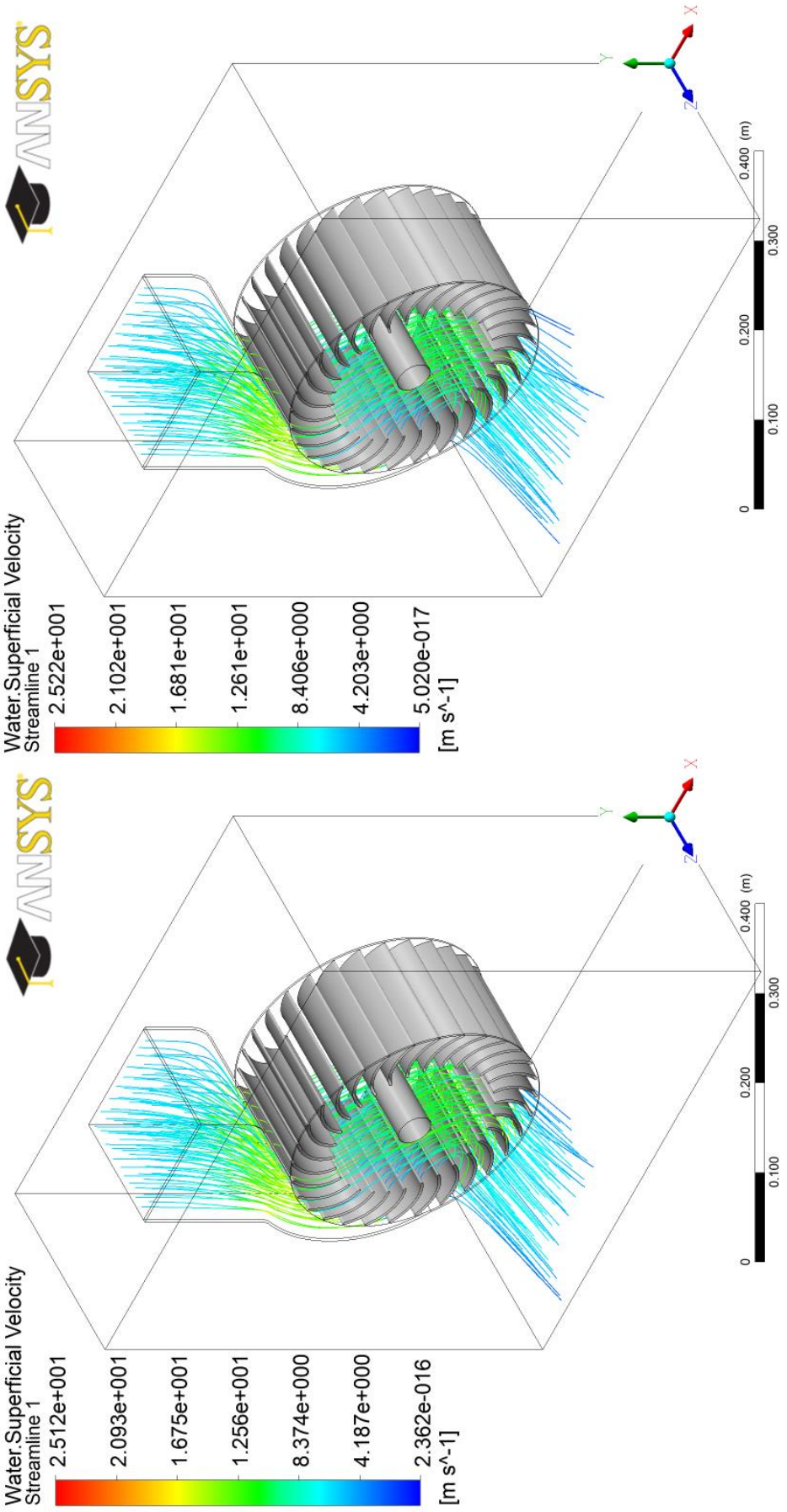

(b) Blade profile (1)

(a) Banki's profile

Fig. 5.46 (a) and (b) Water superficial velocity streamlines in cross-flow turbine of various blade profiles.

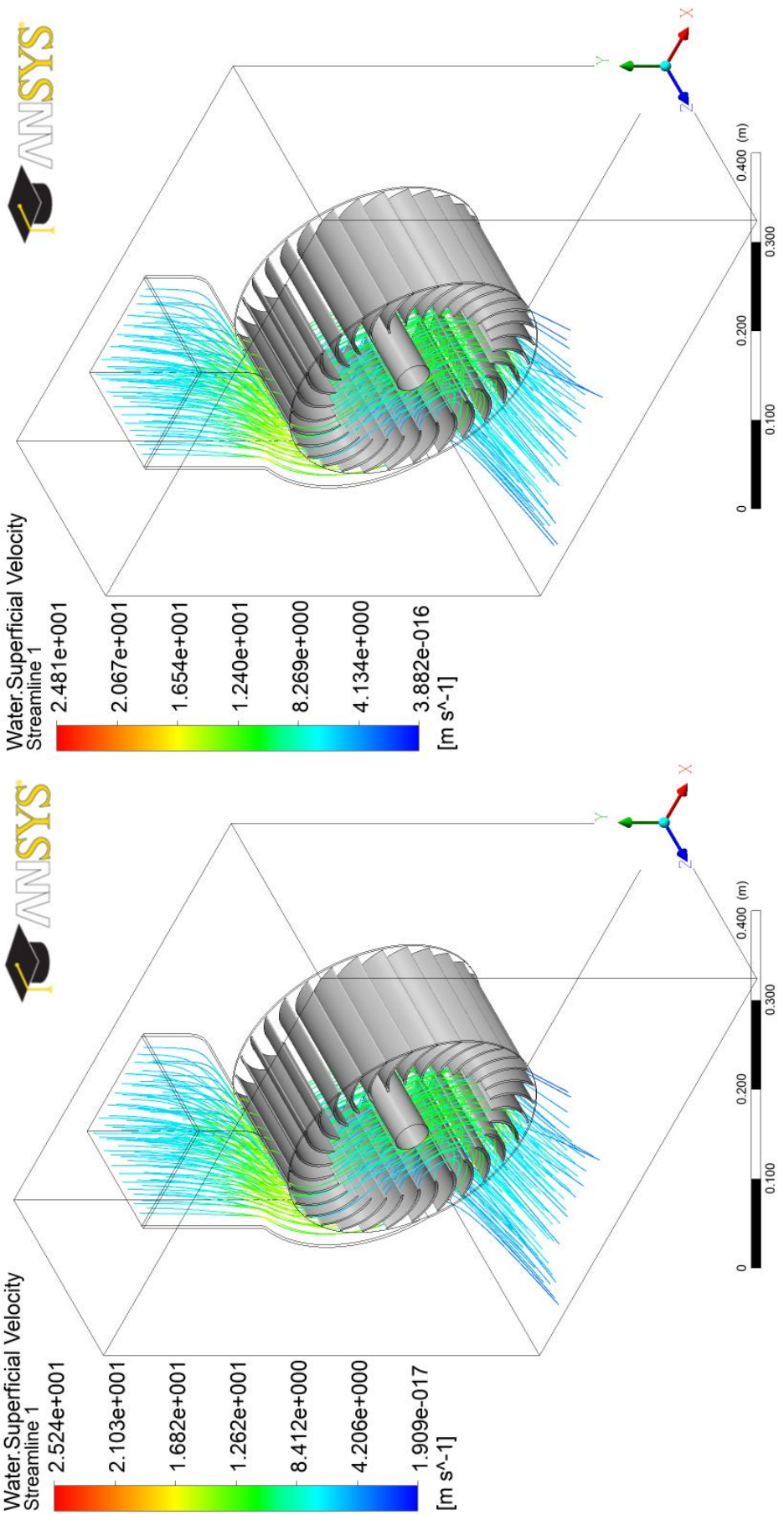

(d) Blade profile (3)

(c) Blade profile (2)

Fig. 5.46 (c) and (d) Water superficial velocity streamlines in cross-flow turbine of various blade profiles.

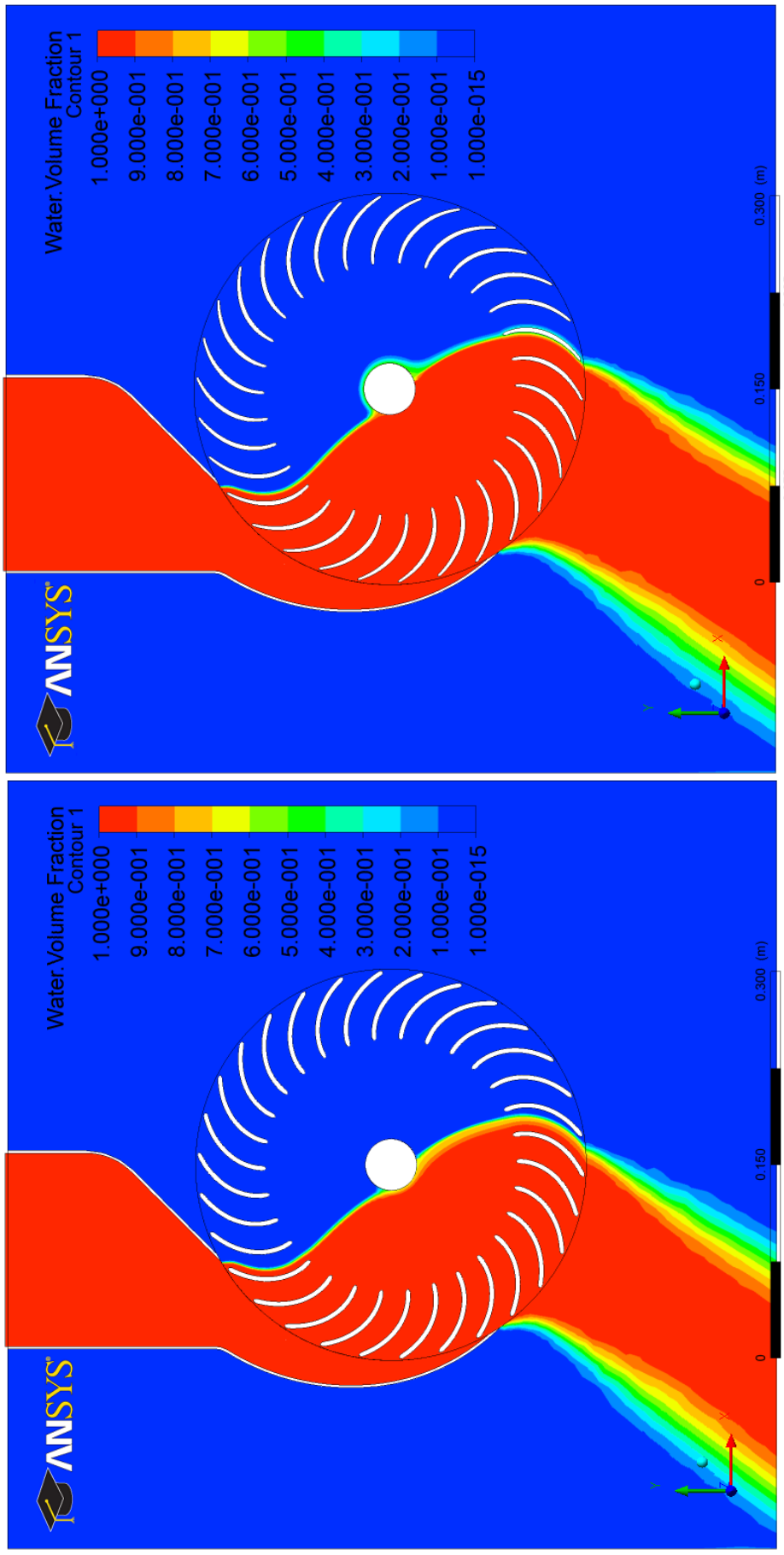

(a) Banki's profile (b) Blade profile (1)

Fig. 5.47 (a) and (b) Water volume fraction contours at the mid span of cross-flow turbine of various blade profiles.

(c) Blade profile (2) (d) Blade profile (3)

Fig. 5.47 (c) and (d) Water volume fraction contours at the mid span of cross-flow turbine of various blade profiles.

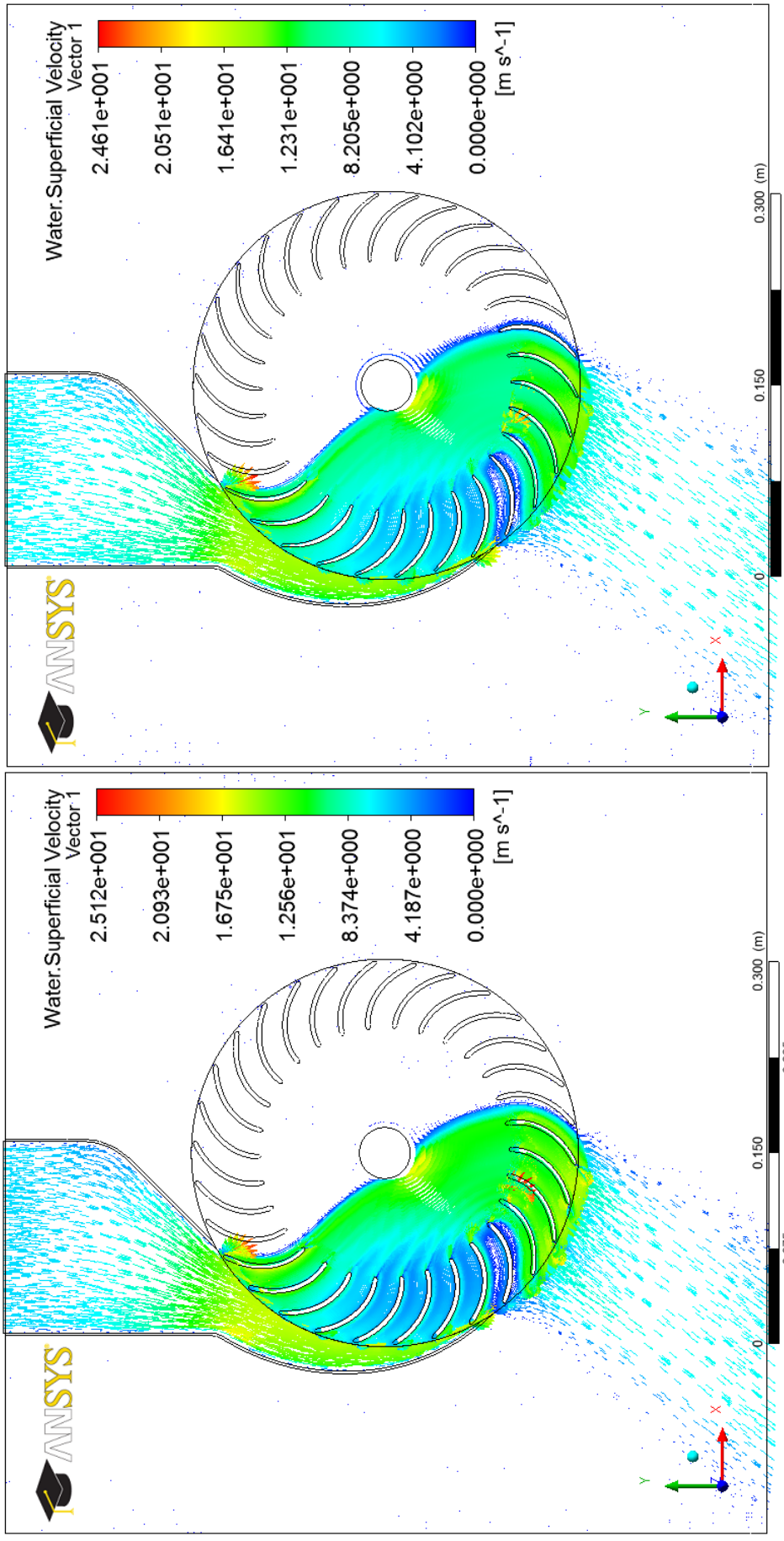

(a) Banki's profile (b) Blade profile (1)

Fig. 5.48 (a) and (b) Water superficial velocity vectors at the mid span of cross-flow turbine of various blade profiles.

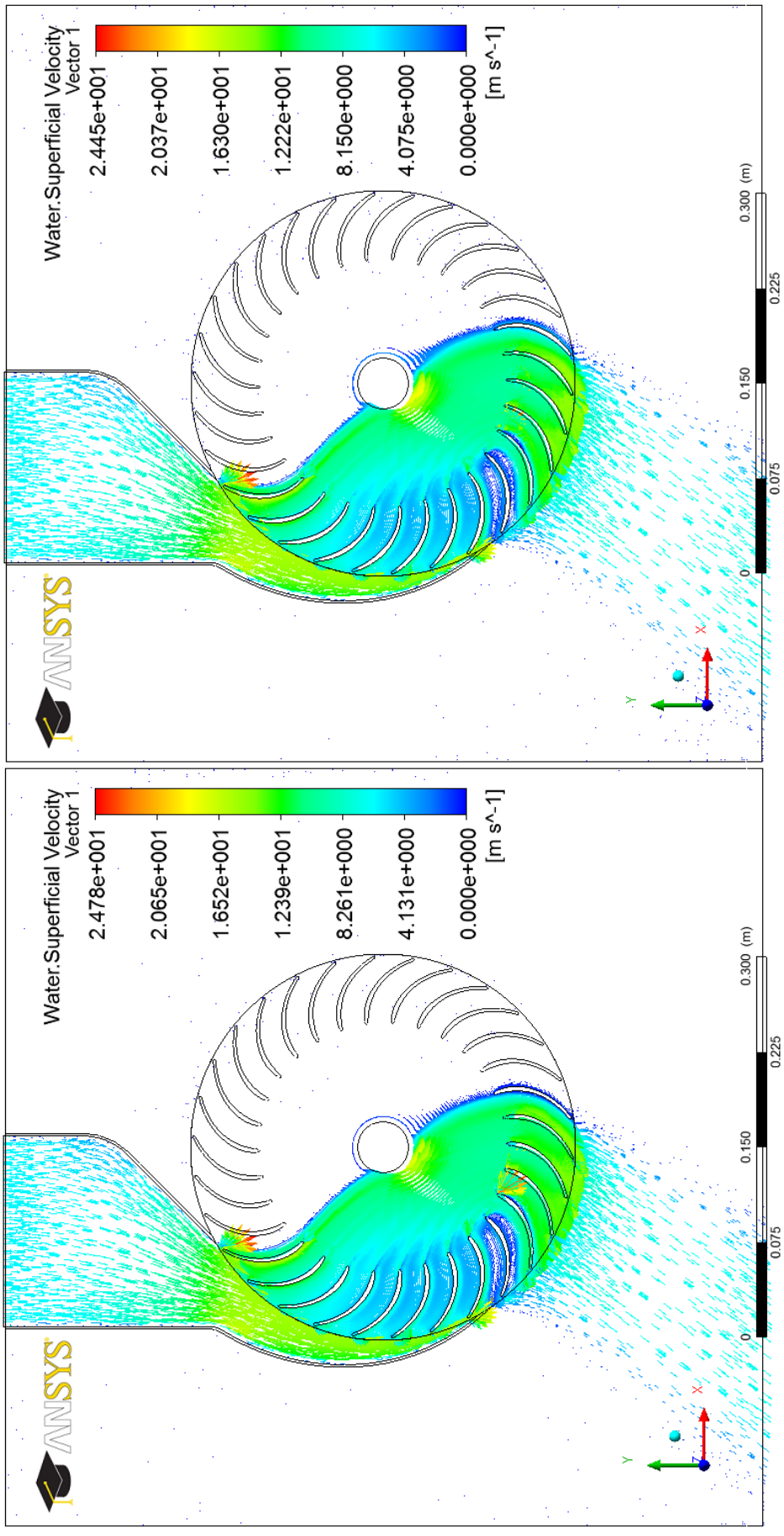

(d) Blade profile (3)

(c) Blade profile (2)

Fig. 5.48 (c) and (d) Water superficial velocity vectors at the mid span of cross-flow turbine of various blade profiles.

The summary of the result of computations shown in Fig. 5.49 reveals that the efficiency of the cross-flow turbine increased significantly by using the new runner blade profiles as compared with Banki's blade profile. This is clearly because the new blade profiles provide better hydrodynamic flow and less collision loss than Banki's blade profile. This is confirmed by the enlarged views of Figs. 5.50 and 5.51. However, there was a small change in the efficiency by using various new runner blade profiles. The turbine efficiency was higher in the case of the blade profile (1) than the blade profile (2) and (3). The cross-flow turbine efficiency with Banki's blade profile was 75.389 % and the most effective blade profile was the blade profile (1) where the efficiency was 77.564 %. According to this, the optimum blade profile can be considered to be the blade profile (1).

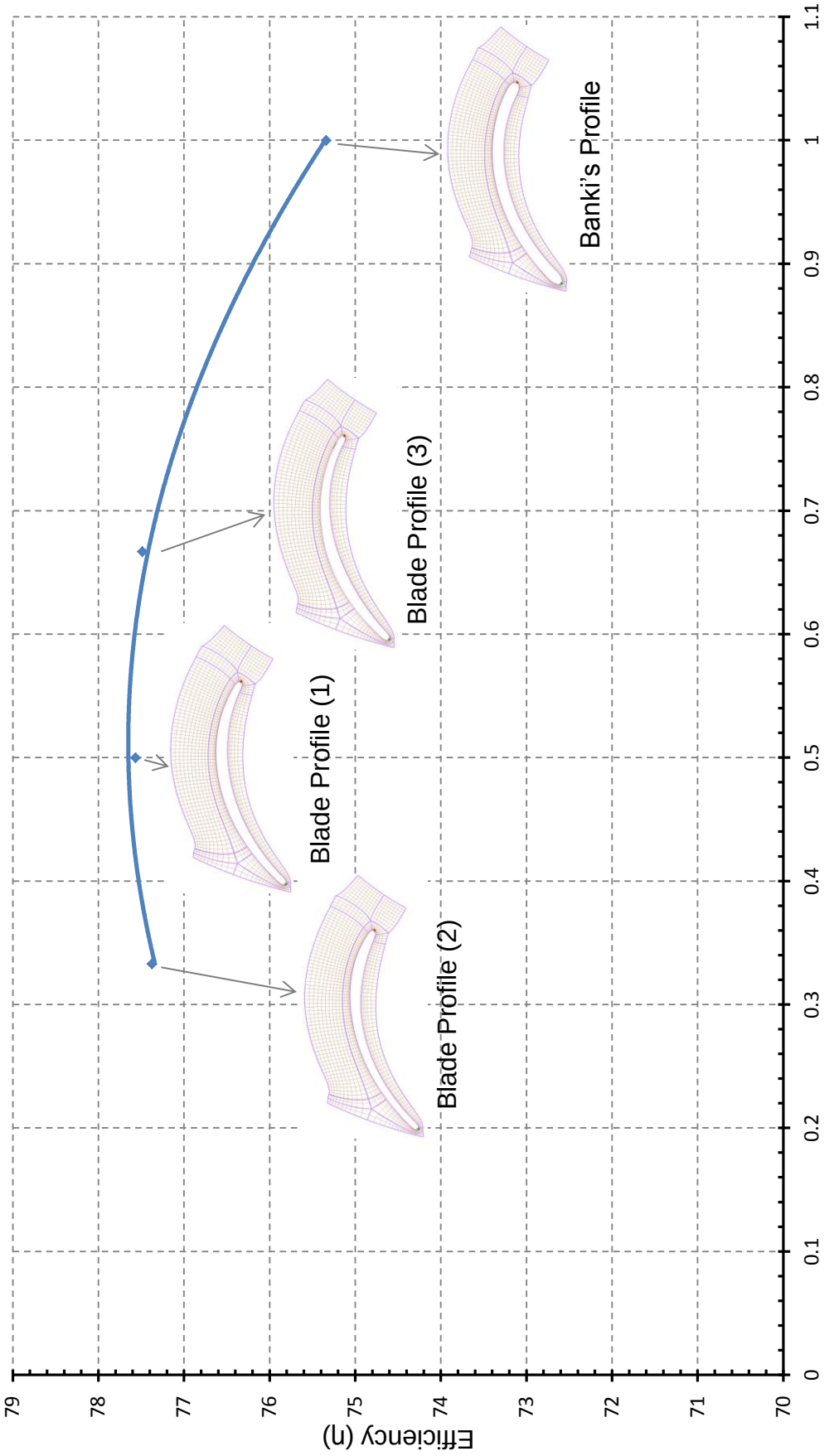

Fig. 5.49 Cross-flow turbine performance characteristics curve for blades of various profiles.

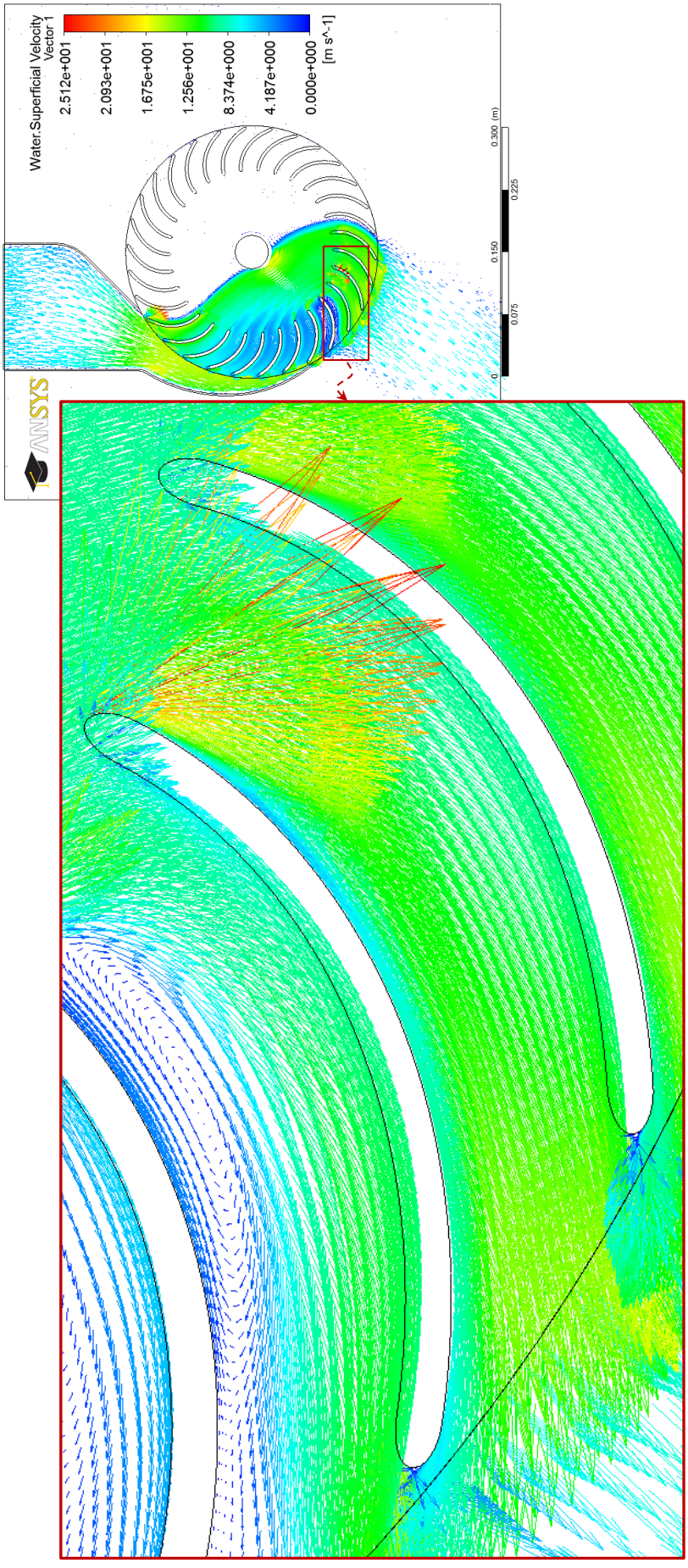

Fig. 5.50 Enlargement of the water superficial velocity vectors at the mid span of cross-flow turbine for Banki's blade profile.

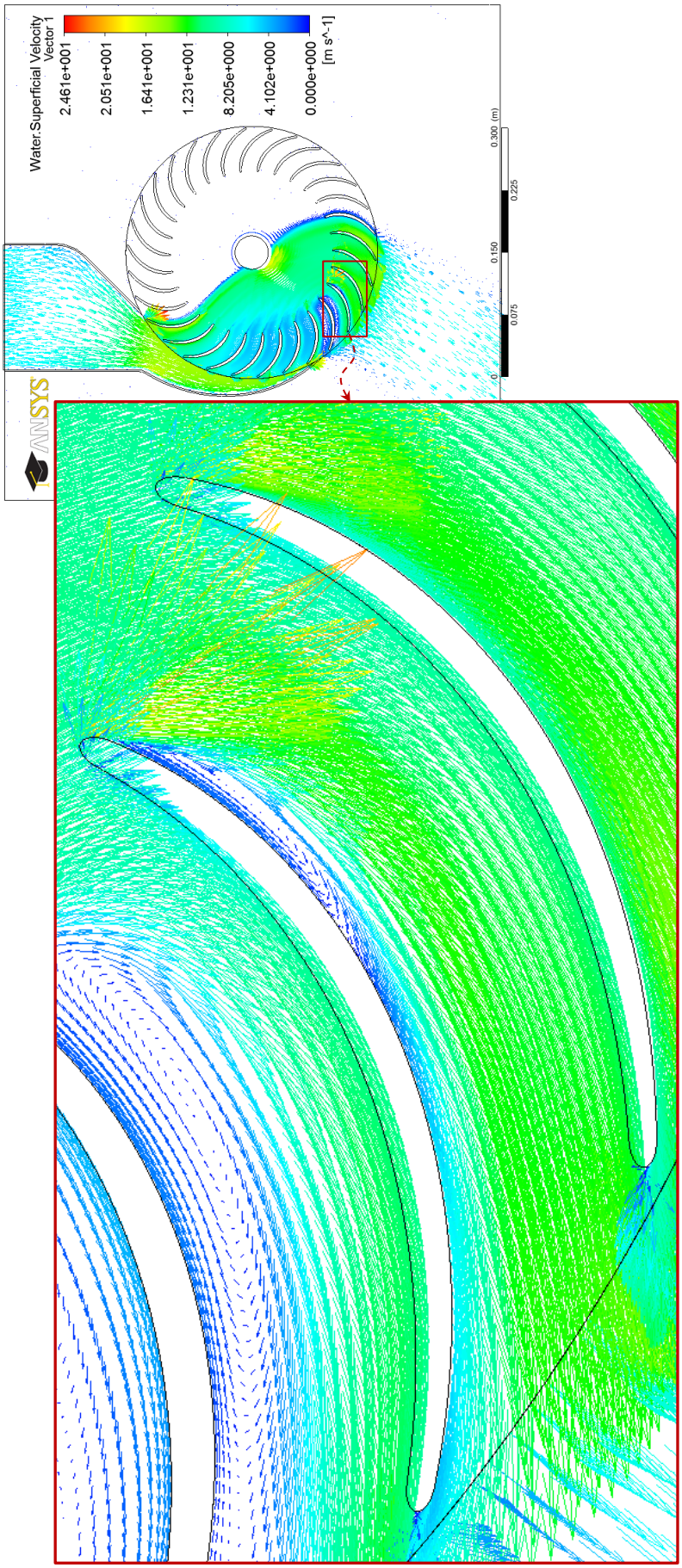

Fig. 5.51 Enlargement of the water superficial velocity vectors at the mid span of cross-flow turbine for blade profile (1).

5.2.6 Optimization of the Nozzle Profile

This section deals with optimization of the nozzle taking into consideration the restrictions imposed. These include a rectangular cross-sectional area with a small angle of attack. According to the equation (3.49) and in order to achieve the maximum efficiency, the angle of attack should be kept as small as possible. The nozzle, which has a rectangular cross-sectional area, converts the flow energy into kinetic energy by directing the water to the full length of the blades at a specified angle of attack. It was evident from the literature available that various cross-flow turbine's nozzle profiles, which may be fitted with or without guide vane, have been investigated by changing most of the geometric parameters of the nozzle. Therefore, it is essential to improve and optimize the turbine operation by selecting the best geometrical shape of the nozzle. The selection and designs created for the cross-flow turbine's nozzle profiles were based on the specifications provided by Aziz and Desai [46] and Kitahora et al. [91]. However, some modifications were made on the original design of the above researchers in order to obtain optimum performance. In the current study, three nozzle profiles were designed by using CATIA V5 computer aided design (CAD) program and investigated by ANSYS CFX simulation code. The geometrical parameters and nozzle profiles' details are shown in table 5.6 and Figs. 5.52, 5.53 and 5.54. The three tested nozzles include a curved profile which gradually reduces the area of the flow in order to keep the flow velocity as constant as possible and as shown in profile (1) of Fig. 5.52. The second nozzle (shown in Fig. 5.53) is of a straight rear wall. This was designed to eliminate the region of flow separation that is likely to take place in the nozzle of profile (1). The third tested nozzle show in Fig. 5.54 was selected so that it contains a

guide vane (profile (3)). All dimensions and angles of Figs. 5.52 to 5.54 are given in table 5.6.

Table 5.6 Details of the nozzles profiles tested.

Geometrical parameter	Specification
Number of blades	$n_b = 30$
External diameter	$d_1 = 300\,mm$
Diameters ratio	$d_2/d_1 = 0.65$
Angle of attack	$\alpha_1 = 15^o$
Inlet blade angle	$\beta_1 = 151.814^o$
Internal blade angle	$\beta_1' = \beta_2' = 90^o$
Outlet blade angle	$\beta_2 = 28.186^o$
Blade thickness	$t_b = 3.6\,mm$
Blade radius of curvature	$r_b = 49.139\,mm$
Width of the nozzle	$N_w = 150\,mm$
Shaft (axle) diameter	$d_s = 40\,mm$
Nozzle profile	1, 2, and 3 *Note: Symbols as detailed in Fig. 3.2.*

Nozzle profile

1 Nozzle profile (1).

2 Nozzle profile (2) with eliminating the convergence at the nozzle rear wall.

3 Nozzle profile (3) with a guide vane.

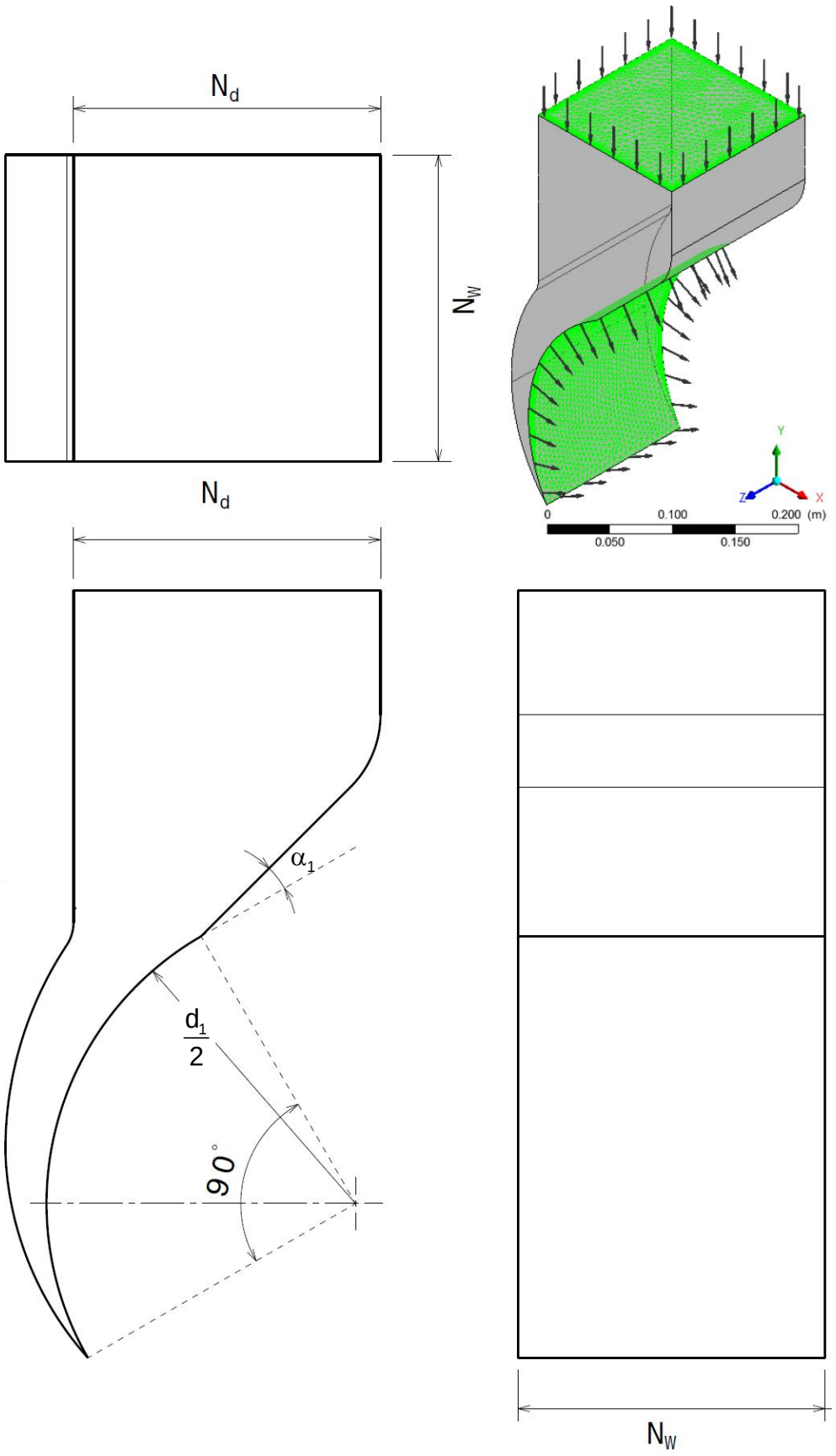

Fig. 5.52 Schematic view of the test nozzle profile (1).

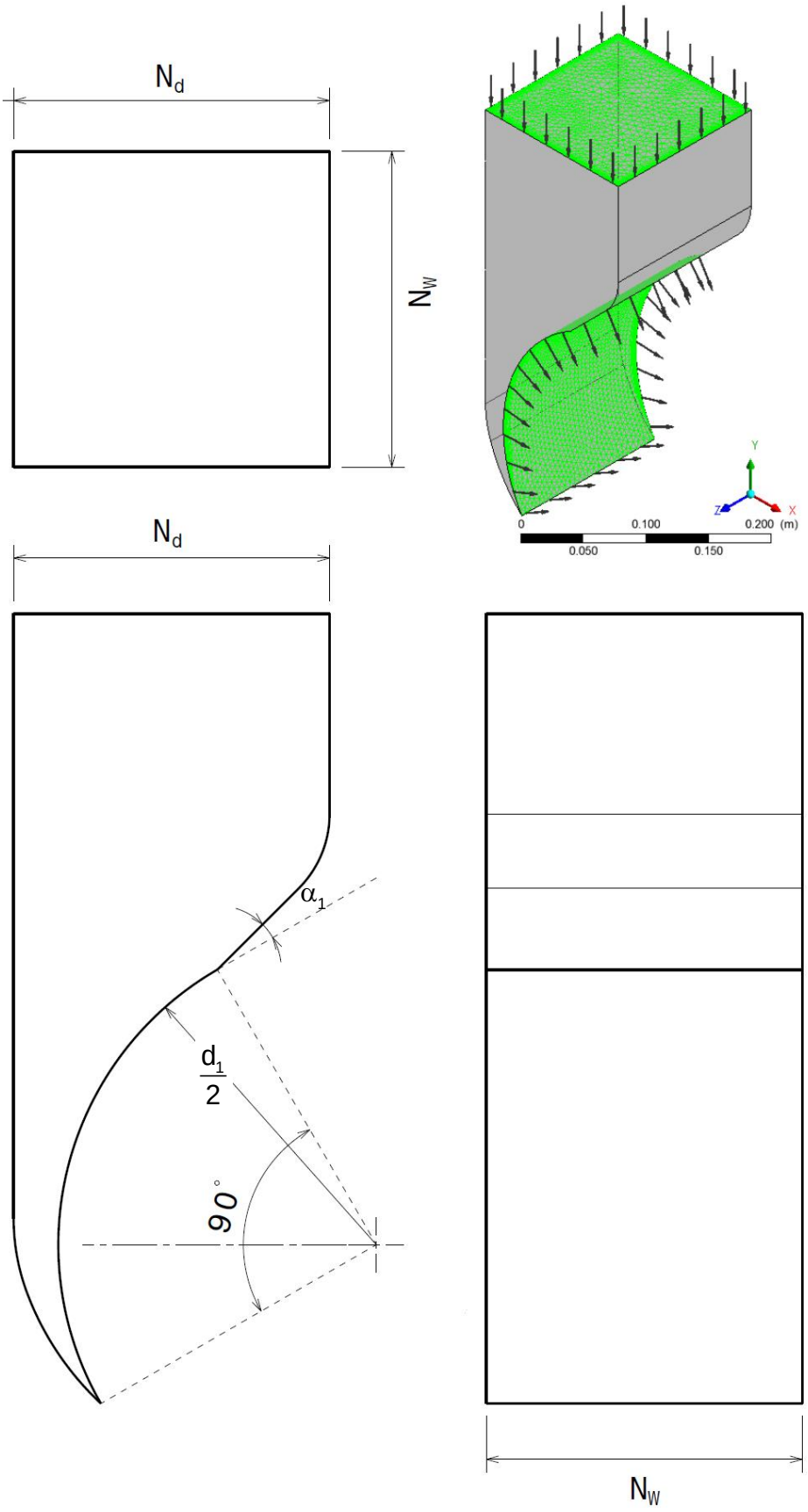

Fig. 5.53 Schematic view of the test nozzle profile (2).

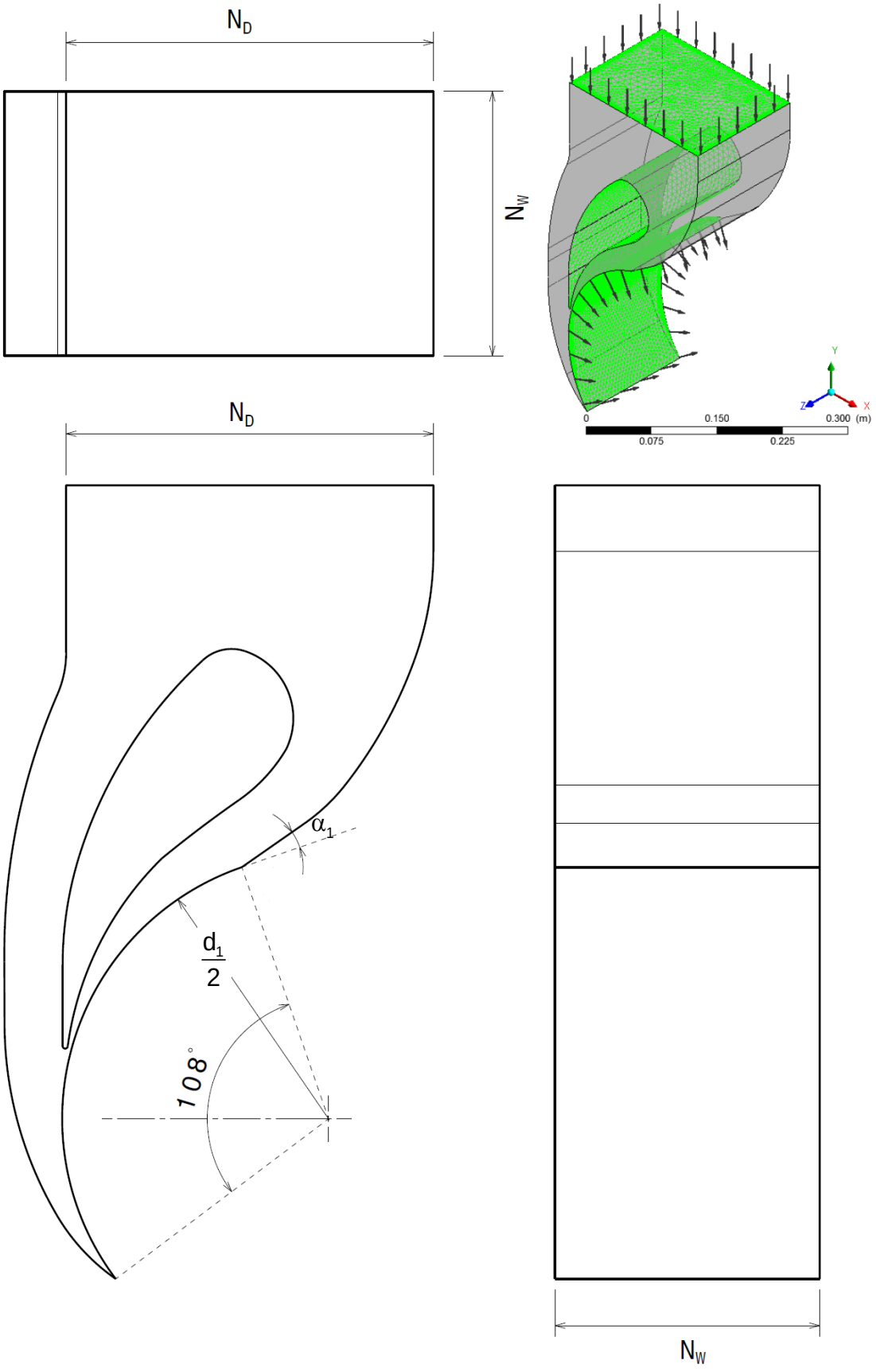

Fig. 5.54 Schematic view of the test nozzle profile (3).

The capability to represent and plot the flow variable of the post-processing of ANSYS CFX simulation code was utilized to perform flow field visualization of the internal flow in the cross-flow turbine. The velocity and pressure distributions provide a comprehensive understanding of the effect of the nozzle profile on the internal flow and the complex flow structure associated with each nozzle profile. The water superficial velocity streamlines were plotted for entire cross-flow turbine with various nozzle profiles (with and without guide vane) as shown in Figs. 5.55 (a) to (c). These figures show the effect of the nozzle profile on the flow structure in the turbine. They clearly indicate that profile (1) is of almost uniform water velocity throughout the nozzle. As it may be expected, this indicates that there are no losses due to flow irregularities, in particular, at the entry to the runner. Hence, this profile should yield the best performance and efficiency.

Water superficial velocity vectors at the mid span of the turbine of various nozzle profiles as shown in Figs. 5.57 (a) to (c) show the water distribution between the runner blade passages. The guide vane in the nozzle profile (3) causes good water distribution, on the other hand; the guide vane increases the impingement of the flow leaving the upper raw of blades on the runner shaft. The shape of the nozzle rear wall of the nozzle profile (1) provides better water distribution than nozzle profile (2).

Figure B.10 (a) reveals the flow tendency to separate along the line close to where the nozzle meets the volute, and also Fig. B.10 (c) reveals the impingement of the flow in the nozzle on the guide vane. The separation and impingement of flow most certainly cause lower power output and lower efficiency as well as causing undesirable vibration and noise.

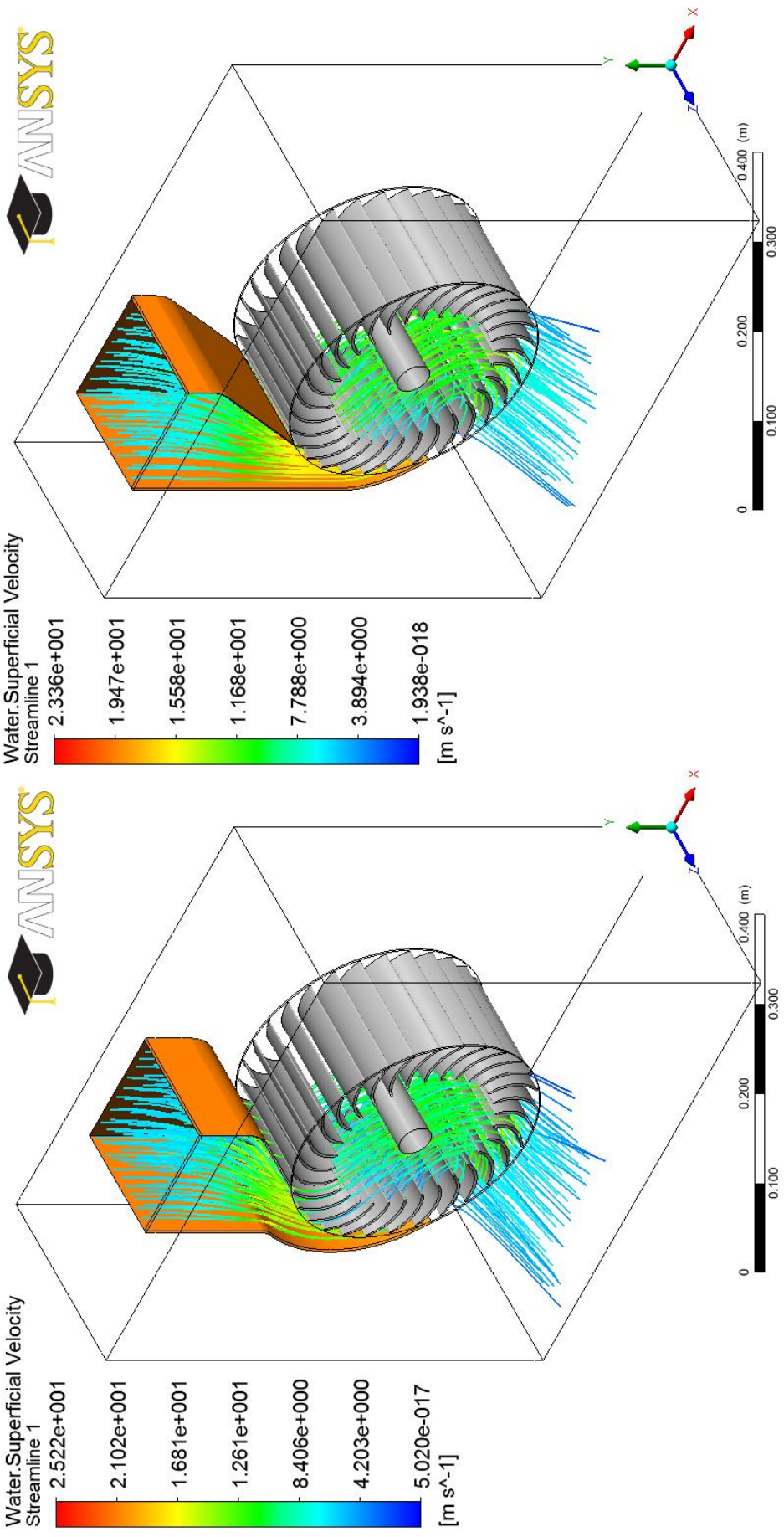

(b) Nozzle profile (2)

(a) Nozzle profile (1)

Fig. 5.55 (a) and (b) Water superficial velocity streamlines in cross-flow turbine of various nozzle profiles.

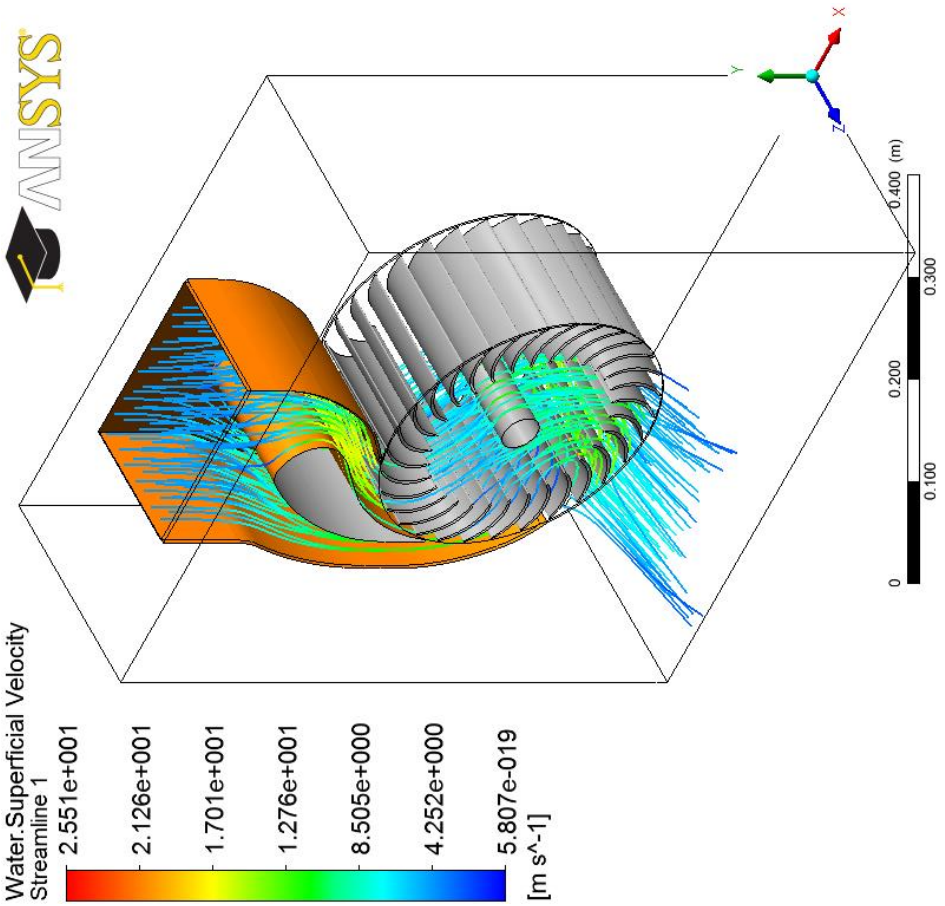

Fig. 5.55 (c) Water superficial velocity streamlines in cross-flow turbine for nozzle profile (3).

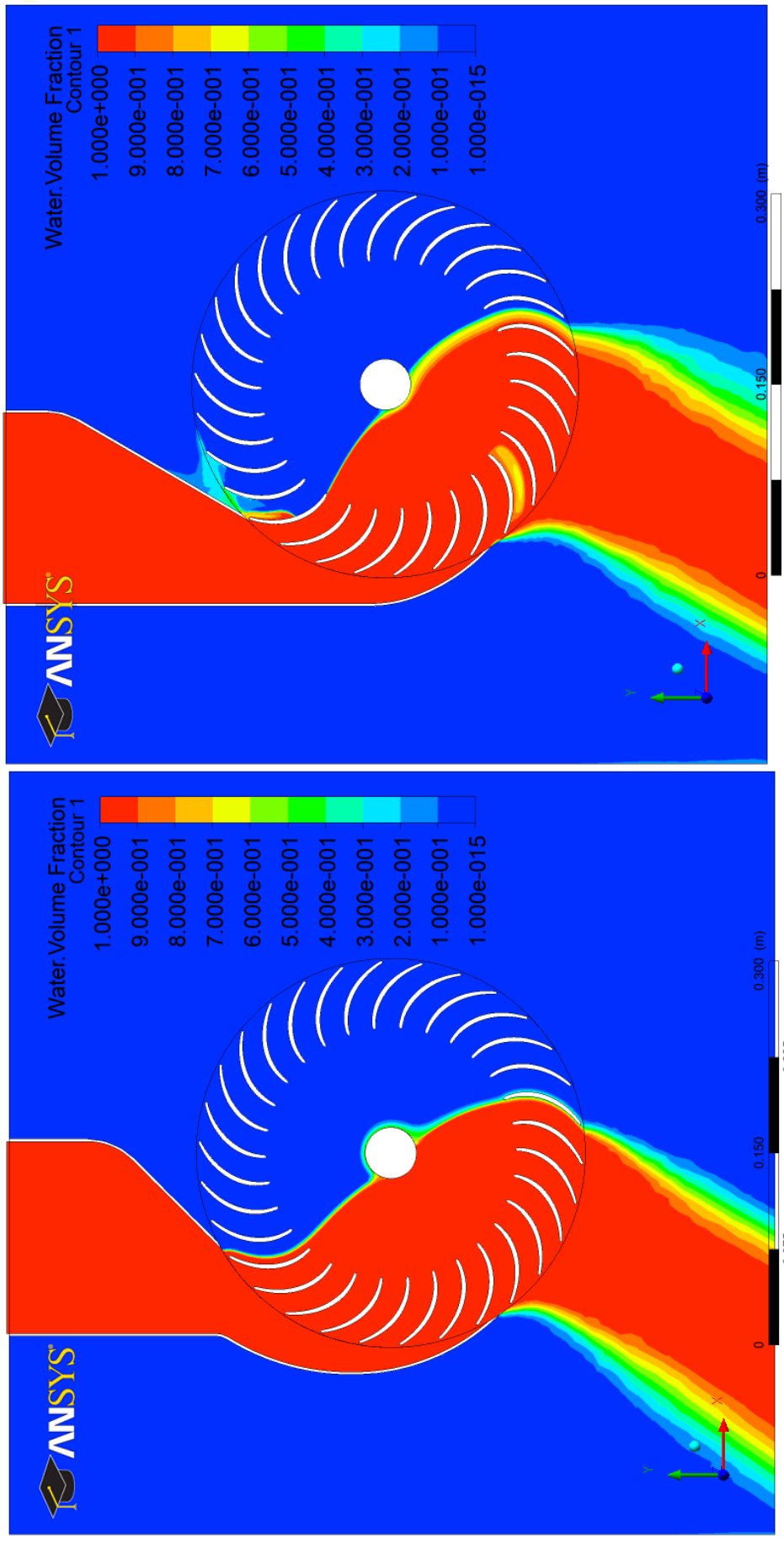

(a) Nozzle profile (1) (b) Nozzle profile (2)

Fig. 5.56 (a) and (b) Water volume fraction contours at the mid span of cross-flow turbine of various nozzle profiles.

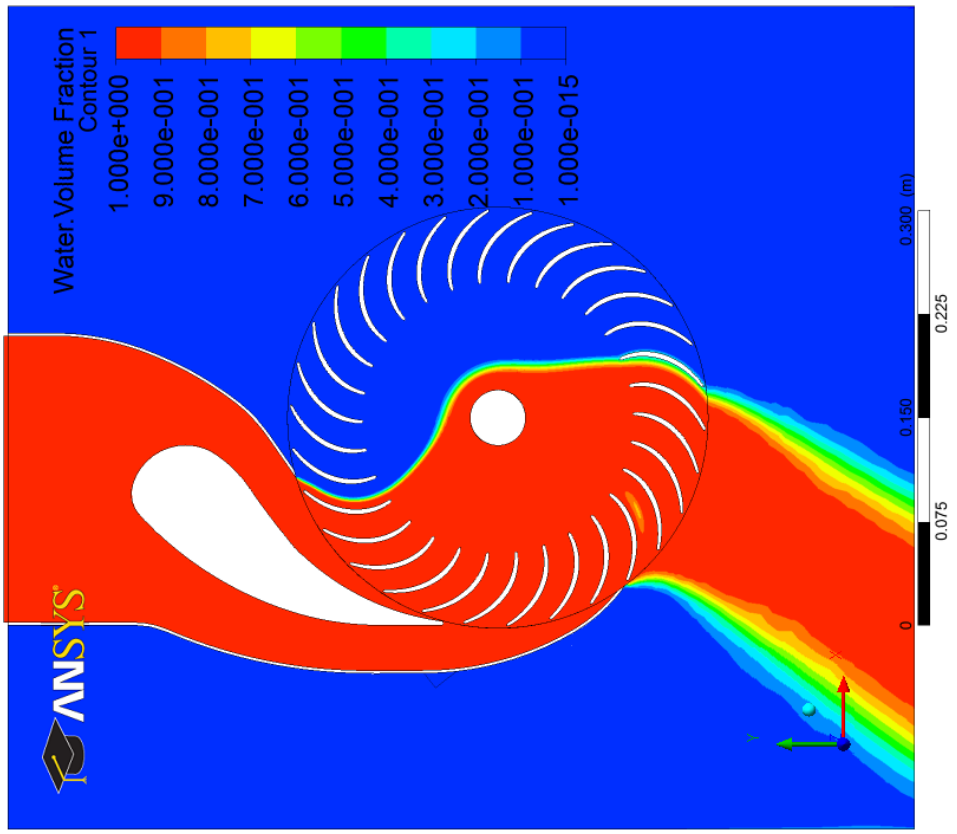

Fig. 5.56 (c) Water volume fraction contours at the mid span of cross-flow turbine for nozzle profile (3).

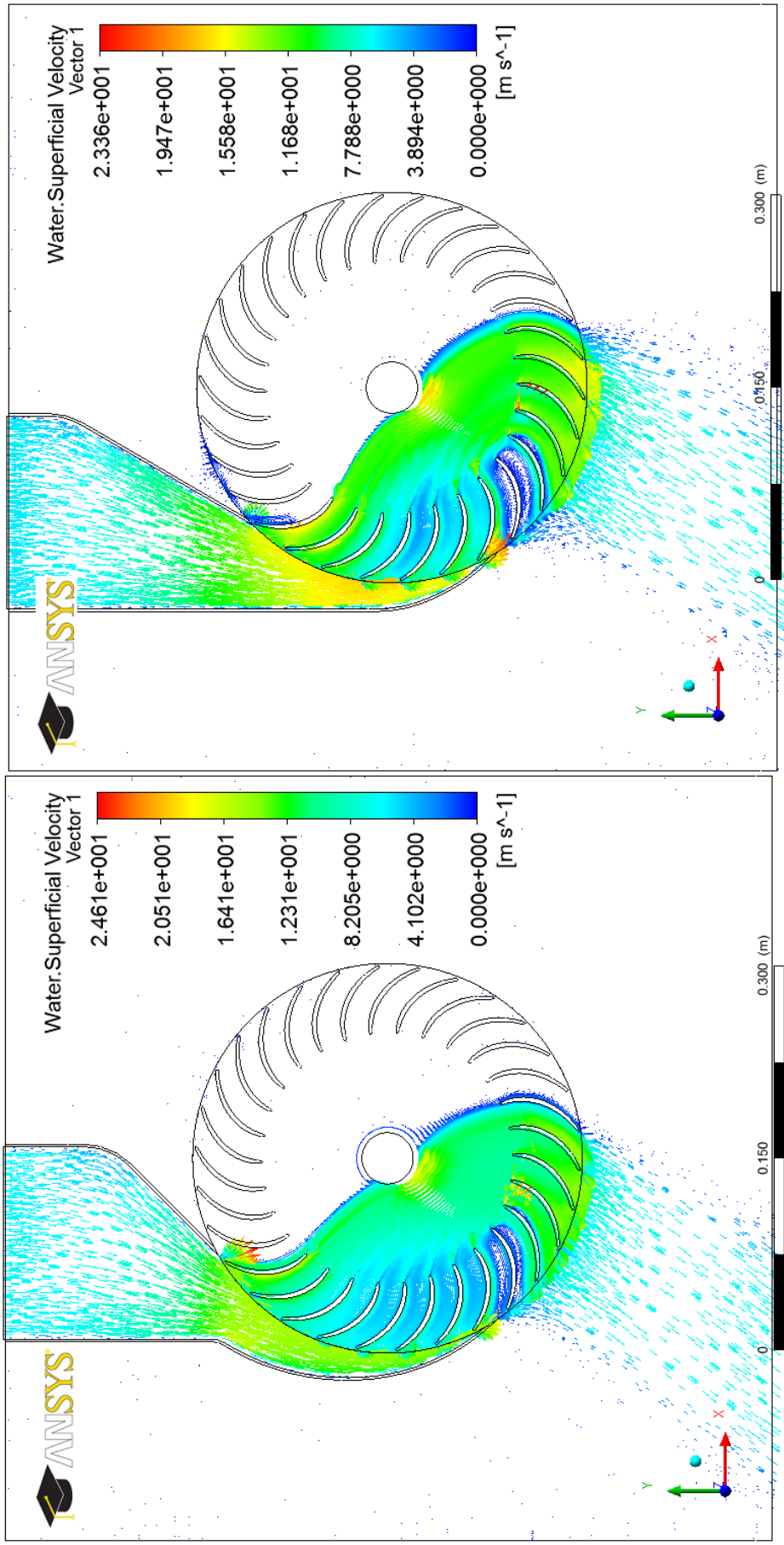

(a) Nozzle profile (1) (b) Nozzle profile (2)

Fig. 5.57 (a) and (b) Water superficial velocity vectors at the mid span of cross-flow turbine of various nozzle profiles.

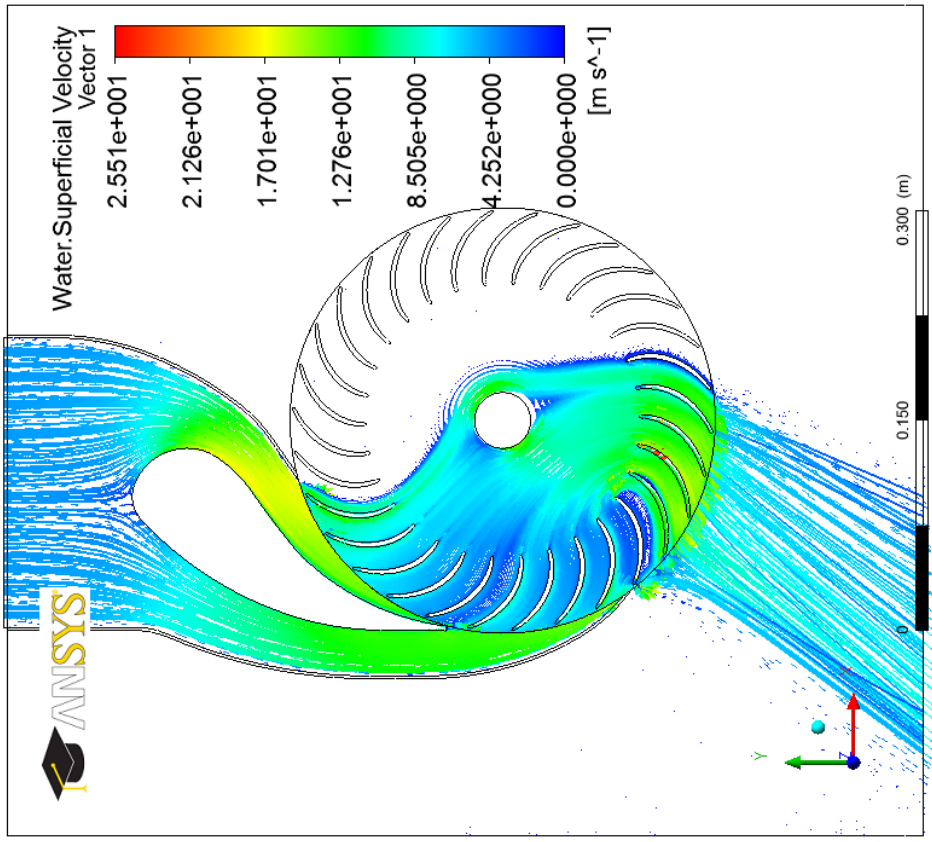

Fig. 5.57 (c) Water superficial velocity vectors at the mid span of cross-flow turbine for nozzle profile (3).

The effect of the nozzle profile on the efficiency of the cross-flow turbine is shown in Fig. 5.58. The results revealed that the turbine efficiency was higher in the case of the nozzle profiles without guide vane than the one with guide vane (the lowest turbine efficiency predicted was for the nozzle fitted with the guide vane 73.166 %). In such arrangement the losses associated with the water impingement on the front of the guide vane seems to be significant enough to cause some performance deterioration. In addition the presence of the guide vane in the nozzle caused the water to be directed towards the runner axle where it also loses some of its energy as clearly indicated by Fig. 5.67. The reason for this was the significant increase in the velocity of the water prior to its entry to the runner blades. Accordingly, the momentum increase of the water caused it to impinge on the runner axle and as shown in the enlarged portions of Figs. 5.65 to 5.67. As it was described, previously, in the case of the nozzle profile without a guide vane, the turbine efficiency with the nozzle profile (1) was higher than the turbine efficiency with the nozzle profile (2). For nozzle profile (2), the turbine efficiency is unsurprisingly lower (76.956 % as compared with 77.564 %) with this profile and as indicated by Figs. 5.60 and 5.61 some of the incoming water seems to reverse direction as it enters the runner blades. Consequently, it opposes the incoming blades and this tends to decrease the available energy of the total water and represents parasitic losses. It is also clear from Figs. 5.62 to 5.64 that energy of the water leaving the second stage blades of the runner is of higher than normal velocity observed for profile (1). In profile (2) the shape of the nozzle is such that it resulted in a very un-even distribution of water in the first stage of the runner blades. The result is a large proportion of the water with high velocity entering the first stage few blade

passages where it leaves the runner from the second stage blades at high energy. The shape of the nozzle rear wall of the nozzle profile (1) provides better water distribution than nozzle profile (2). According to this, the most effective nozzle profile noticed was nozzle profile (1).

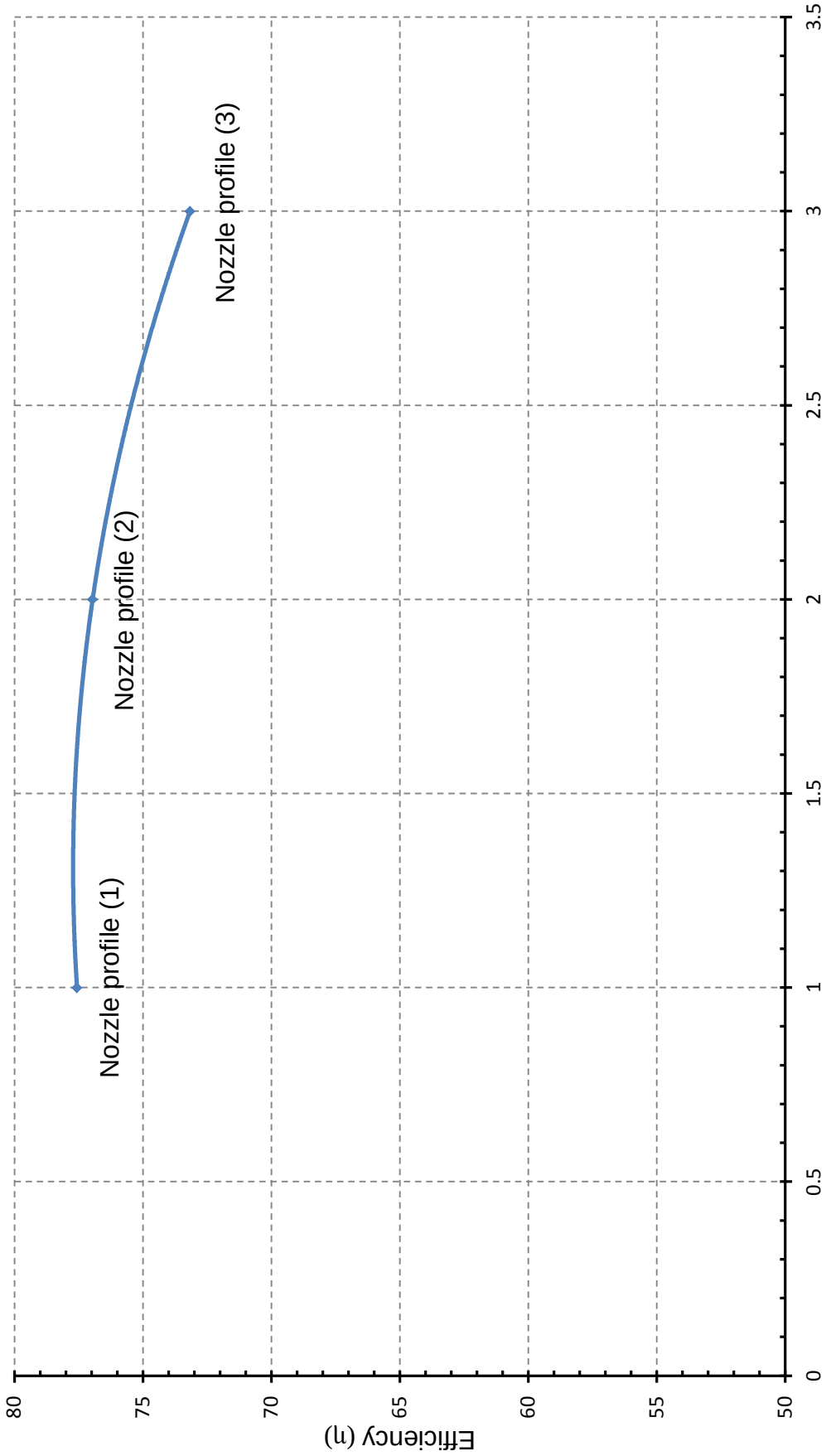

Fig. 5.58 Cross-flow turbine performance characteristics curve for nozzle of various profiles.

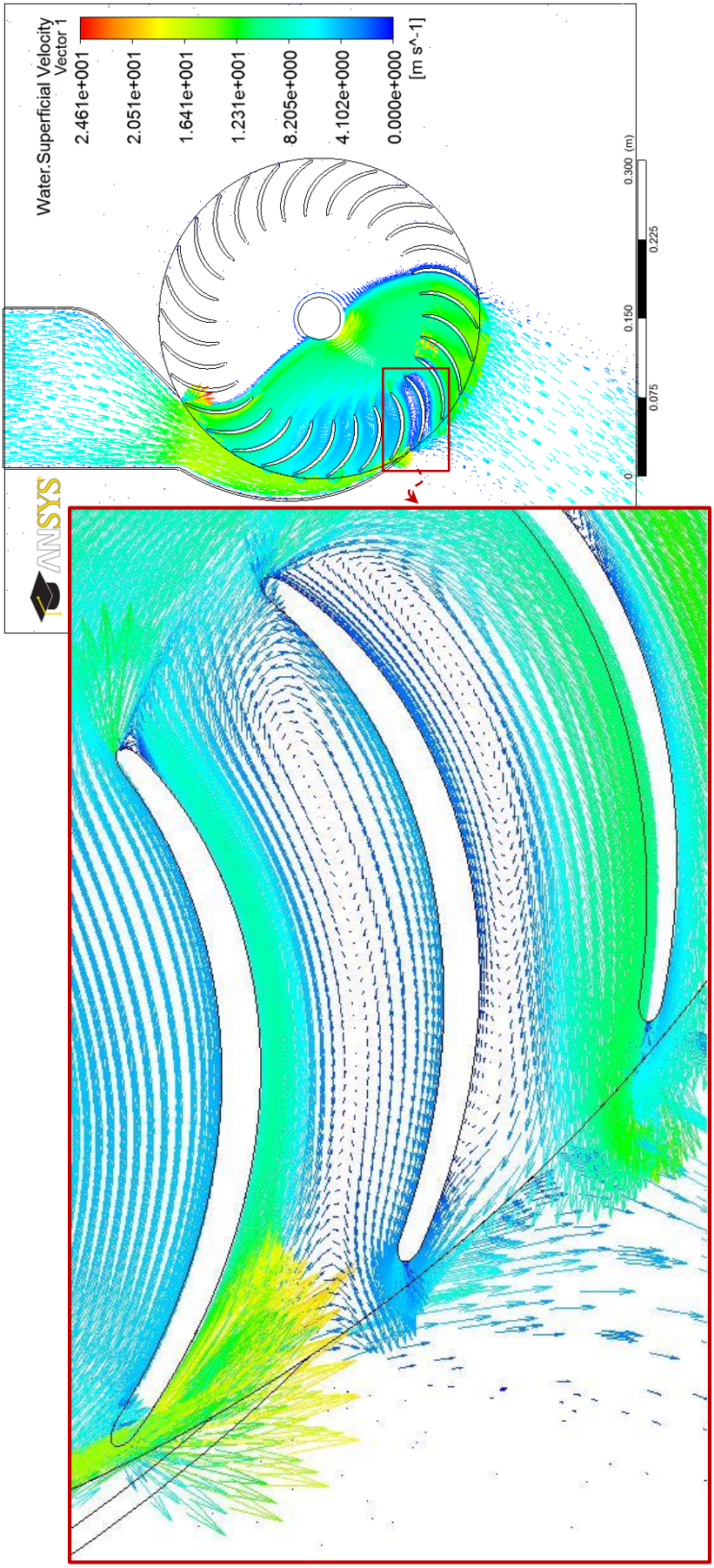

Fig. 5.59 Enlargement of the water superficial velocity vectors on the blades' passages facing the end of the nozzle profile (1).

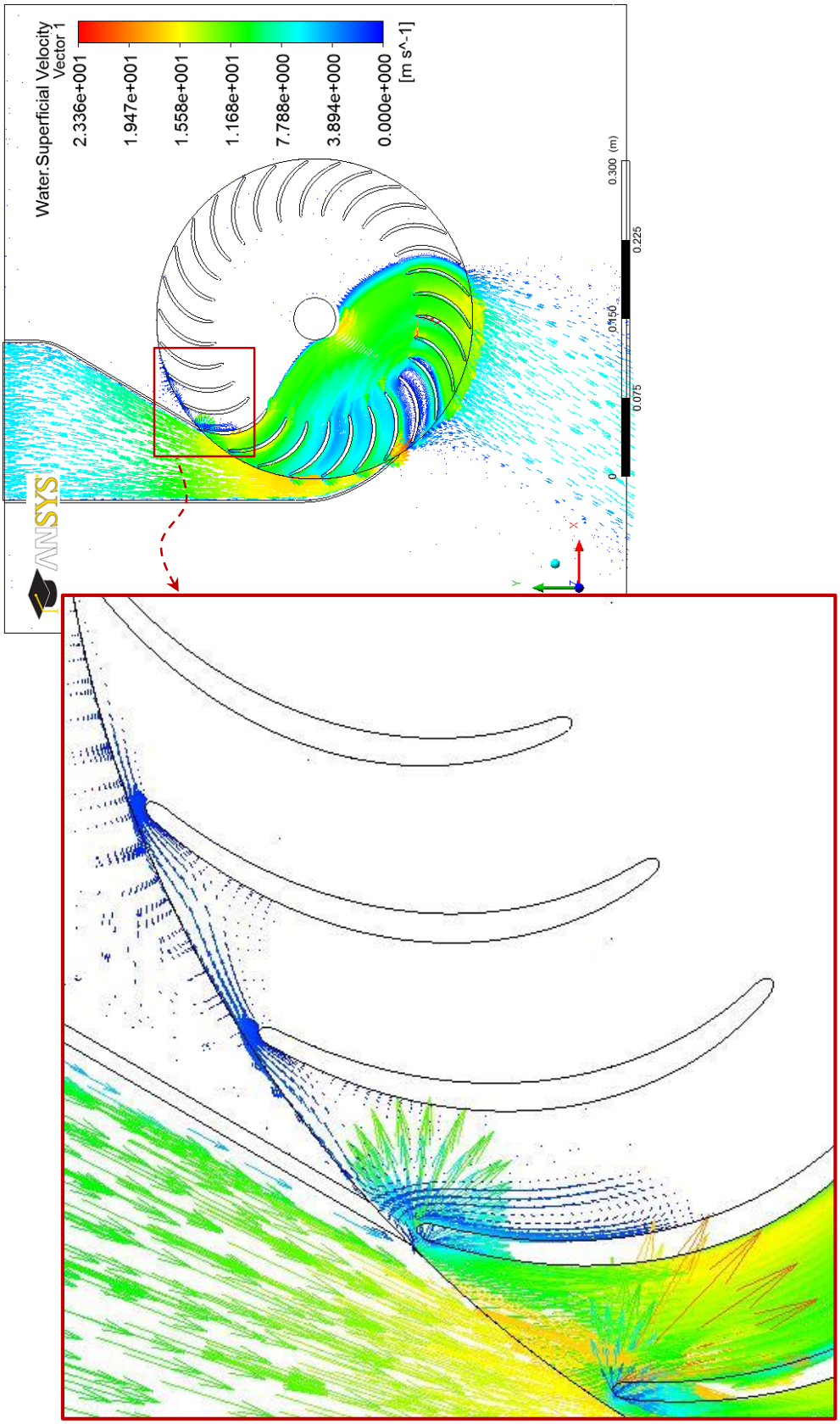

Fig. 5.60 Enlargement of the water superficial velocity vectors on the tip of the first couple of blades at the mid span of cross-flow turbine for the nozzle profile (2).

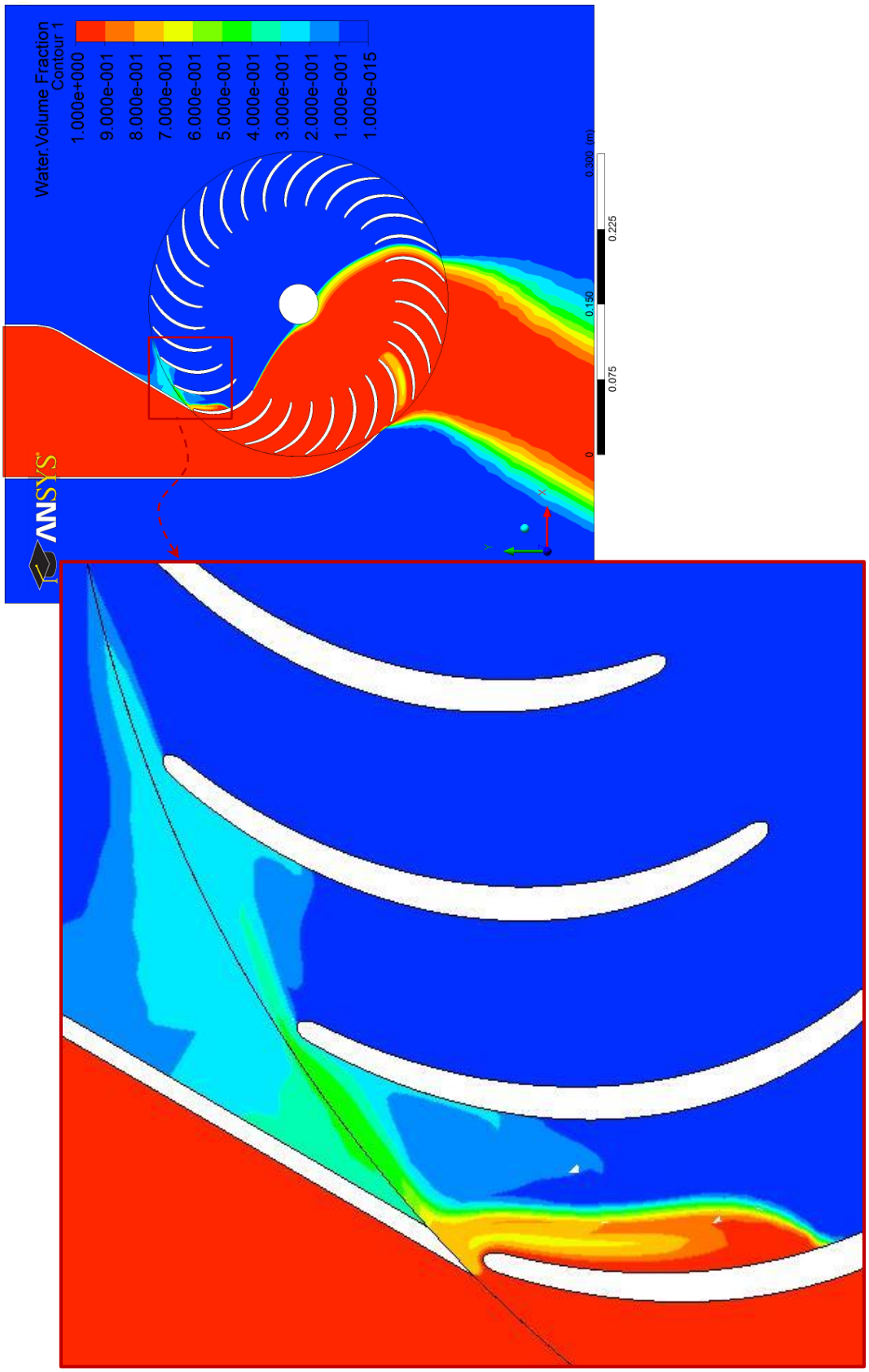

Fig. 5.61 Enlargement of the water volume fraction contour on the tip of the first blade at the mid span of cross-flow turbine for the nozzle profile (2).

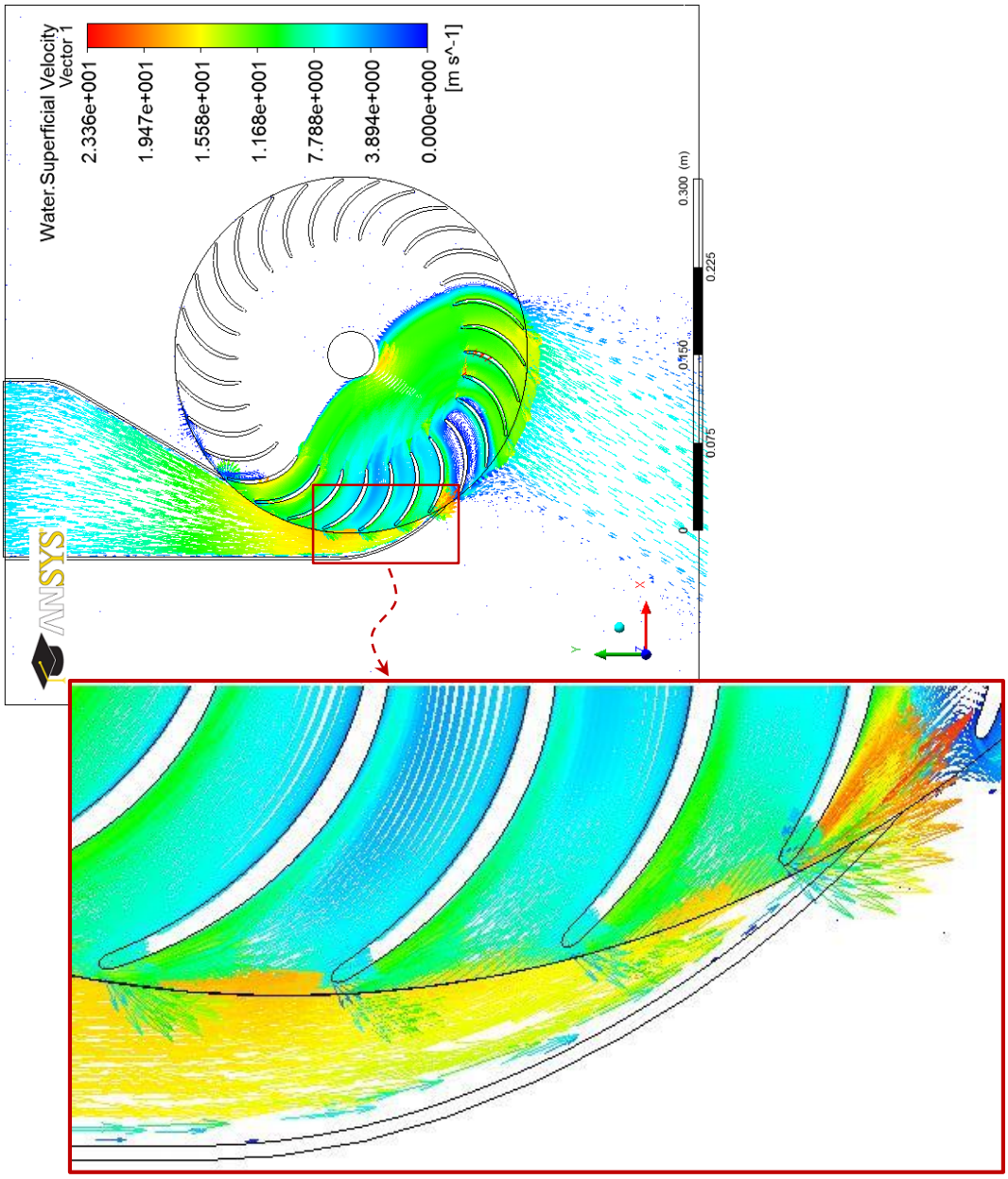

Fig. 5.62 Enlargement of the water superficial velocity vectors at the end of the nozzle profile (2).

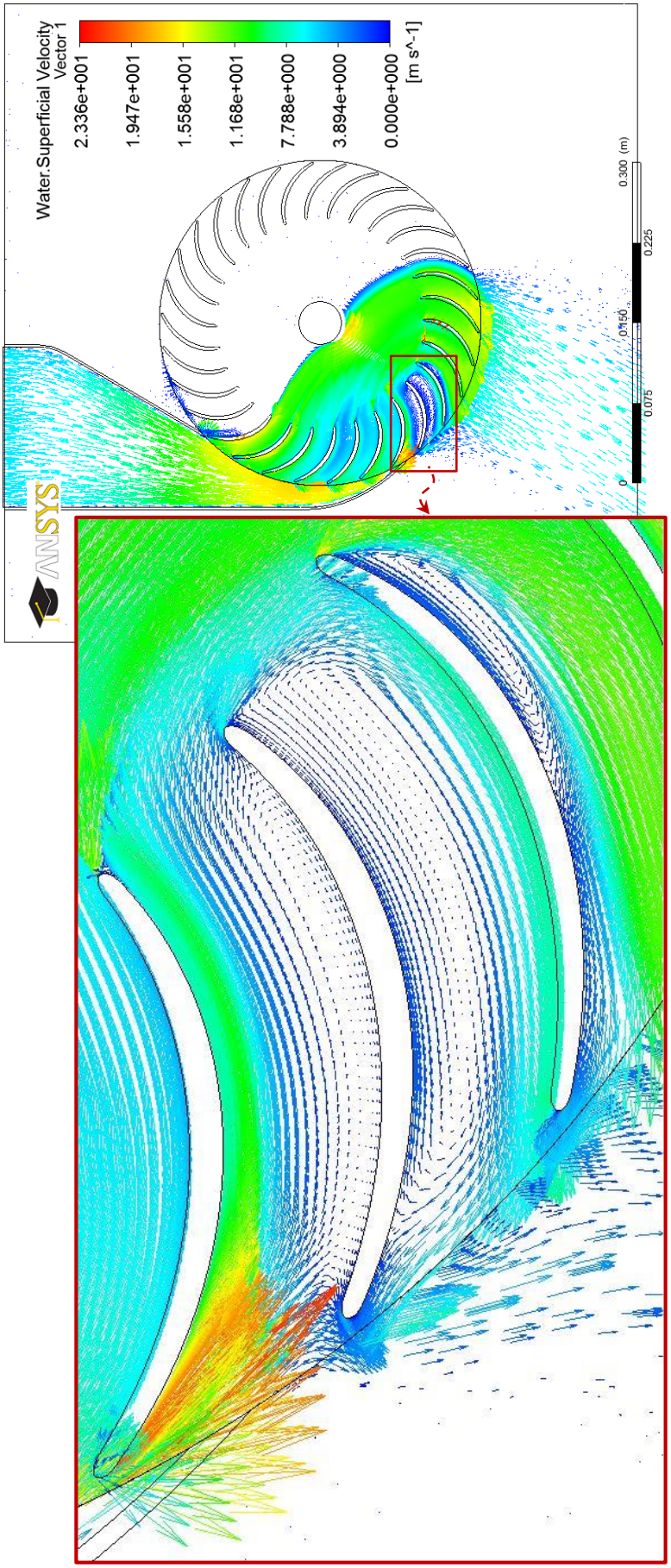

Fig. 5.63 Enlargement of the water superficial velocity vectors on the blades' passages facing the end of the nozzle profile (2).

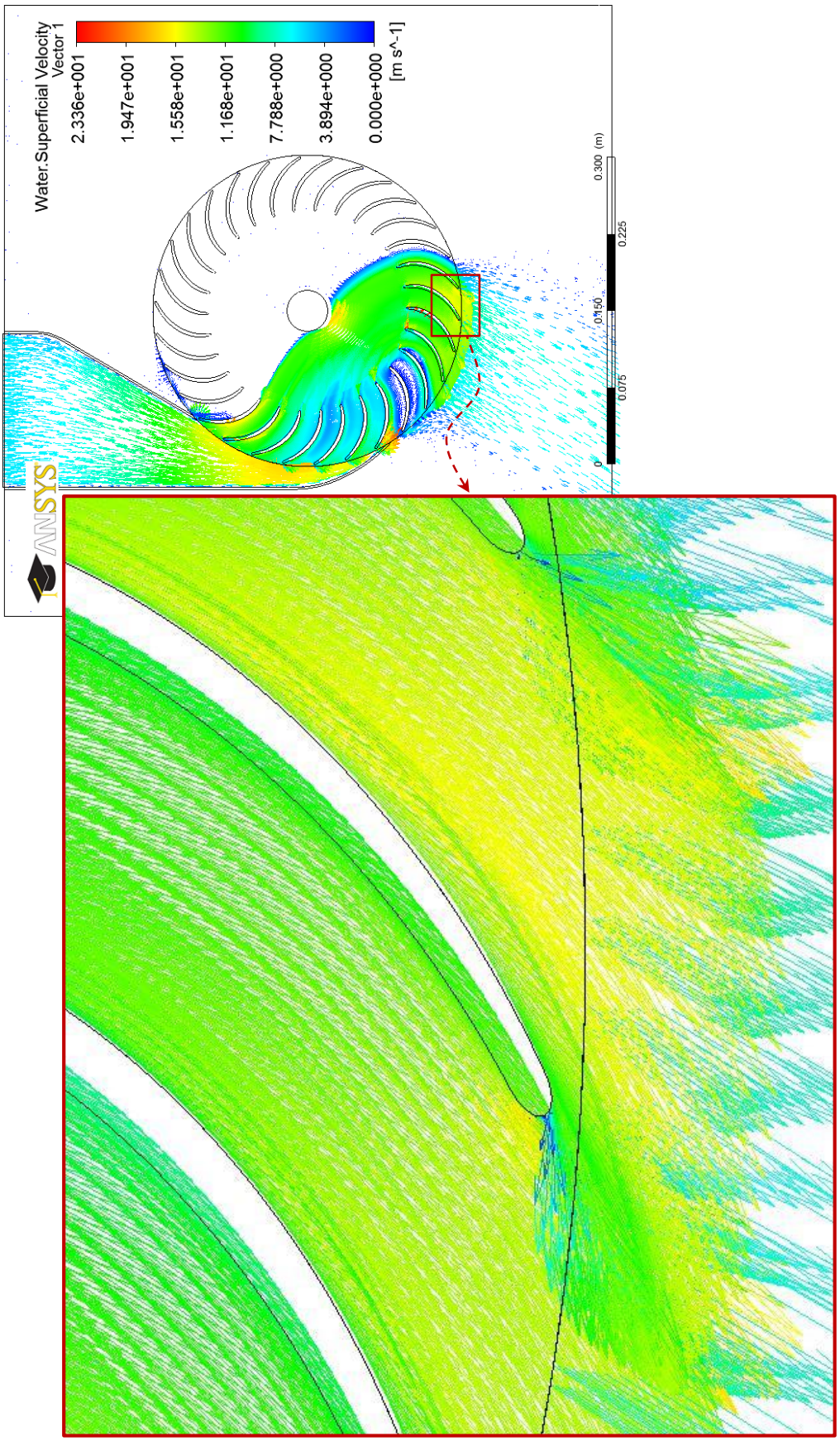

Fig. 5.64 Enlargement of the water superficial velocity vectors at the trailing edges of the second stage blades of the nozzle profile (1).

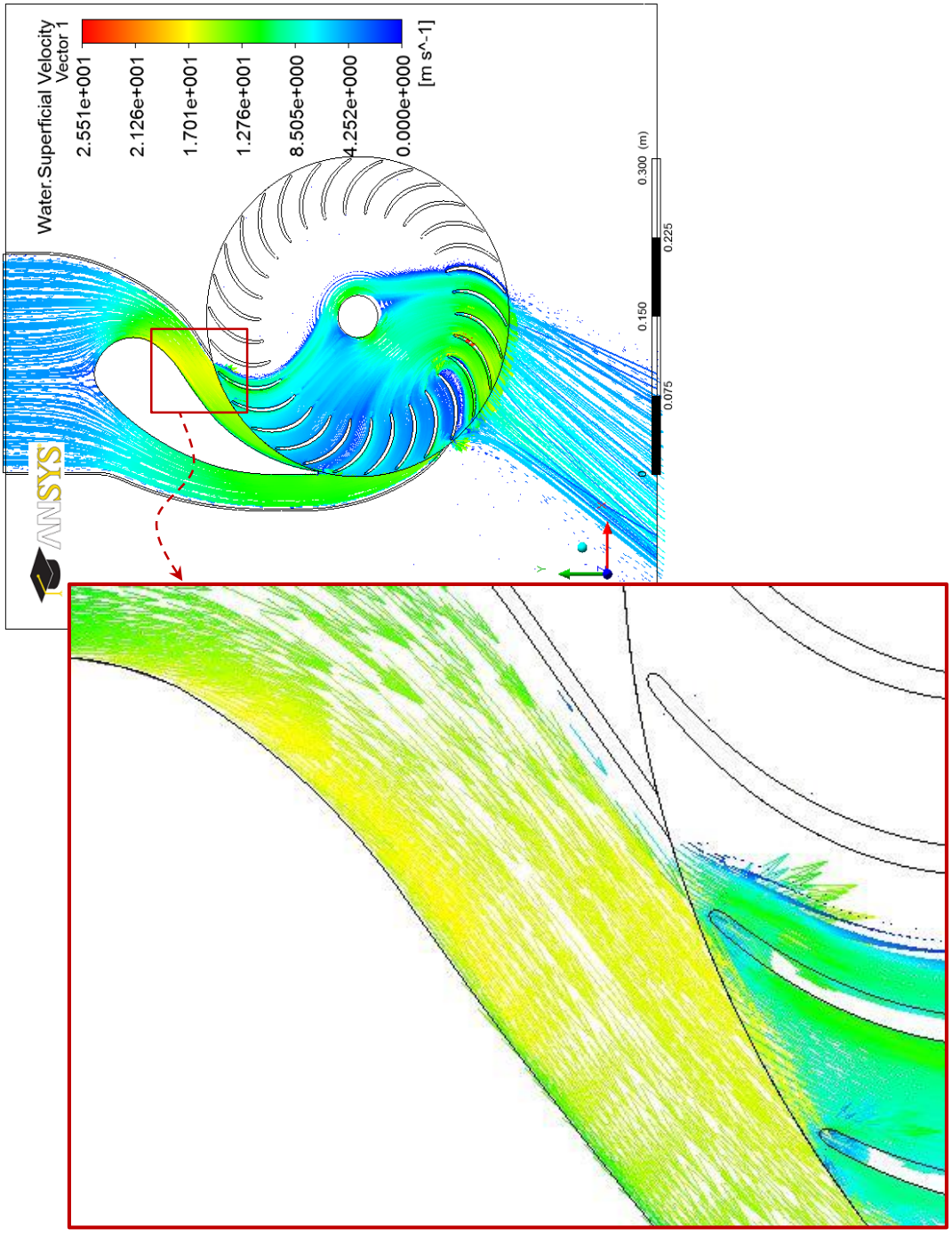

Fig. 5.65 Enlargement of the water superficial velocity vectors on the front passage of the nozzle profile (3).

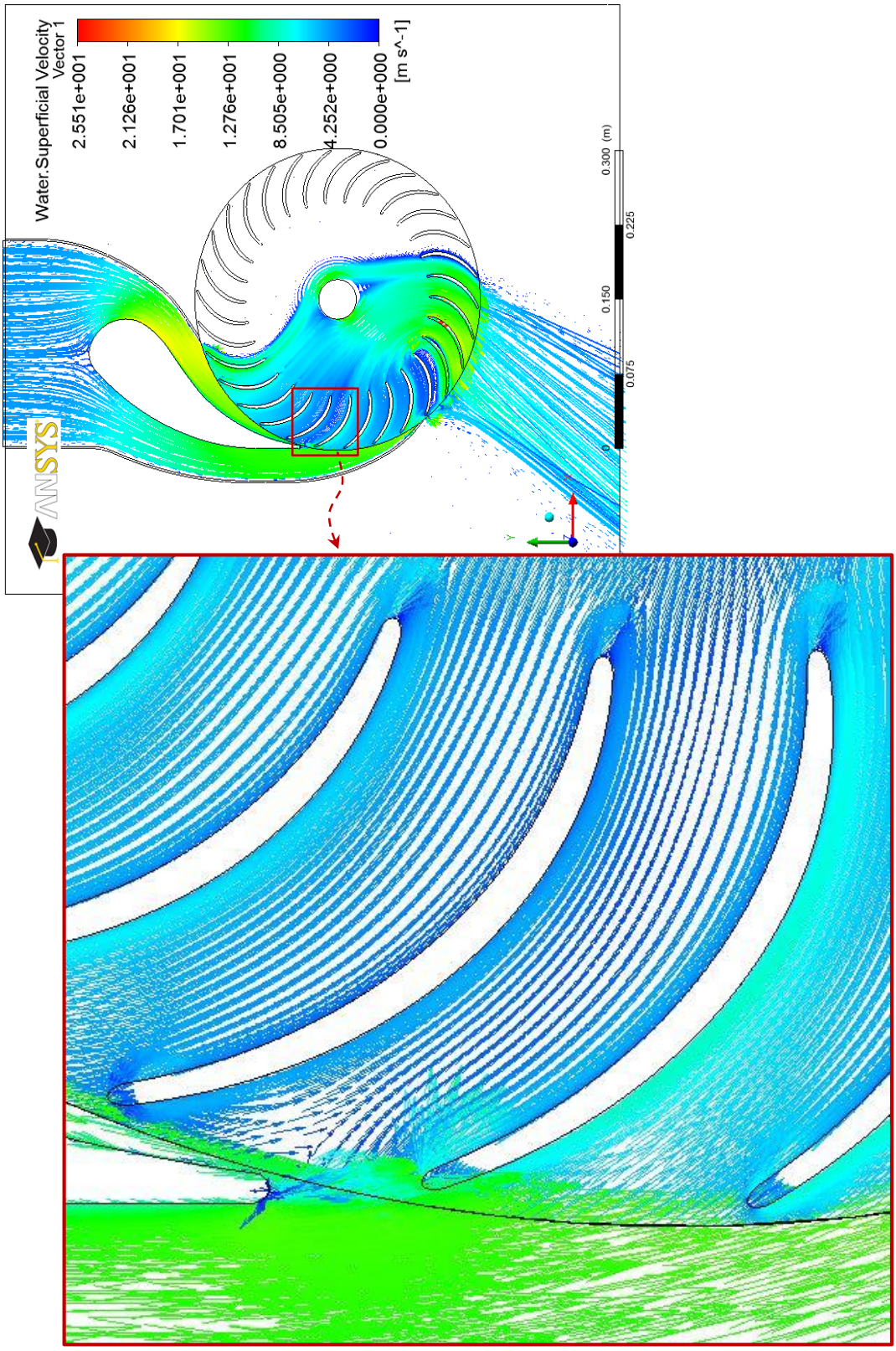

Fig. 5.66 Enlargement of the water superficial velocity vectors on the blades' passages facing the end of the guide vane of the nozzle profile (3).

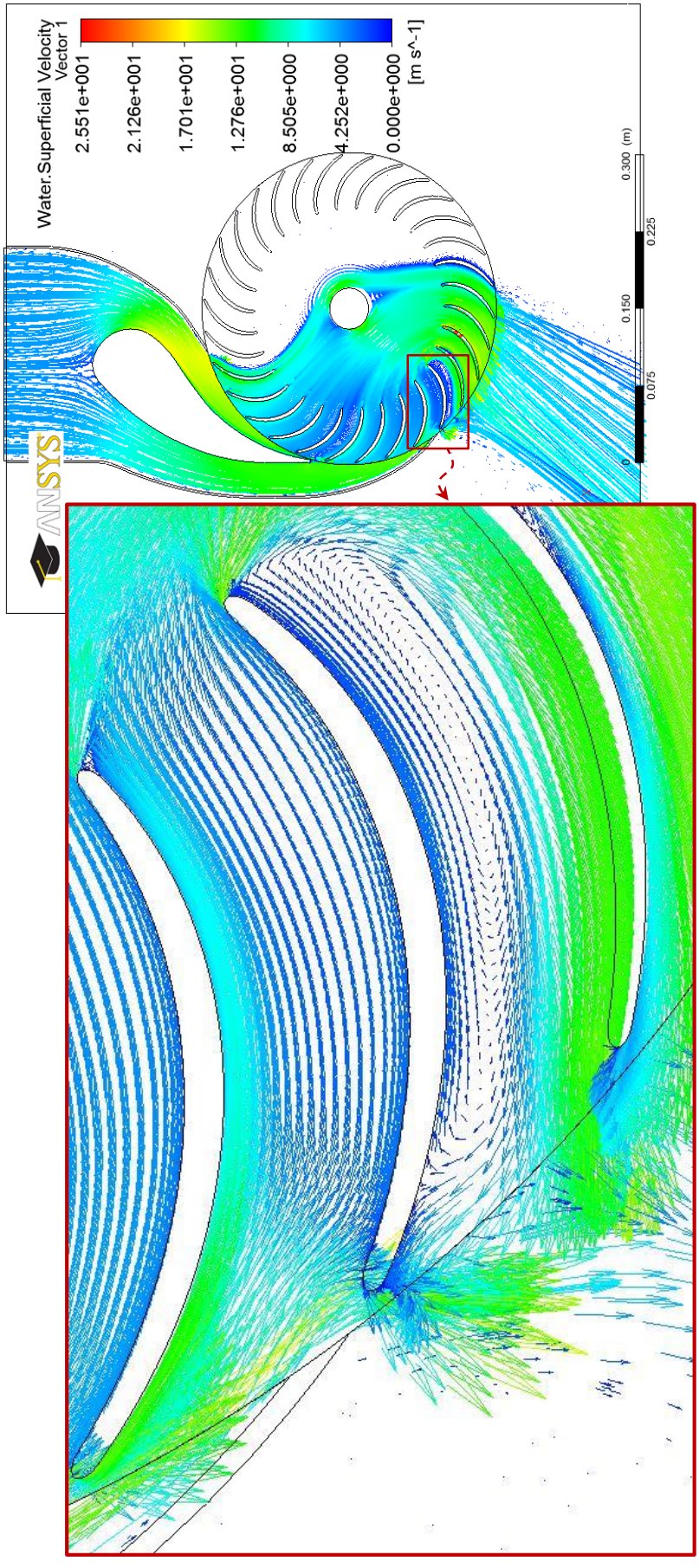

Fig. 5.67 Enlargement of the water superficial velocity vectors on the blades' passages facing the end of the nozzle profile (3).

5.2.7 Optimization of the Nozzle Throat Width (s_0)

The nozzle shape has a significant effect upon the performance of the cross-flow turbine as it controls the water flow velocity and water distribution at the runner inlet. Accordingly, the nozzle throat width s_o is one of the most important geometric parameters of the nozzle. It is defined as the throat width or the water jet thickness, and suggested in the literature to be of a value of 0.1 – 0.2 of the cross-flow turbine's runner outer diameter ($s_o = 0.1d_1 \rightarrow 0.2d_1$) [3]. Naturally, changing this parameter can strongly affect the distribution of the water along the nozzle entry arc λ which in turn affects, the flow characteristics and the hydrodynamic forces within the runner as detailed hereafter in this section. Previously, an experimental investigation to analyze the effect of nozzle shape on the cross-flow turbine performance was conducted by Nakase et al [32]. They concluded that the nozzle throat width ratio $s_o/r_1\lambda$ changes slightly with the nozzle entry arc and $s_o/r_1\lambda$ and a value of 0.26 can produce a highest efficiency when the nozzle entry arc is 90^o. As in the previous sections and in order to determine the optimum nozzle throat width, the cross-flow turbine was simulated in the current study by ANSYS CFX simulation code with nozzle throat width values of $0.1d_1$, $0.15d_1$ and $0.2d_1$ These cover the range of the nozzle throat width ($s_o = 0.1d_1 \rightarrow 0.2d_1$). The geometrical parameters and nozzle throat widths' details of the tested cross-flow turbines are listed in table 5.7 and shown in Figs. 5.68 to 5.70. It is clear from these figures that flow area within the nozzle changes significantly and this in turn changes the flow considerably and as discussed hereafter.

Table 5.7 Details of the nozzle throat width tested.

Geometrical parameter	Specification
Number of blades	$n_b = 30$
External diameter	$d_1 = 300\,mm$
Diameters ratio	$d_2/d_1 = 0.65$
Angle of attack	$\alpha_1 = 15^o$
Inlet blade angle	$\beta_1 = 151.814^o$
Internal blade angle	$\beta_1^{'} = \beta_2^{'} = 90^o$
Outlet blade angle	$\beta_2 = 28.186^o$
Blade thickness	$t_b = 3.6\,mm$
Blade radius of curvature	$r_b = 49.139\,mm$
Nozzle entry arc	$\lambda = 90^o$
Throat width	$s_o = ?$ $0.2d_1, 0.15d_1 \,\&\, 0.1d_1$
Width of the nozzle	$N_W = 150\,mm$
Shaft (axle) diameter	$d_s = 40\,mm$ *Note: Symbols as detailed in Fig. 3.2.*

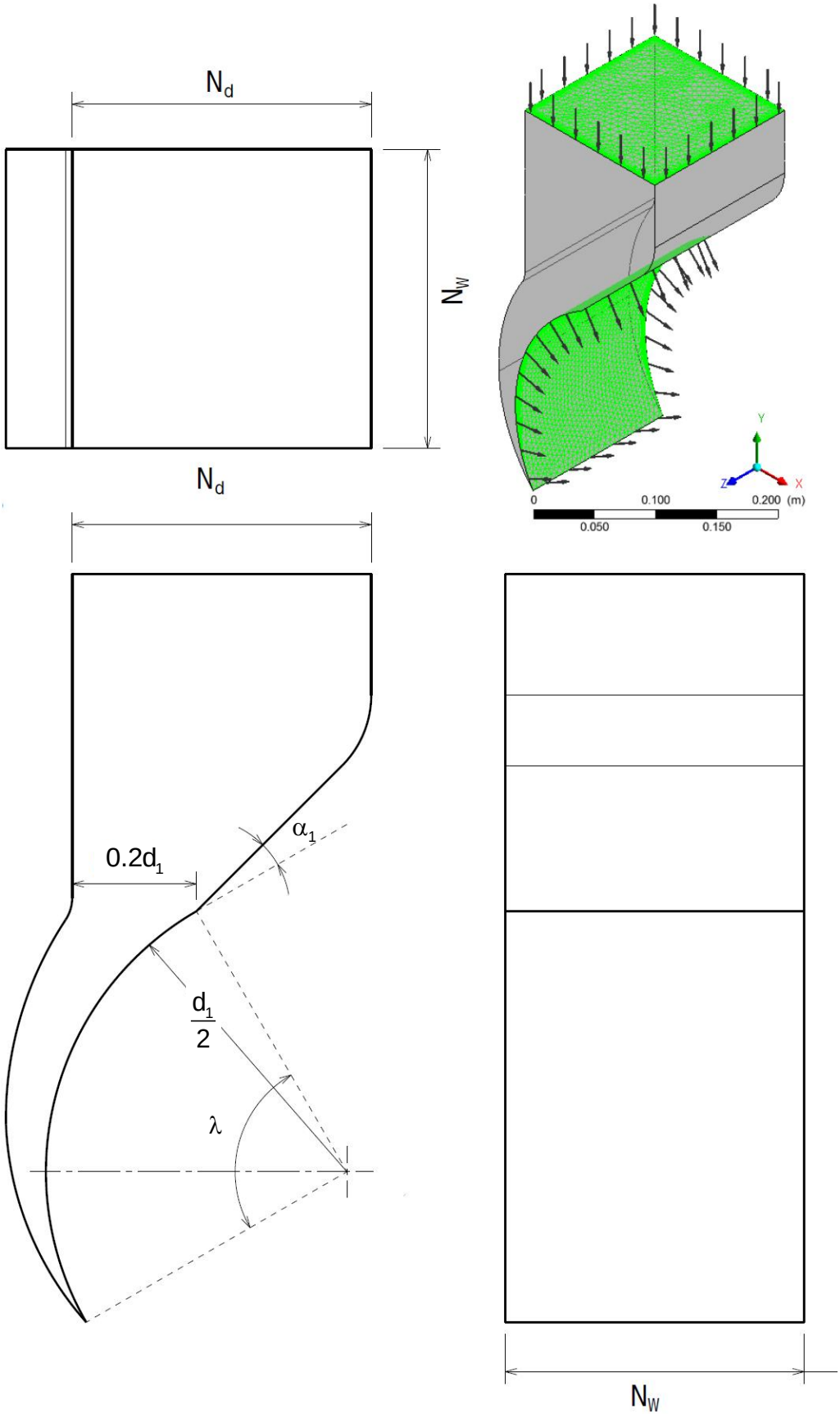

Fig. 5.68 Schematic view of the test nozzle with throat width ($0.2d_1$).

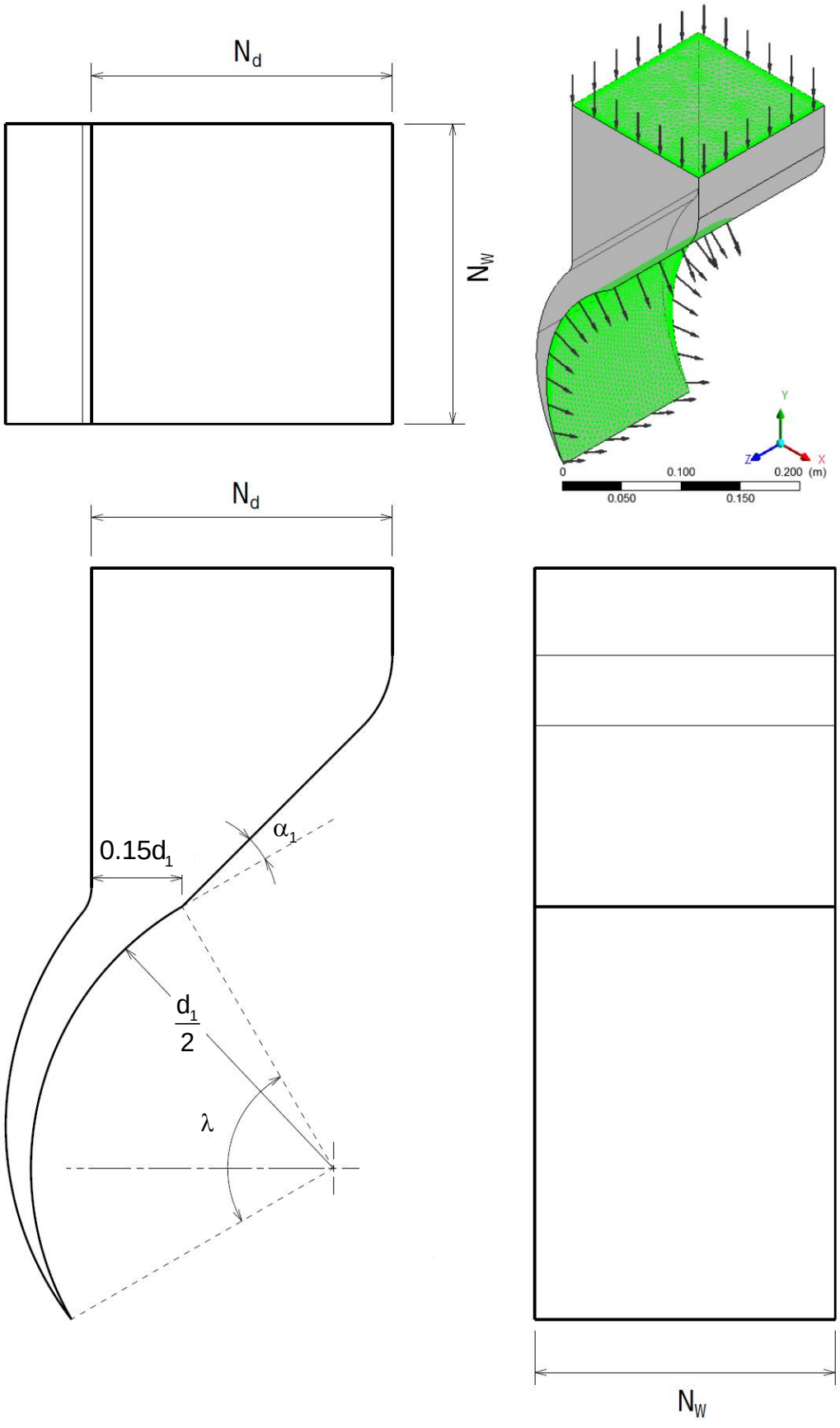

Fig. 5.69 Schematic view of the test nozzle with throat width ($0.15d_1$).

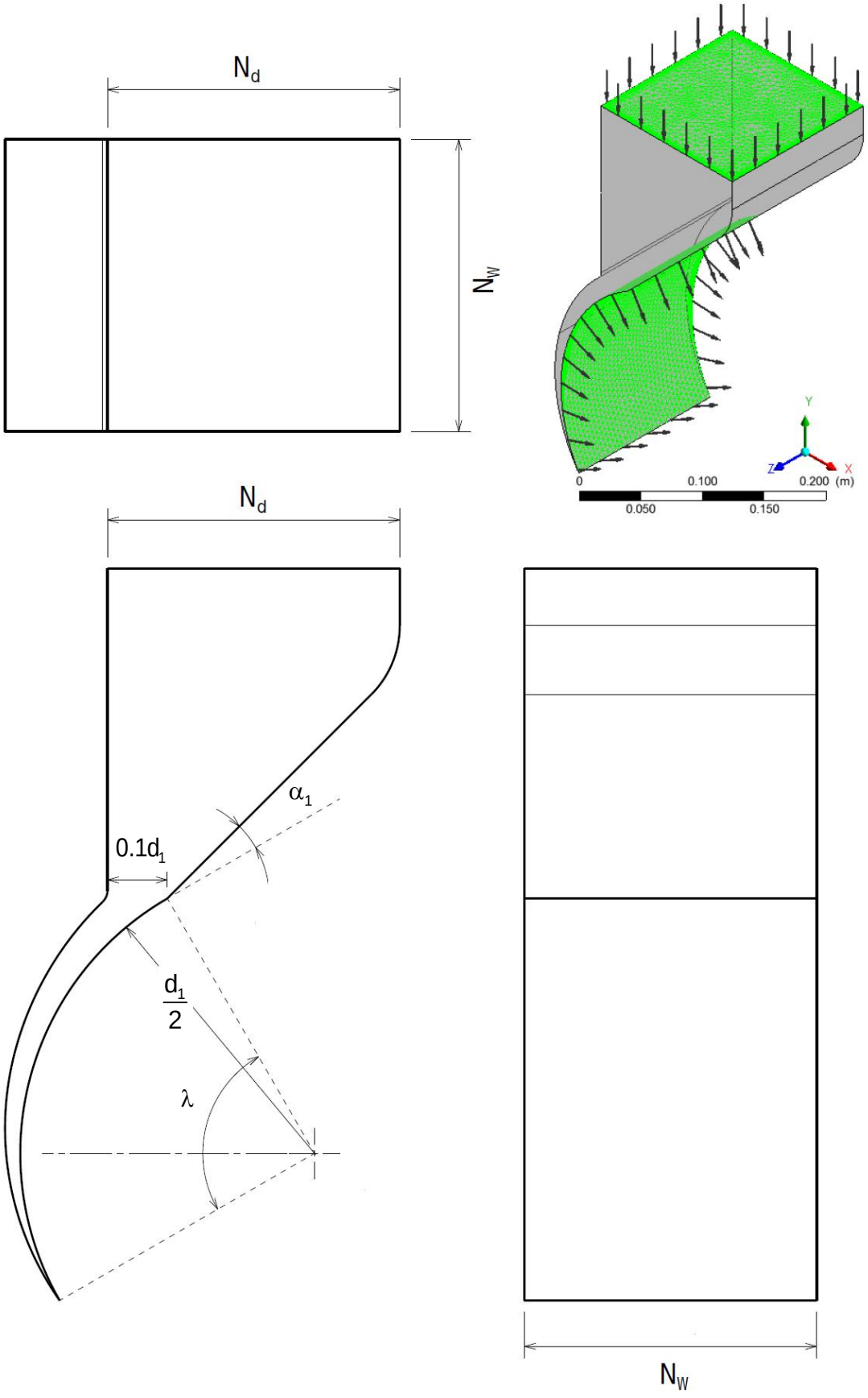

Fig. 5.70 Schematic view of the test nozzle with throat width ($0.1d_1$).

The simulation results are depicted in Figs. 5.71 – 5.74. These figures visualize the internal flow of the turbine and provide important flow structure and details, including the phenomena which are associated the flow separation and water-blades collision.

The streamlines of the flow, in three dimensions, as shown in Figs. 5.71 (a) to (c) clearly illustrate and confirm that in all cases the incoming water passes only through part of the runner. They also show regions (as in Figs. 5.71 (b) and (c)) of intense flow activity indicated by high water velocity. This warrant further consideration as will be detailed later.

The water volume fraction contours shown in Figs. 5.72 (a) to (c) provide a clear and proper visualization of the two-phase flow, with a well-defined interface or shear layer between the air and water. In these figures, the area with blue color represents air and that with the red color represents water. It is important to notice that because of the change in the nozzle shape, the water flow rate of each of Figs. 5.72 (a) to (c) is changeable. This is clearly reflected in these figures by quantity of the water leaving the second stage of runner blades. It is because of that the efficiency of the nozzle with throat width of $0.2d_1$ is expected to be the highest.

Water superficial velocity streamlines and vectors at the mid span of the turbine of various values of the nozzle throat width are shown in Figs. 5.73 and 5.74. These figures illustrate the effect of various values of the nozzle throat width on the performance of cross-flow turbine. The structure of the flow in the runner blades and the nozzle is of similar form to those described earlier, there are interesting areas of high water velocity at the nozzle tip and these were created by the sharp connecting line of the nozzle tip and the volute. The water does not

seem to fill the lower parts of the first stage runner blades (Fig. 5.73 (c)). This in turn should explain the lower efficiency of the turbine with nozzle throat width of $0.1d_1$ as clearly shown in the enlarged section of Fig. 5.76. The impact of the separation of the flow on the performance of the turbine can clearly be seen in Fig. 5.74 and the enlarged section of Fig. 5.74 (c) shown in Fig. 5.77. These separations cause an increase in the velocity of the flow which directs the majority of the water in to first couple of the blade passages and away from the rest of the blades as shown in Fig. 5.74 (c).

Reduce the width of the nozzle throat with some geometric and hydrodynamic imposed restrictions reduces the distance between the nozzle rear wall and the runner and in its turn reduces the amount of water in the passages between the blades (filling and emptying) in lower part of the nozzle entry arc λ, on the other hand, increase the width of the nozzle throat causes the uncertain angle of attack to the flow at the runner inlet as shown in Figs. 5.73 and 5.74.

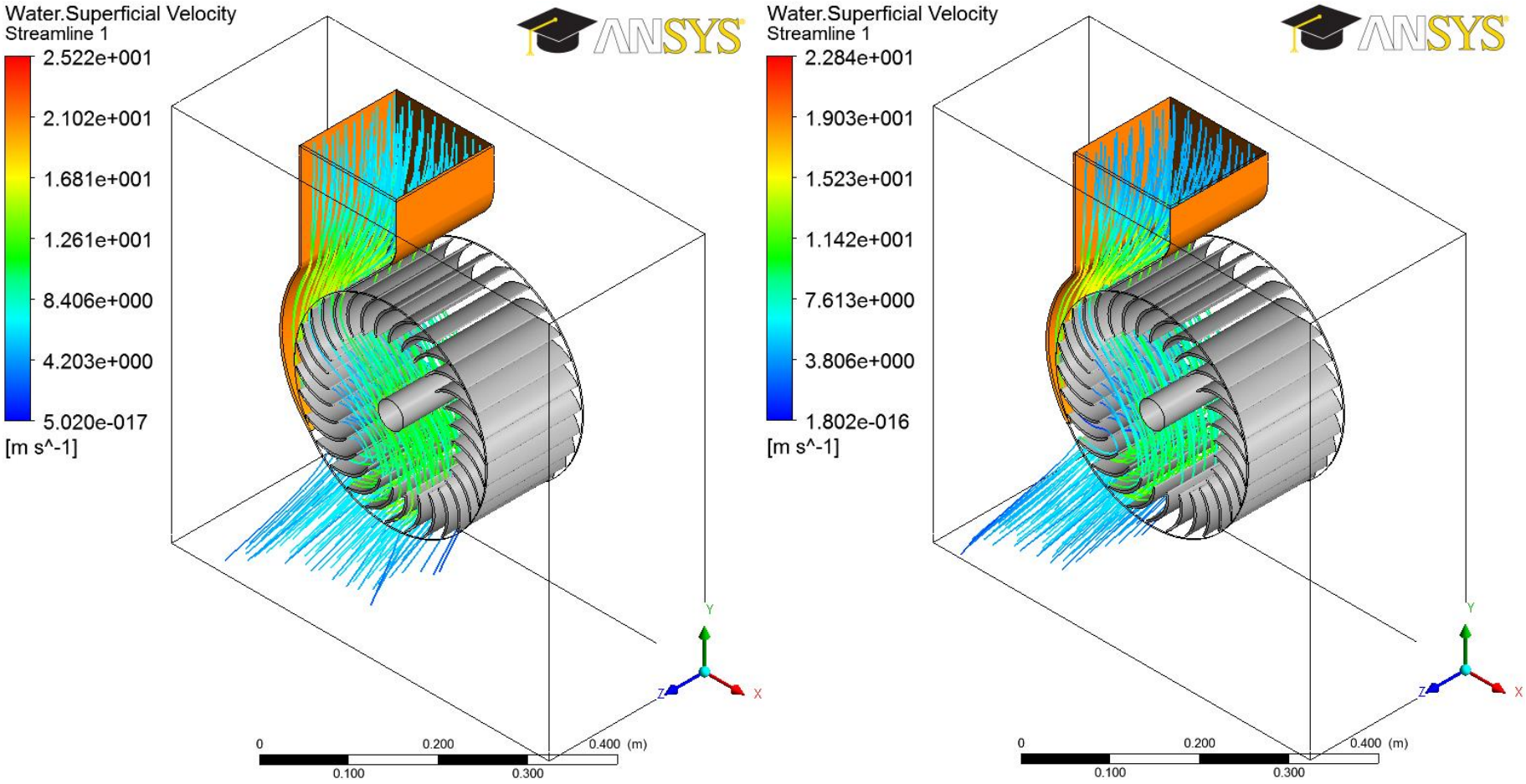

(a) Nozzle throat width ($0.2d_1$)

(b) Nozzle throat width ($0.15d_1$)

Fig. 5.71 (a) and (b) Water superficial velocity streamlines in cross-flow turbine of various nozzle throat widths.

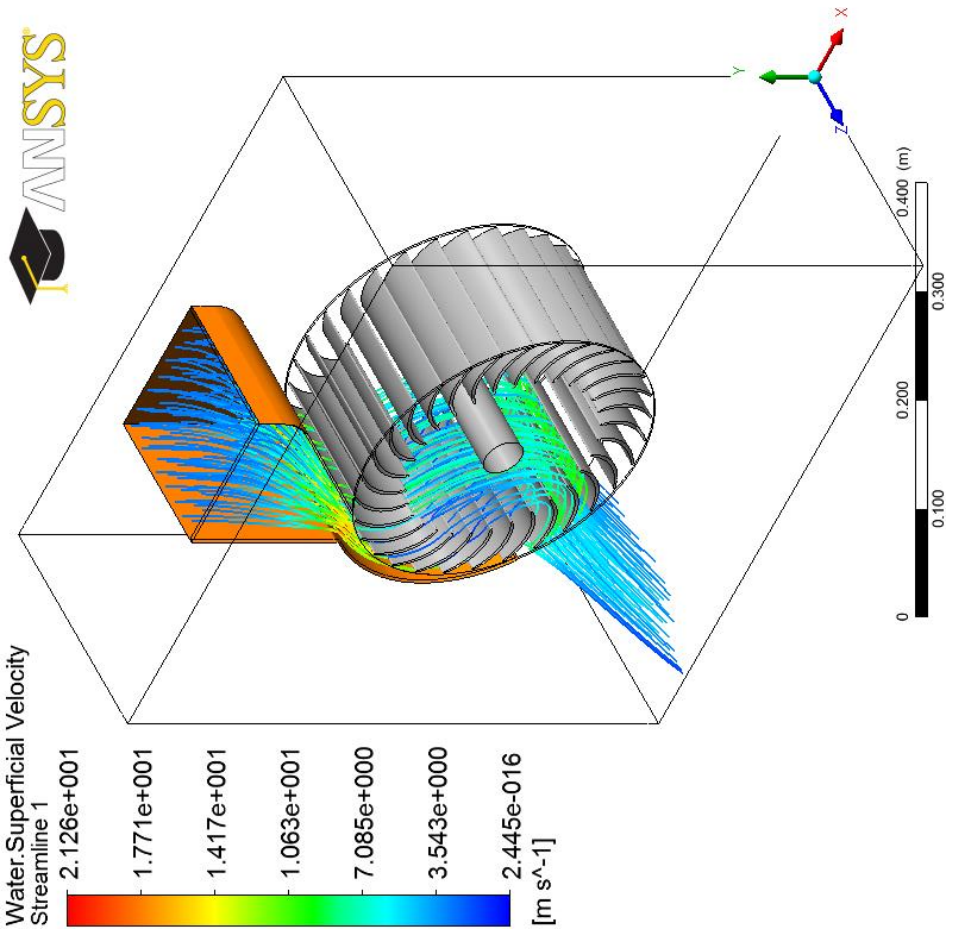

Fig. 5.71 (c) Water superficial velocity streamlines in cross-flow turbine for nozzle throat width ($0.1d_1$).

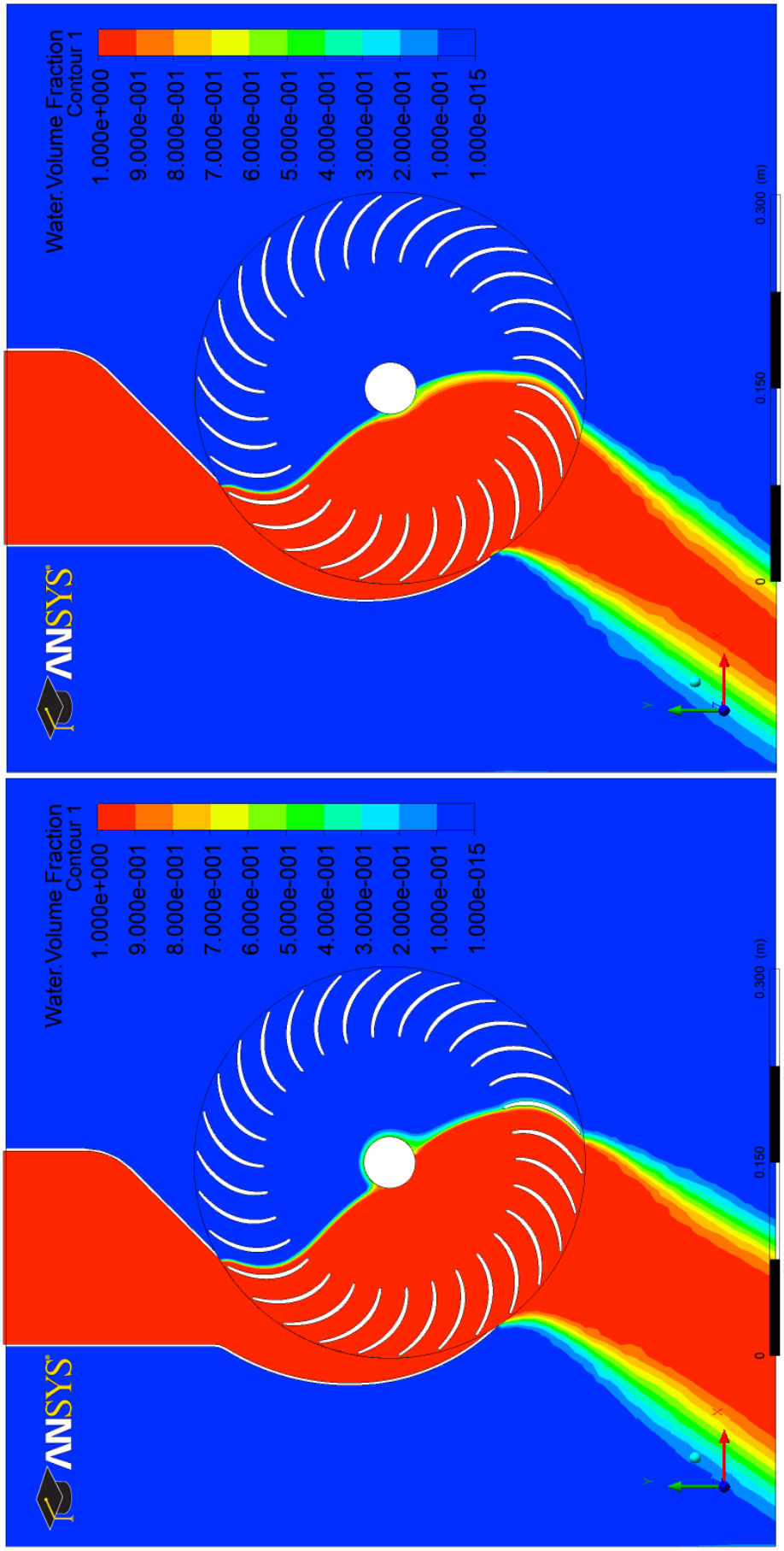

(a) Nozzle throat width ($0.2d_1$) (b) Nozzle throat width ($0.15d_1$)

Fig. 5.72 (a) and (b) Water volume fraction contours at the mid span of cross-flow turbine of various nozzle throat widths.

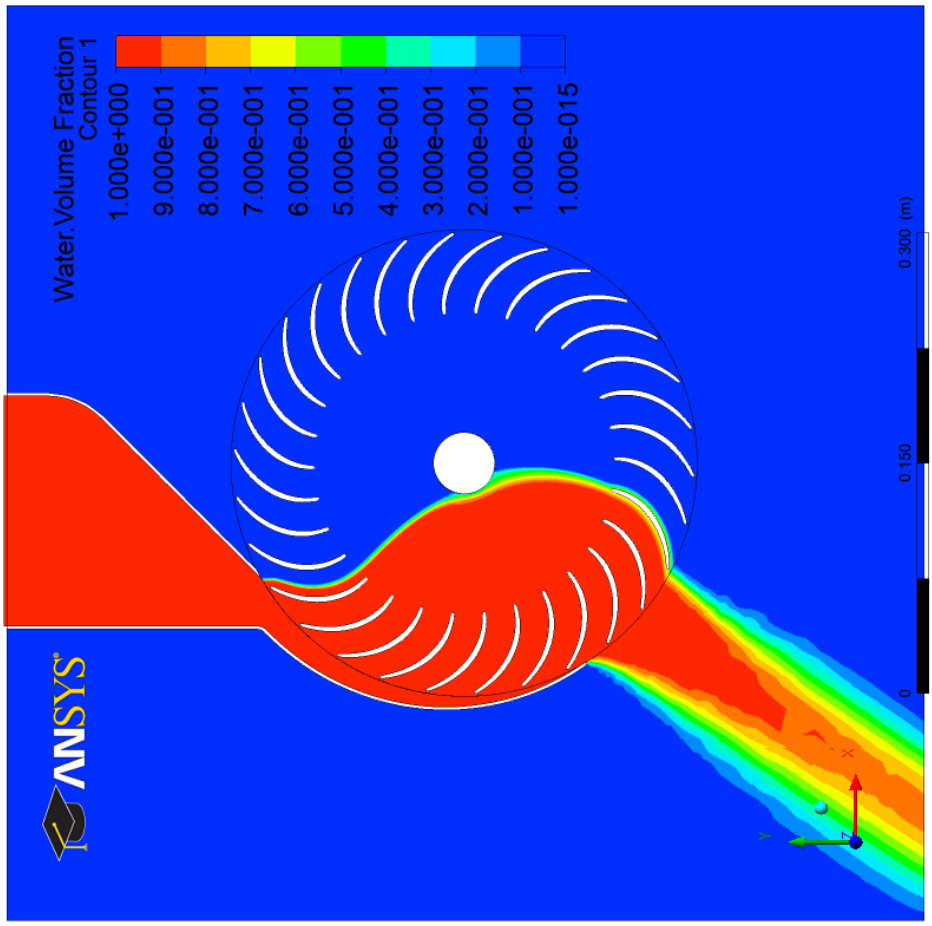

Fig. 5.72 (c) Water volume fraction contours at the mid span of cross-flow turbine for nozzle throat width ($0.1d_1$).

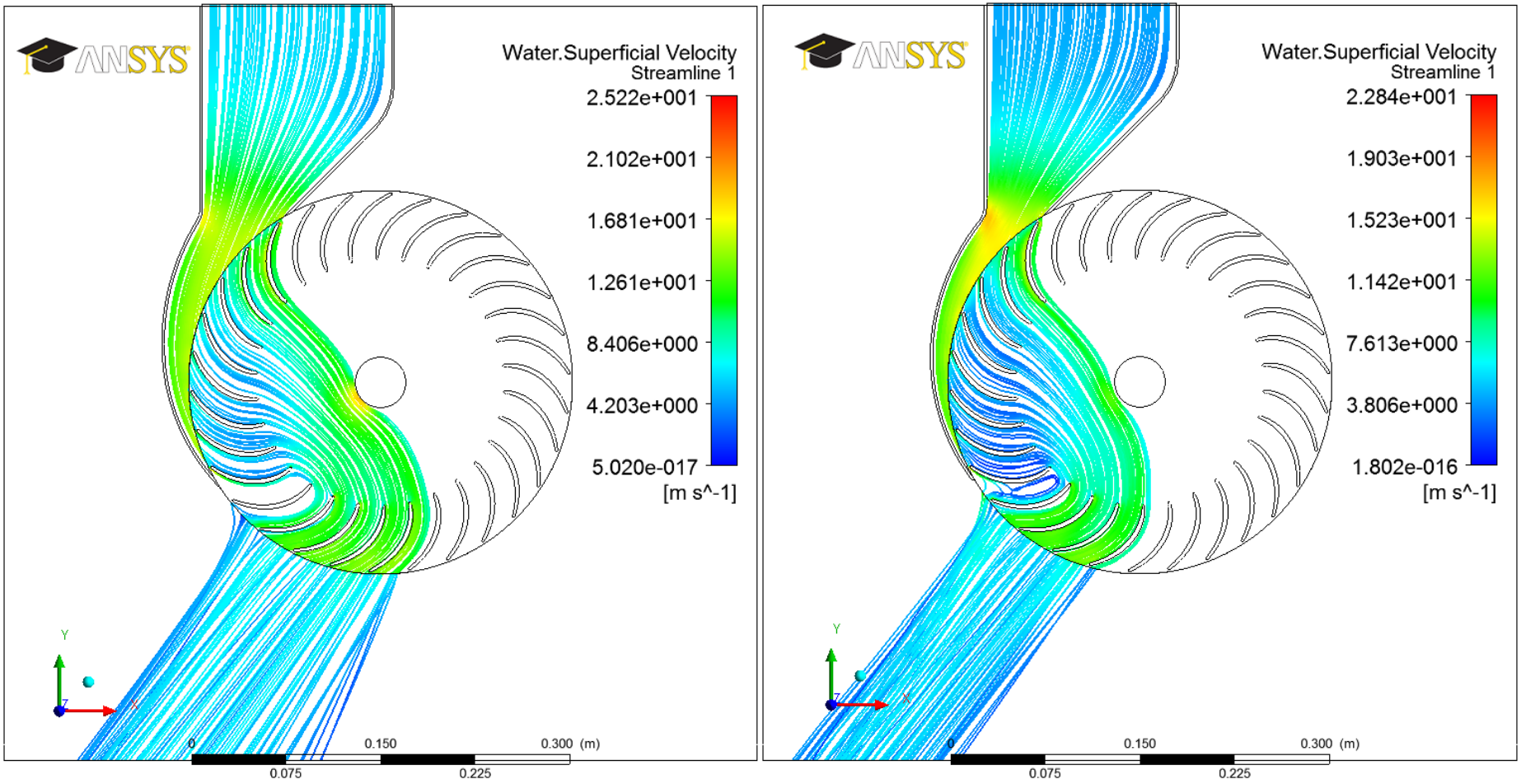

(a) Nozzle throat width ($0.2d_1$)

(b) Nozzle throat width ($0.15d_1$)

Fig. 5.73 (a) and (b) Water superficial velocity streamlines at the mid span of cross-flow turbine of various nozzle throat widths.

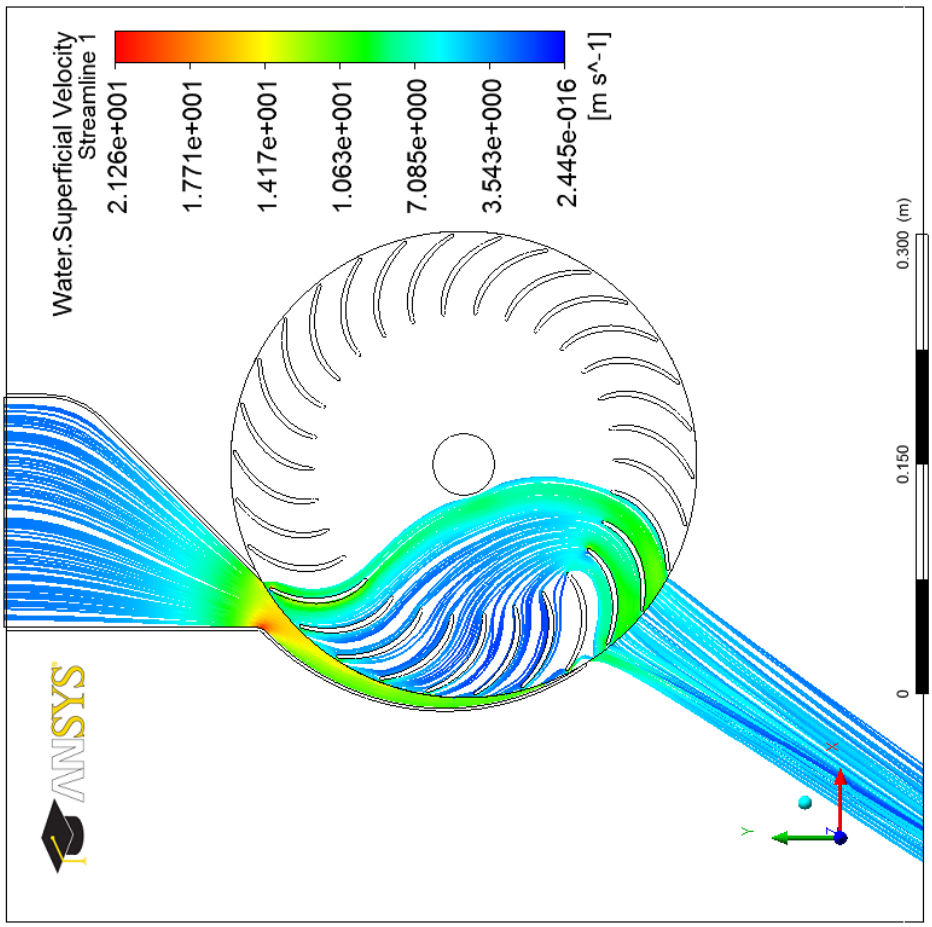

Fig. 5.73 (c) Water superficial velocity streamlines at the mid span of cross-flow turbine for nozzle throat width ($0.1d_1$).

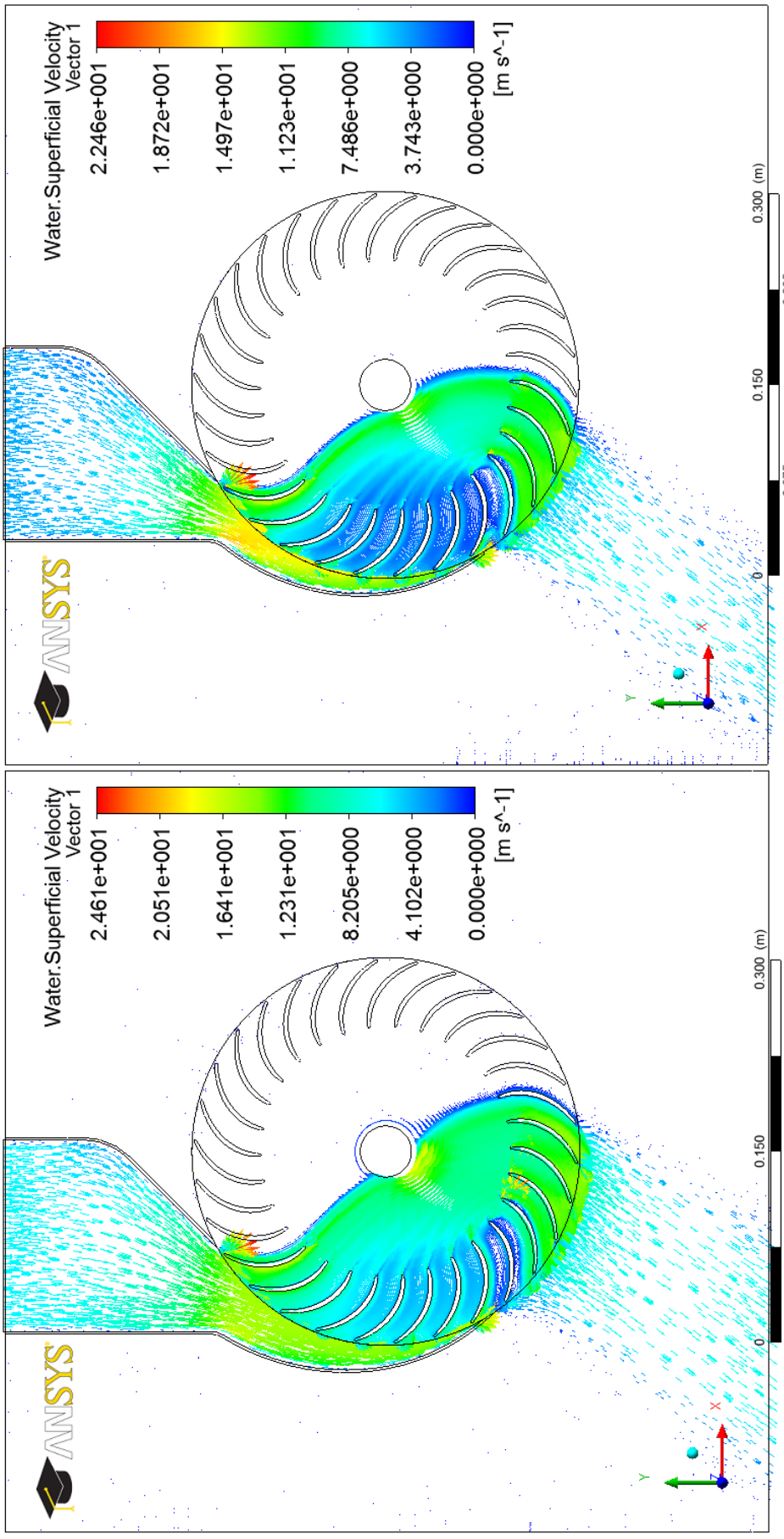

(a) Nozzle throat width ($0.2d_1$) (b) Nozzle throat width ($0.15d_1$)

Fig. 5.74 (a) and (b) Water superficial velocity vectors at the mid span of cross-flow turbine of various nozzle throat widths.

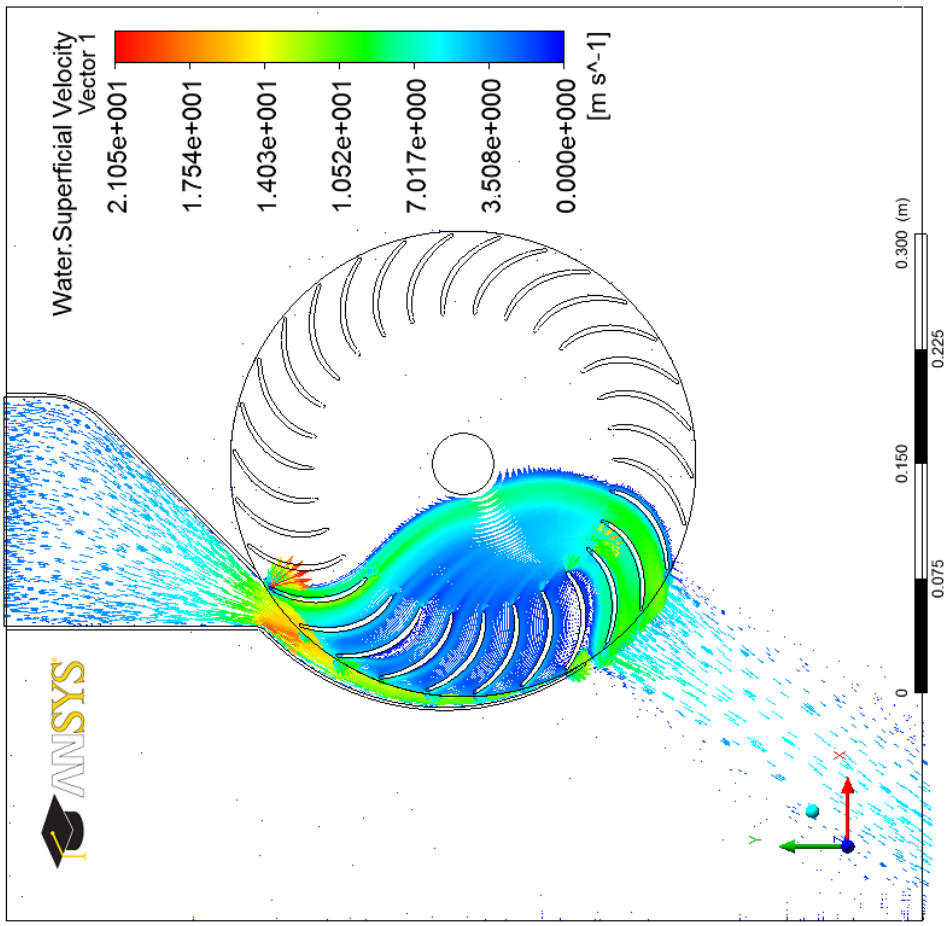

Fig. 5.74 (c) Water superficial velocity vectors at the mid span of cross-flow turbine for nozzle throat width ($0.1d_1$).

The overall effect of the nozzle throat width on the efficiency of the cross-flow turbine is summarized in Fig. 5.75. It is clear that increasing the nozzle throat width from $0.1d_1$ to $0.2d_1$ has a favorable effect on the efficiency of the cross-flow turbine. At small nozzle throat width ($s_o = 0.1d_1$), the turbine efficiency was as low (71.717 %). Decrease the width of the nozzle throat with some geometric and hydrodynamic imposed restrictions decreases the distance between the nozzle rear wall and the runner. This in turn decreases the amount of water in the passages between the blades (filling and emptying) in the lower part of the nozzle entry arc λ. Also decreasing the width of the nozzle strongly affects the volute shape, particularly in the convergent part of the nozzle and close to the runner entry. In that region most of the water from the nozzle directed to the upper part of nozzle entry arc and as a result of that the extracted energy from water by the blades decreases significantly. According to this, the most effective nozzle throat width noticed was $0.2d_1$ where the efficiency was 77.564 %. This result is in full agreement with Nakase et al results [32].

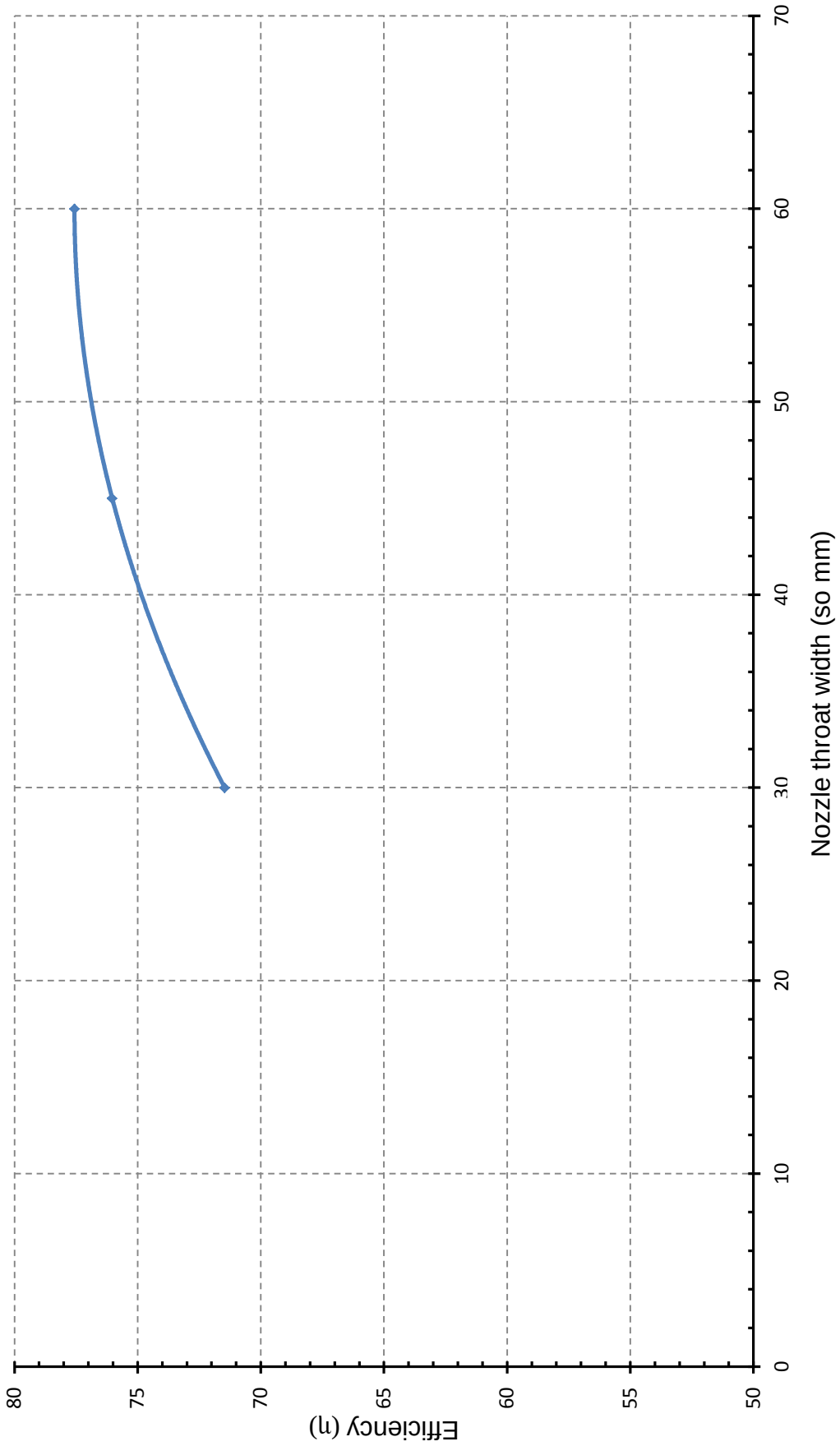

Fig. 5.75 Cross-flow turbine performance characteristics curve for blades of various nozzle throat widths.

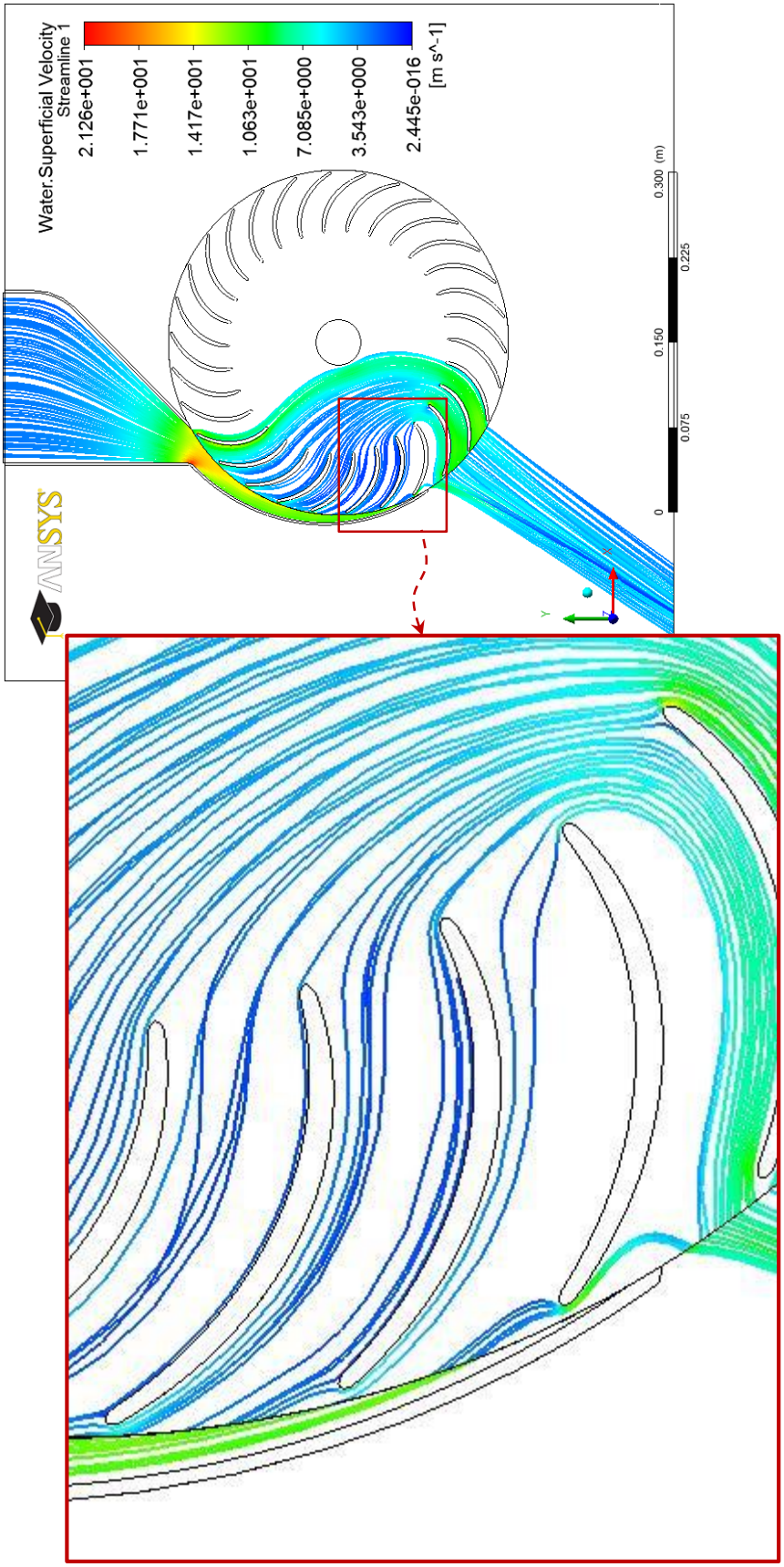

Fig. 5.76 Enlargement of the water superficial velocity streamlines on the blades' passage facing the end of the nozzle throat width ($0.1d_1$).

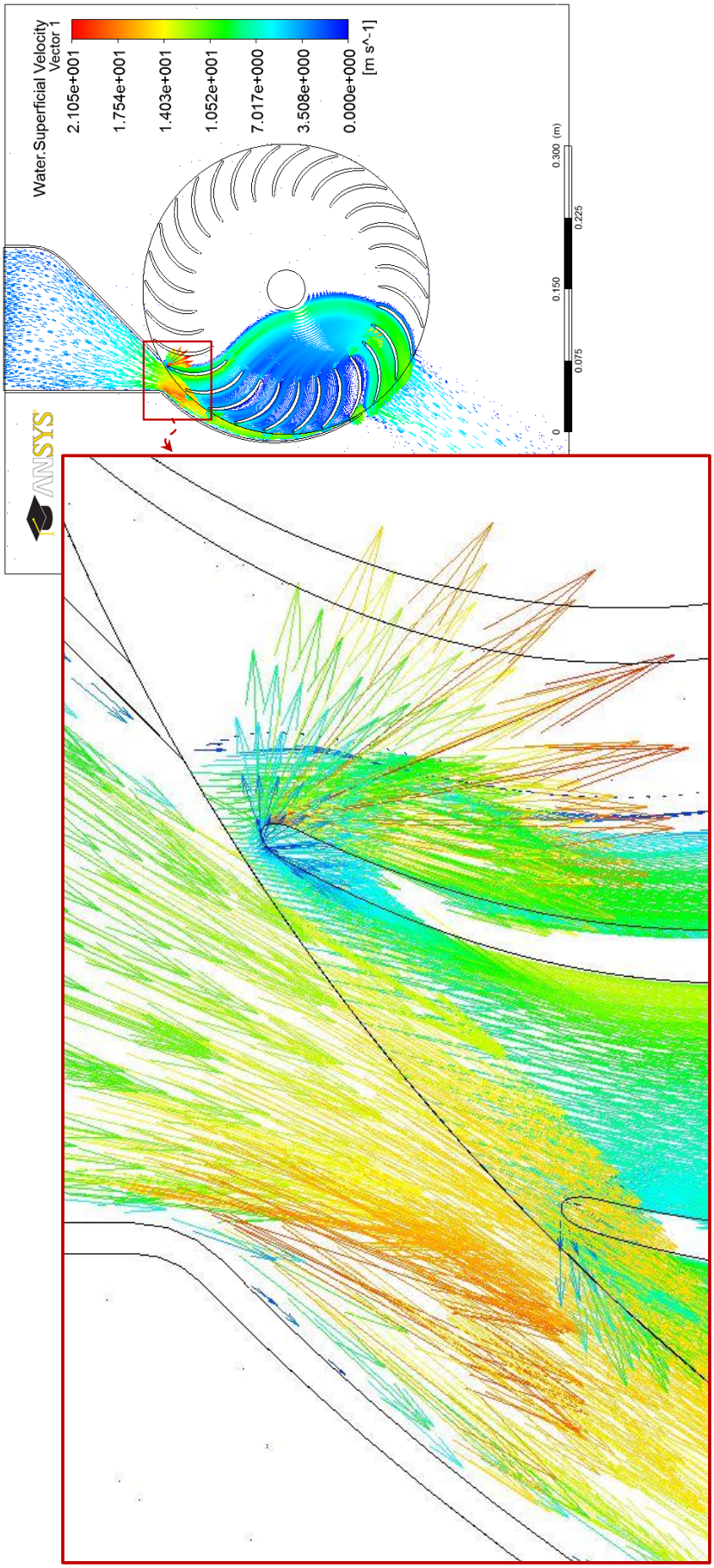

Fig. 5.77 Enlargement of the water superficial velocity vectors on the tip of the volute shape at the mid span of cross-flow turbine for the nozzle throat width ($0.1d_1$).

5.2.8 Optimization of the Nozzle to the Runner Blades Width (N_w/B_w)

As described earlier, the cross-flow turbine elements (runner and nozzle) geometry has a significant effect on the flow characteristics and the hydrodynamic forces within the cross-flow turbine. The nozzle, which has a rectangular cross-sectional area, converts the flow energy into kinetic energy by directing the water to the full length of the runner at a specific angle of attack. The nozzle width N_w, shown diagrammatically in Figs. 5.78 (a) to (d), is one of the most important geometric parameters on the turbine as it limits and directs the water to full width of the blades. Usually the nozzle width N_w to runner blades width B_w ratio is 1.0. Mockmore and Merryfield [31] undertaken an experimental investigation on a laboratory turbine. The turbine was constructed with a nozzle to runner blades width ratio of approximately 1.0. The nozzle width was 304.8 mm (12-in). Both Nakase et al [32] and Desai and Aziz [50] conducted experiments to study the effect of various nozzle to runner blades width ratio N_w/B_w. Contradictory observation regarding the effect of the nozzle to runner blades width ratio on the performance of the cross-flow turbine is evident from the above studies. Nakase et al [32] stated that, the efficiency of the cross-flow turbine increases in the case of a suitable nozzle throat width s_o with an increase of nozzle to runner width ratio of up to 1.0. While Desai and Aziz [50] stated that the nozzle to runner blades width ratio of 2/3 was more efficient than the ratios 1.0, 1/2 and 1/3. It is clear that the conclusions of Nakase et al [32] and Desai and Aziz [50] are highly contradictory. Therefore, it was highly important to predict the optimum nozzle to runner blade width ratio N_w/B_w to optimize the performance of the cross-flow turbine. Hence, in the

current study, this ratio was chosen to be of values of 1/3, 1/2, 2/3 and 1.0. The additional geometrical parameters' details of the tested cross-flow turbines are listed in table 5.8.

Table 5.8 Details of the nozzle to runner blades width tested.

Geometrical parameter	Specification
Number of blades	$n_b = 30$
External diameter	$d_1 = 300\,mm$
Diameters ratio	$d_2/d_1 = 0.65$
Angle of attack	$\alpha_1 = 15^o$
Inlet blade angle	$\beta_1 = 151.814^o$
Internal blade angle	$\beta_1^{'} = \beta_2^{'} = 90^o$
Outlet blade angle	$\beta_2 = 28.186^o$
Blade thickness	$t_b = 3.6\,mm$
Blade radius of curvature	$r_b = 49.139\,mm$
Nozzle entry arc	$\lambda = 90^o$
Throat width	$s_o = 60\,mm$
Width of the nozzle	$N_W = ?$ $150, 100, 75, 50\,mm$
Shaft (axle) diameter	$d_s = 40\,mm$

Note: Symbols as detailed in Fig. 3.2.

A flow field visualization of the internal flow in the cross-flow turbine was predicted to illustrate the impact of the nozzle to the runner blades width ratio N_W/B_W on the flow characteristics and the performance of the turbine. The water superficial velocity streamlines of the entire cross-flow turbine of various ratios of the nozzle to the runner blades width are shown in Figs. 5.78 (a) to (d)

additional front view is provided in the same figures to show the width of the nozzle in each case. These figures clearly show that the water flows over a part of the runner blades width when the nozzle to the runner blades width ratio is less than 1.0. The streamlines of the flow provide extra understanding of the internal flow in the cross-flow turbine at part-flow conditions. Such conditions are encountered during summer season in some sites which suffer from partial drought. Figures 5.78 (b) and (d) also show three dimensional streamlines of partially loaded cross-flow turbine with 1/3 and 2/3 standard division of inlet nozzle flow area (where the water was directed through either 1/3 as shown in Fig. 5.78 (d) or 2/3 of the nozzle width as shown in Fig. 5.78 (b)).

In order to visualize the fluid flow characteristics and their effects on the performance of the turbine more clearly, contours of water volume fraction, vectors of water superficial velocity and contours of pressure were plotted on the mid span planes as shown in Figs. 5.79 to 5.80 and Fig. B.11. Figures 5.79 (a) to (d) clearly show that the water fraction spread decreases with the decreasing of the ratio. This is clearly indicated by the core of the flow and the water-air interface region surrounding this core. Figures 5.79 (a) to (d) also show that a reduction in the ratio results in the main flow to move away from the axle of the runner and reduce the possibility of impingement on the runner axle. This expected to improve the efficiency by reducing the losses. However, as it will be seen, hereafter, it works in favor of decreasing the efficiency as the fraction of the water interacting with the second stage of the runner blades is reduced considerably. A region of intense water splatter due to negative pressure differential is developed at the tip of the first active blade receiving the water from the nozzle. The intensity of these activities seems to increase with

decreasing the ratio. This is confirmed by Figs. 5.80 (a) to (d). It is natural that these activities tend to reduce the power developed and ultimately the efficiency of the turbine. Also, they tend to encounter the effects of less or no impingement of the water on the runner axle observed in Figs. 5.79 (a) to (d). Figures 5.80 (a) to (d) show a considerable increase in the water splatter in the core of the runner with decreasing the ratio. This water quantity does not contribute to power developed and represents parasitical losses. All parts of Fig. 5.80 confirm the conclusions from Fig. 5.79 that the quantity (fraction) of water interacting with the second stage of the runner blades is considerably reduced with reducing the ratio. Figures B.11 (a) to (d) again show the high pressure contours regions of the mid-span reduce with the decreasing the ratio as a result of the tendency of the water to move along the blades' width. It must be noted from Figs. 5.79 (a) to (d) and Figs. B.11 (a) to (d) that as the nozzle to the runner blades width ratio decreases the flow tendency to spread through the free end passages between the blades and also the water tendency to splatter inside the core of the runner. For a nozzle to the runner blades width ratio less than 1.0 considerable changes in the flow patterns in the runner and particularly within the runner blade passages are seen to takes place. Accordingly, it is expected that a nozzle to runner blades width ratio of 1.0 may result in higher efficiency and power output as the splatter of water and flow spread along the blades' width are almost eradicated in this case.

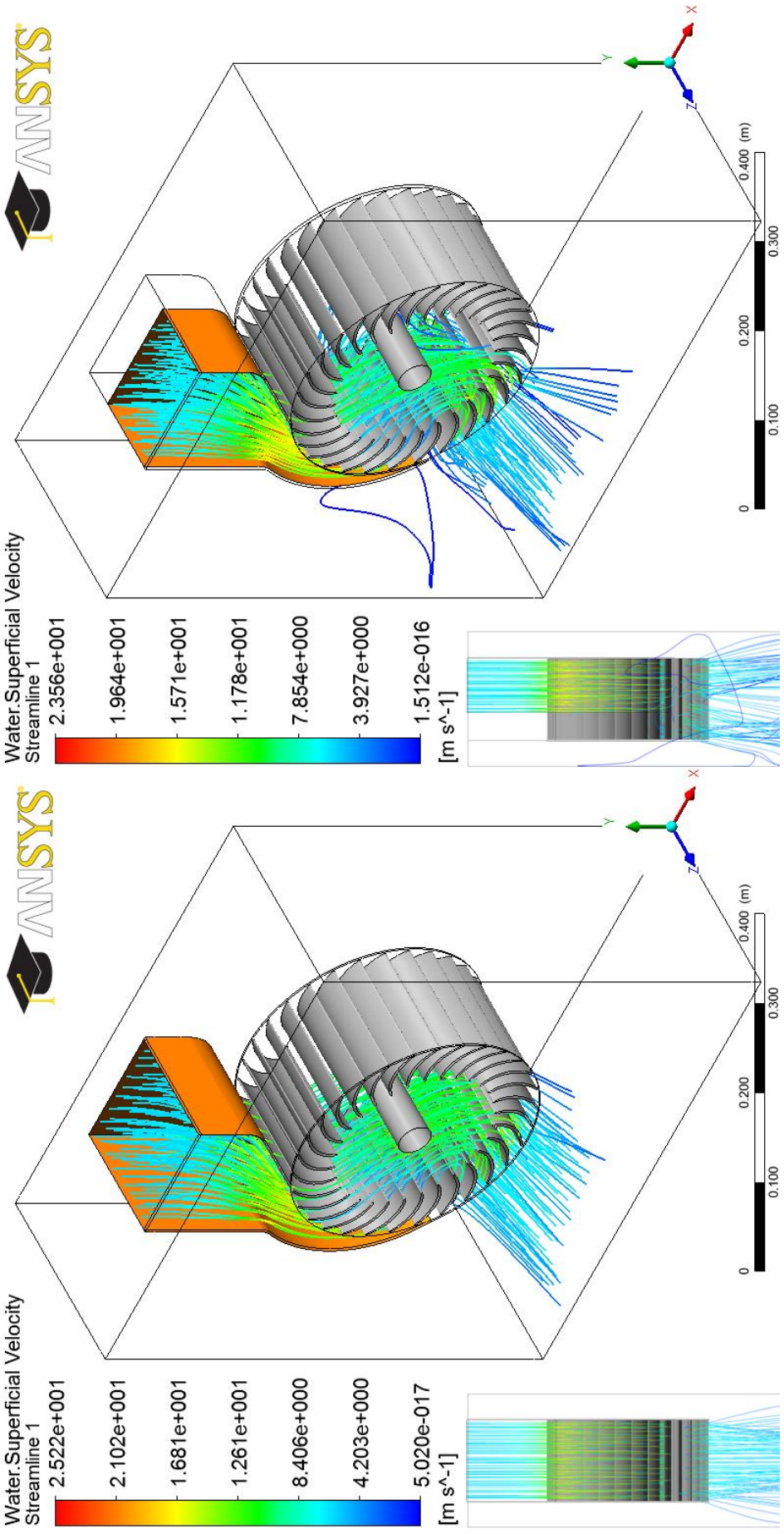

(a) Nozzle to runner blades width (N_w/B_w = 1) (b) Nozzle to runner blades width (N_w/B_w = 2/3)

Fig. 5.78 (a) and (b) Water superficial velocity streamlines in cross-flow turbine of various nozzle to runner blades width ratios.

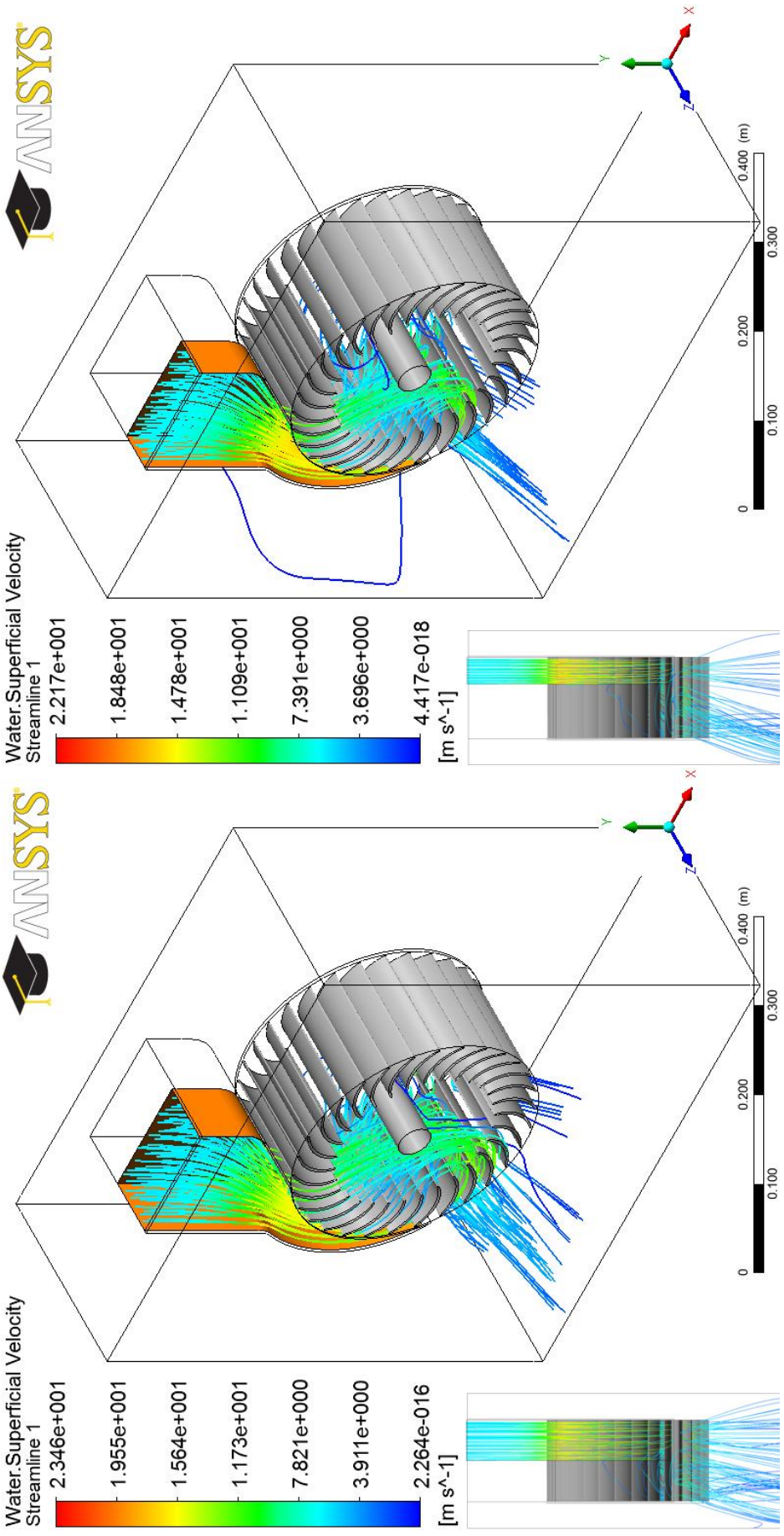

(c) Nozzle to runner blades width (N_w/B_w = 1/2) (d) Nozzle to runner blades width (N_w/B_w = 1/3)

Fig. 5.78 (c) and (d) Water superficial velocity streamlines in cross-flow turbine of various nozzle to runner blades width ratios.

(a) Nozzle to runner blades width (N_w/B_w = 1) (b) Nozzle to runner blades width (N_w/B_w = 2/3)

Fig. 5.79 (a) and (b) Water volume fraction contours at the mid span of various nozzle to runner blades width ratios.

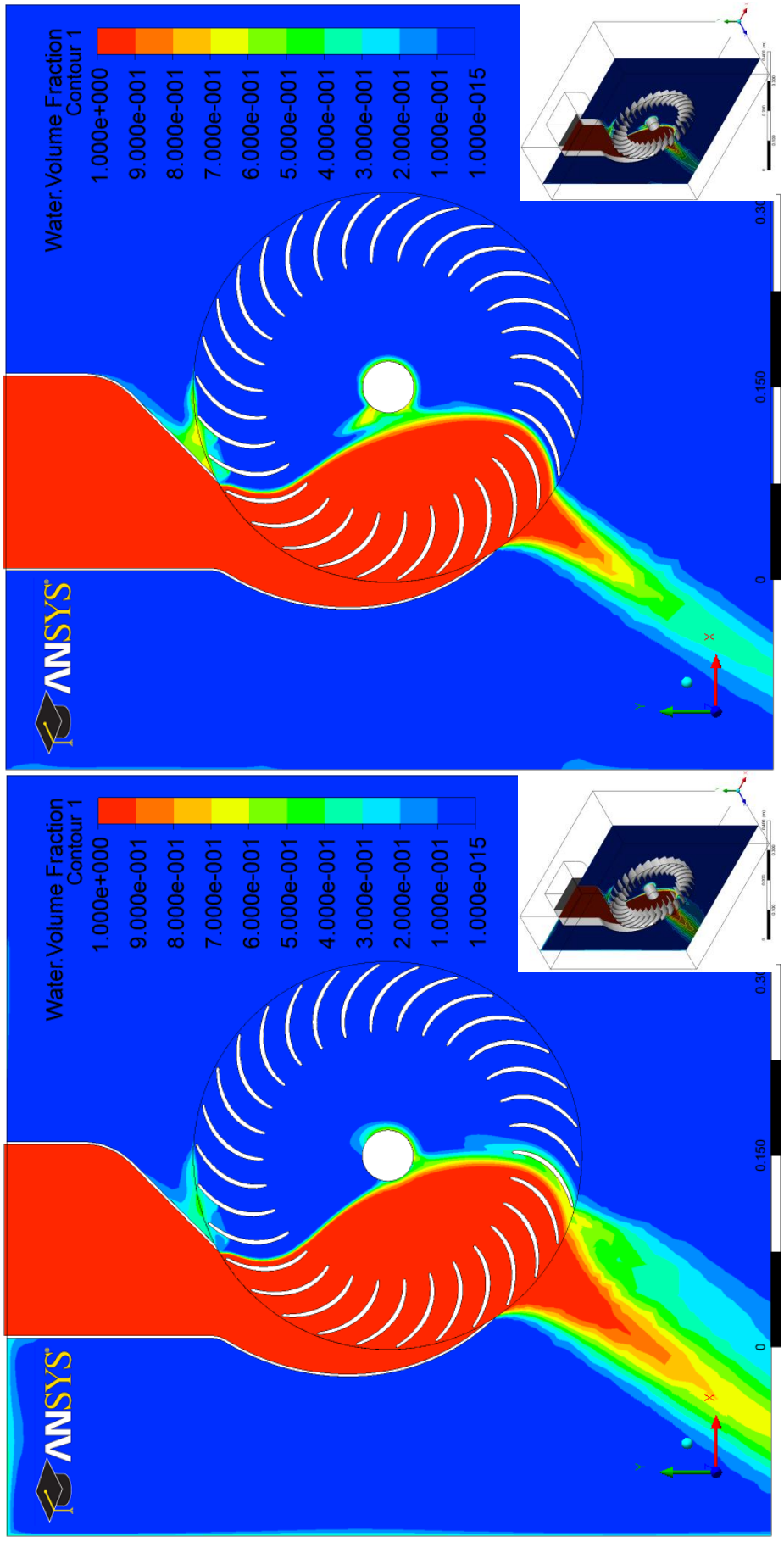

(c) Nozzle to runner blades width (N_w/B_w = 1/2) (d) Nozzle to runner blades width (N_w/B_w = 1/3)

Fig. 5.79 (c) and (d) Water volume fraction contours at the mid span of various nozzle to runner blades width ratios.

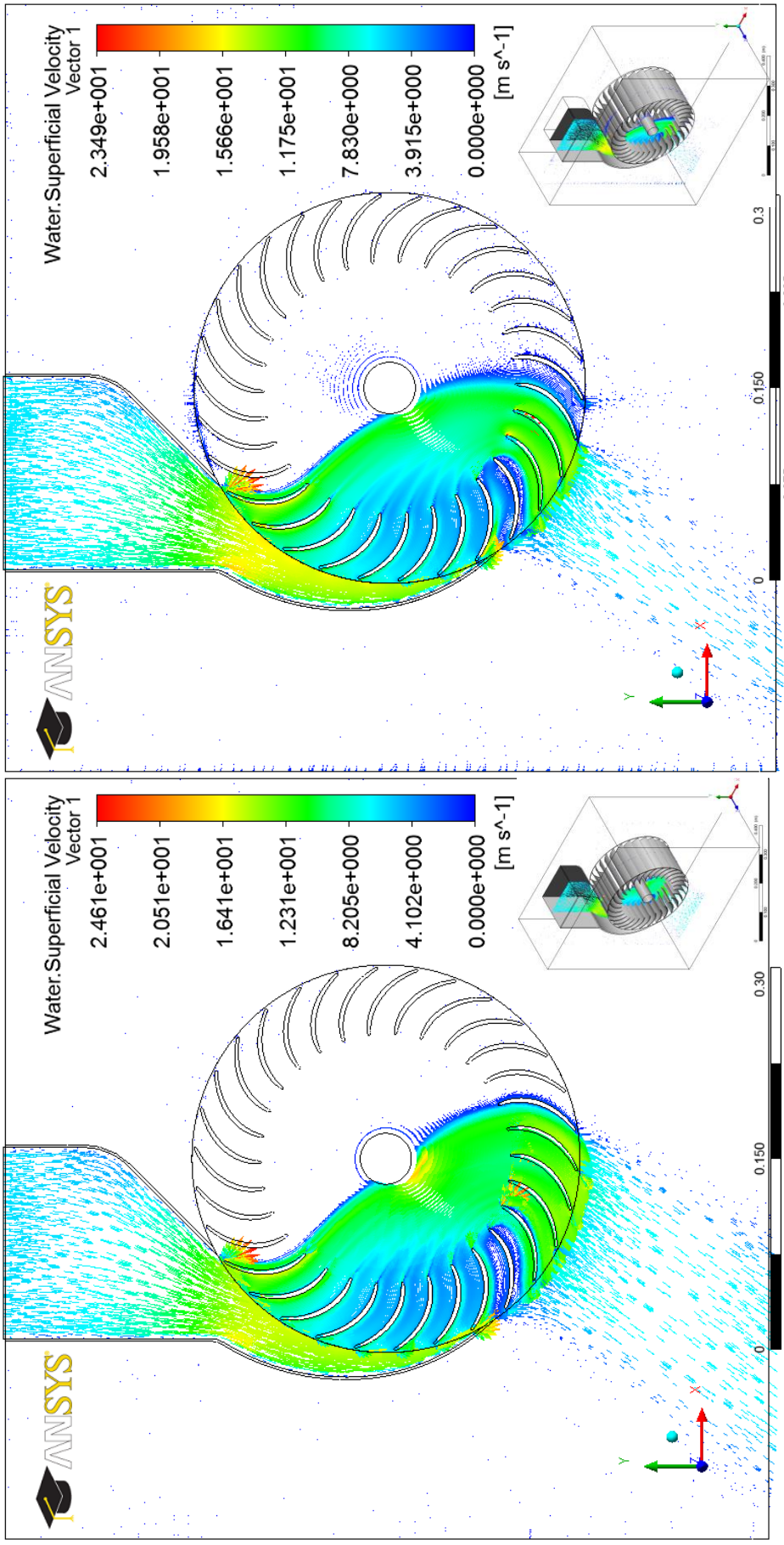

(a) Nozzle to runner blades width (N_w/B_w = 1) (b) Nozzle to runner blades width (N_w/B_w = 2/3)

Fig. 5.80 (a) and (b) Water superficial velocity vectors at the mid span of various nozzle to runner blades width ratios.

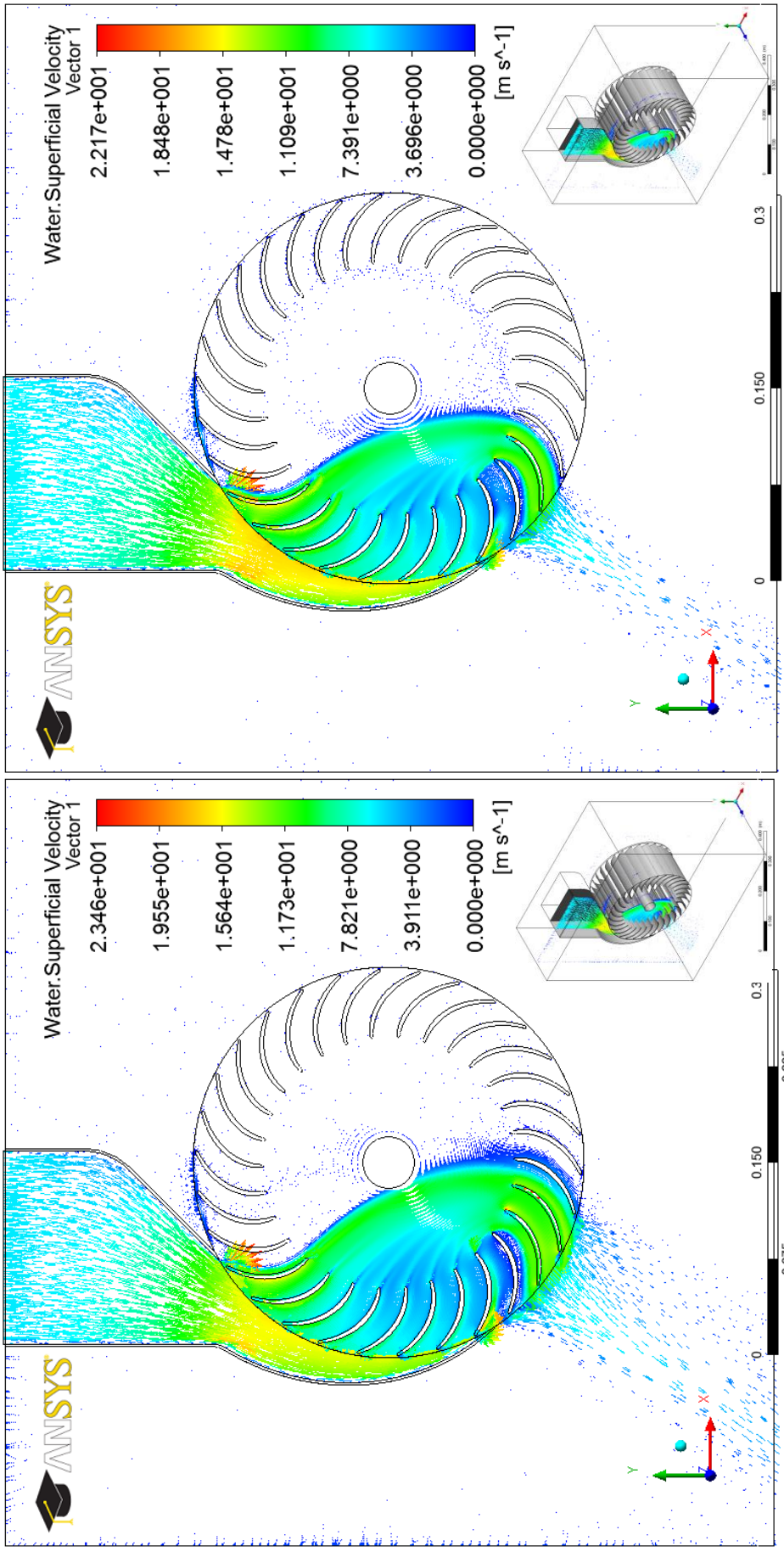

(c) Nozzle to runner blades width (N_w/B_w = 1/2) (d) Nozzle to runner blades width (N_w/B_w = 1/3)

Fig. 5.80 (c) and (d) Water superficial velocity vectors at the mid span of various nozzle to runner blades width ratios.

Figure 5.81 reveals the result of computations of the impact of the nozzle to the runner blades width ratio N_w/B_w on the efficiency of the cross-flow turbine. It is clear that an increase up to unity in the nozzle to the runner blades width ratio N_w/B_w has a favorable effect on the turbine efficiency as indicated above. This shows a full agreement with the Nakase et al [32] and can be explained by the fact that the nozzle outlet covers only part of the width of the runner blades when the nozzle to the runner blades width ratio is less than 1.0. This results in an asymmetrical distribution of the water in from the nozzle after striking the blade along the blade width. Therefore, the energy of the water loses due to the axial movement of water along the blades does not contribute to the second stage in extracting of the energy from water. It can be seen from Fig. 5.81 that at 1/3 nozzle to the runner blades width ratio, the efficiency was low (66.993 %). According to this, the most effective nozzle to the runner blades width ratio N_w/B_w noticed was 1.0 where the efficiency was 77.564 % which is in agreement with the nozzle to the runner blades width ratio constructed by Mockmore and Merryfield [31] which based upon Donat Banki's paper "Neue Wasser-turbine".

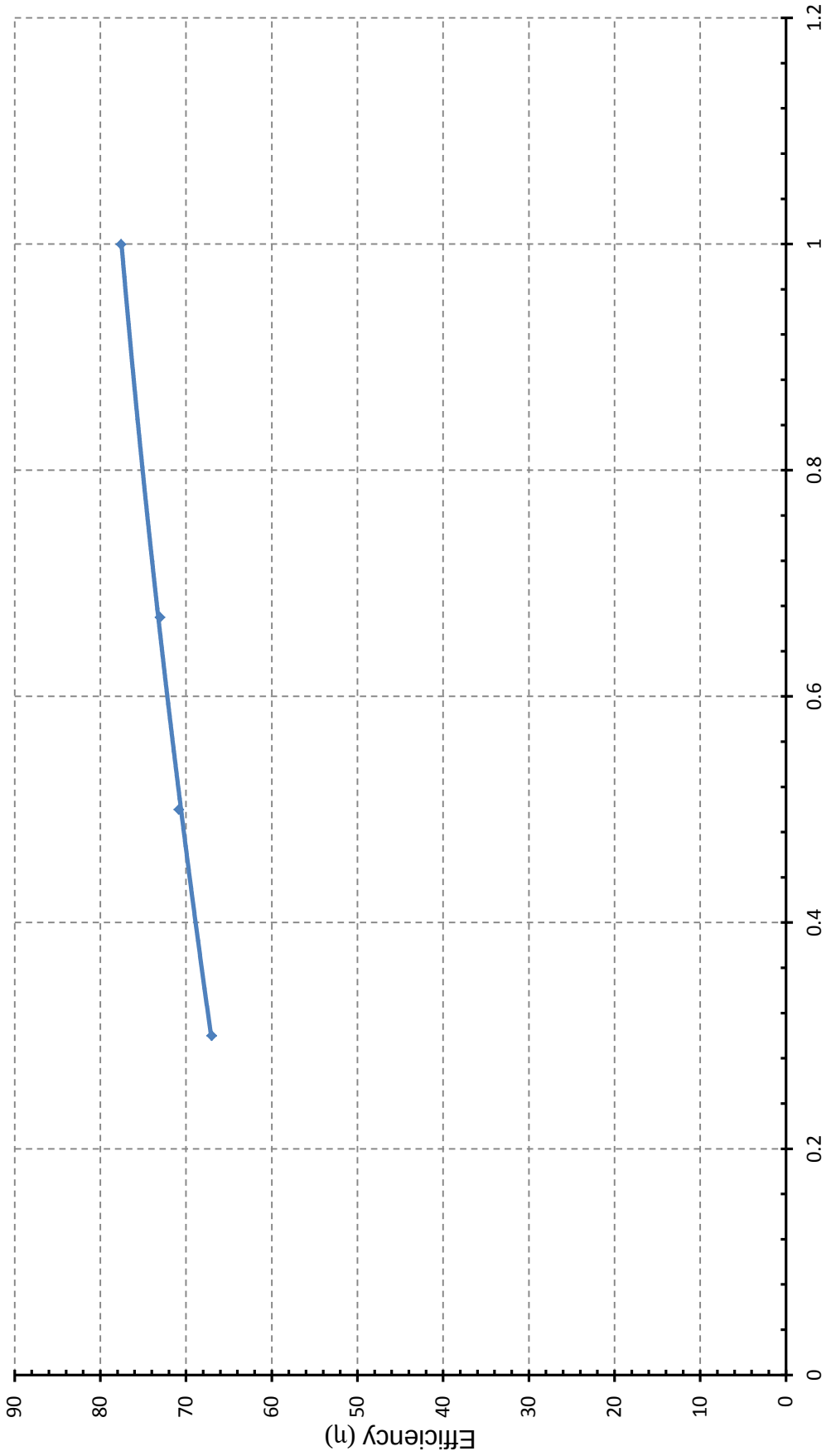

Fig. 5.81 Cross-flow turbine performance characteristics curve f of various nozzle to runner blades width ratios.

5.2.9 Optimization of the Runner Blades Width to Outer Diameter (B_w / d_1)

The unique and inherent advantages of the cross-flow turbine, due to its suitable design for a wide range of operating condition including flow rate and head, has led to a considerable interest and widespread uses in micro hydroelectric power plants. The cross-flow turbine is understood as a water turbine where the runner receives the water in a radial inward direction and discharges it in a substantially radial outward direction, the runner outer diameter is particularly independent of the rate of flow, but the runner blade width can be dependent on the rate of flow. Changing the width of the runner blades will not have effects on the hydraulic characteristics of the cross-flow turbine [3]. However, the available site characteristics, such as the available flow rate and head, are the determinant factors in the selection of a suitable turbine design. Hence, longer runner blades width is suitable for the lower head site of higher flow rate. The impact of the runner blades width to runner outer diameter ratio B_w / d_1 was experimentally investigated by Khosrowpanah et al [43]. They tested two runners of outer diameters of 152.4 mm and 304.8 mm, both were of a width of 152.4 mm. These dimensions correspond to blades width to diameter ratio of 1.0 and 0.5. The results of this experiment showed that the efficiency increases by about 20 % when reducing the ratio of runner width to runner outer diameter from 1.0 to 0.5. In order to provide a comprehensive understanding of the effect of the runner blades width to diameter ratio B_w / d_1 on the performance of the cross-flow turbine, ratios of 1/3, 1/2, 2/3 and 1 were selected for investigation in the current study. The geometrical parameters' details of the tested turbines are listed in table 5.9.

Table 5.9 Details of the runner blades width to outer diameter tested.

Geometrical parameter	Specification
Number of blades	$n_b = 30$
External diameter	$d_1 = 300\,mm$
Diameters ratio	$d_2/d_1 = 0.65$
Angle of attack	$\alpha_1 = 15^o$
Inlet blade angle	$\beta_1 = 151.814^o$
Internal blade angle	$\beta_1^{'} = \beta_2^{'} = 90^o$
Outlet blade angle	$\beta_2 = 28.186^o$
Blade thickness	$t_b = 3.6\,mm$
Blade radius of curvature	$r_b = 49.139\,mm$
Nozzle entry arc	$\lambda = 90^o$
Throat width	$s_o = 60\,mm$
Width of the blade	$B_w = ?$ $300, 200, 150, 100\,mm$
Shaft (axle) diameter	$d_s = 40\,mm$ *Note: Symbols as detailed in Fig. 3.2.*

As described earlier, ANSYS CFX simulation code was adopted to perform flow field visualization of the internal flow inside the turbine. Figures 5.82 – 5.84 and Figs. B.12 – B.13 illustrate the effect of the runner blades width to runner outer diameter ratio B_w / d_1 on the fluid flow characteristics and the performance of the turbine. Also, the water superficial velocity streamlines were plotted for entire turbine as shown in Figs. 5.82 (a) to (d). These figures clearly show the fluid flow in the turbine. To reveal and visualize the two-phase flow more clearly, contours of water volume fraction were plotted on the mid span plane as shown

in Figs. 5.83 (a) to (d). These demonstrate a well-defined interface between the air and water flow. In order to examine the water flow characteristics closely, vectors of water superficial velocity and contours of the pressure were plotted on the mid span planes as shown in Figs. 5.84, B.12 and B.13. These figures clearly show that the runner blades width to runner outer diameter ratio B_w / d_1 does not, in general, effect on the fluid flow characteristics of the cross-flow turbine as the runner receives the water in a radial inward direction and discharges it in a essentially radial outward direction.

The overall effect of the runner blades width to runner outer diameter ratio B_w / d_1 on the efficiency of the cross-flow turbine is shown in Fig. 5.85. The result of computations revealed that an increase in the runner blades width to runner outer diameter ratio from 1/3 to 1.0 has a minimal effect on the turbine efficiency. This revealed total agreement with Harvey et al [3]. They stated that changing the width of the runner blades will not affect the hydraulic characteristics of the cross-flow turbine where the runner receives the water in a radial inward direction and discharges it in an essentially radial outward direction. Therefore, the plant site characteristics, such as the available flow rate and head, are the determined factors in the selection of a suitable turbine design. Hence, the longer runner blades width is suitable for the lower head site of higher flow rate. According to this study, the runner blades width to runner outer diameter ratio B_w / d_1 1.0 was more effective than 1/3, 1/2 and 2/3 where the efficiency was 77.810 %. At low runner blades width to runner outer diameter ratio 1/3, the turbine efficiency was 77.037 %. Therefore, the optimum runner blades width to runner outer diameter ratio can be considered to be 1.0.

(a) Runner blades width to outer diameter ($B_w/d_1 = 1$) (b) Runner blades width to outer diameter ($B_w/d_1 = 2/3$)

Fig. 5.82 (a) and (b) Water superficial velocity streamlines in cross-flow turbine of various runner blades width to outer diameter ratios.

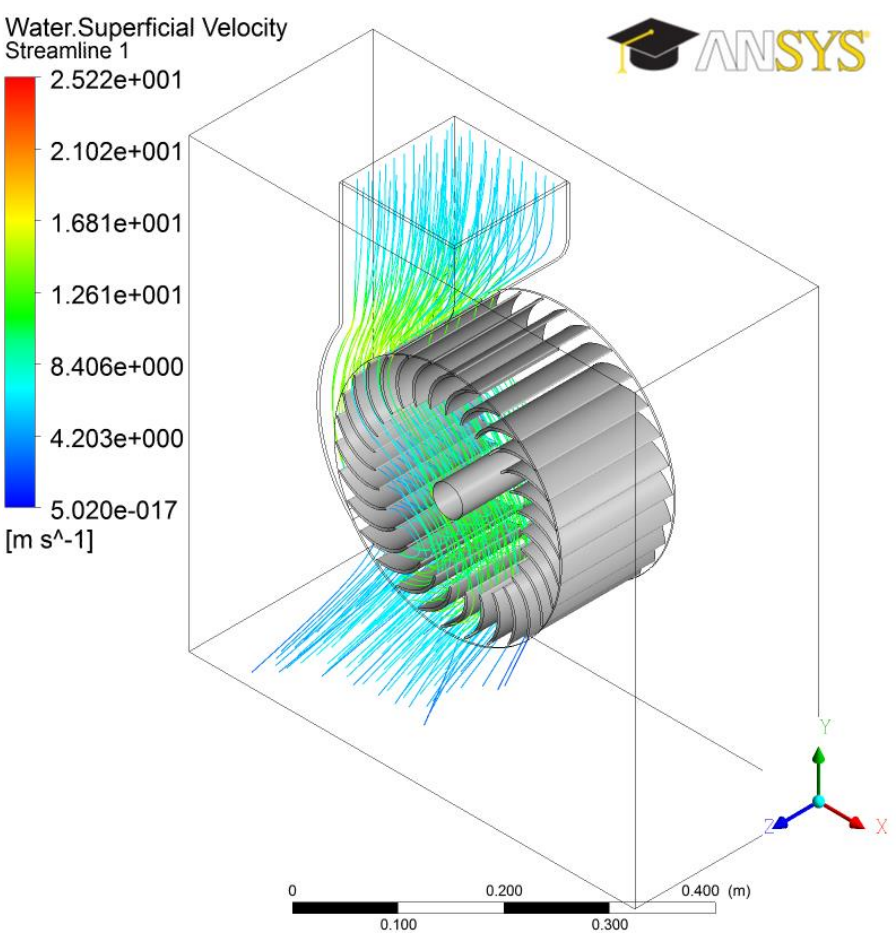

(c) Runner blades width to outer diameter ($B_w / d_1 = 1/2$)

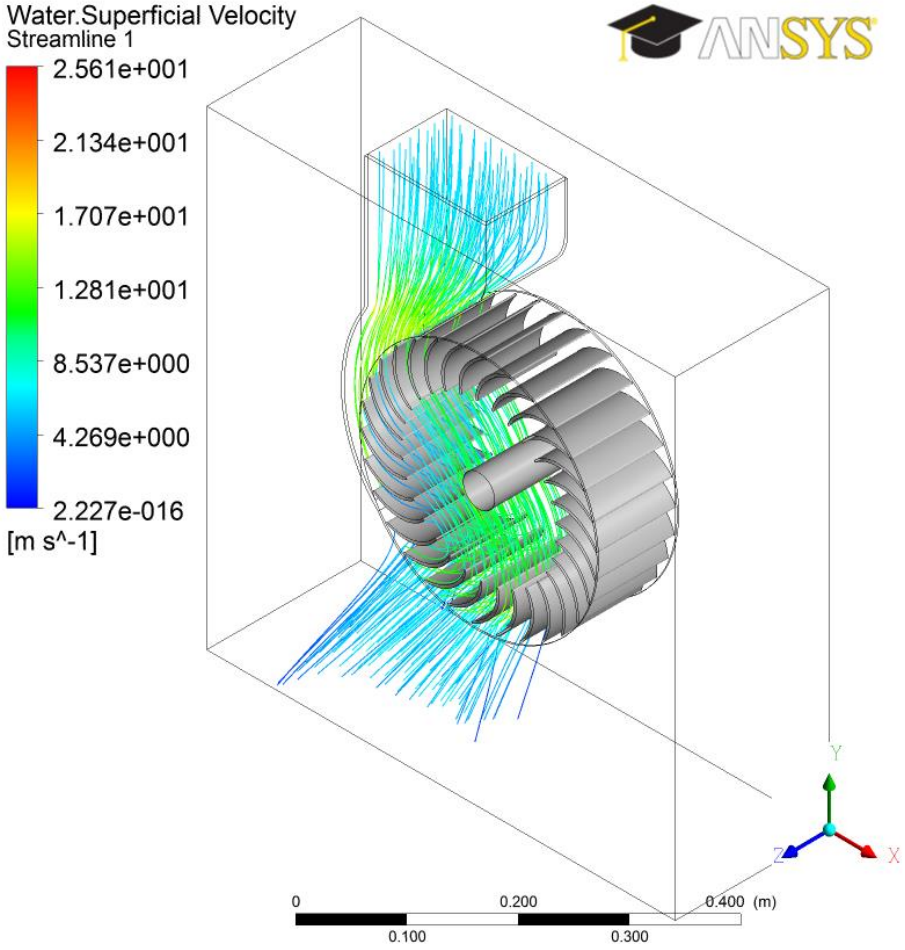

(d) Runner blades width to outer diameter ($B_w / d_1 = 1/3$)

Fig. 5.82 (c) and (d) Water superficial velocity streamlines in cross-flow turbine of various runner blades width to outer diameter ratios.

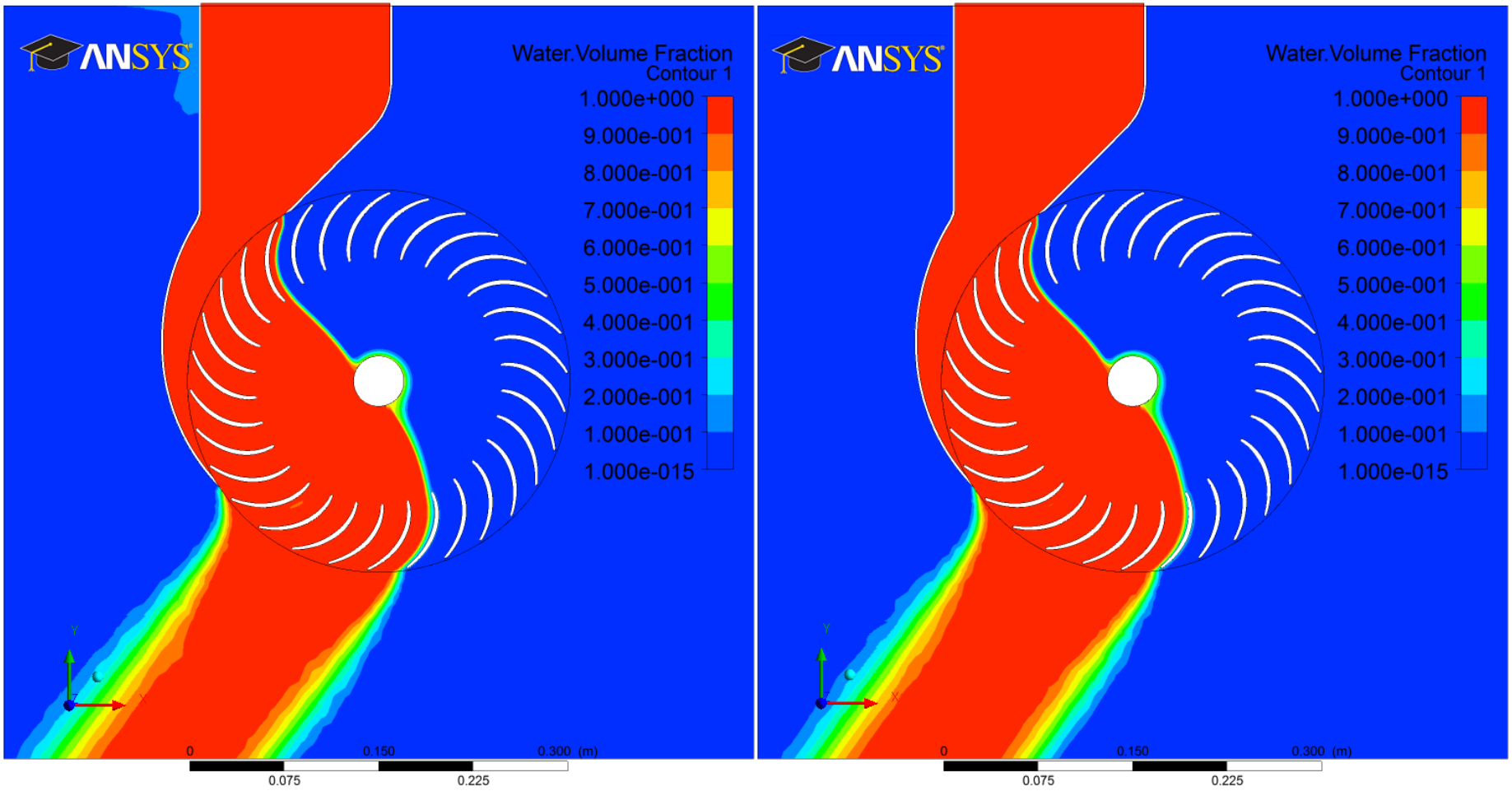

(a) Runner blades width to outer diameter ($B_w / d_1 = 1$) (b) Runner blades width to outer diameter ($B_w / d_1 = 2/3$)

Fig. 5.83 (a) and (b) Water volume fraction contours at the mid span of cross-flow turbine of various runner blades width to outer diameter ratios.

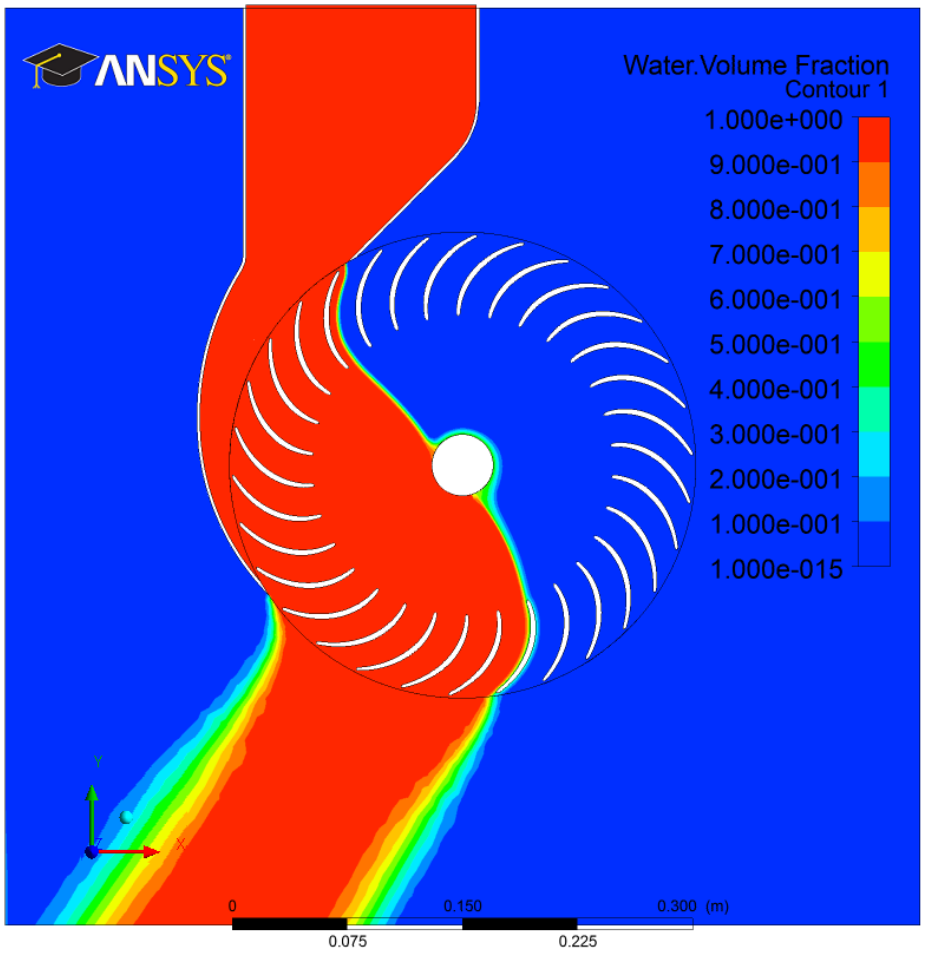

(c) Runner blades width to outer diameter (B_w /d_1 = 1/2)

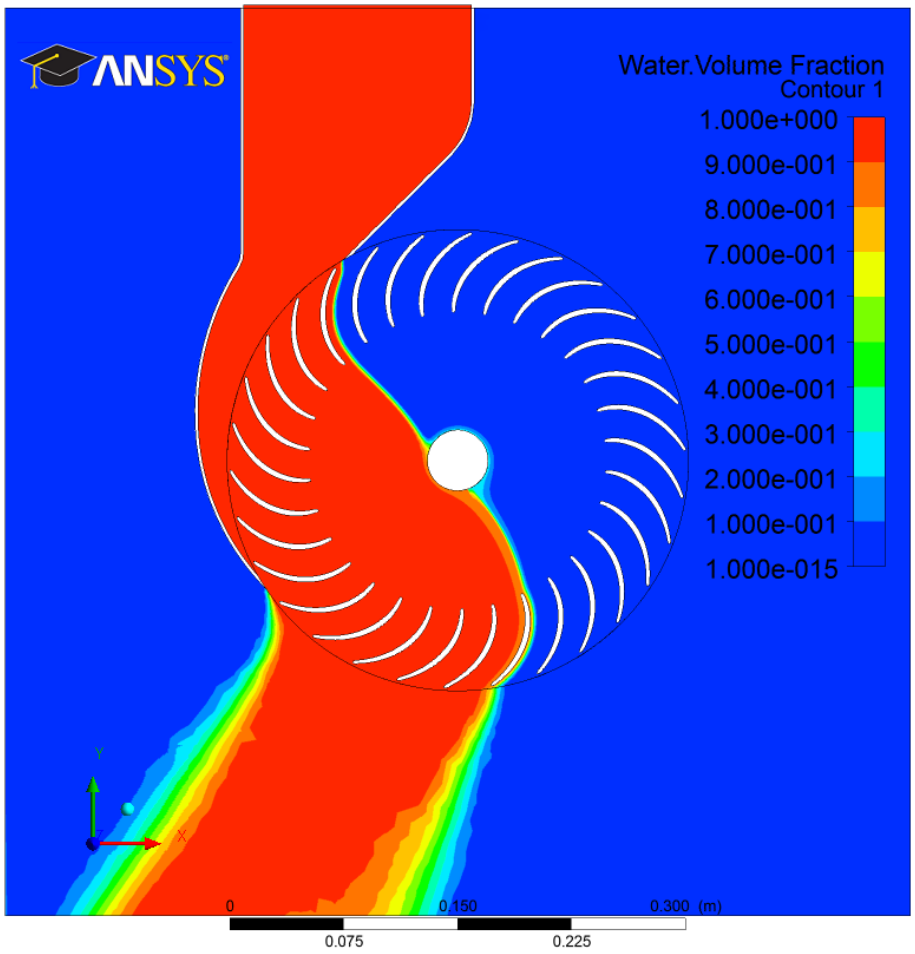

(d) Runner blades width to outer diameter (B_w /d_1 = 1/3)

Fig. 5.83 (c) and (d) Water volume fraction contours at the mid span of cross-flow turbine of various runner blades width to outer diameter ratios.

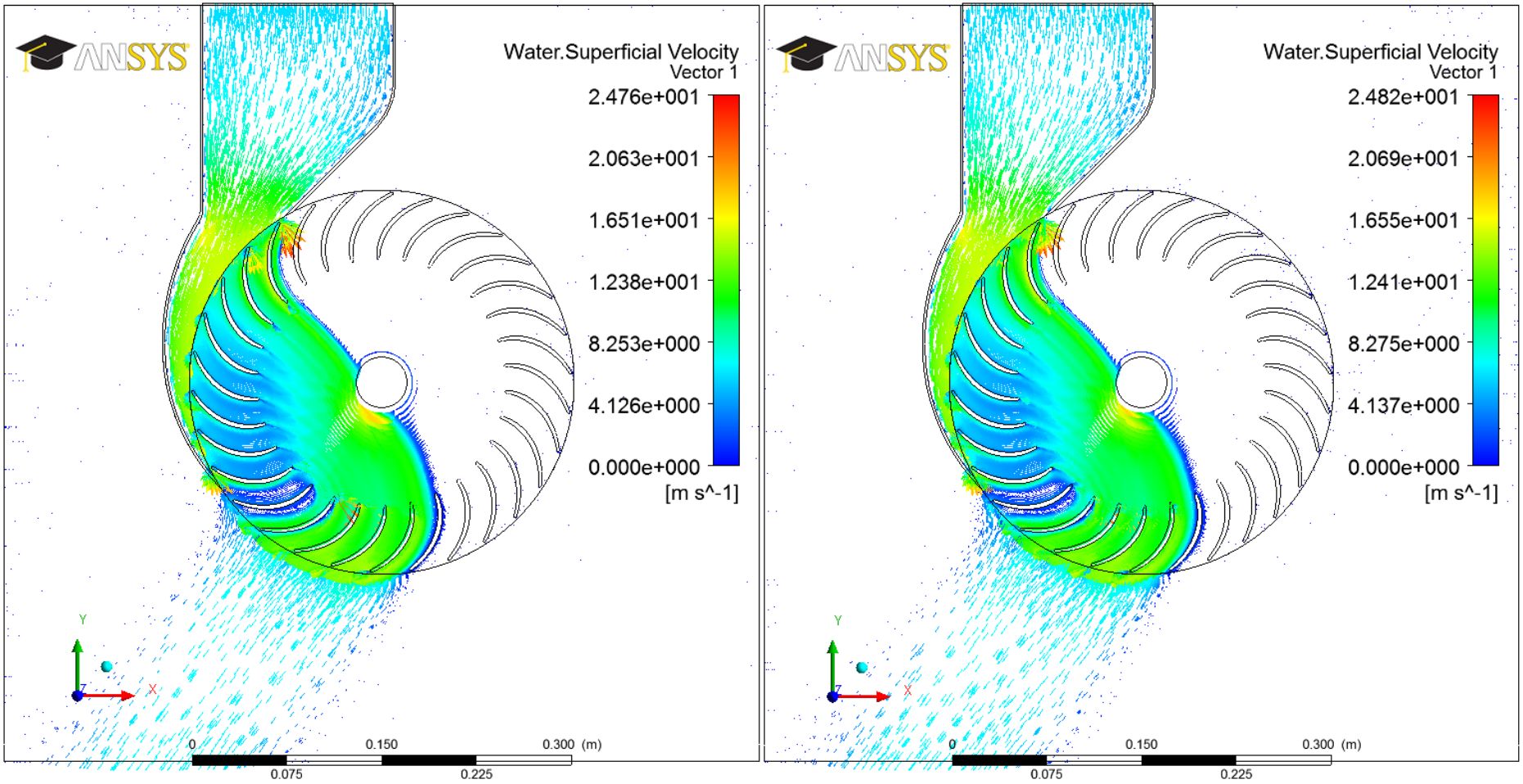

(a) Runner blades width to outer diameter ($B_w / d_1 = 1$)

(b) Runner blades width to outer diameter ($B_w / d_1 = 2/3$)

Fig. 5.84 (a) and (b) Water superficial velocity vectors at the mid span of cross-flow turbine of various runner blades width to outer diameter ratios.

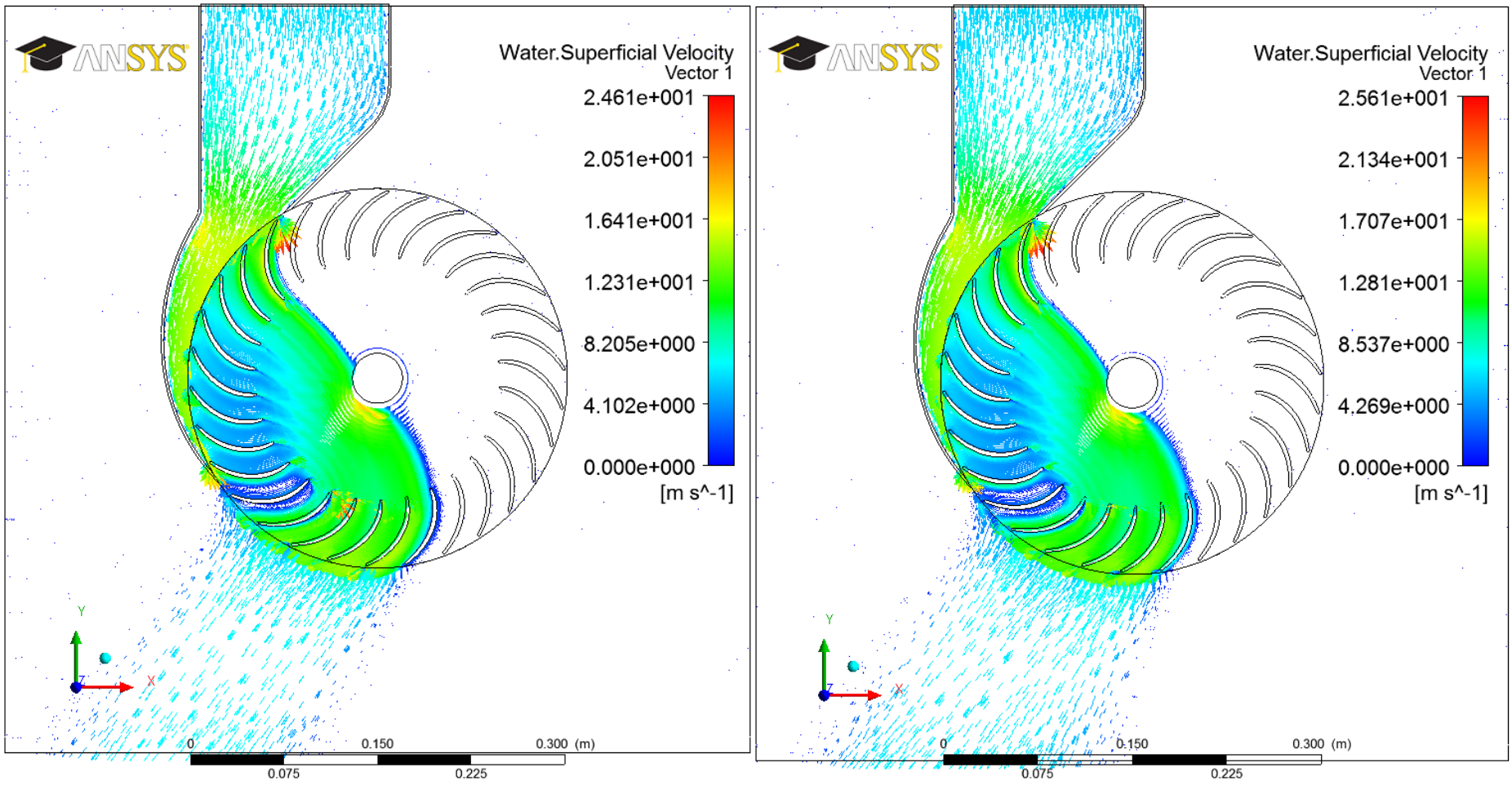

(c) Runner blades width to outer diameter ($B_w / d_1 = 1/2$)

(d) Runner blades width to outer diameter ($B_w / d_1 = 1/3$)

Fig. 5.84 (c) and (d) Water superficial velocity vectors at the mid span of cross-flow turbine of various runner blades width to outer diameter ratios.

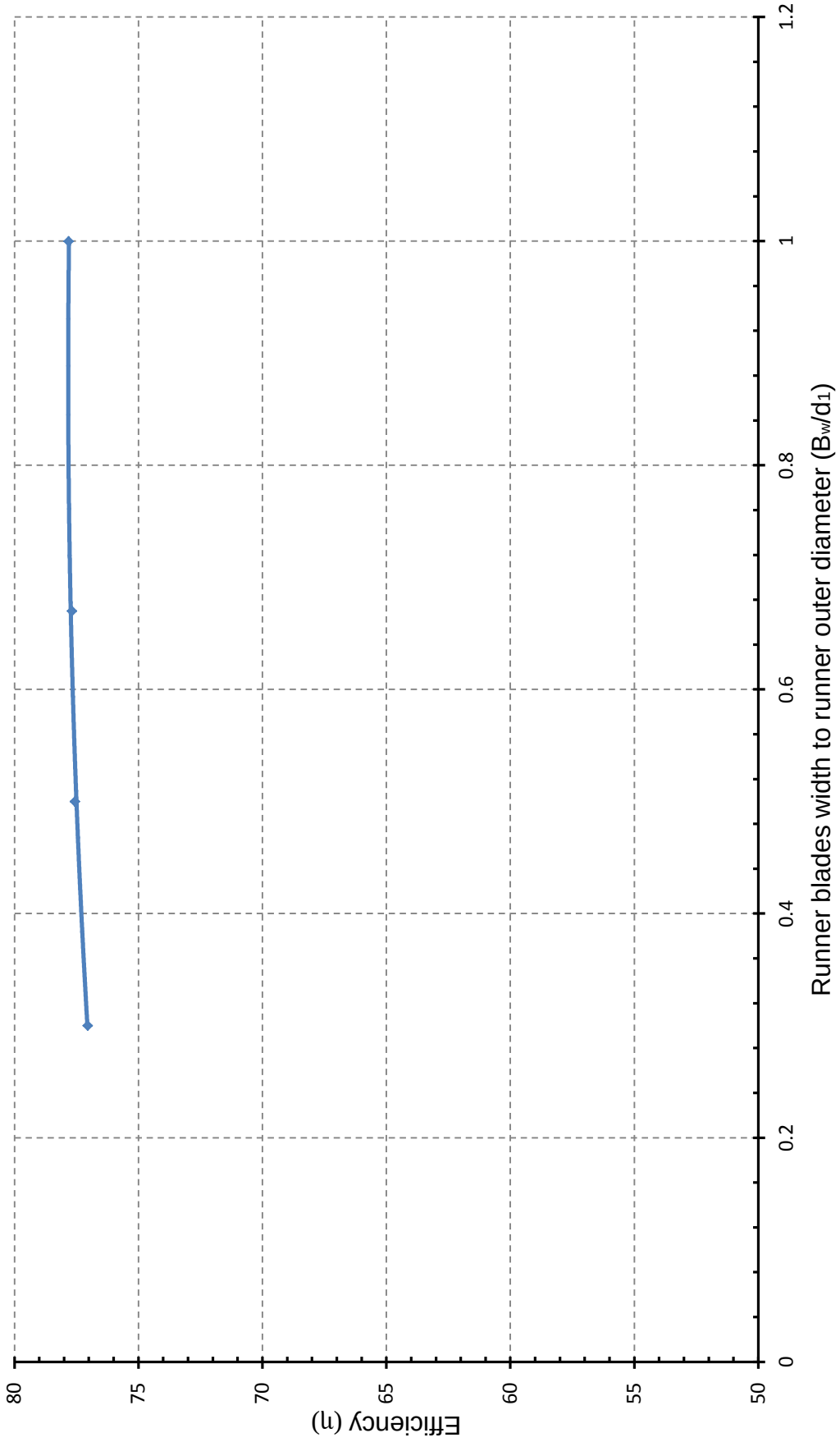

Fig. 5.85 Cross-flow turbine performance characteristics curve for various runner blades width to outer diameter ratios.

5.3 Outline of the Simulation Results

In this chapter, the optimal values for the geometric parameters of the main cross-flow turbine elements, such as the runner and the nozzle were established. Many characteristics of the two major components were numerically and comprehensively investigated. These include the number of runner blades, the ratio of inner to outer diameter, blade profile, and width of the runner blade to outer runner diameter on the performance of the cross-flow turbine. The study reported in this chapter also covered the turbine nozzle improvement by investigating the effects of nozzle entry arc, nozzle throat width, nozzle width to blade width, angle of attack and nozzle shape for two different configurations of the nozzles one installed with an inside guide vane while the other without it on the performance of the cross-flow turbine. The conclusions from the above unique and comprehensive study is reported in the next chapter.

Chapter Six

Conclusions and Recommendations

Chapter Six

Conclusions and Recommendations

6.1 Main Conclusions

This research started with an introduction to the importance and applications of the micro hydroelectric power plants in power generation in isolated and remote communities and the gained environmental benefits. This was followed by selecting an appropriate turbine design (cross-flow micro-turbine) out of several turbine types for such applications. Such turbine is not very complicated in design structure, maintenance, and manufacturing processes. As, such the selected turbine can be used by personnel who on average have moderate or little technical knowledge. A comprehensive and critical review of the literature on various aspects of the cross-flow micro-turbine was then undertaken. The review revealed many important geometrical parameters in the design of cross-flow turbines that influence their performance. Consequently, these parameters were used in modelling the performance of the turbine with the view of optimizing their power output, design and efficiency. ANSYS CFX, advanced and high-performance modelling capabilities, was chosen among several CFD simulation codes (such as PHOENICS, STAR-CCM+ and ANSYS CFX) to perform a complete analysis of the internal flow of cross-flow turbine, which is of turbulent, two-phase and three dimensional nature.

The optimum values for the geometric parameters of the runner and nozzle of the cross-flow turbine were calculated. The analysis and flow prediction performed by ANSYS CFX for the influence of such parameters revealed a fundamental hydrodynamics flow characteristics within the turbine as well as many phenomena associated with the structure of the flow. Such flow structure were not possible at all to be observed by conventional flow visualization methods. The specific concluding points of the present study can be summarized as follows:

i. An increase in the number of runner blades from 15 to 30 has a favorable effect on the efficiency of the cross-flow turbine. This was attributed to the increase in the energy extracted from water by the blades, decrease of the non-cross flow and a reduction in the size of the separation/recirculation flow on the back of the blades. A further increase in the number of runner blades from 30 to 40 has an undesirable effect of reducing the turbine efficiency which was attributed to the increase in the collision loss and the weight of the runner.

ii. There was a minimal effect of the blades diameter ratio within the range 0.65 to 0.68 on the efficiency of the cross-flow turbine. A further change of the diameter ratio below this range had a negative effect on the efficiency. This was most likely caused by the increase in the impingement energy loss and the possibility of the increase of the blades' passage back pressure. Moreover, increasing the value of the diameter ratio over this range tends to increase the separation on the wide blades' passages.

iii. Decreasing the angle of attack α_1 from 32 to 15 has a favorable effect on the efficiency of the cross-flow turbine. This is because of a reduction in the energy extracted from water, by the blades, with any increase in the value of α_1, which in turn increases the inlet blade angle β_1 and blade curvature r_b.

iv. An increase in the nozzle entry arc λ from 60^o to 90^o has a favorable effect on the efficiency of the cross-flow turbine. This was attributed to the increase in the energy extracted from water by the blades. It is natural that any increase in the nozzle entry arc increases the interaction of the same amount of water with larger number blades. A further increase in the nozzle entry arc from 90^o to 120^o has an undesirable effect due to the increase in the impingement loss, flow separation and variation in the angle of attack.

v. The orientation of the nozzle entry arc on the runner circumference has a significant effect on the flow characteristics and the hydrodynamic forces within the cross-flow turbine. Such is the influence of the arc orientation that it can create considerable water splatter which in turn increases losses and decreases turbine efficiency.

vi. The efficiency of the cross-flow turbine increased significantly by using a three new runner blade profiles. This was attributed to the decrease in the collision loss. However, the turbine's efficiency changed very slightly (less than 0.1 %) "among the three new runner blade profiles".

vii. A guide vane has an undesirable effect on the efficiency of the cross-flow turbine by splitting the water flow in the nozzle into two streams. This tends to increase friction losses and consume useful flow energy. Such energy

loss was shown to increase further by the impingement of the water on the guide vane.

viii. The change in the profile of the nozzle rear wall due to change in nozzle entry arc angle and nozzle profile has significant effect on the performance of the cross-flow turbine. Such profile changes the distribution of the water entering the runner from the nozzle.

ix. An increase in the nozzle throat width from $0.1d_1$ to $0.2d_1$ has a favorable effect on the efficiency of the cross-flow turbine. The nozzle throat width controls the water flow condition at the runner inlet. Decreasing the width of the nozzle throat decreases the distance between the nozzle rear wall and the runner and this in turn decreases the amount of water in the passages between the blades in the lower part of the nozzle entry arc (which reduces the water energy extraction by blades).

x. The ratio of the nozzle to the runner blades width N_w/B_w 1.0 provides better performance than the ratios 1/3, 1/2 and 2/3. In case the ratio being less than one the nozzle width covers only part of the runner blades width. This leads to dispersion of water along the blade width, and, therefore, lead to energy loses due to the axial movement of water. The dispersed water does not contribute to the water energy conversion in of the runner, and more specifically, it negatively influences the second stage of energy extraction.

xi. Changing the runner blades width to outer diameter ratio B_w/d_1 has a minimal effect on the flow characteristics and the hydrodynamic forces within

the cross-flow turbine. Hence, turbines with higher runner blades width are suitable for a site with higher flow rate.

Table 6.1 Summarizing the optimum values of the investigated parameters.

Geometrical parameter	Specification
Number of blades	$n_b = 30$
External diameter	$d_1 = 300\,mm$
Diameters ratio	$d_2/d_1 = 0.65$
Angle of attack	$\alpha_1 = 15^o$
Inlet blade angle	$\beta_1 = 151.814^o$
Internal blade angle	$\beta_1' = \beta_2' = 90^o$
Outlet blade angle	$\beta_2 = 28.186^o$
Blade profile	Blade profile (1)
Nozzle profile	Nozzle profile (1)
Blade radius of curvature	$r_b = 49.139\,mm$
Nozzle entry arc	$\lambda = 90^o$ with orientation of 60^o & 30^o
Throat width	$s_o = 60\,mm$
Nozzle to runner blades width	$N_w/B_w = 1$
Runner blades width to outer diameter	$B_w/d_1 = 1$ *Note: Symbols as detailed in Fig. 3.2.*

The above conclusions and the extensive understanding of the flow structure provided by the results of the current work could provide much useful and needed design modification to the current micro-turbine design used in micro hydroelectric power plants. In particular, those micro-turbines used in remote and isolated regions of available water resources which are also not connected to the electricity grid.

6.2 Recommendations for Future Work

The optimization of the geometric parameters by using ANSYS CFX was proven to be a very effective technique in maximizing the performance of the cross-flow turbine. Based on this and in order to refine the results further, some recommendations for future work are listed below:

i. Re-simulate the cross-flow turbine using direct numerical simulation (DNS) or even large eddy simulation (LES) approach. This approach was not followed in the current work due to the limited capacity of the current computers. Perhaps larger capacity computers could allow the use of the above techniques which in turn could reveal more details on the structure of the flow within the turbine.

ii. A total number of 1,713,426 elements were used in the domain of the current work. This number can be increase with the improvement in the future computer capacity. It is natural that this will improve the prediction of the structure of the flow and could reveal better insight into complex flow structure of the cross-flow turbine.

iii. Although grid refinement was used extensively in the current work, however, many regions of interest in both the nozzle and the runner were observed in the predicted results. Such regions of extreme interest can be further investigated by refining the grid to reveal further the complex flow structure and phenomena.

iv. There was a slight drop in the turbine efficiency with increasing the number of the blades from 30 to 35. Hence, investigating the effect of the number of

the blades on the turbine efficiency in smaller steps within the range of 30 to 35 is recommended. Such investigation can shed further light on the effects of this all important parameter (blade numbers) on the structure of the flow within the blades' passages.

v. The nozzle has a significant impact on the performance of the cross-flow turbine. Hence, re-design and simulation analysis of the optimum nozzle profile (nozzle profile 1) is highly recommended as well as investigating new designs of the nozzle rear wall, nozzle throat width and nozzle entry arc.

vi. This study was theoretical in nature, it would be of great interest to produce a prototype turbine and use it in a set of experiments to confirm the conclusions above.

References

References

[1] J. Razak, Y. Ali, M. Alghoul, M. S. Zainol, A. Zaharim, and K. Sopian, "Application of Crossflow Turbine in Off-Grid Pico Hydro Renewable Energy System," in *Processes Proceedings of the American Conference on Applied Mathematics (American-Math '10)*, 2010, pp. 27-29.

[2] B. A. Nasir, "Design of High Efficiency Cross-Flow Turbine for Hydro-Power Plant," *International Journal of Engineering and Advanced Technology,* vol. 2, pp. 308 -311, February 2013.

[3] A. Harvey, A. Brown, P. Hettiarachi, and A. Inversin, *Micro-Hydro Design Manual: A Guide to Small-Scale Water Power Schemes*: Intermediate Technology Publications London, 1993.

[4] P. Fraenkel, O. Paish, V. Bokalders, A. P. Harvey, and S. M. Council, *Micro-Hydro Power: a Guide for Development Workers*: Intermediate Technology Publications, 1991.

[5] A. Patzig, "Optimizing Fluctuating Flows," *Alternative Sources Energy; United States,* vol. 95, 1987.

[6] P. Vintr and P. Kraus, "Type Banki Turbines for Small Hydro-electric Power Plants," *Czechosolvak Heavy Industry,* 1989.

[7] S. Khurana and A. Kumar, "Small Hydro Power-A Review," *International Journal of Thermal Technologies,* vol. 1, pp. 107-110, 2011.

[8] D. Singh, "Micro Hydro Power, Resource Assessment Handbook," Asian and Pacific Center for Transfer of Technology (APCTT), September 2009.

[9] C. S. Ong, "Prototype of an Efficient Gydropower Plant," Mechatronics Engineering, Faculty of Engineering and Science, University of Tunku Abdul Rahman 2011.

[10] L. Ortolano and K. K. Cushing, "Grand Coulee Dam and The Columbia Basin Project, USA," case study report prepared as an input to the World Commission on Dams, www. dams. org, 2000.

[11] "Renewable Energy Technologies: Cost Analysis Series," International Renewable Energy Agency (IRENA), Hydropower, vol.1, June 2012.

[12] A. Akbarzadeh, "Performance Investigation of a Simple Reaction Water Turbine for Power Generation from Low Head Micro Hydro Resources," *Smart Grid and Renewable Energy,* vol. 3, pp. 239-245, 2012.

[13] A. Williams and S. Porter, "Comparison of Hydropower Options for Developing Countries with Regard to the Environmental, Social and Economic Aspects," in *International Conference on Renewable Energy for Developing Countries*, Washington D.C., USA, April 2006.

[14] O. ZIA, O. A. GHANI, S. T. WASIF, and Z. HAMID, "Design, Fabrication and Institute of a Micro-Hydro Power Plant," GIK Institute of Engineering Sciences & Technology, May 2010.

[15] "Environmental and Health Impacts of Electricity Generation," the International Energy Agency Implementing Agreement for Hydropower Technologies and Programms, June 2002.

[16] J. S. Anagnostopoulos and D. E. Papantonis, "Optimal Sizing of a Run-of-River Small Hydropower Plant," *Energy Conversion and Management,* vol. 48, pp. 2663-2670, 2007.

[17] European Small Hydropower Association, Renewable Energy House, ESHS is member of the European Renewable Energy Council, www.esha.be.

[18] C. Dragu, T. Sels, and R. Belmans, "Small Hydro Power–State of the Art and Applications," KU Leuven, ESAT-ELEN, Energy Institute, Leuvan, Belgium, 2001.

[19] M. Singhal and A. Kumar, "Cost Benching for Civil Structures of Micro/mini Hydro Electric Projects Located in Uttaranchal," *Himalayan Small Hydro Summit, Dehradun,* pp. 381-390, 2006.

[20] A. Kunwor, "Technical Specifications of Micro-Hydropower System Design and its Implementation: Feasibility Analysis and Design of Lamaya Khola Micro-Hydro Power Plant," 2012.

[21] S. L. Dixon, *Fluid Mechanics and Thermodynamics of Turbomachinery*: Butterworth-Heinemann, 2005.

[22] C. Brown, "A Feasibility Study into a Proposed Micro Generating Station on the Inverailort Deer Forest Estate," Thesis, Mechanical Engineering Department, Faculty of Engineering, University of Strathclyde Glasgow, September 2006.

[23] G. I. Krivchenko, *Hydraulic Machines: Turbines and Pumps*: Lewis publishers Boca Raton, FL, 1994.

[24] A. T. Chandran, G. Anil, and J. Chandapillai, "Development and Testing of a Cross Flow Turbine," Fluid Control Research Institute, IGHEM, AHEC, IIT Rootkee, India, 2010.

[25] M. Tamburrini, "A Feasibility Study for a Micro-hydro Installation for the Strangford Lough Wildfowlers & Conservation Association," University of Strathclyde, Glasgow, UK, 2004.

[26] C. Penche, *Layman's Handbook on How to Develop a Small Hydro Site*: Published books DG XVII-97/010, ESHA, European Commission, Belgica, June 1998.

[27] D. Shepherd, *Principles of Turbomachinery*. New York, The McMillan Company, 1995.

[28] S. Khosrowpanah, "Historical Overview of Cross-Flow Turbine," *International Water Power and Dam Construction,* vol. 36, p. 38, 1984.

[29] C. C. Warnick, "Hydropower Engineering," Prentice Hall Inc, Englewood Cliffs, New Jersey 1984.

[30] A. Adeyanju, "Technical Feasibility of a Micro Hydro Installation," *Journal of Engineering and Applied Sciences,* vol. 4, pp. 324-334, 2009.

[31] C. A. Mockmore and F. Merryfield, "The Banki Water Turbine," Engineering Experiment Station, Oregon State System of Higher Education, Oregon State College, Corvallis, Buletin Series No. 25, February 1949.

[32] Y. Nakase, J. Fukutomi, T. Watanabe, T. Suetsugu, T. Kubota, and S. Kushimoto, "A Study of Cross-Flow Turbine: Effects of Nozzle Shape on its Performance," in *Proceedings of the ASME Conference on Small Hydro Power Fluid Machinery*, 1982, pp. 13-18.

[33] J. Makansi, "Equipment Options Multiply for Small-Scale Hydro," *Power,* vol. 127, pp. 33-40, May 1983.

[34] J. Chappell, "Recent DOE-Sponsored Hydropower Engineering Research," NTIS Id No. DE84000809, Report No. EGG-M-02983, EG and G Idaho, Inc., Idaho Falls (USA)1983.

[35] L. R. Van Dixhorn, H. L. Moses, and J. Moore, "Experimental Determination of Blade Forces in a Cross-Flow Turbine," *Small Hydro Power Fluid Machinery, the Winter Annual Meeting of ASME, pp. 67-75, New Orleans, LA,* December 1984.

[36] R. Hothersall, "Micro Hydro: Turbine Selection Criteria," *International Water Power and Dam Construction,* pp. 26-29, February 1984.

[37] W. Durgin and W. Fay, "Some Fluid Flow Characteristics of a Cross-Flow Type Hydraulic Turbine," *Small Hydro Power Fluid Machinery, the Winter Annual Meeting of ASME, New Orleans, LA,* pp. 77-83, December 1984.

[38] J. Fukutomi, Y. Nakase, and T. Watanabe, "A Numerical Method of Free Jet from a Cross-Flow Turbine Nozzle," *Bulletin of the JSME,* vol. 28, pp. 1436-1440, July 1985.

[39] O. Thapar and M. L. Albertson, "Ultra Low Head Small Hydro Power System Technology for Economic Development," in *Waterpower'85, Proceeding of an International Conference on Hydropower, Las Vegas, NV*, September 1985, pp. 1905-1924.

[40] G. Smith, "Hydropower Development in Remote Locations of Developing Countries," in *American Institute of Physics (AIP) Conference Proceedings, American Physical Society*, Washington, DC, United States, April 25, 1985, p. 497.

[41] A. Panasyuk, K. Tokombaev, and G. Shainova, "Small Hydroelectric Stations and Prospects of Their Development," *Hydrotechnical Construction,* vol. 21, pp. 366-373, June 1987.

[42] C. S. K. Kpordze, "A New Methodology for Selection of Hydraulic Turbines," Monograph, Idaho Water Resources Research Institute, University of Idaho, Moscow, Idaho, March 1987.

[43] S. Khosrowpanah, A. Fiuzat, and M. L. Albertson, "Experimental Study of Cross-Flow Turbine," *Journal of Hydraulic Engineering,* vol. 114, pp. 299-314, 1988.

[44] A. F. Tongco, "Field Testing of a Crossflow Water Turbine," PhD Thesis, Oklahoma State University., Stillwater, OK (USA), July 1988.

[45] R. F. Ott and J. R. Chappell, "Design and Efficiency Testing of a Cross-Flow Turbine," in *in Proceedings of the International Conference on Hydropower'89, vol. 3*, 1989, pp. 1534-1543.

[46] N. M. Aziz and V. R. Desai, "An Experimental Study of the Effect of Some Design Parameters in Cross-Flow Turbine Efficiency," Engineering Report, Department of Civil Engineering, Clemson University, 1991.

[47] J. Fukutomi, Y. Senoo, and Y. Nakase, "A Numerical Method of Flow through a Cross-Flow Runner," *JSME international journal. Series 2, Fluids engineering, heat transfer, power, combustion, thermophysical properties,* vol. 34, pp. 44-51, 1991.

[48] A. A. Fiuzat and B. P. Akerkar, "Power Outputs of Two Stages of Cross-Flow Turbine," *Journal of Energy Engineering,* vol. 117, pp. 57-70, 1991.

[49] H. Olgun and A. Ulku, "A Study of Cross-Flow Turbine - Effects of Turbine Design Parameters on its Performance," in *Second World Renewable Congress*, Reading, UK, 3 - 18 September, 1992, pp. 2834-2838.

[50] V. Desai and N. Aziz, "Parametric Evaluation of Cross-Flow Turbine Performance," *Journal of Energy Engineering,* vol. 120, pp. 17-34, April 1994.

[51] V. R. Desai and N. M. Aziz, "An Experimental Investigation of Cross-Flow Turbine Efficiency," *Journal of Fluids Engineering;(United States),* vol. 116, pp. 545-550, 1994.

[52] N. Costa Pereira and J. Borges, "Study of the Nozzle Flow in a Cross-Flow Turbine," *International journal of mechanical sciences,* vol. 38, pp. 283-302, 1996.

[53] J. Fukutomi, Y. Nakase, M. Ichimiya, and H. Ebisu, "Unsteady Fluid Forces on a Blade in a Cross-Flow Turbine," *JSME international journal. Series B, fluids and thermal engineering,* vol. 38, pp. 404-410, 1995.

[54] C. Joshi, V. Seshadri, and S. Singh, "Parametric Study on Performance of Cross-Flow Turbine," *Journal of Energy Engineering,* vol. 121, pp. 28-45, 1995.

[55] H. Reddy, V. Seshadri, and D. Kothari, "Effect of Draft Tube Size on the Performance of a Cross-Flow Turbine," *Energy Sources, Part A: Recovery, Utilization and Environmental Effects,* vol. 18, pp. 143-149, 1996.

[56] F. Kenyery and J. Alcala, "Experimental Study of Interior Deflector in Cross Flow Turbines," in *European Conference on Turbomachinery-Fluids Dynamics and Thermodynamics*, Belgium, 1997.

[57] H. Olgun, "Investigation of the Performance of a Cross-Flow Turbine," *International journal of energy research,* vol. 22, pp. 953-964, 1998.

[58] H. Olgun, "Effect of Interior Guide Tubes in Cross-Flow Turbine Runner on Turbine Performance," *International journal of energy research,* vol. 24, pp. 953-964, 2000.

[59] M. Kaniecki, "Modernization of the Outflow System of Cross-Flow Turbines," Institute of Fluid-Flow Machinery, Polish academy of Sciences, No. 4, pp. 601-608, 2002.

[60] Y.-D. Choi, J.-I. Lim, Y.-T. Kim, and Y.-H. Lee, "Performance and Internal Flow Characteristics of a Cross-Flow Hydro Turbine by the Shapes of Nozzle and Runner Blade," *Journal of Fluid Science and Technology,* vol. 3, pp. 398-409, 2008.

[61] Y. Choi, H. Yoon, M. Inagaki, S. Ooike, Y. Kim, and Y. Lee, "Performance Improvement of a Cross-Flow Hydro Turbine by Air Layer Effect," in *25th IAHR Symposium of Hydraulic Machinery and System, IOP Conference Series: Earth and Environmental Science 12*, 2010.

[62] J. Haurissa and R. Soenoko, "Performance and Flow Characteristics Latitude of Nozzle in Turbine Blades Second Level," *Journal of Economics and Engineering,* pp. 448-453, December 2010.

[63] J. De Andrade, C. Curiel, F. Kenyery, O. Aguillón, A. Vásquez, and M. Asuaje, "Numerical Investigation of the Internal Flow in a Banki Turbine," *International Journal of Rotating Machinery,* vol. 2011, 2011.

[64] S.-W. Son and Y.-D. Choi, "Shape Effect of Inlet Nozzle and Draft Tube on the Performance and Internal Flow of Cross-Flow Hydro Turbine," *Journal of the Korean Society of Marine Engineering,* vol. 36, pp. 351-357, 2012.

[65] K. Kokubu, T. Kanemoto, S.-W. Son, and Y.-D. Choi, "Performance Improvement of a Micro Eco Cross-Flow Hydro Turbine," *Journal of the Korean Society of Marine Engineering,* vol. 36, pp. 902-909, 2012.

[66] L. Haimerl, "The Crossflow Turbine," *Water Power,* vol. 12, pp. 5-13, 1960.

[67] M. Durali, "Design of Small Water Turbines for Farms and Small Communities," Thesis, Mechanical Engineering Department, Massachusetts Institute of Technology, 1976.

[68] O. Balje, *Turbomachines: A Guide to Design Selection and Theory*: John Wiley & Sons, New York, 1981.

[69] C. T. Shaw, *Using Computational Fluid Dynamics*: Prentice-Hall, Inc, Englewood Cliffs, New Jersey, 1992.

[70] A. Yangyozov and R. Willinger, "Calculation of Flow Characteristics in Heat Turbomachinery Turbine Stage with Different Three Dimensional Shape of the Stator Blade with Ansys CFX Software," *DIProjektbericht, ZID,* pp. 288-302, 2008.

[71] K. D. Hamman and R. A. Berry, "A CFD Simulation Process for Fast Reactor Fuel Assemblies," *Nuclear Engineering and Design,* vol. 240, pp. 2304-2312, 2010.

[72] H. Cao, "Aerodynamics Analysis of Small Horizontal Axis Wind Turbine Blades by Using 2D and 3D CFD Modelling," Thesis, School of Computing, Engineering and Physical Sciences, University of Central Lancashire, Preston, England, May 2011.

[73] J. Carregal-Ferreira, A. Holzwarth, F. E. T. Menter, and A. Luu, "Advanced CFD Analysis of Aerodynamics Using CFX," *AEA Technology GmbH, Otterfing, Germany,* 2002.

[74] ANSYS Inc, "ANSYS TurboGrid Introduction," ANSYS TurboGrid online product documentation, Release 13.0, November 2010. http://www1.ansys.com/customer/content/documentation/130/tg_intr.pdf.

[75] B. Nennemann, T. Vu, and M. Farhat, "CFD Prediction of Unsteady Wicket Gate-Runner Interaction in Francis Turbines: A New Standard Hydraulic Design Procedure," *Waterpower XIV, Austin, Texas, USA,* 2005.

[76] R. Susan-Resiga, T. C. Vu, S. Muntean, G. D. Ciocan, and B. Nennemann, "Jet Control of the Draft Tube Vortex Rope in Francis Turbines at Partial Discharge," in *Proceedings of the 23rd IAHR Symposium on Hydraulic Machinery and Systems, Yokohama, Japan*, October 2006, p. 192.

[77] P. Drtina and M. Sallaberger, "Hydraulic Turbines—Basic Principles and State-of-the-Art Computational Fluid Dynamics Applications," *Proceedings of the Institution of Mechanical Engineers, Part C: Journal of Mechanical Engineering Science,* vol. 213, pp. 85-102, 1999.

[78] E. Skaperdas and C. Kolovos, "Automated Pre-Processing for High Quality Multiple Variant CFD Models of a City-Class Car," in *3rd ANSA and uETA International conference*, Halkidiki Greece, September 2009.

[79] S. K. Pandey, "CFD Simulation of Hydrodynamics of Three Phase Fluidized Bed," Thesis, Department of Chemical Engineering, National Institute of Technology, Orissa, India, May 2010.

[80] D. Apsley. The CFD Process [Online]. Available: http://personalpages.manchester.ac.uk/staff/david.d.apsley/lectures/comphydr/cfdprocess.pdf

[81] ANSYS Inc, "Introduction to ANSYS CFX," ANSYS Post-Processing Document, Release 14.0, March 2012.

[82] F. Hürlimann, R. Kelm, M. Dugas, K. Oltmann, and G. Kress, "Mass Estimation of Transport Aircraft Wingbox Structures with a CAD/CAE-

Based Multidisciplinary Process," *Aerospace Science and Technology,* vol. 15, pp. 323-333, 2011.

[83] ANSYS Inc, "Introduction to ANSYS Blade Modeler," ANSYS BladeModeler Document, Release 14.0, April 2012.

[84] ANSYS Inc, "ANSYS-CFX Solver Theory Guide," ANSYS CFX Release 11.0, 2006. http://www1.ansys.com/customer/content/documentation/120/wb_cm.pdf.

[85] O. Özgen, "Design Improvements on Mixed Flow Pumps by Means of Computational Fluid Dynamics," Thesis, Mechanical Engineering, Middle East Technology University, December 2006.

[86] ANSYS Inc, "CFX-Mesh," ANSYS CFX online product documentation, Release 12.0, April 2009. http://www1.ansys.com/customer/content/documentation/120/wb_cm.pdf.

[87] N. Y. Luon, M. Z. Yusoff, and N. H. Shuaib, "Development of Improved Three Dimensional Unstructured Tetrahedral Mesh Generator," *World Academy of Science, Engineering and Technology,* vol. 34, pp. 152-159, 2009.

[88] Y.-T. Chiu, "Computational Fluid Dynamics Simulations of Hydraulic Energy Absorber," Thesis, Mechanical Engineering Department, Virginia Polytechnic Institute and State University, Blacksburg, Virginia, July 2000.

[89] ANSYS Inc, "Introduction to ANSYS Meshing," ANSYS Mesh Quality document, Release 14.0, March 2012.

[90] S. Khosrowpanah and M. L. Albertson, "Experimental Study of Cross-Flow Turbine," PhD Thesis, Civil Engineering Department, Colorado State University, Fort Collins, Colorado, 1984.

[91] T. Kitahora, J. Kurokawa, and J. Matsui, "Unsteady Flow Analysis for Cross-Flow Turbine by Use of MAC Method," in *International Conference on Fluid Engineering*, 1997.

[92] M. Abbott and D. Basco, *Computational Fluid Dynamics–An introduction for Engineers: Longman Scientific& Technical*: England, 1989.

[93] H. Liu, J. Wang, R. J. Brown, and N. Kelson, "Computational fluid dynamics (CFD) simulation of ultrahigh velocity abrasive waterjet," *Key Engineering Materials,* vol. 233, pp. 477-482, 2003.

[94] J. D. Anderson, *Computational Fluid Dynamics; the Basic with Application*: McGraw-Hill New York, 1995.

[95] J. H. Ferziger and M. Perić, *Computational Methods for Fluid Dynamics*: Springer Berlin, 2002.

[96] C. J. Roy, "Review of Discretization Error Estimators in Scientific Computing," *AIAA Paper,* vol. 126, 2010.

[97] H. Schlichting and J. Kestin, *Boundary-Layer Theory*: McGraw-Hill New York, 2000.

[98] R. J. Garde, *Turbulent Flow*: John Wiley & Sons 1994.

[99] H. K. Versteeg and W. Malalasekera, *An Introduction to Computational Fluid Dynamics: the Finite Volume Method*. Harlow: Pearson Education Limited: Prentice-hall, England, 1995.

[100] S. B. Pope, *Turbulent Flows*: Cambridge university press, 2000.

[101] T. Chung, *Computational Fluid Dynamics*: Cambridge university press, 2010.

[102] A. Orellano and H. Wengle, "Numerical Simulation (DNS and LES) of Manipulated Turbulent Boundary Layer Flow Over a Surface-Mounted Fence," *European Journal of Mechanics-B/Fluids,* vol. 19, pp. 765-788, 2000.

[103] J. Tu, G. H. Yeoh, and C. Liu, *Computational Fluid Dynamics: a Practical Approach*: Butterworth-Heinemann, 2007.

[104] O. Zikanov, *Essential Computational Fluid Dynamics*: John Wiley & Sons, 2011.

[105] F. M. White, *Fluid Mechanics*: McGraw-Hill Education, 2001.

[106] Y. Nakayama and R. Boucher, *Introduction to Fluid Mechanics*: Butterworth-Heinemann, 1998.

[107] P. K. Kundu and I. M. Cohen, *Fluid Mechanics*. San Diego: Academic Press 2010.

[108] H. Rubin and J. F. Atkinson, *Environmental Fluid Mechanics*: Marcel Dekker, Inc. CRC Press, 2001.

[109] F. R. Menter, "Two-Equation Eddy-Viscosity Turbulence Models for Engineering Applications," *AIAA journal,* vol. 32, pp. 1598-1605, 1994.

[110] D. C. Wilcox, *Turbulence Modeling for CFD*: DCW industries, Inc. La Canada, 1998.

[111] F. Menter, M. Kuntz, and R. Langtry, "Ten years of Industrial Experience with the SST Turbulence Model," *Turbulence, heat and mass transfer,* vol. 4, pp. 625-632, 2003.

[112] ANSYS Inc, "ANSYS-CFX Solver Modeling Guide," ANSYS CFX Release 13.0, 2010. ftp://ftp.stru.polimi.it/incoming/Mirzazadeh/cfx%20docs/cfx_mod.pdf.

[113] D. R. Liles, "Two Phase Flow," *Los Alamos Science,* vol. 2, 1981.

[114] K. Hiltunen, A. Jäsberg, S. Kallio, H. Karema, M. Kataja, A. Koponen, M. Manninen, and V. Taivassalo, "Multiphase Flow Dynamics :Theory and Numerics," VTT Technical Research Centre of Finland, 2009.

Appendices

Appendix A

Governing Equations

A.1 Governing Equations

The governing equations for fluid flow are solved numerically by ANSYS CFX to predict the ways in which fluid flows in a given situation. CFD simulation codes utilize the computer in the numerical calculations to the equations that govern the fluid flow [92]. Understanding of the equations that govern the fluid flow, the characteristics of fluid flow for a given situation, and so must be modelled is necessary in order to achieve acceptable results [93, 94]. Fundamental governing equations, to describe a fluid flow, are Navier Stokes equations for three-dimensional momentum and the continuity equation. The numerical discretization of the partial differential equations of these equations is solved by digital computers [95]. Numerical discretization can be performing by one of the three numerical discretization techniques: the finite volume method, the finite element method and the finite difference method [96]. The finite volume method is used in the numerical discretization of the partial differential equations by ANSYS CFX simulation code.

The majority of flow, for useful engineering applications, is turbulent in nature. As in such applications fast transfer of mass, momentum and energy are

desirable. Successfully simulating turbulent flow requires understanding a few basic characteristics of turbulent flow and modelling techniques in order to choose the best available turbulence models for a given situation. Turbulent flow is difficult to simulate since the turbulent flow is unsteady and three-dimensionally random. Turbulent eddies in all possible orientations appear in turbulent flow with a range of scales. The largest eddies extract energy from the mean flow and transfer it to the smallest eddies where energy is taken out of the flow through viscosity [97, 98]. The largest eddies are responsible for most of the momentum transfer. On the other hand, the smallest eddies are responsible for most the energy dissipation and known as the Kolmogorov [99, 100].

Direct Numerical Simulation (DNS), Large Eddy Simulation (LES) and Reynolds Averaged Navier-Stokes Simulation (RANS) are three approaches to make turbulence computationally tractable [101]. DNS is, the straight forward way, numerically solving the full Navier-Stokes equations directly, without any approximations applied in the calculation. It resolves the whole spectrum scales of motion in a flow down to the Kolmogorov scales [102]. However, it is too expensive. DNS requires a powerful computer and a lot of time; therefore, this method is not practical for engineering applications. LES resolves the large scale eddies directly while the small scale eddies are required to be modelled [103]. LES requires less powerful computer and time than DNS, but this method is still not practical for most engineering applications. RANS is widely used to describe the fluid flow for most engineering applications by solving the time-averaged Navier-Stokes equation. All turbulent eddy scales are required to be modelled in RANS [104].

The governing equations for the fluid flow are the continuity (conservation of mass) and momentum also known as Navier-Stoke equations (conservation of momentum) equations. For fluid flow involving heat transfer, another set of governing equations is required (conservation of energy).

Conservation of mass is a basic principle of engineering and science. It is a fundamental principle in nature. It states that, mass could neither be created nor destroyed. The mathematical statement of the conservation of mass is the continuity equation.

Conservation of mass based on the control volume theorem, let $M = m$, then $\xi = \frac{M}{m} = \frac{m}{m} = 1$, substituting $M = m$ and $\xi = 1$ in equation (3.8).

$$\frac{dm}{dt} = \frac{\partial}{\partial t}\int_{c.v} \rho dV + \int_{c.s} \rho \vec{v} \cdot dA \qquad \ldots (A.1)$$

from conservations law of mass $\frac{dm}{dt} = 0$,

for an infinitesimal control volume

$$\int_{c.v} \frac{\partial \rho}{\partial t} dV + \sum_{out} \dot{m} - \sum_{in} \dot{m} = 0 \qquad \ldots (A.2)$$

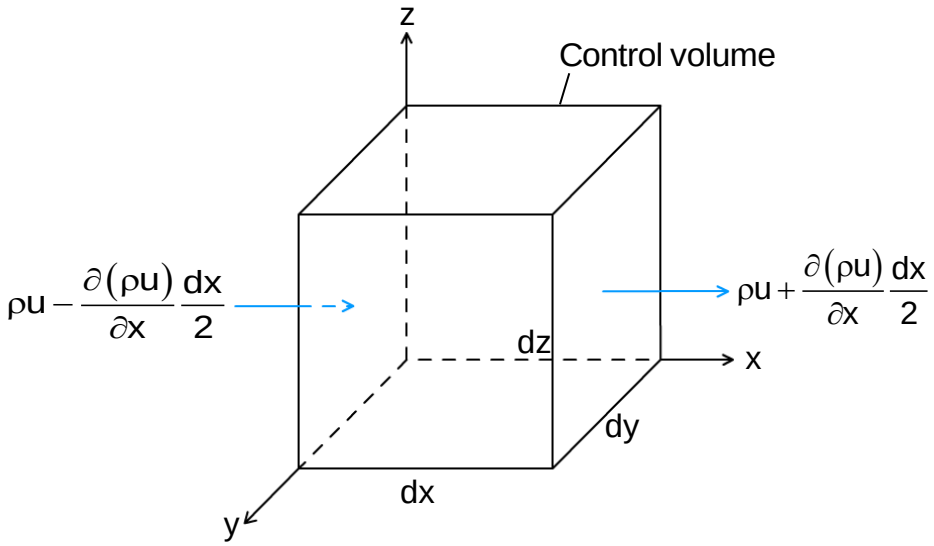

Fig. A.1 Mass flow through the x faces of the infinitesimal control volume.

Consider an infinitesimal fixed control volume of fluid of sides dx, dy and dz as shown in Fig. A.1. The velocities in x, y and z directions are u, v and w respectively. The mass flows in the center of the infinitesimal fixed control volume of fluid in the x-direction is then ρu and the corresponding mass flows in y- and z-direction is ρv and ρw, so the mass flows through each face of the infinitesimal fixed control volume can be written in terms of the mass flows in the center of control volume by using Taylor series.

$$(\rho u)_{\text{center of right face}} = \rho u + \frac{\partial(\rho u)}{\partial x}\frac{dx}{2} + \frac{1}{2!}\frac{\partial^2(\rho u)}{\partial x^2}\left(\frac{dx}{2}\right)^2 + \cdots \qquad \text{… (A.3)}$$

The mass of the fluid entering the control volume, terms of second order and higher are neglected, is

$$\sum_{\text{in}} \dot{m} \cong \left(\rho u - \frac{\partial(\rho u)}{\partial x}\frac{dx}{2}\right)dydz + \left(\rho v - \frac{\partial(\rho v)}{\partial y}\frac{dy}{2}\right)dxdz + \left(\rho w - \frac{\partial(\rho w)}{\partial z}\frac{dz}{2}\right)dxdy \qquad \text{… (A.4)}$$

The mass of the fluid leaving the control volume is

$$\sum_{\text{out}} \dot{m} \cong \left(\rho u + \frac{\partial(\rho u)}{\partial x}\frac{dx}{2}\right)dydz + \left(\rho v + \frac{\partial(\rho v)}{\partial y}\frac{dy}{2}\right)dxdz + \left(\rho w + \frac{\partial(\rho w)}{\partial z}\frac{dz}{2}\right)dxdy \qquad \text{… (A.5)}$$

And the increase in the mass of the control volume equal to

$$\frac{\partial}{\partial t}(\rho dxdydz) \qquad \text{… (A.6)}$$

Substituting equations (A.4), (A.5) and (A.6) into equation (A.2) and simplifying where most terms disappear equation (A.2) becomes

$$\frac{\partial}{\partial t}(\rho dxdydz)+\frac{\partial(\rho u)}{\partial x}dxdydz+\frac{\partial(\rho v)}{\partial y}dxdydz+\frac{\partial(\rho w)}{\partial z}dxdydz=0 \quad \text{… (A.7)}$$

The continuity equation and also known as the differential equation for mass conservation can be obtained by dividing the equation (A.7) by ($dxdydz$),

$$\frac{\partial \rho}{\partial t}+\frac{\partial(\rho u)}{\partial x}+\frac{\partial(\rho v)}{\partial y}+\frac{\partial(\rho w)}{\partial z}=0 \quad \text{… (A.8)}$$

since $\nabla = i\frac{\partial}{\partial x}+j\frac{\partial}{\partial y}+k\frac{\partial}{\partial z}$, and the velocity vector $\vec{v}=iu+jv+kw$, the equation (A.8) can be written in the vector form as

$$\frac{\partial \rho}{\partial t}+\nabla(\rho\vec{v})=0 \quad \text{… (A.9)}$$

Conservation of momentum equations are derived by applying Newton's second law of fluid motion. Conservation of momentum based on the control volume theorem, let $M=m\vec{v}$ then $\xi=\frac{M}{m}=\frac{m\vec{v}}{m}=\vec{v}$, substituting $M=m\vec{v}$ and $\xi=\vec{v}$ in equation (3.8).

$$\frac{d(m\vec{v})}{dt}=\frac{\partial}{\partial t}\int_{c.v}\rho\vec{v}dV+\int_{c.s}\rho\vec{v}\vec{v}\cdot dA \quad \text{… (A.10)}$$

Newton's second law states that the sum of external forces acting on a moving system is equal to the time rate of change of momentum of the system.

$$\sum \vec{F} = \frac{d}{dt}\left(m\vec{v}\right) \quad \text{… (A.11)}$$

Now, we are going to write the system formulation of Newton's law in control volume formulation.

$$\sum \vec{F} = \frac{d\left(m\vec{v}\right)}{dt} = \frac{\partial}{\partial t}\int_{c.v} \rho\vec{v}dV + \sum_{out} \dot{m}\vec{v} - \sum_{in} \dot{m}\vec{v} \quad \text{… (A.12)}$$

the element is so small that the volume integral simply reduces to a derivative term

$$\frac{\partial}{\partial t}\int_{c.v} \rho\vec{v}dV \approx \frac{\partial}{\partial t}\left(\rho\vec{v}\right)dxdydz \quad \text{… (A.13)}$$

The momentum flows occur on the faces of the infinitesimal fixed control volume of fluid, three inlets and three outlets. Figure A.1, shows only the x-component to avoid cluttering up the drawing.

$$\sum_{in} \dot{m}\vec{v} \cong \left(\rho u\vec{v} - \frac{\partial\left(\rho u\vec{v}\right)}{\partial x}\frac{dx}{2}\right)dydz + \left(\rho v\vec{v} - \frac{\partial\left(\rho v\vec{v}\right)}{\partial y}\frac{dy}{2}\right)dxdz + \left(\rho w\vec{v} - \frac{\partial\left(\rho w\vec{v}\right)}{\partial z}\frac{dz}{2}\right)dxdy \quad \text{… (A.14)}$$

$$\sum_{out} \dot{m}\vec{v} \cong \left(\rho u\vec{v} + \frac{\partial\left(\rho u\vec{v}\right)}{\partial x}\frac{dx}{2}\right)dydz + \left(\rho v\vec{v} + \frac{\partial\left(\rho v\vec{v}\right)}{\partial y}\frac{dy}{2}\right)dxdz + \left(\rho w\vec{v} + \frac{\partial\left(\rho w\vec{v}\right)}{\partial z}\frac{dz}{2}\right)dxdy \quad \text{… (A.15)}$$

Substituting equations (A.13), (A.14) and (A.15) into equation (A.12) and simplifying where most terms disappear, equation (A.12) becomes

$$\sum \vec{F} = \left[\frac{\partial}{\partial t}\left(\rho\vec{v}\right) + \frac{\partial}{\partial x}\left(\rho u\vec{v}\right) + \frac{\partial}{\partial y}\left(\rho v\vec{v}\right) + \frac{\partial}{\partial z}\left(\rho w\vec{v}\right)\right]dxdydz \quad \text{… (A.16)}$$

Split up the vector relation in brackets as

$$\frac{\partial}{\partial t}(\rho\vec{v})+\frac{\partial}{\partial x}(\rho u\vec{v})+\frac{\partial}{\partial y}(\rho v\vec{v})+\frac{\partial}{\partial z}(\rho w\vec{v}) = \vec{v}\left[\frac{\partial\rho}{\partial t}+\nabla\cdot(\rho\vec{v})\right]+\rho\left(\frac{\partial\vec{v}}{\partial t}+u\frac{\partial\vec{v}}{\partial x}+v\frac{\partial\vec{v}}{\partial y}+w\frac{\partial\vec{v}}{\partial z}\right) \quad \text{… (A.17)}$$

The terms on the right hand side contain the continuity equation, $\frac{\partial\rho}{\partial t}+\nabla.(\rho\vec{v})=0$, which vanished. The term in parenthesis is the total acceleration

$$\frac{\partial\vec{v}}{\partial t}+u\frac{\partial\vec{v}}{\partial x}+v\frac{\partial\vec{v}}{\partial y}+w\frac{\partial\vec{v}}{\partial z}=\frac{d\vec{v}}{dt} \quad \text{… (A.18)}$$

Thus equation (A.16) can be reduced to

$$\sum\vec{F}=\rho\frac{d\vec{v}}{dt}dxdydz \quad \text{… (A.19)}$$

Express the total force as the sum of body forces and surface forces

$$\sum\vec{F}_{body}+\sum\vec{F}_{surface}=\rho\frac{d\vec{v}}{dt}dxdydz \quad \text{… (A.20)}$$

The forces acting on the control volume are body forces and surface forces [105]. The body forces act on the mass within the control volume. The body forces are gravity, centrifugal, coriolis (a result of centripetal force on a fluid mass moving with a velocity radially outward in a rotating plane), magnetism and electric potential forces. The surface forces are hydrostatic pressure and viscous stresses (τ_{ij}) which acting on the control surface sides arise from motion with velocity gradients [106].

$$\sigma_{ij} = \begin{pmatrix} -p+\tau_{xx} & \tau_{yx} & \tau_{zx} \\ \tau_{xy} & -p+\tau_{yy} & \tau_{zy} \\ \tau_{xz} & \tau_{yz} & -p+\tau_{zz} \end{pmatrix} \quad \ldots (A.21)$$

Stresses subscript notation is shown in Fig. A.2.

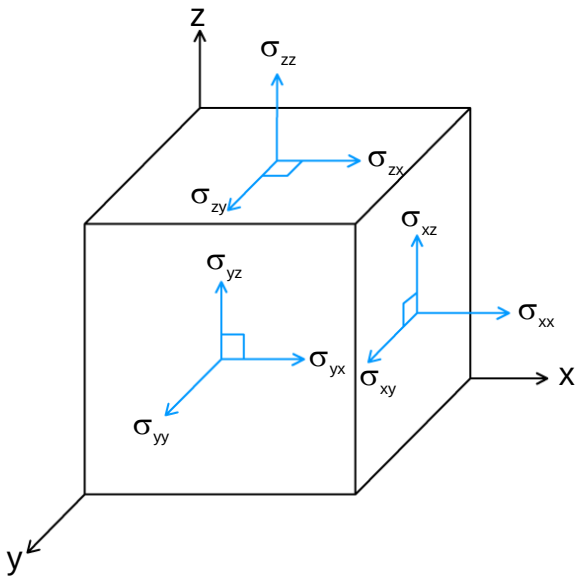

Fig. A.2 Stress components on the faces of an infinitesimal control volume.

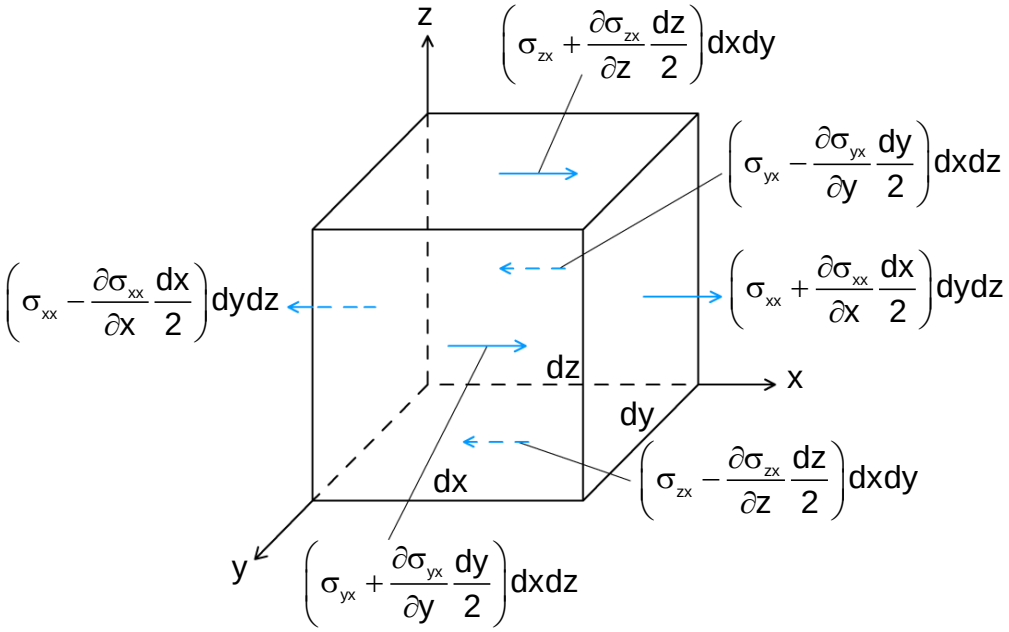

Fig. A.3 The surface force components in x direction of an infinitesimal control volume

Only the x-directed stresses are shown in Fig. A.3 to avoid cluttering up the drawing. The stresses' gradients (or differences) cause a net force on the infinitesimal fixed control surface. For example, the force on the left face ($\sigma_{xx}dydz$) is balanced by the force on the right face ($\sigma_{xx}dydz$) leaving the net force ($\left(\partial\sigma_{xx}/\partial x\right)dxdydz$) on the right face; therefore, in the x direction the net surface force is

$$dF_{x,surfaces} = \left[\frac{\partial}{\partial x}\left(\sigma_{xx}\right) + \frac{\partial}{\partial y}\left(\sigma_{yx}\right) + \frac{\partial}{\partial z}\left(\sigma_{zx}\right)\right]dxdydz \qquad \ldots (A.22)$$

From the equation (A.22) the surface force in the x direction is proportional to the control volume. Since the surface force is pressure and viscous forces equation (A.22) can be written as

$$\frac{dF_x}{dV} = -\frac{\partial p}{\partial x} + \frac{\partial}{\partial x}\left(\tau_{xx}\right) + \frac{\partial}{\partial y}\left(\tau_{yx}\right) + \frac{\partial}{\partial z}\left(\tau_{zx}\right) \qquad \ldots (A.23)$$

Similarly, for the y and z directions, the net surface forces per unit volume on the control surface are

$$\frac{dF_y}{dV} = -\frac{\partial p}{\partial y} + \frac{\partial}{\partial x}\left(\tau_{xy}\right) + \frac{\partial}{\partial y}\left(\tau_{yy}\right) + \frac{\partial}{\partial z}\left(\tau_{zy}\right) \qquad \ldots (A.24)$$

$$\frac{dF_z}{dV} = -\frac{\partial p}{\partial z} + \frac{\partial}{\partial x}\left(\tau_{xz}\right) + \frac{\partial}{\partial y}\left(\tau_{yz}\right) + \frac{\partial}{\partial z}\left(\tau_{zz}\right) \qquad \ldots (A.25)$$

Now, multiply equations (A.23), (A.24) and (A.25) by i, j and k respectively, and add to get the net vector surface force expression as follows,

$$\left(\frac{dF}{dV}\right)_{surface} = -\nabla p + \left(\frac{dF}{dV}\right)_{viscous} \qquad \ldots (A.26)$$

Where the viscous force are

$$\left(\frac{dF}{dV}\right)_{viscous} = i\left(\frac{\partial\tau_{xx}}{\partial x}+\frac{\partial\tau_{yx}}{\partial y}+\frac{\partial\tau_{zx}}{\partial z}\right) + j\left(\frac{\partial\tau_{xy}}{\partial x}+\frac{\partial\tau_{yy}}{\partial y}+\frac{\partial\tau_{zy}}{\partial z}\right) + k\left(\frac{\partial\tau_{xz}}{\partial x}+\frac{\partial\tau_{yz}}{\partial y}+\frac{\partial\tau_{zz}}{\partial z}\right) \quad \ldots (A.27)$$

equation (A.27) can be written in divergence form

$$\left(\frac{dF}{dV}\right)_{viscous} = \nabla\cdot\tau_{ij} \quad \ldots (A.28)$$

$$\left(\frac{dF}{dV}\right)_{surface} = -\nabla p + \nabla\cdot\tau_{ij} \quad \ldots (A.29)$$

where the viscous stress tensor acting on the infinitesimal control volume is

$$\tau_{ij} = \begin{pmatrix} \tau_{xx} & \tau_{yx} & \tau_{zx} \\ \tau_{xy} & \tau_{yy} & \tau_{zy} \\ \tau_{xz} & \tau_{yz} & \tau_{zz} \end{pmatrix} \quad \ldots (A.30)$$

The surface force is the pressure-gradient vector plus the divergence of viscous-stress tensor. Substituting equations (A.20) and (A.29) into equation (A.19), to get the basic differential momentum equation for an infinitesimal element.

$$\rho\frac{d\vec{v}}{dt} = -\nabla p + \nabla.\tau_{ij} + \vec{f} \quad \ldots (A.31)$$

Where $\vec{f}$ is the body force per unit volume and $(d\vec{v}/dt)$ is the acceleration vector of the flow, which is the total time derivative of the velocity vector.

$$\frac{d\vec{v}}{dt} = i\frac{du}{dt} + j\frac{dv}{dt} + k\frac{dw}{dt} \quad \text{… (A.32)}$$

Each velocity component u, v and w is a function of x, y, z and t variables, to get the time derivative of these velocity components we need to use the chain rule.

$$\frac{du(x,y,z,t)}{dt} = \frac{\partial u}{\partial t} + \frac{\partial u}{\partial x}\frac{dx}{dt} + \frac{\partial u}{\partial y}\frac{dy}{dt} + \frac{\partial u}{\partial z}\frac{dz}{dt} \quad \text{… (A.33)}$$

since dx/dt = u, dy/dt = v and dz/dt = w are the local velocity component, equation (A.33) can be written as

$$\frac{du}{dt} = \frac{\partial u}{\partial t} + u\frac{\partial u}{\partial x} + v\frac{\partial u}{\partial y} + w\frac{\partial u}{\partial z} \quad \text{… (A.34)}$$

Similarly for dv/dt and dw/dt components. Summing du/dt, dv/dt and dv/dt into a vector to get the total acceleration.

$$\frac{d\vec{v}}{dt} = \frac{\partial \vec{v}}{\partial t} + u\frac{\partial \vec{v}}{\partial x} + v\frac{\partial \vec{v}}{\partial y} + w\frac{\partial \vec{v}}{\partial z} = \frac{\partial \vec{v}}{\partial t} + (\vec{v}\cdot\nabla)\vec{v} \quad \text{… (A.35)}$$

Substituting equation (A.35) into equation (A.31)

$$\rho\frac{\partial \vec{v}}{\partial t} + \rho(\vec{v}.\nabla)\vec{v} = -\nabla p + \nabla.\tau_{ij} + \vec{f} \quad \text{… (A.36)}$$

Equation (A.36) is, so brief and compact, a vector equation. Therefore, writing out the components of the equation terms, it is required to illustrate the momentum equation.

$$\rho\left(\frac{\partial u}{\partial t} + u\frac{\partial u}{\partial x} + v\frac{\partial u}{\partial y} + w\frac{\partial u}{\partial z}\right) = -\frac{\partial p}{\partial x} + \frac{\partial \tau_{xx}}{\partial x} + \frac{\partial \tau_{yx}}{\partial y} + \frac{\partial \tau_{zx}}{\partial z} + f_x \quad \text{… (A.37)}$$

$$\rho\left(\frac{\partial v}{\partial t}+u\frac{\partial v}{\partial x}+v\frac{\partial v}{\partial y}+w\frac{\partial v}{\partial z}\right)=-\frac{\partial p}{\partial y}+\frac{\partial \tau_{xy}}{\partial x}+\frac{\partial \tau_{yy}}{\partial y}+\frac{\partial \tau_{zy}}{\partial z}+f_y \quad \ldots (A.38)$$

$$\rho\left(\frac{\partial w}{\partial t}+u\frac{\partial w}{\partial x}+v\frac{\partial w}{\partial y}+w\frac{\partial w}{\partial z}\right)=-\frac{\partial p}{\partial z}+\frac{\partial \tau_{xz}}{\partial x}+\frac{\partial \tau_{yz}}{\partial y}+\frac{\partial \tau_{zz}}{\partial z}+f_z \quad \ldots (A.39)$$

The above equations are the differential momentum equations, and they are the equations of motion [107]. However, these equations are not ready to use. The viscous stresses are required to be written in terms of velocity components. The velocity of fluid particles $\vec{v}$ may translate, rotate or deform, in general, it will do all three and the velocity gradient results from distortion and rigid body rotation of the particles. A general formula for a sum of a symmetric strain tensor and asymmetric vorticity tensor parts is $\frac{1}{2}\left(\frac{\partial u_i}{\partial x_j}+\frac{\partial u_j}{\partial x_i}\right)+\frac{1}{2}\left(\frac{\partial u_i}{\partial x_j}-\frac{\partial u_j}{\partial x_i}\right)$ [108]. The velocity gradient may be written in components form as

$$\frac{\partial u}{\partial x}=\frac{1}{2}\left(\frac{\partial u}{\partial x}+\frac{\partial u}{x}\right)+\frac{1}{2}\left(\frac{\partial u}{\partial x}-\frac{\partial u}{\partial x}\right)=\in_{xx}+\Omega_{xx} \quad \ldots (A.40)$$

$$\frac{\partial v}{\partial x}=\frac{1}{2}\left(\frac{\partial v}{\partial x}+\frac{\partial u}{\partial y}\right)+\frac{1}{2}\left(\frac{\partial v}{\partial x}-\frac{\partial u}{\partial y}\right)=\in_{yx}+\Omega_{yx} \quad \ldots (A.41)$$

$$\frac{\partial w}{\partial x}=\frac{1}{2}\left(\frac{\partial w}{\partial x}+\frac{\partial u}{\partial z}\right)+\frac{1}{2}\left(\frac{\partial w}{\partial x}-\frac{\partial u}{\partial z}\right)=\in_{zx}+\Omega_{zx} \quad \ldots (A.42)$$

Similarly,

$$\frac{\partial u}{\partial y}=\frac{1}{2}\left(\frac{\partial u}{\partial y}+\frac{\partial v}{\partial x}\right)+\frac{1}{2}\left(\frac{\partial u}{\partial y}-\frac{\partial v}{\partial x}\right)=\in_{xy}+\Omega_{xy} \quad \ldots (A.43)$$

$$\frac{\partial v}{\partial y}=\frac{1}{2}\left(\frac{\partial v}{\partial y}+\frac{\partial v}{\partial y}\right)+\frac{1}{2}\left(\frac{\partial v}{\partial y}-\frac{\partial v}{\partial y}\right)=\in_{yy}+\Omega_{yy} \quad \ldots (A.44)$$

$$\frac{\partial w}{\partial y}=\frac{1}{2}\left(\frac{\partial w}{\partial y}+\frac{\partial v}{\partial z}\right)+\frac{1}{2}\left(\frac{\partial w}{\partial y}-\frac{\partial v}{\partial z}\right)=\in_{zy}+\Omega_{zy} \quad \ldots (4.45)$$

Also,

$$\frac{\partial u}{\partial z}=\frac{1}{2}\left(\frac{\partial u}{\partial z}+\frac{\partial w}{\partial x}\right)+\frac{1}{2}\left(\frac{\partial u}{\partial z}-\frac{\partial w}{\partial x}\right)=\in_{xz}+\Omega_{xz} \quad \ldots (A.46)$$

$$\frac{\partial v}{\partial z}=\frac{1}{2}\left(\frac{\partial v}{\partial z}+\frac{\partial w}{\partial y}\right)+\frac{1}{2}\left(\frac{\partial v}{\partial z}-\frac{\partial w}{\partial y}\right)=\in_{yz}+\Omega_{yz} \quad \ldots (A.47)$$

$$\frac{\partial w}{\partial z}=\frac{1}{2}\left(\frac{\partial w}{\partial z}+\frac{\partial w}{\partial z}\right)+\frac{1}{2}\left(\frac{\partial w}{\partial z}-\frac{\partial w}{\partial z}\right)=\in_{zz}+\Omega_{zz} \quad \ldots (A.48)$$

We can see that $\in_{xy}=\in_{yx},\in_{xz}=\in_{zx},\in_{yz}=\in_{zy}$, and $\Omega_{xx}=\Omega_{yy}=\Omega_{zz}=0$.

Where the symmetric strain (deformation) rate tensor is

$$\in_{ij}=\begin{pmatrix}\in_{xx} & \in_{xy} & \in_{xz}\\ \in_{yx} & \in_{yy} & \in_{yz}\\ \in_{zx} & \in_{zy} & \in_{zz}\end{pmatrix}=\begin{pmatrix}\frac{\partial u}{\partial x} & \frac{1}{2}\left(\frac{\partial u}{\partial y}+\frac{\partial v}{\partial x}\right) & \frac{1}{2}\left(\frac{\partial u}{\partial z}+\frac{\partial w}{\partial x}\right)\\ \frac{1}{2}\left(\frac{\partial v}{\partial x}+\frac{\partial u}{\partial y}\right) & \frac{\partial v}{\partial y} & \frac{1}{2}\left(\frac{\partial v}{\partial z}+\frac{\partial w}{\partial y}\right)\\ \frac{1}{2}\left(\frac{\partial w}{\partial x}+\frac{\partial u}{\partial z}\right) & \frac{1}{2}\left(\frac{\partial w}{\partial y}+\frac{\partial v}{\partial z}\right) & \frac{\partial w}{\partial z}\end{pmatrix} \quad \ldots (A.49)$$

The viscous stresses for a Newtonian fluid are proportional to the coefficient of viscosity and the element strain rates. The generalization of $\tau=\mu(d\theta/dt)=\mu(du/dy)$ to three-dimensional viscous flow is

$$\left.\begin{aligned}&\tau_{xx}=2\mu\frac{\partial u}{\partial x}+\zeta\nabla\cdot\vec{v} \quad \tau_{yy}=2\mu\frac{\partial v}{\partial y}+\zeta\nabla\cdot\vec{v}, \quad \tau_{zz}=2\mu\frac{\partial w}{\partial z}+\zeta\nabla\cdot\vec{v}\\ &\tau_{xy}=\tau_{yx}=\mu\left(\frac{\partial u}{\partial y}+\frac{\partial v}{\partial x}\right), \qquad \tau_{xz}=\tau_{zx}=\mu\left(\frac{\partial w}{\partial x}+\frac{\partial u}{\partial z}\right),\\ &\tau_{yz}=\tau_{zy}=\mu\left(\frac{\partial v}{\partial z}+\frac{\partial w}{\partial y}\right)\end{aligned}\right\} \quad \ldots (A.50)$$

Substituting the above equations of (τ_{ij}) into equations (A.37), (A.38) and (A.39) gives the differential momentum equation for a Newtonian fluid (the Navier-Stokes equations) for the compressible flow.

$$\rho\left(\frac{\partial u}{\partial t}+u\frac{\partial u}{\partial x}+v\frac{\partial u}{\partial y}+w\frac{\partial u}{\partial z}\right)=-\frac{\partial p}{\partial x}+\frac{\partial}{\partial x}\left(2\mu\frac{\partial u}{\partial x}+\zeta\nabla\cdot\vec{v}\right)+\frac{\partial}{\partial y}\left(\mu\left(\frac{\partial u}{\partial y}+\frac{\partial v}{\partial x}\right)\right)+\frac{\partial}{\partial z}\left(\mu\left(\frac{\partial u}{\partial z}+\frac{\partial w}{\partial x}\right)\right)+f_x \quad \text{… (A.51)}$$

$$\rho\left(\frac{\partial v}{\partial t}+u\frac{\partial v}{\partial x}+v\frac{\partial v}{\partial y}+w\frac{\partial v}{\partial z}\right)=-\frac{\partial p}{\partial y}+\frac{\partial}{\partial x}\left(\mu\left(\frac{\partial u}{\partial y}+\frac{\partial v}{\partial x}\right)\right)+\frac{\partial}{\partial y}\left(2\mu\frac{\partial v}{\partial y}+\zeta\nabla\cdot\vec{v}\right)+\frac{\partial}{\partial z}\left(\mu\left(\frac{\partial v}{\partial z}+\frac{\partial w}{\partial y}\right)\right)+f_y \quad \text{… (A.52)}$$

$$\rho\left(\frac{\partial w}{\partial t}+u\frac{\partial w}{\partial x}+v\frac{\partial w}{\partial y}+w\frac{\partial w}{\partial z}\right)=-\frac{\partial p}{\partial z}+\frac{\partial}{\partial x}\left(\mu\left(\frac{\partial u}{\partial z}+\frac{\partial w}{\partial x}\right)\right)+\frac{\partial}{\partial y}\left(\mu\left(\frac{\partial v}{\partial z}+\frac{\partial w}{\partial y}\right)\right)+\frac{\partial}{\partial z}\left(2\mu\frac{\partial w}{\partial z}+\zeta\nabla\cdot\vec{v}\right)+f_z \quad \text{… (A.53)}$$

For incompressible flow ($\nabla.\vec{v}=0$) and hence ($\tau_{ij}=2\mu\in_{ij}$), Substituting these into equations (A.51), (A.52) and (A.53) gives the differential momentum equation for a Newtonian fluid (the Navier-Stokes equations) for the incompressible flow.

$$\rho\left(\frac{\partial u}{\partial t}+u\frac{\partial u}{\partial x}+v\frac{\partial u}{\partial y}+w\frac{\partial u}{\partial z}\right)=-\frac{\partial p}{\partial x}+\mu\left(\frac{\partial^2 u}{\partial x^2}+\frac{\partial^2 u}{\partial y^2}+\frac{\partial^2 u}{\partial z^2}\right)+f_x \quad \text{… (A.54)}$$

$$\rho\left(\frac{\partial v}{\partial t}+u\frac{\partial v}{\partial x}+v\frac{\partial v}{\partial y}+w\frac{\partial v}{\partial z}\right)=-\frac{\partial p}{\partial y}+\mu\left(\frac{\partial^2 v}{\partial x^2}+\frac{\partial^2 v}{\partial y^2}+\frac{\partial^2 v}{\partial z^2}\right)+f_y \quad \text{… (A.55)}$$

$$\rho\left(\frac{\partial w}{\partial t}+u\frac{\partial w}{\partial x}+v\frac{\partial w}{\partial y}+w\frac{\partial w}{\partial z}\right)=-\frac{\partial p}{\partial z}+\mu\left(\frac{\partial^2 w}{\partial x^2}+\frac{\partial^2 w}{\partial y^2}+\frac{\partial^2 w}{\partial z^2}\right)+f_z \quad \text{… (A.56)}$$

A.2 Reynolds Averaged Navier-Stokes Equations (RANS)

Reynolds Averaged Navier-Stokes equations (RANS) are widely used to describe the fluid flow for most engineering applications. RANS equations are produced by the flow variables decomposition in the Navier-Stokes equations into the mean (time-average) and fluctuating components. The decomposition of a velocity component u recording to Reynolds (1895) is a time-average motion and a turbulent fluctuation [105], as follows,

$$u = \bar{u} + u' \qquad \ldots (A.57)$$

where u is the instantaneous velocity, $\bar{u}$ is the mean (time-average) velocity and u' is the fluctuating velocity, then the flow variables decomposition in the momentum equation (A.36) gives the Reynolds equation as follows,

$$\rho \frac{\partial \vec{\bar{v}}}{\partial t} + \rho\left(\vec{\bar{v}} \cdot \nabla\right)\vec{\bar{v}} = -\nabla \bar{p} + \nabla \cdot \left(\bar{\tau}_{ij} + \tau_t\right) + \vec{\bar{f}} \qquad \ldots (A.58)$$

where τ_t is the Reynolds stress tensor (Turbulent stress tensor). It is symmetrical. The Reynolds stresses are produced by decomposing procedure and they are six unknown terms. These terms must be modeled to solve the RANS equation; therefore, a turbulence model is required.

$$\tau_t = -\rho\overline{\vec{v}'\vec{v}'} = -\rho\begin{pmatrix} \overline{u'^2} & \overline{u'v'} & \overline{u'w'} \\ \overline{v'u'} & \overline{v'^2} & \overline{v'w'} \\ \overline{w'u'} & \overline{w'v'} & \overline{w'^2} \end{pmatrix} \qquad \ldots (A.59)$$

A.2.1 Shear Stress Transport (SST) Model

Shear stress transport (SST) model of Monter [109] is a hybrid two-equation model. SST model is a combination of the standard k-epsilon model and the original Wilcox's k-omega model. It results from adding the transformation of the standard k-epsilon model times $(1-F_1)$ to the original k-omega model times F_1 with modifying the eddy viscosity to account for the transport of the principle turbulent shear stress. Hence, the SST model combines the advantages of the standard k-epsilon model away from walls and the original Wilcox's k-omega model [110] for use near walls using a blending function. A blending function F_1 is equal to one near walls and equal to zero away from the walls. A blend function F_1 activates the k-omega model near walls and the k-epsilon model for the rest of the flow. The turbulent kinetic energy k and the turbulence frequency ω for Wilcox's k-omega and Transformed k-epsilon model are as follows;

Wilcox's k-omega model:

$$\frac{\partial(\rho k)}{\partial t}+\nabla\cdot(\rho\vec{v}k)=\nabla\cdot\left[\left(\mu+\frac{\mu_t}{\sigma_{k1}}\right)\nabla k\right]+p_k-B'\rho k\omega \qquad \ldots (A.60)$$

$$\frac{\partial(\rho\omega)}{\partial t}+\nabla\cdot(\rho\vec{v}\omega)=\nabla\cdot\left[\left(\mu+\frac{\mu_t}{\sigma_{\omega1}}\right)\nabla\omega\right]+A_1\frac{\omega}{k}p_k-B_1\rho\omega^2 \qquad \ldots (A.61)$$

Transformed k-epsilon model:

$$\frac{\partial(\rho k)}{\partial t}+\nabla\cdot(\rho\vec{v}k)=\nabla\cdot\left[\left(\mu+\frac{\mu_t}{\sigma_{k2}}\right)\nabla k\right]+p_k-B'\rho k\omega \qquad \ldots (A.62)$$

$$\frac{\partial(\rho\omega)}{\partial t}+\nabla\cdot(\rho\vec{v}\omega) = \left(\nabla\cdot\left[\left(\mu+\frac{\mu_t}{\sigma_{\omega 2}}\right)\nabla\omega\right]+2\rho\frac{1}{\sigma_{\omega 2}\omega}\nabla k\nabla\omega+A_2\frac{\omega}{k}p_k-B_2\rho\omega^2\right) \quad \ldots (A.63)$$

Now multiplied equations (A.60) and (A.61) by function F_1, and equations (A.62) and (A.63) by $(1-F_1)$ and then adding the corresponding k- and ω-equation to give the new model (p_k is the production rate of turbulence).

$$\frac{\partial(\rho k)}{\partial t}+\nabla\cdot(\rho\vec{v}k)=\nabla\cdot\left[\left(\mu+\frac{\mu_t}{\sigma_{k3}}\right)\nabla k\right]+p_k-B'\rho k\omega \quad \ldots (A.64)$$

$$\frac{\partial(\rho\omega)}{\partial t}+\nabla\cdot(\rho\vec{v}\omega)= \nabla\cdot\left[\left(\mu+\frac{\mu_t}{\sigma_{\omega 3}}\right)\nabla\omega\right]+2(1-F_1)\frac{\rho}{\sigma_{\omega 2}\omega}\nabla k\nabla\omega+A_3\frac{\omega}{k}p_k-B_3\rho\omega^2 \quad \ldots (A.65)$$

where F_1 is a blending function and given by:

$$F_1=\tanh\left(\left(\min\left(\max\left(\frac{\sqrt{k}}{B'\omega y},\frac{500\nu}{y^2\omega}\right),\frac{4\rho k}{CD_{k\omega}\sigma_{\omega 2}y^2}\right)\right)^4\right) \quad \ldots (A.66)$$

With $CD_{k\omega}=\max\left(2\rho\frac{1}{\sigma_{\omega 2}\omega}\nabla k\nabla\omega, 1.0\times10^{-10}\right)$, ν is the kinematic viscosity and y is the distance to the nearest surface. The kinematic eddy viscosity, $\nu_t=\mu_t/\rho$, is

$$\nu_t=\frac{c_1 k}{\max(c_1\omega,\lambda F_2)} \quad \ldots (A.67)$$

where λ is a constant measure of the strain rate.

$$\tilde{\lambda} = \sqrt{2\Omega_{ij}\Omega_{ij}} \quad \text{… (A.68)}$$

and F_2 is a blending function similar to F_1.

$$F_2 = \tanh\left(\left(\max\left(\frac{2\sqrt{k}}{B'\omega y}, \frac{500\nu}{y^2\omega}\right)\right)^2\right) \quad \text{… (A.69)}$$

The new model coefficients are a linear combination of the corresponding coefficients of the $k-\omega$ and modified $k-\varepsilon$ models, $\Phi = \Phi_1 F_1 + \Phi_2(1-F_1)$. And the constant are: $A_1 = 5/9, B_1 = 0.075, \sigma_{k1} = 0.85, \sigma_{\omega 1} = 0.5, B' = 0.09,$ $c_1 = 0.31$ $A_2 = 0.44$, $B_2 = 0.0828$, $\sigma_{k2} = 1$ and $\sigma_{\omega 2} = 1/0.856$ [111].

A.3 Two-Phase Fluid Flow

Two-phase fluid flow is a fluid flow situation in which two fluids are present. A complete analysis of the internal flow of the cross-flow turbine, which is of turbulent, two-phase and three dimensional in nature, was undertaken by simulating it using ANSYS CFX with a two-phase flow and free surface model. Free surface fluid flow is a multiphase fluid flow situation in which the phases are separated by a distinct interface (commonly air and water). Fundamental governing equations, to describe a fluid flow (two-phase flow), are Navier Stokes equations for three-dimensional momentum and the continuity equation. Two-phase fluid flow is expressed by considering each phase independently. Thus, the two-phase (air-water) is formulated in terms of two sets of mass and momentum conservation equations. Each set describes the fluid flow for one phase [112]. However, since each phase is not independent of the other phase,

interaction terms have to be introduced in the conservation equations to the two phases from the interfaces.

The continuity equation taken from Liles [113] for multiphase fluid flow is shown in equation (A.70),

$$\frac{\partial \alpha_n \rho_n}{\partial t} + \nabla.\left(\alpha_n \rho_n \vec{v}_n\right) = \Gamma_n \qquad \ldots (A.70)$$

Where α_n is the volume fraction, therefore, the sum of the volume fraction of the two-phase flow must be one,

$$\sum_{n=1}^{2} \alpha_n = 1 \qquad \ldots (A.71)$$

and Γ_n is the rate of production of the nth phase mass at the interfaces and it must be zero,

$$\sum_{n=1}^{2} \Gamma_n = 0 \qquad \ldots (A.72)$$

The momentum equation taken from Hiltunen [114] for multiphase fluid flow is shown in equation (A.73),

$$\frac{\partial}{\partial t}\left(\alpha_n \rho_n \vec{v}_n\right) + \alpha_n \rho_n \left(\vec{v}.\nabla\right)\vec{v}_n = -\nabla\left(\alpha_n p_n\right) + \nabla.\left(\alpha_n \tau_n + \alpha_n \tau_{t,n} + M_n\right) + \vec{f} \qquad \ldots (A.73)$$

Where M_n is the interfacial force acting on a phase due to the presence of other phase.

Appendix B

Results of Pressure Contours

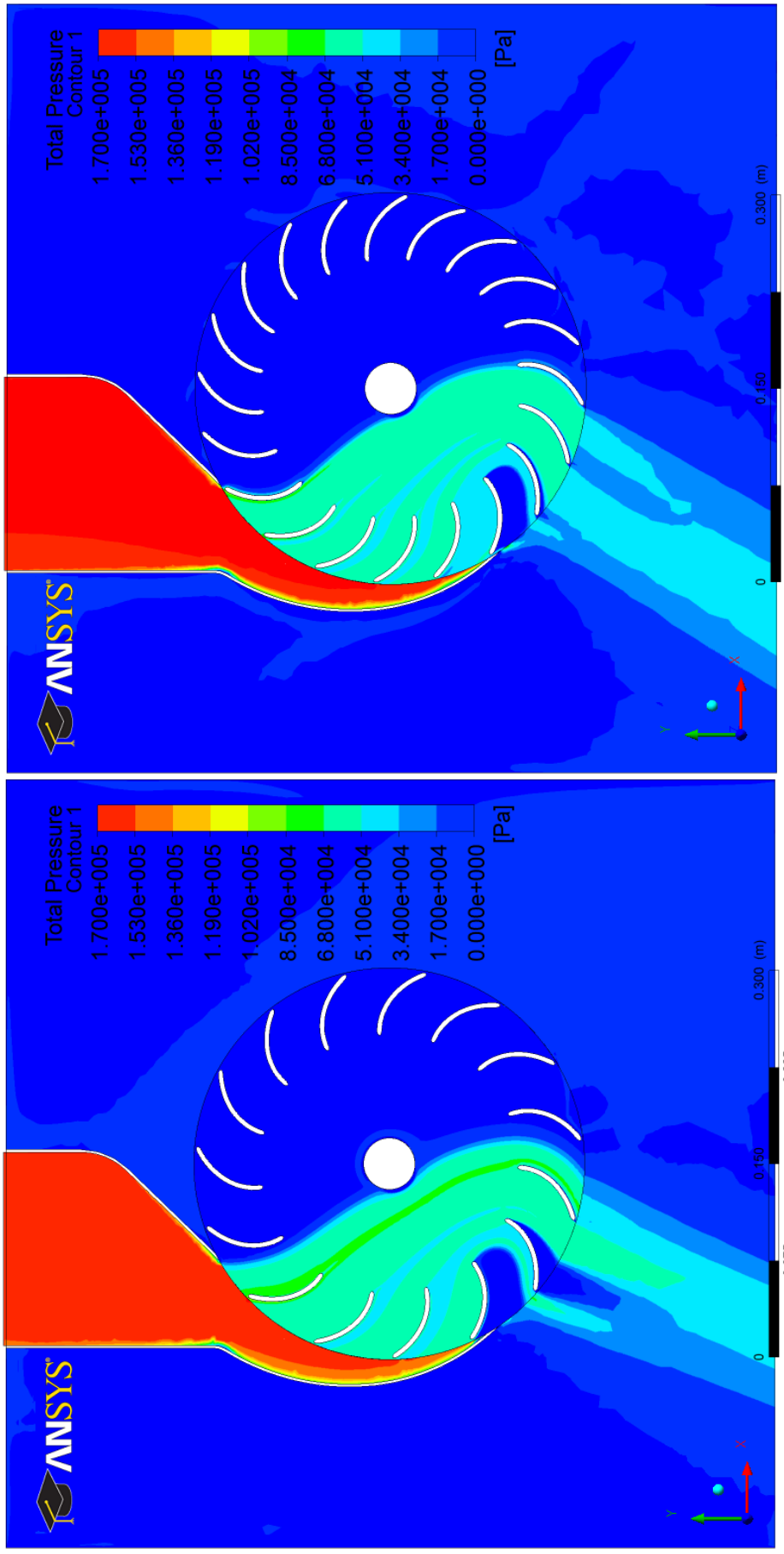

(a) 15-blade (b) 20-blade

Fig. B.1 (a) and (b) Total pressure contours at the mid span of cross-flow turbine for various number of runner's blades.

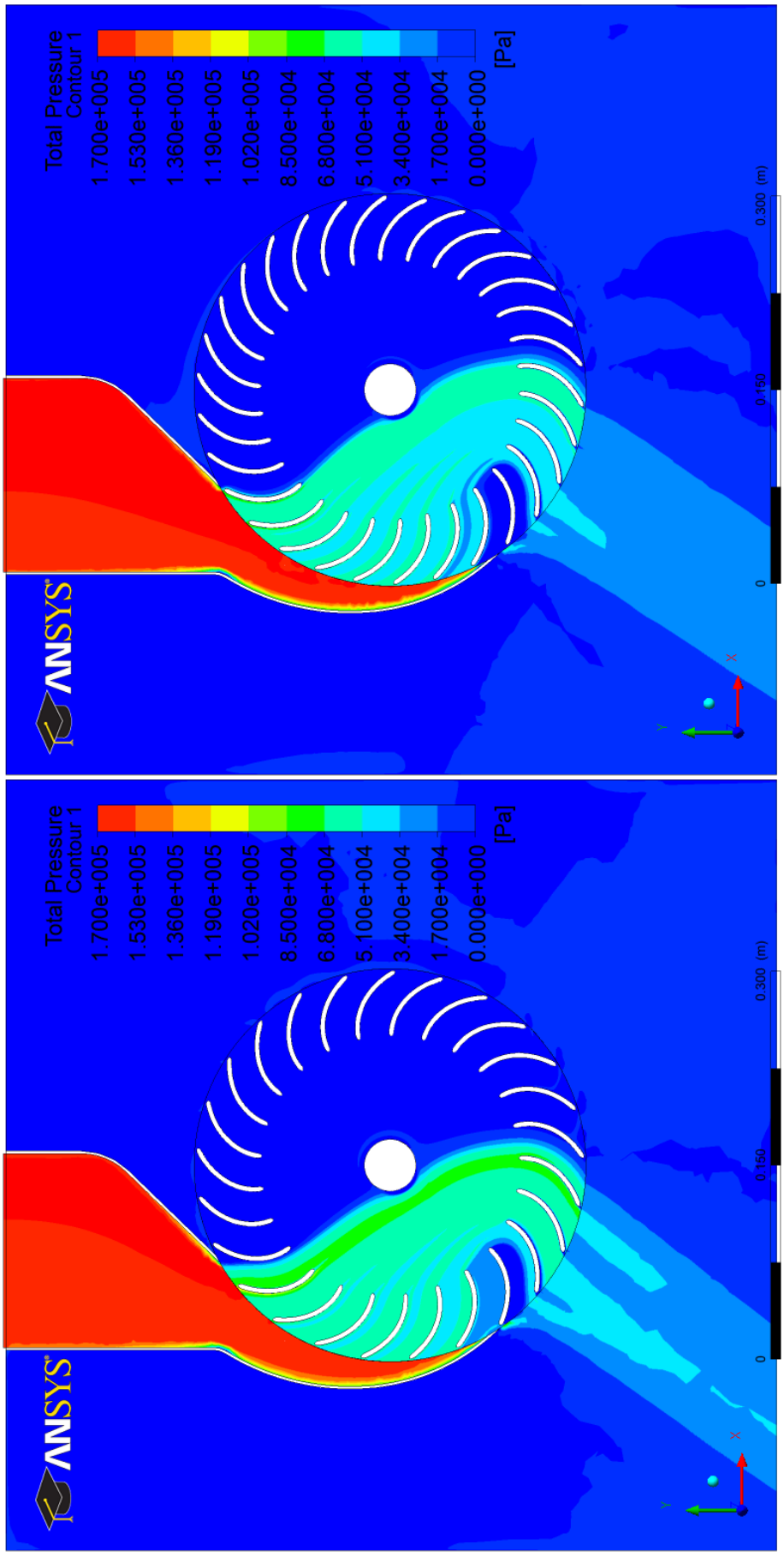

(c) 25-blade (d) 30-blade

Fig. B.1 (c) and (d) Total pressure contours at the mid span of cross-flow turbine for various number of runner's blades.

(e) 35-blade (f) 40-blade

Fig. B.1 (e) and (f) Total pressure contours at the mid span of cross-flow turbine for various number of runner's blades.

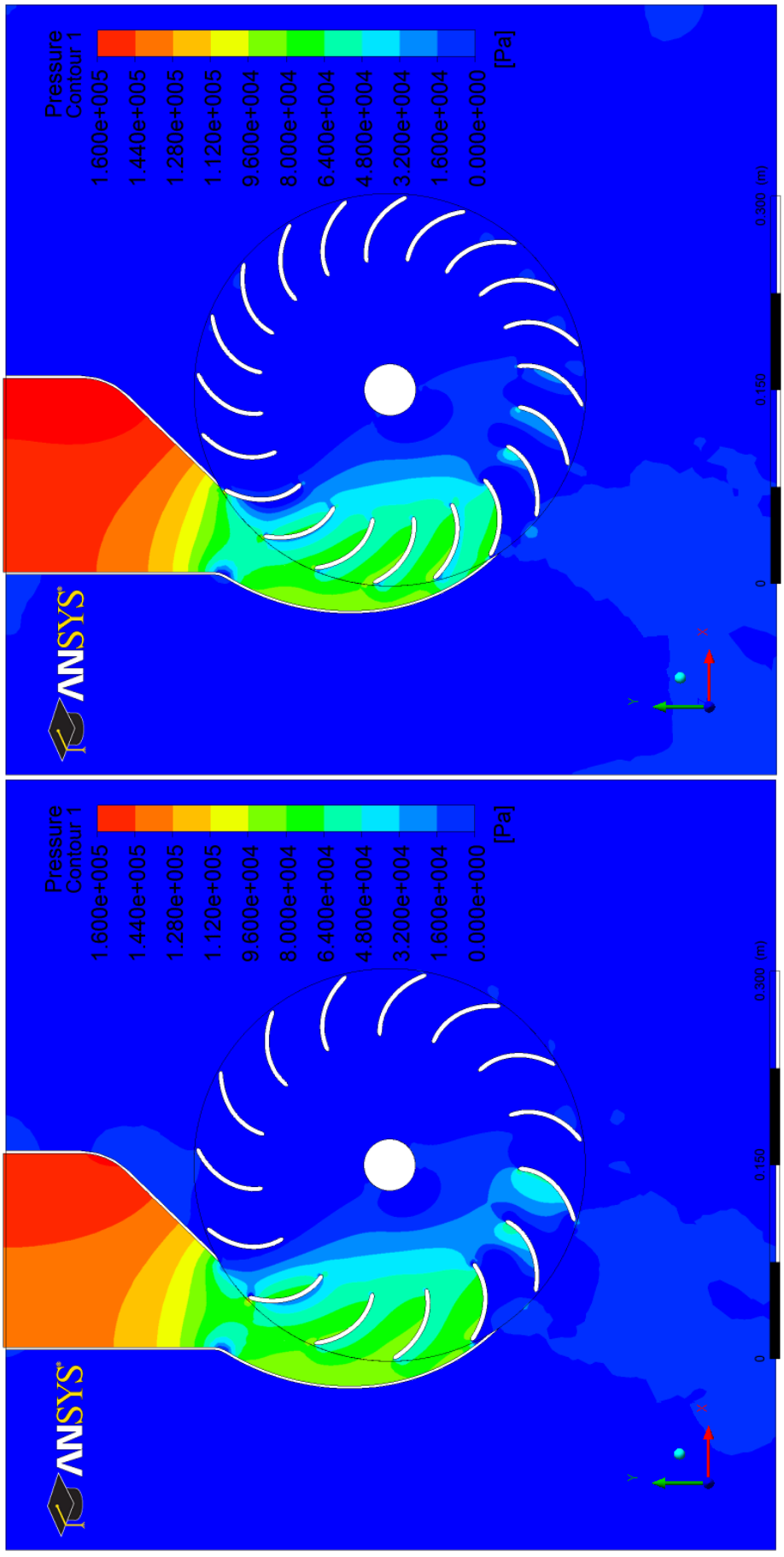

(a) 15-blade (b) 20-blade

Fig. B.2 (a) and (b) Pressure contours at the mid span of cross-flow turbine for various number of runner's blades.

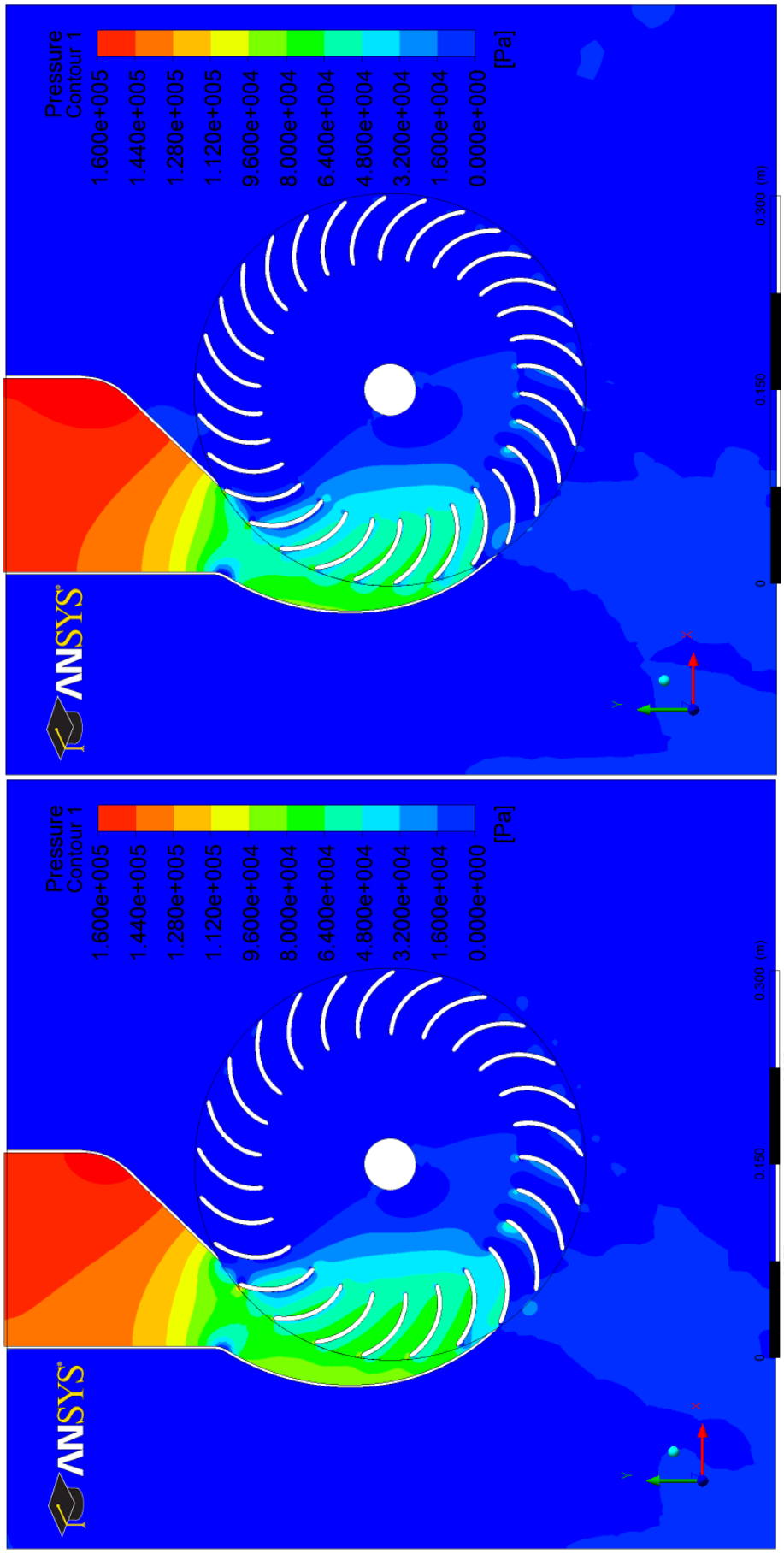

(c) 25-blade (d) 30-blade

Fig. B.2 (c) and (d) Pressure contours at the mid span of cross-flow turbine for various number of runner's blades

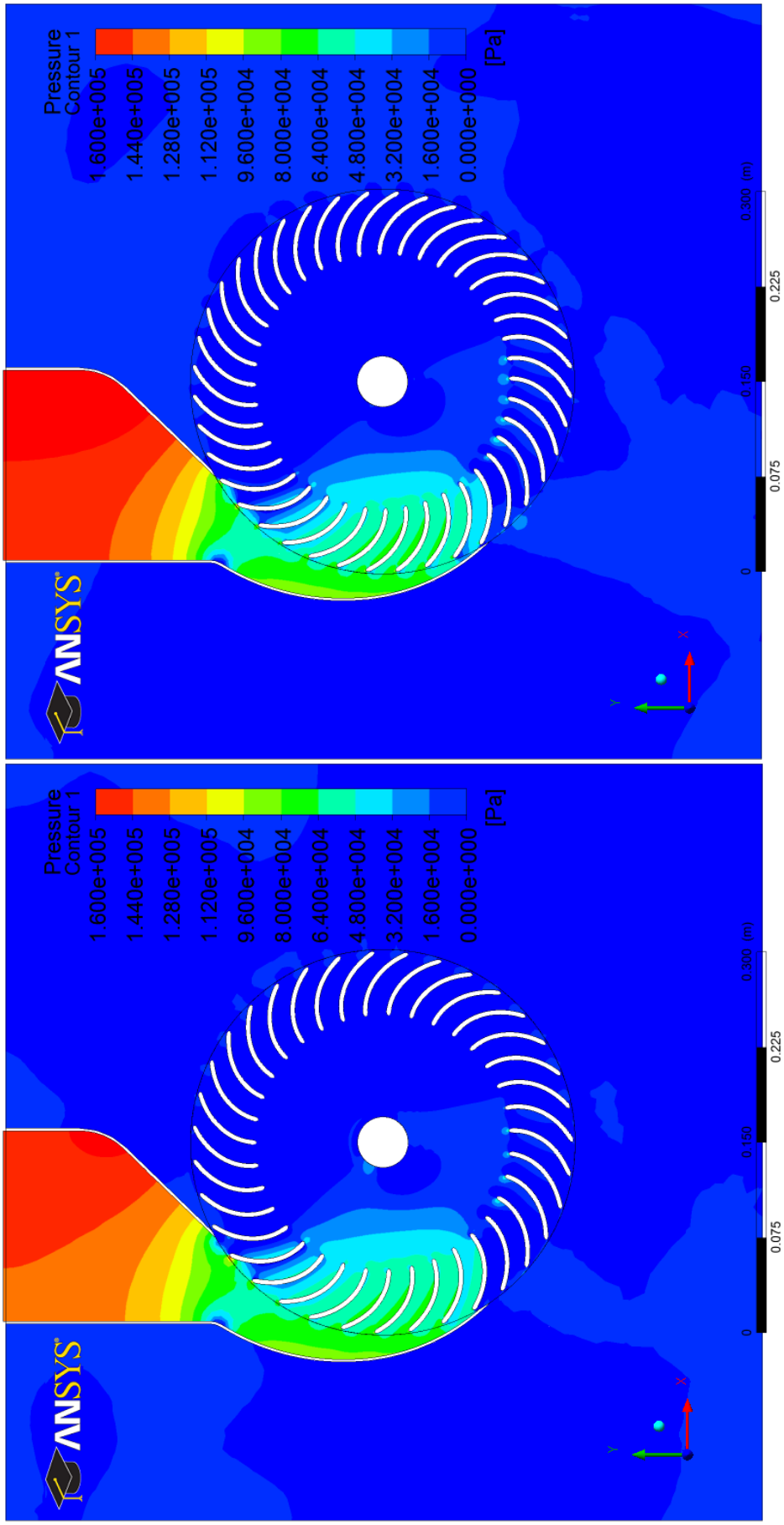

(e) 35-blade (f) 40-blade

Fig. B.2 (e) and (f) Pressure contours at the mid span of cross-flow turbine for various number of runner's blades.

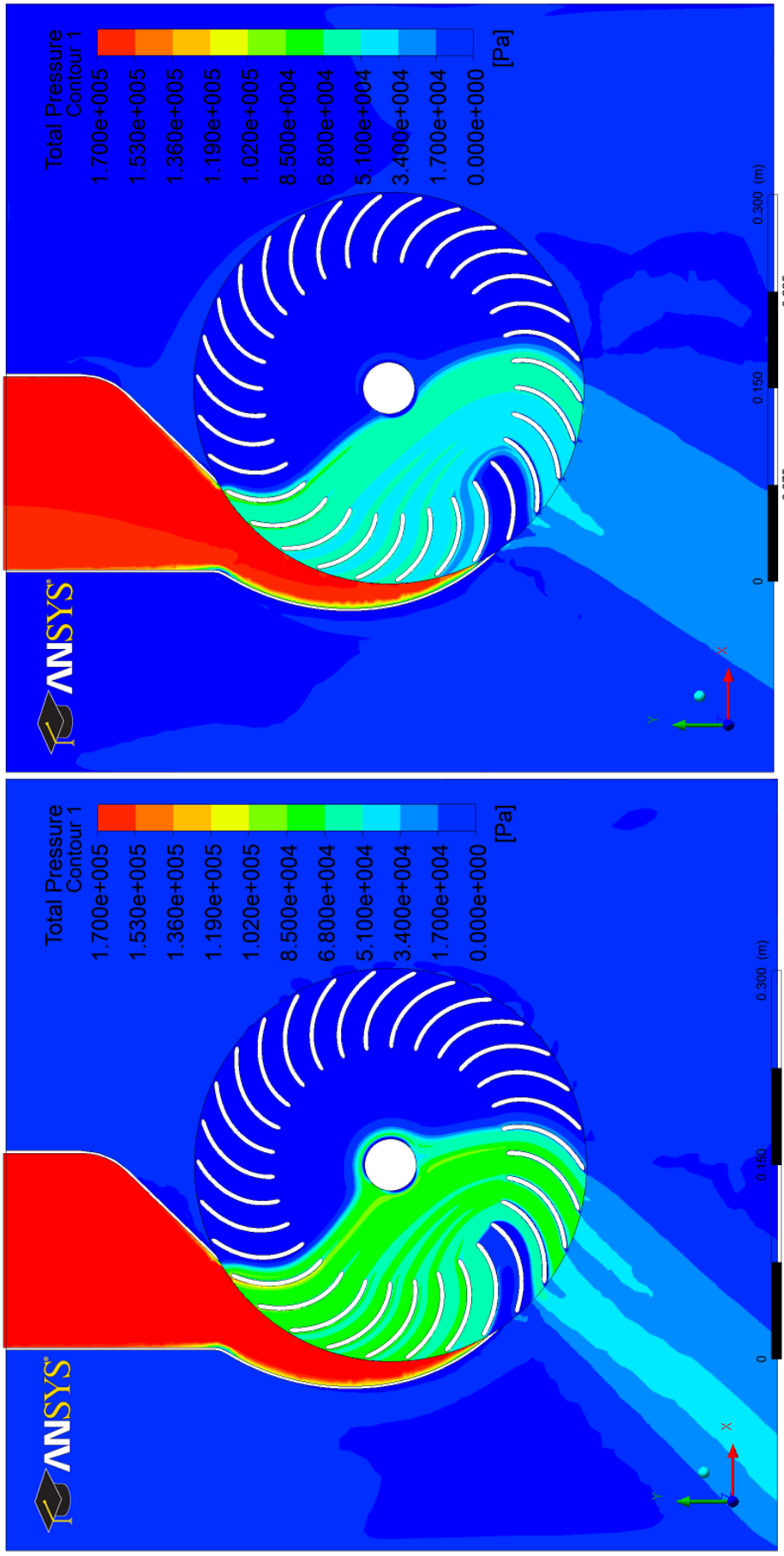

(a) $d_2/d_1 = 0.60$ (b) $d_2/d_1 = 0.65$

Fig. B.3 (a) and (b) Total pressure contours at the mid span of cross-flow turbine of various diameter ratios.

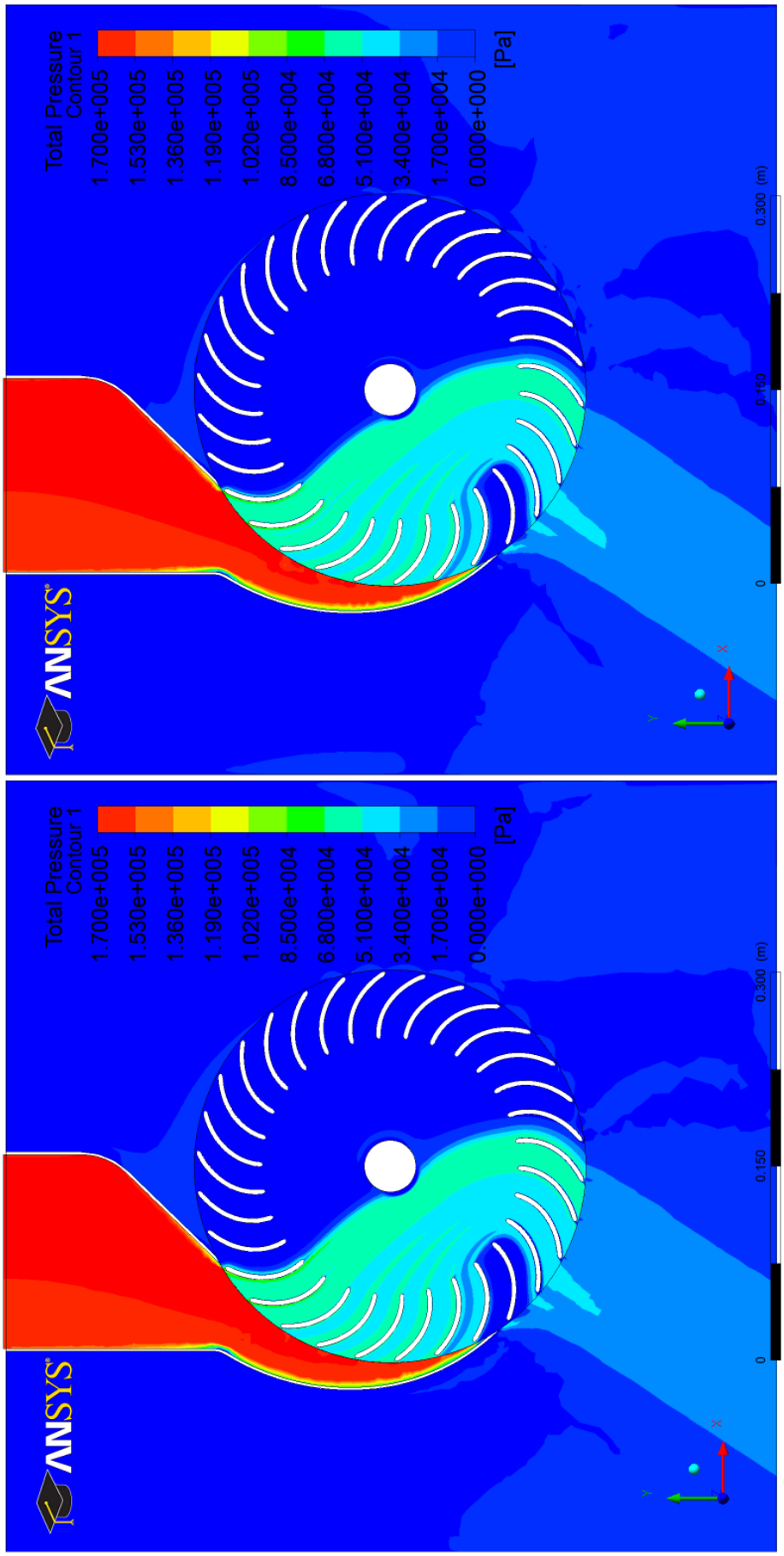

(c) $d_2/d_1 = 0.66$ (d) $d_2/d_1 = 0.67$

Fig. B.3 (c) and (d) Total pressure contours at the mid span of cross-flow turbine of various diameter ratios.

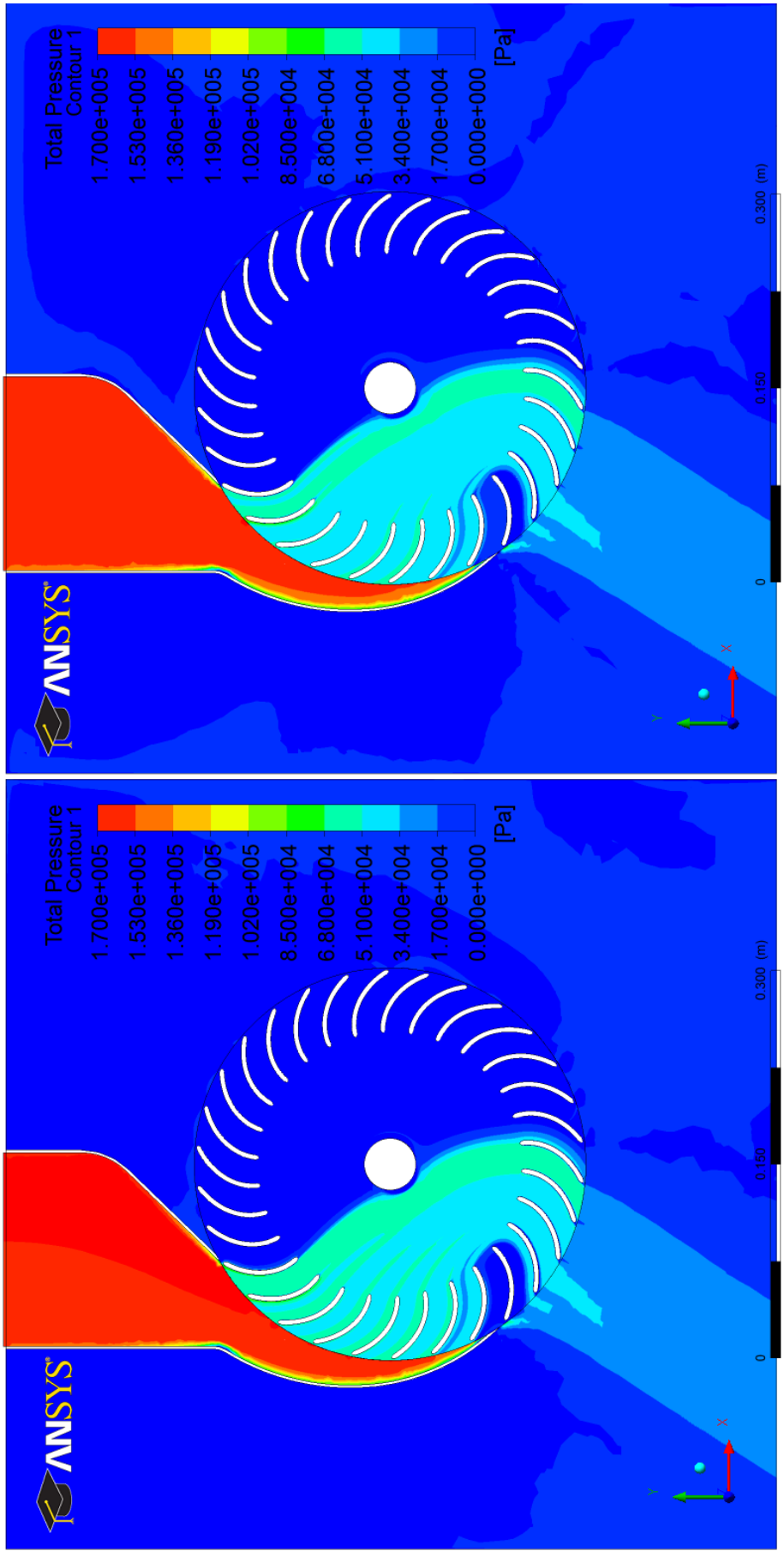

(e) $d_2/d_1 = 0.68$ (f) $d_2/d_1 = 0.70$

Fig. B.3 (e) and (f) Total pressure contours at the mid span of cross-flow turbine of various diameter ratios.

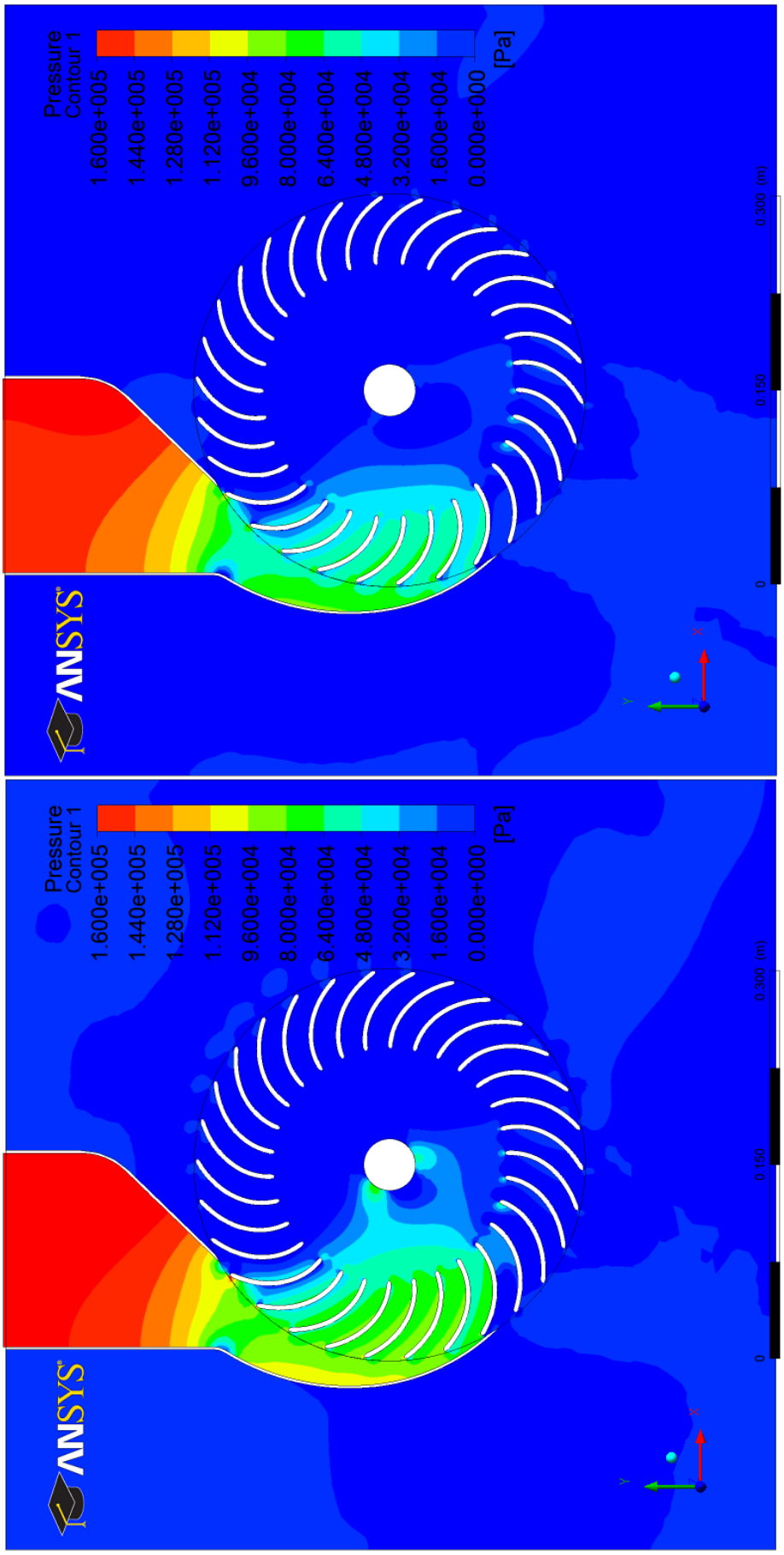

(a) $d_2/d_1 = 0.60$ (b) $d_2/d_1 = 0.65$

Fig. B.4 (a) and (b) Pressure contours at the mid span of cross-flow turbine of various diameter ratios.

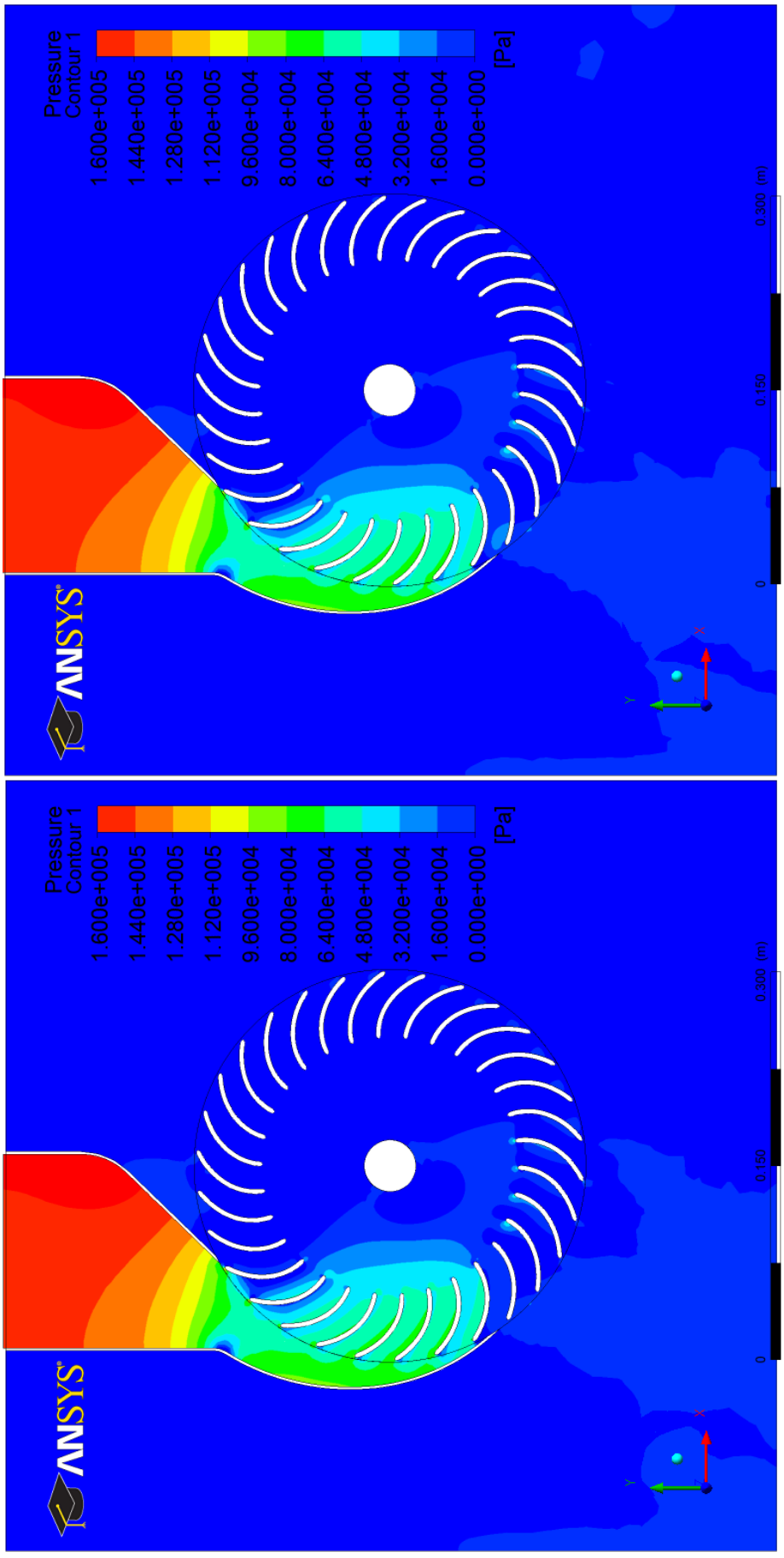

(c) $d_2/d_1 = 0.66$ (d) $d_2/d_1 = 0.67$

Fig. B.4 (c) and (d) Pressure contours at the mid span of cross-flow turbine of various diameter ratios.

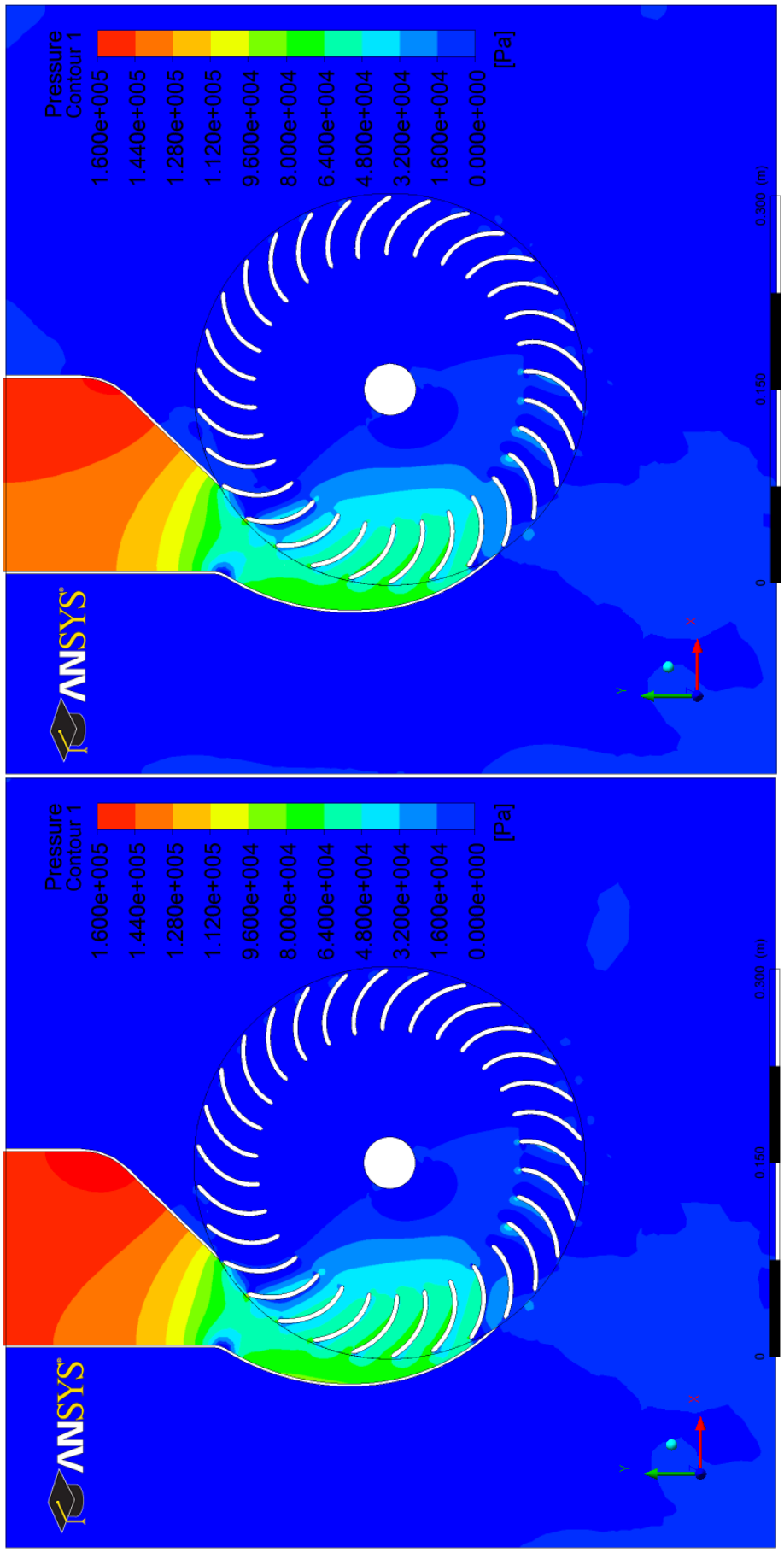

(e) $d_2/d_1 = 0.68$ (f) $d_2/d_1 = 0.70$

Fig. B.4 (e) and (f) Pressure contours at the mid span of cross-flow turbine of various diameter ratios.

(a) Angle of attack 15^{o} (b) Angle of attack 16^{o}

Fig. B.5 (a) and (b) Total pressure contours at the mid span of cross-flow turbine of various angles of attack.

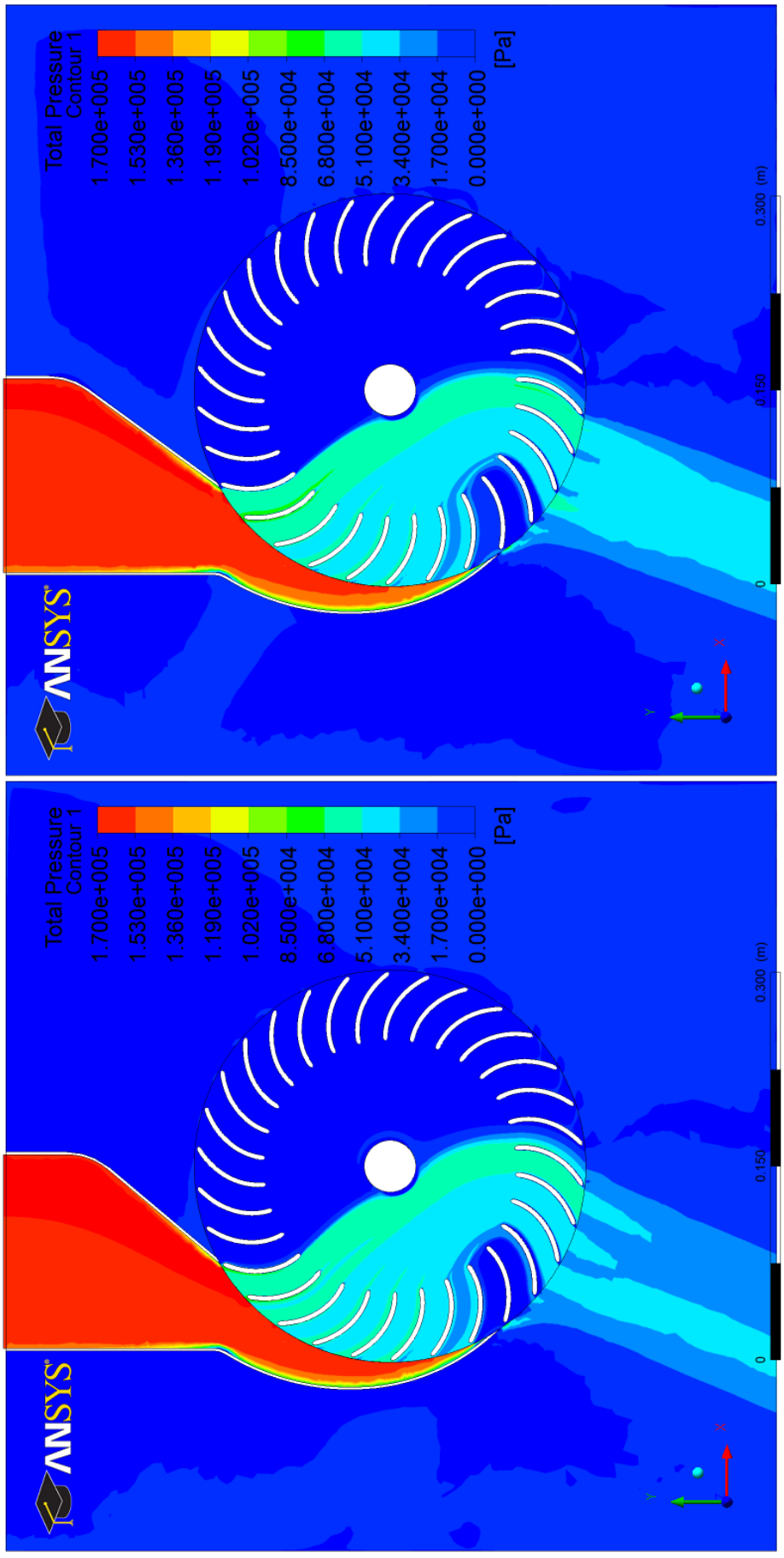

(c) Angle of attack 20°

(d) Angle of attack 24°

Fig. B.5 (c) and (d) Total pressure contours at the mid span of cross-flow turbine of various angles of attack.

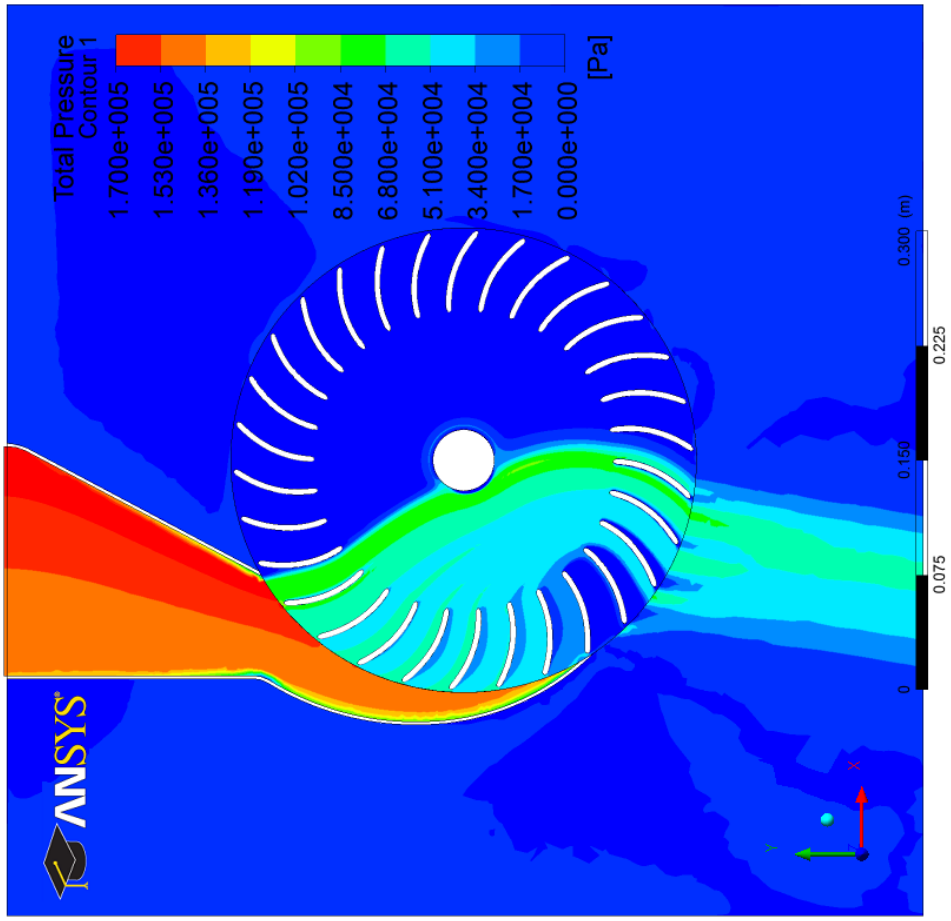

Fig. B.5 (e) Total pressure contours at the mid span of cross-flow turbine for nozzle angle of attack 32^{o}.

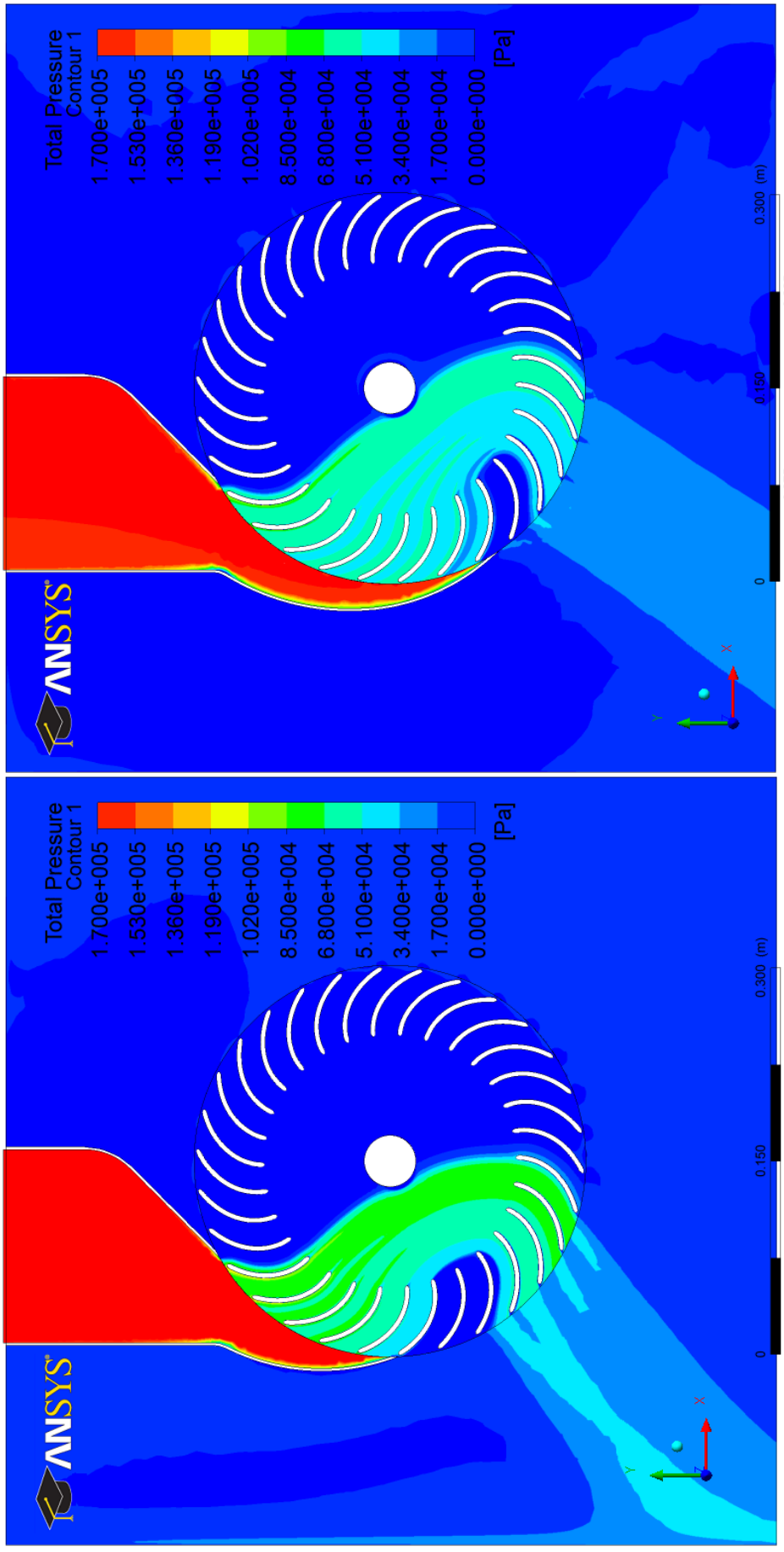

(a) Nozzle entry arc (60^o) (b) Nozzle entry arc 90^o (a)

Fig. B.6 (a) and (b) Total pressure contours at the mid span of cross-flow turbine of various nozzle entry arcs.

(c) Nozzle entry arc 90° (b) (d) Nozzle entry arc (120°)

Fig. B.6 (c) and (d) Total pressure contours at the mid span of cross-flow turbine of various nozzle entry arcs.

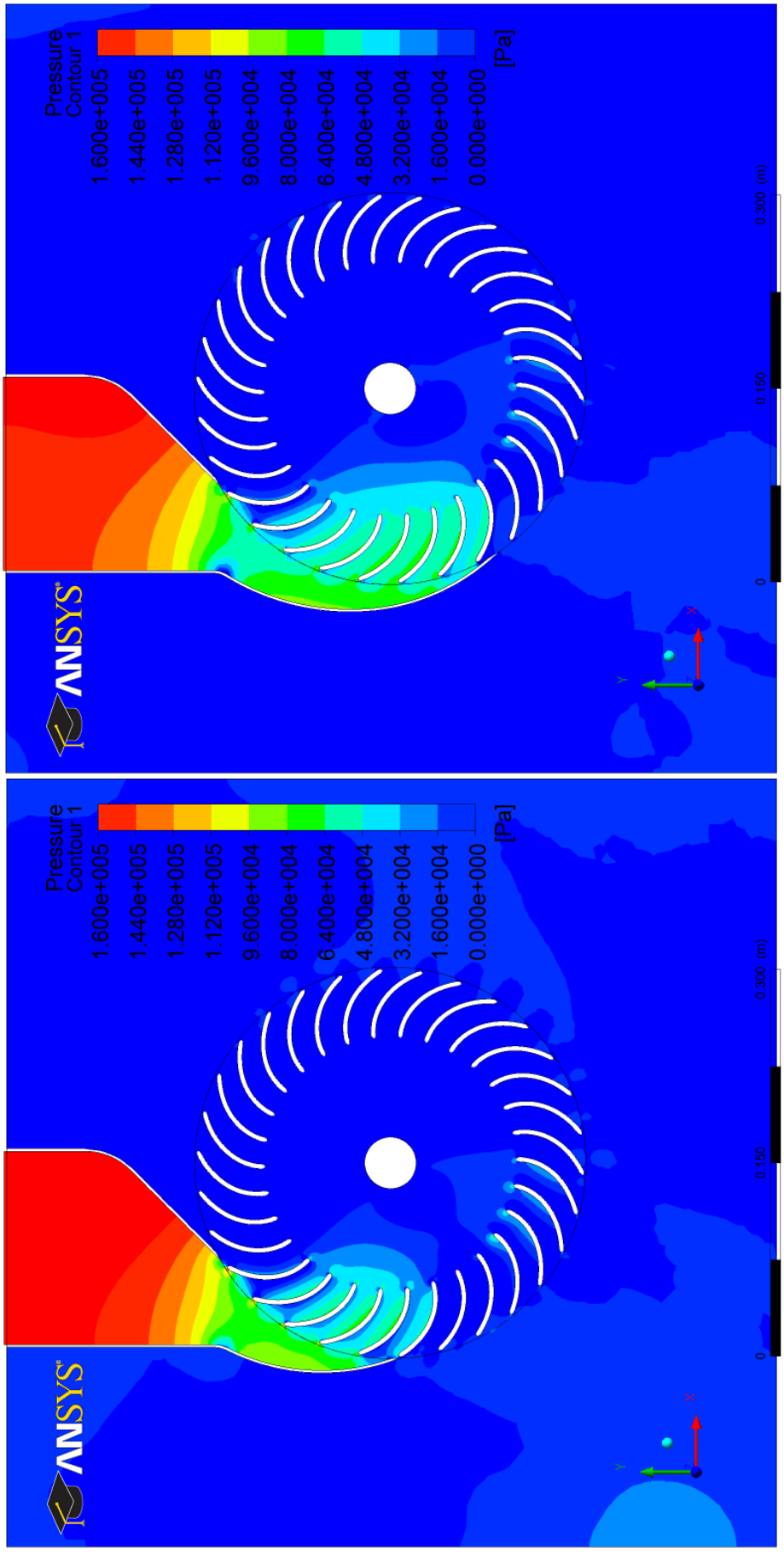

(a) Nozzle entry arc (60^o) (b) Nozzle entry arc 90^o (a)

Fig. B.7 (a) and (b) Pressure contours at the mid span of cross-flow turbine of various nozzle entry arcs.

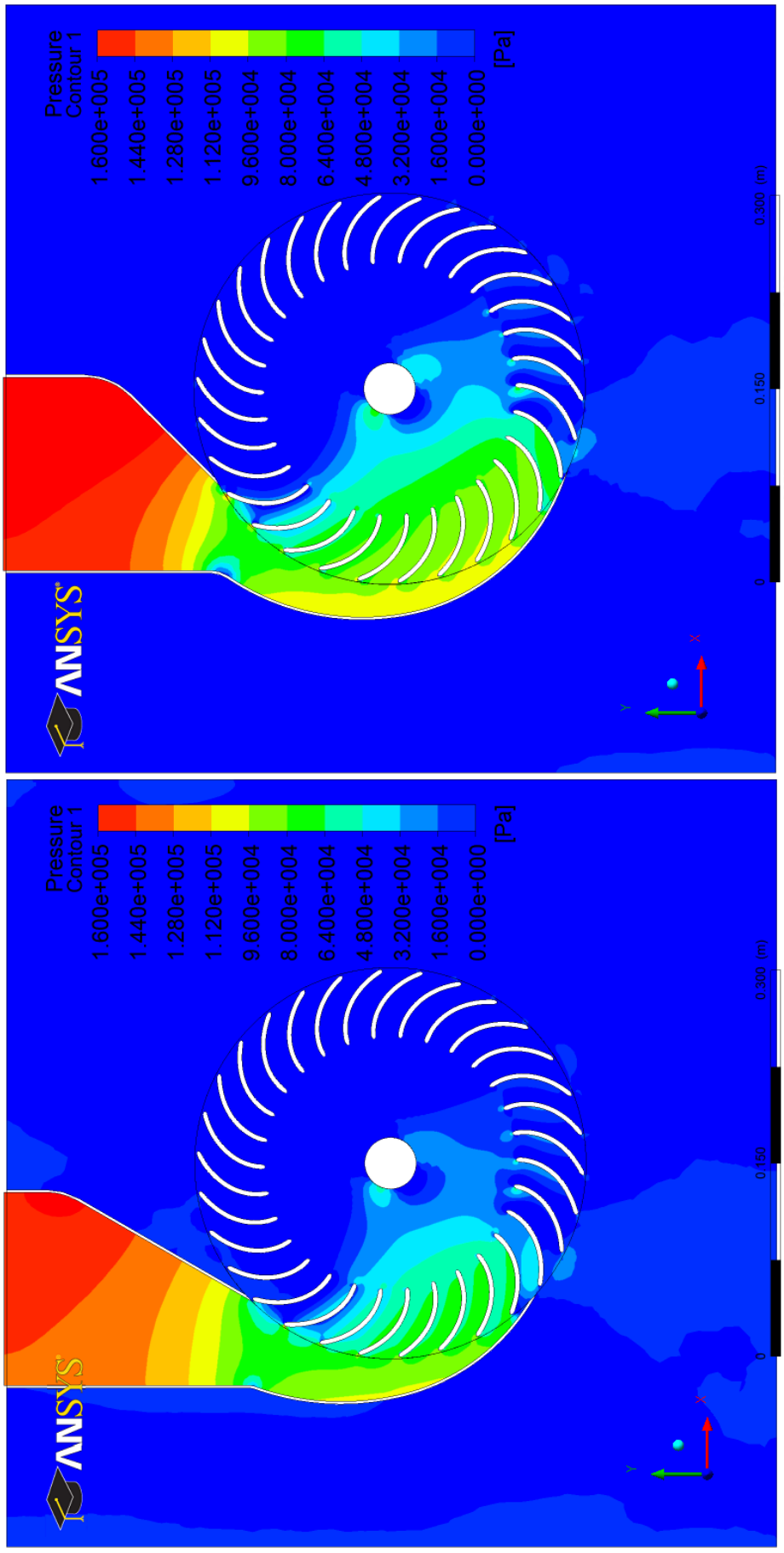

(c) Nozzle entry arc 90° (b) (d) Nozzle entry arc (120°)

Fig. B.7 (c) and (d) Pressure contours at the mid span of cross-flow turbine of various nozzle entry arcs.

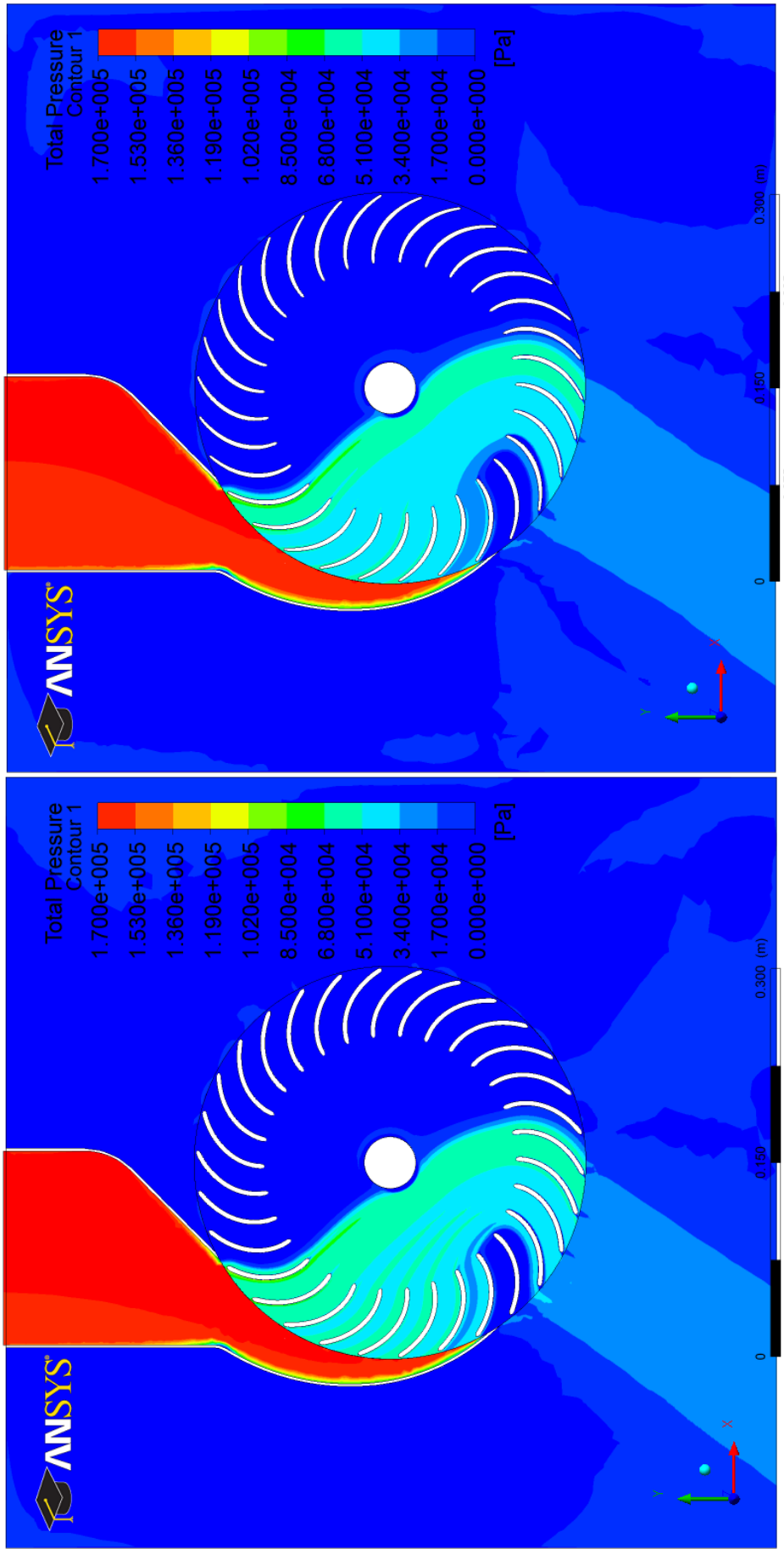

(a) Banki's profile (b) Blade profile (1)

Fig. B.8 (a) and (b) Total pressure contours at the mid span of cross-flow turbine of various blade profiles.

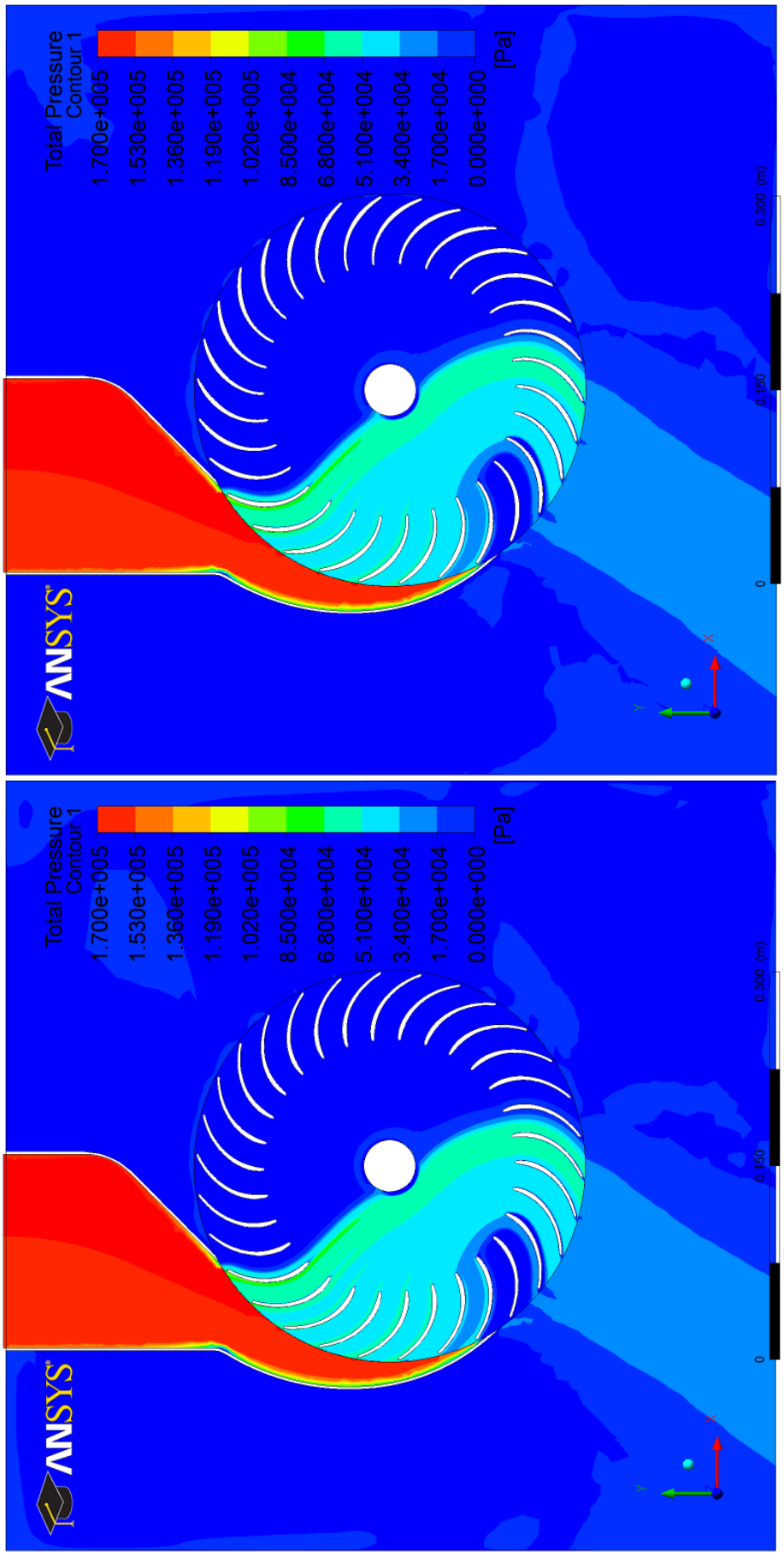

(c) Blade profile (2) (d) Blade profile (3)

Fig. B.8 (c) and (d) Total pressure contours at the mid span of cross-flow turbine of various blade profiles.

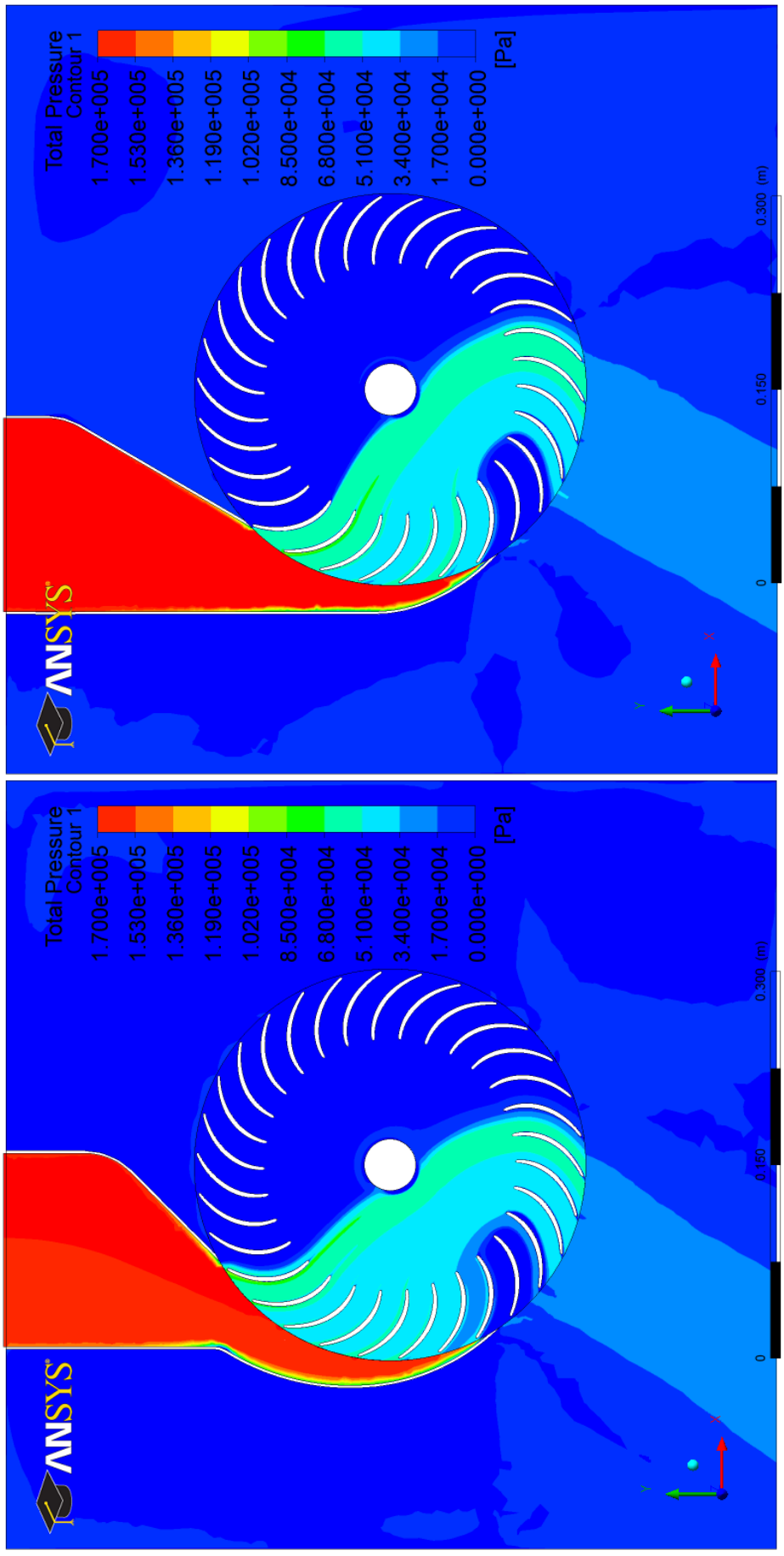

(a) Nozzle profile (1) (b) Nozzle profile (2)

Fig. B.9 (a) and (b) Total pressure contours at the mid span of cross-flow turbine of various nozzle profiles.

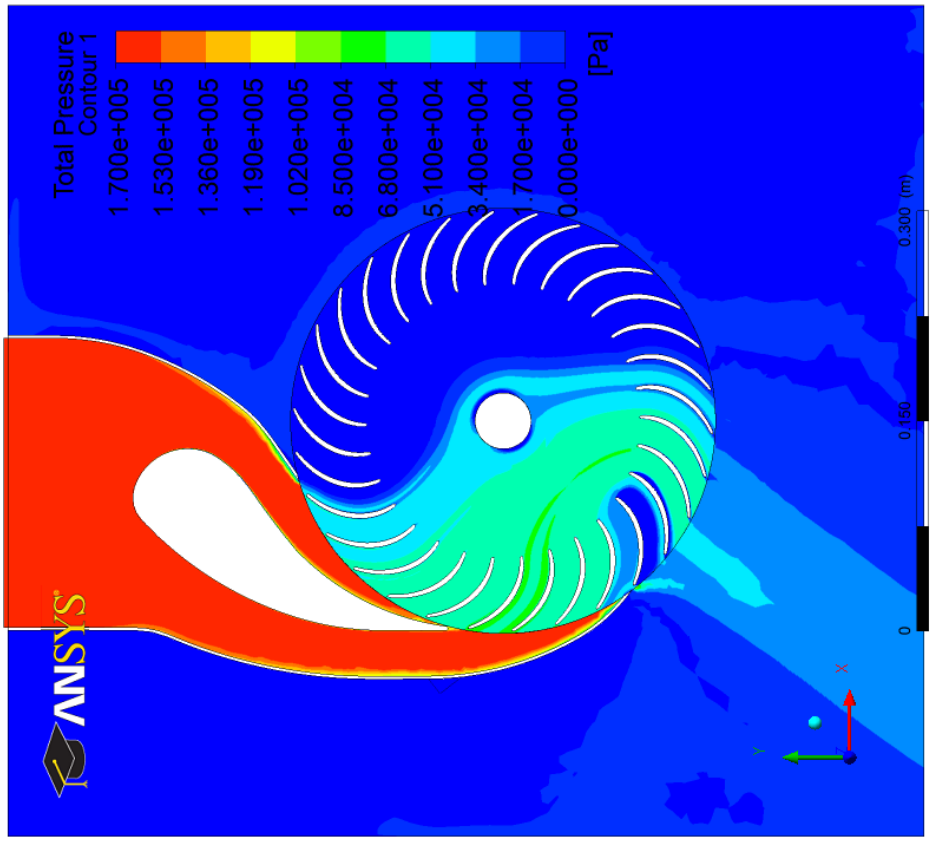

Fig. B.9 (c) Total pressure contours at the mid span of cross-flow turbine for nozzle profile (3).

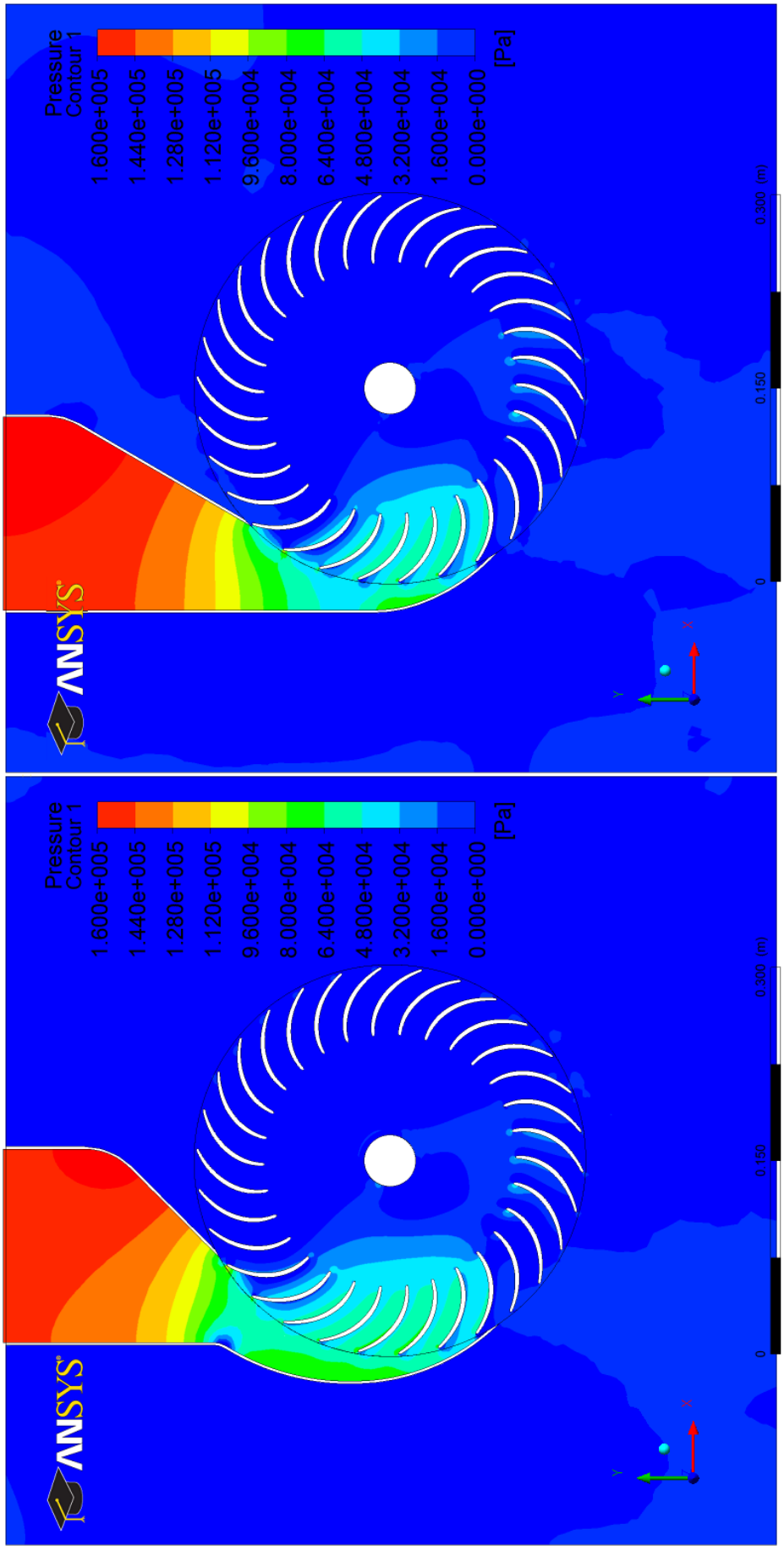

(a) Nozzle profile (1) (b) Nozzle profile (2)

Fig. B.10 (a) and (b) Pressure contours at the mid span of cross-flow turbine of various nozzle profiles.

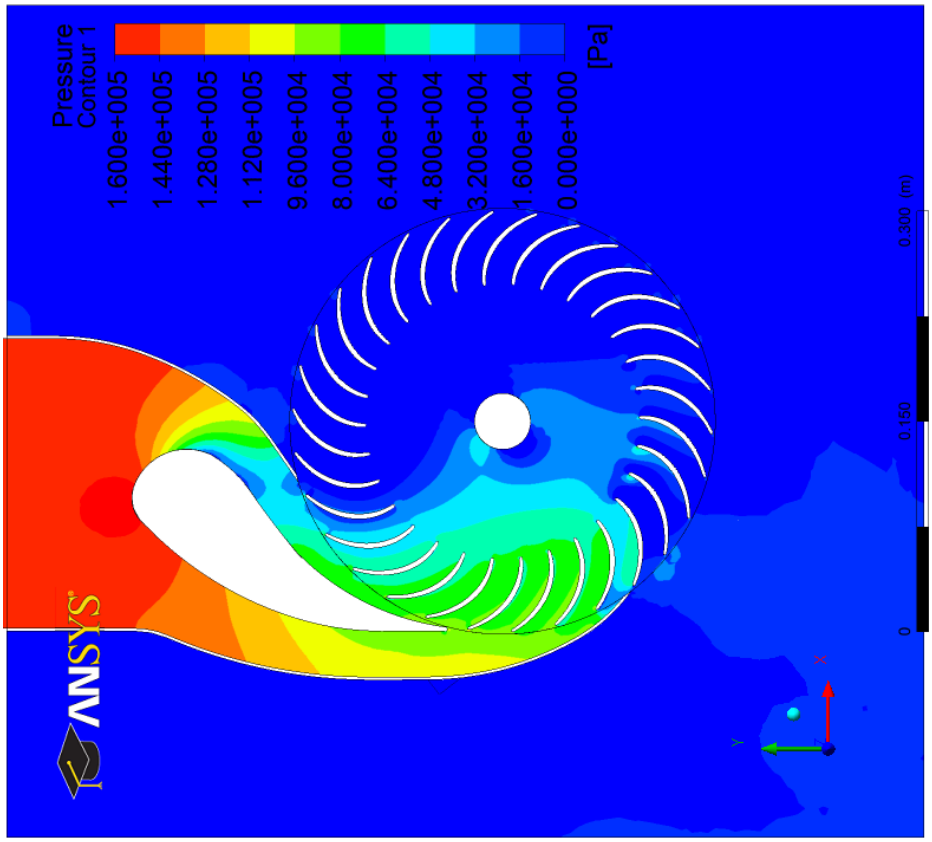

Fig. B.10 (c) Pressure contours at the mid span of cross-flow turbine for nozzle profile (3).

(a) Nozzle to runner blades width (N_w/B_w = 1) (b) Nozzle to runner blades width (N_w/B_w = 2/3)

Fig. B.11 (a) and (b) Pressure contours at the mid span of various nozzle to runner blades width ratios.

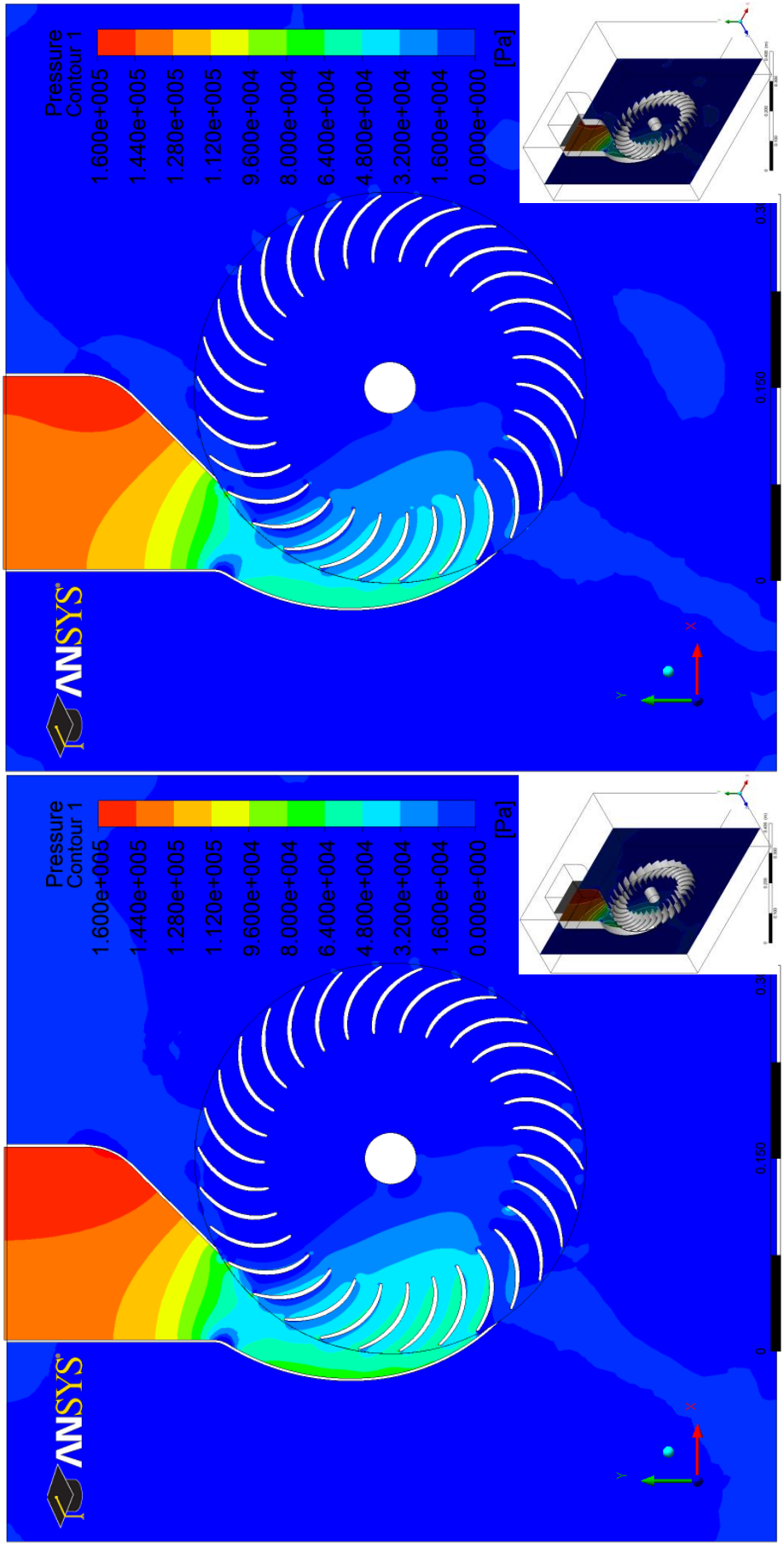

(c) Nozzle to runner blades width (N_w/B_w = 1/2) (d) Nozzle to runner blades width (N_w/B_w = 1/3)

Fig. B.11 (c) and (d) Pressure contours at the mid span of various nozzle to runner blades width ratios.

(a) Runner blades width to outer diameter ($B_w/d_1 = 1$) (b) Runner blades width to outer diameter ($B_w/d_1 = 2/3$)

Fig. B.12 (a) and (b) Total pressure contours at the mid span of cross-flow turbine of various runner blades width to outer diameter ratios.

(c) Runner blades width to outer diameter ($B_w/d_1 = 1/2$) (d) Runner blades width to outer diameter ($B_w/d_1 = 1/3$)

Fig. B.12 (c) and (d) Total pressure contours at the mid span of cross-flow turbine of various runner blades width to outer diameter ratios.

(a) Runner blades width to outer diameter ($B_w/d_1 = 1$) (b Runner blades width to outer diameter ($B_w/d_1 = 2/3$)

Fig. B.13 (a) and (b) Pressure contours at the mid span of cross-flow turbine of various runner blades width to outer diameter ratios.

(c) Runner blades width to outer diameter (B_w /d_1 = 1/2) (d) Runner blades width to outer diameter (B_w /d_1 = 1/3)

Fig. B.13 (c) and (d) Pressure contours at the mid span of cross-flow turbine of various runner blades width to outer diameter ratios.